THÈSE

Pour obtenir le grade de

DOCTEUR DE L'UNIVERSITE GRENOBLE ALPES

Spécialité : **Biologie Structurale et Nanobiologie**

Arrêté ministériel : 25 mai 2016

Présentée par

Waqas JAVED

Thèse dirigée par **Christine EBEL**,
et codirigée par **Jean-Michel JAULT**

préparée au sein du **Laboratoire Institut de Biologie Structurale et du Laboratoire Microbiologie Moléculaire et Biochimie Structurale** dans **l'École Doctorale Chimie et Sciences du Vivant**

Etude des états conformationnels d'un transporteur ABC bactérien de drogues multiples, BmrA

Study of the conformational states of a bacterial multidrug ABC transporter BmrA

Thèse soutenue publiquement le **17 décembre 2020**,
devant le jury composé de :

Madame Christine EBEL
DIRECTRICE DE RECHERCHE, CNRS Delegation Alpes, Directrice de thèse
Monsieur Jean-Michel JAULT
DIRECTEUR DE RECHERCHE, CNRS Delegation Rhone-Auvergne, Co-directeur de thèse
Madame Francesca GUBELLINI
CHARGEE DE RECHERCHE HDR, Institut Pasteur Paris, Rapportrice
Monsieur Guillaume LENOIR
MAITRE DE CONFERENCE HDR, Université Paris-Saclay, Rapporteur
Madame Cécile MORLOT
DIRECTRICE DE RECHERCHE, CNRS Delegation Alpes, Présidente
Monsieur Martial REY
CHARGE DE RECHERCHE, CNRS Delegation Ile-de-France Meudon, Examinateur

Acknowledgement

I am grateful to my family especially my parents, my father, my mother, my mother, and my mother. Their endless efforts, hardwork, countless prayers and relentless support made everything possible. I am greatly indebted to my wife Mehwish, and without her support this work could not have been completed. Thank you Mehwish for always being there for me and managing everything very well whenever I needed to work some extra hours at the lab. I would like to thank my son for being very cooperative all this time and always providing me with the energy boost. I am also grateful to my brother and sister for their encouragement and support and for all the things they taught me. I also thank my mother-in-law for being there for us whenever we needed her support.

I am greatly indebted to Dr. Jean-Michel Jault for providing me with the opportunity for Master leading to PhD at his lab and for all his sincere guidance. I really appreciate his dedicated efforts in reviewing my manuscript in the shortest possible time. My sincere gratitude also goes to Mme. Marie-Pierre Candusso and Dr. Cedric Orelle for enlightening me with the knowledge and skills of research and to be there for me whenever I needed help. Both Cedric and Marie-Pierre never hesitated in even going out of the way to solve all my administrative problems and for always providing the helping hand.

I would also like to thank Dr. Christine Ebel for all her contributions and guidance and her friendly nature. I am thankful to Dr. Anne Martel for all her contributions, and both Christine and Anne for all their efforts that led to my PhD extension. Without their help all this work would not have been possible. My gratitude also goes to Dr. Julien Marcoux who trained me well on HDX and never stopped me from trying new things to improve the sequence coverage. Thank you, Julien, for letting me kill your innocent pepsin columns.

I would like to acknowledge the helping and joyful nature of all my old lab colleagues. The friendly nature of Charlene, Sylvain and Khadija made my work in the lab enjoyable. I am also thankful for all the things I learnt from them.

I am thankful to all my current lab colleagues for making my time at the lab enjoyable. To Matty, Margot and Benjamin for their friendly and helping nature. To Kerstin for the carrot cake and to Agathe and Cecile for their kind and friendly nature.

Margot also contributed to the work in this project. Thank you, Margot, for the productive time we spent in Toulouse and for all the untiring efforts that led to so many interesting results.

Last but not the least, I would like to express my sincere gratitude to everyone who contributed to this manuscript, to the Higher Education Commission (HEC) of Pakistan for providing me with a Master leading to PhD fellowship, to ILL for providing the funds for the 4th year PhD extension.

Thank you everyone for making this moment possible for me!

Table of Contents

List of Figures

List of Tables

List of Annex

List of Abbreviations

ABC: ATP-binding cassette

ADP: Adenosine diphosphate

a.k.a: Also known as

APS: Ammonium persulfate

ATP: Adenosine triphosphate

BCA: Bicinchoninic acid assay

BmrA: *Bacillus* multidrug resistance ATP

BSA: Bovine serum albumin

°C: Degree celsius

CFTR: Cystic fibrosis transmembrane conductance regulator

DDM: n-dodecyl β-D-maltoside

DTT: Dithiothreitol

EDTA: Ethylene diamine tetra acetic acid

ESI-MS: Electrospray ionization mass spectrometry

h: hour

Hepes: 4-(2-hydroxyethyl)-1-piperazineethanesulfonic acid

HDX-MS: Hydrogen Deuterium exchange coupled to mass spectrometry

HIV: Human immunodeficiency viruses

Hoechst: (2′-(4-ethoxyphenyl)-5-(4-methyl-1-piperazinyl)-2,5′-bis-1H-benzimidazole

HPLC: High performance liquid chromatography

ICD: Intracellular domain

ICH: Intracellular helix

ICL: Intracellular loop

IF: Inward-facing

IMVs: Inverted membrane vesicles

IMP: Inner membrane protein

IPTG: Isopropyl-beta-thio-galactoside

kDa: Kilo Dalton

KOH: Potassium hydroxide

L: Liter

LB: Luria-Bertani

LMNG: Lauryl maltose neopentyl glycol

LmrA: *Lactococcus lactis* multi drug resistance ATP

LmrP: *Lactococcus lactis* multi drug resistance protein

LPS: Lipopolysaccharide

MDR: Multi drug resistance

MFP: Membrane fusion protein

min: Minute

MS: Mass spectrometer

MSP: Membrane scaffold protein

MW: Molecular weight

NBD: Nucleotide-binding domain

NBS: Nucleotide-binding site

OG: Octyl glucoside

OD: Optical density

OF: Outward-facing

OMP: Outer membrane protein

PEP: Phosphoenol pyruvate

P-gp: P-glycoprotein

Pi: Inorganic phosphate

PK: Pyruvate kinase

p(r): Distance distribution function

psi: Pounds per square inch

R_g: Radius of gyration

rpm: Revolutions per minute

s: second

SANS: Small angle neutron scattering

SAS: Small angle scattering

SBP: Substrate-binding protein

SDS-PAGE: Sodium dodecyl sulphate-poly acrylamide gel electrophoresis

SEC: Size exclusion chromatography

SLD: Scattering length density

SUR: sulfonyl urea receptor

TEMED: *N*,*N*,*N*′,*N*′-Tetramethylethane-1,2- diamine

TFA: Trifluoroacetic acid

TM: Transmembrane

TM287/288: Thermotoga maritima 287/288

TMD: Transmembrane domain

TMH: Transmembrane helix

TMS: Transmembrane segment

TNP-ATP: 2,4,6 trinitrophenol-adenosine triphosphate

TPP: Tetraphenylphosphonium

Tris-HCl: Tris (hydroxymethyl) aminomethane-hydrochloric acid

UPLC: Ultra performance liquid chromatography

Vi: Vanadate

WT: Wild type

2×YT: Yeast extract tryptone

Abstract

Antibiotic resistance is not the story of the future but a reality today. Bacterial resistance to antibiotics can be conferred by several mechanisms, including the overexpression of dedicated efflux pumps, some of them belonging to the ABC ("ATP-Binding Cassette") transporters superfamily. ABC transporters are ubiquitous proteins that use ATP hydrolysis to pump a wide range of substrates. They are also responsible for the development of MDR ("MultiDrug Resistance") phenotypes in cancer cells and pathogenic microorganisms.

The bacterial ABC exporter BmrA ("Bacillus multidrug resistance ATP"), is structurally and functionally close to ABCB1, a human transporter involved in MDR phenotypes in cancer cells. Together with extensive knowledge in its overexpression and purification, BmrA is a useful archetypical transporter to gain information on the functioning of multidrug ABC transporters. Our goal is to decipher the conformational changes associated with drug transport.

We showed that BmrA exists in at least two different conformations, in detergent micelles or when reconstituted in nanodiscs. In the absence of ligand (apo form), BmrA gets quickly exchanged with deuterium as shown by Hydrogen Deuterium Exchange Coupled to Mass Spectrometry (HDX-MS). The vanadate-induced ADP trapped form shows a large overall protection against deuterium incorporation. Moreover, it was observed that BmrA in nanodiscs shows a different deuteration profile in the presence of drug, indicative of a new intermediate conformation. In addition, using two different catalytic mutants of BmrA, that are trapped in two opposite conformations of the catalytic cycle, it was shown how BmrA changes conformations during the drug export cycle. The results obtained from Small Angle Neutron Scattering (SANS), on WT BmrA and the mutants, paint a similar picture and strengthen the results obtained on the catalytic cycle of BmrA. Moreover, an arginine rich network was revealed that is potentially involved in NBD-TMD communication in BmrA.

These results could potentially lead to a better understanding of the structural basis of MDR.

Résumé

La résistance aux antibiotiques est une réalité à laquelle nous devons faire face. La résistance bactérienne aux antibiotiques peut être conférée par plusieurs mécanismes, dont la surexpression de pompes à efflux, certaines appartenant à la superfamille des transporteurs ABC (“ATP-binding cassette”). Les transporteurs ABC sont des protéines omniprésentes qui utilisent l'hydrolyse de l'ATP pour pomper une large gamme de substrats. Ils sont également responsables du développement des phénotypes de résistance à de multiple drogues dans les cellules cancéreuses et les microorganismes pathogènes.

L'exportateur bactérien ABC BmrA (“Bacillus multidrug resistance ATP”), est homologue à ABCB1, un transporteur humain impliqué dans les phénotypes de résistance dans les cellules cancéreuses. Avec une connaissance approfondie de sa surexpression et de sa purification, BmrA est un archétype utile pour obtenir des informations sur le fonctionnement des transporteurs ABC de multiples drogues. Notre objectif est de déchiffrer les changements conformationnels associés au transport des médicaments.

Nous avons montré que BmrA existe dans au moins deux conformations différentes, dans des micelles de détergent ou reconstitué dans des nanodisques. En l'absence de ligand (forme apo), différentes partie de BmrA fixe rapidement du deutérium comme le montre l'échange hydrogène deutérium couplé à la spectrométrie de masse (HDX-MS). La forme piégée par l'ADP induite par le vanadate montre une grande protection globale contre l'incorporation de deutérium. De plus, il a été observé que BmrA dans les nanodisques présente un profil de deutération différent en présence de médicament, indicatif d'une nouvelle conformation intermédiaire. De plus, en utilisant deux mutants affectés dans différentes étapes du cycle catalytique, il a été montré comment BmrA change de conformations au cours du cycle d'export des médicaments. Les résultats obtenus à partir de la diffusion de neutrons aux petits angles (SANS), brossent un tableau similaire et renforcent les résultats obtenus sur le cycle catalytique de BmrA. De plus, un réseau riche en arginine a été découvert qui est potentiellement impliqué dans la communication NBD-TMD dans BmrA.

Ces résultats conduisent à une meilleure compréhension des changements de conformation de BmrA qui s’opèrent pour permettre le phénotype de résistance aux médicaments.

Literature Review

Chapter 1: Antimicrobial Resistance

The WHO ("World Health Organization") defines antimicrobial resistance as the change in microorganisms (bacteria, fungi, viruses, and parasites) when they are exposed to antimicrobial drugs (such as antibiotics, antifungals, antivirals, antimalarials, and anthelmintics). As a result, they become resistant to the drug therapy and may persist as 'super bugs' (https://www.who.int/news-room/fact-sheets/detail/antimicrobial-resistance).

Urgent Threats
• Carbapenem-resistant *Acinetobacter*
• *Candida auris*
• *Clostriodioides difficile*
• Carbapenem-resistant *Enterobacteriaceae*
• Drug-resistant *Neisseria gonorrhoeae*
Serious Threats
• Drug-resistant *Campylobacter*
• Drug-resistant *Candida*
• Extended-spectrum beta-lactamases (ESBL) producing *Enterobacteriaceae*
• Vancomycin-resistant *Enterococci*
• Multidrug-resistant *Pseudomonas aeruginosa*
• Drug-resistant nontyphoidal *Salmonella*
• Drug-resistant *Salmonella* serotype Typhi
• Drug-resistant *Shigella*
• Methicillin-resistant *Staphylococcus aureus*
• Drug-resistant *Streptococcus pneumoniae*
• Drug-resistant *Mycobacterium tuberculosis*
Concerning Threats
• Erythromycin-resistant group A *Streptococcus*
• Clindamycin-resistant group B *Streptococcus*
Watch List
• Azole-resistant *Aspergillus fumigatus*
• Drug-resistant *Mycoplasma genitalium*
• Drug-resistant *Bordetella pertussis*

Table 1. List of antibiotic-resistant bacteria and fungi classified according to the risk of causing serious infections (O'Neill, 2016).

In 2019 the Centre for Disease Control & Prevention (CDC) in the United States, published a report that apprises about the drug-resistant microorganisms and the risk to the public health posed by them (table 1) (CDC, 2019). According to this report there are more than 2.8 million annual cases of antibiotic resistance in USA alone with more than 35 thousand of them leading to death. This grim picture is not limited to the USA but could be applied to all the countries of the world. In fact, the review on antimicrobial resistance published in 2016 (O'Neill, 2016) predicts that there could be more than 10 million annual deaths worldwide if the menace of antimicrobial resistance is not tackled efficiently.

Multidrug resistance (MDR)

The phenomenon of MDR arises when pathogenic microorganisms become resistant to several classes of antimicrobial drugs leading to the failure of drug therapy, and as a result, more complex, expensive and side effect prone drug therapies are required which might have limited efficacy. Another aspect of MDR related to human health concerns chemotherapy against cancers. Cancer cells can also show MDR phenotypes resulting in the failure of chemotherapy against cancer (Assaraf et al., 2019). With reference to human health, the implications of MDR are hence, twofold. First in case of infection from MDR pathogenic microorganisms and secondly, in case of cancer from MDR cancer cells.

Antimicrobial resistance in Bacteria

Antibiotics are drugs that are used to treat infection caused by bacteria or fungi. They target one or more of the several vital processes required for bacterial survival or growth. Annex 1 lists most of the major classes of antibiotics, their mode of action and resistance mechanisms. Antibiotics can be further divided into two categories based on their ability to either inhibit the

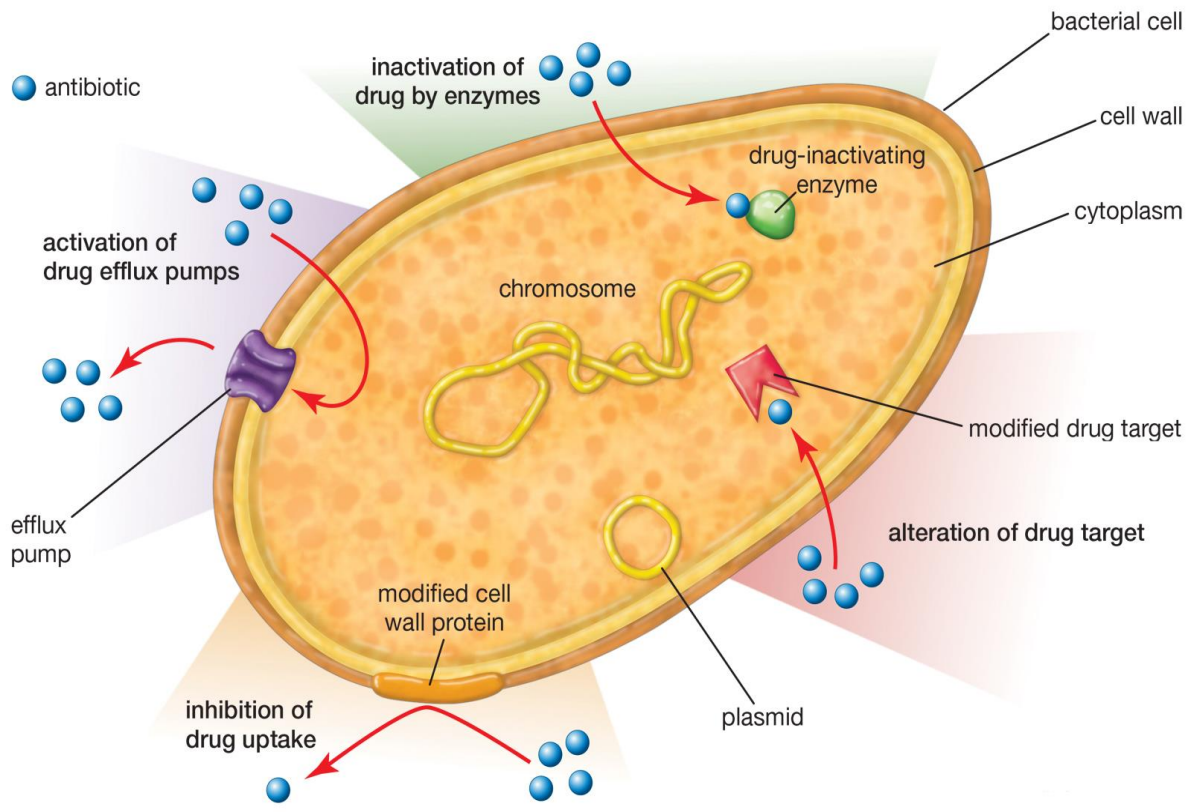

Fig 1. Antibiotic resistance mechanisms in bacteria (Encyclopædia-Britannica©, 2012).

growth of bacterial cells, known as bacteriostatic, or to kill bacteria, hence bactericidal. Bacteria, on the other hand, possess the ability to develop several mechanisms to counteract the lethal effects of these therapeutic agents. These include, 1) reduced therapeutically active drug concentrations inside the cells by, a) drug-inactivation/modification or, b) limiting drug access, 2) drug-target modification (fig. 1). A timeline for the identification of the drug-resistant strain of bacteria or fungi against several classes of antibiotics is provided in annex 2.

1. Drug inactivation:

Bacteria possess several enzymes that can chemically modify the drug by transfer of different chemical groups or by hydrolysis. Beta-lactam antibiotics that include penicillins, cephalosporins, carbapenems and monobactems affect bacteria by inhibiting their cell wall synthesis. The most important form of resistance that bacteria develop against these drugs is by producing beta lactamases. These enzymes are subdivided into several classes (Bush & Jacoby, 2010) and work by hydrolyzing the four membered beta-lactam ring. Beta lactamase inhibitors have been developed which when given in combination with beta-lactam antibiotics, improve their efficacy against beta lactamase producing bacteria, e.g. for treatment of serious *Enterobacteriaceae* and penicillin-resistant staphylococcal infections (Drawz & Bonomo, 2010). These inhibitors include clavulanic acid, sulbactam and tazobactam, but their drawback is their limited spectrum. Two new classes of beta-lactam inhibitors with extended spectrum are now available including diazabicyclooctanones, of which avibactam is the prototype, and boronate-based compounds with vaborbactam as its prototype (Tooke et al., 2019).

Aminoglycosides are a class of drugs that fall under the category of bacterial protein synthesis inhibitors. They can be modified by aminoglycoside n-acetyltransferases, O-nucleotidyltransferases and O-phosphotransferases (Ramirez & Tolmasky, 2010).

The aminoglycoside acyltransferases also modify fluoroquinolones, the bacterial DNA synthesis inhibitors, including ciprofloxacin (Hooper & Jacoby, 2015) (Jacoby et al., 2015).

Other examples of drug-modifying enzymes include chloramphenicol acetyltransferases (Schwarz et al., 2004), macrolide modifying esterases (Morar et al., 2012) and rifamycin modifying ribosyltransferases (Rominski et al., 2017), phosphotransferases (Spanogiannopoulos et al., 2014) and glycosyltransferases (Spanogiannopoulos et al., 2012).

2. Alteration of drug target:

Most of the beta-lactam antibiotics exert their effect by binding to the extra cytoplasmic or periplasmic penicillin binding proteins (PBPs) that are essential for bacterial cell wall synthesis. Alteration of PBPs is a major form of clinically relevant beta lactam resistance in several pathogenic bacteria, including *Staphylococcus aureus*, *Enterococci* and *Streptococcus pneumoniae* (Zapun et al., 2008).

Resistance to quinolones including fluoroquinolones occur because of mutation(s) in one or both drug targets i.e. DNA gyrase and DNA topoisomerase IV (Hooper & Jacoby, 2015). It is a form of plasmid-mediated quinolone resistance (PMQR) which is acquired by resistance conferring genes. As a result, the mutated drug target exhibits reduced drug-binding affinity, leading to loss of drug efficacy.

The target of most of the protein synthesis inhibitor antibiotics include three RNA chains (16S, 23S and 5S) and more than 50 proteins collectively forming two ribosomal subunits (30S and 50S). Mutations in genes coding for the ribosomal chains or ribosomal subunit proteins lead to resistance. This type of resistance is common for aminoglycosides, macrolides, lincosamides, streptogramins B, and ketolides (Lin et al., 2018).

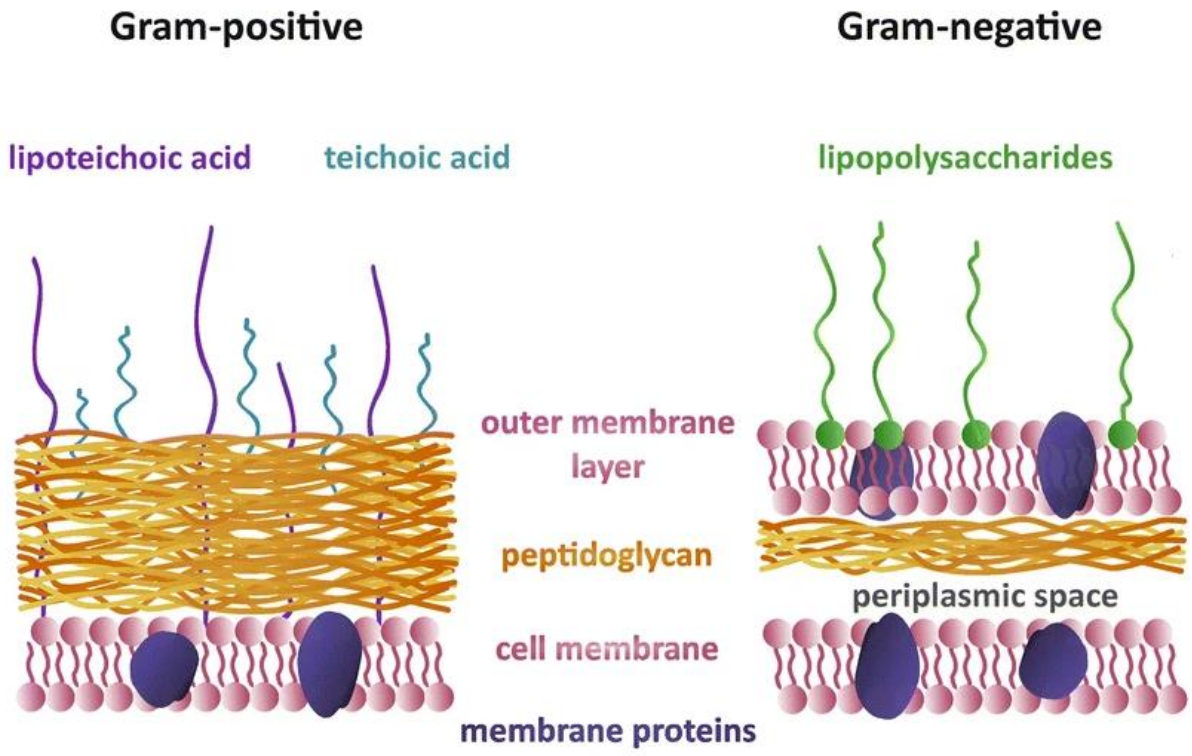

Fig 2. Difference between the cell walls of Gram-positive and Gram-negative bacteria (Pajerski et al., 2019).

3. Inhibition of drug uptake:

One of the major differences between gram positive and gram-negative bacteria is the presence of an outer membrane layer in gram negative bacteria (fig. 2). This layer mainly composed of lipopolysaccharides (LPS) makes a formidable barrier for most of the antibiotics. However, small hydrophilic antibiotics can enter the cell through porins. Consequently, the gram-negative bacteria can develop low level resistance against these agents by either decreasing the number of porins or changing the selectivity of these porins by mutations. An early example of resistance to beta-lactams and aminoglycosides due to porin down expression was reported in *S. marcescens* (Goldstein et al., 1983). One of the major contributors to carbapenem resistance in *Pseudomonas aeruginosa* was shown to be due to the loss of outer membrane porin OprD (Rodríguez-Martínez et al., 2009). In another study, decreased number of outer membrane proteins, possibly porins, were shown to be the leading cause of cross-resistance to nalidixic acid, trimethoprim, and chloramphenicol in *Klebsiella*, *Enterobacter*, and *Serratia* (Gutmann et al., 1985). Since then, various other clinical isolates were found to confer resistance due to the same phenomenon (Kumar & Schweizer, 2005).

In Gram-positive bacteria, cell wall is not considered a true barrier, however, resistance to vancomycin was reported for *Staphylococcus aureus* due to the phenomenon described as cell wall thickening (Cui et al., 2006). Biofilm formation is another mechanism by which bacteria, such as *Pseudomonas aeruginosa*, can prevent the access of antibiotics or immune cells, by forming a physical barrier mainly composed of polysaccharides and proteins (C Reygaert, 2018).

4. Activation of drug efflux pumps:

Another resistance mechanism developed by bacteria is the overexpression of drug efflux pumps to decrease the effective concentration of drug inside the cells. These energy dependent active transporters are located in the cytoplasmic membrane, and in Gram-negative bacteria they may exist as multi-component system spanning both the inner and outer membranes. These molecular machines exist in all kingdoms of life and most of these pumps possess the ability to transport a wide range of substrates, hence leading to multidrug resistant (MDR) phenotypes (Li & Nikaido, 2004). It was in 1966 that Jardetzky proposed a functional mechanism for these pumps and pointed out that one pump may be able to transport multiple molecules (Jardetzky, 1966). In 1970s, P-glycoprotein (P-gp) was identified for its role in multidrug efflux in cancer

cells (Gottesman & Ling, 2006), but it was not until 1980 that active drug efflux as a resistance mechanism in bacteria was identified for tetracycline in *E. coli* (McMurry et al., 1980). Clinical significance of active efflux increased with time, and in 2001, 37 putative drug efflux pumps were reported for *E. coli* (Nishino & Yamaguchi, 2001). These drug transporters work either as primary active transporters using ATP as energy source or secondary active transporters dependent on proton motive force. They are divided into several superfamilies (fig. 3), namely the major facilitator superfamily (MFS) (Quistgaard et al., 2016) (Pao et al., 1998), resistance-nodulation-cell-division (RND) superfamily (Tseng et al., 1999)(Nikaido, 2018), the multidrug and toxic compound extrusion family (MATE) (Chitsaz & Brown, 2017) (Brown et al., 1999) (Kuroda & Tsuchiya, 2009), the small multidrug resistance (SMR) family (Paulsen et al., 1996), the proteobacterial antimicrobial compound efflux (PACE) family (Hassan et al., 2015), the AbgT family (Delmar & Yu, 2016) and the ATP-binding cassette (ABC) superfamily (Van Veen & Konings, 1998) (Locher, 2016) (Orelle et al., 2019).

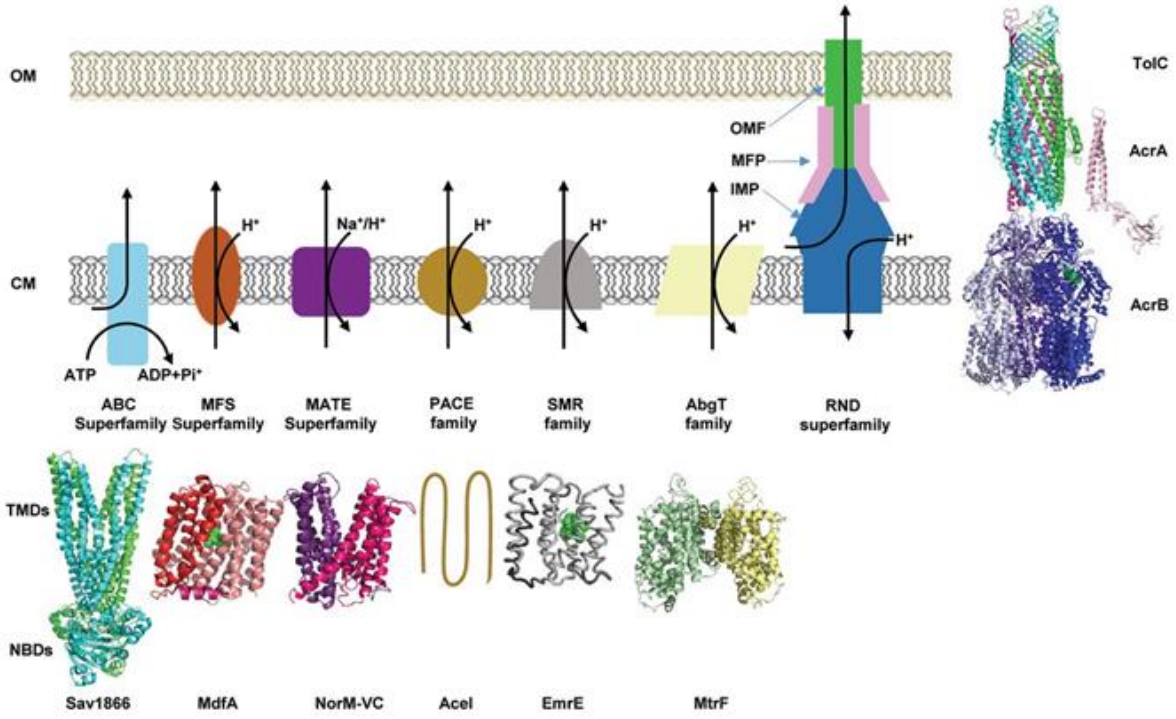

Fig 3. The seven families of multidrug transporters are schematized (Chitsaz & Brown, 2017). Note that, although less frequently, but the MFS and ABC family proteins can also exist as tripartite efflux pumps. The pdb codes are as follows; Sav1866 (2HYD), MdfA (4ZOW), NorM-VC (3MKT), EmrE (3B5D), Mtrf (4R1l), AcrB (2DRD), AcrA (2F1M), TolC (2VDE).

Secondary active transporters

1. The Major Facilitator Superfamily (MFS):

Transporters from this family are present in all forms of life and can transport substrates ranging from sugars, metals to small molecules and drugs, although individual members are mostly substrate specific. They can be uniporters, when transporting substrate without any coupling ion, or symporters or antiporters, when transporting substrate in association with a coupling ion (H^+ or Na^+). They are divided into more than 85 families and typically contain 12 to 14 trans membrane segments (TMSs) (Li, 2017) (http://www.tcdb.org). In Gram-negative bacteria, transporters of this family can also form tripartite complexes spanning across both membranes (Neuberger et al., 2018). In *E. coli* more than 70 members of this family are present including 15 drug exporters (Li et al., 2015) including MdfA (fig. 4) (Heng et al., 2015). Some important multidrug transporters of this family include LmrP from *Lactococcus lactis* (Putman et al., 2001), EmrAB TolC from *E. coli (*Neuberger et al., 2018), Bmr from *Bacillus subtilis* (Neyfakh, 1992) and QacA from *S. aureus* (Brown & Skurray, 2001).

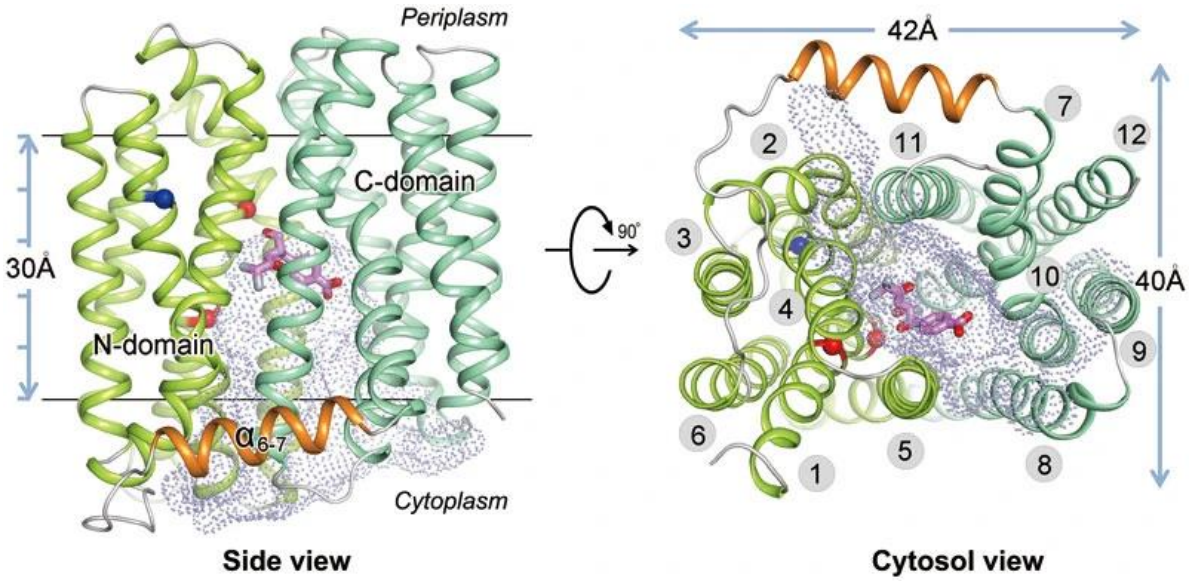

Fig 4. Crystal structure of MdfA in complex with chloramphenicol (Cph) (pdb 4ZOW). The N- and C-domains are colored light and dark green, respectively, and α_{6-7} orange. Cph is shown as magenta sticks. The inward-facing cavity is shown in dot surface representation. In the right panel the transmembrane segments are labeled from 1-12. Figure from (Heng et al., 2015).

2. Resistance-Nodulation-Cell-Division (RND) superfamily:

Transporters from this family are one of the major causes of MDR in Gram-negative bacteria where they mostly exist as tripartite complex spanning both the inner and the outer membranes, directly expelling the drugs into the extra cellular matrix. The prototype RND MDR pumps are AcrAB-TolC from *E. coli* (fig. 5) and MexAB-OprM from *P. aeruginosa*. The tripartite complex contains three components: an inner membrane protein (IMP) component like AcrB, a membrane fusion protein (MFP) like AcrA and an outer membrane protein (OMP) component like TolC (Neuberger et al., 2018). Usually these pumps contain 12 TMHs (TransMembrane Helices) and two large periplasmic loops (Nikaido, 2018) per protomer of AcrB, and function as proton substrate antiporters with a trimer of AcrB. AcrAB-TolC confers resistance to a range of antibiotics including penicillins, chloramphenicol, macrolides, fluoroquinolones, and tetracycline, whereas MexAB-OprM to β-lactams, chloramphenicol, tetracycline, trimethoprim, sulfamethoxazole, and some fluoroquinolones (C Reygaert, 2018). *P. aeruginosa* contains 17 pumps of the RND family (Li, 2017). Some Gram-positive bacteria like *mycobacteria* and *bacillus subtilis* also contain RND member pumps (Schindler & Kaatz, 2016). Other than MDR these molecular machines are also involved in functions such as stress response and pathogenicity (Li et al., 2015).

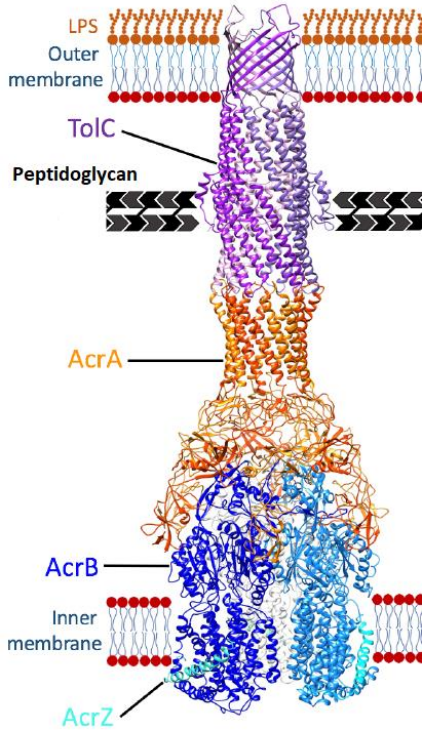

Fig 5. Structure of AcrABZ-TolC. TolC can be seen as a trimer, AcrA as hexamer and AcrBZ as trimer. Figure from (Neuberger et al., 2018).

3. The Multidrug and Toxic Compound Extrusion (MATE) family:

MATE family is part of the multidrug/oligosaccharidyl-lipid/polysaccharide (MOP) transporter superfamily (http://www.tcdb.org) (Hvorup et al., 2003). It contains three subfamilies with around 1000 representatives. Members of this family are Na^+-substrate or H^+-substrate antiporters and typically contain 12 TMHs (Omote et al., 2006). The prototype NorM (fig. 6) was the first member of this family discovered in *Vibrio parahaemolyticus*. It was shown to transport several structurally unrelated compounds including norfloxacin, ethidium, kanamycin, and streptomycin, when overexpressed in *E. coli* (Morita et al., 1998) (Morita et al., 2000). MepA from *Staphylococcus aureus* is another important member, and it was shown to confer resistance against tigecycline (McAleese et al., 2005), an important drug active against methicillin-resistant *S. aureus* (MRSA) and vancomycin-resistant *S. aureus*.

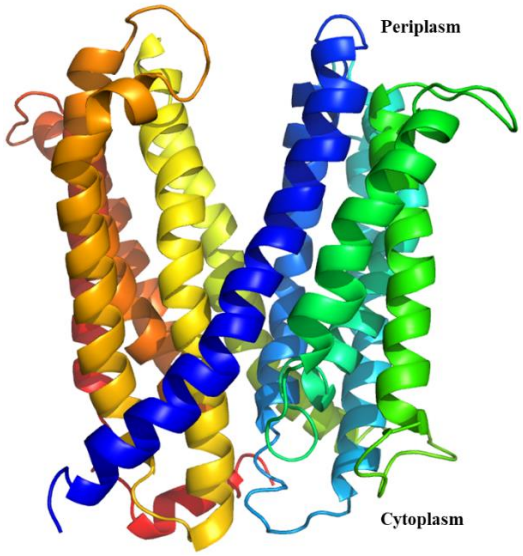

Fig 6. Crystal structure of NorM from *V. cholerae* (pdb 3MKT).

4. The Small Multidrug Resistance (SMR) family:

The SMR family is part of the drug/metabolite transporter (DMT) superfamily (Jack et al., 2001). They are the smallest of bacterial MDR pumps containing only 4 TMSs with 100-140 amino acids and function as dimers (Bay et al., 2008). SMR transporters use proton motive force to pump out quaternary ammonium compounds including a range of antiseptics and some antibiotics. The most studied MDR pump of this family is EmrE (fig. 7) from *E. coli* (Shimon Schuldiner, 2009). The substrates of EmrE include acriflavine, ethidium bromide, tetraphenylphosphonium (TPP), benzalkonium (S. Schuldiner et al., 2001) and some

aminoglycosides (Nasie et al., 2012). Another MDR pump AbeS from *Acinetobacter baumanni* was shown to confer significant resistance to erythromycin as well as novobiocin (Srinivasan et al., 2009), whereas kpnEF from *Klebsiella pneumoniae* was shown to make cells hypersusceptible to several antibiotics when mutated (Srinivasan & Rajamohan, 2013).

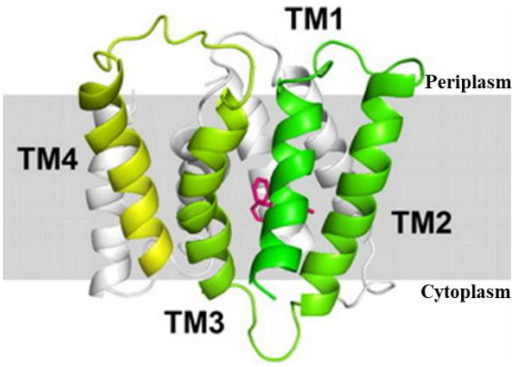

Fig 7. Structure of EmrE dimer in complex with tetraphenylphosphonium (TPP). One monomer is colored and labeled, wheres the other monomer is shown in light grey. The bound TPP is shown in magenta. Figure from (Chen et al., 2007).

5. The Proteobacterial Antimicrobial Compound Efflux (PACE) family:

This is a recent family of MDR transporters with AceI from *Acinetobacter baumannii* to be the first member identified in 2013 (Hassan et al., 2013). Thereafter, 23 homologues of AceI were shown to confer resistance to several biocides including chlorhexidine, dequalinium, benzalkonium, proflavine, and acriflavine (Hassan et al., 2015). Recently, short-chain diamines were shown to be transported by AceI when energized by proton gradient (Hassan et al., 2019). Proteins of this family are highly conserved in gram-negative pathogens and are predicted to contain 4 TMHs (Hassan et al., 2018).

6. AbgT family:

The prototype MDR pumps of the AbgT family include MtrF from *Neisseria gonorrhoeae* (fig. 8) and YdaH from *Alcanivorax borkumensis* and were shown to transport sulfonamide antibiotics (Delmar & Yu, 2016). This is the most recently identified family with members containing 500 residues on average and 9 TMHs, functioning as dimers (Ahmad et al., 2018). Mtrf uses proton motive force whereas YdaH was shown to use both Na^+ and H^+ gradient to energize the transport (Delmar & Yu, 2016).

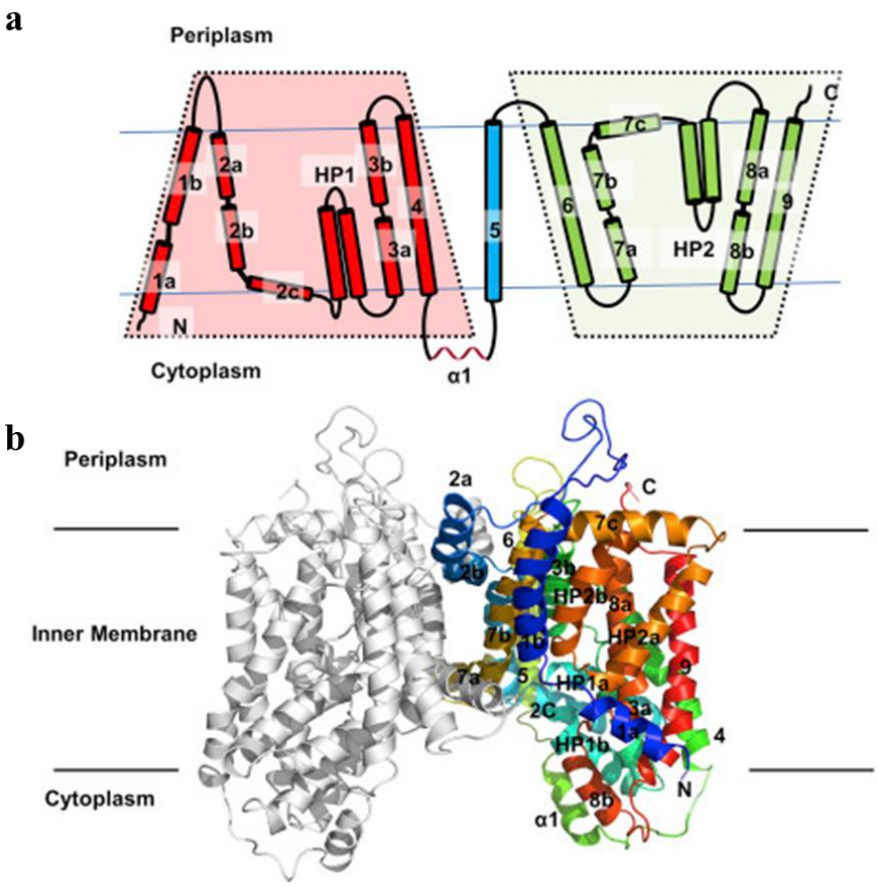

Fig 8. Structure of MtrF from N. gonorrhoeae (pdb 4R1I). (a) Showing transmembrane topology having nine transmembrane helices and two hairpins (HPs). **(b)** Ribbon representation of a dimer of MtrF with the right monomer colored in rainbow gradient from the N terminus (blue) to the C terminus (red), and the left monomer colored in gray. Figure from (Su et al., 2015).

Primary active transporters

The only primary active transporters in the MDR category fall into the ABC ("ATP-Binding Cassette") superfamily. It is one of the largest families of transporters and are present in all forms of life. They use the energy of ATP binding and hydrolysis to fuel the transport of a wide variety of structurally unrelated substrates. LmrA (*Lactococcus* multidrug resistance ATP) from *Lactococcus lactis* was the first ABC MDR pump to be identified in bacteria and was shown to confer resistance to a range of drugs including ethidium, daunomycin, rhodamine 6G and tetraphenylphosphonium, when overexpressed in *E. coli* (Van Veen et al., 1996). A homologue of LmrA, BmrA (*Bacillus* multidrug resistance ATP) from *Bacillus subtilis*, was also shown to export a range of drugs namely ethidium, Hoescht-33342, doxorubicin, 7-aminoactinomycin D, mitoxantrone and a fluorescent analogue of vinblastine after overexpression in *E. coli* (Steinfels et al., 2004). On the other hand, several clinical isolates resistant to fluoroquinolones and dyes

were shown to overexpress PatA/PatB, a heterodimeric ABC MDR pump from *Streptococcus pneumoniae* (Garvey et al., 2011).

Although a multitude of functional & structural studies are available for these transporters, some questions remain unanswered. It will be discussed in detail in the following chapter.

Chapter 2: The ATP-binding Cassette (ABC) Transporters

ABC transporters are ubiquitous membrane proteins involved in the translocation of a myriad of substrates across the membrane, ranging from ions, peptides, polysaccharides, lipids, vitamins, toxins, to xenobiotics (Rees et al., 2009). They could be classified as importers, exporters, or mechanotransducers/extruders (Greene et al., 2018) (Thomas & Tampé, 2018). The importers, which are involved in the uptake of nutrients, are mainly present in prokaryotes, although a few can also be found in eukaryotes (Lee et al., 2008), whereas exporters are found in all living species. In addition to transport function, ABC proteins are also involved in a multitude of other functions such as DNA repair (Goosen & Moolenaar, 2001), regulation of ion channels, iron homeostasis in mitochondria etc. (Rees et al., 2009). Due to their diverse physiological roles, their dysfunction in humans may lead to several disorders namely cystic fibrosis, diabetes, adrenoleukodystrophy, among others (Borst & Oude Elferink, 2002) (Silverton et al., 2011). On the other hand, the overexpression of other therapeutically important ABC exporters is responsible for multidrug resistance (MDR) phenotypes in cancer cells, pathogenic micro-organisms or parasites, as they are involved in the efflux of antimicrobial, antifungals, antiparasitic and anticancer drugs (Ambudkar et al., 2003) (Davidson et al., 2008).

Historically, the first MDR ABC transporter was discovered in 1976; mutants of the chinese hamster ovary cells were isolated for their cross-resistance to several structurally unrelated drugs such as vinblastine, colcemid, daunomycin, puromycin, and cytochalasin B and a strong correlation was established between the level of resistance and the presence of a membrane protein that was named P-glycoprotein (P-gp) (Juliano & Ling, 1976). After two decades since this discovery, the first prokaryotic ABC MDR pump LmrA was found and was later shown to complement P-gp when expressed in human cells (Van Veen et al., 1996) (Van Veen et al., 1998).

Architecture

All the ABC family proteins share some common features: These include two transmembrane domains (TMDs), responsible for substrate binding and translocation, and two highly conserved nucleotide-binding domains (NBDs), that bind and hydrolyze ATP (fig. 9). These four domains can either be linked into a single polypeptide or borne on separate polypeptides, until four. In

bacteria these four domains are mostly distinct subunits or linked together as homo- or heterodimeric half transporters composed of an NBD and a TMD.

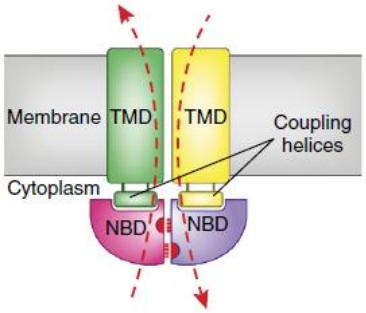

Fig 9. Cartoon depicting the common architecture of ABC transporters. The dotted arrows indicate the probable direction of transport. The red semi-circles represent the Walker-A motif, and the red dashed lines represent the ABC signature motif. Abbreviations: TMD, transmembrane domain; NBD, nucleotide-binding domain. (Locher, 2016)

The Transmembrane Domain (TMD)

The two TMDs form the substrate translocation pathway and are poorly conserved among the ABC transporters family. Conformational changes in the NBDs upon nucleotide binding and hydrolysis are transmitted to the TMDs through the 'coupling helices' (Locher et al., 2002) (Dawson & Locher, 2006). These coupling helices form the NBD-TMD interface and are conserved among the same type/fold of ABC transporters (Locher, 2016). During the catalytic cycle, the TMDs switch between the inward-facing (IF) and outward-facing (OF) conformations becoming alternatively accessible from the cis-side and trans-side of the membrane to enable the transport of substrate (Van Wonderen et al., 2014).

The Nucleotide Binding Domain (NBD)

The NBDs of the ABC transporters are well conserved both in sequence as well as in structure (Oswald et al., 2006). They are a subgroup of P-loop NTPases superfamily and depend on Mg^{2+} ion for catalysis (Vetter & Wittinghofer, 1999). They are further divided into three subdomains; the 'RecA-like' domain which is also present in other P-loop ATPases, the 'α-helical' domain and the 'β-subdomain' (fig. 10a). The latter two subdomains are unique to ABC transporters. The RecA-like subdomain, containing six stranded β sheet and four α-helices, forms the ATP-binding core. The characteristic 'Walker-A' and the 'Walker-B' motifs, the 'Q-loop', the 'D-loop', the 'H-loop' and the 'catalytic glutamate' just downstream of Walker-B, are all part of this subdomain (Orelle et al., 2019). The 'ABC-signature' motif is part of the α-helical subdomain, whereas the three stranded β-subdomain contains the conserved 'A-loop'. Another characteristic feature unique to ABC exporters, is the presence of a so called 'X-loop' which precedes the ABC-signature in the α-helical subdomain.

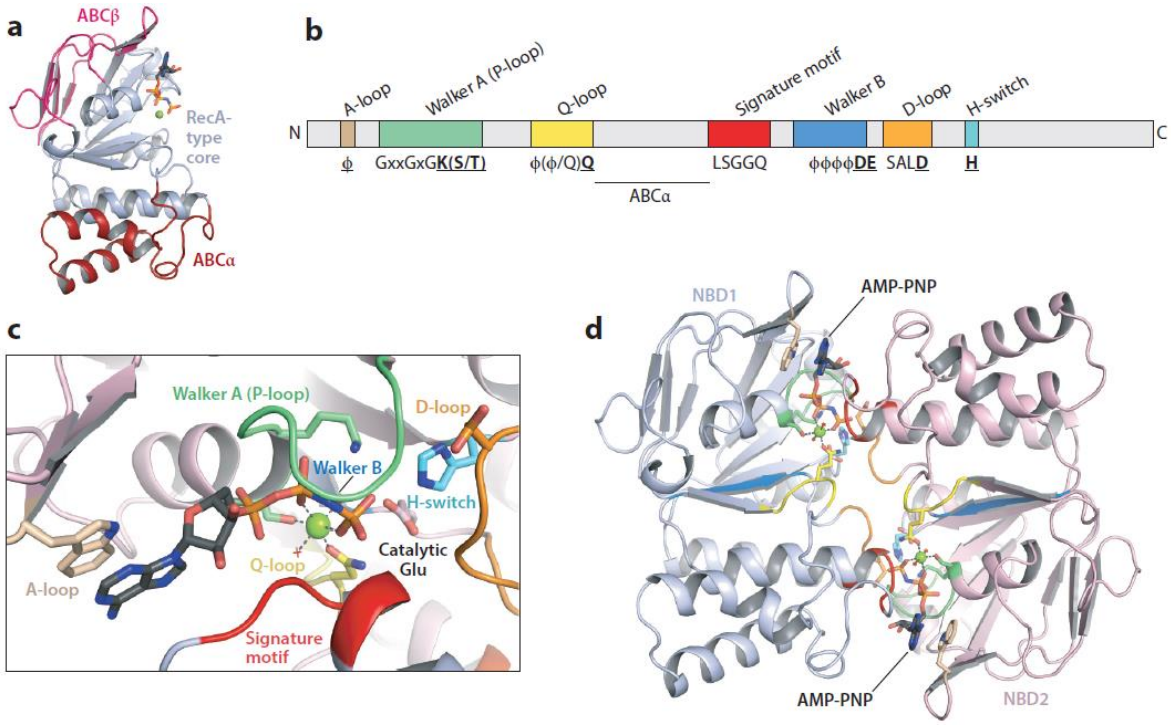

Fig 10. The conserved sequences in the NBDs and their role in ATP binding and hydrolysis is highlighted by using AMP-PNP-bound NBDs of Maltose transporter MalFGK2 (pdb:3RLF). **(a)** An isolated NBD (MalK subunit) of the maltose transporter is shown. The α-helical subdomain, β-subdomain and RecA-like domain are shown in red, pink, and white, respectively. Bound AMP-PMP is shown as sticks and Mg^{2+} ion as sphere. **(b)** Conserved sequence motifs in the NBDs are depicted. **(c)** Nucleotide-binding site in MalK is highlighted with conserved residues involved in ATP binding and hydrolysis shown as sticks and Mg^{2+} ion as sphere. The color scheme is the same as depicted in panel b. Residues 225–234 of NBD2 and residues 118–127 of NBD1 were removed for clear view. **(d)** NBD dimer is shown. The color scheme for the conserved motifs is the same as in panel b. The regulatory domain and the TMD were also removed in panel a and d for clarity. Fig. from (Thomas & Tampé, 2020)

1. A-loop:

The A-loop contains a conserved aromatic residue, hence 'A', and is characteristic of the β-subdomain. It is found upstream of the Walker-A motif and helps to stabilize the adenine ring of the nucleotide through π-π stacking (fig. 10b & 10c) (Geourjon et al., 2001) (Ambudkar et al., 2006).

2. The Walker-A and the Walker-B motifs:

These conserved motifs are also found in many other ATPases (Walker et al., 1982). The Walker-A motif is also known as the 'P-loop' (for Phosphate-binding loop) and is identified by the consensus sequence 'GX_4GKT/S', where 'X' can be any residue (fig. 10b). It stabilizes the β- and γ-phosphate of the bound nucleotide by making hydrogen bonds between the oxygen of the phosphates and the γ-amino group of the conserved lysine (fig. 10c). Mutation of the lysine

has been shown to adversely affect or impair the ATPase activity or ATP-binding, and in turn, transport (Orelle et al., 2008) (Lapinski et al., 2001).

The Walker-B motif is composed of four hydrophobic residues forming a β-strand terminated by an aspartate (ϕϕϕϕD, where 'ϕ' denotes a hydrophobic residue) (fig. 10b). This conserved aspartate coordinates the Mg^{2+} cofactor via hydrogen bonding. The Walker-B motif is immediately followed by another acidic residue glutamate, which forms the catalytic base for ATP hydrolysis (Orelle et al., 2003) (Oldham & Chen, 2011). This catalytic glutamate is conserved among other ATPases (Geourjon et al., 2001). Its mutation leads to complete loss of ATPase activity, however, the NBDs can still dimerize but become incompetent in hydrolyzing ATP (Smith et al., 2002) (Moody et al., 2002) (Orelle et al., 2003) (Mehmood et al., 2012).

3. The Q-loop:

The Q-loop is composed of approximately eight amino acids with a glutamine at the N-terminus (fig. 10b & 10c). It lies at the junction of the RecA-like and the α-helical subdomain and engages with the Mg-ATP, via the conserved Q residue, by forming the active site when Mg-ATP are bound and moving out once ATP is hydrolyzed. It may also be involved in transmitting conformational changes between NBDs and TMDs (Jones & George, 2002).

4. The X-loop:

The X-loop is unique to the ABC exporters. It is defined as the 'TEVGERG' sequence in Sav1866 (Dawson & Locher, 2006) preceding the ABC-signature in the α-helical subdomain. It lies in close proximity to both the ICDs (hence 'X') and is hypothesized to be involved in NBD-TMD communication (Kluth et al., 2015) (Lacabanne et al., 2019).

5. The ABC-signature motif:

The ABC family signature motif, which is not present in other ATPases, is characterized by the 'LSGGQ' sequence (fig. 10b). Also known as the 'C-loop', it is located at the N-terminus of a long α-helix (fig. 10c). The ATP during hydrolysis is sandwiched between the Walker-A motif of one NBD and the LSGGQ sequence of the other NBD, the latter making extensive hydrogen bonds with the ATP and is imperative for ATP hydrolysis (Smith et al., 2002) (Fetsch & Davidson, 2002). Mutants of the C-loop can bind ATP, although with reduced affinity, but their ability to hydrolyze it is strongly affected (Schmees et al., 1999) (Szakács et al., 2001) (Buchaklian & Klug, 2006).

6. The D-loop:

The D-loop typically contains the 'SALD' sequence and is found downstream of the Walker-B motif (fig. 10b). It is involved in the formation of the ATP-binding site by making a network of hydrogen bonds and electrostatic interaction with the Walker-A motif and the H-loop of the opposite NBD (fig. 10c). In this way, the D-loop gets positioned right at the dimer interface where it may be involved in the control and communication between the ATP-binding sites and the directionality of the transport (Grossmann et al., 2014) (Jones & George, 2012). It may also play a role in the stabilization of the catalytic glutamate as well as the attacking water molecule (Prieß et al., 2018).

7. The H-loop:

The H-loop, also known as the H-switch, consists of a highly conserved histidine residue found between a β-strand and an α-helix at the C-terminal end of the NBD (fig. 10b). Its role is to stabilize the ATP-binding site by direct interactions with the D-loop, the catalytic glutamate, and the γ-phosphate of the ATP (fig. 10c) (Zaitseva et al., 2005). It also helps in directing the attacking water and the Mg^{2+} cofactor.

Catalytic site and the ATP hydrolysis

During the catalytic cycle, the two NBDs of ABC transporters dimerize with each other in a head to tail fashion, forming two nucleotide-binding sites (NBS) (fig. 10d) (Moody et al., 2002) (Jones & George, 1999) (Orelle et al., 2019). During this dimer formation the RecA-like domain and the α-helical subdomain of each NBD move towards each other forming the NBS with Walker-A and Walker-B motifs, A-, Q- and H-loops of one NBD and C-loop in trans from the other NBD, sandwiching the two nucleotides between the dimer (Orelle et al., 2019). The hydrolysis of ATP and the resulting Pi/ADP destabilize the dimer forcing the NBDs to move back to their initial position (Cooper & Altenberg, 2013). These conformational changes in the NBDs are coupled to the TMDs resulting in alternating access of the substrate-binding site to either side of the membrane.

The way ATP is hydrolysed and the extent of NBD separation is still a matter of debate (Jones & George, 2012). Several models have been proposed, the most prevalent being the following:

ATP Switch model:

ATP switch model was proposed in 2004 (Higgins & Linton, 2004) and is also known as the processive clamp model (van der Does & Tampé, 2004). According to this model, the NBDs dimerize after binding two molecules of ATP (fig. 11a). This dimerization results in an OF conformation. It is followed by the hydrolysis of ATP and the release of Pi/ADP which leads to the IF conformation with complete separation of NBDs. The backbone of this model is the nucleotide free structures showing NBD separation and nucleotide bound structures of various ABC transporters including Sav1866, MsbA and P-gp (Dawson & Locher, 2006) (Ward et al., 2007) (Jin et al., 2012) (J. Li et al., 2014) (Kim & Chen, 2018).

The constant contact model:

In the constant contact model, the NBDs remain in contact throughout the catalytic cycle while the nucleotides get hydrolyzed at each nucleotide-binding site alternatively (fig. 11b) (Jones & George, 2009). The concept of constant contact was first presented in 1995 when Senior and colleagues observed that orthovanadate-induced ADP trapping in one nucleotide binding site of P-gp was sufficient to inhibit ATP hydrolysis in both sites (Senior et al., 1995). Another observation that favors this model is the normal or stimulated ATPase activity of P-gp when its NBDs are crosslinked (Verhalen & Wilkens, 2011) (Loo et al., 2012) (Loo & Clarke, 2014).

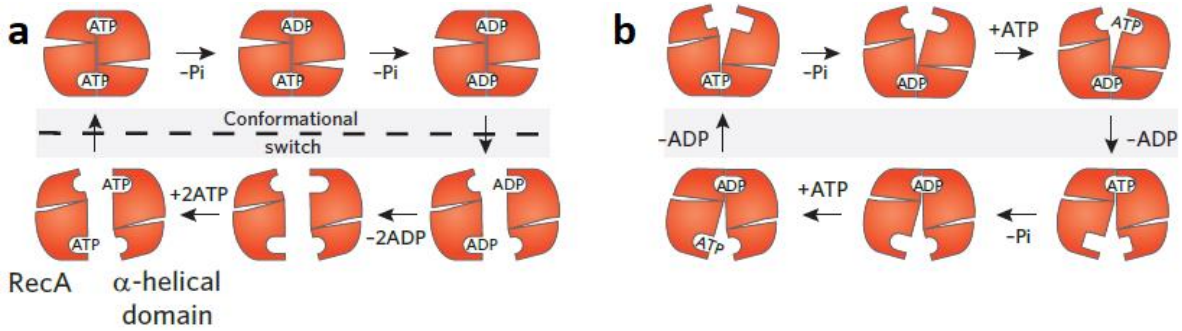

Fig 11. Schematic of NBDs showing **(a)** ATP switch or processive clamp model, and **(b)** Constant contact model of ATP hydrolysis. Details are in the text. (Parcej & Tampé, 2010)

Classification of ABC transporters

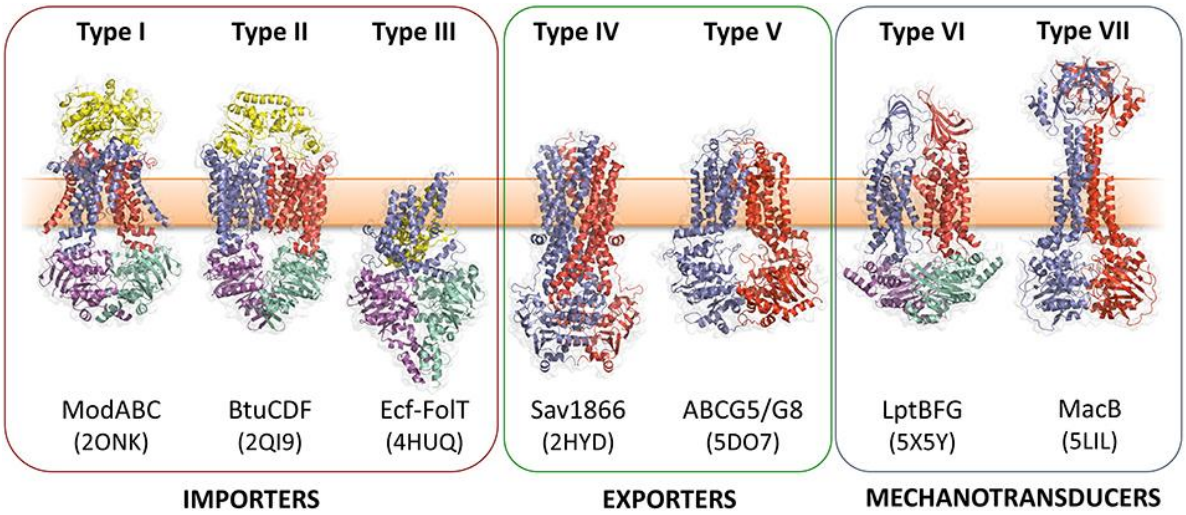

Fig 12. Representative structures of the seven ABC transporter families are shown, conventionally classified as importers, exporters & mechanotransducers. The PDB codes are displayed in parenthesis (Greene et al., 2018).

ABC transporters are conventionally classified into importers, exporters, and mechanotransducers/extruders, based on the direction of the transport (fig. 12) (Greene et al., 2018) (Thomas & Tampé, 2018). Previously, type IV and type V ABC transporters were categorized as type I and type II exporters, respectively (Lewinson & Livnat-Levanon, 2017). Based on the fact that quite a few type IV ABC transporters have been identified having non-exporter functions including cystic fibrosis transmembrane conductance regulator (CFTR) and sulfonyl urea receptor (SUR1 and SUR2), therefore, a new classification has been proposed recently based on the TMD folds and structural features rather than the direction of the translocated substrate (fig. 13) (Thomas & Tampé, 2020).

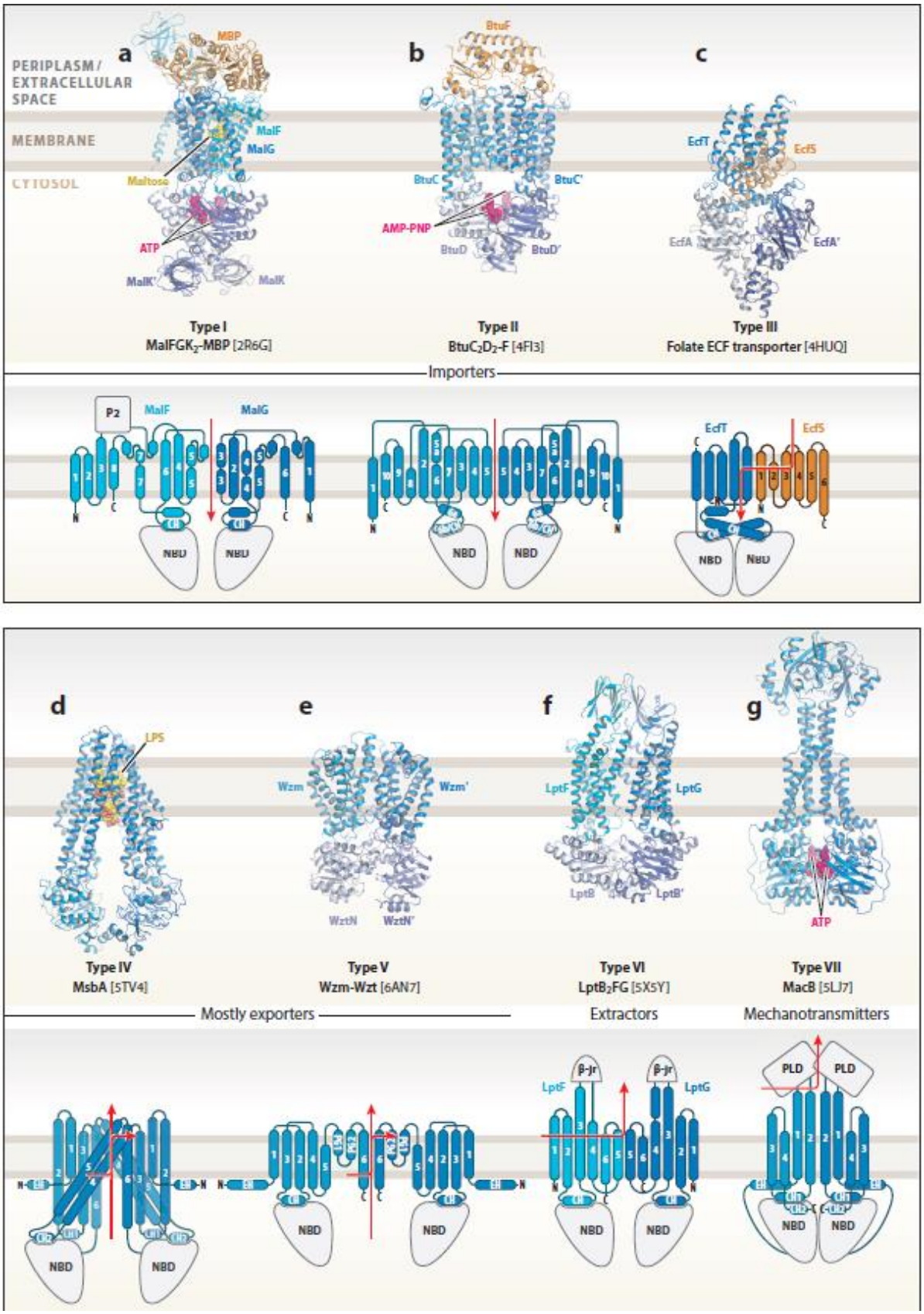

Fig 13. Classification of ABC transporters according to their seven TMD folds/types. Representative structures and their topology diagrams are shown with arrows indicating the direction of transport. The PDB codes are given in brackets. **(a)** Crystal structure of the maltose transporter MalFGK2 from *E. coli*, in complex with the MBP. **(b)** Crystal structure

of the vitamin B12 importer $BtuC_2D_2$ from *E. coli*, in complex with the substrate-binding protein BtuF. **(c)** Crystal structure of the folate energy-coupling factor importer from *Lactobacillus brevis*, in complex with the folate-binding EcfS subunit. **(d)** Cryo–EM structure of MsbA from *E. coli* with bound LPS. **(e)** Crystal structure of the channel-forming O-antigen-flipping Wzm-Wzt from *Aquifex aeolicus*. **(f)** Crystal structure of the LPS-extractor LptB2FG from *Pseudomonas aeruginosa*. **(g)** Crystal structure of the homodimeric ABC transporter MacB from *Aggregatibacter actinomycetemcomitans*. Abbreviations: β-jr, β-jellyroll-like domains; CH, coupling helix; ECF, energy-coupling factor; EH, elbow helix; LPS, lipopolysaccharide; MBP, maltose-binding protein; PG, periplasmic gate helix; PLD, periplasmic domain. (Thomas & Tampe, 2020)

Type/fold I ABC transporters:

Type I transporters are importers that undertake the low to medium affinity uptake of nutrients including oligosaccharides, peptides, and ions. The two TMDs of type I transporters are either identical (homodimer) or structurally similar with at least 5 TMHs present in each TMD, although additional N-terminal TMHs may be present (fig. 13a) (Ter Beek et al., 2014). The prototype for type I ABC transporters is the maltose transporter $MalFGK_2$ (Oldham & Chen, 2011). The transport cycle is explained in fig. 14a. In the first step of the transport, the substrate-binding protein (SBP) captures the substrate and docks onto the TMDs of the transporter in the inward-facing (IF) conformation. The docking of the SBP induces conformational changes in the TMDs which are transferred to the ATP-bound NBDs through the coupling helices, allowing the two NBDs to come closer together (Alvarez et al., 2015). Upon dimerization of NBDs, the transporter adopts an outward-facing (OF) conformation, inducing the SBP to release the substrate into the substrate-binding site on the TMDs (Orelle et al., 2008b). The hydrolysis of ATP and the subsequent release of Pi and ADP triggers the transporter back to the IF conformation, releasing the substrate into the cell.

Type/fold II ABC transporters:

Type II transporters are involved in the high affinity import of micronutrients such as cobalamin (vitamin B12) and metal chelates (Ter Beek et al., 2014). The two TMDs are identical and each TMD contains ten TMHs. This group of ABC transporters also employ coupling helices for TMD-NBD communication (fig. 13b). The vitamin B12 transporter 'BtuCD' is the hallmark of the type II transporters (Korkhov et al., 2012). Type II transporters show high basal ATPase activity, in the absence of the allocrite, in contrast to type I transporters. In the first step, ATP-binding induces NBD dimerization and the transporter switches to the OF conformation. The

SBP together with the bound substrate docks onto the TMDs releasing the substrate. Contrary to type I, type II transporters lack a well-defined substrate-binding site in the TMDs. ATP hydrolysis and Pi release trigger the transporter to switch to the IF conformation, releasing the substrate inside the cell (fig. 14b).

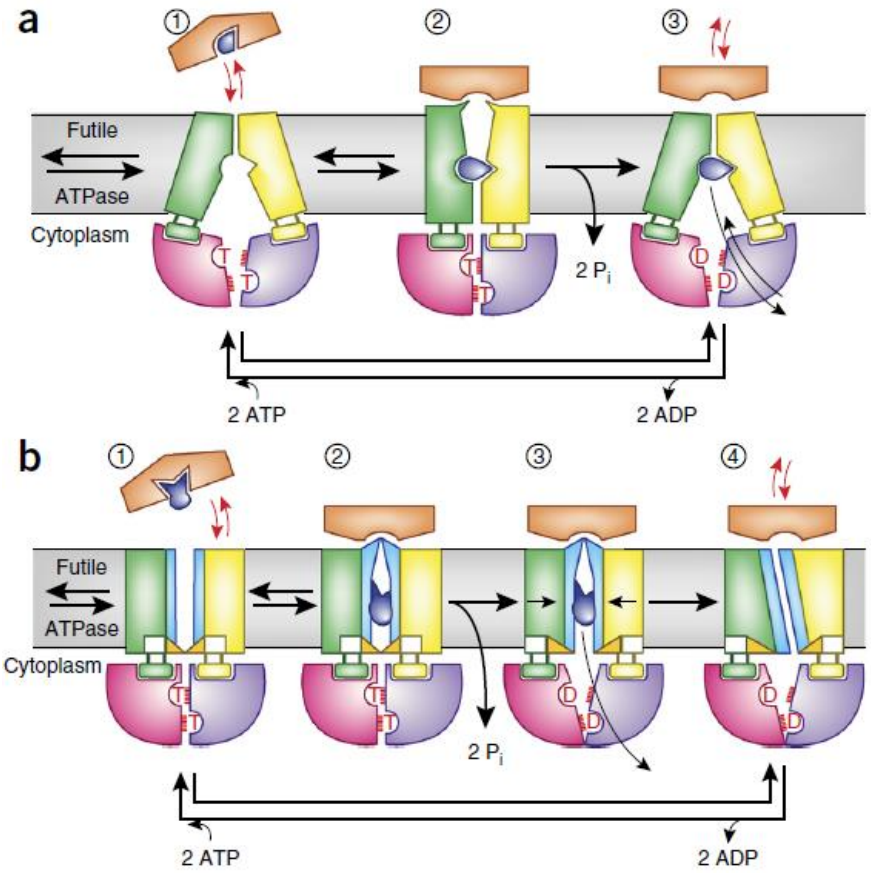

Fig 14. Cartoons representing the transport mechanism of importers with type I and II ABC folds. The substrate-binding proteins are shown in orange and the substrate in blue. Circled numbers represent states during the catalytic cycle. The transport mechanism of **(a)** type I and, **(b)** type II ABC importers is schematized. Abbreviations: T, ATP; D, ADP; Dashed red lines in the NBDs depict the ABC signature motifs; Pi, inorganic phosphate (Locher, 2016).

Type/fold III ABC transporters:

Type III transporters, also known as 'Energy Coupling Factor (ECF)' transporters, are mainly involved in the high affinity import of micronutrients like vitamins and metal ions in prokaryotes (Rempel et al., 2019). Although the folate and thiamine importers from this type were discovered in 1970s (Henderson et al., 1978), it took more than 30 years until they were classified as a distinct group (Rodionov et al., 2009). The two TMDs of ECF-type transporters are unrelated both structurally and functionally. One of them, which is poorly conserved, is

known as EcfT or T-component/subunit and contains 4-8 TMHs (fig. 13c). The EcfT also interacts with the NBDs with its two long coupling helices. The second TMD, which binds the substrate with high affinity, is known as EcfS or S-component/subunit. The EcfS is rather conserved and contains 6 α-helices (Zhao et al., 2015). In the resting state the NBDs adopt an open conformation and the substrate binding site of the EcfS subunit faces the cytosol. ATP binding and subsequent NBD dimerization induces conformational changes in the EcfT subunit which, in turn, activates the EcfS subunit which orients itself to capture the substrate and may detach from the other TMD (fig. 15 state 1). In the 'thermal rachet' model (fig. 15a), substrate bound EcfS reassociates with the EcfT once the NBDs regain the open conformation after ATP hydrolysis and Pi/ADP release. The toppling of EcfS and the release of substrate into the cell is then followed (Swier et al., 2016). In another mechanism termed as the 'power stroke' (fig. 15b), the reassociation of substrate bound EcfS to EcfT triggers the ATP hydrolysis, resulting in toppling over and the release of substrate into the cell by the EcfS (Rempel et al., 2019).

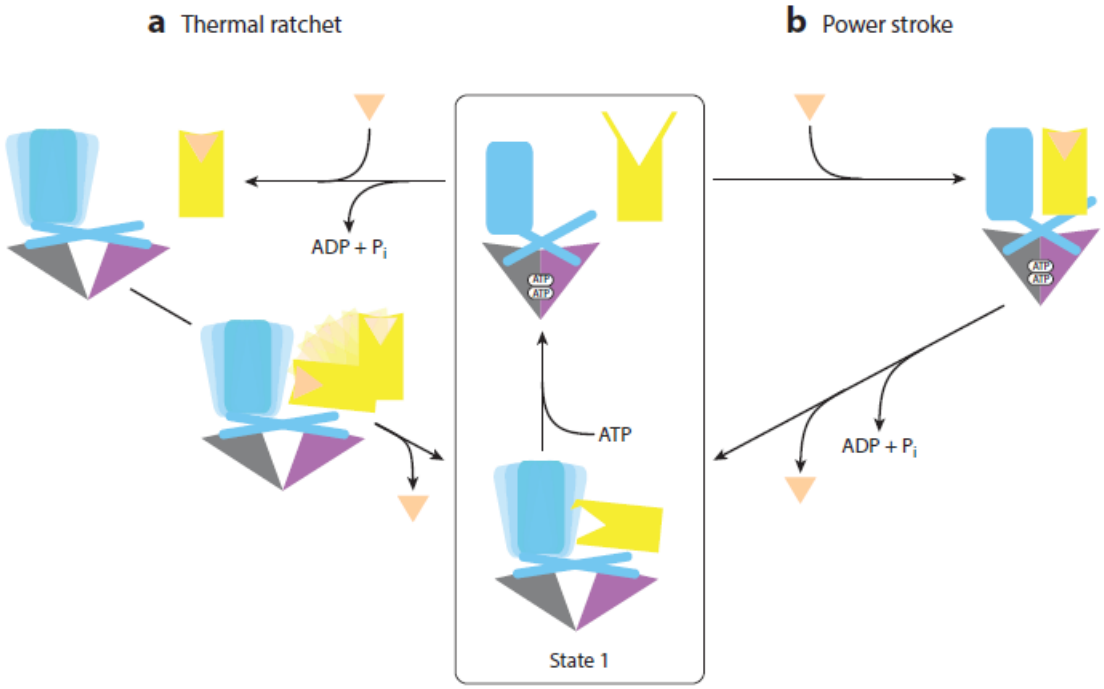

Fig 15. Proposed transport mechanisms for ECF-type ABC transporters. Details are given in the text. Gray and purple triangles depict the NBDs. EcfT is shown in cyan with the two coupling helices shown as bars. The S-component is show in yellow, and transported substrate represented by triangles. The starting point of the catalytic cycle is 'state 1', which is highlighted in the center and leads to, **(a)** the thermal ratchet model of transport or, **(b)** the power stroke mechanism (Rempel et al., 2019).

Type/fold IV ABC trasporters:

The type IV ABC transporters are ubiquitously present and have a very broad substrate spectrum ranging from multiple drugs, peptides to lipids. They are mainly exporters with some exceptions (Thomas & Tampé, 2020). The first true architecture of type IV ABC transporter was revealed by the crystal structure of Sav1866 from *Staphylococcus aureus* (Dawson & Locher, 2006) which was further confirmed by the structure of MsbA that followed soon after (Ward et al., 2007). The core of each TMD consists of 6 TMHs and 2 helices of each TMD cross over to the other TMD (fig. 16).

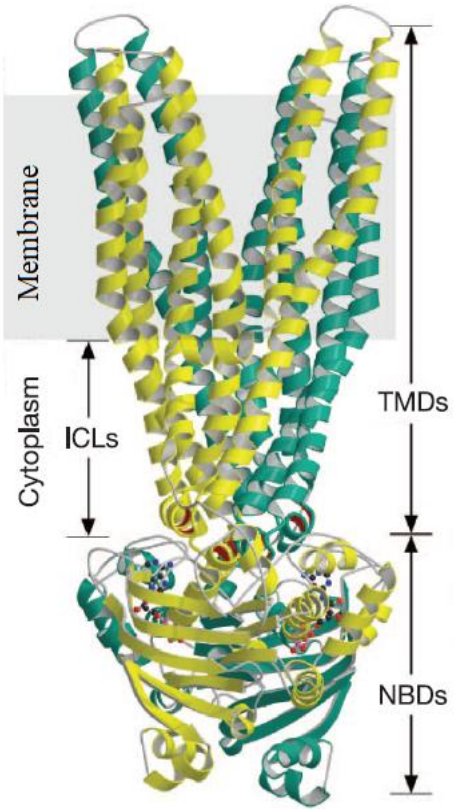

Fig 16. Crystal structure of a multidrug exporter Sav1866 from Staphylococcus aureus (PDB: 2HYD) (Dawson & Locher, 2006).

Another feature of the TMDs is their intra cellular domains (ICDs) that extent well into the cytoplasm to interact with NBDs situated at around 25Å away from the membrane. The ICDs contain coupling helices, with coupling helix 1 of ICD1 situated between TMH2 and 3, whereas, coupling helix 2 of ICD2 situated between TMH4 and 5. The coupling helix 1 interacts with NBD in the same half of the transporter while the coupling helix 2 only interacts with the NBD in the opposite half of the transporter. The site of interaction of the coupling helix 2 lies at the interface of the RecA-like domain and the α-helical domain, whereby, the conformational changes induced by the rotation of these subdomains upon nucleotide binding are transmitted

directly to the TMDs. The transport cycle is governed by an 'alternating access mechanism' (fig. 17) (Locher, 2016). According to the most prevalent 'ATP-switch model', at resting state (state 1), the transporter adopts an IF conformation such that the substrate binding cavity in the TMDs remains accessible from the cytoplasm as well as the inner leaflet of the membrane, resulting in substrate binding. In the following step (state 2), NBD dimerization occurs upon nucleotide binding and the conformational changes are transmitted to the TMDs resulting in an OF conformation (state 3). The reduced affinity of the substrate in the OF conformation allows the release of substrate into the extracellular side. The subsequent ATP hydrolysis and ADP/Pi release completes the transport cycle by resetting the transporter to the initial IF conformation.

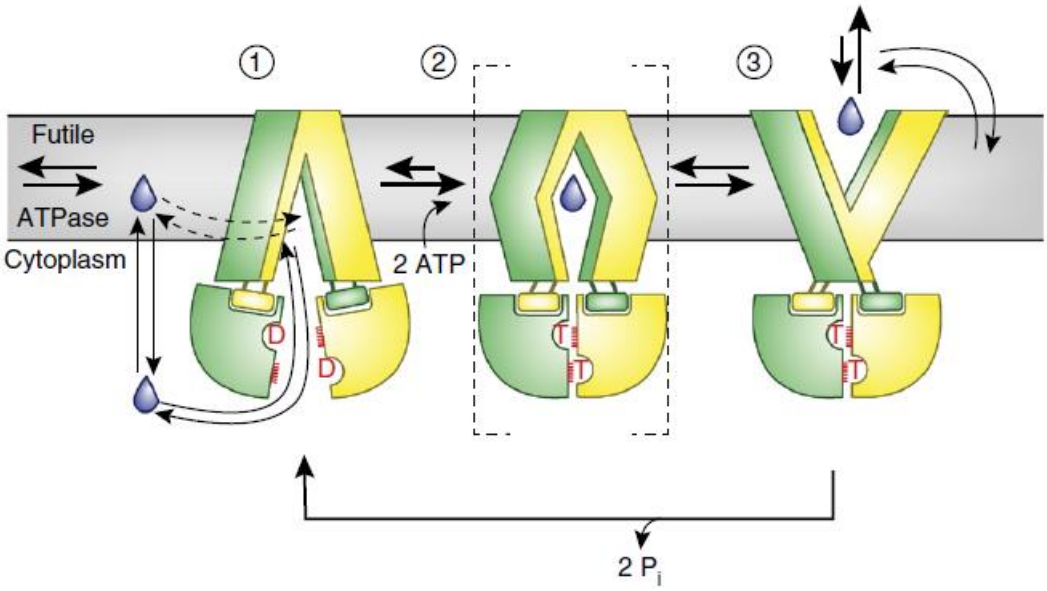

Fig 17. Alternating access mechanism proposed for the type IV ABC transporters. Substrate is shown in blue and the numbers indicate the different states of the catalytic cycle. Abbreviations: T, ATP; D, ADP; Dashed red lines in the NBDs depict the ABC signature motifs; Pi, inorganic phosphate (Locher, 2016).

It is important to note that ATP hydrolysis may not be simultaneous at both sites in the NBDs (Jones & George, 2013) especially for the heterodimeric or asymmetric transporters containing one canonical and one degenerate ATP binding site (Hofmann et al., 2019).

Type/fold V ABC transporters:

This fold was revealed for the first time by the crystal structure of heterodimeric human sterol transporter ABCG5/ABCG8 (Lee et al., 2016) which was soon followed by the structure of homodimeric ABCG2 (Taylor et al., 2017). The distinguishing feature of type 5 ABC transporters is that their 6 TMHs of each half transporter do not cross over to the other TMD of

the other half as seen in the case of type IV ABC transporters (fig. 13e). The NBD-TMD communication is maintained by a coupling helix and a characteristic connecting helix. The coupling helix is found between TMH2 and TMH3 and show similarities with the coupling helices in importers. Another significant difference is the physical contact of NBDs in the nucleotide free state which is quite contrary to the IF conformation of the type IV systems. However, the substrate translocation follows the prevalent 'alternating access mechanism'.

Type/fold VI ABC transporters:

The Lipopolysaccharide (LPS) extractor $LptB_2FG$ is the first ABC transporter identified with this fold (Narita & Tokuda, 2009) (Li et al., 2019) (Owens et al., 2019) (Dong et al., 2017). The ABC transporter $LptB_2FG$ extracts the LPS from the inner membrane which is then delivered and inserted into the outer membrane by the help of LptA, LptC, LptD and LptE. The NBDs of $LptB_2FG$ consists of two LptB subunits whereas TMDs are constituted by LptF and LptG subunits (fig. 13f). The TMDs show folds unique to this group with no domain crossover. In addition to the 6 TMHs, the TMDs also contain characteristic β-jellyroll domains. LptC component contains a single α-helix which docks in between the LptF and LptG subunits. LptC also contains the β-jellyroll domain. The first step in the catalytic cycle is the entry and attachment of LPS to LptF and LptG subunits (fig. 18 state 2). This results in the detachment of LptC from the TMDs. Consequently, the rearrangement of TMDs lead to a more stable interaction with the LPS and the LptC β-jellyroll domain interacts with the LptF β-jellyroll domain (state 3). In the next step, the conformational changes induced by the binding of ATP and the resultant dimerization of LptB subunits cause the TMDs to move inward leading to LPS expulsion into the β-jellyroll assembly (state 4) (Li et al., 2019).

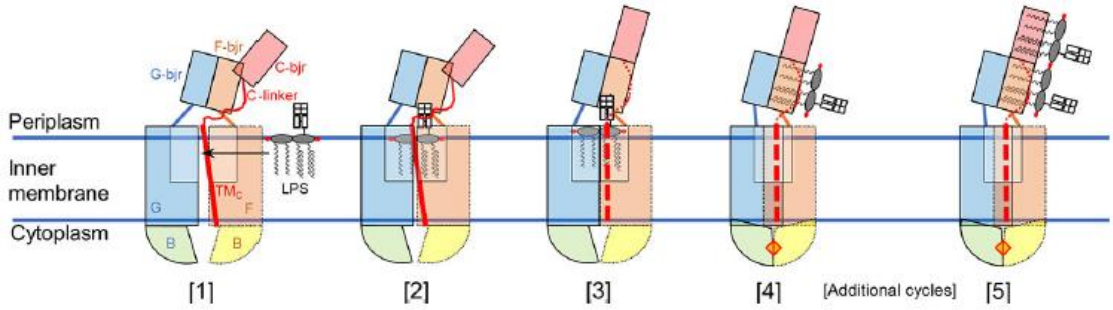

Fig 18. Proposed mechanism for LPS extraction by LptB2FG. Three β-jellyroll domains corresponding to LptC, LptF and LptG are shown in pink, peach, and blue rectangles, respectively. LPS is depicted as a cartoon. The ATP molecule in red is sandwiched between the two LptB subunits in step 4 and 5. The numbers represent the different steps in the catalytic cycle. Details in the text. Abbreviations: G, LptG; B, LptB; F, LptF; C, LptC; bjr, β-jellyroll domains; LPS, lipopolysaccharide (Li et al., 2019).

Type/fold VII ABC transporters:

MacB which is present in various gram-negative pathogens, is the prototype of this type of ABC transporters (Greene et al., 2018). MacB exists as a tripartite efflux pump in complex with the membrane fusion protein 'MacA' and the outer membrane channel protein 'TolC' (Kobyashi et al., 2001) (Okada et al., 2017) (Neuberger et al., 2018). This complex is involved in the mechanotransmission of substrates including macrolide antibiotics and virulence factors from the periplasmic space to the extracellular space. The structure and function of this assembly was revealed by the cryo-EM structure of the MacAB-TolC complex as well as the crystal structures of MacB (Fitzpatrick et al., 2017) (Crow et al., 2017) (Okada et al., 2017). MacB is a homodimer with an inverted topology with an N-terminal NBD fused to C-terminal TMD. TMD of half transporter contains 4 TMHs and a large periplasmic domain (PLD) (fig. 13g). In addition, each TMD also contains 2 coupling helixes but they only contact the NBD of the same protomer for NBD-TMD communication. In the nucleotide free state, the NBDs lie apart and a

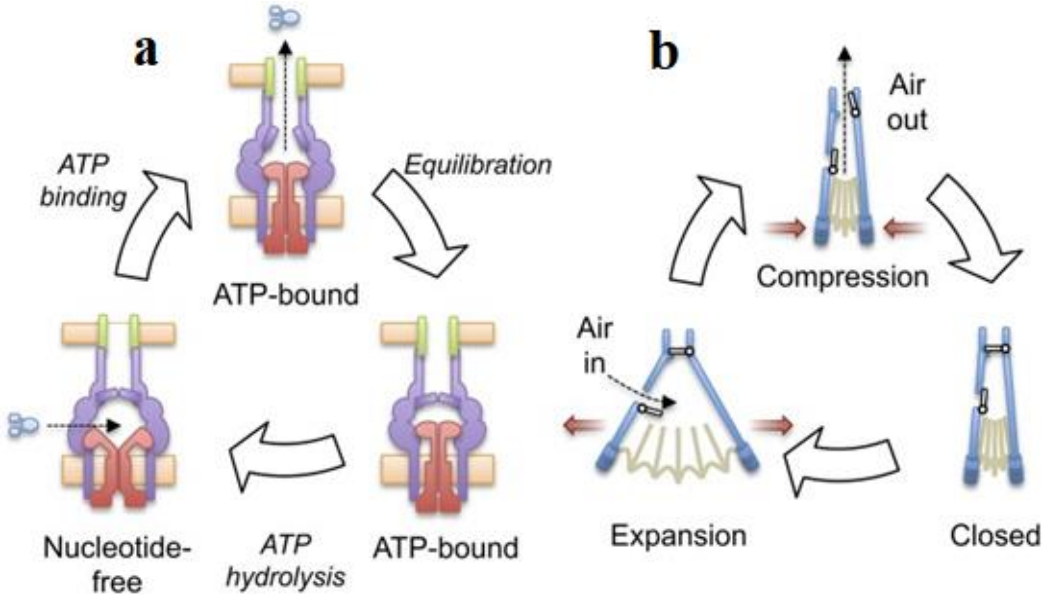

Fig 19. A molecular bellows mechanism for substrate secretion by the MacAB-TolC tripartite efflux pump. (a) Proposed catalytic cycle of the MacAB-TolC efflux pump. MacB is shown red, MacA in purple, TolC in green and substrate in blue. **(b)** Mechanism of a fireplace bellows (Crow et al., 2017).

prominent 'V-shaped' slit was observed in the periplasmic stalk (Crow et al., 2017). This periplasmic opening might be the binding site of the substrate. In the ATP-bound state the V-shaped slit was absent meaning the NBD dimerization induces conformational changes in the TMDs closing the periplasmic opening and mechanically pushing the substrate into the MFP MacA (fig. 19).

Eukaryotic ABC Transporters

In eukaryotes including humans, the ABC transporters are classified into seven subfamilies from ABCA to ABCG, based on amino acid sequence similarity and phylogeny (Dean & Annilo, 2005) (Dassa & Bouige, 2001). All ABC proteins in humans are exporters with few exceptions including one ion channel namely cystic fibrosis transmembrane conductance regulator (CFTR) (Csanády et al., 2019) and the sulfonyl urea receptor (SUR1 and SUR2) which controls a potassium channel (Puljung, 2018), and two importers namely ABCD4 (Coelho et al., 2012) and ABCA4 (Quazi et al., 2012). Member proteins of ABCE and ABCF subfamilies are devoid of TMDs, and thus, are not involved in transport function (Dean & Annilo, 2005). Transporters belonging to the ABCB, ABCC and ABCD subfamilies carry the type IV ABC fold, whereas members of ABCA and ABCG subfamilies are included in the type V ABC proteins (Thomas & Tampé, 2020).

Drug-binding in Type IV ABC Transporters

A very interesting feature of type IV ABC exporters is their broad substrate specificity. As an example, P-glycoprotein's (P-gp) substrates include anticancer drugs (doxorubicin, paclitaxel, vinblastine), antibiotics (gramicidin D), antivirals (ritonavir, saquinavir), dyes (rhodamine 123, daunorubicin), calcium channel blockers (verapamil) and many more (Chufan et al., 2015). The crystal structures of mouse and *C. elegans* P-gp reveal a large hypothetical drug-binding cavity accessible from the membrane inner leaflet (Jin et al., 2012) (Li et al., 2014). Several fold increase in drug affinity was observed for P-gp in membranes as compared to detergent, meaning that it would be more likely for drugs to partition into membrane before binding to the transporter (Jin et al., 2012). But the question remains how the transporter can have a substrate as small as cimetidine (MW 252), and at the same time, a substrate as big as gramicidin D (MW 1882). This can be explained by the intrinsic ability of P-gp and related transporters to adopt a wide range of IF conformations to accommodate substrates of varying size and nature (Esser et al., 2017) (Moeller et al., 2015) (Frank et al., 2016). Generally allocrites (i.e. molecules transported) have been shown to stimulate the ATPase activity of P-gp, whereas inhibitors show the opposite effect (Kimura et al., 2007). Similarly, various biochemical techniques including cysteine cross linking and luminescence resonance energy transfer (LRET) have confirmed the substrate-induced conformational changes in P-gp (Loo et al., 2003) (Zoghbi et al., 2017). In line with this, the cryo-EM structure of nanodisc reconstituted human P-gp bound to paclitaxel

and antigen binding fragment (fab) of UIC2, showed an occluded conformation with a simultaneous closure of inter-NBD gap as compared to the previous IF conformations (Alam et al., 2019) (Alam et al., 2018). A globular drug-binding pocket was identified with mainly hydrophobic amino acids contributing from all the 12 TMDs (fig. 20). Interestingly, in the same study, another cryo-EM structure was resolved with two molecules of the inhibitor zosuquidar bound at the same site as paclitaxel. However, when observed closely, the difference originates from subtle changes in the drug-binding site specially TMD2, which are then transmitted to the NBDs leading to a larger separation between NBDs as compared to the paclitaxel bound form. This can also explain the decrease in ATPase activity in the presence of inhibitors.

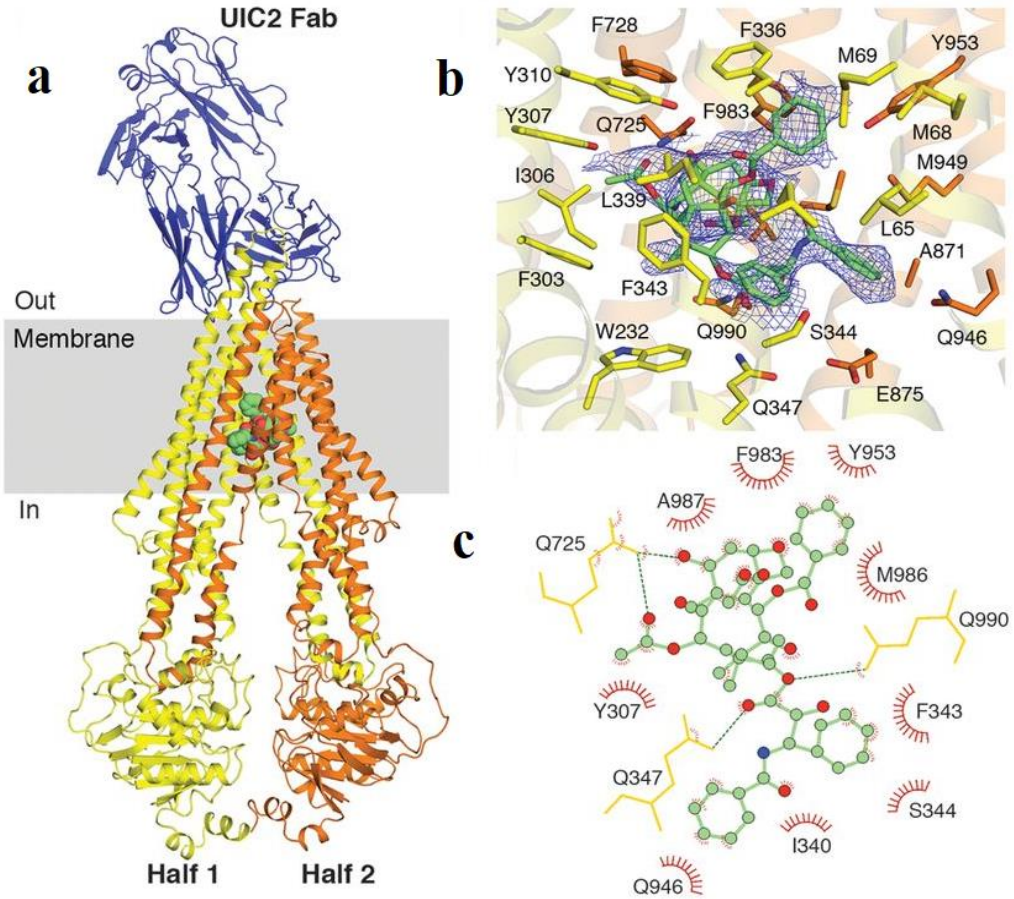

Fig 20. Cryo-EM structure of drug-bound P-gp. (a) Structure of P-gp bound to taxol (green spheres). The N-and C-terminal halves of ABCB1 are colored yellow and orange, respectively with the UIC2 Fab shown in blue. **(b)** Close up of binding site showing side chains of residues within 5Å of bound taxol (green sticks) with EM density shown as a blue mesh. **(c)** Interactions between taxol and P-gp side chains. Non-bonded interactions are represented by spoked arcs and hydrogen bonds are indicated by dashed lines. Fig. from (Alam et al., 2019).

A bacterial homodimeric multidrug exporter 'BmrA'

BmrA (Bacillus multidrug resistance ATP) is a homodimeric multidrug ABC exporter and is a member of type/fold IV ABC transporters. Each monomer consists of one TMD containing 6 TMHs and one NBD. Originally known as 'YvcC', it was identified as MDR pump among 78 putative ABC transporters from *Bacillus subtilis*, due its high sequence similarity to bacterial LmrA (41.5% identity) and to each half of human P-gp (around 28% identity) (Quentin et al., 1999) (Steinfels et al., 2002). It was shown to transport several P-gp substrates including Hoechst 33342, 7-aminoactinimycin D and doxorubicin when overexpressed in *E. coli* inverted membrane vesicles (IMVs) and was renamed BmrA (Steinfels et al., 2004) (Steinfels et al., 2002). Later, a strong upregulation of BmrA due to a promoter mutation was observed in a cervimycin C resistant *Bacillus subtilis* strain (Krugel et al., 2010).

For overexpression, the *E. coli* C41(DE3) strain was shown to be most suited for the optimal functionality of BmrA as compared to BL21(DE3) or T7 express, although the Lemo21(DE3) strain appeared quite efficient too (Mathieu et al., 2019). BmrA was able to bind several classical P-gp substrates when purified in an active form using DDM. Reconstitution into proteoliposomes led to a high ATPase activity which was sensitive to orthovanadate (Vi) inhibition, a classical inhibitor of ATPases (Steinfels et al., 2004). Lately, it was observed that BmrA was more active and stable when purified using LMNG detergent (Breyton et al., 2019). Time-resolved fluorescence energy transfer (FRET) and size exclusion chromatography (SEC) validated that BmrA exists as a homodimer when purified in detergent or reconstituted into proteoliposomes (Dalmas et al., 2005) (Ravaud et al., 2006).

The conserved glutamate residue just downstream of the Walker B motif was identified as the catalytic base for ATP hydrolysis and ATPase inactive mutants were designed to trap the transporter at different steps of the catalytic cycle (Orelle et al., 2003) (Orelle et al., 2008). A low resolution cryo-EM structure of BmrA reconstituted into proteoliposomes was obtained with some residual detergent in which BmrA formed peculiar ring-like structures containing 24 BmrA dimers (Fribourg et al., 2014) (Chami et al., 2002). Interestingly, the addition of Mg^{2+}-ATP prevented the formation of these rings or destroyed the preformed rings in case of WT and the catalytic glutamate mutant (E504) but not in the case of Walker A lysine mutant (K380) (Orelle et al., 2008). From this observation it could be deduced that unlike the WT and E504 BmrA, the K380A BmrA mutant was unable to undergo a significant conformational change required to destroy the ring-like structures.

A disulphide bridge was observed to be spontaneously formed when cysteine residues were introduced in the Q-loop (428 position) of the NBD and the intracellular loop 1 (123 position) of the TMD, which in turn inhibited the ATPase and the transport activity (Dalmas et al., 2005). Addition of Mg^{2+}-ATP and Vi prevented the formation of this disulfide bridge for WT and only Mg^{2+}-ATP for the E504 mutant. This indicates the proximity of these two regions in the resting state and their relative mobility during the catalytic cycle. In another experiment, electron paramagnetic resonance (EPR) spectroscopy revealed the proximity and possible interaction of Q333 of the loop connecting TMD to NBD (intracellular loop 3) to Y408 (Do Cao et al., 2009). This Y408 is located just upstream of one of the three tryptophan residues present in BmrA, W413, which is well conserved in bacterial ABC exporters and is potentially involved in NBD-TMD communication (unpublished work).

In another study, Hydrogen Deuterium exchange coupled to mass spectrometry (HDX-MS) was employed to probe the structural dynamics of BmrA in the apo state (IF conformation) and the ATP-bound state (OF conformation) (Mehmood et al., 2012). It unmasked the incredible flexibility of the intracellular domains, especially ICD2, and highlighted the extraordinary mobility of the NBDs in the resting state. To investigate the molecular determinants of coupling between the NBD and TMDs, mutants in the X-loop of BmrA were designed. Biochemical data showed that the X-loop mutant E474R was ATPase active but defective in drug transport. Using solid-state NMR, it was validated that the E474R mutant was unable to completely switch to the OF conformation in the presence of Mg^{2+}-ATP and Vi, and stiffening of some key residues was imperative to couple the ATP hydrolysis to transport (Lacabanne et al., 2019).

Chapter 3: Techniques Employed

Hydrogen Deuterium Exchange coupled to Mass Spectrometry (HDX-MS)

Background

The first use of hydrogen to deuterium exchange in protein amide backbone was reported in 1953 and was monitored by infrared spectroscopy (Lenormant & Blout, 1953). Since then, several methods were employed to monitor the hydrogen exchange namely scintillation counting, UV spectroscopy, neutron diffraction and quite notably nuclear magnetic resonance (NMR) spectroscopy (Englander, 1963) (Englander et al., 1979) (Bentley et al., 1983) (Barksdale & Rosenberg, 1982). In 1990, the use of electrospray ionization mass spectrometry (ESI-MS) was reported for the first time which was soon followed by the first ever use of HDX coupled to MS (Chowdhury et al., 1990) (Katta & Chait, 1991). The basic advancement in the method and the mass analyzing technology added to the scope of this technique in probing the protein dynamics, interactions, and conformational changes in solution (Hoofnagle et al., 2003) (Trabjerg et al., 2018) (Engen & Komives, 2020).

Fundamentals of HDX

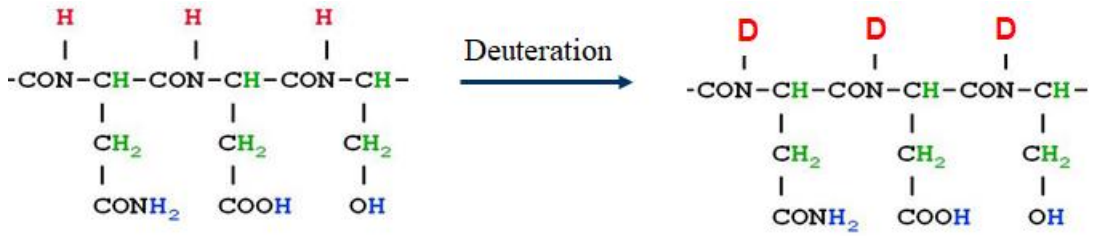

H: Do not exchange or exchange very slowly

H: Too fast to be monitored

H: Best candidates for deuterium exchange

Fig 21. Different types of amide hydrogen atoms in a peptide/protein.

The amino acids in a protein contain hydrogen atoms that are generally categorized as either labile or non-labile. The labile hydrogens are the ones which are bonded to nitrogen, oxygen

and sulfur and get exchanged with the solvent hydrogen (or deuterium in case of deuterated solvent) (Trabjerg et al., 2018). The hydrogens bonded to the main chain and side chain carbon atoms (colored green in fig. 21) are considered non-labile as they get exchanged very slowly with the solvent. In the labile hydrogens, the ones linked to the functional groups in the side chains of amino acids (colored blue in fig. 21) get exchanged at rates that are too fast to be monitored. Only the amide hydrogens (colored in red in fig. 21) that are distributed along the protein backbone (except for proline residues) form the best candidates for HDX, as they exchange at rates that can be easily monitored (Wales & Engen, 2005).

The HDX reaction is either catalyzed by a base or an acid and is governed by the rate constant 'k_{ex}', where k_H, k_{OH} and k_{H2O} are the rate constants for the exchange catalyzed by acid, base and water, respectively (eq. 1).

$$k_{ex} = k_H (H^+) + k_{OH} (OH^-) + k_{H2O} (H_2O) \quad (1)$$

1. pH and amino acid sequence:

As seen above, the pH greatly influences the exchange rate with the lowest exchange occurring at pH 2.5. (Bai et al., 1993) (Hoofnagle et al., 2003). Above this pH base catalyzed reactions dominate, whereas the acid catalyzed reactions are dominant below this pH. Lowering the pH by one unit slows down the exchange rate by a factor of 10. The sequence of amino acids and the nature of their side chains (basic or acidic) can also have an effect on the hydrogen exchange rate by impacting the pH and solvent accessibility in the immediate environment of the amide hydrogens, especially when they are involved in secondary and tertiary structures (Bai et al., 1993).

2. Temperature:

Temperature is known to have a direct relation with the rate of most of the chemical reactions. In a similar way it also directly impacts the hydrogen exchange by effecting the ionization constant of solvent. In addition to it, temperature has a direct impact on the secondary and tertiary elements of a protein as well as its denaturation or unfolding which can gravely effect the hydrogen exchange rate in a solution. As a rule of thumb, every 10°C decrease in temperature slows down the hydrogen exchange rate by a factor of 3 (Zhang & Smith, 1993).

3. Solvent accessibility and protein structure:

The two main factors that greatly affect the amide hydrogen exchange rate in a solvent are solvent accessibility and hydrogen bonding (Englander & Kallenbach, 1983). Amide hydrogens that are exposed to the solvent will have a higher exchange rate. Similarly, unstructured parts of the protein that are not involved in secondary structure formed due to hydrogen bonding, will show higher exchange rates as compared to the structured parts. A typical amide hydrogen located in an unstructured part of folded protein and fully solvent accessible will exchange rapidly according to the following equation, where 'F' denotes the folded form of protein and 'H' and 'D' represent the protonated and deuterated forms, respectively (eq. 2):

$$F_H \underset{D_2O}{\overset{k_{ex}}{\rightleftharpoons}} F_D \qquad (2)$$

Similarly, amide hydrogens in structured part of a folded protein and fully solvent accessible, will undergo similar exchange kinetics as above, albeit 1-2 orders of magnitude slower (Jensen & Rand, 2016) (fig. 22a). For the amide hydrogens buried deep inside the hydrophobic core of a protein, the exchange depends on the 'breathing motion' (transient structural unfolding) of the protein and is governed by the following equation, where 'F' and 'U' denote the folded and unfolded state of protein, and 'H' and 'D' represent the protonated and deuterated forms, respectively. k_2 is the exchange rate constant, whereas, k_1 and k_{-1} are the protein unfolding and folding rate constants, respectively (eq. 3 and fig. 22b):

$$F_H \underset{k_{-1}}{\overset{k_1}{\rightleftharpoons}} U_H \xrightarrow[D_2O]{k_2} U_D \underset{k_1}{\overset{k_{-1}}{\rightleftharpoons}} F_D \qquad (3)$$

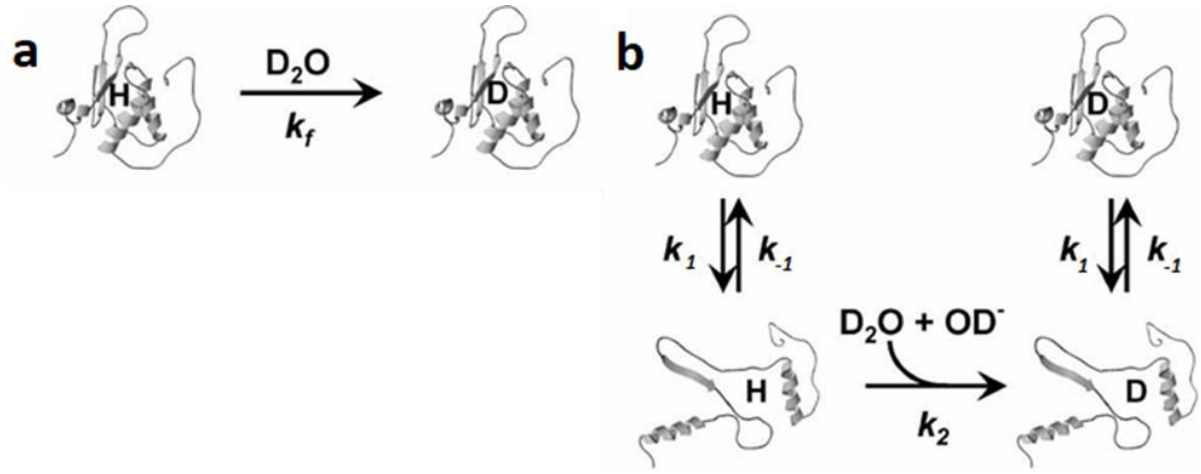

Fig 22. HDX model for **(a)** fully solvent accessible folded protein, **(b)** solvent inaccessible protein where HDX depens on protein unfolding (Wales & Engen, 2005).

When 'k_{-1}<<k_2', meaning the rate of refolding is very slow as compared to the rate of exchange, then the exchange rate directly depends on protein refolding/unfolding and follows 'EX1 kinetics' (Weis et al., 2006). A bimodal distribution in the mass spectrum is a characteristic of EX1 kinetics (fig. 23). It occurs via a 'correlated' exchange pattern in which the upper mass envelope corresponds to the amides that have exchanged (due to unfolding) and the lower mass envelope depicts amides that have not yet exchanged (not unfolded yet). However, the back exchanged carryover can very often lead to a false observation of EX1 kinetics as explained in fig. 24.

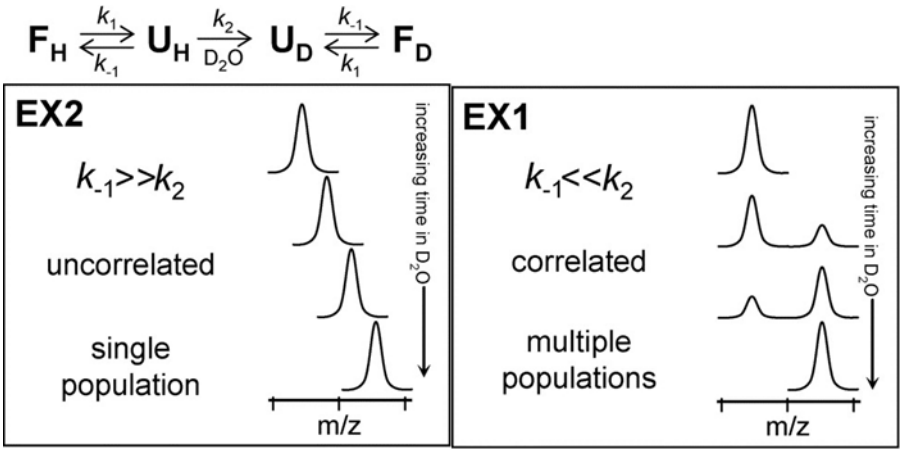

Fig 23. Two types of HDX kinetics that can be observed in HDX-MS (Weis et al., 2006).

Contrary to the above, if 'k_{-1}>>k_2', meaning that the protein refolding rate is much faster than the hydrogen exchange rate which is very often the case for most of the proteins at physiological

conditions, then the hydrogen exchange follows 'EX2' kinetics. In EX2 kinetics, only one isotopic envelope is observed throughout the labeling (with deuterium) kinetics (fig. 23).

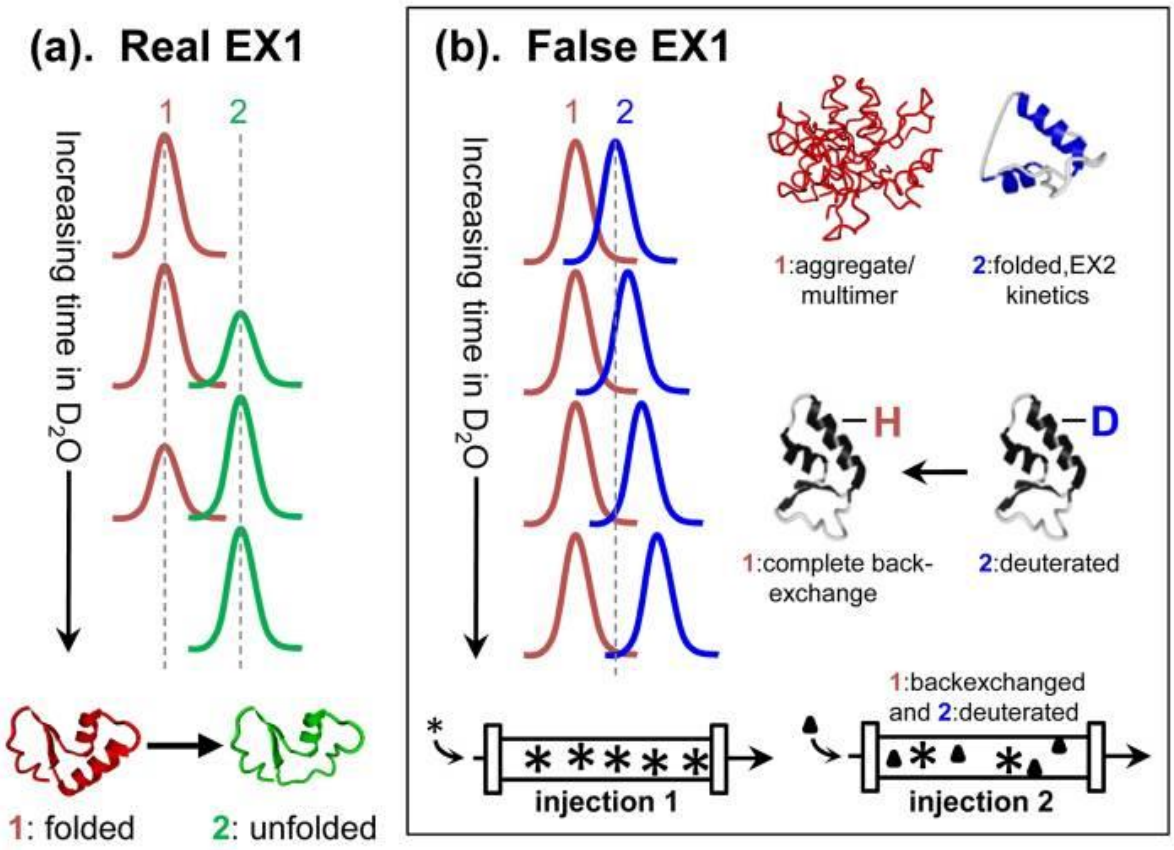

Fig 24. Schematic differentiating the false EX1 kinetics with real EX1 kinetics in HDX. (a) Real EX1 involves two populations but the lower mass peak eventually shifts totally to the higher mass peak with time. **(b)** In False EX1, the lower mass peak persists because it is a result of aggregates, back exchange, or sample carryover (Fang et al., 2011).

HDX-MS workflow:

The workflow of a typical HDX-MS experiment is outlined in fig. 25. This workflow is followed once the 'peptide mapping' has been done for the non-labeled (undeuterated) protein. For peptide mapping, the protein in protonated (normal) buffer is quenched, proteolyzed, the peptides separated by liquid chromatography, identified by MS, and eventually mapped on the protein sequence to get a sequence coverage. The same process is then repeated with the protein diluted in deuterated (labeling) buffer but for varying time periods. This process is known as 'labeling'. The next step is the 'data analysis' which is done by using a software, e.g. 'DynamX' by Waters®, by which deuteration level of each obtained peptide could be assessed leading to useful information on the structural dynamics of the protein.

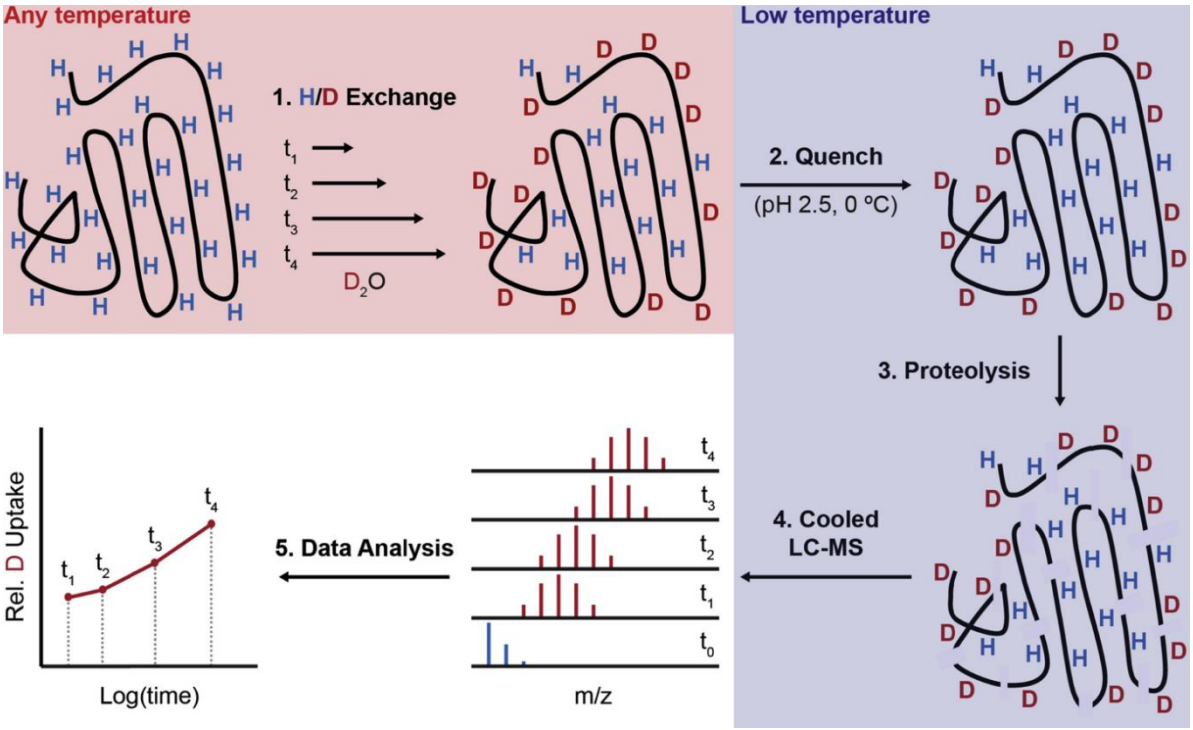

Fig 25. Workflow of a typical 'bottom up' HDX-MS is schematized. Protein is labelled by diluting in deuterated buffer (step 1), followed by quenching (step 2), proteolysis (step 3), separation of peptides (step 4) and analysis (step 5) (Trabjerg et al., 2018).

Applications of HDX-MS

HDX-MS is a powerful technique to gain information on the structural dynamics, interaction, or the folding state of proteins in solution (Pirrone et al., 2015) (Trabjerg et al., 2018) (Konermann et al., 2011). Recently, as a result of the automation, improved methodologies and technological advancements in the MS hardware and the data processing softwares, this technique is being used hand in hand with other high-resolution techniques including cryo-EM, X-ray crystallography and NMR (Engen & Komives, 2020) (Pirrone et al., 2015). The main applications are listed in fig. 26.

1. Protein-ligand/Protein-protein interaction:

Binding of ligands (including drugs, substrates), peptides, antibodies etc. may induce conformational changes in a protein or offer direct protection against HDX at the site of interaction/binding. The allosteric effect of binding/interaction in the form of conformational changes can also be seen as a difference in HDX when compared with the kinetics of the ligand/interacting partner free protein. The applications include antigen-antibody interactions (epitope mapping), receptor-drug/small molecule interaction, protein-effector/inhibitor

interaction (Pirrone et al., 2015) (Zhang et al., 2010) (Underbakke et al., 2014) (Sheff et al., 2017) (Lim et al., 2017).

2. Protein folding and structural characterization:

A classical application of HDX-MS is to study the protein folding either from a denatured state or under different conditions (Yang & Smith, 1997). Additionally, the role of chaperones in folding/unfolding of proteins has also been studied (Pirrone et al., 2015) (Bhat et al., 2017). Pulse labeling is another technique to differentiate the folded parts of protein from unfolded regions at a given instance (Wales & Engen, 2005) (Deng et al., 1999). HDX-MS has also been used to validate structures obtained from other high-resolution techniques such as cryo-EM (Maity et al., 2019) (Bardiaux et al., 2019). This technique has also been successfully employed to gain valuable structural information about a number of viral proteins belonging to hepatitis, ebola, HIV, dengue and many other viruses (Pirrone et al., 2015) (Silva et al., 2012) (Bereszczak et al., 2014).

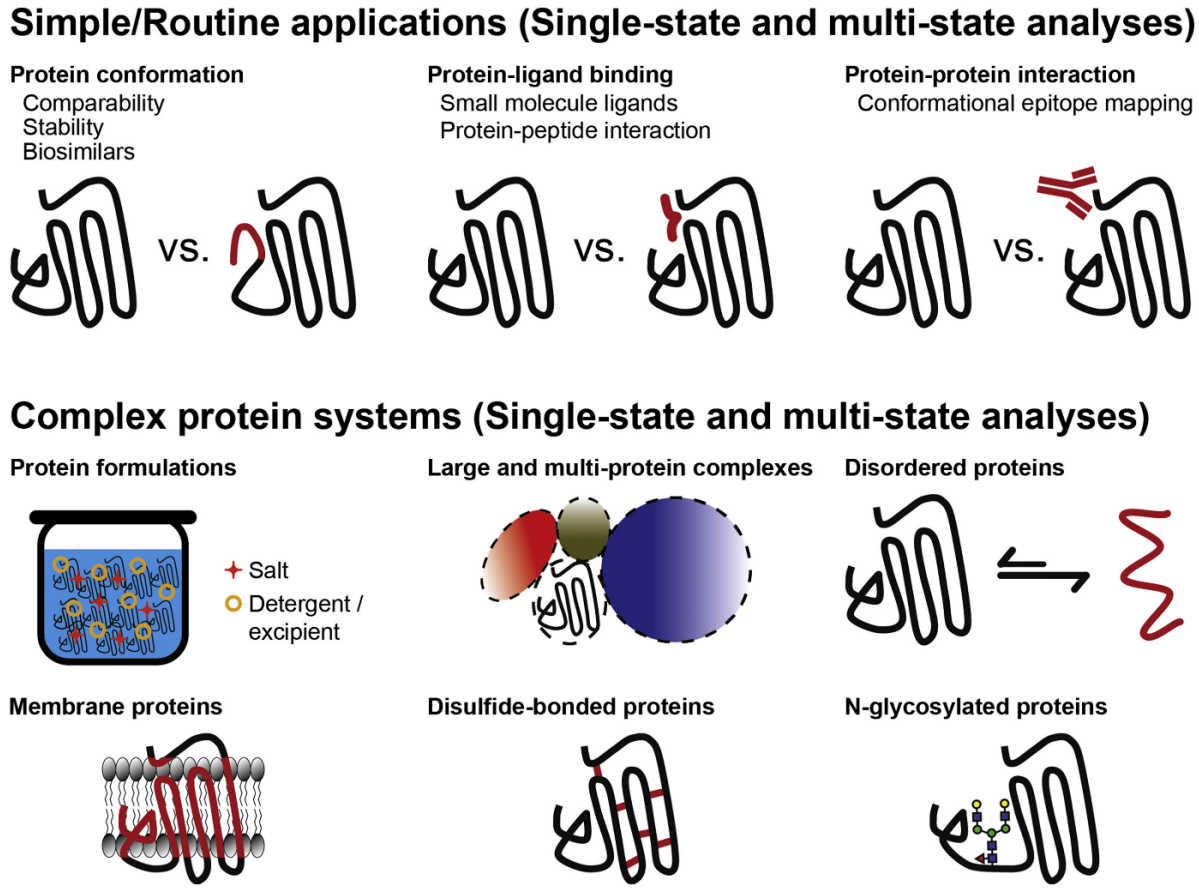

Fig 26. Applications of HDX-MS (Trabjerg et al., 2018).

3. Membrane proteins:

Membrane proteins are involved in important functions such as signal transduction, solute exchange, and in numerous metabolic pathways. Due to this reason they form the target of most of the drugs available in the market (Overington et al., 2006). However, the study of membrane proteins is a challenging task (Baker, 2010). Techniques like X-ray crystallography, NMR, and cryo-EM, that are classically used to study the high-resolution structure, often have prerequisites such as purity, stability, homogeneity, and high protein yield. Very often membrane proteins fall short of these preconditions. HDX-MS offers an alternative solution with low sample requirement and no purity issues. Another advantage of HDX-MS is its ability to probe the structural dynamics and flexibility of proteins in solution, which if combined with the static structural information obtained from other high-resolution techniques, could fill in the missing links about the functioning of proteins (Zheng et al., 2019) (Engen & Komives, 2020).

Membrane proteins, due to their hydrophobic nature, need solubilizing agents for their extraction from the membranes and to retain their solubility. Classically it is achieved using detergents but lipids containing membrane mimetics are also common including liposomes, bicelles, nanodiscs, amphipols and styrene-maleic acid copolymer lipid particles (SMALPS) (Rigaud et al., 1995) (Sanders & Prosser, 1998) (Ritchie et al., 2009) (Tribet et al., 1996) (Knowles et al., 2009). Detergents have the tendency to contaminate the liquid chromatography and MS system and often coelutes with the peptides of interest leading to signal suppression. Several methods have been developed to overcome this problem (Rey et al., 2010) (Yeung et al., 2008). Similarly, phospholipids in the membrane mimetics like nanodiscs and liposomes can shorten the life of the HPLC/UPLC column and are also incompatible with the MS. Zirconium beads, having natural affinity for the phosphate group, were shown to be quite efficient in removing the contaminating phospholipids right after the quenching reaction (Hebling et al., 2010) (Anderson et al., 2018).

The ABC exporter P-gp, solubilized in a mixture of two detergents, was studied recently using HDX-MS revealing three distinct conformations during its catalytic cycle (Kopcho et al., 2019). In another study, the role of a mutation and the mechanism of inhibition of DDM solubilized AcrB, by an efflux pump inhibitor was investigated (Reading et al., 2020). The conformational dynamics of a DDM solubilized multidrug exporter BmrA were also probed by this technique and the extraordinary flexibility of the two intracellular domains was highlighted (Mehmood et al., 2012). HDX-MS is also compatible with membrane proteins reconstituted in nanodiscs

(Martens et al., 2019) (Parker et al., 2014) (Jiarong Li et al., 2018). A rhomboid protease GlpG in SMALP nanodiscs was studied and the role of native lipids on its conformational dynamics were highlighted (Reading et al., 2017).

Native membrane mimicking 'Nanodiscs'

Nanodiscs are native membrane mimics consisting of a phospholipid bilayer held together by membrane scaffold proteins (MSPs) (fig. 27) (Denisov & Sligar, 2017). MSP is a modified form of the human serum apolipoprotein A-1 which wraps around the phospholipid bilayer as a belt, keeping the assembly in place. Several MSPs with varying sizes and affinity tags are commercially available giving rise to nanodiscs of 8-16 nm diameter (Ritchie et al., 2009). The transmembrane part of a membrane protein gets incorporated into the lipid bilayer making it soluble while the hydrophilic parts are exposed to the solvent.

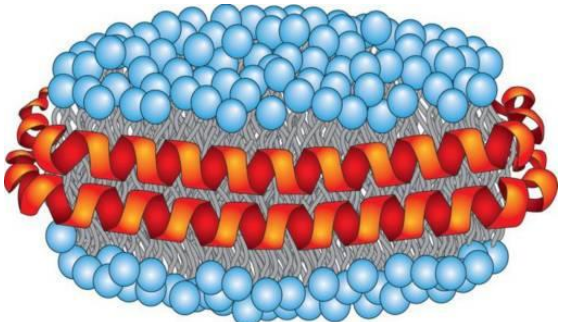

Fig 27. Schematic view of a nanodisc composed of a phospholipid bilayer encircled by two helical MSPs (Denisov & Sligar, 2017).

Nanodiscs were first introduced by Sligar's lab in 2002 (Bayburt et al., 2002). Since then, the popularity of nanodisc reconstitution for structural and functional characterization of membrane proteins has grown tremendously over the years because of several reasons. The self-assembly process of nanodiscs is very convenient and rapid and is achieved by solubilizing all the components in detergent including lipids, membrane protein and MSP, followed by the removal of detergent, either by using polystyrene bio-beads or through dialysis. Membrane proteins can be reconstituted in the nanodiscs either after purification or directly from the membranes after the solubilization in detergent (fig. 28). The diameter of the nanodiscs can be conveniently optimized according to the size of the target protein owing to the range of available MSPs, whereas, the molar ratio of MSP to the target protein can be optimized to favor the incorporation of the monomeric form of the target protein (Ritchie et al., 2009). Nanodisc technology also offers flexibility in the choice of lipids, and indeed, the influence of different lipids on the

stability and conformational dynamics of membrane proteins has been the topic of many studies (Martens et al., 2019). Another feature of nanodiscs is the accessibility from both sides of the bilayer, which is quite favorable to study the effect of ligands/effectors/inhibitors on the target protein. The high stability which is retained even at very high concentrations and the ease of concentrating, adds to the advantages of nanodiscs.

Although nanodiscs are a multicomponent system, they are compatible with a range of analytical techniques (Denisov & Sligar, 2016). The cryo-EM structure of the nanodisc reconstituted ABC transporter $LptB_2FG$ was obtained in the nucleotide free and Vi-trapped states (Li et al., 2019). At another instance, the different conformational states of the nanodisc reconstituted ABC transporter MsbA were probed by small angle scattering (SAS) (Josts et al., 2018). The compatibility of nanodiscs with HDX-MS has also been well elaborated (Hebling et al., 2010) (Martens et al., 2019) (Parker et al., 2014) (Jiarong Li et al., 2018).

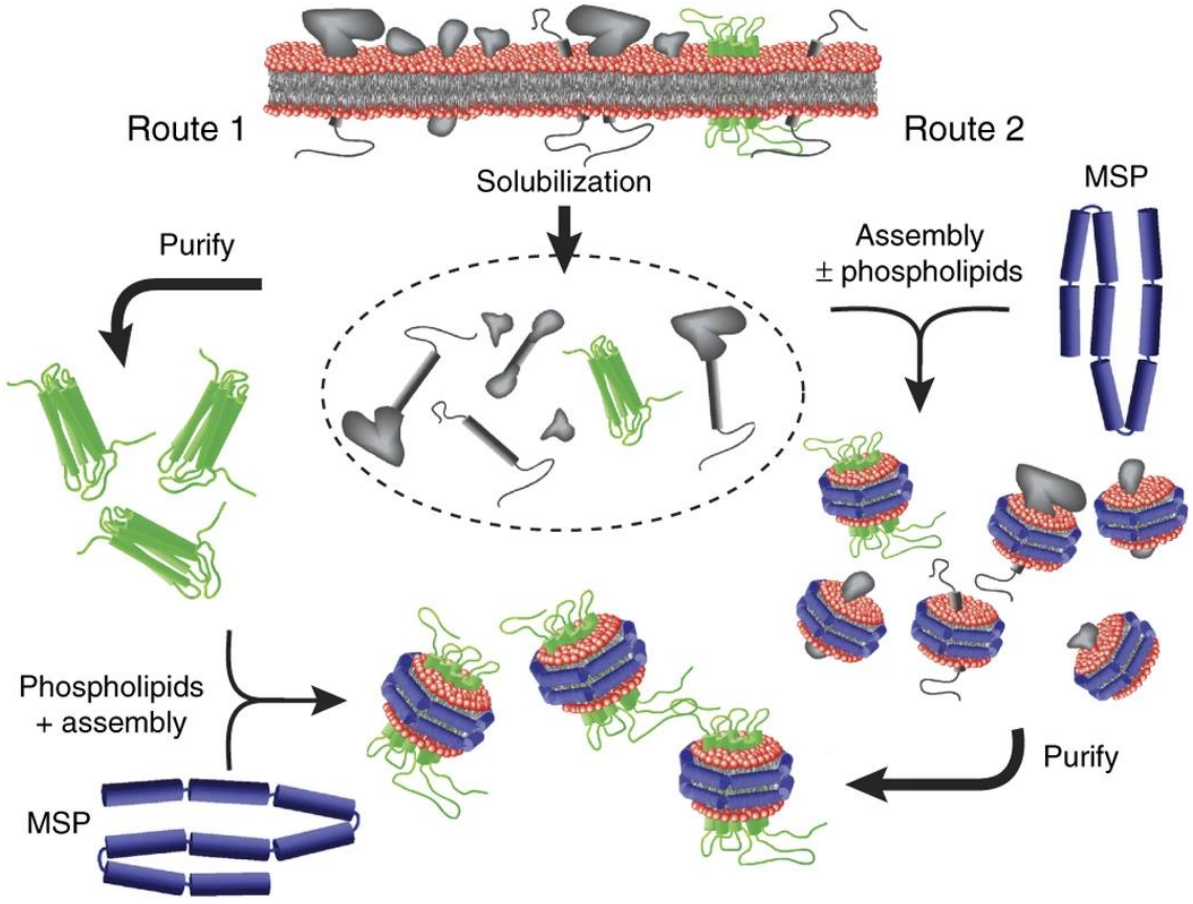

Fig 28. Schematic showing two different methods of reconstituting membrane proteins into nanodiscs. In route 1, the required membrane protein is first purified using detergent and then reconstituted in nanodiscs. In route 2, membrane proteins are directly reconstituted after solubilization in detergent and then the required reconstituted membrane protein is purified (Denisov & Sligar, 2016).

Small angle neutron scattering (SANS)

SANS is a useful technique to study the conformational dynamics of proteins in solution. It can give an estimate of the overall shape and size of the protein leading to a low-resolution structure (Jacrot, 1976) (Koch et al., 2003). It ideally complements the static structural information gained from other high-resolution techniques such as X-ray crystallography and cryo-EM. If high resolution structures or models are available, then by using modeling techniques, they could be optimized in view of the SANS in-solution data (Svergun, 2010). For membrane proteins, SANS offers an invaluable tool of contrast variation, by which, the contribution from the solubilizing agents such as detergents and lipids can be efficiently masked, to provide protein specific information (Breyton et al., 2013) (Midtgaard et al., 2018).

Scattering length density (SLD) & Contrast variation

In SANS, when neutrons interact with the atoms in a molecule, they are either absorbed or scatter coherently or incoherently. It is coherent scattering that leads to useful structural information about the target macromolecule. Neutrons are scattered by the nuclei of the atoms of all the components in a solution, including the macromolecule of interest as well as the solvent. Each component has its own neutron scattering length density (SLD) (eq. 4):

$$\rho_N = \sum b / V \qquad (4)$$

Where 'ρ_N' is the SLD, 'b' in cm, is the coherent neutron scattering by individual atoms and 'V' is volume of the target macromolecule in cm^3.

The difference between the SLD of the macromolecule of interest and the SLD of the solvent determines the 'contrast' (eq. 5).

$$\Delta\rho_N = \rho_N - \rho_{N^o} \qquad (5)$$

Where '$\Delta\rho_N$' is the difference in SLD between the SLD of the target molecule 'ρ_N' and the SLD of the solvent 'ρ_{N^o}'.

Each element and its isotopes in the periodic table has a characteristic scattering length independent of the atomic number (fig. 29) (Jacrot, 1976). Generally, scattering length (b) is positive for all the atoms including carbon, nitrogen, oxygen as well as deuterium, and ranges from 0.28 and 0.94 10^{-12} cm. However, a very useful exception is the hydrogen atom which has

a negative scattering length of -0.37 10^{-12} cm. Therefore, by controlling the ratios of light (H_2O) and heavy water (D_2O) in the solvent or by selective deuteration of the molecule of interest, the contrast can be effectively fine-tuned (fig. 29). At a specific percentage of D_2O in the solvent, the SLD of the molecule of interest will become equal to the SLD of the solvent, nulling the contrast. This is known as 'contrast match point'.

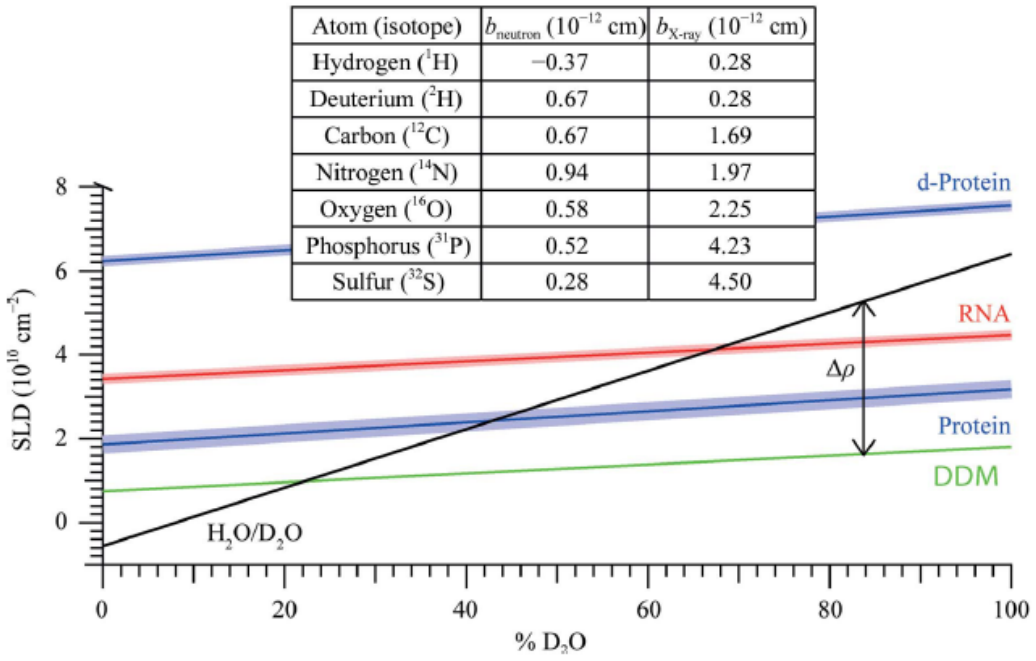

Fig 29. Scattering length densities of biological molecules shown as a function of D_2O. Inset table lists the neutron and X-ray scattering lengths of some common elements and their isotopes found in biomolecules (Mahieu & Gabel, 2018).

This is of particular interest for multicomponent systems like protein-DNA/RNA complexes, in which contribution from one component can be contrast matched, whereas selective deuteration of the other component could lead to information specific to that component. This could also be applied to membrane proteins that contain either bound or free detergent or lipid containing membrane mimetics including nanodiscs. It was demonstrated that the detergent lauryl maltose neopentyl glycol (LMNG) gets completely matched out at 21.4% D_2O in the buffer (C. Breyton et al., 2019). Although the membrane protein to be studied at this percentage of D_2O needs to be deuterated to get a reasonable contrast. Another way is to selectively deuterate the detergent so that it gets matched out at 100% D_2O, and in that case, the non-deuterated membrane protein would have an adequate contrast. This was done with octyl glucoside (OG) and dodecyl maltoside (DDM) to study five different membrane proteins (Midtgaard et al., 2018). Using the same principle, deuterated nanodiscs were prepared using selectively deuterated lipids and MSP which were contrast matched at 100% D_2O (Maric et al.,

2014). The structure of non-deuterated ABC transporter MsbA was investigated in 100% D_2O buffer using these 'stealth carrier nanodiscs' (Josts et al., 2018).

SANS technique

A simplified scheme of SANS experiment and outcome is showed in fig. 30.

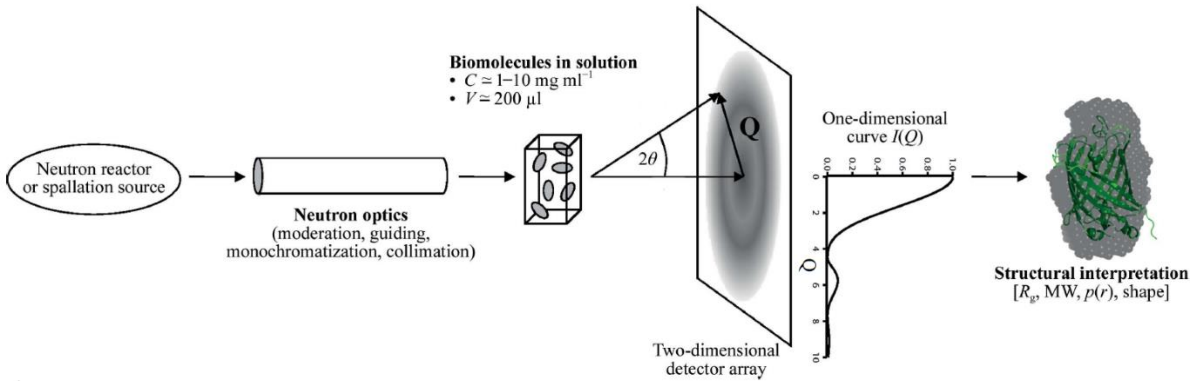

Fig 30. An overview of the SANS instrument, experiment and expected results. Fig. modified from (Mahieu & Gabel, 2018).

Neutrons are bombarded at the sample at a specific wavelength λ and are scattered in all directions by the randomly arranged molecules in solution. A 2-D curve is obtained by radially averaging the scattered intensity I measured as a function of the scattering vector Q in $Å^{-1}$. Where Q is related to the wavelength and scattering angle as follows:

$$Q = (4\pi/\lambda) \sin(\theta) \qquad (6)$$

Data analysis

The initial analysis of SANS data focuses on more classical approaches including Guinier analysis, distance distribution function $p(r)$ and kratky plot (Jacrot, 1976) (fig. 31). This provides information about the global shape of molecule, molar mass, radius of gyration (R_g) and the maximum distances within the molecule. The next step in the analysis is directed towards the modelling approaches, starting from the ab initio bead modeling to the more complex structure-based modeling (Blanchet & Svergun, 2013).

1. Guinier analysis:

The Guinier analysis is used to calculate the radius of gyration (R_g) in *nm* and the molar mass (M) in *g/mol*, by extrapolating the forward intensity I_o:

$$\ln I_Q = \ln I_o - 1/3\, R_g^2\, Q^2 \qquad (7)$$

The forward intensity (I_o) is directly related to the concentration (c) and the molar mass (M) of the macromolecule in the following manner:

$$I_o = (1/N_A)\, c\, M\, (\partial\rho_N/\partial c)^2 \qquad (8)$$

Where N_A is the Avogadro constant and $(\partial\rho_N/\partial c)^2$ is the contrast.

2. Distance distribution function *p*(*r*):

p(*r*) is the Fourier transform of the scattering intensity *I* as a function of the scattering vector *Q*. It demonstrates the probability of finding a nucleus at distance *r* from another nucleus in the macromolecule. This real space data informs about the overall shape of the molecule as well as the maximum distance D_{max}. Globular proteins have a characteristic bell-shaped curve with the maximum at $D_{max}/2$. Using the distance distribution function, one can also calculate the radius

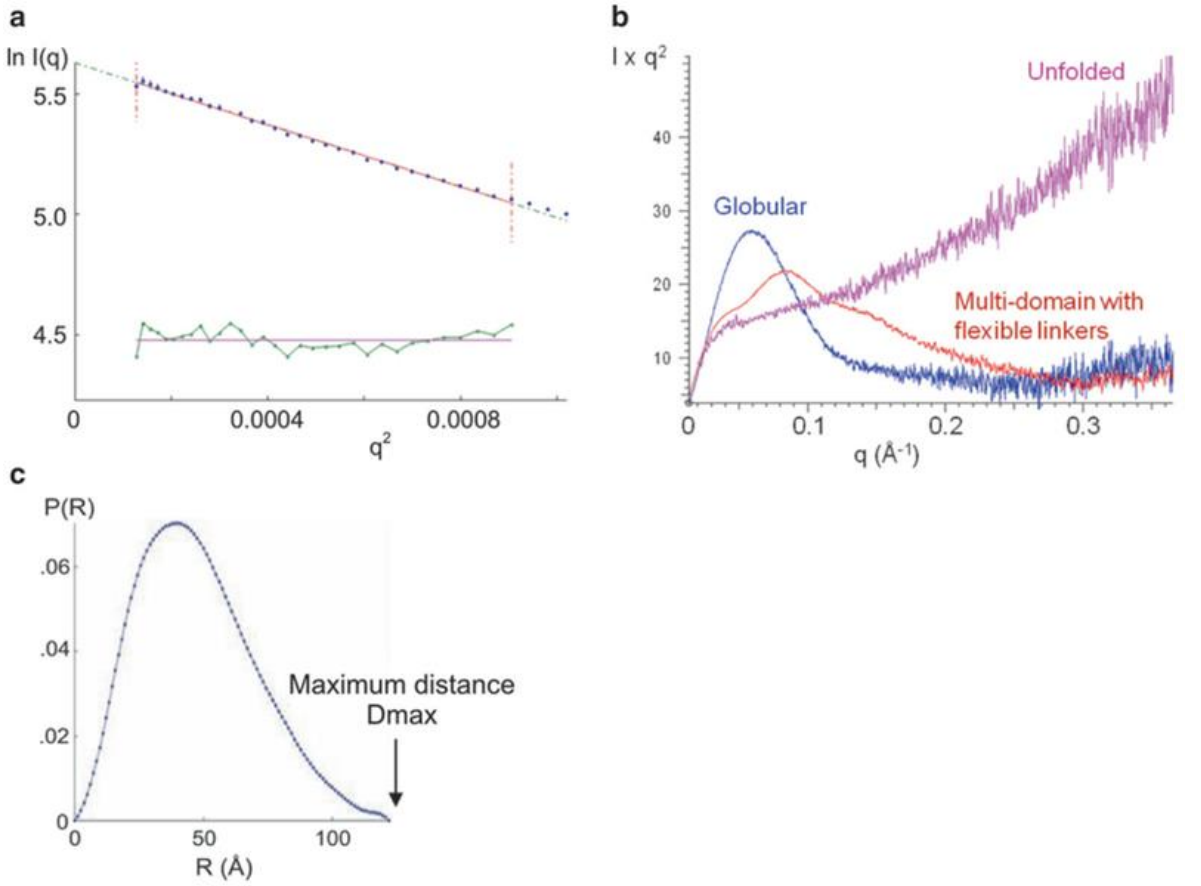

Fig 31. SANS primary data analysis. (a) Guinier plot is shown with the fit of the Guinier equation shown in red. The slope of the Guinier plot is used to calculate the radius of gyration. **(b)** Kratky plot showing characteristic curves for different types of proteins. **(c)** Distance distribution function *p*(r). The shape of the curve shown here is asymmetric with a tailing profile at higher distances, indicative of an elongated shape of the protein (modified from (Choi & Morais, 2014).

of gyration in the real space which could be compared to the one calculated by the Guinier analysis.

3. The Kratky plot:

The Kratky plot provides information about the folding state and the compactness of the protein and is represented as follows:

$$I_Q (Q)^2 \text{ vs } Q \qquad (9)$$

A globular folded protein will have a characteristic bell-shaped curve, whereas an unfolded protein will form a plateau. A multidomain protein will show a broad multi peak profile.

4. Modeling or model-based approaches:

The first step in modeling could be the 'ab-initio' construction using the ATSAS based DAMMIN or DAMMIF softwares (Franke et al., 2017). A variety of bead models are created, and their theoretical scattering curves can be calculated and compared with the experimental data. The best model gives information about the general shape of the protein. If a high-resolution structure or model of the protein under investigation is available, then its theoretical scattering curve can be calculated and compared with the experimental curve by using a software like CRYSON from ATSAS.

Another approach could be to create ensemble of structures based on available high-resolution model or structure, and then compare the experimental scattering to the theoretical scattering of each of the individual structures, to determine which generated structure or ensemble of structures fit the data. This could be achieved by using, for example, the programs SASSIE (Curtis et al., 2012).

Thesis Objective

The objective of this thesis project is to get a deep understanding of the conformational events which allow drug export from cells via ABC transporters. My aims include:

- Identification and characterization of the different conformational states of BmrA involved in drug transport
- Understand the mechanism underlying drug export
- Understand the connection and transfer of information between ATP and drug-binding site

To answer these questions, a homodimeric MDR ABC exporter BmrA (Steinfels et al., 2004), a bacterial homologue of P-glycoprotein (P-gp), will be studied. P-gp is known to be involved in MDR against cancer cells in humans (Martinez et al., 2014). To shed light on the different conformational states of BmrA involved in drug transport, mutants of BmrA (K380A and E504Q) (Orelle et al., 2008), trapped at different stages of the catalytic cycle, are to be analysed by various techniques. To gain insight into the NBD-TMD coupling, W413 mutants of BmrA, which can hydrolyze ATP but are affected in drug transport (Orelle, thesis 2004), are to be focused. Lastly, drug-bound forms of BmrA are to be studied to determine induced conformational changes and the residues involved in drug-binding.

Materials and Methods

Buffers

Buffer	Composition
Lysis buffer	50 mM Tris-HCl pH 8, 5 mM $MgCl_2$, 1 mM DTT, protease inhibitor cocktail tablet (Roche) (1 tab/50 mL)
Resuspension buffer	50 mM Tris-HCl pH 8, 1.5 mM EDTA, 1 mM DTT
Storage buffer	20 mM Tris-HCl pH 8, 300 mM sucrose, 1 mM EDTA
Solubilization buffer	50 mM Tris-HCl pH 8, 10% glycerol, 100 mM NaCl, 1 mM DTT, 10 mM imidazole, protease inhibitor cocktail tablet (Roche) (1 tab/50 mL)
Washing buffer 1	50 mM Tris-HCl pH 8, 10% glycerol, 500 mM NaCl
Washing buffer 2	50 mM Tris-HCl pH 8, 10% glycerol, 100 mM NaCl, 20 mM imidazole
Elution buffer	50 mM Tris-HCl pH 8, 10% glycerol, 100 mM NaCl, 500 mM imidazole
Dialysis buffer	50 mM Hepes pH 8, 10% glycerol, 50 mM NaCl
SANS buffer	50 mM Tris-HCl pH 8, 150 mM NaCl, 10% Glycerol, 0.01% LMNG and 21.4% D2O

Overexpression, purification and reconstitution of BmrA in nanodiscs/liposomes

Cloning of BmrA

The protein BmrA (WT, K380A, E504Q & W413F/L) was overexpressed in *E. coli* C41 (DE3) using the plasmid pET 23b containing the WT or mutated *bmrA* gene (Steinfels et al., 2004) (Orelle et al., 2003) (Orelle et al., 2008) (Orelle, thesis 2004). In all *BmrA* constructs, the hexa-histidine tag is present at the C-terminus. For the production of deuterated BrmA for SANS requiring kanamycin resistance, the following constructs were designed.

1. Construction of *pET28-WT BmrA*

BmrA gene fragment was PCR-amplified from *pET23-WT BmrA* with the primers *TataccatggcaCCAACCAAGAAACAAAAATCTAAAAGTAAATTGAA* and *CTTGTCGACCCCGGCTTT*. *WT bmrA gene* was cloned in *pET28* by using the NcoI and SalI restriction sites.

2. Construction of pET28-E504Q BmrA

The plasmid *pET28-BmrA* was digested with SalI and PstI for 3 hours at 37 °C. After electrophoresis, the 6436 pb fragment was extracted from the agarose gel. The plasmid *pET23-E504Q BmrA* was similarly digested with SalI and PstI and the 587 bp fragment was extracted. Next, a ligation with the two fragments was performed with T4 DNA ligase for 4 hours at room temperature, before transformation of TOP10 cells.

3. Construction of *pET28-K380A BmrA*

The plasmids *pET23-K380A BmrA* and *pET28-WT BmrA* were digested with StuI and SacII restriction enzymes for 1 hour at 37 °C. After electrophoresis, the smaller fragment corresponding to *K380A-BmrA* from *pET23* and the bigger fragment lacking *WT-BmrA* from *pET28* were extracted from the agarose gel. Next, a ligation with the two fragments was performed with T4 DNA ligase for 1 hour at room temperature, before transformation of TOP10 cells.

Transformation of *E. coli* C41 (DE3) competent cells with the plasmid *pET 23-bmrA*

In a microtube containing 50 µl of competent cells (*E. coli* C41 DE3), 10-30 ng of plasmid (*pET 23-bmrA* or *pet 28-BmrA*) was added which was then incubated on ice for 5 min. Thermal shock was performed at 42°C in water bath for 45 s to make the insertion of plasmid easier. The microtube was then immediately put on ice for 5 min. 200 µL of sterile LB broth was added for the recovery of bacteria and the microtube was incubated in a shaking incubator at 37°C and 180 rpm for 1 h. 20 µL of the transformed bacteria were spread on agar plate containing 100 µg/ml of ampicillin. The agar plate was then incubated overnight at 37°C.

Pre-culture and culture of bacteria transformed with non-deuterated BmrA (*pET 23-BmrA*)

For the pre-culture, one of the colonies of the transformed bacteria from the agar plate was inoculated into 250 mL sterile LB broth containing 100 µg/mL of ampicillin. The flask was then incubated at 37°C and 180 rpm overnight in a shaking incubator. The next morning, O.D. of the pre-culture was measured at 600 nm and enough pre-culture was added to 1L 2xYT medium to get an O.D. of 0.1. The flasks were then incubated at 37°C and 180 rpm until the O.D. reached 0.6. At this O.D., the over expression was induced by the addition of 0.7 mM IPTG (final concentration) and the culture was further grown for 4 h at 25°C and 180 rpm.

Afterwards, the bacterial cells were harvested by centrifugation at 5000g for 15 min at 4°C and the obtained pellet was frozen at -80°C.

Culture of bacteria transformed with deuterated BmrA (*pET 28-BmrA*)

Expression of partially deuterated ("match-out labeled") BmrA (d-BmrA) for neutron scattering was carried out by the ILL Deuteration Laboratory (D-Lab) at the Institut Laue-Langevin (ILL), Grenoble, France, according to the previously established protocols (Haertlein et al., 2016). After adaptation to growth in deuterated minimal medium C41(DE3) cells containing the expression vector pET28a with the coding sequence for wild-type or mutant BmrA (K380A or E504Q) inserted, were grown in a high-cell density fermenter culture at 30°C. The deuterated minimal medium contained 85% (v/v) D_2O and unlabeled glycerol as carbon source. During the batch and fed-batch phases, the pD was adjusted to 6.9 by the addition of NaOD (Eurisotop, France). The culture was induced with 0.5 mM IPTG at an OD_{600} of around 13 and deuterated cells (about 50g wet weight from 1-2 L of fermenter culture) were harvested after overnight expression and stored at -80°C.

Preparation of Inverted Membrane Vesicles (IMVs)

The pellet of bacteria was resuspended in lysis buffer which was then passed through Microfluidizer™ thrice at 18,000 psi to get inverted membrane vesicles. Cell debris was then removed by centrifugation of the samples at 15,000g for 30 min at 4°C. IMVs were then collected by centrifugation at 150,000g for 1 h at 4°C and were resuspended in resuspension buffer. The IMVs were centrifuged again at 150,000g for 1 h at 4°C and, afterwards, resuspended in storage buffer. IMVs were flash frozen and stored at -80°C after being divided into aliquots.

For deuterated BmrA, the difference was: bacterial pellet was resuspended with, additionally, 1 mg/mL lysozyme to facilitate cell lysis. The bacterial cells were lysed by three 5 min cycles of sonication and the membrane fraction was obtained by one ultracentrifugation only.

BmrA Purification

The hexa-histidine tagged BmrA was purified by Ni-affinity chromatography by either using 0.01% LMNG or a mixture of DDM/cholate (0.0675/0.04%). For purification in LMNG, the IMVS were solubilized in 1% LMNG, whereas for purification in DDM/cholate, the IMVs were

solubilized in 1% DDM. The final dialysis buffer contained either 0.01% LMNG or 0.035/0.01% of DDM/cholate. The general purification protocol is as follows:

BmrA enriched IMVs, at 2 mg/mL final membrane protein concentration, were solubilized for 1 h at 4 °C in solubilization buffer containing 1% detergent (either LMNG or DDM). The soluble fraction obtained after ultra-centrifugation, at 150,000 g for 1 h at 4 °C, was injected into a 1 mL HisTrap HP column (GE Healthcare), which was pre-equilibrated with the solubilization buffer containing either 0.01% LMNG or 0.0675/0.04% of DDM/cholate. The column was first washed with 3-5 column volumes of washing buffer 1, and then with 20 column volumes of the washing buffer 2, both containing either 0.01% LMNG or 0.0675/0.04% of DDM/cholate. Gradient elution was then performed with the imidazole gradient from 20 to 500 mM using elution buffer containing the relevant detergent. The protein fractions were dialyzed twice, overnight, and for 4 h the next day, at 4 °C against dialysis buffer containing either 0.01% LMNG or 0.035/0.01% of DDM/cholate. The protein concentration was determined from UV absorbance at 280 nm by using Nanodrop spectrophotometer, and a $\varepsilon 280nm=38,850\ M^{-1}.cm^{-1}$. The protein concentration was further assayed with Bradford method. Protein was stored at -80°C after flash freezing.

Deuterated BmrA Purification and SANS samples

SANS measurements were performed in two sessions, corresponding to two slightly different purification protocols. The first session was undertaken by another team member but is mentioned here because of its relevance. The initial steps of the two purifications were essentially as above, with the following modifications. The solubilization was done for 1.5 h at 4 °C in 100 mM NaPi pH 8 (session 1) or 100 mM Tris-HCl pH 8 (session 2), 15% glycerol, 100 mM NaCl, 1 mM DTT, 10 mM imidazole and 1% LMNG. The 1 mL HisTrap HP column was pre-equilibrated with 50 mM NaPi pH 8 (session 1) or 50 mM Tris-HCl pH 8 (session 2), 15% glycerol, 100 mM NaCl, 20 mM imidazole and 0.01% LMNG. The column was washed with 20 column volumes of the same buffer before the imidazole gradient. Then, the most concentrated fractions were pooled, and dialysed overnight at 4 °C against either 50 mM Hepes pH 8 (session 1) or 50 mM Tris-HCl pH 8 (session 2), 10% glycerol, 50 mM NaCl, 0.01% LMNG, before flash freezing. Then, protein was concentrated using 4 mL 100 kDa cutoff Millipore concentrator, and injected into a Superdex 200 10/300 GL SEC column equilibrated with 50 mM Tris-HCl pH 8, 150 mM NaCl, 10 % Glycerol, 0.01 % LMNG and 21.4% D_2O (SANS buffer), at a flow rate of 0.25 mL/min. The most concentrated fractions were pooled,

concentrated, and re-injected into the same column. The final samples were obtained by pooling the most concentrated fractions, filled in 1mm quartz cuvette and required ligands added for SANS measurements. Note in session 1, ligands were added before filling the cuvette, whereas in session 2, the ligands were eventually added in the cuvette after acquisition of the data for the Apo form.

1. **SANS BmrA samples measured in session 1:** WT Apo (A_{280} = 1.64); WT + 10 mM $MgCl_2$ + 10 mM ADP (A_{280} = 1.59); WT + 10 mM $MgCl_2$ + 10 mM ATP + 1 mM Vi (A_{280} = 1.55); E504Q Apo (A_{280} = 1.395); E504Q + 10 mM $MgCl_2$ + 10 mM ATP (A_{280} = 1.35).
2. **SANS BmrA samples measured in session 2:** WT Apo (A_{280} = 0.55); WT + 10 mM $MgCl_2$ + 10 mM ATP + 1 mM Vi (A_{280} = 0.54, and A_{280} = 1.21); K380A Apo (A_{280} = 0.23, and A_{280} = 0.91); K380A + 10 mM $MgCl_2$ + 10 mM ATP (A280 = 0.22); K380A + 10 mM $MgCl_2$ + 10 mM ATP + 1 mM Vi (A_{280} = 0.91).

Reconstitution of BmrA into Liposomes

Proteoliposomes were prepared as described before (Orelle et al., 2003). Briefly, 80 µl of 25 mg/ml *E. coli* phospholipid total extract (Avanti polar lipids) in water was added to 20 µl of DDM 10% and left at room temperature for 1 h under slow magnetic stirring. After 1 h, 100 µg of purified BmrA in detergent was added and the volume made up to 250 µl by 50 mM Hepes/KOH pH 8. After 45-min incubation, three successive additions of 40 mg Bio-Beads SM2 (Bio-Rad), were performed every hour, and the resulting proteoliposomes were kept at 4 °C until used.

Reconstitution of BmrA into nanodiscs

Nanodiscs were prepared as described before with a molar ratio of BmrA dimer: lipids: MSP of 1: 360: 4 (Alvarez et al., 2010). Briefly, 9.3 µl of 25 mg/ml *E. coli* phospholipid total extract (Avanti polar lipids) in water was added to 15 µl of DDM 10% and left at room temperature for 1 h under slow magnetic stirring. After 1 h, 100 µg of purified BmrA in detergent (either in LMNG or DDM/cholate) was added and the volume made up to 250 µl by 50 mM Hepes/KOH pH 8, 50 mM NaCl. After 45-min incubation, 170 mg Bio-Beads SM2 (Bio-Rad) were added and allowed to mix for 3 h at room temperature. The resulting nanodiscs were kept at 4 °C until used.

Determination of total membrane protein concentration in IMVs by the Bicinchoninic Acid (BCA) Method

BCA is a colorimetric assay for the quantification of the total protein. Proteins, in an alkaline medium, reduce the Cupric ion (Cu^{2+}) to the Cuprous ion (Cu^{1+}) which is the principle of the famous Biuret reaction. Each Cuprous ion, in turn, chelates two molecules of BCA forming a purple colored reaction product, which exhibits a strong absorbance at 562 nm, measured by a spectrophotometer. The absorbance is directly proportional to the protein concentration over a wide range of 20-2000 µg/ml of protein. The advantage of this method, over the other methods to determine the protein concentration like Lowry and Bradford, is that it is quite sensitive as well as tolerant to a wide range of detergents, lipids, and nucleic acids.

A reference range of 0-2000 µg/ml of protein was made from a standard solution of BSA (bovine serum albumin) in a 96-well flat-bottomed transparent plate. Varying amount of protein samples were added into different wells and the final volume was made up to 25 µl with the corresponding buffer (depending on the sample). The basic reagent was then prepared i.e. 0.08% Cupric Sulfate in BCA, and 200 µl of this reagent was added into each well of standard as well as the samples. The 96 well plate was incubated at 37°C for 30 min, after which the absorbance was measured with a spectrophotometer. A standard curve was plotted using the reference concentrations of BSA, from which, the protein concentration in the samples were derived.

Determination of BmrA functionality

Drug Transport Assay in IMVs

Fluorometric analysis was performed to measure the transport of a fluorescent drug doxorubicin by IMVs containing WT or mutant BmrA. As the NBDs are present on the external surface of IMVs so the drug is transported from outside to the inside of the vesicles. Once inside, the fluorescence of doxorubicin gets quenched upon binding to DNA (Guiral et al., 1994). The resultant decrease in fluorescence is recorded and analyzed by spectrofluorometer.

The 2 ml quartz cuvette containing the buffer (50 mM Hepes/KOH pH 8, 8.5 mM NaCl, 4 mM PEP, 60 µg/ml PK, 2 mM $MgCl_2$) was placed in the spectrofluorometer for 5 min to attain the required temperature (25ºC for doxorubicin assay). 100 µg of IMVs containing BmrA was then added followed by the addition of drug (10 µM doxorubicin) and fluorescence was recorded for

1-2 min. ATP was then added to a final concentration of 2 mM and fluorescence intensity was monitored for several minutes.

ATPase Activity Assay

To determine the ATPase activity of BmrA, ADP release coupled to the disappearance of reduced NADH was measured by spectroscopic analysis. The reaction involves regeneration of ATP from ADP by pyruvate kinase at the expense of PEP (phosphoenol pyruvate) which is converted to pyruvate in the process. Another enzyme, lactate dehydrogenase, catalyzes the conversion of pyruvate to lactate at the cost of NADH which is oxidized to NAD^+. Disappearance of reduced NADH is proportional to ATP hydrolysis by the transporter which can be measured by the decrease in absorbance at 340 nm. The protocol is detailed as follows:

The buffer, containing 50 mM Hepes-KOH pH 8, 10 mM MgCl2, 4 mM phosphoenolpyruvate, 0.3 mM NADH, 32 µg/mL lactate dehydrogenase, 60 µg/mL pyruvate kinase and 10 mM ATP, was added into the cuvette and was allowed to attain the desired temperature i.e. 37 °C for 5 min, before adding the protein, and measuring the absorbance at 340 nm for 20 min at 37 °C. For BmrA in LMNG, 0.01% LMNG, and for BmrA in DDM/cholate, 0.035/0.01% of DDM/cholate, was also added in the cuvette. In case of BmrA in detergent, 3 µg of protein was added, whereas, in case of BmrA reconstituted in nanodiscs or liposomes, 1 µg of protein was added for measurement.

Limited proteolysis of BmrA

Limited Proteolysis of BmrA in detergent or in nanodiscs

For the Apo condition, BmrA was diluted to 0.5 µg/µL in buffer. For purified BmrA, the buffer was the dialysis buffer supplemented with the relevant detergent, whereas for BmrA in nanodiscs, the buffer was 50 mM Hepes pH 8, 50 mM NaCl. After 15 min of incubation at room temperature, trypsin (1 µg/250 µg of protein for BmrA in detergent and 1 µg/125 µg for BmrA in nanodiscs) was added. Samples of 10 µL (5 µg BmrA) were withdrawn at 0, 2, 5, 15, 30, 60, 120, 180 and/or 300 minutes. 2.5 µL of 5% trifluoroacetic acid was added immediately to each sample to stop the reaction. 3.2 µL of Laemmli 5x was then added and the samples were placed in ice before resolving them by 12% SDS-PAGE. Before adding BmrA and incubating for 15 min at room temperature, the buffer was supplemented with either 3 mM $MgCl_2$ + 2 mM ATP or 10 mM $MgCl_2$ + 10 mM ATP, for the ATP-incubated conditions, and with 3 mM $MgCl_2$

+ 2 mM ATP + 1 mM Vi, for the Vi-incubated condition. For the drug-incubated condition, the buffer was supplemented with 100 µM drug before 15 min incubation with the protein. Samples were treated thereafter in the same way as done for the apo condition.

Limited Proteolysis of BmrA in IMVs

The overall protocol is same as for BmrA in detergent or nanodiscs. The difference is, BmrA enriched IMVS were diluted to 2 µg/µL in storage buffer. After 15 min of incubation at room temperature, trypsin (1 µg/250 µg of protein) was added. Samples of 10 µL (20 µg IMVs) were withdrawn.

Thermal unfolding

Thermal denaturation and aggregation analysis were done by differential scanning fluorimetry coupled to back scattering using the Prometheus NT.48 instrument and analyzed using the PR. thermocontrol V2.0.4. software (Nanotemper technologies, DE). The ratio of fluorescence intensity at 350 nm/330 nm was used to determine melting temperatures, T_m, and back-scattering intensity to determine onsets of aggregation, T_{agg}. All the BmrA samples were at 1-3 mg/mL in corresponding buffer eventually supplemented with ATP and /or ADP, $MgCl_2$, Vi, or drugs where specified. Samples were incubated for 15 min at room temperature after the addition of ligands before analysis.

Small Angle Neutron Scattering experiment

BmrA SANS samples were measured on ILL SANS-D22 instrument at room temperature. Samples were measured in Hellma suprasil quartz cells (Hellma, Müllheim, Germany) 100QS with 1 mm optical pathlength, using a 22-position sample changer. Scattering data were recorded at two instrumental detector/collimator configurations, 1.4 m/2 m or 1.6 m/2.8 m and 8 m/8 m, using a neutron wavelength $\lambda = 6$ A° ± 10%. At each instrumental configuration, the neutron flux reaching the sample was precisely measured, as well as the direct beam transmission, the scattering of a boron-enriched material, and the scattering and transmission of an empty cell, of the buffer and of all samples.

SANS data reduction

Data were scaled to absolute intensity I (q) in absolute scale (cm^{-1}) *vs.* q (where $q = 4\pi\sin\theta/\lambda$, 2q is the scattering angle, λ is the neutron wavelength) as follows. The neutron flux at sample position was used to calibrate scattering intensity to absolute scale. The empty beam transmission was used to set the center of the patterns and to calculate the transmission of the empty cell, the buffers, and the samples. The scattering of the piece of boron-enriched material, absorbing the totality of the beam flux, was subtracted from all other patterns because it results from ambient and electronic noise. The raw data was reduced (detector efficiency, electronic and empty cell background subtraction, angular averaging, transmission, and thickness correction) using GRASP software package (https://www.ill.eu/users/support-labs-infrastructure/software-scientific-tools/grasp/). The scattering curves measured at the two different configurations and covering different but overlapping q ranges were merged after respective buffer subtraction using SANS reduction macros written by S. Kline for Igor software (Kline, 2006). For analysis using the ATSAS suite, the resolution column and data at $q > 0.25$ $Å^{-1}$ were removed, and the q-values were expressed in nm^{-1}.

SANS data analysis

SANS data has been submitted to a classical Guinier analysis using NCNR-developped Igor Macros (Kline, 2006) and ATSAS based Primus (Konarev et al., 2003), to extract the radii of gyration (Rg) and the intensities scattered in the forward direction ($I(_0)$) of all samples. Pair distance distribution fonctions (called p(r)) were obtained using Gnom from Primus (Svergun, 1992) and SASVIEW (https://www.sasview.org). Then, they have been evaluated using Ambimeter online tool (Petoukhov & Svergun, 2015). Finally, they have been analyzed using ab initio methods.

1. Ab initio modelling

For the ab-initio modelling, the low ambiguity Vi-trapped WT in LMNG data, DAMMIN online (Svergun, 1999) was run 20 times, without symmetry constraints, to collect 20 independant bead models. The 20 DAMMIN models being very similar and uncorrelated according to CorMap (Franke et al 2015), they have been averaged using DAMAVER and the low-occurence pieces of the structure have been filtered out using DAMFILT (Volkov & Svergun, 2003). The resulting model has been refined using DAMMIN locally with

DAMSTART parameters, in expert mode, with 25 harmonics and 80 knots, and superimposed to the BmrA cryo-EM structure using SUPCOMB.

Hydrogen deuterium exchange coupled to mass spectrometry

HDX-MS of BmrA in LMNG

HDX-MS experiments were performed using an automated Hydrogen Deuterium Exchange system coupled to Synapt G2Si mass spectrometer from Waters™. The reactions were carried out by Leap HDX PAL robot (Leap tech, USA). Labeling was initiated by diluting 5.5 µL of typically 15 µM protein in 104.5 µL D_2O labeling buffer (5 mM Hepes pD 8, 50 mM NaCl, 0.01% LMNG). For the Vi-trapped and ATP-incubated conditions, the labeling buffer additionally contained 10 mM ATP, 10 mM $MgCl_2$, 1 mM Vi and 10 mM ATP, 10 mM $MgCl_2$, respectively. Prior to labeling, the samples were incubated with the respective ligands for 15 min at room temperature. Samples were labeled for 0.5 min, 2 min, 5 min, 15 min, 30 min & 60 min at 20 °C. Subsequently, the reactions were quenched by adding 22 µL of ice-cold quenching buffer to 100 µL of labelled sample at 4°C. For the WT, the quenching buffer contained 0.5 M glycine pH 2.2, 4 M guanidine-HCl and pepsin with protein to pepsin ration of 4:1 wt/wt, and digestion was done for 2 min in quenching buffer before injecting 110 µL of the quenched sample into a 100 µL loop. For K380A BmrA, the quenching buffer consisted of 0.5 M glycine pH 2.2 & 8 M guanidine-HCl and digestion was done in-line at 10°C using a pepsin column (Waters Enzymate™ BEH Pepsin Column 300Å, 5 µm, 2.1 mm X 30 mm). The resulting peptides were desalted for three minutes and trapped on a C18 precolumn (Waters™.UPLC BEH C18 Vanguard Pre-column) before separating them with a C18 column (Waters™ Acquity UPLC BEH C18 column) using a linear Acetonitrile gradient of 5-95% in 25 min. The valve position was adjusted to divert the sample after 14 min of each run from C18 column to waste to avoid contaminating the mass spectrometer with detergent. Three full kinetics were run for each condition, one after the other, to get triplicates of each timepoint. Blanks with equilibration buffer (5 mM Hepes pH 8, 50 mM NaCl) were injected after each sample injection and pepsin column washed (when present) during each run with pepsin wash (1.5 M guanidine-HCl, 4% acetonitrile, 0.8% formic acid pH 2.5) to minimize the carryover.

Electrospray ionization Mass spectra were acquired in positive mode in the m/z range of 50−2000 and with a scan time of 0.3 s. For the identification of non-deuterated peptides, data was collected in MS^E mode and the resulting peptides were identified using PLGS™ software

(ProteinLynx Global SERVER 3.0.2 from Waters™). Deuterated peptides were identified using DynamX 3.0 software (Waters™), using the following parameters: minimum intensity of 1000, minimum products per amino acid of 0.3 and file threshold of 2. A web-based application 'HDX Viewer' was used to plot the HDX data on BmrA model or structure (Bouyssié et al, 2019), which was then visualized on 'PyMOL' (https://pymol.org). Deuteros 2.0 software (Lau et al., 2020) was used for data visualization and statistical analysis.

HDX of BmrA in Nanodiscs reconstituted from BmrA in DDM/cholate

HDX-MS experiments were performed using a Hydrogen Deuterium Exchange system coupled to Synapt G2Si mass spectrometer from Waters™. All the reactions were carried out manually. Labeling was initiated by diluting 5 µL of typically 15 µM BmrA in Nanodiscs, in 95 µL labeling buffer (5 mM Hepes pD 8, 50 mM NaCl). For the Vanadate-incubated condition, the labeling buffer additionally contained 10 mM ATP, 10 mM $MgCl_2$ and 1 mM Vanadate. For the drug-bound condition, the labeling buffer additionally contained 100 µM doxorubicin. For all the ligand/drug incubated conditions, BmrA was incubated for 15 min with the specified ligand/drug before labeling. Samples were labeled for 2, 5, 15, 30 and/or 60 minutes at 20 °C. Subsequently, the reactions were quenched by adding 22 µL of ice-cold quenching buffer (0.5 M glycine, 8 M Guanidine-HCl pH 2.2, 0.035% DDM and 0.03% sodium cholate) to 100 µL of labelled sample, in ice bath. After 1 minute, the 122 µL quenched sample was added into a microtube containing 200 µg of activated zirconium magnetic beads (MagReSyn Zr-IMAC from Resyn Biosciences, USA), to remove the phospholipids (Hebling et al., 2010). After 1 minute, the magnetic beads were removed, and the supernatant injected immediately using a 100 µL loop. Labelled proteins were then subjected to in-line digestion at 15°C using a pepsin column (Waters Enzymate™ BEH Pepsin Column 300Å, 5 µm, 2.1 mm X 30 mm). The resulting peptides were desalted for three minutes and trapped on a C4 precolumn (Waters ACQUITY UPLC Protein BEH C4 VanGuard Pre-column 300Å, 1.7 µm, 2.1 mm X 5 mm, 10K - 500K) before separating them with a C4 column (Waters ACQUITY UPLC Protein BEH C4 Column 300Å, 1.7 µm, 1 mm X 100 mm) using a linear acetonitrile gradient of 5-40% in 15 min and then four alternative cycles of 5% and 95% until 25 minutes. The valve position was adjusted to divert the sample after 11.2 min of each run from C4 column to waste to avoid contaminating the mass spectrometer with detergent. Two full kinetics were run for each condition, one after the other, to get duplicate of each deuteration timepoint. Blanks, with

equilibration buffer (5 mM Hepes pH 8, 50 mM NaCl) were injected after each sample injection and pepsin column washed during each run with pepsin wash (1.5 M guanidine-HCl, 4% acetonitrile, 0.8% formic acid pH 2.5) to minimize the carryover.

Electrospray ionization Mass spectra were acquired in positive mode in the m/z range of 50−2000 and with a scan time of 0.3 s. For the identification of non-deuterated peptides, data was collected in MS^E mode and the resulting peptides were identified using PLGS™ software (ProteinLynx Global SERVER 3.0.2 from Waters™). Deuterated peptides were identified using DynamX 3.0 software (Waters™), using the following parameters: minimum intensity of 1000, minimum products per amino acid of 0.3 and file threshold of 2. A web-based application 'HDX Viewer' was used to plot the HDX data on BmrA model or structure (Bouyssié et al, 2019), which was then visualized on 'PyMOL' (https://pymol.org). Deuteros 2.0 software (Lau et al., 2020) was used for data visualization and statistical analysis.

HDX of BmrA in Nanodiscs reconstituted from BmrA in LMNG

The protocol is generally the same as for the other nanodisc preparation with few exceptions. The quenching buffer contained 0.1% DDM as detergent. The peptides after in-line digestion were desalted for three minutes and trapped on a C18 precolumn (Waters™.UPLC BEH C18 Vanguard Pre-column) before separating them with a C18 column (Waters™ Acquity UPLC BEH C18 column) using a linear Acetonitrile gradient of 5-95% in 25 min. The valve position was adjusted to divert the sample after 14 min of each run from C18 column to waste to avoid contaminating the mass spectrometer with detergent.

Results and Discussion

Chapter 1: Insight into the catalytic cycle of BmrA

BmrA is a homodimeric ABC exporter having type IV TMD fold. The most widely accepted functioning mechanism for type IV ABC transporters is the 'alternating access mechanism'. According to this mechanism, the transporter fluctuates between an inward-facing (IF) and outward-facing (OF) conformation during the transport cycle. However, the catalytic cycle and the extent of NBD separation is still a matter of debate. Therefore, to shed light on the catalytic cycle of a typical type IV bacterial ABC exporter, several biochemical and biophysical techniques were used, including limited proteolysis, nano DSF (nano Differential Scanning Fluorimetry), HDX-MS (Hydrogen Deuterium exchange coupled to Mass Spectrometry) and SANS (Small Angle Neutron Scattering). In addition to the WT BmrA, two catalytic inactive BmrA mutants, the Walker-A lysine K380A mutant and the catalytic glutamate E504Q mutant were also utilized. These mutants are hypothesized to be trapped at different steps of the catalytic cycle (fig. 32) (Orelle et al., 2008). The Walker-A lysine at 380 position in BmrA is involved in the stabilization of gamma-phosphate of ATP during nucleotide binding and sandwiches the ATP together with the C-loop. The glutamate at E504 position, on the other hand, is the catalytic glutamate that acts as a base for ATP hydrolysis (Orelle et al., 2003).

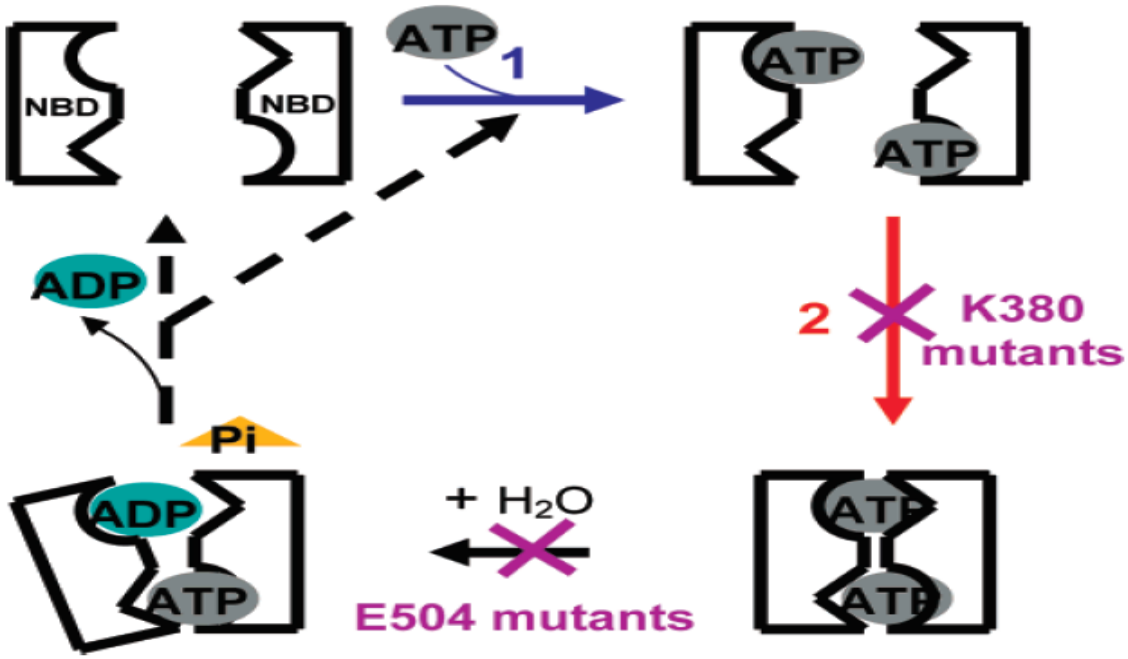

Fig 32. Schematic representation of the ATPase cycle of WT BmrA and the steps where the two mutants are arrested. ATP/Mg^{2+} binds to each of the two NBDs (step 1), inducing the dimerization of NBDs (step 2). ATP hydrolysis and products release (ADP+Pi) dissociate the NBDs and BmrA returns to its resting state. The steps impaired in the two sets of mutants, E504 and K380, are also indicated (Orelle, *et al*., 2008).

Overexpression of WT BmrA and mutants and doxorubicin transport assay in inverted membrane vesicles (IMVs)

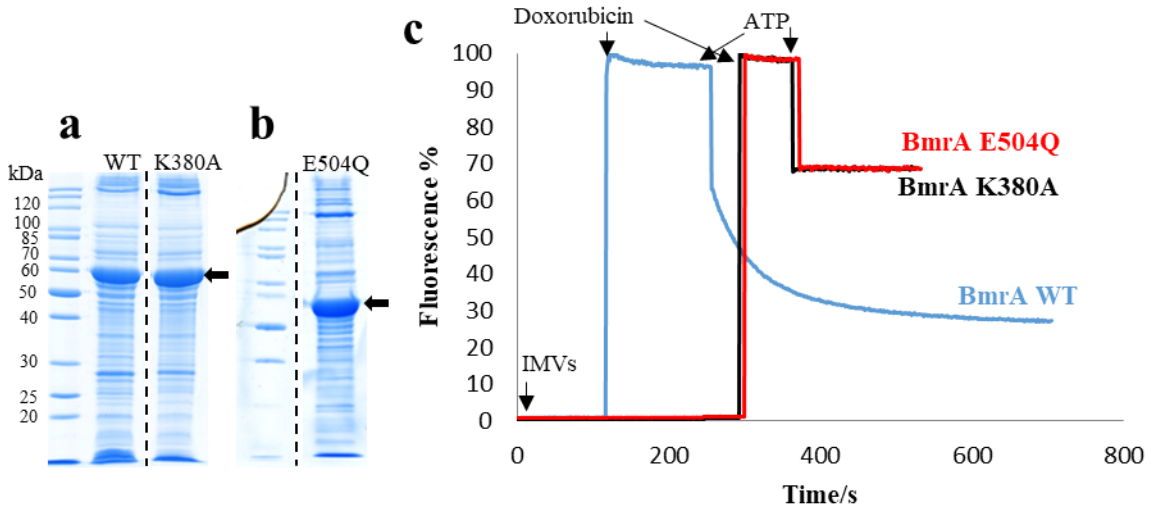

Fig 33. Overexpression of WT BmrA and mutants, and doxorubicin transport assay in inverted membrane vesicles (IMVs). SDS-PAGE stained with coomassie blue showing the overexpression of **(a)** WT and K380A BmrA mutant in IMVs and **(b)** E504Q BmrA in IMVs. The black arrows highlight the BmrA band on the gel with apparent size around 55 kDa. **(c)** Doxorubicin transport by WT BmrA and mutants. The result is representative of triplicates. The arrows indicate the addition of different components of the assay.

IMVs were prepared after the overexpression of the WT BmrA and the two catalytic inactive mutants, K380A and E504Q, in *E. coli* C41 (DE3) strain. The overexpression level is shown in fig. 33a and 33b. The functionality of the protein in IMVs was determined by the fluorescent drug transport assay using doxorubicin, known to be a substrate of BmrA (Steinfels et al., 2004). The sharp decrease in the slope, after the addition of ATP, shows that the WT BmrA is able to transport the drug, whereas the flat graph observed for the two mutants indicate their inability to transport the allocrite (fig. 33c). The sharp decrease in fluorescence right after the addition of ATP is not to be confused with transport as it is an effect of fluorescence quenching by ATP.

Limited proteolysis of WT BmrA and mutants reveals two BmrA forms in IMVs

The WT BmrA and the two mutants were subjected to limited proteolysis by trypsin, in the absence or presence of ATP/Mg^{2+} and/or Vi. Vanadate is a classical inhibitor of ATPases and traps ADP in the nucleotide-binding site (NBS) of the transporter by mimicking the gamma phosphate of ATP (Urbatsch et al, 2003).

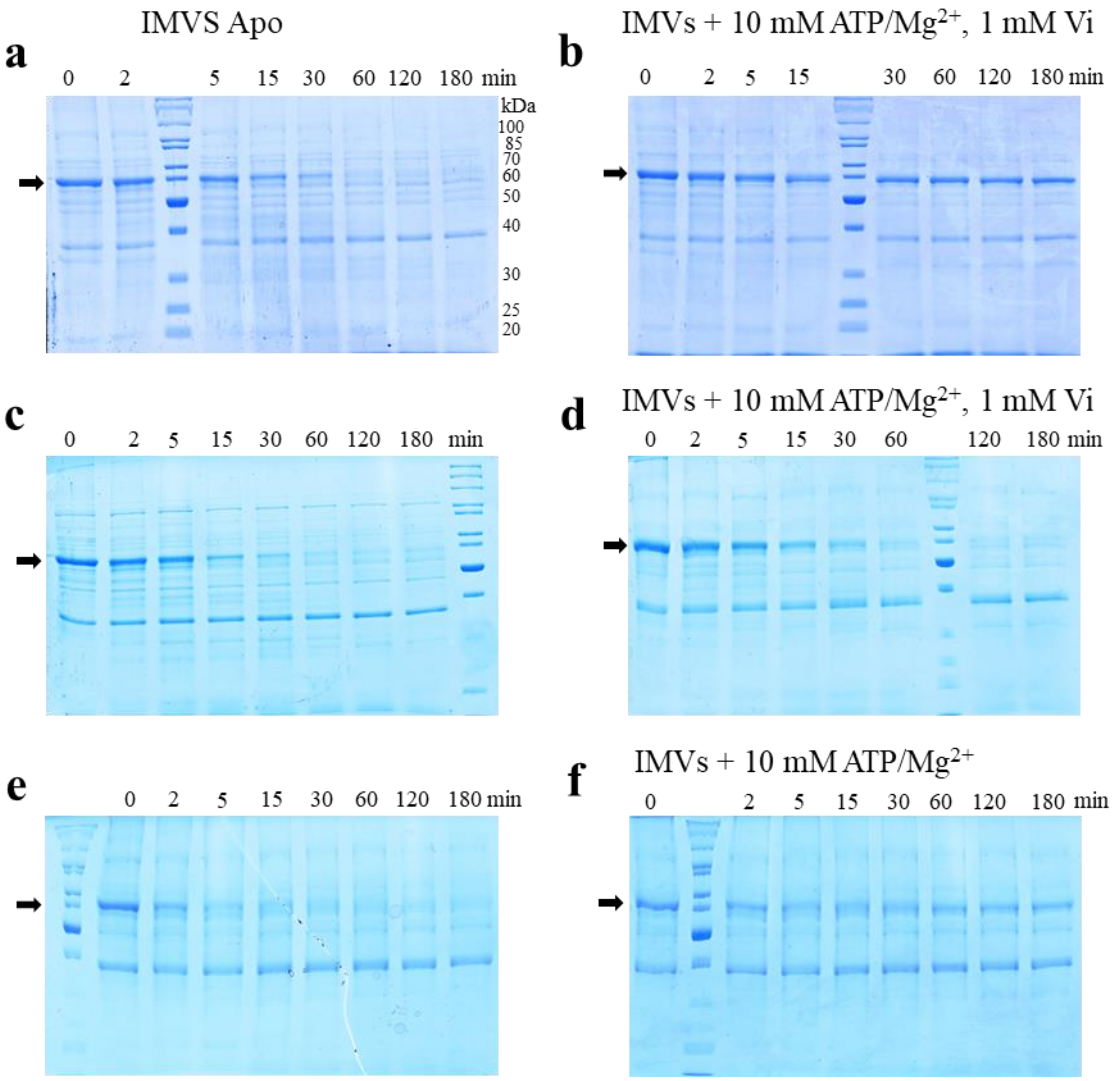

Fig 34. Limited proteolysis of BmrA in IMVs using trypsin. IMVs containing overexpressed BmrA were proteolysed in the presence or absence of mentioned ligands, for the indicated periods of time, and the digestion progress was visualized on SDS-PAGE gels stained with coomassie blue. **(a)** WT BmrA in the apo (without ligand) and **(b)** Vi-trapped condition. **(c)** K380A BmrA in the apo and **(d)** ATP/Mg^{2+}/Vi-incubated condition. **(e)** E504Q BmrA in the apo and **(f)** ATP-trapped condition. The black arrows indicate the intact BmrA band.

The disappearance of the intact BmrA band for the apo condition of the WT and both the mutants in less than 30 min, points to their flexible nature and/or a conformation in which most of the cleavage sites are quite accessible to trypsin (fig. 34a, 34c & 34e). Conversely, in the Vi-trapped condition of the WT and the ATP-trapped condition of the E504Q mutant, we see a significant protection against the action of trypsin that lasts for at least 3 hours (fig. 34b & 34f). This highlights the rigid nature of the protein in these conditions presumably reflecting a 'closed conformation' in which most of the trypsin cleavage sites are shielded. It can be inferred from

this experiment that the E504Q mutant might not need vanadate to get trapped in the 'closed conformation' and that, only ATP might be enough to induce the trapping.

Interestingly, in the case of the K380A mutant, even the presence of ATP, Mg^{2+} and Vanadate does not induce the rigid and/or 'closed conformation' in the IMVs (fig. 34d). This is evident from the disappearance of the intact BmrA band between 30 and 60 min for this condition.

WT BmrA is active in detergent or after reconstitution into nanodiscs or liposomes

WT BmrA, the K380A and E504Q mutants were purified using a range of detergents including DDM, LMNG or a mixture of DDM/Cholate. The DDM preparation will be discussed in detail in the Chapter 5 of the results so it will not be discussed in this chapter.

The purified proteins were also reconstituted into nanodiscs or liposomes from the initial detergent preparations, hence named nanodiscs DDM/cholate, if reconstituted from protein in DDM/cholate, or nanodiscs LMNG, if reconstituted from protein in LMNG. The simplified molar ratio of BmrA dimer: lipids: MSP (membrane scaffold protein) for nanodisc reconstitution was kept at 1: 360: 4 for both nanodisc preparations.

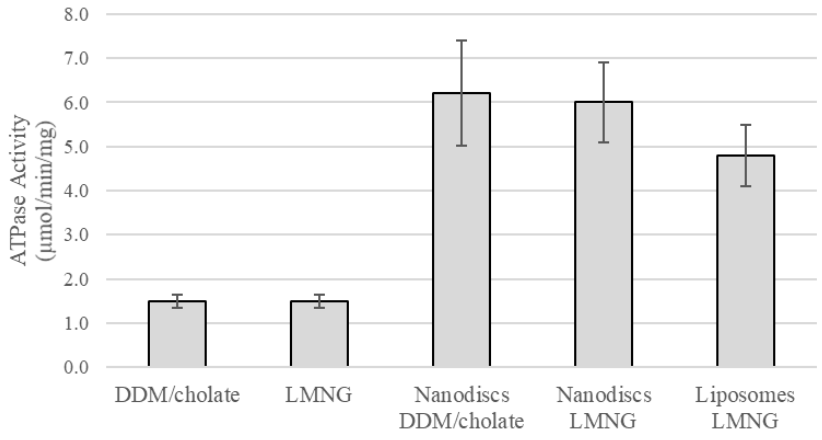

Fig 35. ATPase activity of WT BmrA after purification in detergents or reconstitution in nanodiscs or liposomes from the mentioned detergent preparations of protein. The data represents the average of triplicates for DDM/cholate and nanodiscs DDM/cholate, and seven replicates for all others. The error bars indicate the standard deviation.

The ATPase activity of WT BmrA from different detergent preparations or after reconstitution in nanodiscs or liposomes, is represented in fig. 35. The ATPase activity of the K380A and E504Q mutant was also determined but was found to be almost zero. It can be seen from the

data that WT BmrA is equally active in LMNG or DDM/Cholate mixture, however, the activity is increased three-fold after reconstitution in liposomes and four-fold after reconstitution in nanodiscs, regardless of the initial detergent preparation from which the nanodiscs were reconstituted.

Limited proteolysis reveals two global forms of BmrA in LMNG or after reconstitution in nanodiscs

Limited proteolysis was performed on WT BmrA in LMNG or in nanodiscs in the apo and Vi-trapped conditions. Note that there was no difference observed between the results of nanodiscs reconstituted from BmrA in LMNG or from BmrA in DDM/cholate. The results are very similar to what was observed in IMVs in similar conditions, i.e., a significant protection against trypsin can be seen in the Vi-trapped condition, both in LMNG as well as in nanodiscs, indicative of a compact or 'closed' conformation (fig. 36b & 36d). Whereas the protein is prone to digestion in the apo condition in both environments, pointing to a more 'flexible' or accessible conformation (fig. 36a & 36c).

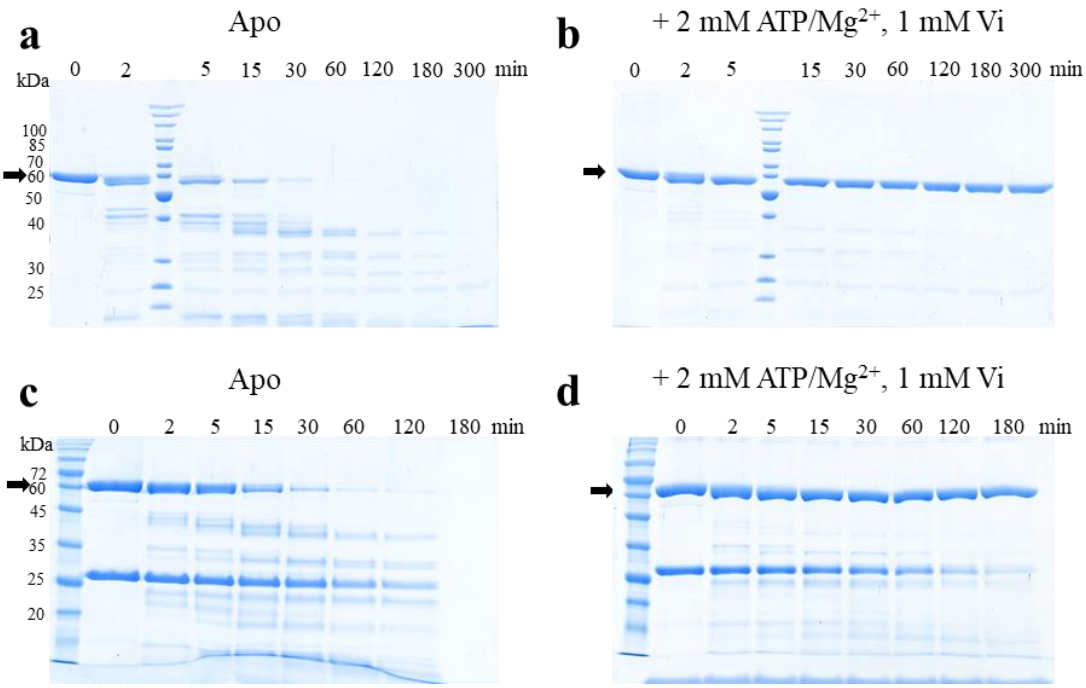

Fig 36. Limited proteolysis of purified WT BmrA in 0.01% LMNG and after reconstitution in nanodiscs, using trypsin. Purified WT BmrA in LMNG or after reconstitution in nanodiscs, was proteolysed in the presence or absence of mentioned ligands, for the indicated periods of time and the progress was visualized on SDS-PAGE stained with coomassie blue. **(a)** BmrA in LMNG in the apo condition (without ligand). **(b)** BmrA in LMNG in the Vi-trapped condition. **(c)** BmrA in nanodiscs in apo condition **(d)** BmrA in nanodiscs in the Vi-trapped condition. The black arrows indicate the intact BmrA band.

For the K380A mutant in LMNG, a slight protection against the action of trypsin is observed in the presence of 2 mM ATP/Mg^{2+}, and a more pronounced protection in the presence of higher concentration of ATP (fig. 37b & 37c). However, Vi seems to have no additional effect when present in addition to 2 mM ATP/Mg^{2+}, implying that Vi is not able to stabilize the 'closed' conformation for this mutant (fig. 37b & 37d). On the other hand, 10 mM ATP/Mg^{2+} induces a significant protection against trypsin digestion.

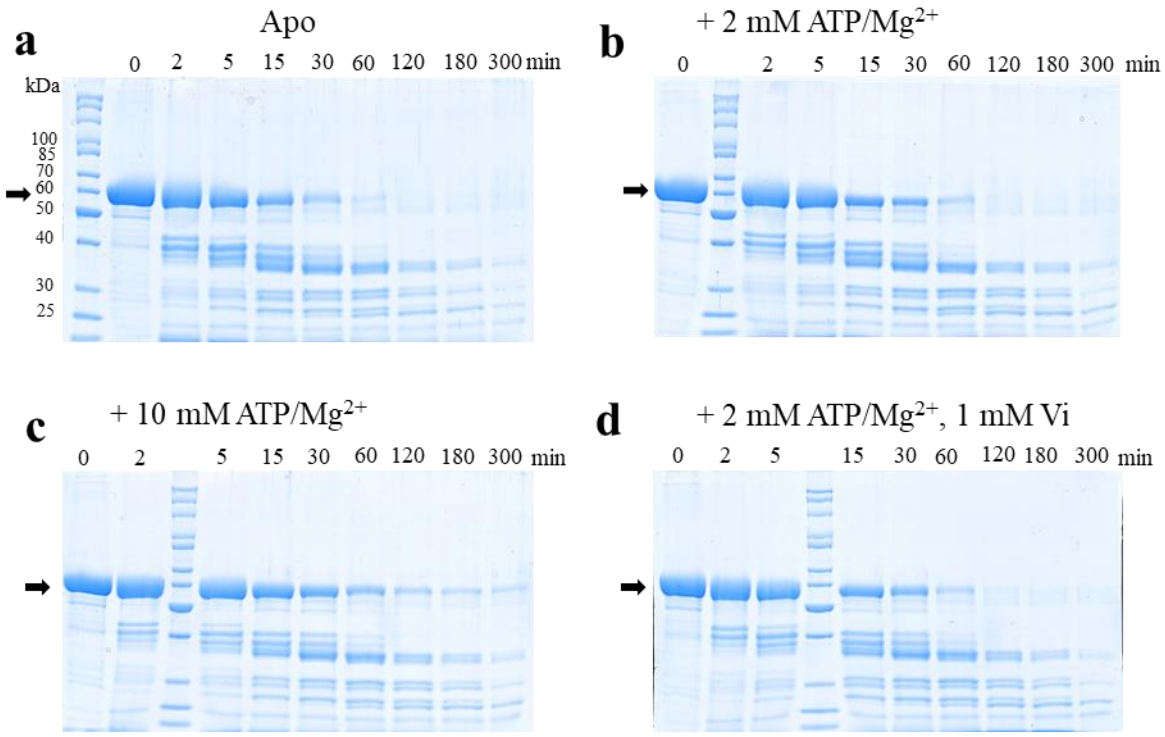

Fig 37. Limited proteolysis of purified K380A BmrA in 0.01% LMNG using trypsin. K380A BmrA was proteolysed in the presence or absence of mentioned ligands, for the indicated periods of time and the progress was visualized by SDS-PAGE stained with coommassie blue. **(a)** In the apo condition (without ligand). **(b)** After incubation with 2 mM ATP/Mg^{2+} **(c)** After incubation with 10 mM ATP/Mg^{2+} **(d)** After incubation with 2 mM ATP/Mg^{2+}, 1 mM Vi. The black arrows indicate the intact BmrA band.

Thermal denaturation of WT BmrA and mutants confirms the presence of at least two forms of BmrA

Nano differential scanning fluorimetry (NanoDSF) was used to measure the stabilizing effect of ligands on WT BmrA and its mutants. This technique measures the ratio of intrinsic fluorescence of tryptophan and tyrosine residues emitted at 350 and 330 nm wavelength. The ratio of fluorescence emitted at these wavelengths is very critical and highly depends on the immediate environment of these residues. A change in environment, for instance due to protein unfolding, would trigger a change in the ratio and then the gradient of the ratio (derivative)

could be plotted to get the melting temperature of the protein. On the same instrument there is another interesting feature of back reflection of light, that can simultaneously measure the onset of aggregation in the samples.

The ADP trapping by Vi stabilizes WT BmrA by more than 16 °C in nanodiscs and by 13 °C in LMNG, pointing towards a large change in conformation (Fig. 38a, 38b & table 2). Interestingly, when WT BmrA in nanodiscs is preincubated with ADP/Mg^{2+} and Vi, we also

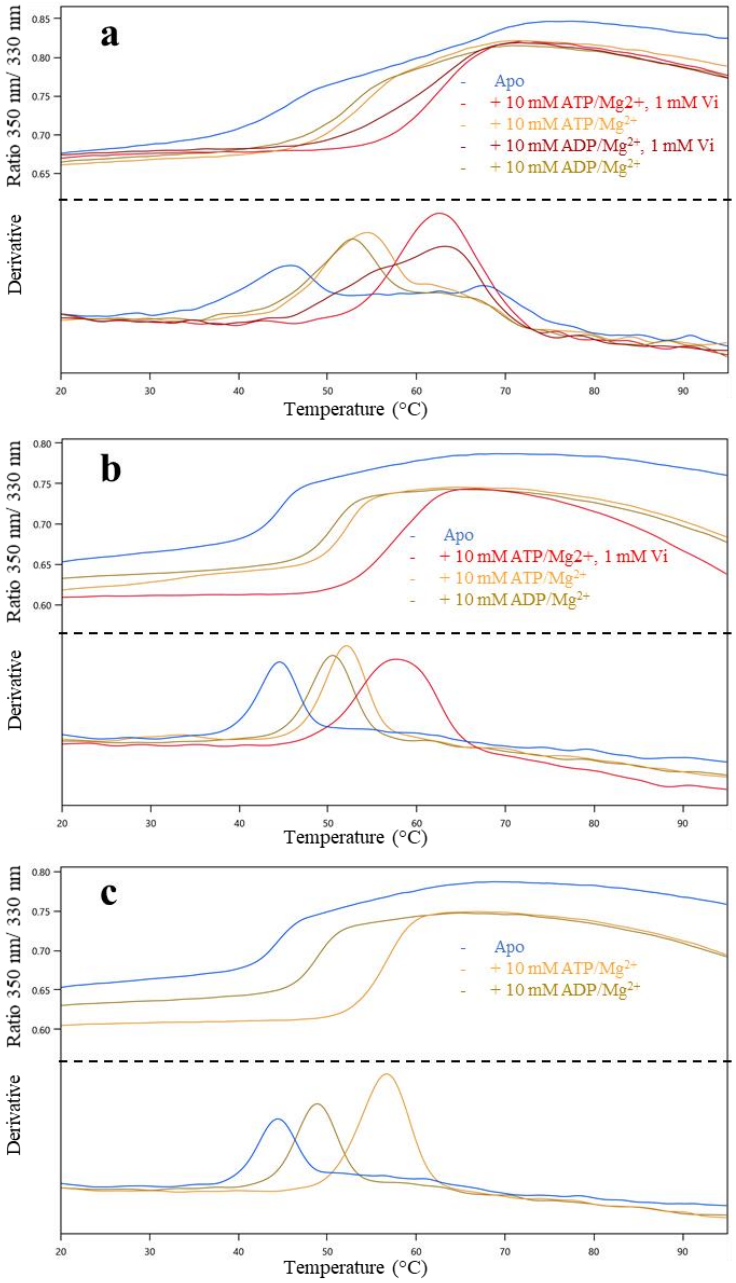

Fig 38. Melting temperature (T_m) of BmrA in the absence (apo) or presence of the mentioned ligands, recorded by nanoDSF. The upper panel in each case represents the ratio of fluorescence emitted at 350 and 330 nm, whereas the lower panel reports the first derivative. **(a)** WT BmrA in nanodiscs. **(b)** WT BmrA in LMNG. **(c)** E504Q BmrA in LMNG.

see a large shift in T_m, but a shoulder is observed at a lower temperature, hinting at the presence of a second less stable population. This shows that ADP/Mg^{2+} and Vi is less efficient than ATP/Mg^{2+} and Vi to induce the more stable 'closed' conformation of BmrA. The presence of ATP or ADP with Mg^{2+} also stabilize the WT transporter considerably but significantly less than Vi, as they are not able to trap the protein in the most stable conformation. In the presence of ATP/Mg^{2+}, BmrA is supposed to switch between the less stable IF, and the more stable OF conformation, thereby increasing the T_m.

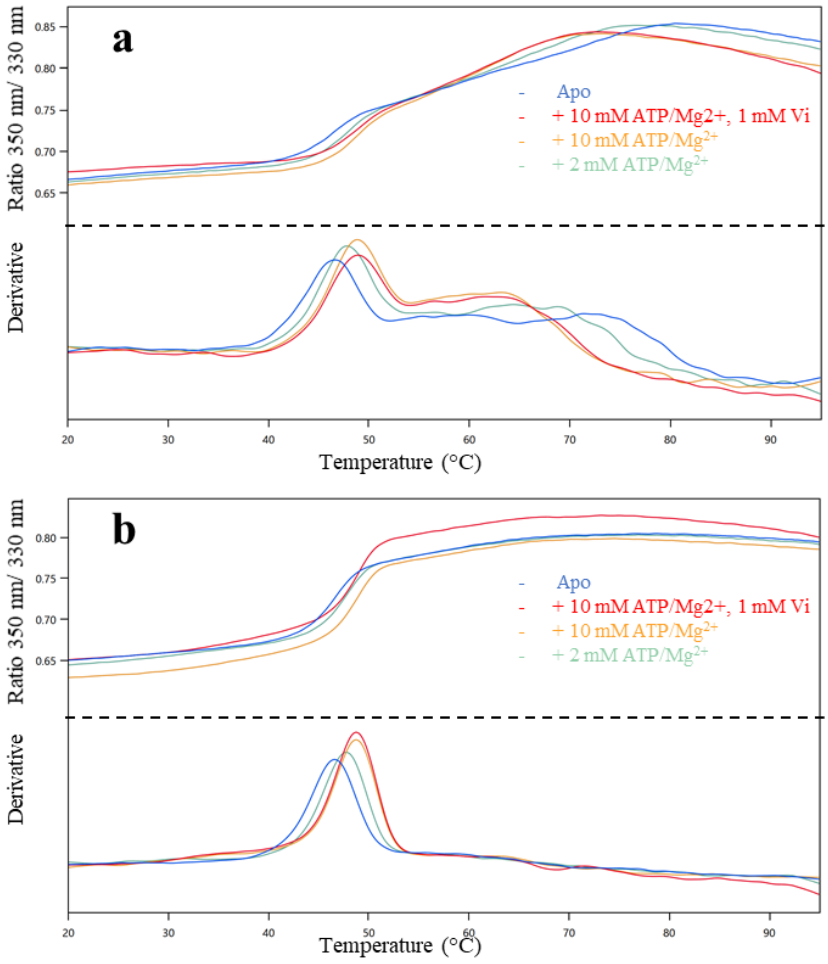

Fig 39. Melting temperature (T_m) of K380A BmrA in the absence (apo) or presence of the mentioned ligands, recorded by nanoDSF. The upper panel in each case represents the ratio of fluorescence emitted at 350 and 330 nm, whereas the lower panel reports the first derivative. **(a)** K380A BmrA in nanodiscs. **(b)** K380A BmrA in LMNG. The data is representative of triplicates having standard deviations of typically 0.1°C for T_m, and 1°C for T_{agg}.

In the case of the catalytic glutamate mutant (E504Q), ATP/Mg^{2+} only is sufficient to increase the T_m by more than 12 °C, which is equivalent to the Vi-trapped condition of the WT (fig. 38c & table 2). This is because the E504Q BmrA is catalytically inactive and was hypothesized to

get trapped in the OF conformation in the presence of ATP (no turnover is necessary). The change in T_m by a mere 4 °C by the addition of ADP/Mg^{2+} proves that ADP/Mg^{2+} only is not sufficient to trap E504Q in the more stable 'closed' conformation.

Protein	Condition	Ligand concentration (mM)	T_m (°C)	T_{agg} (°C)
WT BmrA in Nanodiscs	Apo		45.6	76
WT BmrA in Nanodiscs	ATP/Mg^{2+}/Vi	10/10/1	62.5	60
WT BmrA in Nanodiscs	ATP/Mg^{2+}	10/10	54.3	62
WT BmrA in Nanodiscs	ADP/Mg^{2+}	10/10	52.8	60
WT BmrA in Nanodiscs	ADP/Mg^{2+}/Vi	10/10/1	63.0	60
WT BmrA in LMNG	Apo		44.5	64
WT BmrA in LMNG	ATP/Mg^{2+}/Vi	10/10/1	57.8	52
WT BmrA in LMNG	ATP/Mg^{2+}	10/10	52.0	52
WT BmrA in LMNG	ADP/Mg^{2+}	10/10	50.5	56
E504Q BmrA in LMNG	Apo		44.4	64
E504Q BmrA in LMNG	ATP/Mg^{2+}	10/10	56.6	54
E504Q BmrA in LMNG	ADP/Mg^{2+}	10/10	48.8	60
K380A BmrA in LMNG	Apo		46.5	66
K380A BmrA in LMNG	ATP/Mg^{2+}/Vi	10/10/1	48.7	54
K380A BmrA in LMNG	ATP/Mg^{2+}	10/10	48.7	52
K380A BmrA in LMNG	ATP/Mg^{2+}	2/3	47.7	56
K380A BmrA in Nanodiscs	Apo		46.5	70
K380A BmrA in Nanodiscs	ATP/Mg^{2+}/Vi	10/10/1	48.9	60
K380A BmrA in Nanodiscs	ATP/Mg^{2+}	10/10	48.9	56
K380A BmrA in Nanodiscs	ATP/Mg^{2+}	2/3	47.9	65

Table 2. Melting temperature (T_m) of WT BmrA and mutants, either in the absence (apo) or presence of the mentioned ligands, measured by nano-DSF. The onset of aggregation temperature is also listed which was measured by the back reflection of light. All experiments were done in at least triplicate having standard deviations of typically 0.1°C for T_m, and 1°C for T_{agg}.

The T_m results for the K380A BmrA mutant show that it cannot be trapped in the most stable 'closed' conformation even in the presence of Vi (fig. 39a, 39b & table 2). However, we do

observe a slight increase in T_m with increasing concentrations of ATP. This might be a result of mere binding of ATP resulting from local effects at the level of NBDs, the probability of which increases with higher concentration of ATP.

Small Angle Neutron Scattering (SANS) reveals several types of mean conformations for BmrA in solution

SANS experiments were designed to investigate BmrA conformations in LMNG for the WT and the two mutants, K380A and E504Q, that are hypothesized to be trapped at different steps of the catalytic cycle. The contrast match point (CMP) of LMNG micelles is 21.4 % D_2O, meaning that at this percentage of D_2O in buffer, the SANS signal from LMNG is efficiently masked, getting structural information about the protein of interest only (Breyton et al., 2019). However, the CMP of hydrogenated BmrA is ≈ 38 %, which is quite close to that of LMNG (21.4%), so to increase its contrast, selective deuteration of BmrA was undertaken. It was achieved by over-expression in a deuterated minimal media containing 85 % D_2O and unlabeled glycerol as carbon source. The theoretical CMP of the deuterated BmrA is 100% D_2O, providing a significant contrast at 21.4% D_2O.

The SANS data of the three deuterated proteins in LMNG at ≈ 2 mg/mL (WT, E504Q and K380A BmrA) was recorded in absence (apo) or presence of ligands (ATP/Mg^{2+}, ADP/Mg^{2+}, or ATP/Mg^{2+}/Vi). These ligands are known to induce conformational changes in BmrA. The protein buffer contained 21.4% D_2O, at which LMNG is invisible to the neutrons. The resulting SANS data therefore provided information concerning the shape of the protein only, within the protein detergent complex.

From a first glance at the raw scattering curves (Figure 40a), their flatness for all samples at low angle, indicates the absence of aggregation. From the Guinier plot of each sample (40b), the radius of gyration, Rg, was calculated. The Rgs are in the same range (44-45 Å) for the three constructs (WT, K380A, E504Q) in the apo condition, indicative of similar conformations (table 3). The Rgs are significantly lower (40-42.5 Å) for the Vi-trapped condition of WT and ATP-trapped condition of E504Q mutant. This shows that the WT and the E504Q mutant adopt a compact conformation under these conditions. WT BmrA in the presence of ADP/Mg^{2+} and K380A BmrA in the presence of ATP/Mg^{2+}, show intermediate R_g, indicative of indermediate conformations.

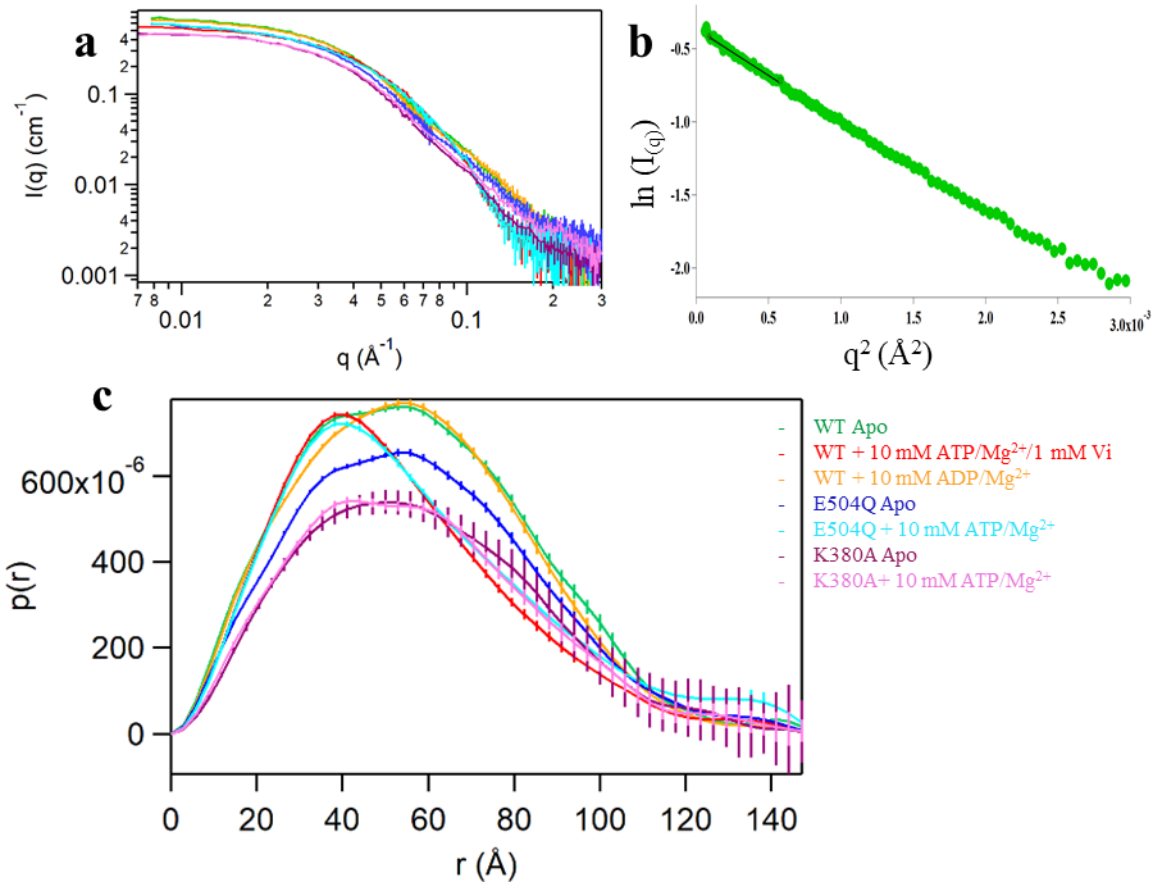

Fig 40. SANS data and plots. (a) Raw SANS curves of deuterated WT BmrA and mutants, in the absence or presence of the mentioned ligands. **(b)** The Guinier plot of WT BmrA in apo condition. The black line defines the q range used to calculate the R_g. **(c)** The Pair distance distribution functions of the WT BmrA and mutants. The color scheme for all the panels is kept same. Note that *p*(r) is not normalized according to the concentration.

The pair distance distribution functions, *p*(r), calculated as the Fourier transform of the scattering data, provide information about the general shape of the molecule. The largest distance within the macromolecule, D_{max}, is determined as the large distance at which *p*(r) tends to be null. A globular compact protein will present a well-defined maximum at about $D_{max}/2$, while the presence of shoulders or asymmetric *p*(r) is indicative of non-globular shapes.

The *p*(r) of the various BmrA samples clearly show different mean conformations. The Vi-trapped form of WT (red) and ATP-trapped E504Q (cyan) display very similar *p*(r), with a maximum at ≈ 38Å, i.e., more populated for the smallest internal distances, indicating the presence of a very compact 'closed' conformation (fig. 40c). This means that the E504Q mutant does not need Vi to reach the closed conformation. All other BmrA samples show broader *p*(r)

BmrA construct	WT			E504Q		K380A	
Ligand	-	ADP/Mg^{2+}	ATP/Mg^{2+}/Vi	-	ATP/Mg^{2+}	-	ATP/Mg^{2+}/Vi
R_g (Å)	44.3 ± 0.2	43.8 ± 0.3	40.3 ± 0.3	45.0 ± 0.3	42.5 ± 0.4	45.7 ± 0.5	44.1 ± 0.4

Table 3. Radii of gyration (R_g) of WT BmrA and mutants, in the absence or presence of ligands, obtained from the Guinier analysis.

distributions, with the appearance of another maximum at ≈ 53 Å compatible with a non-compact shape. The *p*(r) of WT and E504Q BmrA in the Apo form (green and blue curves, respectively) are undistinguishable. The *p*(r) of ADP-bound WT BmrA (yellow) is slightly but significantly different from that of the apo form, suggesting a more open mean conformation, although the R_g of ADP-bound WT BmrA was found to be less than that of the apo form. This means that in the presence of ADP/Mg^{2+}, the WT BmrA exists predominantly in a slightly open conformation, but at the same time, this open conformation is more compact than the average open conformations observed in the apo form. In short, the WT in apo form might exist in several conformations ranging from more open to closed, whereas, binding to ADP might shift the equilibrium to a less open conformation. In case of K380A mutant, the presence of Vi (light pink curve) does not induce the 'closed' conformation as observed in the case of Vi-trapped WT. However, it does show a comparatively compact intermediate conformation as compared to its apo form (purple).

Reconstructing the ab initio 3D shape of the protein from its scattering curve is a common technique. However, the small angle scattering data is often ambiguous, meaning that several shapes can lead to the same scattering curve. To estimate the level of ambiguity of the scattering curves of BmrA samples, the ATSAS based web application "Ambimeter" was used. The results showed that the SANS data on all the BmrA samples was ambiguous except for the Vi-trapped WT. Therefore, an ab-initio reconstruction was initiated only for this data set. The resulting envelope obtained using the ATSAS based program DAMMIN, is shown in fig. 41, superimposed with the closed OF conformation of the cryo-EM structure of ATP-trapped E504A BmrA (recently solved, unpublished result), which fits rather well. This indicates that, in solution, the ATP-trapped E504A/Q BmrA mutant and the Vi-trapped WT BmrA, might exist in a similar 'closed' OF conformation.

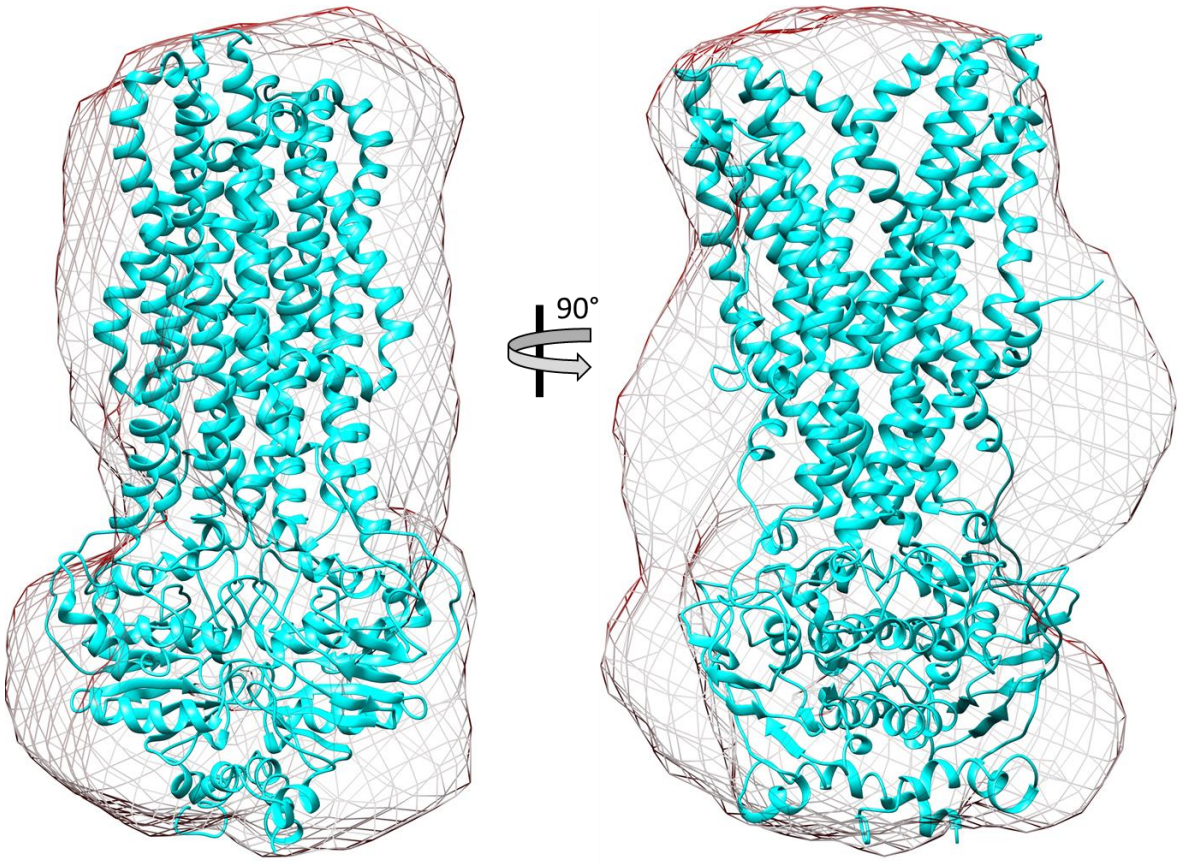

Fig 41. Vi-trapped WT BrmA SANS data fits the cryo-EM BmrA structure. Superimposition of the cryo-EM structure of E504A BmrA (PDB: 6R81) in the presence of ATP/Mg^{2+} (cyan ribbon) and the *ab-initio* reconstruction from SANS data of WT BmrA in the presence of ATP/Mg^{2+}/Vi (mesh).

Hydrogen Deuterium Exchange coupled to Mass Spectrometry (HDX-MS) confirms the presence of different conformations of BmrA in solution

Hydrogen Deuterium exchange (HDX) coupled to mass spectrometry is now a well-established technique to study the structural dynamics of membrane proteins. It can probe the conformational changes, solvent accessibility and secondary structural elements within a protein. Labelling is initiated by incubation in a deuterated buffer followed by a rapid quenching of the exchange reaction. The partially deuterated protein is then digested by a protease, and the fragments analyzed by mass spectrometry, to identify the specific peptides that exchange with deuterium. A significant protection against HDX is measured for hydrogen amides involved in strong hydrogen bonds (i.e. secondary structure), in protein-protein contacts, or for amides buried inside the hydrophobic core of proteins. Importantly, upon interaction of a protein with another compound (e.g. substrates, inhibitors or effectors), a protection against

HDX is observed at the binding site, or distant sites involved in allosteric interaction, allowing for the delineation of the residues involved in this interaction.

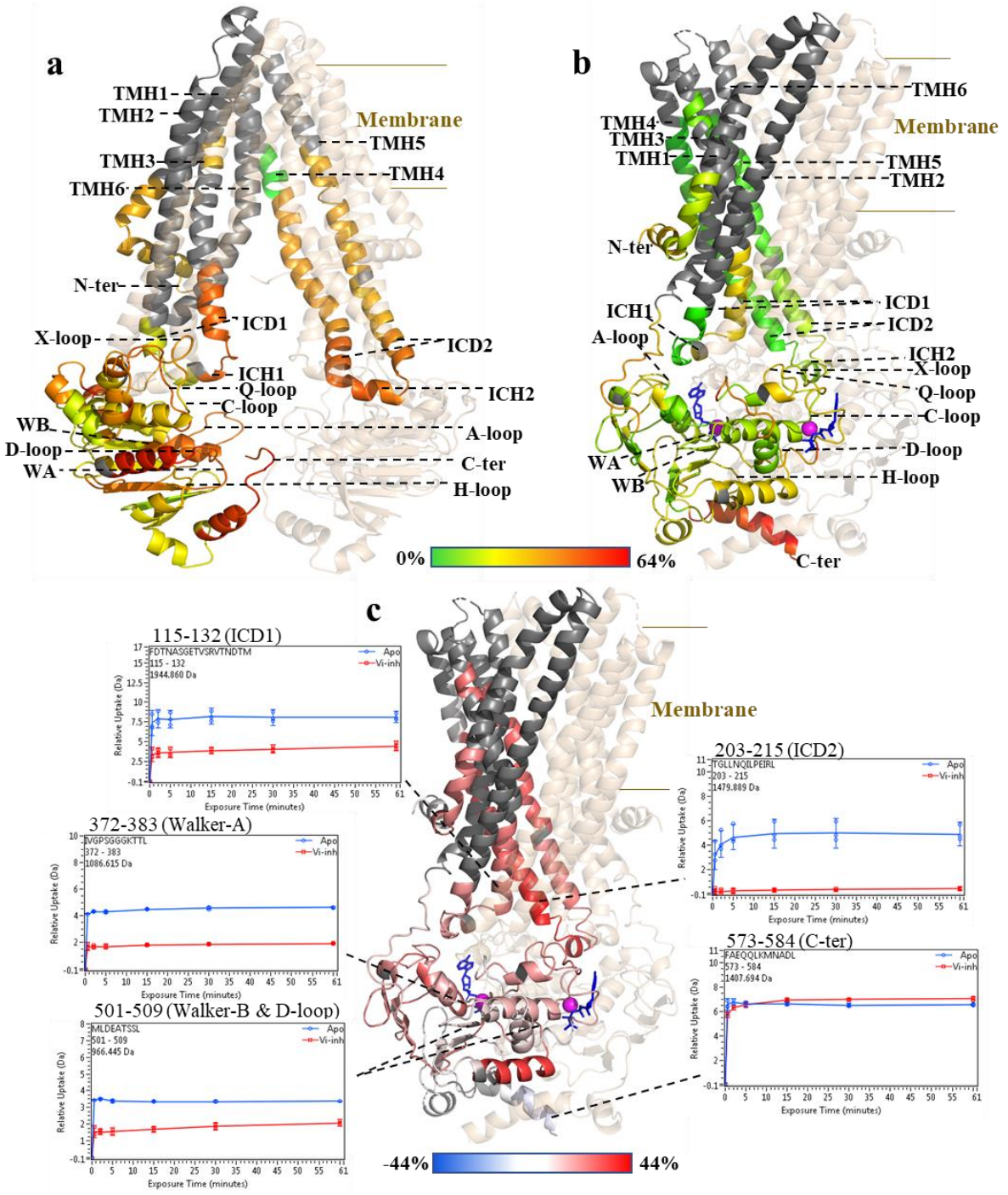

Fig 42. Hydrogen Deuterium Exchange (HDX) of WT BmrA in LMNG in two different conditions after 1-hour deuteration. **(a)** HDX data of WT BmrA in apo condition (without ligand) is plotted on a homology model of BmrA based on the inward-facing (IF) structure of mouse P-gp (PDB: 3WME). **(b)** HDX data of WT BmrA in the Vanadate trapped (Vi-trapped) condition is depicted on the cryo-EM structure of E504A BmrA mutant (PDB: 6R81). One BmrA monomer in each case is colored in translucent wheat, whereas the second monomer in green, yellow, orange and red, with a deuteration scale of 0 to 64%. 64% was the maximum percentage deuteration observed in these conditions. The TMHs and the

conserved sequences in the NBDs are labelled. The bound ATP molecules are shown in blue while the magnesium ions are shown in magenta. **(c)** The differential deuterium uptake between the apo and the Vi-trapped condition of WT BmrA is mapped on the cryo-EM structure of E504A BmrA. The differential deuteration scale is set from -44% to 44%, which was the maximum differential HDX observed, represented by the colors blue, white and red. Blue signifies the peptides that show less deuteration in the apo condition. White highlights the peptides with no difference in deuteration level between the two conditions, whereas red pinpoints the peptides that get protected from deuteration in the Vi-trapped condition. The box inserts show, in dalton, the relative deuterium uptake in the apo (blue) and Vi-trapped (red) conditions, of some important peptides. The error bars in the inserts show the standard deviation between the triplicates with sigma multiplier '2'. Abbreviations: C-ter, C-terminal; ICD, intracellular domain; ICH, intracellular helix; NBD, nucleotide-binding domain; N-ter, N-terminal; TMH, transmembrane helix; WA, Walker-A; WB, Walker-B.

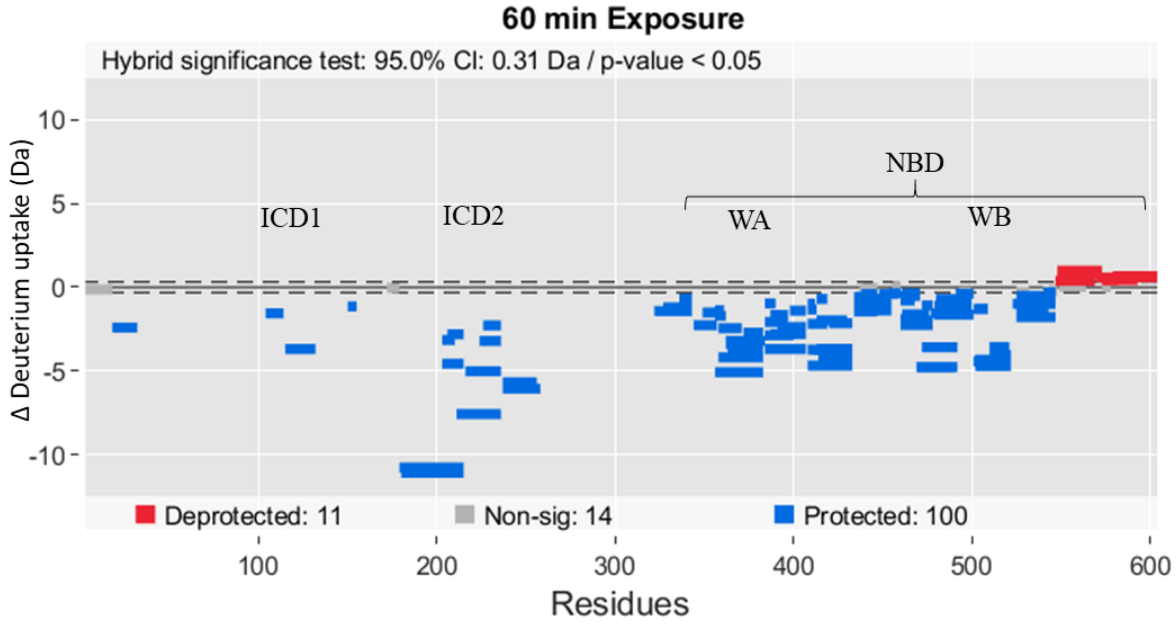

Fig 43. Differential HDX plot of WT BmrA in LMNG between the Apo and Vi-trapped conditions at 60 min D_2O exposure. Blue signifies the peptides protected against deuteration in Vi-trapped condition, whereas red signifies the deprotected peptides. Grey represents peptides with HDX below the 95% confidence interval shown by dotted lines and having p-value more than 0.05. All measurements were done in triplicate.

HDX was performed on WT BmrA and mutants in LMNG or after reconstitution in nanodiscs with the aim to get structural insights into the catalytic cycle of BmrA. There was no significant difference observed between the two nanodiscs preparations mentioned earlier (reconstituted from the protein in LMNG or from the protein in DDM/cholate). So, the results from nanodiscs reconstituted from the protein in DDM/cholate would be discussed here due to the higher sequence coverage obtained in this condition (fig. 45). The sequence coverage maps of all the other conditions, together with the uptake plots, are provided in annex.

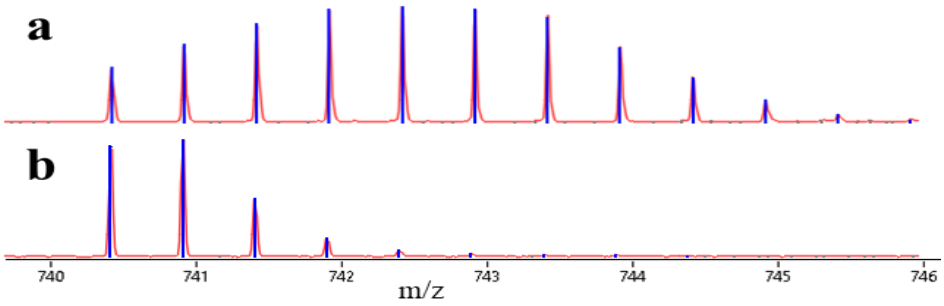

Fig 44. Isotopic envelope of the peptide 203-215 from ICD2 (charge state 2^+), after 30s deuteration in the (a) apo condition and, (b) after incubation with ATP/Mg^{2+}/Vi. Waters™ synapt G2-Si mass spectrometer was used to acquire the data.

As seen in fig. 42a, WT BmrA in LMNG shows an overall high deuterium uptake in the apo condition. A very high deuterium uptake can be observed in the D-loop region, C-terminus, the peptide 408-412 (adjacent to W413), at the level of NBD, and both the ICDs at the level of TMD, just after 30s deuteration (see box inserts in fig. 42). In the NBD, in addition to flexibility, the high deuterium exchange can be directly linked to the high solvent accessibility, as all of the peptides showing high exchange face the solvent in the model. The high exchange observed in the ICDs, especially ICD2, however, seems to be due to the highly flexible nature of this part of the protein. Another prominent feature observed in ICD2 is the big standard deviation in the triplicates. This also points to its flexible or accessible nature. The isotopic envelopes of most of the peptides in ICD2 in the apo condition, are observed to be widespread (fig. 44). This might indicate the presence of several populations concerning this region. In the whole transporter, the only peptide that is well protected from exchange even after 1-hour deuteration in the apo condition, lies in the TMH4 and possibly buried deep in the hydrophobic core of the protein surrounded by the detergent belt. On the other hand, in the Vi-trapped condition of WT, we observe a significant overall protection against deuteration even after 1-hour deuteration (fig. 42b). The only peptide in the covered region, that exchanges very quickly with deuterium, lies at the solvent accessible and possibly unstructured C-terminal part. In fig. 42c the peptides that are protected from deuteration in the Vi-trapped condition as compared to apo, can be seen in red. Significant protection can be observed against deuterium uptake in all the conserved sequences in the NBD that are involved in ATP and/or Mg^{2+} binding or stabilization, including Walker-A, Walker-B, A-loop, C-loop, and the D-loop (fig 42c & 43).

Fig 45. Sequence coverage map of WT BmrA in nanodiscs (DDM/cholate). The blue bars represent the recovered peptides, mapped on the primary sequence of the protein. A 95 % final sequence coverage was achieved. Note that residues 29-309 constitute the TMD and 341-576 form the NBD.

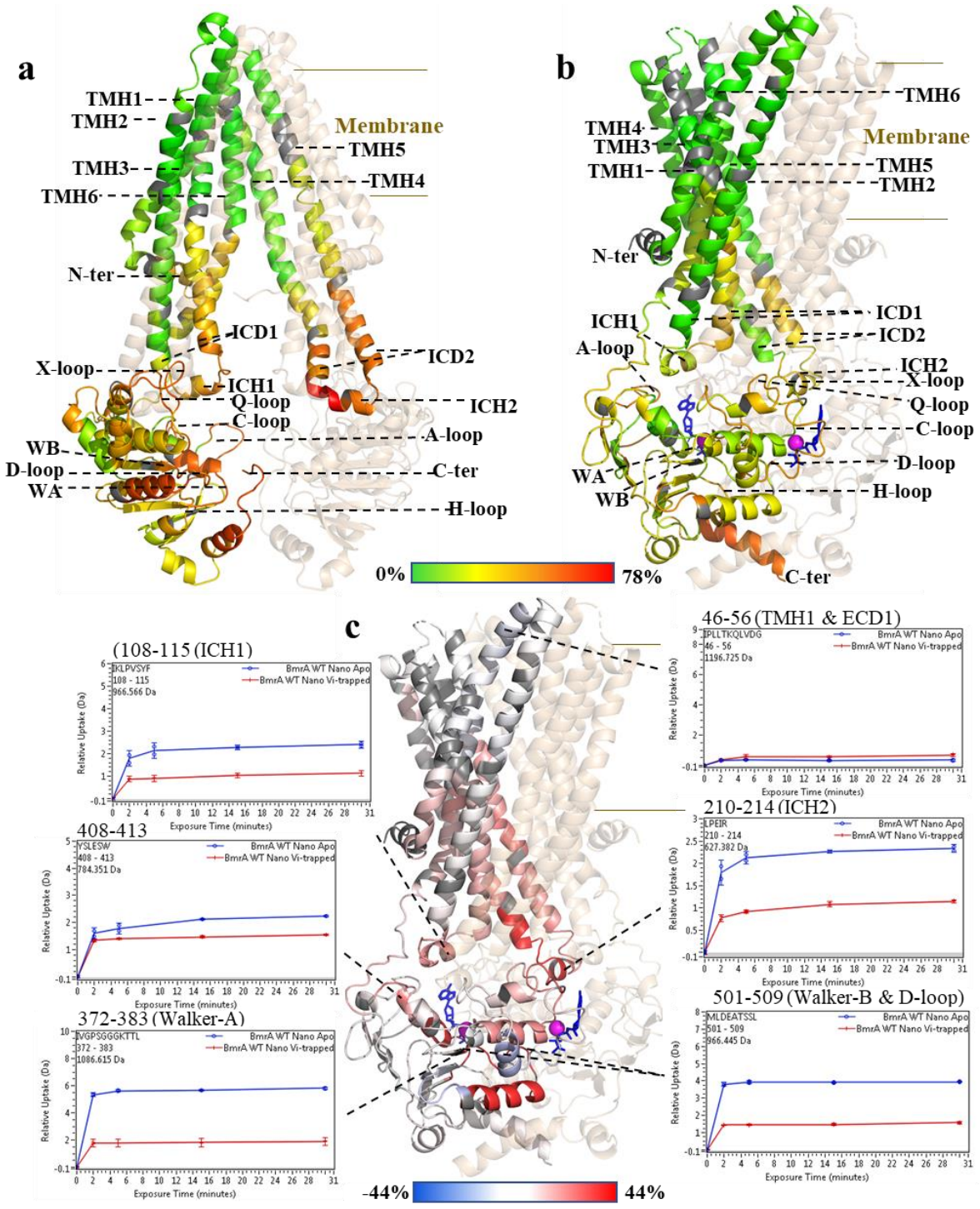

Fig 46. HDX of WT BmrA reconstituted in nanodiscs, after 30 min deuteration. **(a)** HDX data of WT BmrA in apo condition (without ligand) is plotted on a homology model of BmrA based on the inward-facing (IF) structure of mouse P-gp (PDB: 3WME). **(b)** HDX data of WT BmrA in the Vanadate trapped (Vi-trapped) condition is depicted on the cryo-EM structure of E504A BmrA mutant (PDB: 6R81). One BmrA monomer in each case is colored in translucent wheat, whereas the second monomer in green, yellow, orange and red, with a deuteration scale of 0 to 78%. 78% was the maximum percentage deuteration observed in these conditions. The TMHs and the conserved sequences in the NBDs are labelled. The bound ATP molecules are shown in blue while the magnesium ions are shown in magenta. **(c)** The differential deuterium uptake between the apo and the Vi-trapped condition of WT

BmrA is mapped on the cryo-EM structure of E504A BmrA. The differential deuteration scale is set from -44% to 44%, which was the maximum differential HDX observed, represented by the colors blue, white and red. Blue signifies the peptides that show less deuteration in the apo condition. White highlights the peptides with no difference in deuteration level between the two conditions, whereas red pinpoints the peptides that are protected from deuteration in the Vi-trapped condition. The box inserts show, in dalton, the relative deuterium uptake in the apo (blue) and Vi-trapped (red) conditions, of some important peptides. The error bars in the inserts show the standard deviation between the duplicates with sigma multiplier '2'. Abbreviations: C-ter, C-terminal; ECD, extracellular domain; ICD, intracellular domain; ICH, intracellular helix; NBD, nucleotide-binding domain; N-ter, N-terminal; TMH, transmembrane helix; WA, Walker-A; WB, Walker-B.

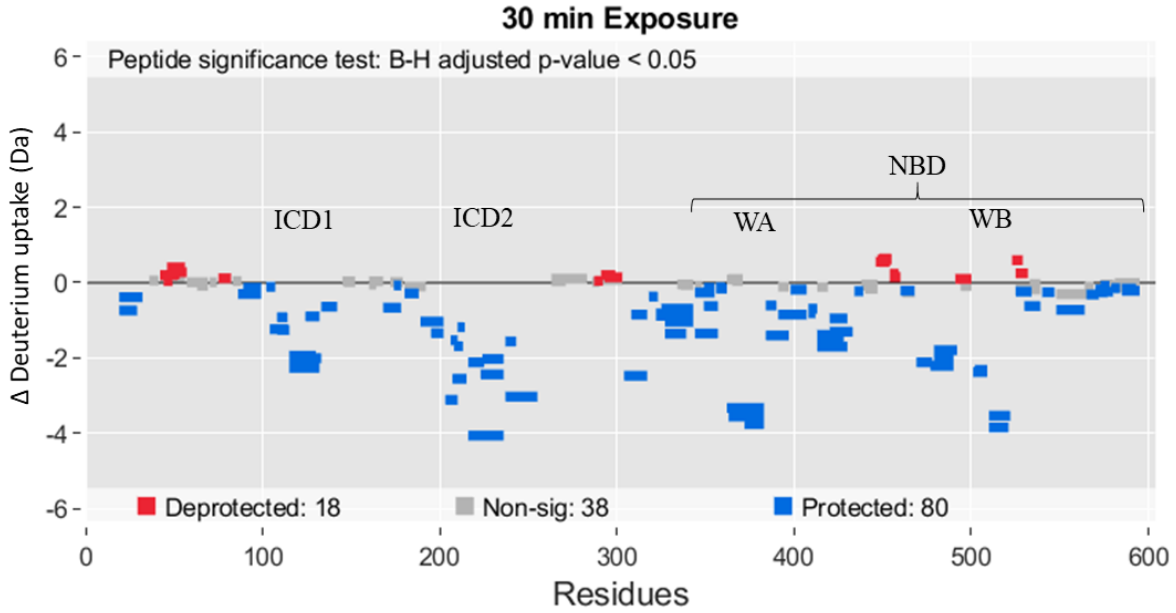

Fig 47. Differential HDX plot of WT BmrA in nanodiscs between the Apo and Vi-trapped condition at 30 min D2O exposure. Blue signifies the peptides protected against deuteration in Vi-trapped condition, whereas red signifies the deprotected peptides. Grey represents peptides with p-value more than 0.05. All measurements were done in duplicate.

In addition to this, the potential loops or sequences involved in the NBD-TMD communication namely, the X-loop, Q-loop and the sequence 408-413 (adjacent to R414), also show a significant protection against deuterium uptake. In the TMD region, we see a prominent protection in the ICDs, especially ICD2, which could be explained by its rigid or fixed nature in this condition. Overall, the large change in deuterium uptake between the two conditions, demonstrates a major change of conformation of the protein induced by the addition of ATP/Mg^{2+} and Vi.

Please note that inline digestion was employed in all cases including WT in nanodiscs except for WT in LMNG, which was digested offline leading to an overall higher back exchange.

Nevertheless, the HDX results of WT BmrA in nanodics are globally similar to the results obtained in LMNG. The only major difference in apo condition is observed in the ICDs that show overall less deuterium uptake in nanodiscs as compared to the apo condition in LMNG (fig. 46a). This might be due to a comparatively more compact nature of the transporter in nanodiscs. Although, both the ICHs show similar deuterium uptake profile in the lipidic environment of nanodiscs compare to the detergent environment of LMNG, again highlighting their highly flexible or accessible nature. In the TMD, almost all the TMHs in nanodiscs show protection against deuteration most probably due to solvent inaccessibility due to the presence of the lipids. Exception to this is the peptide 46-56 that forms part of TMH1 & ECD1 (fig. 46c). This peptide shows higher deuterium uptake in Vi-trapped condition compared to WT, which is consistent with the OF conformation of BmrA hypothesized to exist in this condition. As observed in LMNG, WT BmrA in nanodiscs also shows a large conformational change from apo condition to Vi-trapped condition, demonstrated by the considerable protection against deuterium observed between the two conditions (fig. 46b, 46c & 47).

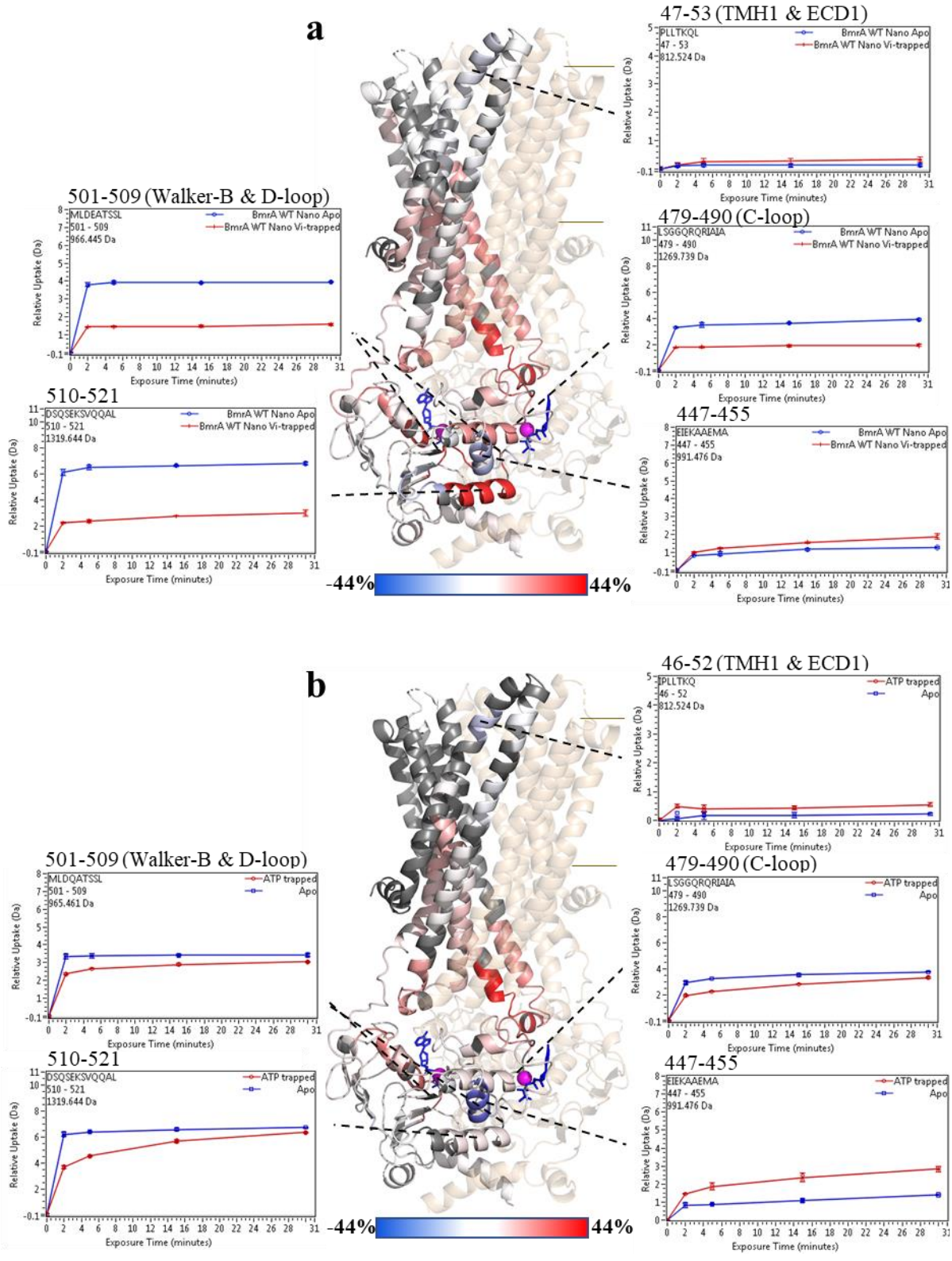

Fig 48. The differential HDX in nanodiscs, after 30 min deuteration, between **(a)** apo and Vi-trapped WT BmrA and, **(b)** apo and ATP-trapped E504Q BmrA mutant, is plotted on the OF cryo-EM structure of E504A BmrA (PDB: 6R81). The differential deuteration scale is set from -44% to 44% in both cases as the maximum differential deuteration was similar in both conditions. The scale is represented by the colors blue, white and red. Blue signifies the peptides that show more deuteration in the ATP/Vi-trapped conditions. White highlights the

peptides with no difference in deuteration level between the two conditions, whereas red pinpoints the peptides that are protected from deuteration in the ATP/Vi-trapped conditions. The box inserts show, in dalton, the relative deuterium uptake in the apo (blue) and ATP/Vi-trapped conditions (red), of some important peptides including the ones that show significant difference between the ATP-trapped E504Q and Vi-trapped WT BmrA. The error bars in the inserts show the standard deviation between the duplicates with sigma multiplier '2'. The brown lines indicate the boundary of the cell membrane. Abbreviations: ECD, extracellular domain; TMH, transmembrane helix.

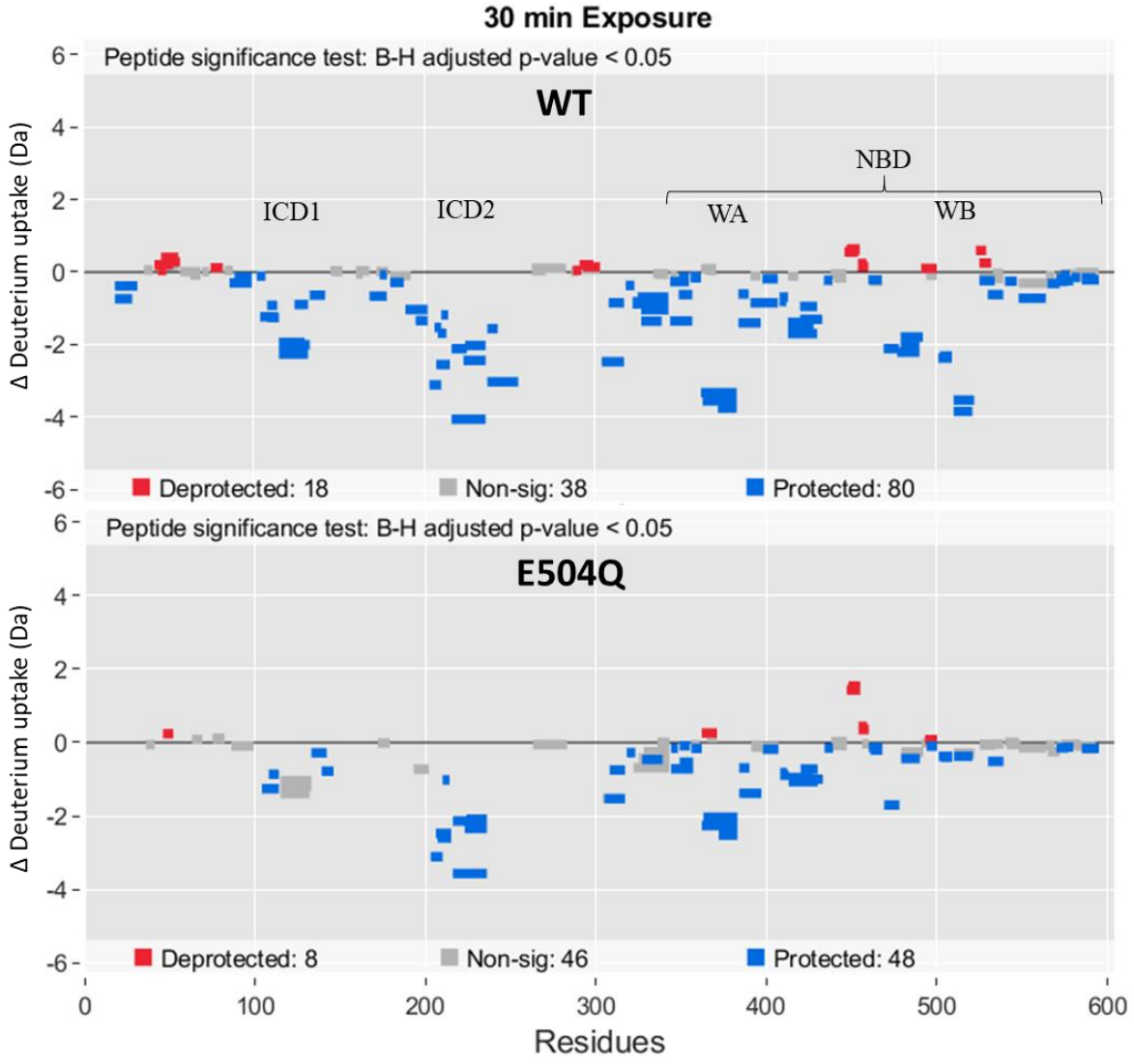

Fig 49. Differential HDX plot of WT and E504Q BmrA in nanodiscs between the Apo and Vi-trapped conditions for WT or Apo and ATP-trapped for E504Q at 30 min D2O exposure. Blue signifies the peptides protected against deuteration in Vi-trapped condition for WT or ATP-trapped for E504Q, whereas red signifies the deprotected peptides. Grey represents peptides having p-value more than 0.05. All measurements were done in duplicate.

The HDX analysis was also performed on the E504Q BmrA mutant in nanodiscs. In the apo condition the results of the mutant are very similar to the apo condition of the WT in nanodiscs

so they will not be discussed. In the presence of ATP/Mg^{2+}, the E504Q mutant shows a very similar overall protection against deuterium uptake, as observed for the WT in the Vi-trapped condition (fig. 48a & 48b). The most notable exception being the Walker-A, D-loop and the following peptide 510-520. All these peptides show significantly higher deuteration in ATP-trapped E504Q as compared to Vi-trapped WT (fig. 48 & 49). The reason for this could be the local effect of high concentration of Vi (1 mM), that may offer some additional protection in case of WT compared to the mutant. An interesting peptide 46-52 (47-53 in WT) that forms part of TMH1 and ECD1, shows a slightly higher deuterium uptake in the ATP- or Vi-trapped conditions of the E504Q and WT, respectively, compared to their apo conditions. This is in line with the presence of an OF conformation of both the E504Q and WT, in the ATP- or Vi-trapped conditions, respectively.

For the apo K380A BmrA mutant in nanodiscs, the results are similar to WT and E504Q in their apo conditions. However, in the ATP/$Mg^{2+/}$Vi-incubated condition, the K380A mutant shows very contrasting behaviour (fig. 50). An overall protection against deuteration cannot be observed as seen in case of WT for the same condition or in case of ATP-trapped E504Q mutant. Therefore, the possibility of a large conformational change towards a 'closed' conformation is completely ruled out. Interestingly, we do observe some minor protection against deuteration in the conserved sequences involved in ATP/Mg^{2+} binding and stabilization, including Walker-A, Walker-B and the D-loop, in the ATP/Mg^{2+}/Vi-incubated condition of this mutant. The protection is more prominent in the shorter deuteration times, meaning that the protection is transient. This transient protection is very likely caused by ATP binding to these sequences in the NBD, inducing some local effects. Surprisingly, these local effects are also observed to be transmitted to the ICDs, especially the ICD2, through the coupling helices, making ICD2 less flexible and hence protected against deuteration (fig. 50c & 51).

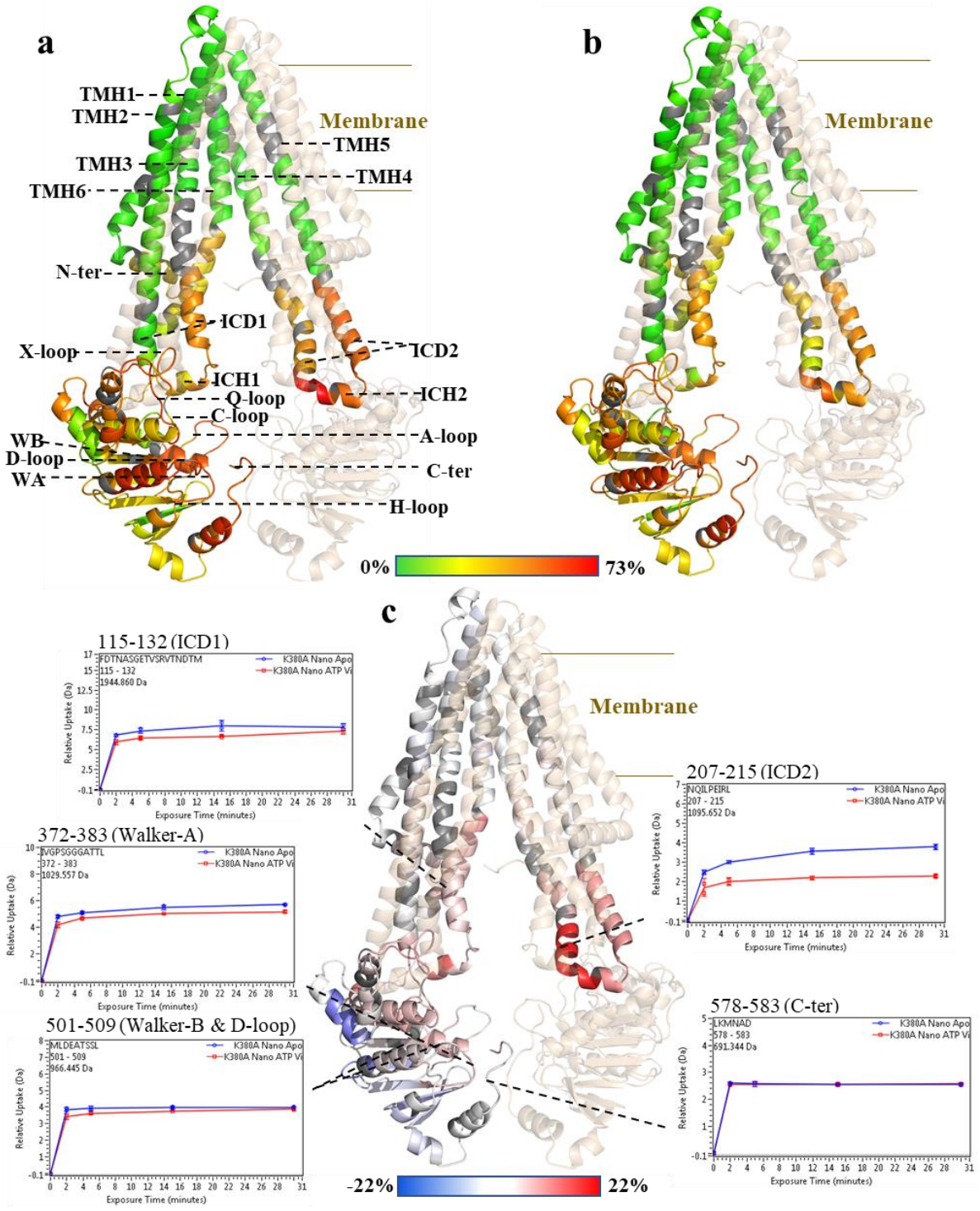

Fig 50. HDX of K380A BmrA in nanodiscs in two different conditions after 30 min deuteration, plotted on BmrA inward-facing (IF) model. **(a)** HDX data of K380A BmrA in apo condition (without ligand) is plotted on a homology model of BmrA based on the IF structure of mouse P-gp (PDB: 3WME). **(b)** HDX data of K380A BmrA, incubated with 10 mM ATP/Mg^{2+} and 1 mM Vi, is depicted on the same IF model. One BmrA monomer in each case is colored in translucent wheat, whereas the second monomer in green, yellow, orange and red, with a deuteration scale of 0 to 73%. 73% was the maximum percentage deuteration observed in these conditions. The TMHs and the conserved sequences in the NBDs are labelled. **(c)** The differential deuterium uptake between the apo and the ATP/Mg^{2+} and Vi-incubated conditions is mapped on the BmrA IF model. The differential deuteration scale is set from -

22% to 22%, which was the maximum differential HDX observed, represented by the colors blue, white and red. Blue signifies the peptides that show less deuteration in the apo condition. White highlights the peptides with no difference in deuteration level between the two conditions, whereas red pinpoints the peptides that are protected from deuteration in the ATP/Mg^{2+} and Vi-incubated condition. The box inserts show, in dalton, the relative deuterium uptake in the apo (blue) and ATP/Mg^{2+} and Vi- incubated condition (red), of some important peptides. The error bars in the inserts show the standard deviation between the duplicates with sigma multiplier '2'. Abbreviations: C-ter, C-terminal; ICD, intracellular domain; ICH, intracellular helix; NBD, nucleotide-binding domain; N-ter, N-terminal; TMH, transmembrane helix; WA, Walker-A; WB, Walker-B.

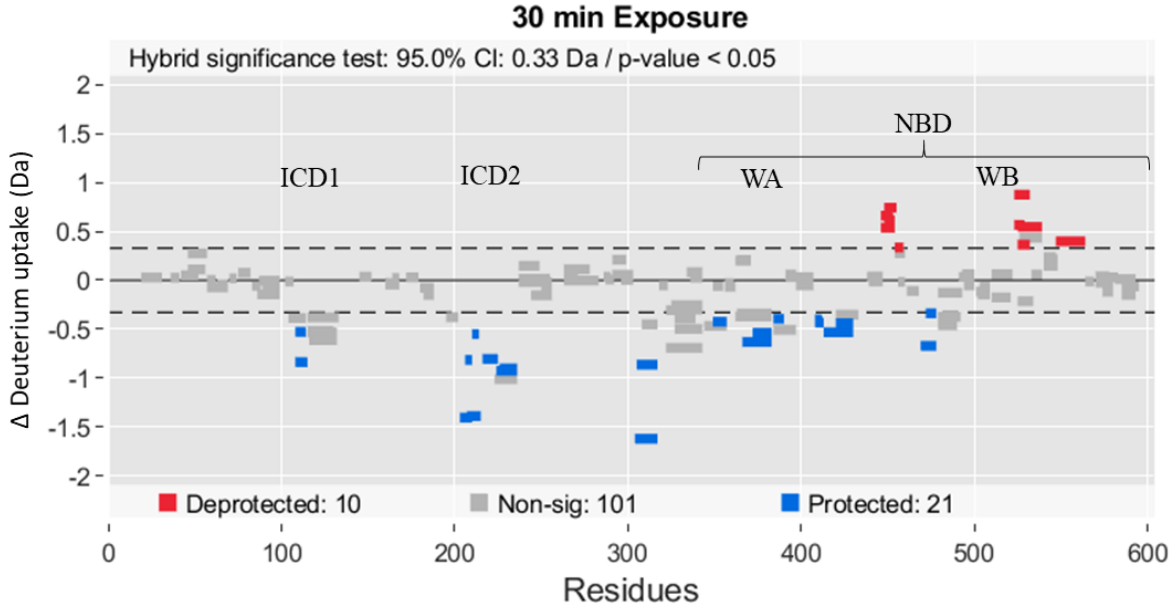

Fig 51. Differential HDX plot of K380A BmrA in nanodiscs between the Apo and Vi-incubated (10 mM ATP/Mg2+ and 1 mM Vi) conditions at 30 min D2O exposure. Blue signifies the peptides protected against deuteration in Vi-incubated condition, whereas red signifies the deprotected peptides. Grey represents peptides with HDX below the 95% confidence interval shown by dotted lines and having p-value more than 0.05. All measurements were done in duplicate.

The HDX result of K380A BmrA in LMNG paint a similar picture as observed in nanodiscs (fig. 52 & 53). Although, the second condition tested for K380A mutant in LMNG was in the presence of ATP and Mg^{2+} only, in the absence of Vi, but still the result is identical to the ATP/Mg^{2+}/Vi-incubated condition in nanodics (fig. 52b). Meaning that Vi has no observable effect on this mutant. The only difference between the results in LMNG vs nanodiscs for this mutant, is the slightly higher deuteration level in ICD1 and part of TMH6 observed in the apo condition in LMNG vs the same condition in nanodiscs, afforded by the greater flexibility of the protein in detergent. Overall, the HDX results of K380A BmrA in LMNG or nanodiscs, validate the results obtained by other techniques for this mutant.

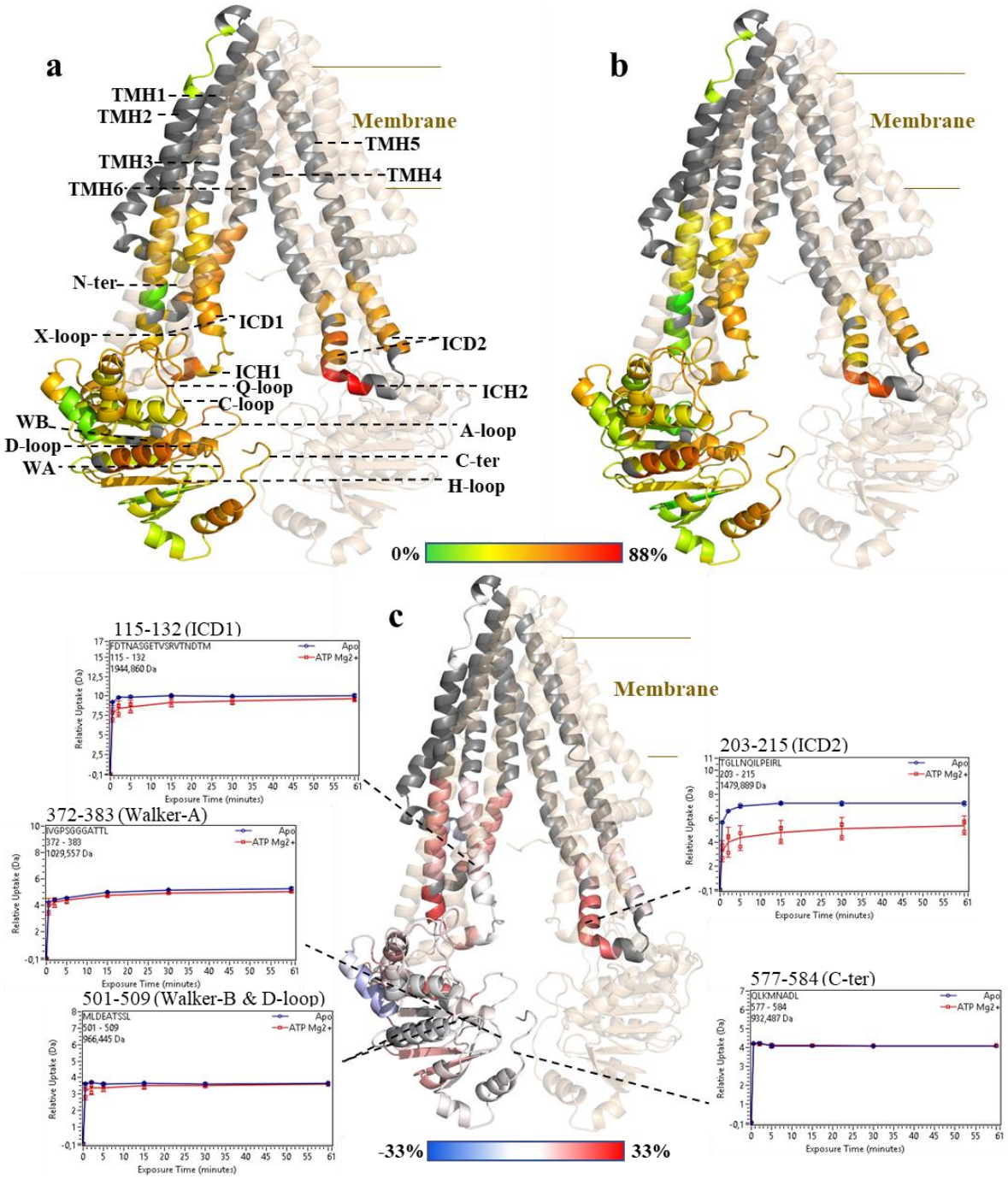

Fig 52. HDX of K380A BmrA in LMNG in two different conditions after 1 h deuteration, plotted on BmrA IF model. **(a)** HDX data of K380A BmrA in apo condition (without ligand) is plotted on a homology model of BmrA based on the IF structure of mouse P-gp (PDB: 3WME). **(b)** HDX data of K380A BmrA, incubated with ATP/Mg^{2+}, is depicted on the same IF model. One BmrA monomer in each case is colored in translucent wheat, whereas the second monomer in green, yellow, orange, and red, with a deuteration scale of 0 to 88%. 88% was the maximum percentage deuteration observed in these conditions. The TMHs and the conserved sequences in the NBDs are labelled. **(c)** The differential deuterium uptake between the apo and the ATP/Mg^{2+} incubated condition is mapped on the BmrA IF model. The differential deuteration scale is set from -33% to 33%, which was the maximum differential HDX observed, represented by the colors blue, white and red. Blue signifies the peptides that show less deuteration in the apo condition. White highlights the peptides with no difference in deuteration level between the two conditions, whereas red pinpoints the peptides that are

protected from deuteration in the ATP and Mg^{2+} incubated condition. The box inserts show, in dalton, the relative deuterium uptake in the apo (blue) and ATP and Mg^{2+} incubated condition (red), of some important peptides. The error bars in the inserts show the standard deviation between the triplicates with sigma multiplier '2'. Abbreviations: C-ter, C-terminal; ICD, intracellular domain; ICH, intracellular helix; NBD, nucleotide-binding domain; N-ter, N-terminal; TMH, transmembrane helix; WA, Walker-A; WB, Walker-B.

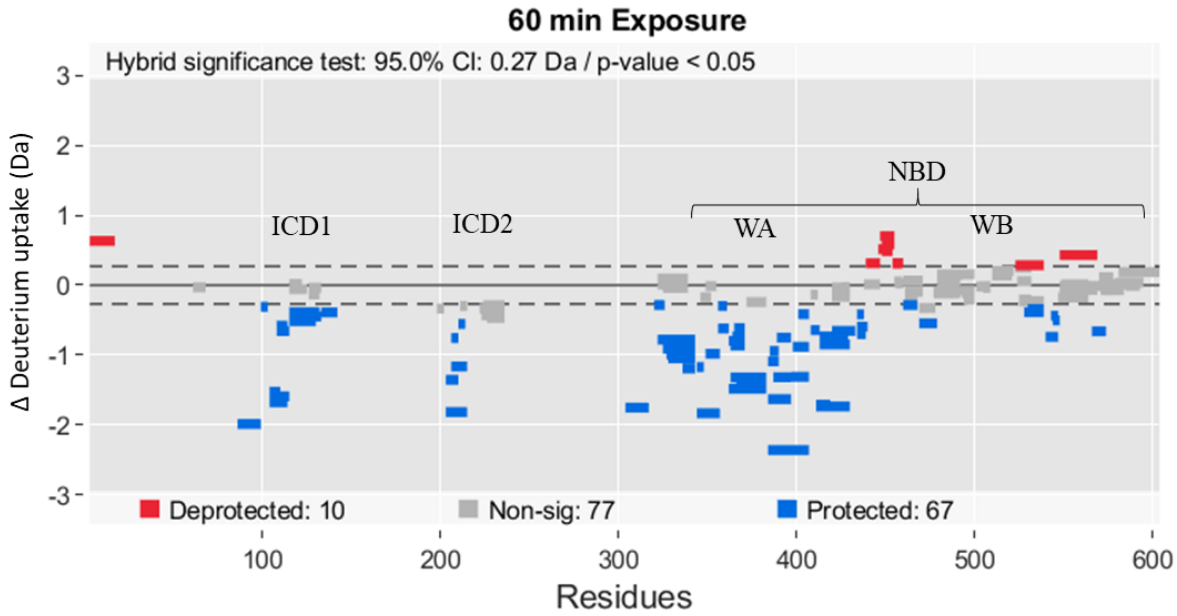

Fig 53. Differential HDX plot of K380A BmrA in LMNG between the Apo and ATP-incubated (10 mM ATP/Mg^{2+}) conditions at 60 min D2O exposure. Blue signifies the peptides protected against deuteration in ATP-incubated condition, whereas red signifies the deprotected peptides. Grey represents peptides with HDX below the 95% confidence interval shown by dotted lines and having p-value more than 0.05. All measurements were done in triplicate.

Conclusion & Discussion

The results obtained through limited proteolysis, nano-DSF, SANS and HDX-MS complement each other and paint a global picture of the catalytic cycle of BmrA. The proposed conformations of BmrA, under the light of these results, are schematized in fig. 54. The apo form of the protein, whether WT or mutant (K380A or E504Q) was found to be in a conformation prone to proteolysis by trypsin, having a high R_g with pair distances having two maxima, with lower T_m and showing a globally higher deuterium uptake. All these finding suggest that BmrA in the apo form is quite flexible and is able to adopt multiple conformations ranging from a wide open IF to less open IF conformation in detergent as well as nanodiscs. Although, in nanodiscs the wide open IF conformation may not be present due to the compact nature of nanodiscs, as observed by comparatively less deuterium uptake by ICDs in nanodiscs vs LMNG. The flexibility of the transporter in apo form is not surprising. MsbA crystal structures were also found to be present in two different IF open conformations (Ward et al.,

2007). MsbA from *E. coli* was crystallized in a wide open IF conformation, whereas one from *V. cholerae* was present in a less open IF conformation. It was also shown by single particle electron microscopy that *E. coli* MsbA and mouse P-gp exist in IF conformations with a range of NBD opening (Moeller et al., 2015). The IF crystal structures of P-gp obtained from various organisms with varying NBD separations go in line with this finding (Jin et al., 2012) (Li et al., 2014) (Ward et al., 2013) (Alam et al., 2019).

The WT BmrA in the presence of ATP/Mg^{2+}/Vi, on the other hand, displays profiles very similar to the catalytic glutamate mutant E504Q in the presence of ATP/Mg^{2+}, in all the techniques utilized. On top of this, the SANS envelope of Vi-trapped WT BmrA fits well the cryo-EM structure of the E504A BmrA (pdb 6R81) mutant in the OF conformation, meaning that both adopt the closed OF conformation in these conditions. This is in line with the solid-state NMR result which showed that ATP binding is sufficient for BmrA to transition to the OF conformation (Lacabanne et al., 2019).

The WT in the presence of ADP/Mg^{2+} displays a very interesting result. In nano DSF, an increase in T_m, hence stability, was observed. However, the observed increase in T_m was lower than that obtained with similar ATP concentration. Similar result was obtained by limited proteolysis of WT BmrA in IMVs (annex. 5). This shows that ADP does stabilize the transporter but less than ATP. It is important to note that, in the latter case, Mg^{2+} was also present in addition to ATP, thereby triggering the constant turnover of the transporter and thus a switch between the IF and OF, until ATP depletion occurs and/or ADP inhibition takes place. In SANS, the R_g observed for ADP-bound BmrA (43.8 Å) was lower than that observed in apo condition (44.3 Å), meaning that ADP-bound BmrA adopts a slightly more compact conformation as compared to apo BmrA. Interestingly, the p(r) of SANS data showed that ADP-bound BmrA only exhibits one maximum representative of larger pair distances, as opposed to apo condition which displays an additional maximum also representing smaller pair distances. In short, ADP-bound BmrA exists in an intermediate IF conformation in which the NBDs are neither too close together, nor too far apart. This result was also observed in human P-gp using single particle electron microscopy, in which the ADP-incubated P-gp was found to exist in IF conformations with varying separation of NBDs but not in the closed-conformation as opposed to the apo condition (Frank et al., 2016). This is very interesting because this condition represents the post hydrolysis condition of ABC transporters which is still under intense debate.

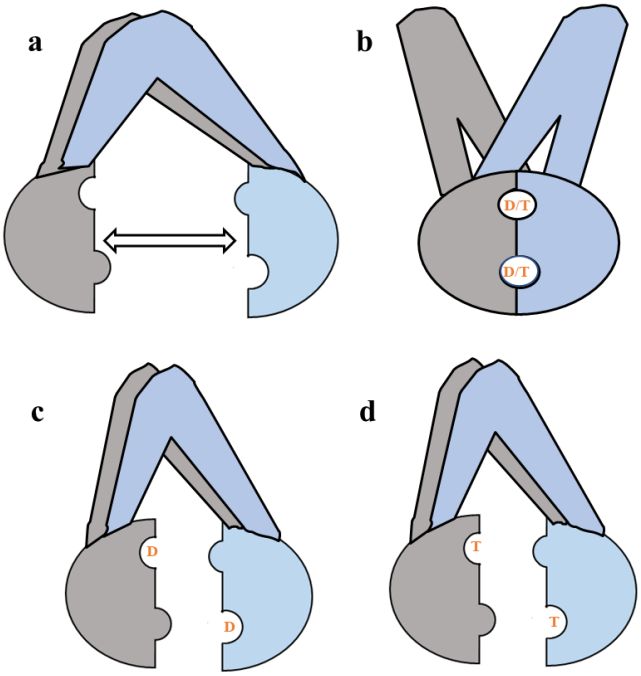

Fig 54. The different conformations of WT BmrA and mutants are schematized. **(a)** WT, K380A & E504Q BmrA in apo condition. **(b)** Vi induced ADP-trapped WT or ATP-trapped E504Q BmrA. **(c)** WT in the presence of ADP/Mg^{2+}. **(d)** K380A in the presence of ATP/Mg^{2+}. One BmrA monomer is shown in blue and the other in grey. Abbreviations: D, ADP; T, ATP.

The Walker-A K380A BmrA mutant, in the presence of ATP/Mg^{2+} or ATP/Mg^{2+}/Vi, features same profiles in all the techniques used, so only ATP-incubated condition (also containing Mg^{2+}) will be discussed. The R_g from SANS in this condition was observed to be slightly lower as compared to apo condition, indicative of a slightly more compact conformation. In the nano-DSF and HDX, we observed an increased stability and less flexibility as compared to the apo condition, again pointing to a more compact conformation. However, all these changes were far less pronounced as observed for the Vi-trapped WT or ATP-trapped E504Q, thus excluding the possibility of the closed OF conformation. Although, in limited proteolysis of 10 mM ATP-incubated condition of K380A in LMNG, we did observe a small band that remained protected from digestion for the entire duration of the experiment. This band was absent in 2 mM ATP-incubated condition. Also, the *p*(r) of 10 mM ATP-incubated K380A SANS data, displays two maxima, one representative of shorter pair distances and the other one for larger distances. To summarize, the K380A mutant exists in a slightly compact IF conformation in the presence of ATP. Moreover, under high concentrations of ATP (10 mM) a small population of this mutant might exist in a more compact conformation. Yet, this mutant is unable to reach the closed state, a result consistent with its total lack of ATPase activity (Orelle et al, 2008). Similar conclusions

were also reached for the equivalent mutations in the two NBDs of the P-gp (Urbatsch et al, 1998) (Tombline et al., 2005).

Based on the obtained results, the catalytic cycle of BmrA is schematized in fig. 55.

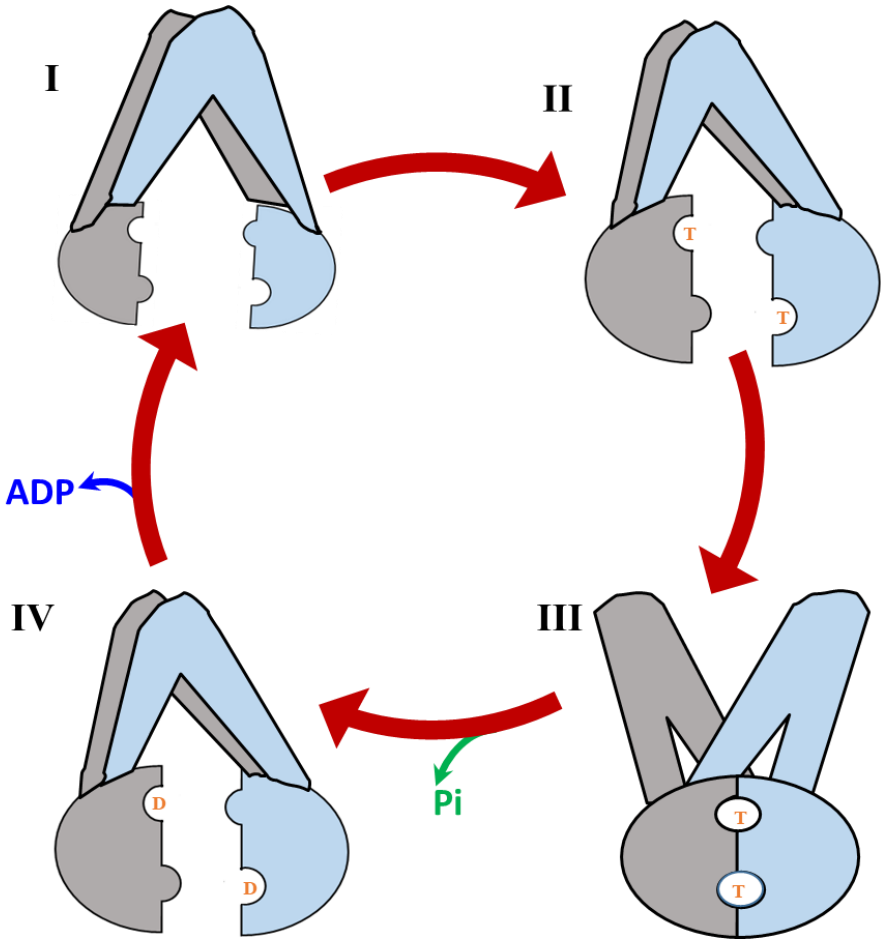

Fig 55. BmrA catalytic cycle is schematized. State I represents the IF conformation in the apo condition without bound ligand. State II signifies the ATP-bound predimerization conformation. State III represents the OF conformation induced by the binding of ATP and subsequent dimerization of the NBDs. State IV depicts the post-hydrolytic ADP-bound conformation. Note that one BmrA monomer is colored blue and the other is colored grey. Magnesium is also present in states II, III & IV. Abbreviations: D, ADP; T, ATP.

Chapter 2: W413 acts as a relay between NBD-TMD communication in BmrA

The 'alternating access mechanism' is the most widely accepted mechanism for the functioning of type IV ABC transporters. According to this mechanism, the ATP binding induces the dimerization of NBDs, and the conformational changes are transmitted to the TMDs through the coupling helices. However, the exact mechanism by which this information is transferred or the residues involved still remain a black box. In order to shed some light on this crucial coupling between the NBDs and TMDs, we utilized a W413F mutant of BmrA, previously identified and characterized as uncoupled in the laboratory (Orelle, thesis 2004). Each BmrA monomer contains 3 tryptophan residues and among these, only one is present in the NBD, W413, which is located between the Walker-A and the Q-loop in RecA-like subdomain. Interestingly, the W413 is followed by R414, whose position is strictly conserved in type IV ABC transporters (fig. 56). Based on this information, the W413 mutant of BmrA was chosen for further investigation.

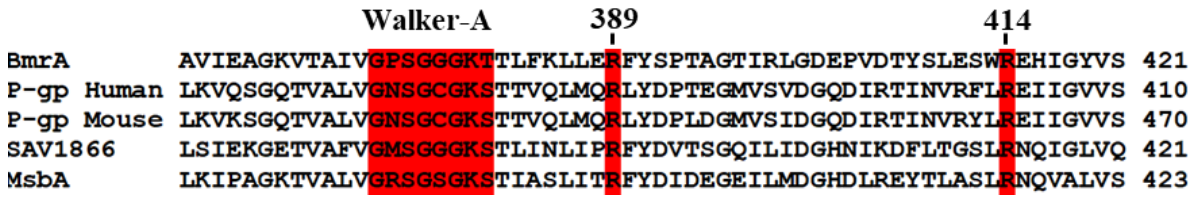

Fig 56. Sequence alignment of some type IV ABC transporters. The sequences were obtained and aligned on 'UniProt' (Pichler et al., 2018).

The W413 BmrA mutants are decoupled in ATPase and drug-tranport

Two W413 mutants, W413F and W413L, were selected from several mutants already engineered and assayed by our team, and IMVs were prepared after their overexpression in *E. coli* C41 (DE3) cells (fig. 57a). The functionality of these mutants in IMVs was re-checked by fluorescent drug transport assay. The W413 mutants were verified to be almost dead in drug transport (fig. 57b). To study this mutation further, W413F mutant was purified in LMNG and then reconstituted in lipid bilayer nanodiscs. The SDS-PAGE after purification and reconstitution in nanodiscs, can be seen in fig. 57c and 57d, respectively. The ATPase activity was determined and the W413F BmrA mutant was found to be 75-80% active in LMNG or in

nanodiscs, compared to the WT under same conditions (fig. 57e). This means that although this mutant shows a fairly good ATPase activity, this ATPAse activity is not, or at least poorly coupled to drug transport.

Thermal denaturation uncovers the existence of two conformations of W413F BmrA

The T_m of W413F mutant in LMNG was determined using nano-DSF, in the apo condition and in the presence of ATP/Mg^{2+}/Vi. A large change in T_m was observed from apo to ATP/Mg^{2+}/Vi-incubated condition, indicative of a large conformational change (fig. 58 & table 4). The T_m of ATP/Mg^{2+}/Vi-incubated W413F (58.3 °C) is very similar to that of the WT (57.8 °C) in similar condition. However, in the apo condition, the T_m of W413F (39.6°C) is significantly lower than the apo WT (44.5 °C). This interesting result confirms that the W413F mutant is able to switch

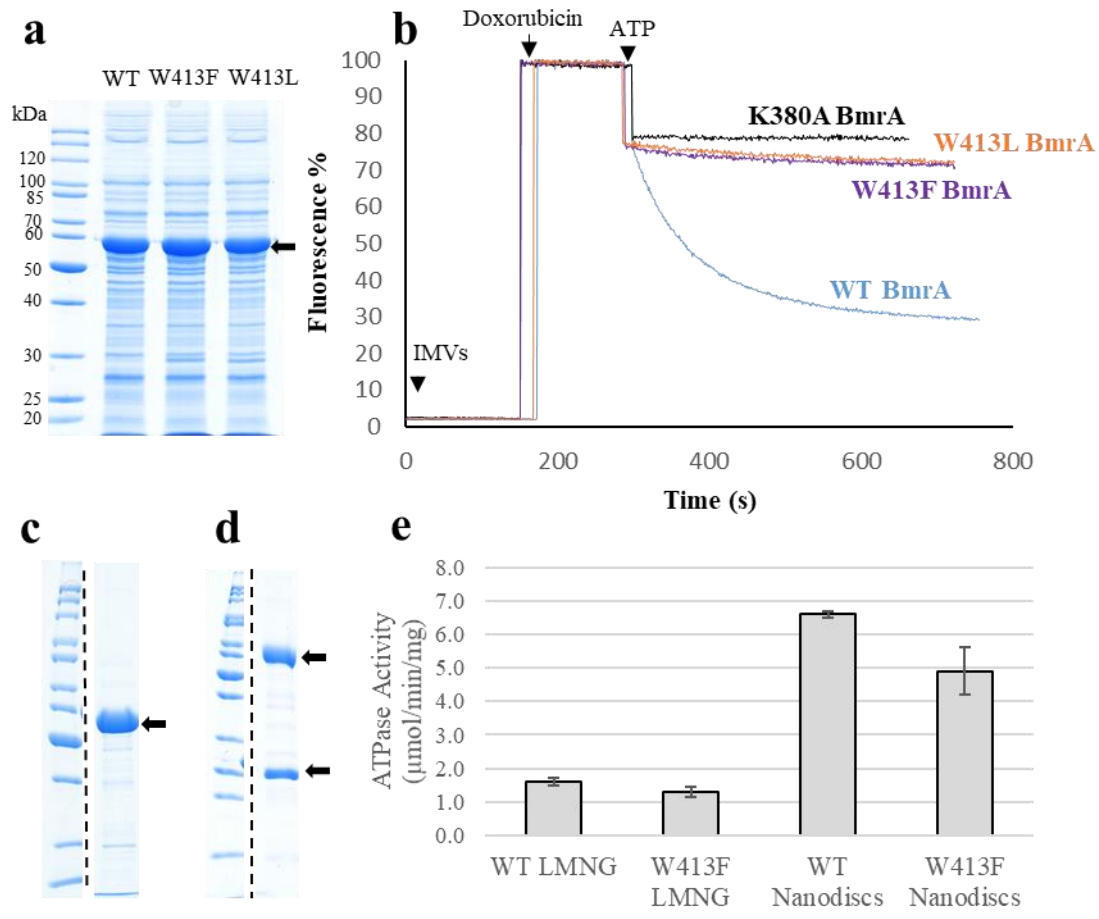

Fig 57. Overexpression, purification, reconstitution in nanodiscs, and functional assays of W413 BmrA mutants. **(a)** SDS-PAGE stained with coomassie blue showing the overexpression of WT and W413 BmrA mutants in IMVs. The black arrow highlights the BmrA band on the gel around 60 kDa. **(b)** Doxorubicin transport by WT BmrA and mutants at 25 °C with 10 µM doxorubicin. The result is representative of duplicates. The arrows indicate the addition

of different components of the assay. SDS-PAGE stained with coomassie blue showing **(c)** W413F BmrA after purification in LMNG and, **(d)** W413F BmrA after reconstitution in nanodiscs. The lower black arrow in nanodiscs pinpoints membrane scaffold protein (MSP). **(e)** ATPase activity assays of WT and W413F BmrA in LMNG or after reconstitution in nanodiscs. The result is an average of triplicates and the error bars indicate the standard deviation.

to the more stable 'closed' conformation induced by ADP-trapping by Vi, but as shown earlier, this 'closed' conformation of W413F is incapable to convey the conformational change allowing doxorubicin efflux. Another interesting result regarding this mutant is the existence of a less stable conformation in apo condition, inferred from its significantly reduced T_m compared to WT.

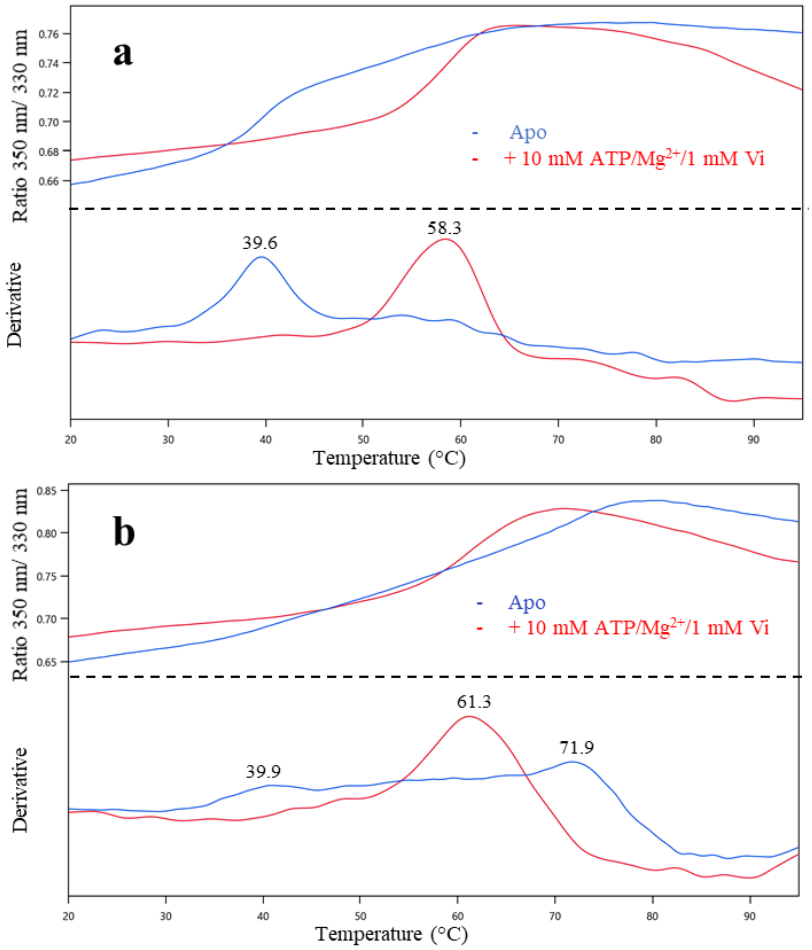

Fig 58. Melting temperature (T_m) of W413F BmrA in the apo condition or after incubation with 10 mM ATP/Mg^{2+}/1 mM Vi, measured by nano-DSF. **(a)** W413F in LMNG or, **(b)** reconstituted in nanodiscs (from purified protein in LMNG). The upper panel represents the ratio of fluorescence emitted at 350 and 330 nm, whereas the lower panel reports the first-derivative with T_m (in °C) indicated on top of each observed peak. The data is representative of triplicates for nanodiscs having standard deviations of typically 0.2 °C for T_m, and 1 °C for T_{agg}.

Protein	Condition	Ligand concentration (mM)	T_m (°C)	T_{agg} (°C)
WT LMNG	Apo		44.5	64
WT LMNG	ATP/Mg^{2+}/Vi	10/10/1	57.8	52
W413F LMNG	Apo		39.6	64
W413F LMNG	ATP/Mg^{2+}/Vi	10/10/1	58.3	52
WT Nanodiscs	Apo		46.1	62
WT Nanodics	ATP/Mg^{2+}/Vi	10/10/1	64.1	56
W413F Nanodiscs	Apo		39.9	56
W413F Nanodiscs	ATP/Mg^{2+}/Vi	10/10/1	61.3	66

Table 4. Melting temperature (T_m) of WT and W413F BmrA. Nanodics were reconstituted from the preparations of protein in LMNG. The onset of aggregation temperature is also listed which was measured by the back reflection of light. The data is representative of triplicates (except for W413F in LMNG) having standard deviations of typically 0.2 °C for T_m, and 1 °C for T_{agg}.

W413F BmrA mutant is unable to switch to a competent drug-expelling OF conformation

HDX analysis was done on W413F BmrA reconstituted in nanodiscs in the apo condition and in the presence of ATP/Mg^{2+}/Vi. At the level of NBDs, we see a similar deuteration profile for this mutant compared to the corresponding conditions of WT, with an overall high level of deuteration in the apo condition and a significant protection against deuteration in the ATP/Mg^{2+}/Vi-incubated condition (fig. 59 & 60). However, a moderate difference can be observed at the level of ICDs, especially ICD1, which do not show the same level of protection against deuteration in the Vi-trapped condition, as observed for the WT (fig. 62 & 63).

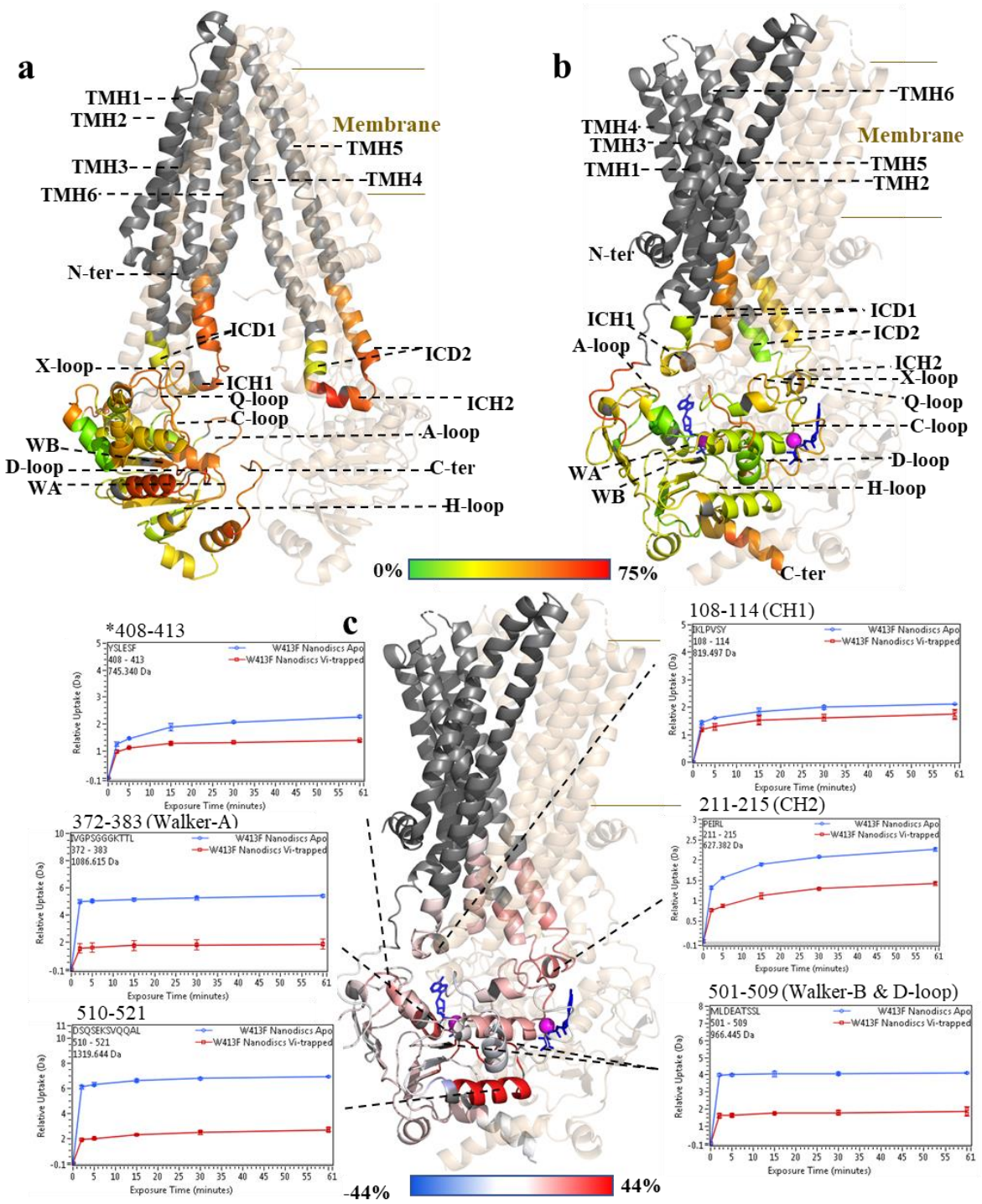

Fig 59. Hydrogen Deuterium Exchange (HDX) of W413F BmrA reconstituted in nanodiscs, after 1-h deuteration. **a)** HDX data of W413F BmrA in apo condition (without ligand) is plotted on a homology model of BmrA based on the inward-facing (IF) structure of mouse P-gp (PDB: 3WME). **b)** HDX data of W413F BmrA in the Vanadate trapped (Vi-trapped) condition is depicted on the cryo-EM structure of E504A BmrA mutant (PDB: 6R81). One BmrA monomer in each case is colored in translucent wheat, whereas the second monomer in green, yellow, orange and red, with a deuteration scale of 0 to 75%. 75% was the maximum percentage deuteration observed in these conditions. The TMHs and the conserved sequences in the NBDs are labelled. The bound ATP molecules are shown in blue while the magnesium ions are shown in magenta. **c)** The differential deuterium uptake between the apo and the Vi-

trapped condition of W413F BmrA is mapped on the cryo-EM structure of E504A BmrA. The differential deuteration scale is set from -44% to 44%, represented by the colors blue, white and red. Blue signifies the peptides that show less deuteration in the apo condition. White highlights the peptides with no difference in deuteration level between the two conditions, whereas red pinpoints the peptides that are protected from deuteration in the Vi-trapped condition. The box inserts show, in dalton, the relative deuterium uptake in the apo (blue) and Vi-trapped (red) conditions, of some important peptides. The error bars in the inserts show the standard deviation between the duplicates with sigma multiplier '2'. Abbreviations: C-ter, C-terminal; ECD, extracellular domain; ICD, intracellular domain; CH, coupling helix; NBD, nucleotide-binding domain; N-ter, N-terminal; TMH, transmembrane helix; WA, Walker-A; WB, Walker-B.

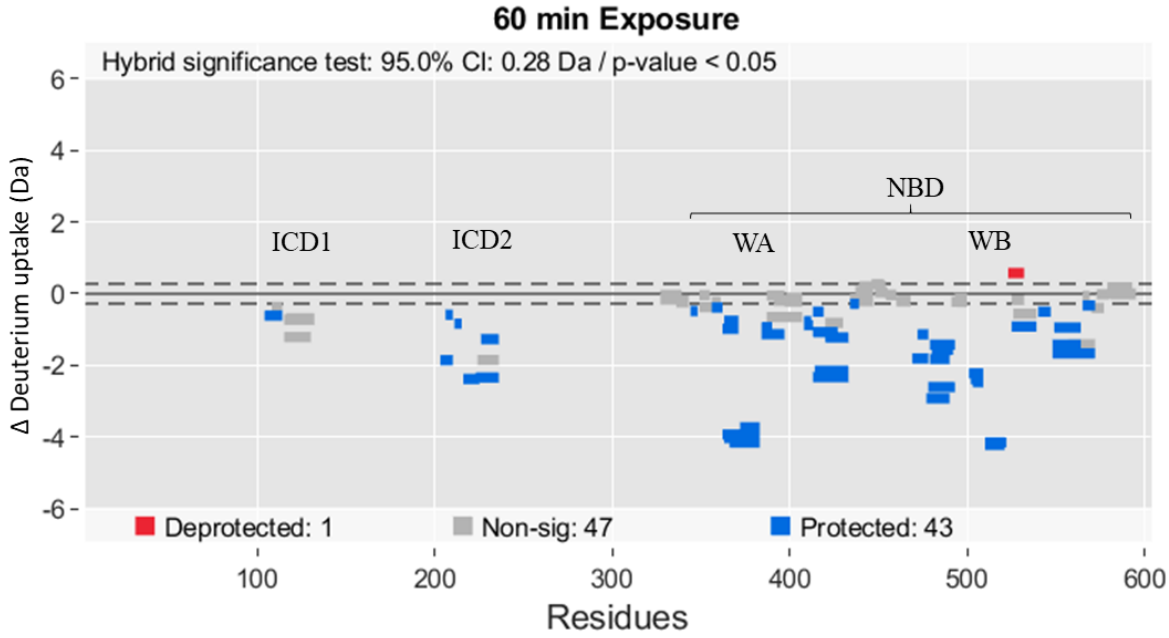

Fig 60. Differential HDX plot of W413F BmrA in nanodiscs between the Apo and Vi-trapped (10 mM ATP/Mg2+ and 1 mM Vi) conditions at 60 min D2O exposure. Blue signifies the peptides protected against deuteration in Vi-trapped condition, whereas red signifies the deprotected peptides. Grey represents peptides with HDX below the 95% confidence interval shown by dotted lines and having p-value more than 0.05. All measurements were done in duplicate.

This simply means that, although the dimerization of NBDs is taking place, the conformational changes are not being efficiently transferred to the TMDs in the W413F mutant. It can be seen in fig. 62, that the peptide 408-413 preceeding the mutation, displays exactly the same deuteration profile for WT and the mutant in similar conditions. This suggests that the conformational changes associated with nucleotide binding are being efficiently transferred to this peptide. However, due to the mutation W413 to F, this sequence is unable to properly transmit the information to the TMDs via ICDs, leading to a failure in adopting a competent drug expelling OF conformation.

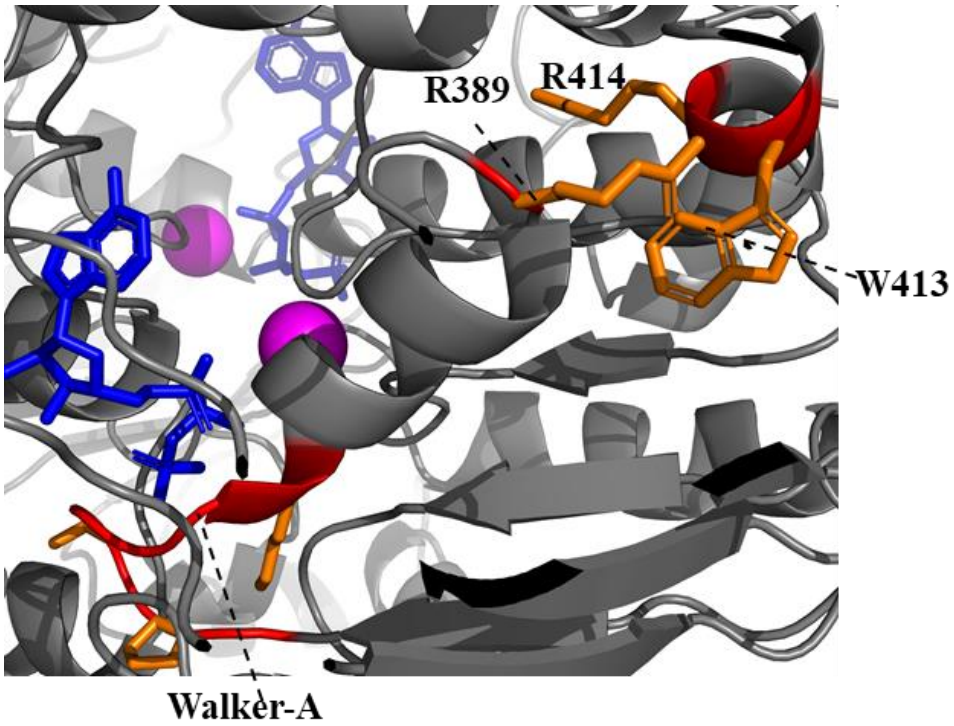

Fig 61. Position of W413 as a relay between the conserved Walker-A motif and R414, shown on the cryo-EM structure of E504A BmrA (PDB: 6R81). The labeled residues and their sidechains are colored red and orange, respectively. Bound ATP is shown in blue and Mg^{2+} ion in magenta.

Another important insight coming from this study is a higher deuterium uptake by at least two major peptides, 384-390 & 344-348, of apo W413F mutant compared to WT. The first peptide contains arginine at 389 position which lies just downstream of Walker-A motif and likely functions as a relay between the Walker-A and the W413 or R414 residues (fig. 61). Quite interestingly, the R389 is also well conserved in type IV ABC transporters. The second peptide also contains an arginine at 345 position which is just upstream of A-loop. A-loop is known to be involved in the stabilization of adenine ring of ATP during the catalytic cycle. The higher deuteration of these peptides is also in line with the decreased T_m of the apo W413F vs apo WT in LMNG.

We also observe a significant difference for the peptide 501-509 that includes the Walker-B motif and the D-loop (fig. 62a, 62b & 63). In W413F mutant, this peptide shows a higher deuterium uptake in the Vi-trapped condition compared to the same condition of WT. As the D-loop lies at the interface of the NBD-NBD dimer in the 'closed' conformation, a slightly higher deuteration may suggest a less tightly closed NBD-NBD dimer. This may also explain the 20-25% loss in ATPase activity observed in case of mutant.

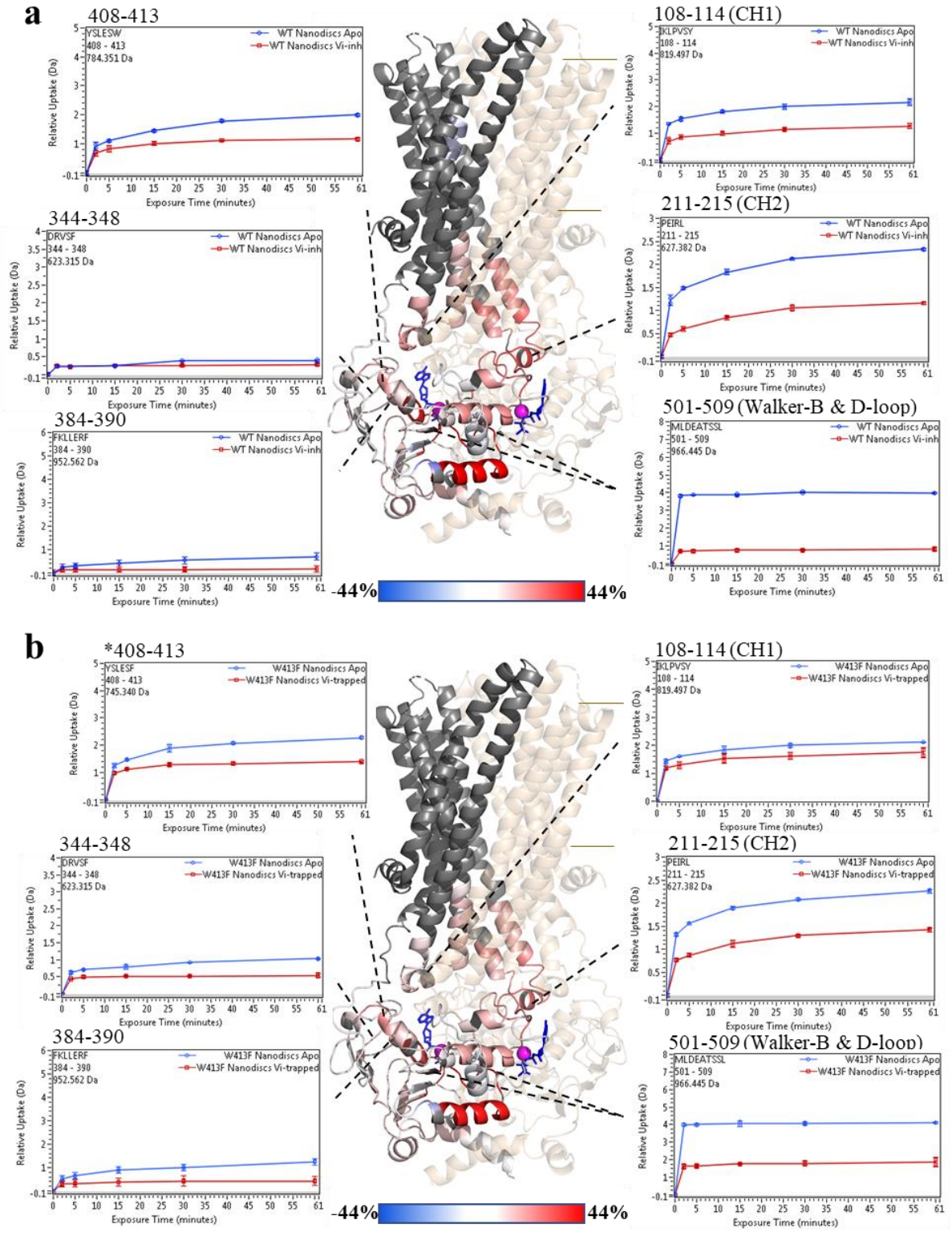

Fig 62. The differential HDX in nanodics, after 30 min deuteration, between **(a)** apo and Vi-trapped WT BmrA, and **(b)** apo and Vi-trapped W413F BmrA mutant is plotted on the OF cryo-EM structure of E504A BmrA. The differential deuteration scale is set from -44% to 44% in both cases as the maximum differential deuteration was similar in both conditions. The scale is represented by the colors blue, white and red. Blue signifies the peptides that show more deuteration in the Vi-trapped condition. White highlights the peptides with no difference in deuteration level between the two conditions, whereas red pinpoints the peptides

that are protected from deuteration in the Vi-trapped condition. The box inserts show, in dalton, the relative deuterium uptake in the apo (blue) Vi-trapped condition (red), of some important peptides including the ones that show significant difference between the WT BmrA and the mutant. The error bars in the inserts show the standard deviation between the duplicates with sigma multiplier '2'. The brown lines indicate the boundary of the cell membrane. Abbreviations: CH, coupling helix.

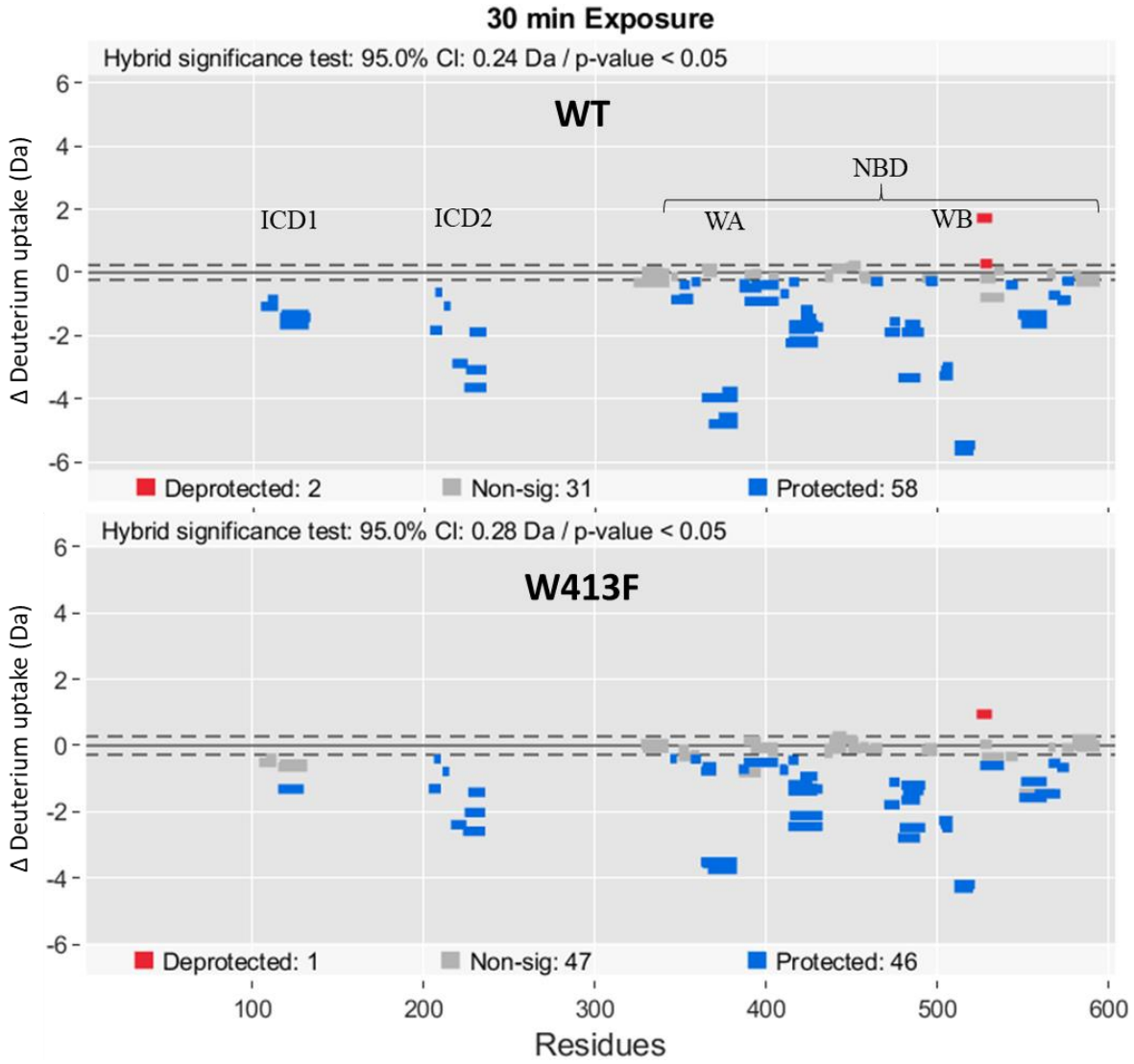

Fig 63. Differential HDX plot of WT and W413F BmrA in nanodiscs between the Apo and Vi-trapped (10 mM ATP/Mg2+ and 1 mM Vi) conditions at 30 min D2O exposure. Blue signifies the peptides protected against deuteration in Vi-trapped condition, whereas red signifies the deprotected peptides. Grey represents peptides with HDX below the 95% confidence interval shown by dotted lines and having p-value more than 0.05. All measurements were done in duplicate.

HDX of drug-bound W413F BmrA mutant in nanodiscs confirms its role in NBD-TMD communication in type IV ABC multidrug transporters

HDX experiment was carried out on WT and W413F BmrA in the apo condition and after incubation with doxorubicin, a known substrate of BmrA. Both the WT and the mutant were reconstituted in nanodiscs after purification in LMNG, for this experiment. A differential HDX between the apo and the drug-bound form of the proteins was plotted on BmrA model, as shown in fig. 64 & 65. In the WT, an increased deuterium uptake can be seen in the ICDs, especially ICD2, induced by the binding of drug. This conformational change is getting transferred via the coupling helix 2, to the peptide 408-412 in the NBDs, which is right upstream of W413 and R414. In the BmrA OF structure, A218 in ICD1 seems to be well positioned to interact with R414 in the NBDs, transferring the conformational changes in the process. The coupling helix 2 also contains an arginine at position 214, which is moderately conserved in type IV ABC transporters (Steinfels et al., 2004). This R214, is also positioned well to interact with the coupling helix 1 and also the NBDs.

The results of W413F BmrA mutant in the same conditions, confirm the above finding. It can clearly be observed that the conformational change in the ICDs, induced by drug-binding to this mutant, is poorly transferred to the peptide 408-412 in the NBDs (fig. 64b & 65). This suggests that the connection between the NBD and TMD, secured by residues encompassing R214 and R414, is greatly affected by the mutation.

Another interesting finding for this mutant is a significantly less difference in deuteration level between the apo and drug-bound condition of the shown peptides, when compared to the WT under similar conditions (fig. 64 & 65). The loss in difference in W413F mutant can be attributed to a higher deuterium uptake in the apo condition compared to WT. A visibly higher deuteration can be seen for the ICH, 408-412, 384-389 and 344-348 peptides in the apo condition of W413F. It can be deduced from this observation that W413F/R414 are not only involved in NBD-TMD connection, they are also, either directly or indirectly, involved in the stabilization of R389 (peptide 384-389) and R345 (peptide 344-348). According to the results it can be assumed that, in comparison to WT, the apo W413F BmrA mutant may exist in an IF conformation with a wider NBD opening or higher flexibility, due to more flexible ICDs.

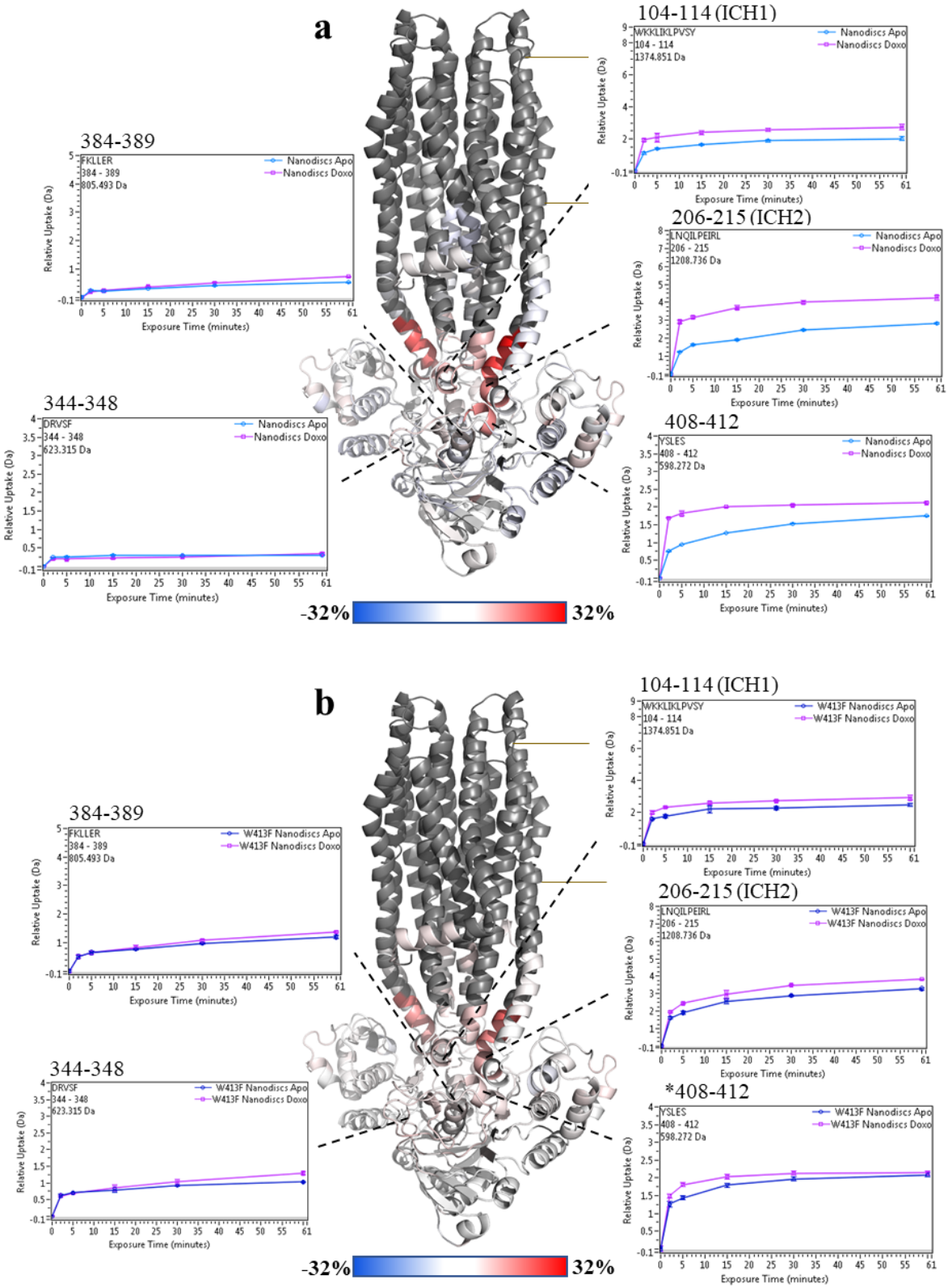

Fig 64. The differential HDX, at 30 min deuteration, between apo (without ligand) and doxorubicin-bound conditions of **(a)** Nanodisc reconstituted WT BmrA, and **(b)** Nanodisc reconstituted W413F BmrA. Both proteins were reconstituted in nanodiscs after purification in LMNG. The data is plotted on a homology model of BmrA based on the inward-facing (IF) structure of mouse P-gp (PDB: 3WME). The differential deuteration scale is set according to the maximum differential deuteration observed in WT and was kept same for

the mutant for comparison. The scale is represented by the colors blue, white and red. Blue signifies the peptides that show less deuteration in the doxorubicin-bound condition. White highlights the peptides with no difference in deuteration level between the two conditions, whereas red pinpoints the peptides that are highly deuterated in the doxorucicin-bound condition. The box inserts show, in dalton, the relative deuterium uptake in the apo (blue) and doxorubicin-bound conditions (magenta), of the peptides that show difference between the WT and the mutant. The error bars in the inserts show the standard deviation between the duplicates, with sigma multiplier '2', except for the apo condition of BmrA WT nanodiscs reconstituted after purification in LMNG. The peptide preceeding the mutation is indicated by asterisk. The brown lines indicate the boundary of the cell membrane. Abbreviations: ICH, intracellular helix.

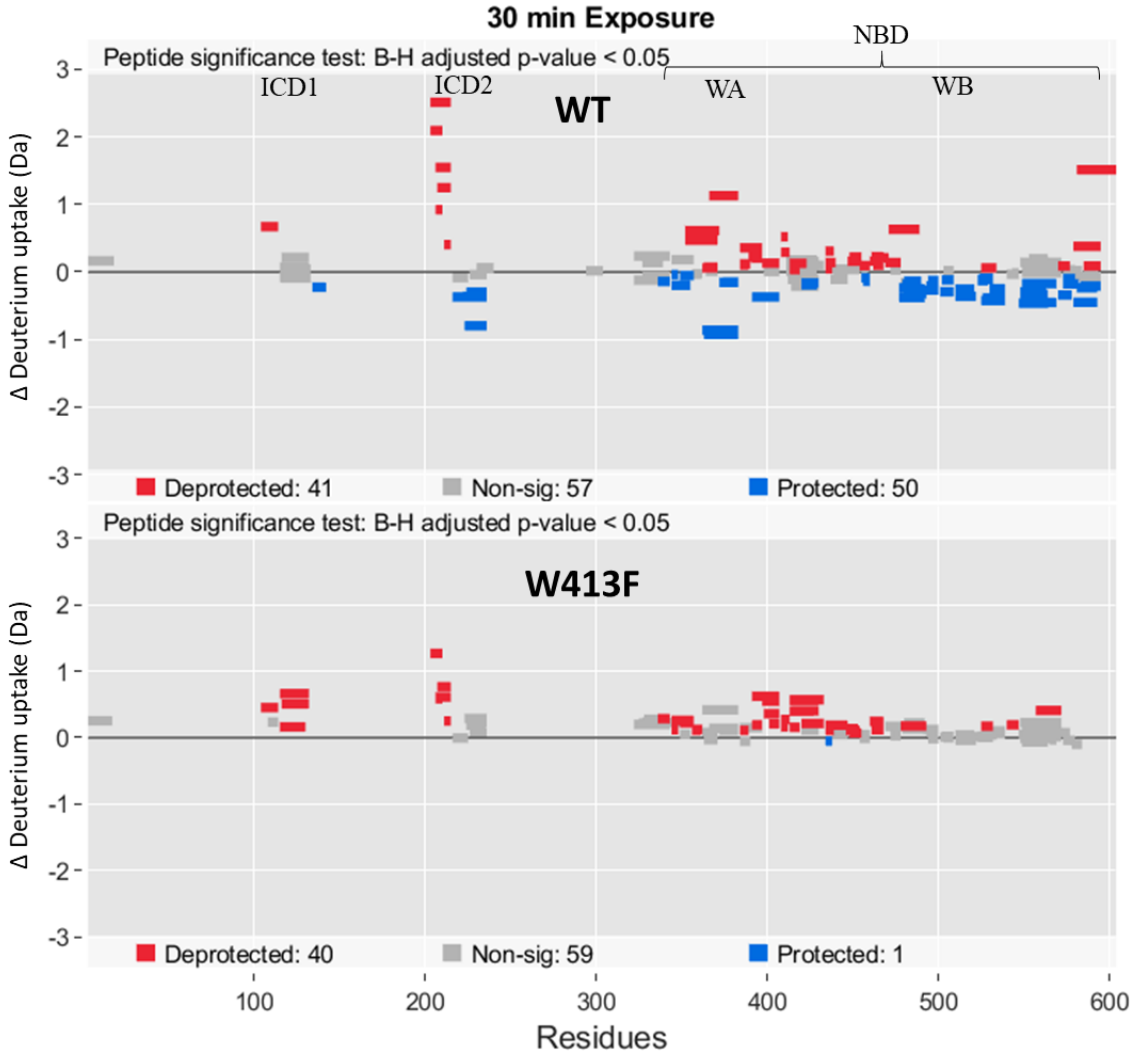

Fig 65. Differential HDX plot of WT and W413F BmrA in nanodiscs between the Apo and doxorubicin-bound (100 µM doxo) conditions at 30 min D2O exposure. Blue signifies the peptides protected against deuteration in doxo-bound condition, whereas red signifies the deprotected peptides. Grey represents peptides having p-value more than 0.05. All measurements were done in duplicate except for WT apo.

This also explains very well the lower Tm observed for apo W413F compared to the WT.

A pre-dimerization ATP-bound state of Walker-A lysine BmrA mutant highlights the NBD-TMD communication pathway

HDX analysis on the catalytically inactive K380A BmrA, in LMNG or after reconstitution in nanodiscs, was performed. The differential HDX between the apo or ATP/Mg^{2+}-incubated condition is plotted on BmrA model in fig. 66. This mutant is unable to hydrolyze ATP but can still bind it at the high concentration present (10 mM). In the figure, the dashed lines indicate the position of the residues (mentioned in parentheses) that show significant protection against deuteration in the ATP-bound state. This critical ATP-bound state is representative of the chain of events, right after ATP binding, before the dimerization of NBDs, in the catalytic cycle of ABC transporters.

The protection against deuteration is likely caused by conformational changes induced by ATP-binding. Either in LMNG or in nanodiscs, we can observe the conformational changes induced at R389 by ATP-binding at Walker-A (fig. 66a & 66b). This change is getting transferred to R414 through W413. The next event in the chain, is the transfer of conformational change from R414 to the coupling helix 2 that forms the major contact between the NBD and TMD. The information then gets transferred to the coupling helix1 via R214 of the coupling helix 2. In this way the conformational change, right at the ATP-binding site, gets transmitted all the way to the ICDs, and in turn, to the TMDs (fig. 67).

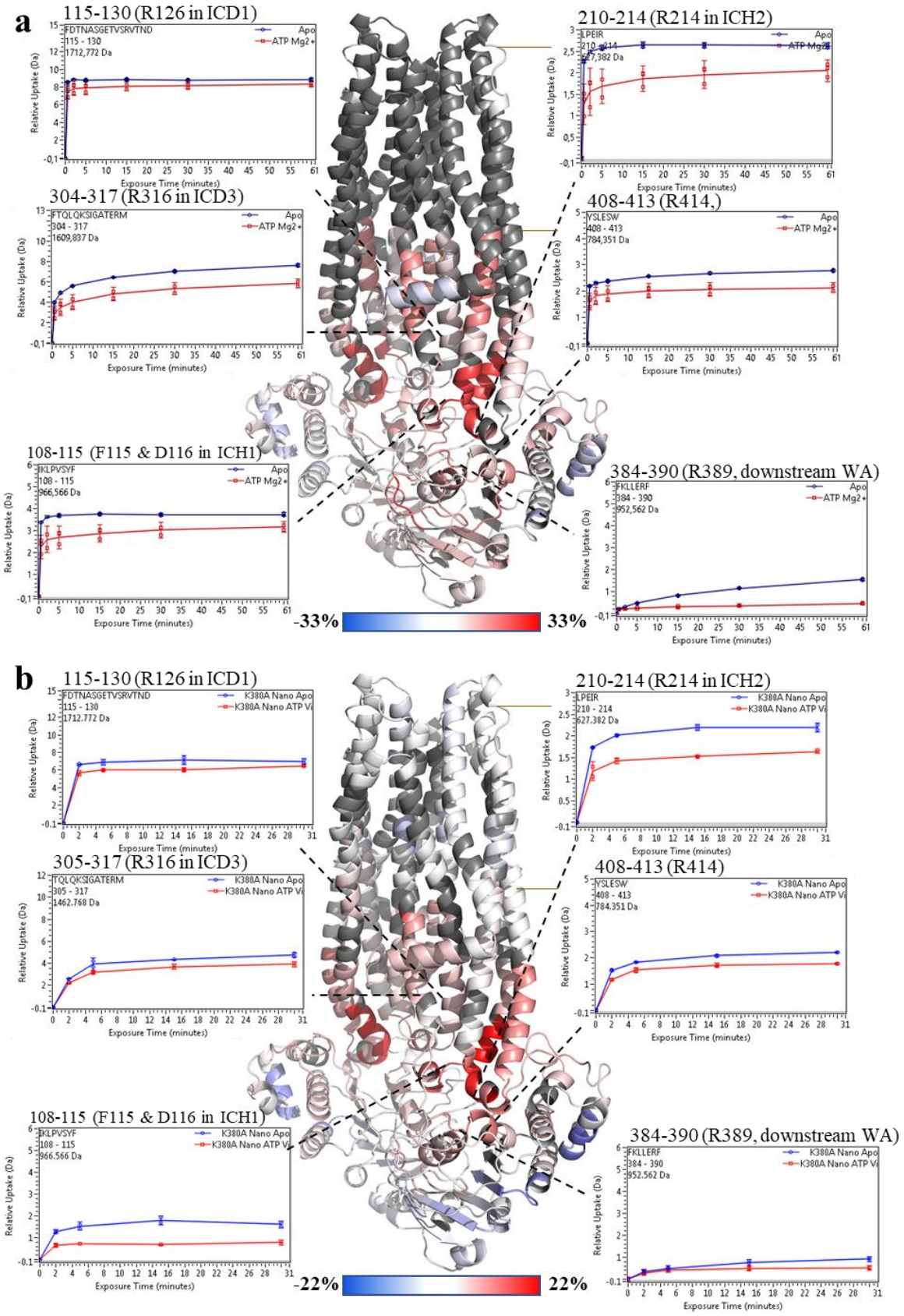

Fig 66. The differential HDX between apo (without ligand) and ATP/Mg^{2+} incubated conditions of K380A BmrA, after 30 min deuteration, is plotted on a homology model of BmrA based on the inward-facing (IF) structure of mouse P-gp (PDB: 3WME) for **(a)** K380A mutant purified

in LMNG, and **(b)** K380A mutant reconstituted in nanodiscs. In nanodiscs, Vi is also present in the ATP/Mg^{2+} incubated condition. The differential deuteration scale is set from -33% to 33% for BmrA in LMNG and, -22% to 22% for BmrA in nanodiscs. The scale was chosen based on the maximum differential HDX obtained for each condition and is represented by the colors blue, white and red. Blue signifies the peptides that show less deuteration in the apo condition. White highlights the peptides with no difference in deuteration level between the two conditions, whereas red pinpoints the peptides that are protected from deuteration in the ATP and Mg^{2+}/Vi incubated conditions. The box inserts show, in dalton, the relative deuterium uptake in the apo (blue) and ATP and Mg^{2+}/Vi incubated conditions (red), of some important peptides including the ones hypothesized to be involved in NBD-TMD communication. The dashed lines indicate the position of the residues present in parentheses, that are conserved among type IV ABC transporters. The error bars in the inserts show the standard deviation between the triplicates for LMNG, and duplicates for nanodiscs, both with sigma multiplier '2'. The brown lines indicate the boundary of the cell membrane. Abbreviations: ICD, intracellular domain; ICH, intracellular helix; NBD, nucleotide-binding domain; TMD, transmembrane domain; WA, Walker-A.

Conclusion & Discussion

The results from all these experiments clearly show that the W413F BmrA mutant is decoupled in ATPase and drug transport. The evidence from nanoDSF and HDX further suggests that this mutant might exist in a more open/flexible IF conformation permitted by more flexible ICDs compared to WT (fig. 68). HDX data also indicates that the W413F mutant may not be able to transition into a competent drug expelling OF conformation upon nucleotide trapping by Vi, due to an inadequate connection between W413/R414 and the coupling helix 2.

Based on the results, a pathway could be traced involved in the transfer of conformational change from ATP binding site to the TMDs involving R389, W413/R414, and R214 (fig. 67).

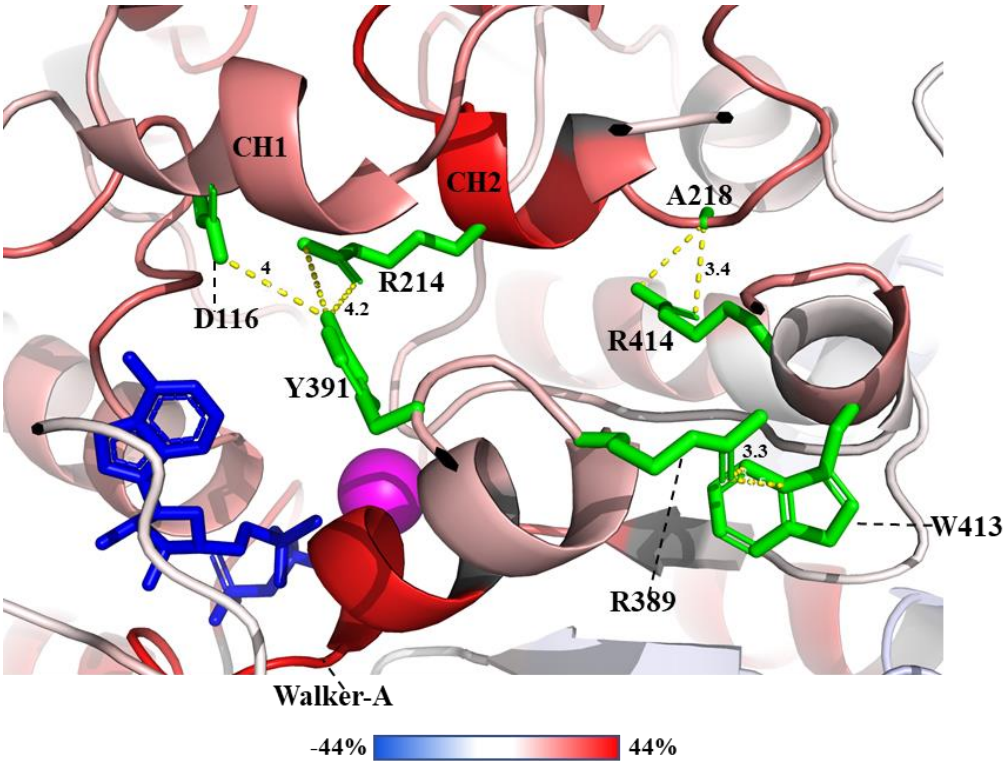

Fig 67. The potential NBD-TMD connection pathway is shown on the OF cryo-EM structure of E504A BmrA (PDB: 6R81). The differential HDX of WT BmrA in nanodics, after 30 min deuteration, between the apo and Vi-trapped condition is also plotted. The differential deuteration scale is set from -44% to 44% represented by the colors blue, white and red. Red signifies the peptides that show protection from deuteration in the Vi-trapped condition. The sidechains of the labelled residues are shown in green and the inter-residue distances are highlighted by yellow dotted lines. The distances are in angstrom. Bound ATP is shown in blue and Mg^{2+} ion in magenta. Abbreviations: CH, coupling helix.

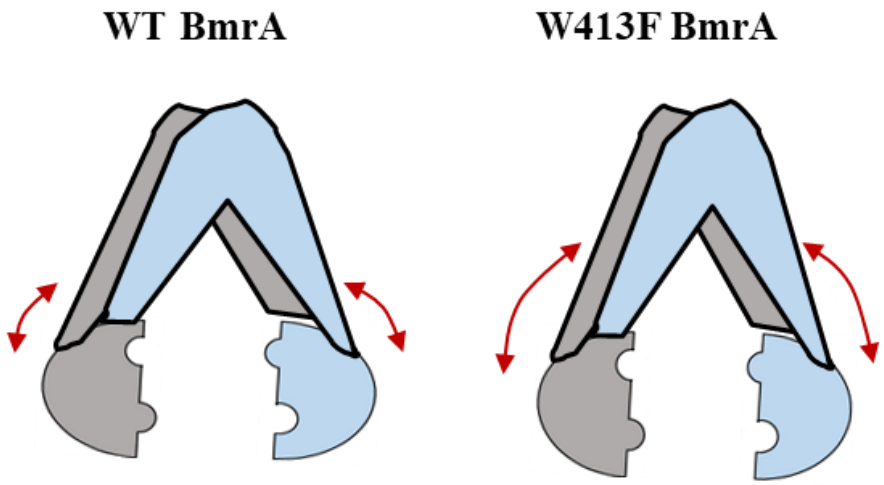

Fig 68. The hypothesized higher flexibilty of W413F BmrA mutant in comparison to WT is schematized. The arrows depict the flexibilty of NBDs. One BmrA monomer is colored blue and the other is colored grey.

Chapter 3: Conformational changes induced by drug-binding to BmrA

A very interesting feature of type IV ABC exporters is their broad substrate specificity. This gives rise to equally interesting questions; that how substrates of different sizes can be transported by the same transporter; do all the drugs bind to the same residues and what are the conformational changes induced by drug-binding?

To answer these questions, the effect of drugs on BmrA was studied using limited proteolysis, nano-DSF and HDX-MS. Limited proteolysis is a very simple but effective technique in detecting conformational changes in proteins. In case of a conformational change, the digestion profile of the protein under investigation would change, depending on the accessibility to cleavage sites to the enzyme. Additionally, if a protein is more flexible in one conformation then it would be digested faster as compared to the more rigid conformation. Based on this, the trypsin digestion profiles of BmrA in IMVs were studied in the presence of several drugs including known substrates of BmrA. The results are given in fig. 69.

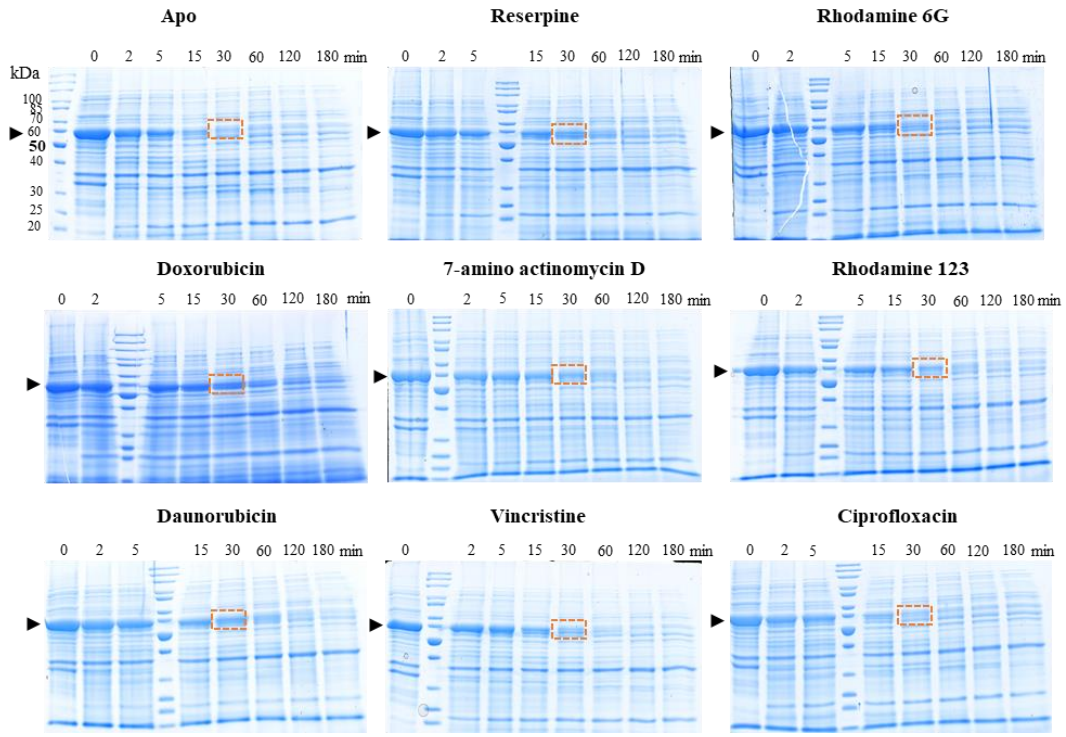

Fig 69. Limited proteolysis of WT BmrA in IMVs using trypsin. IMVs containing overexpressed BmrA were proteolysed in the absence (apo) or presence of different drugs at 100 µM concentration each, for the indicated periods of time. The progress of digestion was visualized on SDS-PAGE stained with coomassie blue. The black arrows indicate the intact BmrA band and the red dotted rectangles highlight the progress at 30 min of digestion.

Doxorubicin and 7-AAD are known to be transported by BmrA in IMVs and as the results show, a protection against digestion can be observed in the presence of these drugs at the 30 min timepoint highlighted on the fig. 69, although more significant in case of doxorubicin. The other drugs that induce significant protection include reserpine and daunorubicin. Reserpine was shown to be an inhibitor of drug-transport by BmrA (Steinfels et al., 2004), whereas daunorubicin is structurally very close to doxorubicin (fig. 70).

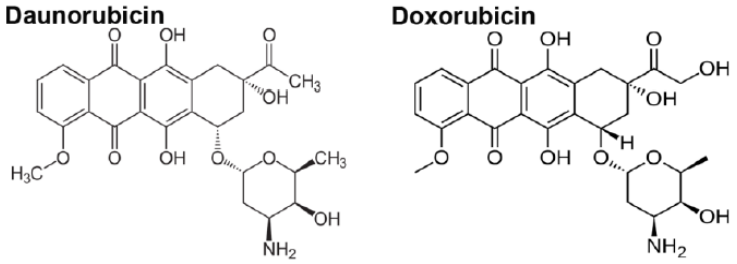

Fig 70. Chemical structures of doxorubicin and daunorubicin (Tyleckova et al., 2012).

On the other hand, ciprofloxacin, which is not known to be a substrate of BmrA, does not induce any protection against proteolysis.

Purification of BmrA and reconstitution into nanodiscs

The limited proteolysis results in IMVs were quite promising, but the drawback was the presence of other membrane proteins increasing the background. Therefore, WT BmrA was affinity purified using either LMNG or a mixture of DDM/cholate as detergents (fig. 71a & 71b). The purified BmrA was further reconstituted into nanodiscs from their parent preparations in detergents (fig. 71c & 71d), for e.g., the nanodiscs reconstituted from BmrA in LMNG were named nanodiscs LMNG. It can be seen in fig. 71e that BmrA is at least 4 times more active in nanodiscs as compared to the mentioned detergents. Also note that both the nanodisc preparations show similar level of ATPase activity.

To further test the homogeneity of BmrA nanodiscs, the sample was injected into a superdex 200 10/300 GL SEC column. Fig. 72a shows the elution profile of BmrA nanodiscs that confirms its homogeneity. Next, the ratio of BmrA to MSP in nanodiscs was estimated by comparison to known quantities of the two proteins (fig. 72b).

Based on the SDS-PAGE in fig. 72b and by using the software ‘imageJ’, the concentration of BmrA and MSP in nanodiscs was estimated to be 8.5 µg and 3.8 µg, respectively. This gives an estimated BmrA dimer to MSP molar ratio of 1:2, meaning that on average each nanodisc

contains one BmrA dimer (two half transporters) in a phospholipid bilayer, surrounded by two MSPs.

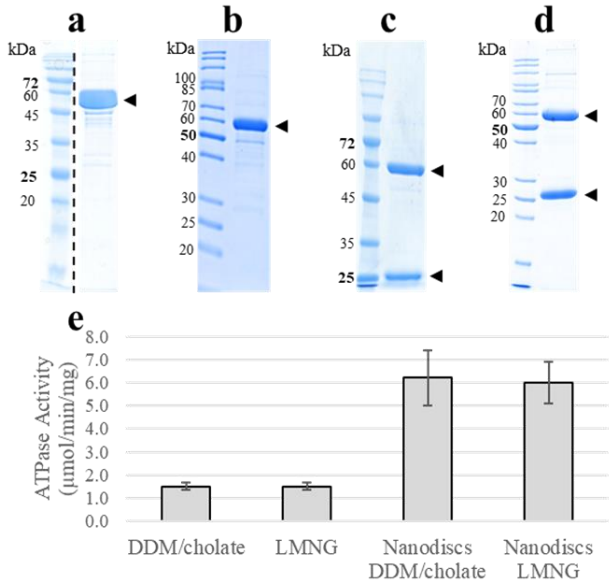

Fig 71. Purification and reconstitution of WT BmrA into nanodiscs and ATPase assay. SDS-PAGE stained with coomassie blue showing BmrA **(a)** affinity purified after solubilization by DDM/cholate, **(b)** or after solubilization by LMNG, **(c)** reconstituted into nanodiscs from purified BmrA in DDM/cholate, and **(d)** reconstituted into nanodiscs from purified BmrA in LMNG. The black arrows indicate either BmrA around 60 kDa, or MSP around 25 kDa. **(e)** ATPase activity assays of BmrA in detergent or after reconstitution into nanodiscs. The data represents the average of triplicates for DDM/cholate and nanodiscs DDM/cholate, and seven replicates for LMNG and nanodiscs LMNG. The error bars indicate the standard deviation.

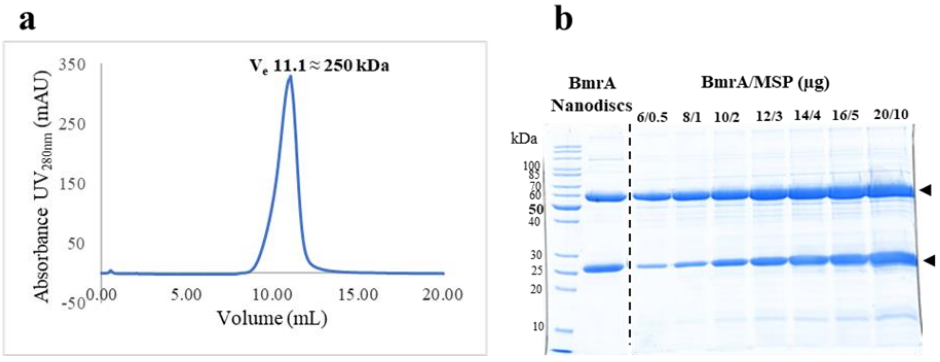

Fig 72. Characterization of WT BmrA in nanodiscs by size-exclusion chromatography (SEC) and SDS-PAGE. The nanodiscs were reconstituted from purified BmrA in LMNG and the empty nanodiscs were removed by affinity chromatography before SEC. (a) Elution profile of BmrA in nanodiscs through a superdex 200 10/300 GL SEC column. The column was calibrated with standard proteins, therefore, an elution volume (V_e) of 11.1 corresponds to approximately 250 kDa Mw. (b) SDS-PAGE of BmrA in nanodiscs in comparison to known quantities of BmrA and MSP to estimate the ratio of BmrA to MSP in nanodiscs.

Doxorubicin & tariquidar may induce conformational change in BmrA in nanodiscs

It was previously observed that the presence of some drugs induced protection against tryptic digestion in BmrA when present in IMVs. So, to test if it holds true for reconstituted BmrA, the same experiment was repeated with nanodiscs this time.

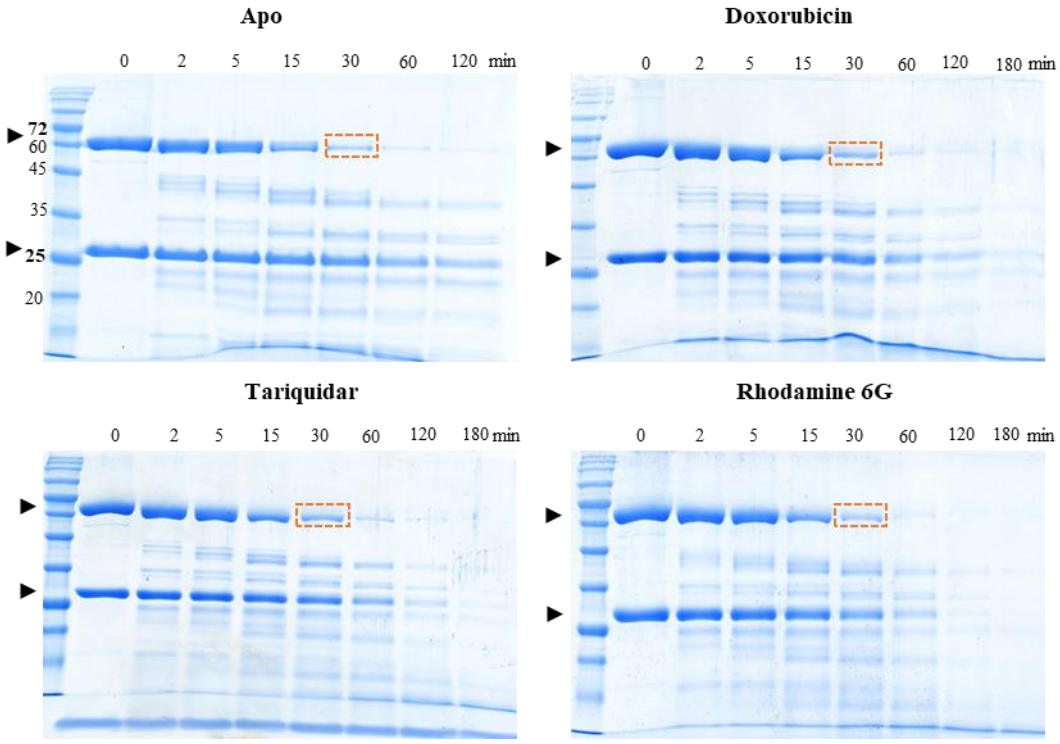

Fig 73. Limited proteolysis of WT BmrA in nanodiscs using trypsin. The nanodiscs reconstituted from BmrA in DDM/Cholate were proteolysed in the absence (apo) or presence of different drugs, at 100 µM each, for the indicated periods of time. The progress of digestion was visualized on SDS-PAGE stained with coomassie blue. The upper and lower black arrow heads indicate the intact BmrA and MSP band, respectively. The red dotted rectangles highlight the progress at 30 min of digestion.

As shown in fig. 73, a slight protection against proteolysis can be observed when BmrA nanodiscs were incubated with doxorubicin or tariquidar. Tariquidar is a known inhibitor of P-gp activity (Chufan et al., 2016), whereas protection in case of doxorubicin was also observed for BmrA in IMVs.

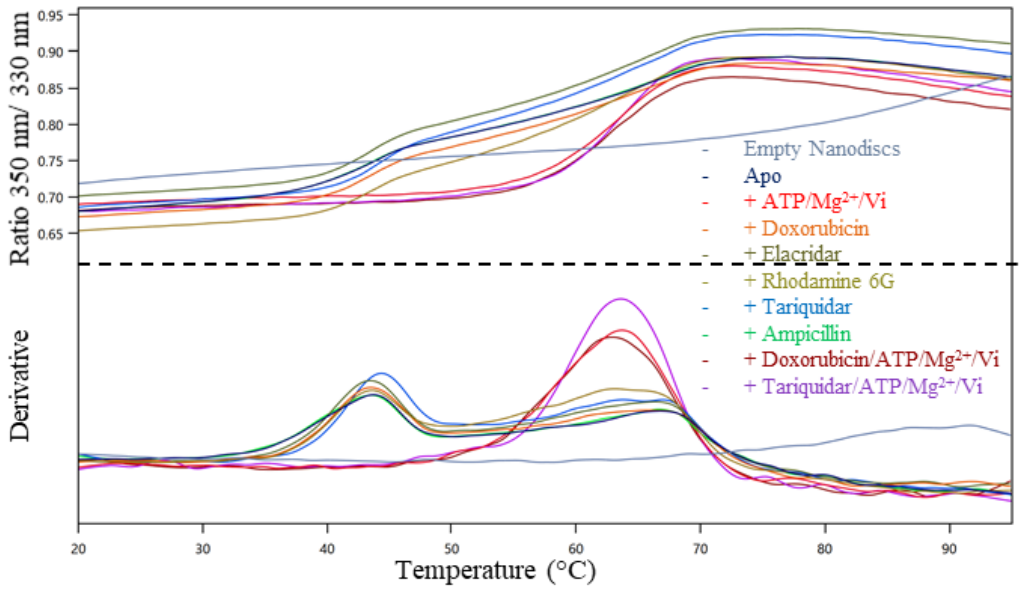

Fig 74. Melting temperature (T_m) of WT BmrA in nanodiscs (DDM/cholate) in the apo condition, or after incubation with 10 mM ATP/Mg^{2+}/1 mM Vi or 100 µM drug, or both. Note that all the drugs were solubilized in DMSO, so all the samples tested contain 5% DMSO (final concentration) to keep the conditions similar. The upper panel represents the ratio of fluorescence emitted at 350 and 330 nm, whereas the lower panel reports the first derivative. All experiments were done in duplicate having standard deviations of typically 0.2 °C for T_m, and 1 °C for T_{agg}.

Condition	T_m (°C)	Δ T_m (°C)	T_{agg} (°C)
Empty Nanodiscs	Not observed	-	Not observed
Apo	43.5	-	64
ATP/Mg^{2+}/Vi	63.6	+ 20.1	64
Doxorubicin	43.5	0	67
Elacridar	43.5	0	36
Rhodamine 6G	43.6	+ 0.1	65
Tariquidar	44.3	+ 0.8	38
Ampicillin	43.3	- 0.2	68
Doxorubicin/ATP/Mg^{2+}/Vi	62.9	+ 19.4	62
Tariquidar/ATP/Mg^{2+}/Vi	63.6	+ 20.1	25

Table 5. Melting temperature (T_m) of WT BmrA in nanodiscs DDM/cholate, either in the absence (apo) or presence of the mentioned ligands/drugs, measured by nano DSF. The onset of aggregation temperature is also listed which was measured by the back reflection of light. All experiments were done in duplicate having standard deviations of typically 0.2 °C for T_m, and 1 °C for T_{agg}.

Thermal denaturation of BmrA in nanodiscs

It was seen in previous chapters that a change in conformation of BmrA significantly impacts its T_m. Therefore, the impact of different drugs on the T_m of WT BmrA in nanodiscs was

analysed by nanoDSF. The results are presented in fig. 74 and summarized in table 5. The nanodiscs additionally contain membrane scaffold protein (MSP) which could potentially interfere with the signal from BmrA. To rule out this possibility, empty nanodiscs were used as a control. It can be seen in fig. 61 that the MSP in nanodiscs is quite stable and does not get denatured till at least 80 °C. On the other hand, we see a very well-defined T_m for BmrA in nanodiscs for the apo condition (43.5 °C) which jumps more than 20 °C upon ADP-trapping by Vi. Among the drugs, a significant increase in T_m in the presence of tariquidar could be observed. However, the start of aggregation in this condition is at 38 °C which could potentially impact the T_m. Another change in T_m is observed when BmrA was incubated with doxorubicin before the addition of ATP/Mg^{2+}/Vi.

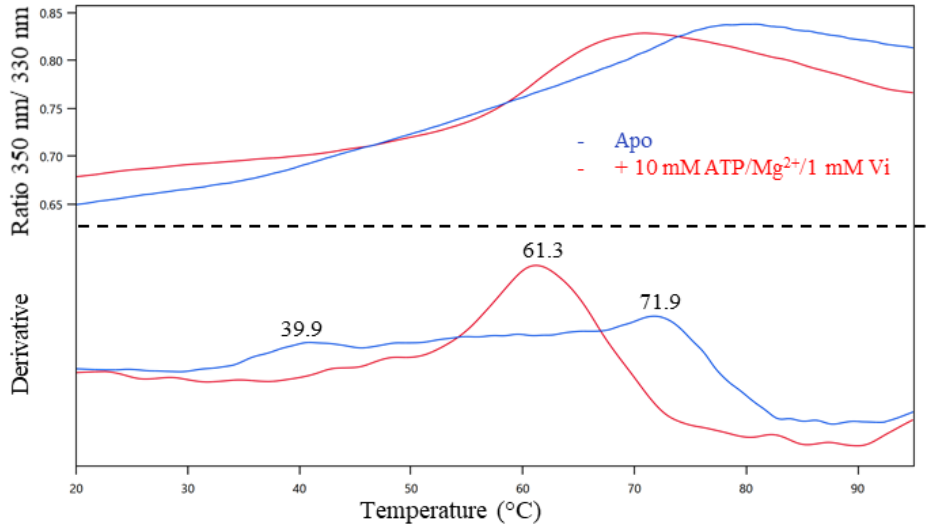

Fig 75. Melting temperature (T_m) of W413F BmrA in nanodiscs LMNG in the apo condition or after incubation with 10 mM ATP/Mg^{2+}/1 mM Vi. The upper panel represents the ratio of fluorescence emitted at 350 and 330 nm, whereas the lower panel reports the first-derivative with T_m (in °C) indicated on top of each observed peak. The data is representative of triplicates having standard deviations of typically 0.2 °C for T_m, and 1 °C for T_{agg}.

Another interesting observation is the appearance of a second T_m (≈ 68 °C) for apo condition of BmrA in nanodiscs which was not detected when BmrA was present in detergent. It is unlikely that it is the T_m of MSP because; first it is not present in the Vi-trapped condition and second, we did not observe any T_m in the empty nanodiscs till at least 80 °C. The second explanation could be that as discussed in chapter 1, BmrA may exist in a range of conformations with varying NBD separation. So, the second T_m could be coming from the population that exists in the more stable 'closed conformation. If this is the case then we need to assume that the 'closed' conformation present in the apo condition is more stable than the one stabilized by

ADP-trapping by Vi, as the former has a higher T_m compared to the latter. This is again highly unlikely. Note here that each BmrA monomer has only 3 tryptophan residues, and out of these three, only one (W413) is present in the NBD. A possible explanation would be that the first T_m in the apo condition of BmrA in nanodiscs is the T_m of the NBDs recorded by the change in the environment of W413. The second T_m (≈ 68 °C) would be from the tryptophan residues present in the TMD, which is highly stabilized because of the presence of the nanodiscs, hence not observed in detergent. The next question could arise that why we do not observe this two T_m phenomenon in the Vi-induced ADP trapped condition. This is because in this condition BmrA predominantly exists in the OF conformation as shown in the chapter 1 of this thesis. In the OF conformation, the NBDs dimerize and as a result, the T_m of NBDs increases a staggering 20 °C to 63.6 °C. However, the TMDs may be more flexible or exposed in the OF conformation, thereby, decreasing their T_m by ≈ 5 °C to coincide with that of the NBDs at 63.6 °C. Evidence for this hypothesis is presented in fig. 75 which clearly shows that the first T_m observed in case of apo WT in nanodiscs, is almost non-existent in W413F BmrA mutant in nanodiscs, whereas the rest of the profile is very similar between the two.

Opposite deuteration profiles observed for BmrA nanodiscs reconstituted from two different detergent preparations

To further study the effect of drugs on the conformational changes induced in BmrA, HDX-MS analysis was carried out on two types of BmrA nanodiscs; one reconstituted from BmrA purified in LMNG (nanodiscs LMNG) and the other from BmrA purified in the mixture of DDM/cholate (nanodiscs DDM/Cholate). The conditions for the experiment were optimized to get an exceptional sequence coverage of 95% for nanodiscs DDM/cholate, which in our knowledge is the first time for an ABC transporter in nanodiscs (fig. 76).

Fig 76. Sequence coverage map of WT BmrA in nanodiscs (DDM/cholate). The blue bars represent the recovered peptides, mapped on the primary sequence of the protein. A 95 % final sequence coverage was achieved.

WT BmrA in the two types of nanodiscs showed a totally opposite deuteration profile in the presence of 100 µM doxorubicin (fig. 77 & 78). In case of nanodiscs LMNG, the two ICDs of BmrA, especially ICD 2, demonstrate an increased deuterium uptake in the presence of drug. This effect is being transferred to the NBDs through the peptide 408-412 which lies adjacent to the W413 and R414 residues. R414 is conserved among type IV ABC transporters as shown in last chapter. Contrastingly, in the presence of drug, BmrA in nanodiscs DDM/cholate displays protection against deuteration in almost all the TMHs, the most prominent being TMH5. This protective effect is getting transmitted to the ICDs, especially ICD2 and from there to the NBDs via the peptide 408-413.

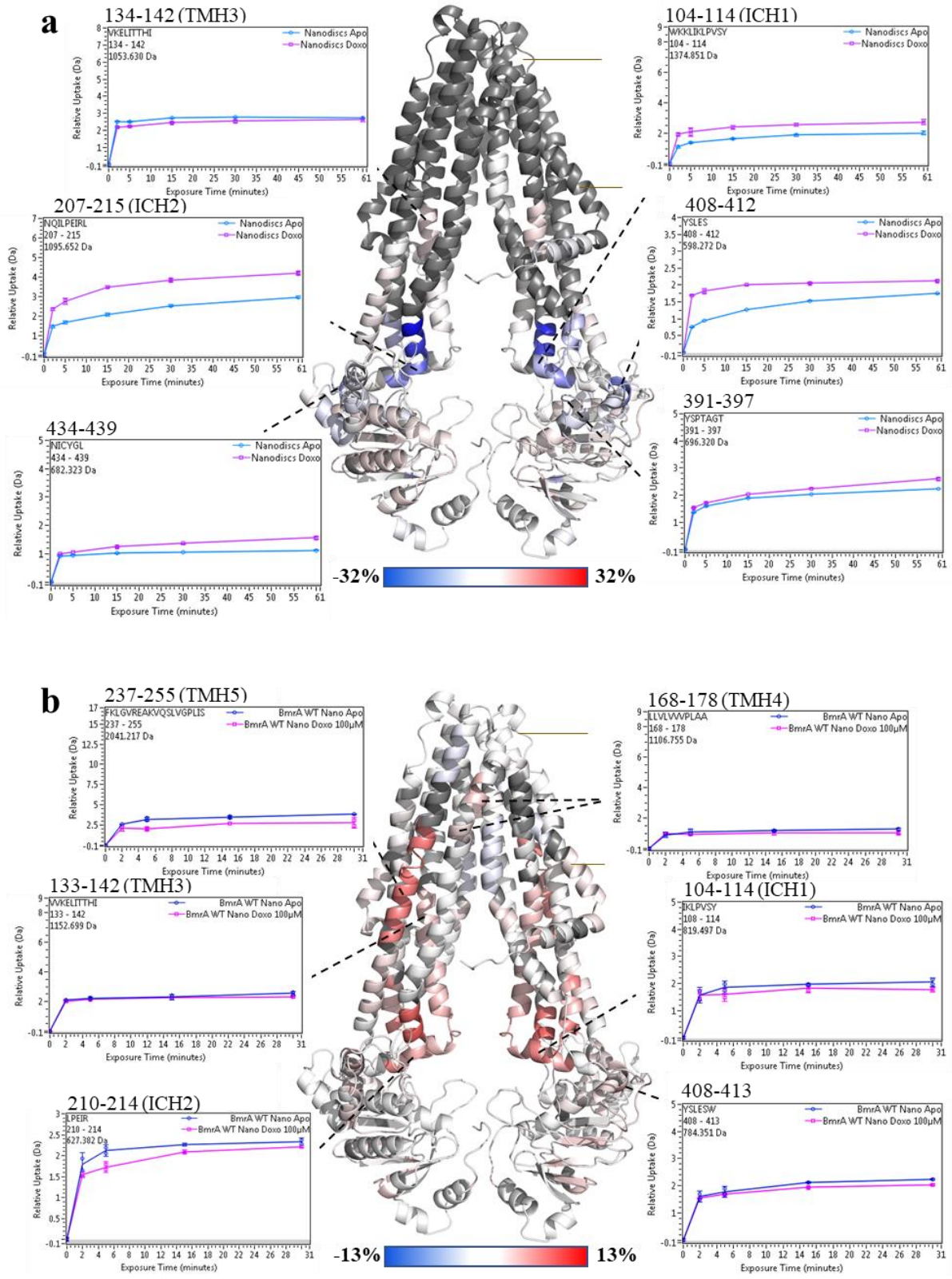

Fig 77. The differential HDX between apo (without ligand) and doxorubicin-bound conditions of nanodisc reconstituted WT BmrA, after 30 min deuteration, is plotted on a homology model of BmrA based on the inward-facing (IF) structure of mouse P-gp (PDB: 3WME) for **(a)** Nanodiscs reconstituted with WT BmrA after purification in LMNG, and **(b)** Nanodiscs reconstituted with WT BmrA after purification in DDM/cholate mixture. The differential deuteration scale is set according to the maximum differential deuteration observed in each

condition and is represented by the colors blue, white and red. Blue signifies the peptides that show more deuteration in the doxorubicin-bound condition. White highlights the peptides with no difference in deuteration level between the two conditions, whereas red pinpoints the peptides that are protected from deuteration in the doxorubicin-bound condition. The box inserts show, in dalton, the relative deuterium uptake in the apo (blue) and doxorubicin-bound conditions (magenta), of some important peptides. The error bars in the inserts show the standard deviation between the duplicates, with sigma multiplier '2', except for the apo condition of BmrA WT nanodiscs reconstituted after purification in LMNG. The brown lines indicate the boundary of the cell membrane. Abbreviations: ICH, intracellular helix; TMH, transmembrane helix.

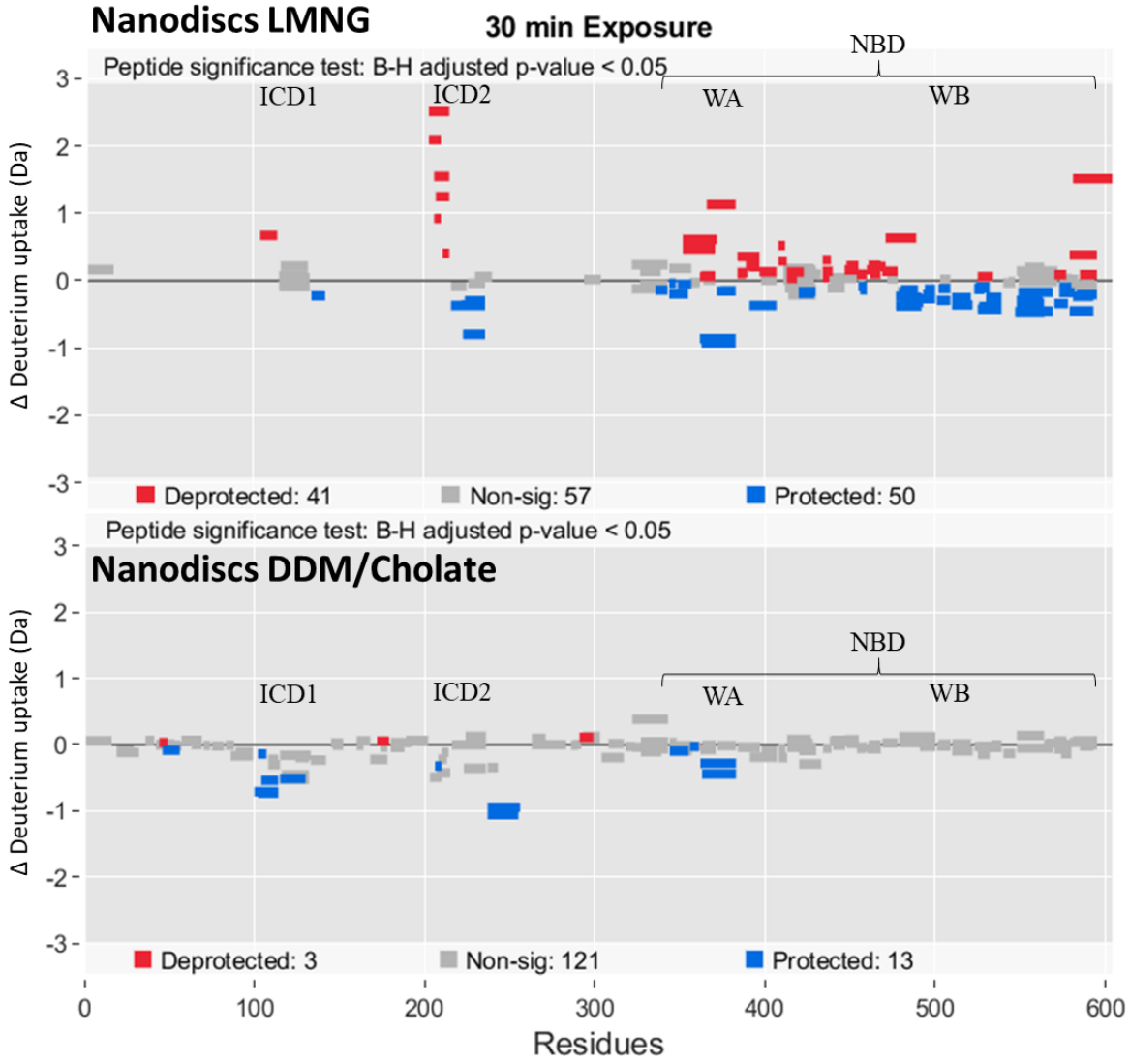

Fig 78. Differential HDX plot of WT BmrA in nanodiscs, reconstituted from WT purified using LMNG or using DDM/Cholate, between the Apo and doxorubicin-bound (100 µM doxo) conditions at 30 min D2O exposure. Blue signifies the peptides protected against deuteration in doxo-bound condition, whereas red signifies the deprotected peptides. Grey represents peptides having p-value more than 0.05. All measurements were done in duplicate except WT apo in nanodisc LMNG.

The only peptide in the TMDs that shows similar result is the peptide 133-142 from TMH3 that shows a slight protection from deuterium incorporation in the presence of doxorubicin.

The residues in BmrA corresponding to the ones involved in taxol binding in P-gp are colored green in fig. 79. The involvement of TMH5 in taxol binding can be clearly seen and this is the region where the maximum protection against deuteration was observed for BmrA in the presence of drug. The residue S255 in the protected peptide visibly overlaps the taxol-binding site. Most of the other taxol-binding residues are buried deep inside, which are not solvent accessible even in the apo condition. However, the conformational change induced by drug-binding can very well be seen being transmitted from the TMHs to the ICDs.

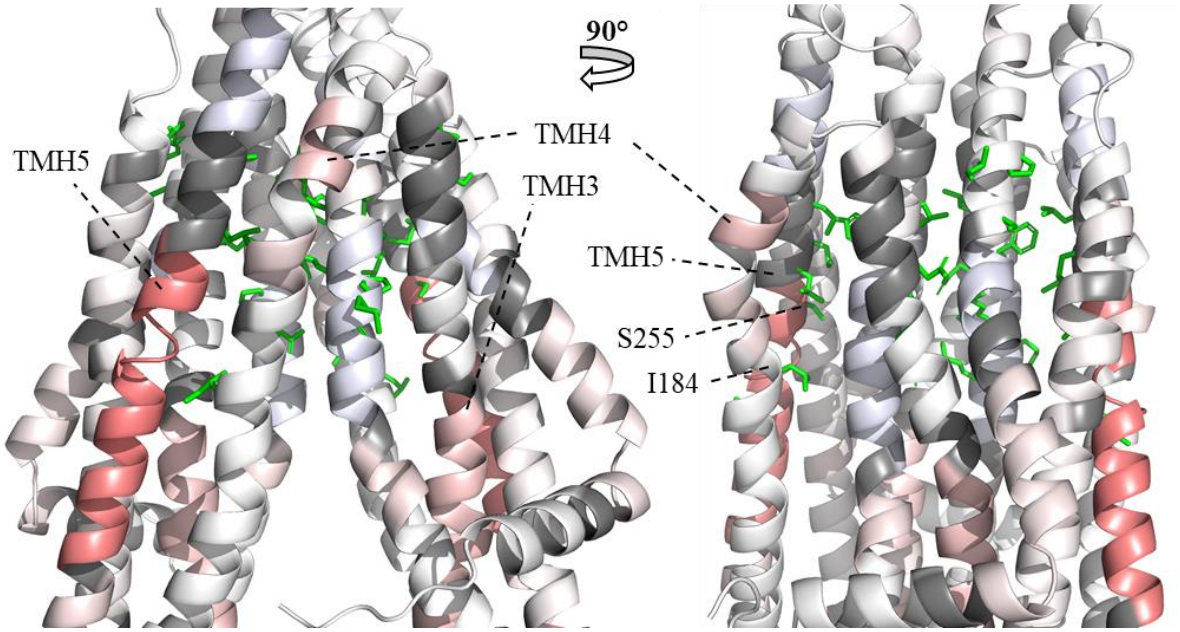

Fig 79. BmrA model based on the inward-facing (IF) structure of mouse P-gp (PDB: 3WME), showing in shades of red the residues protected from deuteration in the presence of 100 µM doxorubicin in nanodiscs DDM/cholate. The side chains of the corresponding residues found to be involved in taxol binding in P-gp are colored green (Alam et al., 2019).

Conclusion & Discussion

The limited proteolysis and HDX results prove that doxorubicin induces conformational change in BmrA. However, in nanodiscs the induced conformational change highly depended on the type of detergent present before reconstitution. In the protocol of nanodiscs, first the lipids are solubilized in DDM (irrespective of the solubilizing detergent used for BmrA) and then, BmrA in either LMNG or DDM/cholate is added, with a subsequent addition of MSP. Eventually, the detergent is removed by the addition of polystyrene bio-beads. It was hypothesized that LMNG might not be efficiently removed by the bio-beads and that residual traces of LMNG could be

responsible for a totally opposite drug-bound profile observed in HDX. Mass spectrometry analysis was carried out on the BmrA nanodiscs LMNG sample, before and after the treatment of bio-beads, to test for the presence of LMNG. And indeed, the signal from LMNG could be seen even after the bio-beads treatment, whereas the signal from DDM (used for the solubilization of lipids) disappeared, confirming our hypothesis (fig. 80).

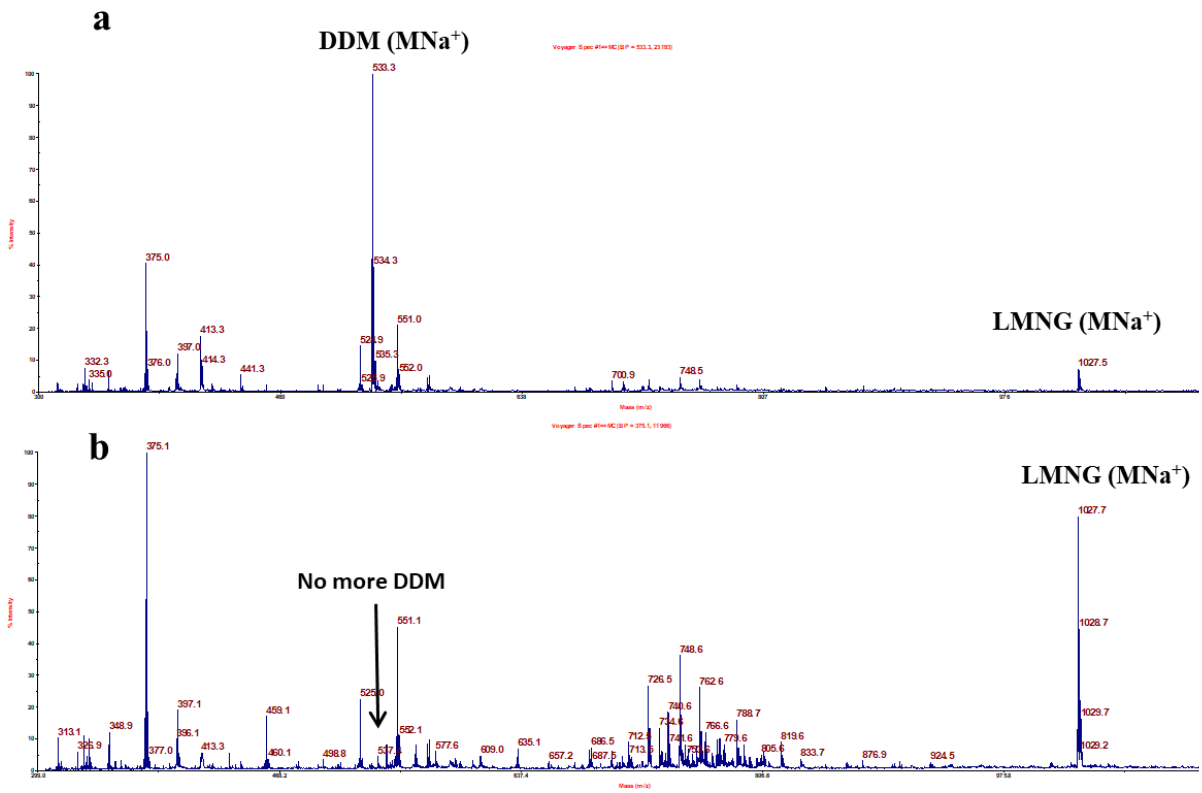

Fig 80. MALDI-TOF MS spectra showing the presence or absence of molecular sodiated ions (MNa+) of DDM & LMNG in the nanodiscs (a) before detergent removal with bio-beads and, **(b)** after detergent removal with bio-beads.

The contrast in HDX results from the two BmrA nanodisc preparations could be explained by the presence of residual LMNG in one of the preparations. It is probable that the residual LMNG binds to the high affinity drug-binding pocket forcing doxorubicin to bind to the low affinity site. Whereas, in case of BmrA nanodiscs DDM/cholate, there is no residual detergent so the drug can bind to the high affinity site. Binding to two different potential drug-binding sites by doxorubicin, may have induced opposite conformational changes in the two types of nanodiscs. In fact, several studies on P-gp proposed the existence of multiple drug-binding sites (Shapiro & Ling, 1997) (Loo et al., 2003) (Garrigos et al., 1997). In their studies, Shapiro and Ling proposed the existence of three drug-binding sides in P-gp namely the R (Rhodamine), H (Hoechst) and P (Prazosin & Progesterone) site. The R and the H sites were shown to be

transport competent with a positive cooperativity between the two whereas the P site was found to be an allosteric site (Shapiro et al., 1999).

Conclusion and Perspectives

During the course of my PhD, BmrA was studied in different environments and indermediate conformations of BmrA were unraveled for the first time for the catalytic cycle of BmrA including ATP-bound predimerization state and ADP-bound post hydrolysis state. These are indicated by arrows in fig 81.

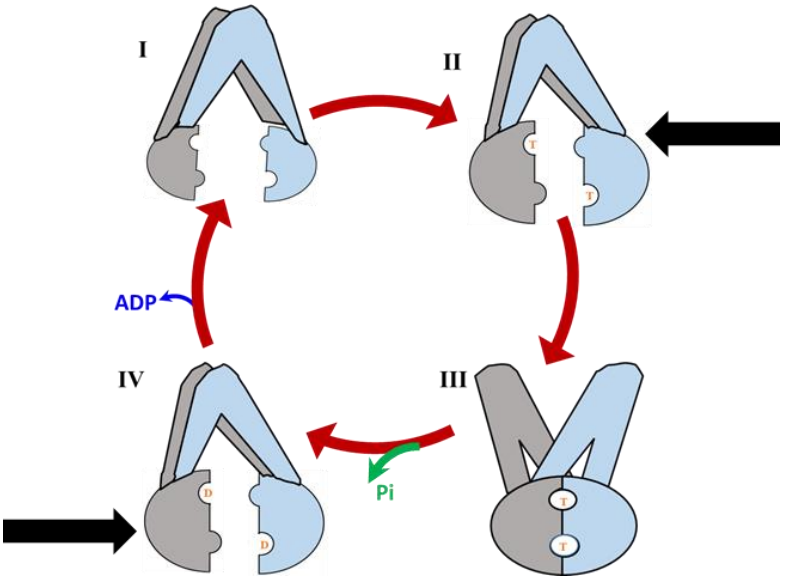

Fig 81. Proposed catalytic cycle of BmrA. All features same as fig 55.

In addition to this, a new drug-bound conformation was revealed for BmrA in nanodiscs. In this conformation, the doxorubicin binding site was observed to partially overlap with the corresponding taxol binding site in P-gp (fig 82).

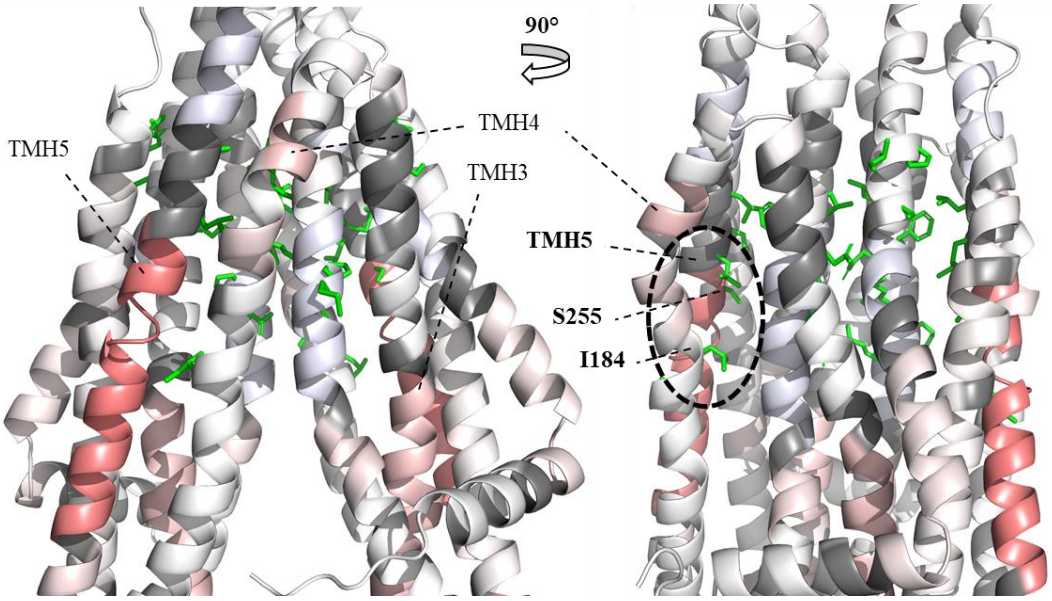

Fig 82. BmrA model based on the inward-facing (IF) structure of mouse P-gp (PDB: 3WME), showing in shades of red the residues protected from deuteration in the presence of 100 µM doxorubicin in nanodiscs DDM/cholate. The black oval highlights the corresponding residues involved in taxol binding in P-gp.

Moreover, tryptophan W413 was identified as a relay between NBD and TMD communication (fig. 83).

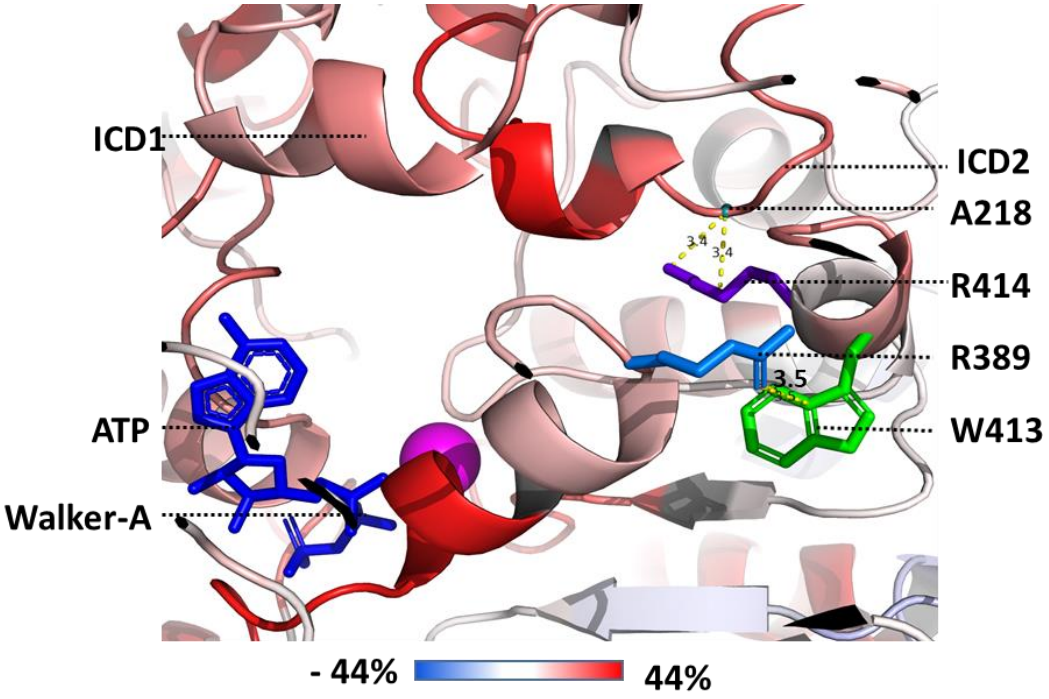

Fig 83. W413 shown to be a relay between NBD and TMD communication. All features same as fig 67.

Although the lipid containing environment of nanodiscs mimic the native environment of the protein, but it would be equally interesting to investigate by HDX-MS, the different conformations of BmrA in inverted membrane vesicles which are the closest mimic to the native environment. This would further confirm the results already obtained in detergent and nanodiscs. It would also be time saving, work saving and cost effective as the purification and reconstitution steps are not required. To achieve this, after thorough optimization process, a protocol was established to study BmrA in IMVs by HDX-MS. Quite interestingly, a sequence coverage of 78% was achieved (fig. 84) for BmrA in IMVs which is higher than the one achieved for BmrA in detergent. This sequence coverage was achieved with C18 UPLC column and using DDM to destabilize the IMVs in order to remove the excessive phospholipids by zirconium beads. There is a huge margin for improvement and a higher sequence coverage could be achieved if C4 UPLC column is used instead of C18. This was seen for BmrA in nanodiscs where a sequence coverage of around 95% was touched by using C4 column. The other important point is the addition of DDM/Cholate mixture in quench buffer for the destabilization of membranes, just before the addition of zirconium beads to remove the phospholipids.

Regarding the NBD-TMD communication in BmrA, another interesting observation was made for K380A BmrA in LMNG in the presence of ATP. As already concluded that this mutant is unable to dimerize upon ATP binding although it is still able to bind ATP. The stabilization of the adenine ring of ATP by the A-loop (Y350) was observed to be sensed by the highly conserved F348 (fig. 86) and the conformational change was transferred to the conserved Y391

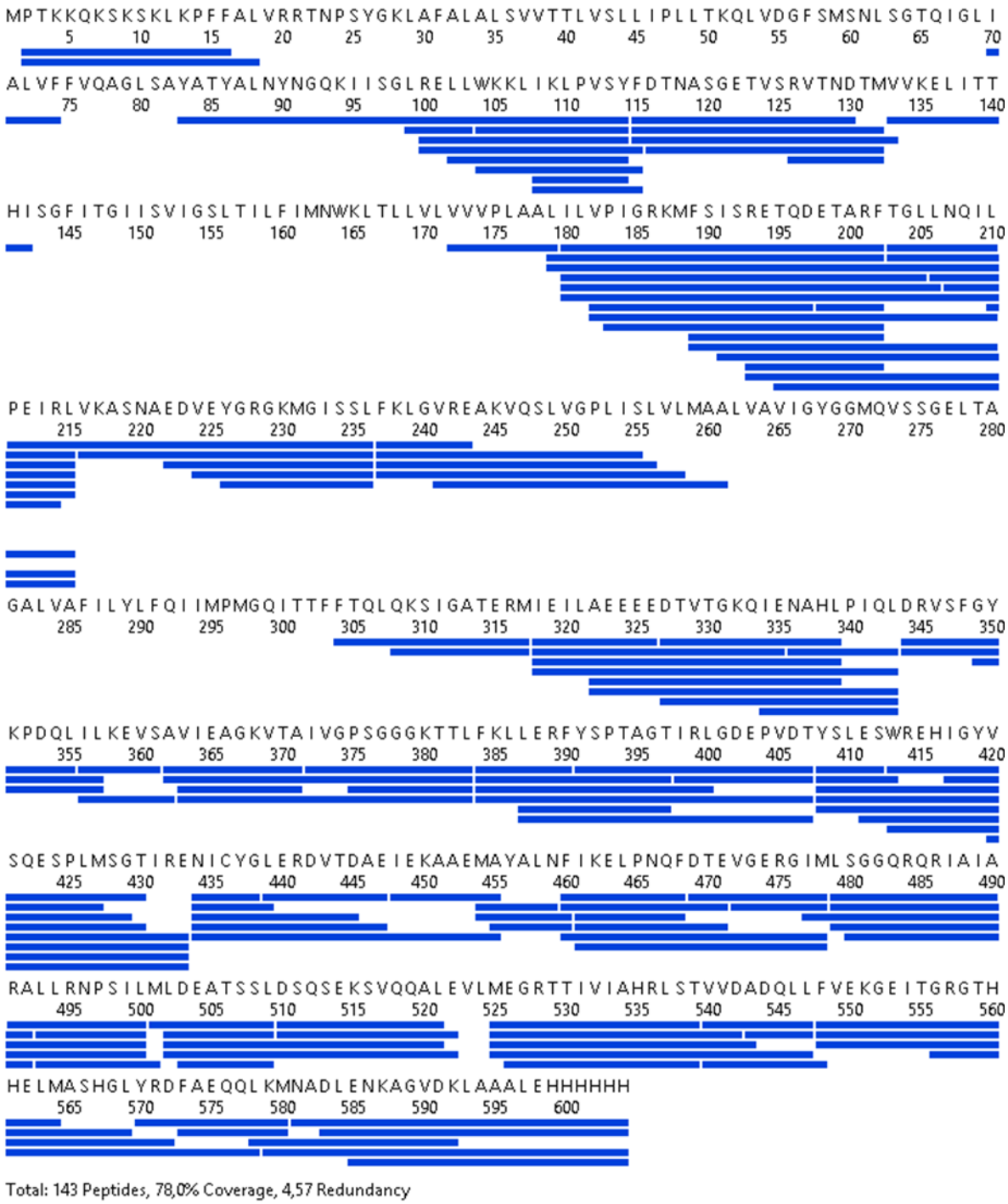

Fig 84. Sequence coverage map of WT BmrA in IMVs. The blue bars represent the recovered peptides, mapped on the primary sequence of the protein. A 78 % final sequence coverage was achieved. Note that residues 29-309 constitute TMD and 341-576 form the NBD.

and from there to D116 in ICD1 (fig 85). This D116 is also conserved among type IV multidrug transporters and may also communicate with the R214 of the ICD2. In the homology model of BmrA based on IF structure of P-gp, all these residues lie in the range of 3.5Å to one another making the interaction highly probable. Therefore, this NBD-TMB communication pathway from A-loop to coupling helix 1 seems very interesting and needs to be further investigated by mutating, one by one, the residues highlighted and then analyzing through drug transport and ATPase activity assays and by using HDX-MS.

All these results may pave the way for designing targeted inhibitors of these multidrug exporters and eventually help in countering multidrug resistance.

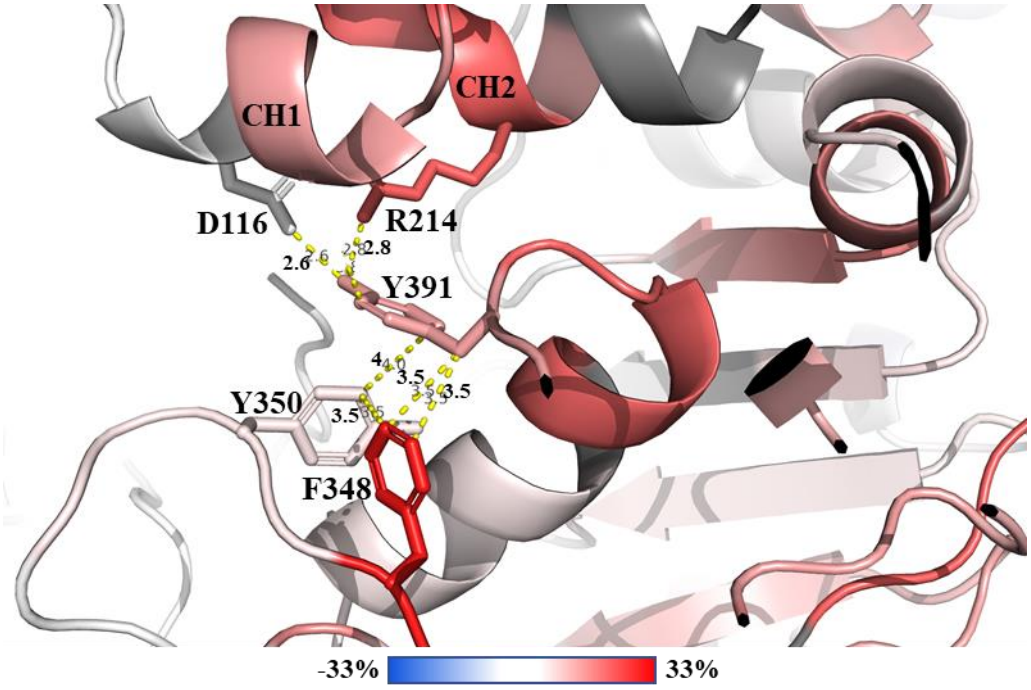

Fig 85. The potential NBD-TMD connection pathway is shown for K380A BmrA in LMNG. The homology model of BmrA based on the inward-facing (IF) structure of mouse P-gp (pdb 3WME) is used to plot the differential HDX of K380A BmrA in LMNG after 60 min deuteration, between the apo and ATP-incubated conditions (10 mM ATP/$MgCl_2$). The differential deuteration scale is set from -33% to 33% represented by the colors blue, white and red. Red signifies the peptides that show protection from deuteration in the ATP-incubated condition. The sidechains of the labelled residues are also shown and the inter-residue distances are highlighted by yellow dotted lines. The distances are in angstrom. Abbreviations: CH, coupling helix.

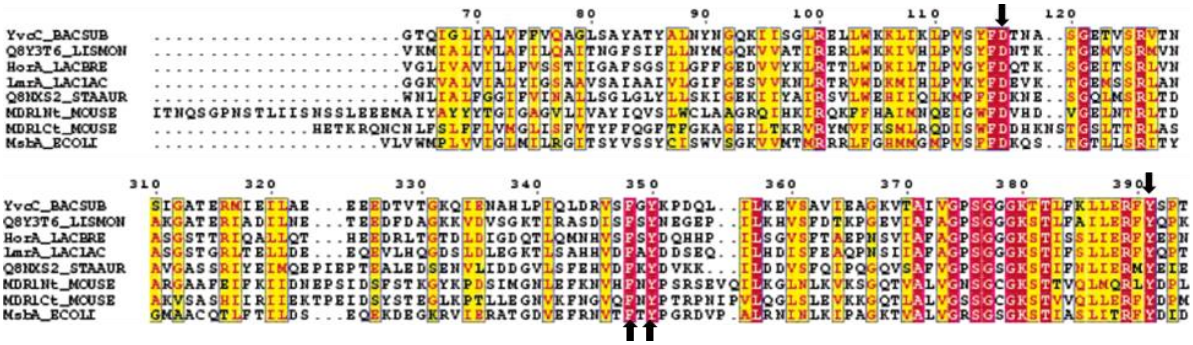

Fig 86. Sequence alignment of some type IV ABC transporters. YvcC is the old name of BmrA. Red highlights the highly conserved residues and yellow signifies similarity. The black arrows indicate residues D116, F348, Y350 and Y391. Abbreviations: BACSUB, *B. subtilis*; LISMON, *L. monocytogenes*; LACBREV, *L. brevis*; LACLAC, *L. lactis*; STAAUR, *S. aureus*; ECOLI, *E. coli*. Figure adapted from (Steinfels et al., 2004).

Chapter 4: Publication 1

Functionality of membrane proteins overexpressed and purified from *E. coli* is highly dependent upon the strain

My contribution includes complete fig. 3 and fig. 6C and 6D, and all the related experimental work.

SCIENTIFIC REPORTS

OPEN

Functionality of membrane proteins overexpressed and purified from *E. coli* is highly dependent upon the strain

Received: 15 October 2018
Accepted: 22 January 2019
Published online: 25 February 2019

Khadija Mathieu[1], Waqas Javed[1,3], Sylvain Vallet[1], Christian Lesterlin[1], Marie-Pierre Candusso[1], Feng Ding[2], Xiaohong Nancy Xu[2], Christine Ebel[3], Jean-Michel Jault[1] & Cédric Orelle[1]

Overexpression of correctly folded membrane proteins is a fundamental prerequisite for functional and structural studies. One of the most commonly used expression systems for the production of membrane proteins is *Escherichia coli*. While misfolded proteins typically aggregate and form inclusions bodies, membrane proteins that are addressed to the membrane and extractable by detergents are generally assumed to be properly folded. Accordingly, GFP fusion strategy is often used as a fluorescent proxy to monitor their expression and folding quality. Here we investigated the functionality of two different multidrug ABC transporters, the homodimer BmrA from *Bacillus subtilis* and the heterodimer PatA/PatB from *Streptococcus pneumoniae*, when produced in several *E. coli* strains with T7 expression system. Strikingly, while strong expression in the membrane of several strains could be achieved, we observed drastic differences in the functionality of these proteins. Moreover, we observed a general trend in which mild detergents mainly extract the population of active transporters, whereas a harsher detergent like Fos-choline 12 could solubilize transporters irrespective of their functionality. Our results suggest that the amount of T7 RNA polymerase transcripts may indirectly but notably impact the structure and activity of overexpressed membrane proteins, and advise caution when using GFP fusion strategy.

Membrane proteins account for about 20–30% of synthesized proteins in all organisms[1]. They play key roles in human diseases and are targeted by more than half of therapeutic drugs. Native membrane proteins are generally insufficiently abundant to isolate material for biochemical and structural studies. Therefore, membrane proteins are often overexpressed in heterologous systems. The bacterium *Escherichia coli* is the most convenient and widely used system for overexpression of both soluble and membrane proteins[2,3]. The reason is largely historical due to a wealth of knowledge regarding its physiology, the availability of effective genetic tools and well-known advantages: (i) easy DNA transformation; (ii) fast growth and high cell density cultures; (iii) inexpensive culture costs and (iv) high yield of overexpression. The *E. coli* BL21(DE3) strain together with T7 promoter-based plasmids have been extensively employed to massively overexpress proteins. In this system, the T7 RNA polymerase gene is located in the DE3 prophage of the chromosome under the control of the IPTG-inducible L8-UV5 *lac* promoter, which is a more powerful variant of the wild-type lac promoter. Two base pair substitutions make the −10 promoter sequence closer to the consensus one recognized by bacterial sigma factors, thereby recruiting the RNA polymerase more effectively and decreasing its dependence on CAP/cAMP stimulation for full activation. A third mutation, located in the CAP/cAMP binding site, decreases the affinity for CAP/cAMP. These 3 mutations thus create a stronger promoter that is less sensitive to catabolic repression[4]. The BL21(DE3) strain is also deficient in Lon and OmpT proteases, and the T7 RNA polymerase transcribes ~8 times faster than native *E. coli* RNA polymerases[5] to generate high level of mRNA available for protein synthesis. However, such strategy may not be the most appropriate for some proteins, especially those that are toxic. As such, the overexpression of

[1]Université de Lyon, CNRS, UMR 5086 "Molecular Microbiology and Structural Biochemistry", IBCP, 69367, Lyon, France. [2]Department of Chemistry & Biochemistry, Old Dominion University, Norfolk, VA, 23529, USA. [3]Université Grenoble Alpes, CNRS, CEA, IBS, 38000, Grenoble, France. Correspondence and requests for materials should be addressed to J.-M.J. (email: jean-michel.jault@ibcp.fr) or C.O. (email: cedric.orelle@ibcp.fr)

membrane proteins may have detrimental effects by their intrinsic function, improper folding or by exceeding the capabilities of the machineries involved in membrane protein biogenesis and protein secretion[6–8]. Twenty years ago, Miroux and Walker designed a simple screening approach to isolate BL21(DE3) mutant strains displaying improved membrane protein overexpression abilities[9]. BL21(DE3) cells expressing toxic membrane proteins were plated on medium containing the IPTG inducer to select for surviving colonies that can cope with the toxic effects associated with membrane protein overexpression. With this approach, the C41(DE3) and C43(DE3) strains were selected and are now widely used to overexpress membrane proteins, although they do not improve yields for all of them. Much later, it was discovered that the C41(DE3) and C43(DE3) contained 3 mutations in the lacUV5 promoter[10]. The two mutations in the -10 region turned back the lacUV5 promoter into the much weaker wild-type lac promoter. Moreover, in contrast to the lacUV5 promoter, the wild-type lac promoter is susceptible to catabolite regulation. Therefore, a reduced transcription rate in these derivative strains likely explains why overexpression of many membrane proteins is hardly toxic for their growth and results in substantially improved membrane protein overexpression yields. Although the identified genetic differences lie in the lacUV5 promoter, they may have indirect effects on mRNA stability, protein translation and folding or stress response. For instance, Wagner and colleagues hypothesized that high transcription levels of membrane proteins is counterproductive because it leads to the saturation of the Sec translocon[10]. As a result, most overexpressed and endogenous membrane proteins fail to insert into the membrane and aggregate, resulting in cellular deleterious effects. Based on these observations, this team successfully engineered a BL21(DE3) variant strain named Lemo21(DE3), in which the activity of the T7 RNA polymerase can be finely tuned by its natural inhibitor T7 lysozyme, whose gene is under the control of the rhamnose promoter[10,11]. The optimization of membrane protein synthesis and their insertion into the membrane can thus strongly minimize the toxic effects associated with membrane protein overexpression, resulting in higher bacterial biomass and protein yield. However, it is unclear whether the quality of membrane proteins successfully incorporated into the membrane can also be affected by the T7 polymerase expression. The most popular tool for quality control of membrane proteins remains the use of GFP fusion to monitor the level of fluorescence produced by the host, which was shown to directly correlate with the amount of protein of interest properly inserted in the cytoplasmic membrane[12].

Here, we report the overexpression of two different multidrug ABC transporters in various *E. coli* expression strains governed by T7 RNA polymerase/promoter system. The first one is the heterodimeric PatA/PatB transporter from *Streptococcus pneumoniae*. Although its biochemical characterization is at early stages[13,14], its implication in clinical resistance to antibiotics was clearly demonstrated by the group of Piddock[15–17]. The second one is the homodimeric BmrA transporter from *Bacillus subtilis*[18]. BmrA is a fairly robust membrane protein, which can be produced and purified from *E. coli* in high yields for mechanistic characterization[19,20], detergent/reconstitution method developments[21–24] and structural studies, i.e. cryo-EM[25] or solid-state NMR[26]. Here, we show that these membrane proteins can be expressed and addressed to the membrane equally well in different *E. coli* strains, but they are substantially more functional and easier to solubilize by mild detergents when overexpressed in the C41(DE3) strain. In addition, we also analyzed a BmrA-GFP chimeric construct since such a strategy has been widely used to screen for the production and structural integrity of membrane proteins, based on the assumption that a fluorescent GFP is a direct readout of the proper folding of the fused protein of interest. Overall, our data strongly suggest that membrane proteins may be targeted to *E. coli* membranes but not necessarily in a properly folded form. Our study illustrates that functionality of membrane proteins drastically depends on the *E. coli* expressing strain and cautions against choosing an expression strain based solely on expression levels. Moreover, the fluorescence of the fused GFP will not necessarily attest of the quality of the membrane protein of interest and this assay should thus be used with caution.

Results

Overexpression of PatA/PatB in various *E. coli* strains. PatA/PatB is a heterodimeric multidrug ABC transporter from *Streptococcus pneumoniae*[13,27,28] involved in clinical resistance to fluoroquinolones. We overexpressed this transporter in different *E. coli* strains: BL21(DE3), C41(DE3), and T7 express. The latter is a BL21 derivative in which the T7 polymerase gene is inserted in the lactose operon and is thus expressed under the control of the lac promoter. This design permits controlled induction of the polymerase and consequently, inducible control of transcription of genes downstream of the T7 promoter. This system provides potential advantages over strains that carry the T7 RNA polymerase on a lysogenic prophage DE3. Although λDE3 is normally dormant in the host chromosome, the expression of toxic proteins may results in the induction of the SOS cascade that directly or indirectly damage the *E. coli* chromosome leading to cell lysis. The expression of PatA/PatB was induced overnight at 25 °C by IPTG addition at high $OD_{600\,nm}$ (~1.7), as published before[13,14]. In addition, the BL21(DE3) strain was either induced by IPTG or by using an auto-induction media. Auto-induction under diauxic growth conditions in media containing glucose, lactose, and glycerol is a convenient approach for *lac*-based expression systems in *E. coli*. It relies on inducer exclusion between glucose and lactose, preventing the induction by lactose before glucose consumption[29]. In these conditions, similar amounts of the transporter were overexpressed in the membrane fractions of all strains (Figs 1A and S1 for empty vector control). These results indicate that the transporter could be efficiently addressed to the *E. coli* membrane regardless of the strains employed.

Drug transport catalyzed by PatA/PatB in inverted membrane vesicles. Exceeding the capacity of the bacterial cell to process the nascent membrane protein correctly may result in the production of aggregated material that fail to insert in the membrane and that end up in inclusion bodies[3,30]. The similar overexpression of PatA/PaB in the membrane fraction of the various strains suggested *a priori* that PatA/PatB was correctly folded in the experimental conditions tested here. However, misfolded material can also be found associated with the membrane[30], and we sought to verify whether the transporters overexpressed from the various strains were equally functional. The transport functionality was assayed at 25 °C by using Hoechst 33342, which is a

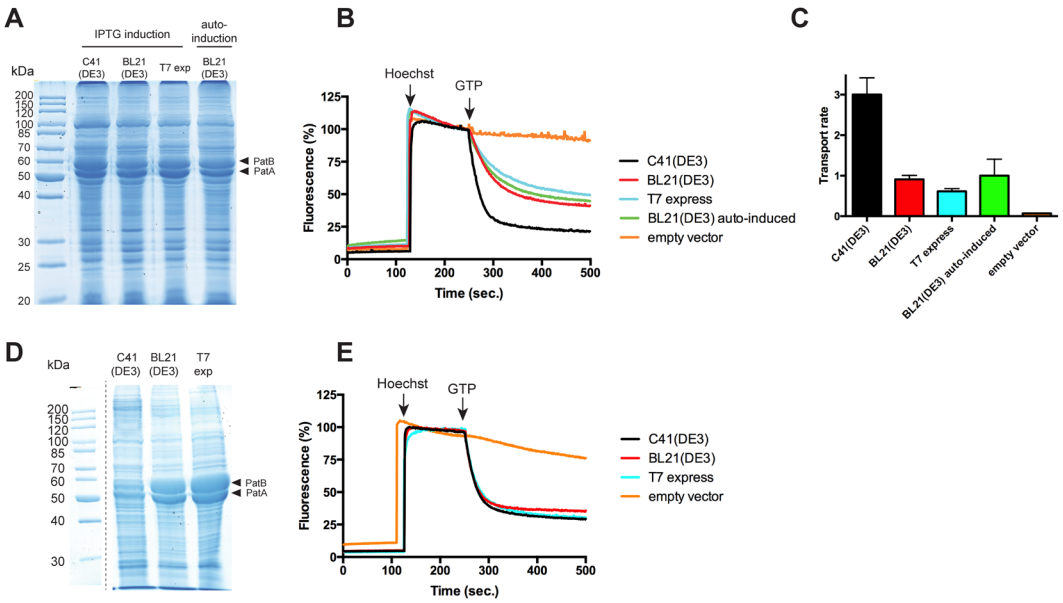

Figure 1. Overexpression of PatA/PatB in various *E. coli* strains and functionality of the transporter. (**A**) Expression of the transporter was either induced overnight by IPTG when cells reached OD_{600}~1.8 or by auto-induction. Membrane fractions were analyzed by 12% SDS-PAGE stained with Coomassie blue. Twenty µg of proteins were loaded in each lane. (**B**) Hoechst 33342 transport assays with inverted membrane vesicles prepared from the various strains in panel A. 50 µg of total membrane proteins were used for each sample. (**C**) Hoechst 33342 transport rates were measured by initial slopes following GTP addition. The empty vector was used in the C41(DE3) strain. The data represent the average of two independent experiments, each with triplicates, and error bars indicate the standard deviation. (**D**) Expression of the transporter was induced by IPTG in exponential phase for 5 h. Membrane fractions were analyzed by 12% SDS-PAGE stained with Coomassie blue. Twenty µg of proteins were loaded in each lane. Dash line delineates cropped images from different parts of the same gel. (**E**) Hoechst 33342 transport assays with inverted membrane vesicles prepared from the various strains in panel (D). The empty vector was used in the C41(DE3) strain. Two hundred µg of total membrane proteins were used for each assay. Data shown are representative of two independent experiments.

fluorescent drug translocated by PatA/PatB and many drug transporters (e.g. P-glycoprotein[31]). Transport was energized by GTP, which is the preferred energy source for PatA/PatB[14]. Strikingly, Hoechst 33342 was much better transported (>3 fold) when PatA/PatB was expressed in C41(DE3) strain as compared to the other strains (Fig. 1B,C). In the absence of PatA/PatB (see Fig. S1 for coomassie-stained gel), C41(DE3) membranes display no Hoechst transport at that temperature (Fig. 1B). Next, we induced the expression of the transporter at exponential phase (when $OD_{600\,nm}$ was between 0.3 and 1), for 5 hours at 25 °C. While expression of PatA/PatB was much less efficient in the C41(DE3) strain (Fig. 1D), transport of Hoechst 33342 was fairly similar from all three strains tested when equivalent amounts of total membrane proteins were used (Fig. 1E), showing again that the transport activity of PatA/PatB, i.e. related to the total amount of the transporter in the membrane, was far superior when expressed in C41(DE3) strain. In order to address the possibility that the rate of transport reached a saturation level in this experiment, 4 times less membrane vesicles were used but a similar level of transport activity was again found with the three different strains (Fig. S2). Thus, despite being addressed to the membrane, a large fraction of PatA/PatB is not functional in BL21(DE3) or T7 express cells.

Detergent solubilization of PatA/PatB. Since the conformation of PatA/PatB appears dependent on the strain used for overexpression, we next investigated the capacity of different detergents to solubilize the transporter from these three strains. Strikingly, detergents like n-dodecyl-β-D-maltoside (DDM), lauryl maltose neopentyl glycol (LMNG), triton X-100 and lauryldimethylamine N-oxide (LDAO) solubilized much better PatA/PatB overexpressed in C41(DE3) as compared to the two other strains (Fig. 2). The n-octyl-β-D-glucoside (OG) was less efficient to solubilize PatA/PatB from the C41(DE3) strain but was inefficient when used with membranes prepared from the two other strains. In contrast, the harsher detergent Fos-Choline 12 (FC12) was able to solubilize the transporter regardless of the strain used for the overexpression. These experiments suggest that PatA/PatB is less extractable by milder detergents when it is not optimally folded and functional in membranes.

Overexpression and functionality of BmrA in several *E. coli* strains. The choice of overexpressing strain appeared critical for the functionality of PatA/PatB. Does this hold true for other membrane proteins whose activity can be directly and easily probed before any detergent extraction? We took advantage of functional tests developed with BmrA, a multidrug ABC transporter from *B. subtilis*[18] that we historically expressed in C41(DE3) strain[32], to address this question. In contrast to PatA/PatB[13,14], BmrA is a homodimeric transporter[33]

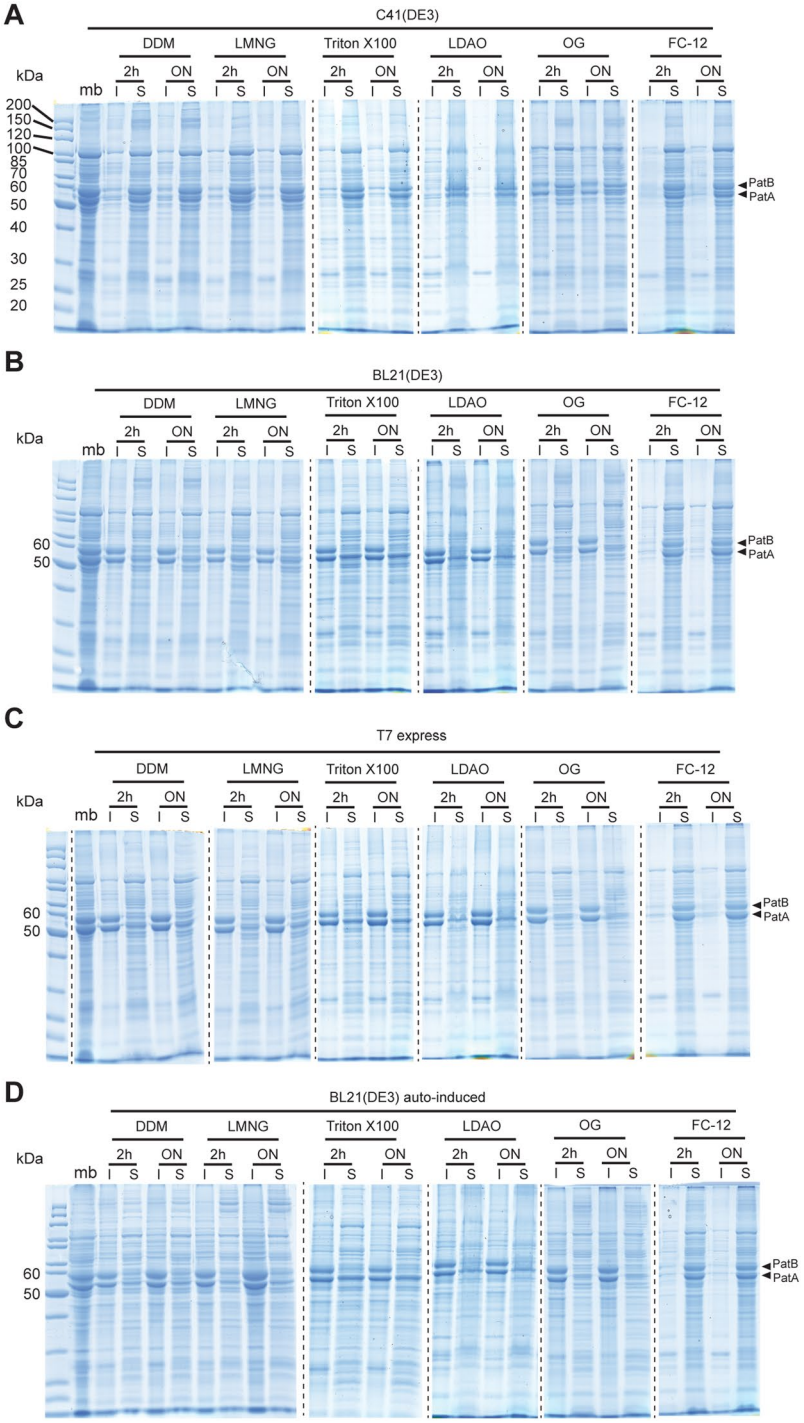

Figure 2. Detergent solubilization of overexpressed PatA/PatB from membranes isolated from various strains. A selection of detergents was employed to extract PatA/PatB from the membranes (10 µg of total proteins) displayed in Fig. 1A, either for 2 h or for overnight incubation. After ultracentrifugation, the soluble (S) and insoluble (I) fractions were submitted to 12% SDS-PAGE. Twenty µg of proteins were loaded in the membrane lane (mb). (**A**) PatA/PatB solubilization from C41(DE3) membranes. (**B**) PatA/PatB solubilization from BL21(DE3) membranes. (**C**) PatA/PatB solubilization from T7 express membranes. (**D**) PatA/PatB solubilization from BL21(DE3) membranes prepared after auto-induction expression. Dash lines delineate cropped images from different parts of the same gel or from different gels.

and it is also classically powered by ATP binding and hydrolysis. BmrA was efficiently overexpressed in C41(DE3) and T7 express strains, while the level of membrane expression was lower in BL21(DE3) strain (Fig. 3A). Of note, BL21(DE3) was also difficult to transform by the plasmid carrying BmrA, with 10 to 100 times less transformants

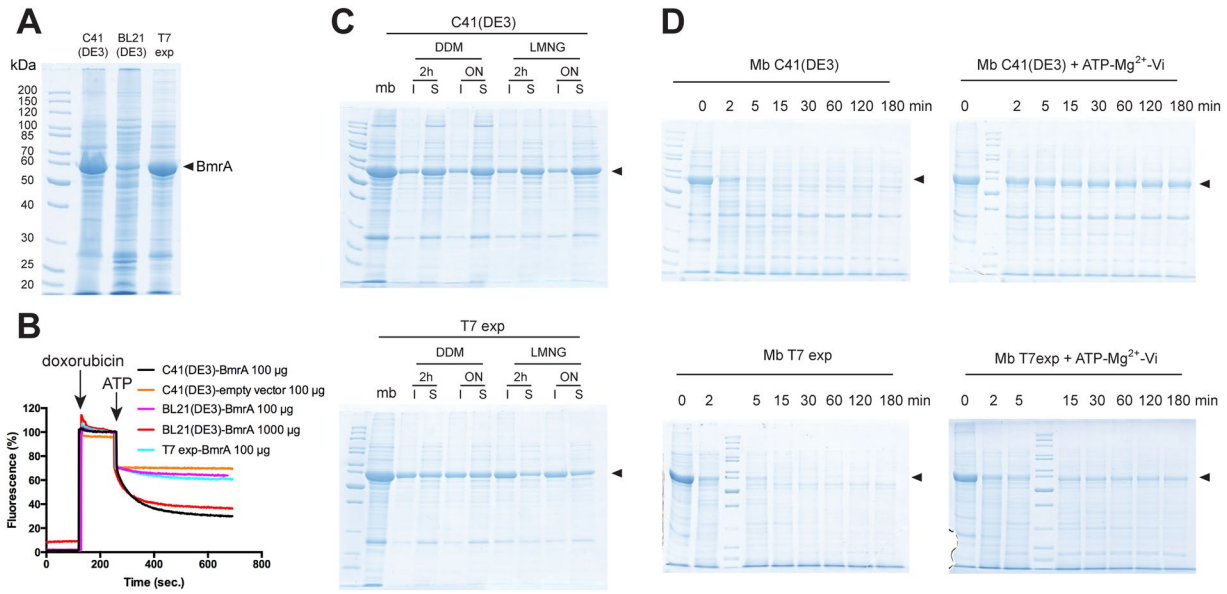

Figure 3. Overexpression of BmrA in the membrane of various *E. coli* strains and functionality of the transporter. The expression of the transporter was induced by IPTG in exponential phase for 4 h. (**A**) Membrane protein expressions were visualized by 12% SDS-PAGE stained with Coomassie blue. Twenty µg of proteins were loaded in each lane. (**B**) Doxorubicin transport assays with inverted membrane vesicles prepared from the various strains. For the assays, 100 µg of total proteins were used for C41(DE3) and T7 express membranes, while 100 or 1000 µg were used for BL21(DE3) membranes. A representative experiment of 2–3 replicates is shown. (**C**) Detergent solubilization of membranes containing BmrA overexpressed from various strains. DDM or LMNG detergents were employed to extract BmrA from the membranes (10 µg of total proteins), either for 2 h or for overnight incubation. After ultracentrifugation, the soluble (S) and insoluble (I) fractions were submitted to 12% SDS-PAGE. Twenty µg of proteins were loaded in the membrane lane (mb). (**D**) Limited proteolysis of BmrA by trypsin. Membranes (Mb) from C41(DE3) or T7 express strains containing overexpressed BmrA were submitted to trypsin digestion for the indicated times, in the absence of ligand or after an incubation with ATP, Mg^{2+} and orthovanadate.

as compared to the other strains. We performed transport assays with doxorubicin, and not Hoechst 33342, for the following reason. Since BmrA is less expressed in BL21(DE3) membranes, we aimed to add a higher amount of these membranes in transport assays to have similar amounts of BmrA. We estimated by coomassie-stained SDS-PAGE that BmrA was about 10 times less expressed in BL21(DE3) strain as compared to the two other strains (Fig. S3). Hoechst fluorescence is highly dependent on the amount of membranes because its quantum yield drastically increases in hydrophobic environments[31], whereas doxorubicin fluorescence is not sensitive to that and is simply quenched by DNA when transported inside the inverted membrane vesicle[34]. In addition, there is no basal transport of doxorubicin in *E. coli* membranes[18], giving us the opportunity to freely increase the quantity of BL21(DE3) membranes in doxorubicin transport assay. As observed in Fig. 3B with equivalent amounts of BmrA in the assay medium (~10 times more membrane of BL21(DE3) as compared to the other strains), BmrA efficiently transports doxorubicin when expressed in C41(DE3) or BL21(DE3) strains, but not in T7 express strain. As shown previously for PatA/PatB, the DDM and LMNG detergents solubilized BmrA more efficiently when expressed in C41(DE3) strain as compared to T7 express strain (Fig. 3C), while FC12 solubilized nearly all BmrA in each strain (Fig. S4A). Of note and in contrast to PatA/PatB, Triton X100 solubilized 50% of BmrA in all strains (Fig. S4B). To check whether BmrA could properly cycle between the inward- and outward-facing conformations in membranes, limited digestion with trypsin was carried out as performed before[19]. In C41(DE3) membranes, BmrA in the apo (inward-facing) conformation was rapidly digested by trypsin, i.e. within 5 min (Fig. 3D). In the closed vanadate-trapped conformation (outward-facing), however, most of BmrA was resistant to this protease for about 180 min. This result corroborated the ability of BmrA to switch between two very different conformations when functionally overexpressed in C41(DE3) membranes[19]. In contrast, less than 30% of BmrA (quantification made using ImageJ software) expressed in T7 express membranes switched from the inward- to the outward-facing conformations as it was rapidly digested by trypsin in both conditions, apo and vanadate-trapped conformations. Of note, ~30% of BmrA expressed in T7 express strain was solubilized by LMNG (Fig. 3C). Thus, these results suggest that the majority of the protein was improperly folded in this strain.

Overexpression and functionality of BmrA-GFP fusions in *E. coli* strains. Fusing GFP to the C-terminus of membrane proteins has been widely used as a strategy to monitor the levels of membrane proteins properly addressed to the membrane[3]. The GFP does not fold properly and does not fluoresce when the overexpressed protein ends up in inclusion bodies[12]. Although this tool does not provide direct information on the functionality of the synthesized proteins, GFP fluorescence was correlated with the functional overexpression

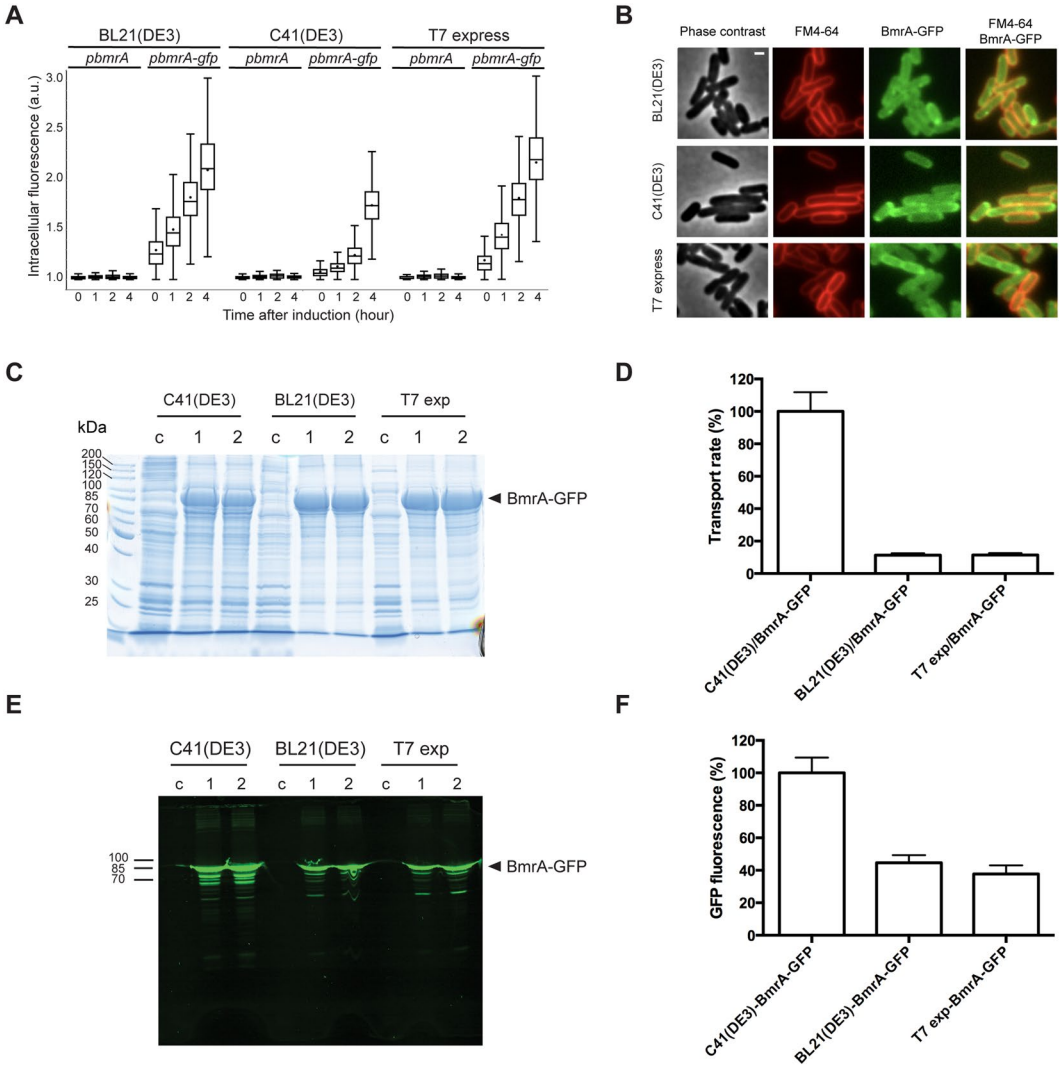

Figure 4. Overexpression of BmrA-GFP fusions in various *E. coli* strains and functionality of the transporter. (**A**) Analysis of BmrA-GFP production by live-cells fluorescence microscopy. Quantification of GFP intracellular signal was performed in BL21(DE3), C41(DE3) and T7 express strains containing plasmids that encode IPTG-inducible BmrA-GFP (*pbmrA-gfp*) or BmrA (*pbmrA*) proteins. Box-and-whisker plots show the statistical distribution of cellular fluorescence normalised to background before, and 1, 2 and 4 h after addition of IPTG (0.7 mM) (between 600 and 1800 cells analysed). (**B**) BmrA-GFP membrane localisation. Microscopy images taken 3 h after IPTG induction show BmrA-GFP (green channel) colocalisation with FM4-64 membrane-staining dye (red channel) in all three strains containing *pbmrA-gfp* plasmid. Scale bar, 1 μm. (**C**) membrane fractions were isolated from the strains after 4 h of induction and analyzed by 12% SDS-PAGE with Coomassie blue staining. Two preparations of BmrA-GFP (indicated as 1 and 2) and one control preparation with an empty vector (indicated as c) were analyzed for each strain. Twenty μg of proteins were loaded in each lane. (**D**) Doxorubicin transport rates with inverted membrane vesicles prepared from the various strains. Rates were calculated from initial slopes (Fig. S5). The data represent the average of triplicates, and error bars indicate the standard deviation. (**E**) In-gel fluorescence of BmrA-GFP was scanned with a typhoon imager. (**F**) Green fluorescence displayed by BmrA-GFP in membranes, as quantified with a spectrofluorometer and corrected from the amount of BmrA-GFP in each membrane (as determined in Figs S6 and S7). The data represent the average of triplicates, and error bars indicate the standard deviation. Panels 4C–F were analyzed with the same batches of membrane preparation.

of a number of fused membrane proteins[30]. We thus sought to determine if this assumption was correct with BmrA as a case study. Previously, The functionality of BmrA fused to GFP was shown to be retained in *B. subtilis*[35]. First, overexpression of a BmrA-GFP fusion was monitored as a function of induction time in C41(DE3), BL21(DE3) and T7 express strains (Fig. 4A). By looking at the kinetics, the induction of BmrA-GFP was slower in C41(DE3) as compared to the other strains in which fluorescence raised much earlier. Moreover, after 4 h of induction the level of fluorescence was very high in both the T7 express and the BL21(DE3) strains, but a bit reduced in the C41(DE3) strain. In these three strains, the BmrA-GFP fusion appears to be present in, or close to, the membrane (Fig. 4B), suggesting that a significant fraction of the fusion protein was both properly targeted to

the membrane and functional. Next, the amount of BmrA-GFP fusion in the membranes of the different strains was assessed. It was found to be fairly similar for the three strains, although a bit reduced for C41(DE3) strain (Fig. 4C). Nevertheless, as shown previously for BmrA alone, the fusion BmrA-GFP was ~10 times more efficient at transporting doxorubicin when expressed in C41(DE3) strain (Figs 4D and S5). We also analyzed the levels of GFP fluorescence in each membrane sample after migration on a SDS-PAGE, since it was reported that correctly folded GFP is not denatured in SDS-polyacrylamide gel under certain conditions[30]. We observed a higher fluorescence level in the C41(DE3) membranes as compared to the other strains (Fig. 4E). Furthermore, we measured the fluorescence associated with the non-denatured membranes with a spectrofluorometer (Fig. S6). After subtracting the background fluorescence of the control membranes, the latter quantification allowed us to determine the GFP fluorescence associated with a normalized amount of BmrA from each membrane source (Figs S7 and 4F). Despite the fact that the transport activity of BmrA-GFP is reduced by more than 90% when expressed in BL21(DE3) and T7 express strains (Fig. 4D), the fused BmrA-GFP fluoresces to about 40% when expressed in T7 and BL21(DE3) strains as compared to C41(DE3) strain (Fig. 4F). We found similar results (∼35%) by quantifying the in-gel fluorescence of the full-length BmrA-GFP by typhoon fluorescence imaging and ImageJ. Therefore, while a higher GFP fluorescence intensity was visible in the C41(DE3) strain (Fig. 4E) thereby correlating with a higher functionality of BmrA in this strain, a substantial amount of GFP fluorescence was visible in the membrane of the strains in which the functionality of BmrA was severely impaired. Therefore, these data suggest that fluorescence and thus folding of GFP can occur independently of the folding of the target membrane protein fused to its C-terminus.

Expression in Lemo21(DE3) strain. This strain was engineered to provide an "All in One" platform for membrane protein overexpression, since the activity of the T7 polymerase can be controlled by rhamnose concentration[10]. Surprisingly, the expression of PatA/PatB was much lower in Lemo21(DE3) as compared to C41(DE3) strain (Fig. 5A), although the IPTG induction was performed in a similar way (induction at OD ~1.7 during overnight at 25 °C in TB media). Accordingly, drug transport was much faster in the latter strain (Fig. 5B), although membranes prepared from Lemo21(DE3) cells displayed a bell-shape rate of transport dependent on the rhamnose concentration used during induction (Fig. 5C). We performed a western-blot analysis, which suggests that the highest transport seen at 0.1–0.25 mM rhamnose corresponded to a higher expression of PatA/PatB in these conditions (Fig. S8). Moreover, ~5 times less C41 membranes was sufficient to detect a similar band intensity, suggesting that PatA/PatB was about 5 times more expressed in the membranes of C41(DE3) strain. Knowing that drug transport was approximately 5 times faster in C41(DE3) membranes (Fig. 5C), these results suggest a similar quality of PatA/PatB expressed in C41(DE3) and Lemo21(DE3) strains, although the level of production was much higher in the former. The expression of BmrA was also attempted in Lemo21(DE3) cells with various rhamnose concentrations, in TB medium (25 °C and 37 °C) or LB medium (37 °C). At 25 °C in TB, none of the rhamnose conditions permitted a high overexpression of the transporter, in contrast to the C41(DE3) strain (Fig. S9A). However, while transport activity from C41(DE3) membranes was ~3 times higher as compared to the highest one from Lemo21(DE3) membranes, protein quantification by Western blot showed that BmrA was markedly more abundant in the C41(DE3) as compared to the Lemo21(DE3) strain, much more than 3 fold in the former strain. This suggested that the lower expression in Lemo21(DE3) strain at 0.5 mM rhamnose produced a higher fraction of functional transporters. When the induction was performed at 37 °C in TB (Fig. S9B), we found some conditions in which Lemo21(DE3) strain overexpressed BmrA as well as in C41(DE3) strain (or better, ~1.5 fold at 0.5 mM rhamnose, see Western Blot), and the Lemo21(DE3) membranes were about 3 times more active. When the induction was performed at 37 °C in LB (Fig. S9C), the overexpression of BmrA in Lemo21(DE3) strain showed a bell-shape that correlated with transport activities. At 0.2 and 0.5 mM rhamnose, both the expression and transport of BmrA in the Lemo21(DE3) strain was ~3 times higher than in C41(DE3) strain.

Functionality of the transporters purified from various strains. As described above, the functionality of PatA/PatB and BmrA is highly influenced by the choice of the T7 expression strain. Because milder detergents seem to extract a higher proportion of active transporters in the host membrane, this raises two important questions. First, could a mild detergent indeed selectively extract the population of functional membrane proteins? Second, since a detergent like FC12 was able to extract the transporters irrespective of the quality of the transporter, how does such detergent preserve or affect the functionality of the transporters? To address these questions, we solubilized and purified PatA/PatB that was expressed in C41(DE3) and BL21(DE3) strains, with either LMNG or FC12 (see Table S1 for purification yields). The first noticeable observation we made was that, in contrast to LMNG that seems to preserve a constant stoichiometry of the PatA and PatB subunits, FC12 at least partially dissociated PatA and PatB during the elution of the affinity chromatography leading to an uneven distribution of the two subunits in the different fractions (Fig. S10). We next characterized the GTPase activity of the purified transporters, both in detergent or reconstituted in proteoliposomes. Interestingly, the PatA/PatB population solubilized and purified in LMNG from both strains remained highly active (Fig. 6A). Upon reconstitution, although the GTPase activities were reduced by 2–3 fold, as reported before[14], they remained similar for PatA/PatB overexpressed and purified from both strains (Fig. 6B). In contrast, no significant GTPase activity could be measured when FC12 was used to purify PatA/PatB, regardless of the strain used, and even after reconstitution into proteoliposomes (Fig. 6A,B). For BmrA (see Table S1 for purification yields), the activity of the protein purified from each strain with LMNG was also similar (Fig. 6C), even after reconstitution (Fig. 6D), except that 2–3 fold higher ATPase activities were measured upon proteoliposome reconstitution. When FC12 was used to solubilize and purify BmrA from either strain, a much-reduced ATPase activity was observed as compared to LMNG (~7 times) (Fig. 6C). BmrA purified by FC12 from the C41(DE3) regained a full ATPase activity upon reconstitution, comparable to that obtained with LMNG (Fig. 6D). In contrast, BmrA extracted by FC12 from the T7 express did not regain a level of ATPase activity similar to that obtained from the LMNG treated sample

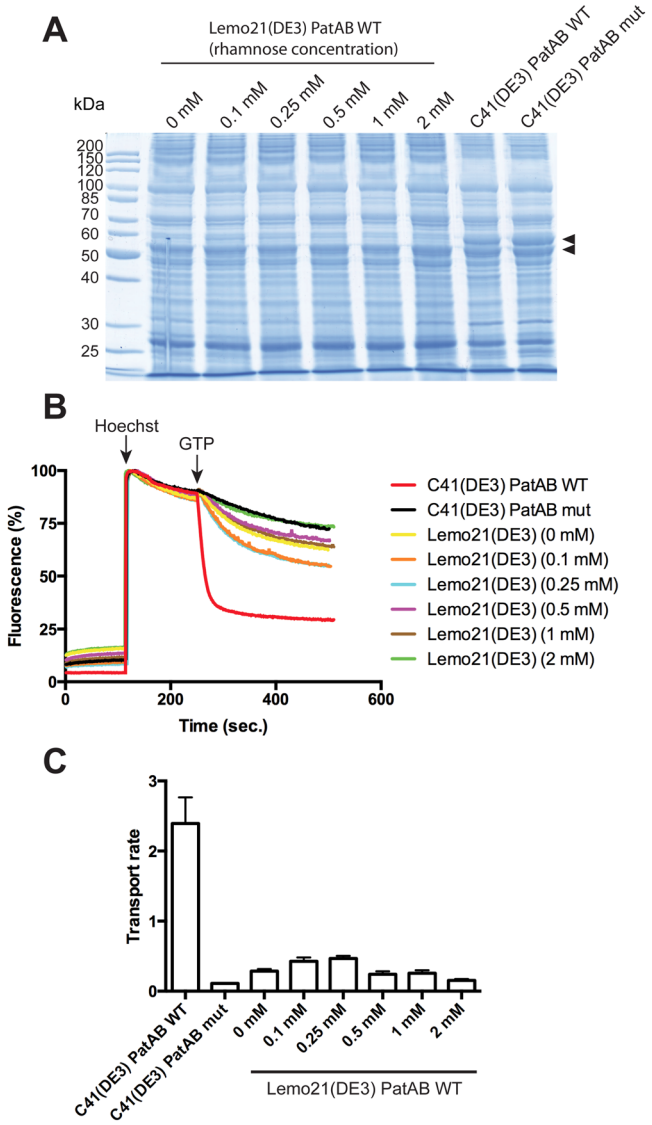

Figure 5. Expression of PatA/PatB in Lemo21(DE3) strain and functionality of the transporter. (**A**) Membrane proteins in Lemo21(DE3) and C41(DE3) strains were visualized by 12% SDS-PAGE stained with Coomassie blue. Twenty µg of proteins were loaded in each lane. As a negative control, a mutant of PatA/PatB was used in which the conserved Walker-A lysine was mutated in each subunit (PatA-K367A/PatB-K388A). (**B**) Hoechst 33342 transport assays with inverted membrane vesicles prepared from the various strains. 50 µg of total membrane proteins were used for each assay. (**C**) Hoechst 33342 transport rates as measured by initial slopes following GTP addition and calculated from panel B. The data represent the average of triplicates, and error bars indicate the standard deviation.

upon reconstitution. The ATPase activity of the FC12 treated BmrA was ~2–3 times lower than the LMNG treated BmrA. Presumably, this is due to the fact that FC12 extracted both folded and unfolded forms of BmrA from the T7 express cells. Upon reconstitution in proteoliposomes, the inactive co-purified fraction failed to regain activity. On the other hand, in the C41(DE3), a large majority of BmrA is properly folded and can be solubilized using either LMNG or FC12. Although the latter strongly inhibits the ATPase activity of BmrA, removal of the detergent during the reconstitution process allowed BmrA to recover its activity.

Discussion

Overexpression represents the first major bottleneck in structural and functional studies of integral membrane proteins. In the recent years, substantial progress has been accomplished in producing both prokaryotic and eukaryotic membrane proteins in bacterial hosts, especially *E. coli* but also *Lactococcus lactis* and *B. subtilis*[3]. Notably, it was shown that many strains with strongly improved membrane protein overexpression ability could be selected for[9,36–42] or engineered[43–47]. However, the tools to assess the overall quality of the overexpressed proteins are limited. The most commonly used strategy has been to fuse GFP to the C-terminal end of membrane proteins[12,48], although it should be kept in mind that fusing fluorescent protein tags may introduce artifacts

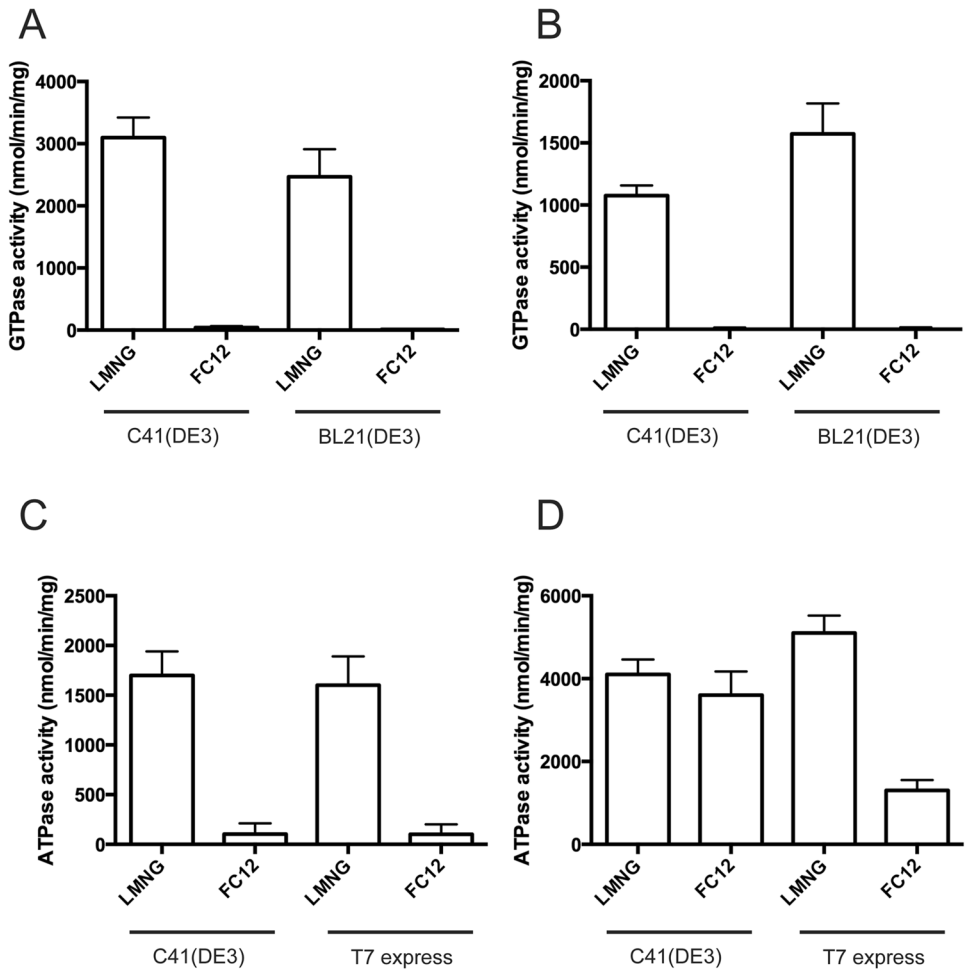

Figure 6. NTPase activities of purified PatA/PatB and BmrA in detergent or after reconstitution into proteoliposomes. (**A**) GTPase activities of PatA/PatB solubilized from C41(DE3) or BL21(DE3) with the indicated detergent and purified by Ni-affinity. (**B**) GTPase activities of PatA/PatB solubilized from C41(DE3) or BL21(DE3) with the indicated detergent, purified and reconstituted into proteoliposomes. (**C**) ATPase activities of purified BmrA solubilized from C41(DE3) or T7 express with the indicated detergent and purified by Ni-affinity. (**D**) ATPase activities of BmrA solubilized from C41(DE3) or T7 express with the indicated detergent, purified and reconstituted into proteoliposomes. The data represent the average of triplicates (panels A and B) or six replicates (panels C and D), and error bars indicate the standard deviation.

in the localization and/or stability of the proteins of interest[49]. It was reported that proper folding and fluorescence of GFP fused to the C-terminus of a target protein depends on the appropriate folding of the latter, and thus only folded fusion protein is fluorescent. Instead, if the fusion protein is present in inclusion bodies, the GFP does not fold properly and thus does not fluoresce. Methods employing GFP fusion seem therefore extremely useful to assess a first quality control for membrane protein production[30,36]. Membrane protein biogenesis is indeed complex and tightly controlled in order for the synthesized membrane proteins to be correctly targeted, inserted and then folded into the membrane[50,51]. GFP-fusions also allowed using minimal amounts of detergent-solubilized whole cells/membranes to rapidly assess both membrane protein production levels and their degree of monodispersity using fluorescence-detection size-exclusion chromatography precrystallization screening[52]. However, these methods do not directly provide any information on the functionality of the proteins that are overexpressed. Here, we took advantage of two different membrane proteins for which functional assays can be easily and directly performed at the level of membrane vesicles, i.e. before their solubilisation with detergents that might compromise their active conformation. Our study clearly illustrates that membrane proteins that are seemingly properly addressed to the membrane is not a guarantee for quality. In addition, when working with the widely employed GFP fusion strategy, we showed a lack of correlation between the GFP fluorescence and the functionality of BmrA, revealing that the two proteins in the chimeric construct can fold independently of each other. At the cell level (Fig. 4A), BL21(DE3) and T7 express displayed higher fluorescence intensity than C41(DE3), which would encourage investigators toward choosing the former strains for downstream work. When the membrane fraction was isolated (Fig. 4E), a higher GFP fluorescence was associated with C41(DE3) membranes, although we demonstrated that about 35–40% of fluorescence was associated with inactive BmrA in the other strains (Fig. 4D,F). To explain this apparent discrepancy between cell and membrane levels, it is possible

that some fluorescent BmrA-GFP was not targeted to the membrane in BL21(DE3) and T7 express cells and/or that a fraction of fluorescent BmrA-GFP in their membranes was very unstable and degraded during membrane preparation. Regardless of the explanation for this difference, it is clear that considering just the global level of GFP fluorescence for fusion of membrane proteins could be quite misleading. It is very likely that this downside of using GFP fusion might also be a problem when one works with soluble proteins.

Overall, we found that PatA/PatB and BmrA transporters appear much more functional when expressed in the C41(DE3) strain as compared to the BL21(DE3) and T7 express strains, as evidence by a series of assays. First, real-time drug transport assays clearly showed that these transporters are more active in the membranes prepared from this strain. Second, limited proteolysis on BmrA suggested its ability to operate conformational changes when expressed as an active form in membranes, but not as inactive ones. Third, a screening with a variety of detergents indicated that functional membrane proteins could be solubilized from the membrane by milder detergents, whereas inactive proteins are generally less extractable by these detergents. The LMNG and DDM detergents were indeed able to extract high amounts of the transporters from the membranes of the best strains, while little amounts of transporters were solubilized from the strains with a poorer capacity for functional overexpression. However, the extracted fraction of proteins was active in all cases. In contrast, a harsh detergent such as FC12 was able to extract the protein irrespective of the membrane strain. Neither PatA/PatB nor BmrA was active in FC12, although the activity of the latter could be almost fully recovered upon reconstitution in proteoliposomes. These observations are notable because direct functional tests are not always available for overexpressed membrane proteins, and this simple detergent assay may provide a valuable tool to suggest whether heterologously expressed membrane proteins are indeed properly folded. Interestingly, similar observations were recently described for membrane proteins expressed in eukaryotic systems[53]. The proper choice of detergent is fundamental for functionality of membrane proteins and protein structure determination[21,54,55]. The right balance between the ability of the detergent to solubilize the protein of interest and stabilize its native structure is key for such goals[55]. Indeed, detergents can compete with stabilizing intramolecular interactions within membrane proteins, leading to their inactivation[56–58] or the alteration of their properties that can be recovered once reconstituted in lipids[59,60]. Although Foscholine detergents appear to be detrimental for the native conformation of many membrane proteins[61,62], there are a few examples in which the functionality of the purified proteins could be regained after incorporation into proteoliposomes[54], as found here for BmrA. This is in agreement with a previous study where the ATPase activity of BmrA solubilized in FC12 could be restored after detergent exchange[63]. In contrast, the heterodimeric transporter PatA/PatB appears much more sensitive to FC12, as also reported for a related heterodimeric transporter from *B. subtilis*, BmrCD[64]. As seen with our study, the choice of the overexpressing strain can also influence the choice of detergent for further applications, since milder detergents can both extract and maintain the protein function when used with the proper expression strain.

While BL21(DE3) strain was originally developed for the production of soluble proteins, overexpression of proteins, and especially membrane proteins, may have toxic effects and induces a wide range of physiological perturbations[6,10,65]. In 1996, Miroux and Walker cleverly isolated mutant derivatives of BL21(DE3) with improved yields and reduced toxicity for membrane protein production[9]. These C41(DE3) and C43(DE3) strains are now widely used to produce membrane proteins[66], although they do not improve yields for all membrane proteins. Very recently, Miroux's laboratory selected additional BL21(DE3) mutants, C44(DE3) and C45(DE3) strains, that appeared better suited to overproduce some eukaryotic transporter[36]. Regarding the C41(DE3) and C43(DE3), it was much later shown that mutations in the lacUV5 promoter governing expression of the T7 RNA polymerase were key to the improved membrane protein production characteristics of these strains, because such mutations would result in the production of much lower amounts of T7 RNA polymerase upon induction than in BL21(DE3) strain[10]. Based on this observation, a derivative strain of BL21(DE3), termed Lemo21(DE3), was constructed in which the activity of the T7 RNA polymerase can be precisely tuned by its natural inhibitor T7 lysozyme. In Lemo21(DE3) the gene encoding the T7 lysozyme is on a plasmid under the control of a well titratable rhamnose promoter, thereby offering the possibility of a wide window of expression levels[10,11]. It has been proposed that subsequent lower synthesis rates of the mRNA for the target membrane protein ensure that the capacity of the Sec-translocon machinery is sufficient to incorporate the produced proteins in the membrane, thereby decreasing toxicity[8,10,11,67]. Although this hypothesis is certainly true, it may not be the sole explanation. Our results show that the amounts of PatA/PatB and BmrA incorporated in BL21(DE3) and T7 express membranes can be as high (or even higher) as in C41(DE3) membranes, apparently suggesting that the Sec-translocon could handle in all strains the insertion of these overexpressed membrane proteins. However, more PatA/PatB and BmrA proteins are appropriately folded in C41(DE3) strain than in the other strains. How can we explain this? First, membrane protein insertion in the membrane can occur without translocon as seen with cell-free translation systems supplemented with liposomes or vesicles, although the mechanism is poorly understood[68–70]. It is thus possible that, under the non-physiological high level of protein synthesis (as here with the T7 system), some membrane proteins may not be processed by the Sec machinery and insert/fold improperly into the membrane. Second, transcription and translation are normally coupled in bacteria[71]. The *E. coli* RNA polymerase (RNAP) transcribes approximatively 60 nucleotides per second, and a ribosome initiating translation on the mRNA nascent chain proceeds with a rate of 20 amino acids per second, i.e. 20 codons (60 nucleotides) per second. Therefore, during active transcription/translation, there is no significant gap between the transcriptase and the following ribosome. The nascent mRNA chain cannot form secondary structures that would prevent translation elongation or transcription via R-loop formation. Moreover, the presence of ribosomes also protects the mRNA against RNAseE degradation[72]. However, the T7 RNAP is up to eight times faster than *E. coli* RNAP, thus breaking the tight coupling between transcription and translation with possible adverse consequences[5]. Strong secondary RNA structures can form and hinder the path of the translating ribosome along the mRNA, likely impairing the co-translational folding and thus the yield of active proteins[73]. As shown in recent years, translation pace and its changes can regulate protein folding, and native translation is in fact uneven along each mRNA[74].

Most likely, a combination of all these factors is responsible for the impaired functionality of membrane proteins when overexpressed from high levels of transcription. The fine-tuning of transcription, mRNA stability and translation is often required for optimal protein synthesis[73,75,76]. Although our study only focused here on two membrane proteins, our data suggested that the Lemo21(DE3) strain did not overexpress well at 25 °C, as compared to the C41(DE3) strain. However, we found some conditions in which the Lemo21(DE3) strain outperform the C41(DE3) strain for functional overexpression of BmrA at 37 °C. Overall, our study clearly advises against choosing a bacterial strain based solely on expression levels in the membranes, even though some harsh detergents are able to extract these proteins. Although activity assays are the gold standard to assess quality, alternate tools can be used when functional tests are not readily achievable. Limited proteolysis can assess conformational changes, and detergent solubilization can provide valuable hints regarding the quality of overexpressed membrane proteins. With the technical advances and successes of structural methods such as X-ray crystallography, Cryo-Electron Microscopy and solid-state NMR, the high-resolution structures of membrane proteins is at much closer reach than before, but the overexpression in a functional and homogeneous state remain the second hurdle encountered for the structural analysis and biochemical characterization of membrane proteins. Identifying and counteracting the pitfalls of membrane protein expression remain at stake and will require the efforts from all the community with a broad range of case studies.

Methods

Bacteria and growth conditions. C41(DE3), BL21(DE3) and T7express strains were transformed either by pETDuet-1-PatA/PatB[13] or pET23b-BmrA[32]. For PatA/PatB, a fresh colony was inoculated into 500 mL of Terrific broth medium containing 100 µg/ml of ampicillin and grown at 37 °C with shaking at 190 rpm. Protein expression was induced by 0.7 mM of IPTG either when the $OD_{600\,nm}$ reached 0.3–1 or 1.6–2, and during respectively 5 h or overnight at 25 °C with shaking at 190 rpm. For auto-induced BL21(DE3), a pre-culture was done in the morning from an individual clone inoculated into 100 mL of LB at 37 °C with shaking at 200 rpm. In the evening, the preculture was inoculated into 500 mL of auto-induced medium (1% N-Z-amine, 0.5% yeast extract, 25 mM Na_2HPO_4, 25 mM KH_2PO_4, 50 mM NH_4Cl, 5 mM Na_2SO_4, 2 mM $MgSO_4$, 0.05% Glucose, 0.2% Lactose, 0.5% Glycerol) such as the initial $OD_{600\,nm}$ was about 0.2. The culture was left overnight at 25 °C with shaking at 190 rpm. For BmrA, a freshly transformed colony was inoculated into 1 L of Terrific broth containing 100 µg/ml of ampicillin. The flask was then incubated at 25 °C and 180 rpm overnight. The next morning, when the $OD_{600\,nm}$ reached 0.6, overexpression was induced by addition of 0.7 mM IPTG (final concentration) and the culture was induced for 4 h at 25 °C and 180 rpm. Then, the medium was centrifuged at 4000 × g for 20 min at 4 °C to obtain the pellet of bacteria which was either frozen at −80 °C or used directly.

Membrane Preparation. Bacteria collected by low speed centrifugation were resuspended in a buffer (50 mM Tris-HCl pH 8.0, 5 mM $MgCl_2$, 1 mM dithiotreitol, protease inhibitor cocktail tablet (Roche)). Bacteria were then lysed by three successive passages through a Microfluidizer™ at 18 000 psi. Unbroken cells were removed by a 30 min centrifugation at 15,000 × g. Membrane vesicles were collected by an ultracentrifugation at 150,000 × g during 1 h. Pellets were re-suspended in a buffer (50 mM Tris-HCl pH 8.0, 1.5 mM EDTA, 1 mM dithiotreitol) and centrifuged again 1 h at the same speed. Final membrane vesicles were resuspended in a buffer (20 mM Tris-HCl pH 8.0, 1 mM EDTA and 300 mM sucrose) then flash-frozen in liquid nitrogen and conserved at −80 °C. Protein concentrations in membrane vesicles were measured by a BCA assay and protein overexpression was checked by SDS-PAGE subsequently stained by Coomassie Brilliant Blue.

Solubilization tests. Detergent solubilization was performed in a final volume of 200 µL at 2 mg/mL of membrane protein in a buffer (50 mM Tris-HCl pH 8.0, 100 mM NaCl, 15% Glycerol) at 4 °C. Various detergents were used (LMNG, DDM, Triton X100, LDAO, OG, Fos-Choline-12) at different concentrations (1% for all of them, except for OG where 2% was used). The solubilization was performed either during 2 h or overnight. Solubilized proteins were collected in the supernatant after an ultracentrifugation at 150,000 × g during 1 h. The insoluble pellets were resuspended in equal volume of the same buffer. 5 µL of samples in Laemmli buffer were loaded and migrated in a 12% SDS-PAGE during 1 h at 200 Volts and proteins were stained by Coomassie Brilliant Blue.

Transport assays. Experiments were performed in a 2 mL quartz cuvette with a final volume of 1 mL in a buffer (50 mM Hepes-KOH pH 8.0, 8.5 mM NaCl, 4 mM phosphoenolpyruvate, 60 µg/mL pyruvate kinase (Roche), 2 mM $MgCl_2$) and monitored by a Photon Technology International Quanta Master I fluorimeter. Excitation and emission wavelengths were set at 355 and 457 nm, respectively, for Hoechst 33342 [2-(4-eth oxyphenyl)-5-(4-methyl-1-piperazinyl)-2,5-bis-1H-benzimidazole] or at 480 and 590 nm, respectively, for doxorubicin. After incubation at 25 °C during 1 min, inside-out membrane vesicles (IMVs) were added and the fluorescence was recorded. After 2 min, 1 µM of Hoechst 33342 or 10 µM of Doxorubicin was added. Two min later, the transport was induced by adding 2 mM of ATP or GTP and recorded during around 8–10 min until stabilization. Doxorubicin fluorescence is quenched by *E. coli* native DNA that was trapped inside the vesicles during cell disruption[18].

Limited proteolysis of BmrA. Inside-out membrane vesicles (IMVs) containing overexpressed BmrA were added into a buffer (20 mM Tris-HCl pH 8, 1 mM EDTA) and after 15 min of incubation, trypsin (1 µg/250 µg of BmrA) was added. For the Vi-inhibited form, before the addition of IMVs containing overexpressed BmrA, 3 mM $MgCl_2$, 2 mM ATP and 1 mM Vi were also added into the buffer. Samples of 10 µl (20 µg) each were withdrawn at 0, 2, 5, 15, 30, 60, 120 and 180 min. 2.5 µl of TFA 5% was added immediately to each sample to stop the reaction. 3 µl of Laemmli buffer (5x concentrated) was then added and the samples were placed on ice before resolving them on SDS-PAGE.

BmrA-GFP fusion. The *egfp* gene containing the mutations F64L and S65T[77] was amplified by PCR and cloned between restriction sites SalI and NotI in the plasmid pET23b-*bmrA* thereby fusing the eGFP at the *C*-terminus of BmrA with a linker VDAAAAVDAAAA. A freshly transformed colony was inoculated into 500 mL of Terrific broth medium containing 100 µg/ml of ampicillin and grown overnight at 22 °C. Protein expression was induced by addition of 0.7 mM of IPTG when the $OD_{600\,nm}$ reached 0.6 and was pursued for 4 h at 25 °C with shaking at 180 rpm. Membranes were prepared as described above for BmrA. For in-gel analysis of GFP fluorescence, samples were prepared in a Laemmli buffer containing 0.4% SDS instead of 2%. SDS-PAGE was then run at 4 °C. After migration, gels were scanned for fluorescence with a typhoon imager. For quantification of BmrA-eGFP fluorescence in membranes, *E. coli* membranes containing 100 µg of total proteins were diluted in 1 mL of 50 mM Hepes-KOH pH 8, 8.5 mM NaCl and placed in a PTI spectrofluorometer. Samples were excited at 488 nm and their fluorescence was recorded between 500 and 600 nm. Integrated fluorescence intensities (between 500 and 530 nm) from the membranes overexpressing BmrA-GFP were corrected from the background fluorescence displayed by the control membranes prepared with empty pET23 vector (Fig. S6). A second correction was then made by estimating the amounts of BmrA overexpressed in each membrane preparation (Fig. S7) to assess the GFP fluorescence associated with a normalized amount of BmrA in membranes (Fig. 4F).

Microscopy imaging and analysis. Several colonies were diluted into 5 mL of Terrific broth media supplemented with 100 µg/mL of ampicillin. These culture were grown overnight at 23 °C (130 rpm) such that the $OD_{600\,nm}$ on next morning was around 0.6 for all the strains. IPTG (0.7 mM final concentration) was added to the cell cultures and, after 1, 2 or 4 hours, 5 µl cell samples were transferred to a slide mounted with 1% agarose in Terrific medium[78]. When needed, cell membranes were visualized using 1 µg/mL FM4-64 (Life Technologies). Conventional wide-field fluorescence microscopy imaging was carried out on an Eclipse Ti-E microscope (Nikon), equipped with x100/1.45 oil Plan Apo Lambda phase objective, FLash4 V2 CMOS camera (Hamamatsu), and using NIS software for image acquisition. Acquisition settings were 10 ms for GFP and 10 ms for FM4-64, using 50% power of a Fluo LED Spectra X light source at 488 nm and 560 nm excitation wavelengths, respectively. Intracellular fluorescence intensity was analysed using MicrobeJ[79] and ImageJ software (http://rsb-web.nih.gov/ij/).

Protein expression in Lemo21(DE3) strain. Commercially competent cells (New England Biolabs) were transformed with pETDuet-1/*patA-patB*[13] or pET23/*bmrA*[32] and plated onto LB-agar plates containing 30 µg/mL of chloramphenicol and 100 µg/mL of ampicilline. For PatA/PatB expression, one colony was first diluted into 600 µl of Terrific Broth. Then, 100 µl of this culture was inoculated into 500 mL of Terrific Broth containing 30 µg/mL of chloramphenicol, 100 µg/mL of ampicilline and 0 to 2 mM of rhamnose. Cells were grown at 37 °C with shaking. When the $OD_{600\,nm}$ reached ~2, protein expression was induced by 0.7 mM IPTG overnight at 25 °C. Membranes were prepared as described above. For BmrA expression, an overnight LB preculture containing 30 µg/mL of chloramphenicol and 100 µg/mL of ampicilline was diluted at $OD_{600\,nm} = 0.1$, cells were grown at 37 °C with shaking in TB or LB medium containing 30 µg/mL of chloramphenicol, 100 µg/mL of ampicilline and 0 to 2 mM of rhamnose. At $OD_{600\,nm}$ ~0.6, protein expression was induced with 0.7 mM IPTG for 4 h at 25 °C or 37 °C.

Western Blot analysis. For PatA/PatB expression, a 12% SDS-PAGE was performed with 0.5 µg purified PatA/PatB, 30 µg of total proteins for Lemo21(DE3) membranes and 6 µg of total proteins for C41(DE3) membranes. For BmrA expression, a 12% SDS-PAGE was performed with 0.2 µg purified BmrA, 0.1 to 1 µg of total membrane proteins for Lemo21(DE3) and 0.3 µg of total membrane proteins for C41(DE3) (see legend of Fig. S9 for details). Proteins were then transferred at 300 mA for 1.5 h onto a PVDF membrane preactivated in ethanol in a buffer containing 25 mM Tris base, 192 mM glycine, 20% ethanol and 0.02% SDS. The PVDF membrane was first rinced with TBS (50 mM Tris-HCl pH 7.6, 150 mM NaCl), then blocked 1 h in buffer TBS supplemented with 0.1% tween and 10% semi-skimmed milk (powder). Next, the membrane was incubated during 1 h with a HRP-conjugated anti-pentaHis antibody (Qiagen) diluted 2000 or 10000 times (for PatA/PatB and BmrA, respectively) in a new blocking buffer. The membrane was washed 3 times with TBS buffer supplemented with 0.1% tween. Finally, the membrane was revealed with Luminata™ Forte reagents from Millipore.

Purification of PatA/PatB and BmrA. For PatA/PatB, 50 mg of total membrane proteins were solubilized in a buffer containing 50 mM Tris-HCl pH 8, 100 mM NaCl, 15% glycerol and 1% of detergent (LMNG or FC-12). After an ultracentrifugation at 150,000 × g for 1 h, solubilized proteins were applied to a 1 mL Histrap HP column (GE Healthcare) that was pre-equilibrated with a buffer containing 50 mM Tris-HCl pH 8, 100 mM NaCl, 15% glycerol and 0.02% LMNG or 0.3% FC-12. The column was then washed with the same buffer. Elution was performed with the same buffer containing an imidazole gradient up to 250 mM. Purified proteins were dialyzed in a buffer 50 mM Tris-HCl pH 8, 100 mM NaCl, 15% glycerol and 0.02% LMNG or 0.15% FC-12. The concentration of the purified PatA/PatB proteins was measured with Bradford assay. For BmrA, total membrane proteins (30 mg from C41(DE3), or 9–12 mg from T7 express) at 2 mg/mL final concentration were solubilized for 1 h in a buffer containing 50 mM Tris-HCl pH 8, 100 mM NaCl, 10% glycerol, 1 mM DTT, protease inhibitor cocktail tablet (Roche) (1 tab for 50 mL buffer) and 1% of detergent (LMNG or FC-12). After an ultracentrifugation at 150,000 × g for 1 h, solubilized proteins were applied to a 1 mL Histrap HP column (GE Healthcare) that was pre-equilibrated with a buffer containing 50 mM Tris-HCl pH 8, 100 mM NaCl, 10% glycerol, 20 mM imidazole and 0.01% LMNG or 0.3% FC-12. The column was then washed with the same buffer. Elution was performed with the same buffer containing an imidazole gradient up to 500 mM. Purified proteins were dialyzed in a buffer 50 mM Hepes-KOH pH 8, 50 mM NaCl, 10% glycerol and 0.01% LMNG or 0.15% FC-12. The concentration of the purified BmrA was measured with Nanodrop (UV absorbance at 280 nm).

Membrane protein reconstitution. BmrA and PatA/PatB proteoliposomes were prepared as described before[20].

ATPase and GTPase activities. Activities were measured in 700 µL total volume in buffer Hepes-KOH 50 mM pH 8, 10 mM $MgCl_2$, 4 mM phosphoenolpyruvate, 0.43 mM NADH (for GTPase measurements) or 0.3 mM NADH (for ATPase measurements), 32 µg/mL of lactate deshydrogenase, 60 µg/mL pyruvate kinase, and 4 mM GTP (for PatA/PatB) or 10 mM ATP (for BmrA). The buffer was heated at 37 °C during 5 min before adding the protein. Activities of 2 µg of PatA/PatB or BmrA (or 1 µg for BmrA proteoliposomes) were then measured by absorbance at 340 nm during 20 min at 37 °C. For measurements in detergent, LMNG was supplemented at 0.02% (PatA/PatB) or 0.01% (BmrA), while FC12 was supplemented at 0.15% in the cuvette.

Data Availability

The datasets generated during and/or analyzed during the current study are available from the corresponding author on reasonable request.

References

1. Almen, M. S., Nordstrom, K. J., Fredriksson, R. & Schioth, H. B. Mapping the human membrane proteome: a majority of the human membrane proteins can be classified according to function and evolutionary origin. *BMC biology* **7**, 50, https://doi.org/10.1186/1741-7007-7-50 (2009).
2. Rosano, G. L. & Ceccarelli, E. A. Recombinant protein expression in Escherichia coli: advances and challenges. *Frontiers in microbiology* **5**, 172, https://doi.org/10.3389/fmicb.2014.00172 (2014).
3. Schlegel, S., Hjelm, A., Baumgarten, T., Vikstrom, D. & de Gier, J. W. Bacterial-based membrane protein production. *Biochimica et biophysica acta* **1843**, 1739–1749, https://doi.org/10.1016/j.bbamcr.2013.10.023 (2014).
4. Novy, R. & Morris, B. Use of glucose to control basal expression in the pET system. *inNovations* **13**, 8–10 (2001).
5. Iost, I., Guillerez, J. & Dreyfus, M. Bacteriophage T7 RNA polymerase travels far ahead of ribosomes *in vivo*. *Journal of bacteriology* **174**, 619–622 (1992).
6. Gubellini, F. *et al*. Physiological response to membrane protein overexpression in *E. coli*. *Molecular & cellular proteomics: MCP* **10**, M111 007930, https://doi.org/10.1074/mcp.M111.007930 (2011).
7. Klepsch, M. M., Persson, J. O. & de Gier, J. W. Consequences of the overexpression of a eukaryotic membrane protein, the human KDEL receptor, in Escherichia coli. *Journal of molecular biology* **407**, 532–542, https://doi.org/10.1016/j.jmb.2011.02.007 (2011).
8. Wagner, S. *et al*. Consequences of membrane protein overexpression in Escherichia coli. *Molecular & cellular proteomics: MCP* **6**, 1527–1550, https://doi.org/10.1074/mcp.M600431-MCP200 (2007).
9. Miroux, B. & Walker, J. E. Over-production of proteins in Escherichia coli: mutant hosts that allow synthesis of some membrane proteins and globular proteins at high levels. *Journal of molecular biology* **260**, 289–298, https://doi.org/10.1006/jmbi.1996.0399 (1996).
10. Wagner, S. *et al*. Tuning Escherichia coli for membrane protein overexpression. *Proceedings of the National Academy of Sciences of the United States of America* **105**, 14371–14376, https://doi.org/10.1073/pnas.0804090105 (2008).
11. Schlegel, S. *et al*. Optimizing membrane protein overexpression in the Escherichia coli strain Lemo21(DE3). *Journal of molecular biology* **423**, 648–659, https://doi.org/10.1016/j.jmb.2012.07.019 (2012).
12. Drew, D. E., von Heijne, G., Nordlund, P. & de Gier, J. W. Green fluorescent protein as an indicator to monitor membrane protein overexpression in Escherichia coli. *FEBS letters* **507**, 220–224 (2001).
13. Boncoeur, E. *et al*. PatA and PatB form a functional heterodimeric ABC multidrug efflux transporter responsible for the resistance of Streptococcus pneumoniae to fluoroquinolones. *Biochemistry* **51**, 7755–7765, https://doi.org/10.1021/bi300762p (2012).
14. Orelle, C. *et al*. A multidrug ABC transporter with a taste for GTP. *Scientific reports* **8**, 2309, https://doi.org/10.1038/s41598-018-20558-z (2018).
15. Baylay, A. J. & Piddock, L. J. Clinically relevant fluoroquinolone resistance due to constitutive overexpression of the PatAB ABC transporter in Streptococcus pneumoniae is conferred by disruption of a transcriptional attenuator. *The Journal of antimicrobial chemotherapy* **70**, 670–679, https://doi.org/10.1093/jac/dku449 (2015).
16. El Garch, F. *et al*. Fluoroquinolones induce the expression of patA and patB, which encode ABC efflux pumps in Streptococcus pneumoniae. *The Journal of antimicrobial chemotherapy* **65**, 2076–2082, https://doi.org/10.1093/jac/dkq287 (2010).
17. Garvey, M. I., Baylay, A. J., Wong, R. L. & Piddock, L. J. Overexpression of patA and patB, which encode ABC transporters, is associated with fluoroquinolone resistance in clinical isolates of Streptococcus pneumoniae. *Antimicrobial agents and chemotherapy* **55**, 190–196, https://doi.org/10.1128/AAC.00672-10 (2011).
18. Steinfels, E. *et al*. Characterization of YvcC (BmrA), a multidrug ABC transporter constitutively expressed in Bacillus subtilis. *Biochemistry* **43**, 7491–7502, https://doi.org/10.1021/bi0362018 (2004).
19. Mehmood, S., Domene, C., Forest, E. & Jault, J. M. Dynamics of a bacterial multidrug ABC transporter in the inward- and outward-facing conformations. *Proceedings of the National Academy of Sciences of the United States of America* **109**, 10832–10836, https://doi.org/10.1073/pnas.1204067109 (2012).
20. Orelle, C., Dalmas, O., Gros, P., Di Pietro, A. & Jault, J. M. The conserved glutamate residue adjacent to the Walker-B motif is the catalytic base for ATP hydrolysis in the ATP-binding cassette transporter BmrA. *The Journal of biological chemistry* **278**, 47002–47008, https://doi.org/10.1074/jbc.M308268200 (2003).
21. Chaptal, V. *et al*. Quantification of Detergents Complexed with Membrane Proteins. *Scientific reports* **7**, 41751, https://doi.org/10.1038/srep41751 (2017).
22. Lacabanne, D. *et al*. Gradient reconstitution of membrane proteins for solid-state NMR studies. *Journal of biomolecular NMR* **69**, 81–91, https://doi.org/10.1007/s10858-017-0135-4 (2017).
23. Morrison, K. A. *et al*. Membrane protein extraction and purification using styrene-maleic acid (SMA) copolymer: effect of variations in polymer structure. *The Biochemical journal* **473**, 4349–4360, https://doi.org/10.1042/BCJ20160723 (2016).
24. Nguyen, K. A. *et al*. Glycosyl-Substituted Dicarboxylates as Detergents for the Extraction, Overstabilization, and Crystallization of Membrane Proteins. *Angewandte Chemie* **57**, 2948–2952, https://doi.org/10.1002/anie.201713395 (2018).
25. Fribourg, P. F. *et al*. 3D cryo-electron reconstruction of BmrA, a bacterial multidrug ABC transporter in an inward-facing conformation and in a lipidic environment. *Journal of molecular biology* **426**, 2059–2069, https://doi.org/10.1016/j.jmb.2014.03.002 (2014).
26. Wiegand, T. *et al*. Solid-state NMR and EPR Spectroscopy of Mn(2+) -Substituted ATP-Fueled Protein Engines. *Angewandte Chemie* **56**, 3369–3373, https://doi.org/10.1002/anie.201610551 (2017).
27. Marrer, E. *et al*. Involvement of the putative ATP-dependent efflux proteins PatA and PatB in fluoroquinolone resistance of a multidrug-resistant mutant of Streptococcus pneumoniae. *Antimicrobial agents and chemotherapy* **50**, 685–693, https://doi.org/10.1128/AAC.50.2.685-693.2006 (2006).

28. Robertson, G. T., Doyle, T. B. & Lynch, A. S. Use of an efflux-deficient streptococcus pneumoniae strain panel to identify ABC-class multidrug transporters involved in intrinsic resistance to antimicrobial agents. *Antimicrobial agents and chemotherapy* **49**, 4781–4783, https://doi.org/10.1128/AAC.49.11.4781-4783.2005 (2005).
29. Studier, F. W. Protein production by auto-induction in high density shaking cultures. *Protein expression and purification* **41**, 207–234 (2005).
30. Geertsma, E. R., Groeneveld, M., Slotboom, D. J. & Poolman, B. Quality control of overexpressed membrane proteins. *Proceedings of the National Academy of Sciences of the United States of America* **105**, 5722–5727, https://doi.org/10.1073/pnas.0802190105 (2008).
31. Shapiro, A. B., Corder, A. B. & Ling, V. P-glycoprotein-mediated Hoechst 33342 transport out of the lipid bilayer. *Eur J Biochem* **250**, 115–121 (1997).
32. Steinfels, E. *et al*. Highly efficient over-production in *E. coli* of YvcC, a multidrug-like ATP-binding cassette transporter from Bacillus subtilis. *Biochimica et biophysica acta* **1565**, 1–5 (2002).
33. Dalmas, O. *et al*. Time-resolved fluorescence resonance energy transfer shows that the bacterial multidrug ABC half-transporter BmrA functions as a homodimer. *Biochemistry* **44**, 4312–4321, https://doi.org/10.1021/bi0482809 (2005).
34. Guiral, M., Viratelle, O., Westerhoff, H. V. & Lankelma, J. Cooperative P-glycoprotein mediated daunorubicin transport into DNA-loaded plasma membrane vesicles. *FEBS letters* **346**, 141–145 (1994).
35. Ding, F., Lee, K. J., Vahedi-Faridi, A., Huang, T. & Xu, X. H. Design and probing of efflux functions of EGFP fused ABC membrane transporters in live cells using fluorescence spectroscopy. *Analytical and bioanalytical chemistry* **400**, 223–235, https://doi.org/10.1007/s00216-011-4727-7 (2011).
36. Angius, F. *et al*. A novel regulation mechanism of the T7 RNA polymerase based expression system improves overproduction and folding of membrane proteins. *Scientific reports* **8**, 8572, https://doi.org/10.1038/s41598-018-26668-y (2018).
37. Baumgarten, T. *et al*. Isolation and characterization of the *E. coli* membrane protein production strain Mutant56(DE3). *Scientific reports* **7**, 45089, https://doi.org/10.1038/srep45089 (2017).
38. Gul, N., Linares, D. M., Ho, F. Y. & Poolman, B. Evolved Escherichia coli strains for amplified, functional expression of membrane proteins. *Journal of molecular biology* **426**, 136–149, https://doi.org/10.1016/j.jmb.2013.09.009 (2014).
39. Linares, D. M., Geertsma, E. R. & Poolman, B. Evolved Lactococcus lactis strains for enhanced expression of recombinant membrane proteins. *Journal of molecular biology* **401**, 45–55, https://doi.org/10.1016/j.jmb.2010.06.002 (2010).
40. Massey-Gendel, E. *et al*. Genetic selection system for improving recombinant membrane protein expression in *E. coli*. *Protein science: a publication of the Protein Society* **18**, 372–383, https://doi.org/10.1002/pro.39 (2009).
41. Schlegel, S., Genevaux, P. & de Gier, J. W. Isolating Escherichia coli strains for recombinant protein production. *Cellular and molecular life sciences: CMLS* **74**, 891–908, https://doi.org/10.1007/s00018-016-2371-2 (2017).
42. Skretas, G. & Georgiou, G. Simple genetic selection protocol for isolation of overexpressed genes that enhance accumulation of membrane-integrated human G protein-coupled receptors in Escherichia coli. *Applied and environmental microbiology* **76**, 5852–5859, https://doi.org/10.1128/AEM.00963-10 (2010).
43. Gialama, D. *et al*. Development of Escherichia coli Strains That Withstand Membrane Protein-Induced Toxicity and Achieve High-Level Recombinant Membrane Protein Production. *ACS synthetic biology* **6**, 284–300, https://doi.org/10.1021/acssynbio.6b00174 (2017).
44. Leviatan, S., Sawada, K., Moriyama, Y. & Nelson, N. Combinatorial method for overexpression of membrane proteins in Escherichia coli. *The Journal of biological chemistry* **285**, 23548–23556, https://doi.org/10.1074/jbc.M110.125492 (2010).
45. Makino, T., Skretas, G. & Georgiou, G. Strain engineering for improved expression of recombinant proteins in bacteria. *Microbial cell factories* **10**, 32, https://doi.org/10.1186/1475-2859-10-32 (2011).
46. Marino, J., Hohl, M., Seeger, M. A., Zerbe, O. & Geertsma, E. R. Bicistronic mRNAs to enhance membrane protein overexpression. *Journal of molecular biology* **427**, 943–954, https://doi.org/10.1016/j.jmb.2014.11.002 (2015).
47. Niesen, M. J. M., Marshall, S. S., Miller, T. F. III & Clemons, W. M. Jr. Improving membrane protein expression by optimizing integration efficiency. *The Journal of biological chemistry* **292**, 19537–19545, https://doi.org/10.1074/jbc.M117.813469 (2017).
48. Drew, D., Lerch, M., Kunji, E., Slotboom, D. J. & de Gier, J. W. Optimization of membrane protein overexpression and purification using GFP fusions. *Nature methods* **3**, 303–313, https://doi.org/10.1038/nmeth0406-303 (2006).
49. Swulius, M. T. & Jensen, G. J. The helical MreB cytoskeleton in Escherichia coli MC1000/pLE7 is an artifact of the N-Terminal yellow fluorescent protein tag. *Journal of bacteriology* **194**, 6382–6386, https://doi.org/10.1128/JB.00505-12 (2012).
50. Bowie, J. U. Solving the membrane protein folding problem. *Nature* **438**, 581–589, https://doi.org/10.1038/nature04395 (2005).
51. Luirink, J., Yu, Z., Wagner, S. & de Gier, J. W. Biogenesis of inner membrane proteins in Escherichia coli. *Biochimica et biophysica acta* **1817**, 965–976, https://doi.org/10.1016/j.bbabio.2011.12.006 (2012).
52. Kawate, T. & Gouaux, E. Fluorescence-detection size-exclusion chromatography for precrystallization screening of integral membrane proteins. *Structure* **14**, 673–681, https://doi.org/10.1016/j.str.2006.01.013 (2006).
53. Thomas, J. & Tate, C. G. Quality control in eukaryotic membrane protein overproduction. *Journal of molecular biology* **426**, 4139–4154, https://doi.org/10.1016/j.jmb.2014.10.012 (2014).
54. Chipot, C. *et al*. Perturbations of Native Membrane Protein Structure in Alkyl Phosphocholine Detergents: A Critical Assessment of NMR and Biophysical Studies. *Chemical reviews* **118**, 3559–3607, https://doi.org/10.1021/acs.chemrev.7b00570 (2018).
55. Seddon, A. M., Curnow, P. & Booth, P. J. Membrane proteins, lipids and detergents: not just a soap opera. *Biochimica et biophysica acta* **1666**, 105–117, https://doi.org/10.1016/j.bbamem.2004.04.011 (2004).
56. Bowie, J. U. Stabilizing membrane proteins. *Current opinion in structural biology* **11**, 397–402 (2001).
57. Garavito, R. M. & Ferguson-Miller, S. Detergents as tools in membrane biochemistry. *The Journal of biological chemistry* **276**, 32403–32406, https://doi.org/10.1074/jbc.R100031200 (2001).
58. Henrich, E. *et al*. Lipid Requirements for the Enzymatic Activity of MraY Translocases and *in Vitro* Reconstitution of the Lipid II Synthesis Pathway. *The Journal of biological chemistry* **291**, 2535–2546, https://doi.org/10.1074/jbc.M115.664292 (2016).
59. Alvarez, F. J. *et al*. Full engagement of liganded maltose-binding protein stabilizes a semi-open ATP-binding cassette dimer in the maltose transporter. *Molecular microbiology* **98**, 878–894, https://doi.org/10.1111/mmi.13165 (2015).
60. Smirnova, I., Kasho, V., Sugihara, J. & Kaback, H. R. Opening the periplasmic cavity in lactose permease is the limiting step for sugar binding. *Proceedings of the National Academy of Sciences of the United States of America* **108**, 15147–15151, https://doi.org/10.1073/pnas.1112157108 (2011).
61. Kurauskas, V. *et al*. How Detergent Impacts MembraneProteins: Atomic-Level Views of Mitochondrial Carriers in Dodecylphosphocholine. *The journal of physical chemistry letters* **9**, 933–938, https://doi.org/10.1021/acs.jpclett.8b00269 (2018).
62. Zoonens, M. *et al*. Dangerous liaisons between detergents and membrane proteins. *The case of mitochondrial uncoupling protein 2. Journal of the American Chemical Society* **135**, 15174–15182, https://doi.org/10.1021/ja407424v (2013).
63. Matar-Merheb, R. *et al*. Structuring detergents for extracting and stabilizing functional membrane proteins. *PloS one* **6**, e18036, https://doi.org/10.1371/journal.pone.0018036 (2011).
64. Galian, C. *et al*. Optimized purification of a heterodimeric ABC transporter in a highly stable form amenable to 2-D crystallization. *PloS one* **6**, e19677, https://doi.org/10.1371/journal.pone.0019677 (2011).
65. Dumon-Seignovert, L., Cariot, G. & Vuillard, L. The toxicity of recombinant proteins in Escherichia coli: a comparison of overexpression in BL21(DE3), C41(DE3), and C43(DE3). *Protein expression and purification* **37**, 203–206, https://doi.org/10.1016/j.pep.2004.04.025 (2004).

66. Hattab, G., Warschawski, D. E., Moncoq, K. & Miroux, B. Escherichia coli as host for membrane protein structure determination: a global analysis. *Scientific reports* **5**, 12097, https://doi.org/10.1038/srep12097 (2015).
67. Zhang, Z. *et al*. High-level production of membrane proteins in *E. coli* BL21(DE3) by omitting the inducer IPTG. *Microbial cell factories* **14**, 142, https://doi.org/10.1186/s12934-015-0328-z (2015).
68. Katzen, F. & Kudlicki, W. Efficient generation of insect-based cell-free translation extracts active in glycosylation and signal sequence processing. *Journal of biotechnology* **125**, 194–197, https://doi.org/10.1016/j.jbiotec.2006.03.002 (2006).
69. Long, A. R., O'Brien, C. C. & Alder, N. N. The cell-free integration of a polytopic mitochondrial membrane protein into liposomes occurs cotranslationally and in a lipid-dependent manner. *PloS one* **7**, e46332, https://doi.org/10.1371/journal.pone.0046332 (2012).
70. Niwa, T. *et al*. Comprehensive study of liposome-assisted synthesis of membrane proteins using a reconstituted cell-free translation system. *Scientific reports* **5**, 18025, https://doi.org/10.1038/srep18025 (2015).
71. Gowrishankar, J. & Harinarayanan, R. Why is transcription coupled to translation in bacteria? *Molecular microbiology* **54**, 598–603, https://doi.org/10.1111/j.1365-2958.2004.04289.x (2004).
72. Iost, I. & Dreyfus, M. The stability of Escherichia coli lacZ mRNA depends upon the simultaneity of its synthesis and translation. *The EMBO journal* **14**, 3252–3261 (1995).
73. Iskakova, M. B., Szaflarski, W., Dreyfus, M., Remme, J. & Nierhaus, K. H. Troubleshooting coupled *in vitro* transcription-translation system derived from Escherichia coli cells: synthesis of high-yield fully active proteins. *Nucleic acids research* **34**, e135, https://doi.org/10.1093/nar/gkl462 (2006).
74. Rodnina, M. V. The ribosome in action: Tuning of translational efficiency and protein folding. *Protein science: a publication of the Protein Society* **25**, 1390–1406, https://doi.org/10.1002/pro.2950 (2016).
75. Boel, G. *et al*. Codon influence on protein expression in *E. coli* correlates with mRNA levels. *Nature* **529**, 358–363, https://doi.org/10.1038/nature16509 (2016).
76. Schlesinger, O. *et al*. Tuning of Recombinant Protein Expression in Escherichia coli by Manipulating Transcription, Translation Initiation Rates, and Incorporation of Noncanonical Amino Acids. *ACS synthetic biology* **6**, 1076–1085, https://doi.org/10.1021/acssynbio.7b00019 (2017).
77. Cormack, B. P., Valdivia, R. H. & Falkow, S. FACS-optimized mutants of the green fluorescent protein (GFP). *Gene* **173**, 33–38 (1996).
78. Lesterlin, C. & Duabrry, N. Investigating Bacterial Chromosome Architecture. *Methods in molecular biology* **1431**, 61–72, https://doi.org/10.1007/978-1-4939-3631-1_6 (2016).
79. Ducret, A., Quardokus, E. M. & Brun, Y. V. MicrobeJ, a tool for high throughput bacterial cell detection and quantitative analysis. *Nature microbiology* **1**, 16077, https://doi.org/10.1038/nmicrobiol.2016.77 (2016).

Acknowledgements

CO is grateful and in debt to his current and former colleagues (from Di Pietro, Gros, Davidson and Mankin's laboratories) for their mentoring and support throughout his career. We thank Vincent Chaptal and Josiane Kassis for the generous gift of auto-induction medium, and Annick Dedieu for help with typhoon imager. This work was supported by FINOVI foundation (AO10 to CO and JMJ), Agence Nationale de la Recherche (ANR-17-CE11-0045-01 to CO). CO is also grateful to the "Fondation pour la Recherche Médicale" (FRM) for the financial support of SV (FRM ING20150532264). KM is a recipient of a 6-month PhD extension fellowship from the FRM (FRM FDT201805005394). FD and XNX thank the support of NSF (CBET 0507036) and NIH (R01GM076440). CL was supported by the ATIP-avenir program in partnership with the FINOVI foundation.

Author Contributions

C.O. and J.M.J. conceived the experiments. K.M., W.J., S.V., C.L., F.D. performed experiments; K.M., W.J., S.V., C.L., J.M.J. and C.O. analyzed the data; C.O., J.M.J., C.L., M.P.C., X.N.X. and C.E. supervised experiments; C.O. wrote the manuscript with the help of J.M.J.; all authors read and corrected the manuscript.

Additional Information

Supplementary information accompanies this paper at https://doi.org/10.1038/s41598-019-39382-0.

Competing Interests: The authors declare no competing interests.

Publisher's note: Springer Nature remains neutral with regard to jurisdictional claims in published maps and institutional affiliations.

Chapter 5: Publication 2

Assemblies of lauryl maltose neopentyl glycol (LMNG) and LMNG- solubilized membrane proteins

My contribution includes all the work done on BmrA except Fig 7A and 7B.

BBA - Biomembranes 1861 (2019) 939–957

Contents lists available at ScienceDirect

BBA - Biomembranes

journal homepage: www.elsevier.com/locate/bbamem

Assemblies of lauryl maltose neopentyl glycol (LMNG) and LMNG-solubilized membrane proteins

Cécile Breyton[a], Waqas Javed[a,b], Annelise Vermot[a], Charles-Adrien Arnaud[a], Christine Hajjar[a], Jérôme Dupuy[a], Isabelle Petit-Hartlein[a], Aline Le Roy[a], Anne Martel[c], Michel Thépaut[a], Cédric Orelle[b], Jean-Michel Jault[b], Franck Fieschi[a], Lionel Porcar[c], Christine Ebel[a,*]

[a] Univ. Grenoble Alpes, CNRS, CEA, Institute for Structural Biology (IBS), 38000 Grenoble, France
[b] University of Lyon, CNRS, UMR5086, Molecular Microbiology and Structural Biochemistry, IBCP, Lyon 69367, France
[c] Institut Max Von Laue Paul Langevin, 38042 Grenoble, France

ARTICLE INFO

Keywords:
Membrane proteins
Detergent
LMNG
Homogeneity
Crystallization
Rods

ABSTRACT

Laurylmaltose neopentylglycol (LMNG) bears two linked hydrophobic chains of equal length and two hydrophilic maltoside groups. It arouses a strong interest in the field of membrane protein biochemistry, since it was shown to efficiently solubilize and stabilize membrane proteins often better than the commonly used dodecylmaltopyranoside (DDM), and to allow structure determination of some challenging membrane proteins. However, LMNG was described to form large micelles, which could be unfavorable for structural purposes. We thus investigated its auto-assemblies and the association state of different membrane proteins solubilized in LMNG by analytical ultracentrifugation, size exclusion chromatography coupled to light scattering, centrifugation on sucrose gradient and/or small angle scattering. At high concentrations (in the mM range), LMNG forms long rods, and it stabilized the membrane proteins investigated herein, *i.e.* a bacterial multidrug transporter, BmrA; a prokaryotic analogous of the eukaryotic NADPH oxidases, SpNOX; an *E. coli* outer membrane transporter, FhuA; and the halobacterial bacteriorhodopsin, bR. BmrA, in the Apo and the vanadate-inhibited forms showed reduced kinetics of limited proteolysis in LMNG compared to DDM. Both SpNOX and BmrA display an increased specific activity in LMNG compared to DDM. The four proteins form LMNG complexes with their usual quaternary structure and with usual amount of bound detergent. No heterogeneous complexes related to the large micelle size of LMNG alone were observed. In conditions where LMNG forms assemblies of large size, FhuA crystals diffracting to 4.0 Å were obtained by vapor diffusion. LMNG large micelle size thus does not preclude membrane protein homogeneity and crystallization.

1. Introduction

Detergents are amphipatic molecules that auto-assemble into micelles above the critical micelle concentration (CMC). Above the CMC, they are able to solubilize lipids and membrane proteins, forming protein-detergent complexes of small and well-defined size [1]. Detergents are essential for membrane protein solubilization and purification steps, as well as functional and structural studies. However, they often lead to membrane protein inactivation. One of the mechanisms leading to inactivation (for a recent review, see [2]) is the dissociation of subunits, loss of essential lipids or other hydrophobic cofactors. As an example, cytochrome b_6f inactivation and monomerization was related to lipid loss [3]. Detergent dynamics, *i.e.* detergent exchange between the free monomers, or between micelles, and bound detergent at the surface of the transmembrane protein surface, could trigger transient exposure to the solvent of this hydrophobic surface,

Abbreviations: AUC, Analytical Ultracentrifugation; DSF, Differential Scanning Fluorimetry; SEC-LS, size exclusion chromatography coupled to light scattering; SAXS, small angle X-ray scattering; SANS, Small Angle Neutron Scattering; SLD, scattering length density; TLC, Thin Layer Chromatography; CMC, critical micelle concentration; DDM, dodecyl-β-D-maltopyranoside; DDAO, decyldimethylamine-*N*-oxide; LDAO, lauryldimethylamine-*N*-oxide; LMNG, lauryl maltose neopentyl glycol; OTG, octyl-β-D-thioglucopyranoside; bR, bacteriorhodopsin from *Halobacterium*; BmrA, Bacillus multidrug resistance ATP; SpNOX, *S. pneumoniae* NOX protein; FhuA, *E. coli* outer membrane ferrichome-iron transporter; Vi, orthovanadate

* Corresponding author at: Institut de Biologie Structurale (IBS), Univ. Grenoble Alpes, CEA, CNRS 71 avenue des Martyrs, CS 10090 38044, Grenoble, Cedex 9, France.
E-mail address: christine.ebel@ibs.fr (C. Ebel).

https://doi.org/10.1016/j.bbamem.2019.02.003
Received 1 December 2018; Received in revised form 8 February 2019; Accepted 8 February 2019
Available online 15 February 2019
0005-2736/

leading to irreversible protein aggregation. Detergent binding can also alter protein structure: molecular dynamics simulation indeed showed, for a thermostable mutant of the adenosine receptor, that the harsh octylglucoside detergent molecules intercalate between trans-membrane helices, moving them apart in the 200 ns simulation [4]. The structure and dynamics of different α-helical membrane proteins solubilized in alkyl phosphocholines appear deeply altered [5]. For example, NMR, molecular dynamics simulations, and functional studies, among other techniques, show that mitochondrial carriers are incorrectly folded in these detergents. Some parts of the transmembrane segments are disordered, with molecules of detergent penetrating between the helices; the proteins are in a highly dynamic state with unstable tertiary contacts; and weak ligand binding results from non-specific interactions [5]. In the challenging aim to obtain high resolution structure of membrane proteins by crystallography, a usual strategy is to select detergents that not only preserve membrane protein stability, function and solubility, but also form small micelles (*e.g.* by adding compounds decreasing the micelle size), in order to favor protein-protein contacts [6,7].

The propensity of detergents to inactivate membrane proteins drove the search for new amphiphilic environments (for a review, see [6,8,9]). Peptides that form an α-helix or a β-sheet [10–13], amphipatic polymers with multiple hydrophobic tails [14,15], fluorinated surfactants (reviewed in [8,16,17]), Calixarene based detergents (*e.g.* [18]) or detergents with varying architectures: tripod amphiphiles (*e.g.* [19,20]), facial amphiphiles [21–23], polycyclic based [24], bi-tails [25–29], tri-tails [30], and other compounds [31–33] have been synthetized to decrease their exchange kinetics, and/or reinforce interactions with membrane protein surfaces. This is done noticeably by increasing the rigidity as well as the surface of their hydrophobic moieties. Among these compounds, neopentyl glycols (MNG) constitute a class of detergents with notable interest [25,26]. Members with different chain lengths or with different sugar head groups have been described and are commercialized (Anatrace). We will focus here on the most commonly used one, lauryl maltose neopentyl glycol (LMNG), also named MNG3 (MNG3, however, designates the related family of compounds in [26]). Its structure (Scheme 1) is formed by two molecules of n-dodecyl-β-D-maltopyranoside (DDM) linked at the junction between the hydrophilic and hydrophobic moieties of the molecule. The presence of the two hydrophobic chains of equal length mimics better the structure of lipids than classical detergents having a single hydrophobic tail. According to the authors who designed this detergent in 2010, the central quaternary carbon, was “intended to place subtle restraints on conformational flexibility” [26]. In this work, LMNG was shown to display a set of very interesting features: to extract integral membrane proteins from membranes; to improve substantially the stability of various membrane proteins, including G protein-coupled receptors and respiratory complexes. It also allowed diffraction up to 3.4 Å resolution of LMNG-solubilized cytochrome b_6f crystals obtained by vapor diffusion [26]. Shortly after this first publication, high resolution structures of the challenging β2 adrenergic receptor, in complex with G-proteins [34] or with covalently bound agonist [35], were obtained. The proteins were solubilized and purified in LMNG followed by crystallization in mesophase. LMNG was then described as successfully used for various applications, including membrane solubilization and membrane protein stabilization (*e.g.* [26,36–40]), excited state intermediates [37,41–44], NMR studies [44], H/D exchange coupled to mass spectroscopy (*e.g.* [45,46]), negative stain electron microscopy (*e.g.* [43,46,47]), or reconstitution in lipid vesicles [48]. Impressively, LMNG has now been used to solve the structure of more than ten G-protein coupled receptors (*e.g.* refs in [49]; in all cases, LMNG was used for protein purification and crystallization was performed in mesophase). Other proteins, *e.g.* ABC transporters [41,50,51] or channels [52], were purified and crystallized in LMNG by vapor diffusion. Furthermore, LMNG was also successfully used to solve the high resolution structures of membrane proteins by single particle cryo-electron microscopy (*e.g.* [47,53–55]).

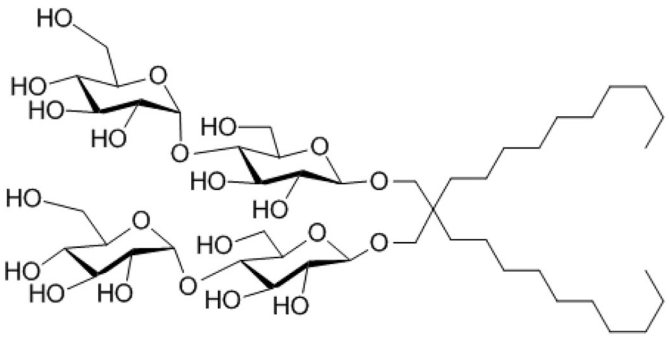

Scheme 1. Chemical structure of LMNG.

Regarding the β2 adrenergic receptor in complex with G-proteins, not only does the complex display long term stabilization in LMNG, but surprisingly, its ligand binding activity is preserved even after diluting LMNG 1000 fold below its CMC [34]. The kinetics of interconversion between the different β2 adrenergic receptor conformations are significantly slower for the protein solubilized in LMNG *vs.* DDM, as shown by F-NMR on labelled proteins [44]. Notably, it was proposed that this was related to the very low CMC of LMNG. From simple considerations, assuming that the on-rate for a monomer forming a micelle is diffusion-limited (thus related only to the detergent monomer size, similar for LMNG and DDM), the detergent off-rates are expected to be lower for LMNG than that for DDM, by a factor being the ratio of their CMCs [44] (the value of the CMC of LMNG will be discussed below). The large off-rate of LMNG may be an explanation for the slower protein dynamics. The fact that individual monomers dissociate much slower from the protein than other standard detergents would also explain the exceptional stabilization of protein-LMNG complexes, and the presence of residual activity measured after dilution below the CMC: LMNG “sticks” to the protein surface, and protein-detergent complexes are preserved. A protocol (GraDeR) was indeed proposed to prepare samples at 1 CMC of LMNG, thus devoid of excess LMNG, for obtaining cryo-electron microscopy images of significantly enhanced quality [47].

However, probably due to the particular geometry of this molecule, the LMNG detergent assemblies formed in solution may be rather large: a hydrodynamic radius of 7.2 nm was determined for a 0.5% solution of LMNG [49]. The questions to be addressed are therefore: how are the large LMNG assemblies/micelles organized in solution? Does the large size of LMNG micelles lead to large protein-detergent complexes? What is the homogeneity and the quaternary structure of the solubilized membrane proteins, and how do they compare to those in more usual detergents? Is the crystallization process affected by the large size of the detergent micelles and/or the possible large size of the solubilized protein-detergent complexes?

To answer these questions, and having in mind that the effects of detergents are protein dependent, we characterized the assemblies in solution of LMNG alone and in complex with four different membrane proteins, FhuA, SpNOX, BmrA and bacteriorhodopsin (bR). We confirmed the stabilization propensity of LMNG compared to DDM, by measuring thermal denaturation by Differential Scanning Fluorimetry (DSF) of the four proteins, limited proteolysis of BmrA, and specific activities of BmrA and SpNOX. We also used complementary techniques such as small angle X-ray and Neutron scattering (SAXS and SANS), Analytical Ultracentrifugation Sedimentation Velocity (AUC-SV) and size exclusion chromatography coupled to light scattering (SEC-LS) and dynamic light scattering (DLS). We showed that, although LMNG alone forms increasingly large assemblies with increasing concentration, the protein-LMNG complexes are of comparable size to those formed with other detergents, with overall the same weight amount of bound detergent, and the oligomeric state of each protein remains unchanged. Furthermore, FhuA solubilized in LMNG showed an overall increased

number of hits when screened for crystallization, suggesting that the large size of LMNG micelles does not prevent protein crystallization.

2. Materials and method

2.1. Chemicals and buffers

Detergents are from Anatrace, except octyl-β-D-thioglucopyranoside (OTG) from Acros, other chemicals are typically from Sigma-Aldrich.

Buffer A: 50 mM Tris-HCl pH 7.0, 300 mM NaCl.

2.2. FhuA purification

FhuA was purified from the *E. coli* strain AW740 transformed with a plasmid encoding the *fhuA* gene in which a 6xHis-tag has been inserted in the extracellular loop L5 [56]. Cells were grown in LB medium at 37 °C in the presence of 100 mM of the iron-chelating agent dipyridine, and broken with a microfluidizer (10 passages at 15 kpsi) in a 20 mM Tris-HCl pH 8, 150 mM NaCl buffer with a pinch of DNase I. Unbroken cells were removed by a first centrifugation (15 min, 6000 rpm, rotor SX4250), and the membrane fraction was recovered by ultracentrifugation (20 min, 35,000 rpm, 45Ti). A first solubilization with 2% OPOE (octylpolyoxyethylene), 20 mM Tris-HCl pH 8.0, 30 min at 37 °C under gentle shaking solubilized the inner membranes, and the outer membrane pellet (20 min, 35,000 rpm, 45Ti) was solubilized in 1% lauryldimethylamine-*N*-oxide (LDAO), 20 mM Tris-HCl pH 8, 1 mM EDTA for 1 h at 37 °C. Insoluble material was removed (20 min, 35,000 rpm, 45Ti). The protein was purified by Nickel affinity chromatography (HiTrap Chelating, 5 mL, GE Healthcare). The LDAO supernatant was supplemented with 5 mM $MgCl_2$ and 5 mM Imidazole, loaded onto the column and thoroughly washed (20 mM Tris-HCl pH 8, 150 mM NaCl, 0.1% LDAO). A delipidation step was achieved by washing with 10 mL of the same buffer containing 1% LDAO. The protein was eluted with 20 mM Tris-HCl pH 8.0, 200 mM Imidazole, 0.1% LDAO. Fractions containing the protein were pooled and loaded onto an anion-exchange chromatography (HiTrap Q, 1 mL, GE Healthcare) equilibrated with 20 mM Tris-HCl pH 8.0, 0.05% LDAO and the protein was eluted by a linear gradient of NaCl in 20 mM Tris-HCl pH 8, 0.05% (2.2 mM) LDAO (final NaCl concentration ~150 mM). The concentration of FhuA was determined using $\varepsilon_{280nm} = 103{,}690\ M^{-1}\ cm^{-1}$.

2.3. FhuA detergent exchange

For LDAO - LMNG exchange, the protein sample was diluted 50 times with water, to reach a detergent concentration far below the LDAO CMC. Protein aggregation was checked by spectrometry (scattering), and the protein was recovered as a pellet by ultracentrifugation (20 min, 35,000 rpm, 45 Ti or 20 min, 80,000 rpm TLA 100.3 depending on the volume). The protein pellet was rinsed with water, and resuspended in 11.9 mM LMNG, 20 mM Tris-HCl pH 8.0 to reach a final protein concentration of 7–10 mg mL^{-1}. A different protocol is described below for the thermal denaturation assays.

2.4. FhuA crystallization

Crystallization screening was carried out using commercial screens (Qiagen and Hampton Research). Sitting drops, consisting of 100 nL protein and 100 nL crystallization buffer, were dispensed in 96-well plates (Greiner Crystal Quick plates) using a Cartesian PIXSYS 4200 robot (Genomic Solutions) and equilibrated at 20 °C against 100 mL of crystallization buffer. Hits were then manually reproduced and improved using the vapor diffusion hanging drop technique. The drops, consisting of 0.8 mL protein and 0.8 mL crystallization buffer, were equilibrated against 250 mL of crystallization buffer at 20 °C in 48-well plates (Hampton Research). Crystals were transferred to the crystallization buffer supplemented with 20% (v/v) glycerol for 30 s, flash-cooled and stored in liquid nitrogen.

2.5. FhuA LMNG data processing

The final data set was collected at 4 Å on beamline FIP-BM30A at the European Synchrotron Radiation Facility, Grenoble, France [57]. Data reduction was performed using the XDS program [58]. The space group was $C222_1$ (a = 149.53 Å, b = 210.96 Å, c = 188.70 Å) with two molecules per asymmetric unit (solvent content of 73%). The structure was solved by molecular replacement performed with the Phaser program [59] using the model of the *E. coli* protein available in the Protein Data Bank (code 2FCP). A refinement was carried out with the *phenix.refine* program [60,61] in the 48–4 Å resolution range.

2.6. SpNOX production

SpNOX was overexpressed and purified in typically 0.025 mM LMNG, as previously described [62]. When using DDM as the detergent, the same purification protocol was used but with adjustments for DDM concentrations in the purification buffers corresponding to each step. Indeed, the solubilization step was performed using 5.1 mM DDM, the loaded Ni-HisTrap column was washed in the corresponding buffer containing 2 mM DDM, and eluted with 0.3 mM DDM in the elution buffer. Final size exclusion was performed in 50 mM Tris-HCl pH 7.0, 300 mM NaCl, 0.3 mM DDM.

2.7. BmrA production

Typical bacterial culture protocol: pET23b-*bmrA* [63] was used to transform C41(DE3) strain of *E. coli*. For preculture, 200 mL LB medium containing 100 μg mL^{-1} ampicillin was inoculated with a freshly transformed colony and growth allowed overnight at 37 °C and 180 rpm. The next morning, enough preculture was added into 1 L 2× YT medium, containing 100 μg mL^{-1} ampicillin, to get an optical density of 0.1, and growth then allowed at 37 °C 180 rpm. When the optical density reached 0.6, the culture was induced for the overexpression of BmrA for 4 h at 25 °C and 180 rpm by the addition of 0.7 mM IPTG (final concentration). Thereafter, the cells were harvested by centrifugation at 4000*g* at 4 °C for 20 min and the bacterial pellet was frozen at −80 °C until further use. Inverted Membrane Vesicles preparation: The bacterial pellet was resuspended in 50 mM Tris-HCl pH 8, 5 mM $MgCl_2$, 1 mM dithiotreitol, with an anti-protease cocktail from Roche. The bacterial cells were lysed by passing them thrice through Microfluidizer™ at 18,000 psi. Next, the cellular debris was removed by centrifugation at 15,000*g* for 30 min at 4 °C. The membrane fraction was subsequently obtained by centrifugation at 150,000*g* for 1 h at 4 °C. The membrane fraction was resuspended and centrifuged again, with the same conditions as before, after resuspension in 50 mM Tris-HCl pH 8, 1.5 mM EDTA, 1 mM dithiotreitol. Finally, the obtained membrane vesicles were resuspended in 20 mM Tris-HCl pH 8, 300 mM sucrose, 1 mM EDTA and flash frozen in liquid nitrogen before storage at −80 °C. The total protein concentration in membrane vesicles was analyzed by BCA assay. BmrA purification: BmrA enriched Inverted Membrane Vesicles were solubilized for 1 h at 4 °C in 50 mM Tris-HCl pH 8, 10% glycerol, 100 mM NaCl, 1 mM dithiotreitol, anti-protease cocktail from Roche, with 1% detergent (LMNG or DDM). The soluble fraction obtained after ultra-centrifugation, at 150,000*g* for 1 h at 4 °C, was injected into a 1 mL HisTrap HP column (GE Healthcare) which was pre-equilibrated with the same buffer with 20 mM imidazole, and 0.1% (2 mM) DDM or 0.01% (0.1 mM) LMNG. The column was washed with 20 column volumes of the same buffer. Gradient elution was eventually performed with the same buffer with imidazole gradient from 20 mM to 500 mM. The protein fractions were dialyzed overnight at 4 °C against 50 mM Hepes pH 8, 10% glycerol, 50 mM NaCl, 2 mM

DDM or 0.1 mM LMNG. The protein concentration, 2.2 mg mL^{-1} for both BmrA in 2 mM DDM and BmrA in 0.1 mM LMNG, was determined from UV absorbance at 280 nm by using Nanodrop spectrophotometer, and a ε_{280nm} = 38,850 M^{-1} cm^{-1}. Reconstitution of BmrA in proteoliposomes was performed as previously described [64].

2.8. Limited proteolysis of BmrA

Apo form: Purified BmrA in detergent was added to buffer 50 mM Hepes-KOH pH 8, 50 mM NaCl, 10% glycerol and the specified detergent, in case of trypsin, or 100 mM ammonium bicarbonate pH 7.8 with the specified detergent, in case of protease V8. After 15 min of incubation, either trypsin (1 μg/250 μg of protein) or protease V8 (1 μg/20 μg of protein) was added. Samples of 10 μL (5 μg BmrA) were withdrawn at 0, 2, 5, 15, 30, 60, 120, 180 and 300 min. 2.5 μL of TFA 5% was added immediately to each sample to stop the reaction. 3 μL of Laemmli 5× was then added and the samples were placed in ice before resolving them on SDS-PAGE. Vanadate-inhibited form: For the Vi-inhibited form, before the addition of purified BmrA, the buffer was supplemented with 3 mM $MgCl_2$, 2 mM ATP and 1 mM Vi. The samples were then incubated for 15 min before the addition of protease. Samples of 10 μL were withdrawn and treated thereafter in the same way as the Apo form.

2.9. bR solubilization and detergent exchange by sucrose gradient

Purified purple membrane was solubilized for 40 h at 4 °C with 89 mM OTG (CMC = 9 mM) at a membrane concentration of 1.5 g L^{-1} in 20 mM sodium phosphate buffer, pH 6.8. Samples were diluted to reach a final OTG concentration of 15 mM, supplemented with 2 mM of the surfactant to be tested, and incubated 15 min prior to being loaded onto a 10–30% (w/w) sucrose gradient containing 20 mM sodium phosphate buffer pH 6.8 and 0.2, 2 or 20 mM LMNG. A control gradient contained 1 mM DDM. Gradients were centrifuged for 15 h at 55,000 rpm (200,000*g*) in the TLS55 rotor of a TL100 ultracentrifuge (Beckman). Bands containing the colored protein were collected with a syringe, and protein samples were kept at 4 °C in the dark for UV–visible spectrophotometry. To check for detergent exchange, 10 μL of each recovered bR band was deposited onto a Thin Layer Chromatography (TLC) silica plate (Macherey-Nagel, ref. 818423), and migration performed in a Chloroform/Methanol/Water solvent (65/35/5). After drying, the plate was first stained with iodine vapor and then with orcinol (0.1% orcinol in 3% H_2SO_4 and 72.5% ethanol) and charring at 120 °C.

2.10. Thermal denaturation and activity assays

Thermal unfolding experiments and analysis were performed by differential scanning fluorimetry coupled to back scattering using a Prometheus NT.48 instrument (Nanotemper Technologies, Munich, DE), and the provided software PR.thermocontrol v2.0.4. Up to 48 capillary containing 10 μL of sample are sequentially illuminated at 280 nm, and fluorescence intensity at 350 (F350) and 330 (F330) nm, and back scattering measured as a function of temperature. The derivatives of F350/F330 and of the back scattering were used to estimate the melting temperature, T_m, and the onset of aggregation, T_{agg}, respectively. For FhuA: samples were prepared by diluting 48 times a stock sample of 1.92 mg mL^{-1} FhuA, in 2.2 mM LDAO, 20 mM Tris pH 8.0, ~150 mM NaCl, into 20 mM Tris pH 8.0 with the appropriate detergent, leading to a final residual LDAO concentration of ≈0.05 mM (0.05 CMC), with FhuA at 0.04 mg mL^{-1}. For SpNOX: samples were prepared after purification in LMNG, and possible detergent exchange in DDM, and concentration. Buffer is 50 mM Tris HCl pH 7.0, 300 mM NaCl, 10 μM FAD, with 0.025 mM LMNG or 0.2 mM DDM initial concentrations, 0.21 LMNG and 1.27 mM DDM final estimated concentrations, considering co-concentration of protein and detergent, and SpNOX at 8.3 mg mL^{-1}, for the T_m assays. For activity assays, SpNOX was diluted to 1 μg mL^{-1} in 50 mM Tris HCl pH 7.0, 300 mM NaCl, 10 μM FAD, with 0.025 mM LMNG or 0.2 mM DDM. Activity assays were performed in the presence of 100 μM Cytochrome *c*, 10 μM FAD, 200 μM NADPH, following Cytochrome *c* absorbance at 550 nm. For BmrA: for T_m measurements, samples were prepared at a final protein concentration of 1 mg mL^{-1}, from dilution of the purified protein in 50 mM Hepes pH 8, 10% glycerol, 50 mM NaCl, with 2 mM DDM or 0.1 mM LMNG. For Vi-inhibited form of BmrA, the dilution buffer also contained 10 mM ATP, 10 mM $MgCl_2$ and 1 mM Vi (all final concentrations). BmrA samples were incubated for 15 min at room temperature before allowing them to be filled in the capillaries for Nano DSF analysis. The activity assays of BmrA were done in a quartz cuvette in a final volume of 700 μL. The buffer, containing 50 mM Hepes-KOH pH 8, 10 mM $MgCl_2$, 4 mM phosphoenolpyruvate, 0.3 mM NADH, 32 μg mL^{-1} lactate dehydrogenase, 60 μg mL^{-1} pyruvate kinase, 10 mM ATP and either 2 mM DDM or 0.1 mM LMNG, was added into the cuvette and was allowed to attain the desired temperature *i.e.* 37 °C for 5 min, before adding 3 μg protein, and measuring the absorbance at 340 nm for 20 min at 37 °C. For bR: to perform T_m measurements, after the solubilization step (see above), solubilized bR was incubated 40 min at 4 °C in the presence of biobeads (10 g g^{-1} OTG), that reduced the concentration of OTG to 70 mM estimated from TLC, from the comparison with OTG aqueous solution at 10, 25, 50, 75 and 100 mM. TLC was performed as described above in bR preparation, but the mobile phase was Chloroform/Methanol 2/1, and the volume deposited was 1 μL. Imaging and quantification were done with the Gel Doc XR system and Image lab software (Biorad). The bR was then diluted 18 times in 0.1 M NaCl, 0.02 M Na phosphate buffer supplemented with the appropriate detergent, residual OTG concentration being estimated as 0.4 its CMC, and final bR concentration to 0.14 mg mL^{-1}. In the thermal denaturation assays, the temperature was increased by 1 (FhuA, bR, SpNOX) or 0.5 (BmrA) °C/min from 15 °C (FhuA, bR, SpNOX) or 20 °C (BmrA) up to 95 °C.

2.11. Density measurements

31.8 mg of dried LMNG was dissolved in 1.99948 g of water. From the density of water (0.998205 ± 0.000001 g mL^{-1}) and sample (1.001416 ± 0.000002 g mL^{-1}) determined from triplicate measurements at 20 °C using a DMA 58 density meter (Anton Paar, Graz, Austria), we derived [65] a LMNG concentration of 15.68 mg mL^{-1} and a partial specific volume $\bar{\nu}$ = 0.797 mL g^{-1}.

2.12. AUC-SV

AUC-SV experiments were conducted in an XLI analytical ultracentrifuge (Beckman, Palo Alto, CA) using an ANTi-50 rotor, using double channel Ti centre pieces (Nanolytics, Germany) of 12, 3, or 1.5 mm optical path length equipped with sapphire windows, with the reference channel being typically filled with solvent without detergent. For BmrA, LMNG was in the buffer in the reference channel, and we used double sector capillary type cells (Beckman, Palo Alto, CA) allowing perfect matching of the channel heights upon centrifugation 90 min at 7000 rpm (3600*g*). Acquisition was done at 42,000 rpm (130,000*g*), overnight, using absorbance (280 nm, and additionally for SpNOX, 412 nm) and interference detection. Data processing and analysis was done using the program SEDFIT [66] from P. Schuck (NIH, USA), REDATE [67] and GUSSI [68] from C. Brautigam (USA), and using standard equations and protocols described in [65,69–71]. LMNG samples in water were prepared from precise weight dilution from a stock solution at 9.88 mM. The sedimentation velocity profiles for LMNG at 23.2 and 35 mM in 20 mM Tris-HCl pH 8.0, 150 mM NaCl showed an optical artefact, and *s*-values were determined from (r_b/

r_m) = $s\omega^2 t$, with r_b the radial position at half the plateau signal, r_m the meniscus position, ω the angular velocity, and t the time. Corrected s-values for solvent density and viscosity, s_{20w}, are calculated, for membrane proteins, considering for their partial specific volume, the mean value between protein and detergent.

2.13. Dynamic light scattering (DLS) of LMNG

LMNG at 20 mM in water was measured using the DynaPro NANOSTAR (Wyatt, Santa-Barbara, USA) instrument, at room temperature, and analyzed with the associated software DYNAMICS.

2.14. SEC-LS

SEC-LS experiments were conducted at 4 or 6 °C on a HPLC consisting of a degasser DGU-20AD, a LC-20AD pump, an autosampler SIL20-AC_{HT}, a communication interface CBM-20A and a UV–vis detector SPD-M20A (Schimadzu, Kyoto, Japan), a column oven XL-Therm (WynSep, Sainte Foy d'Aigrefeuille, France), a static light scattering miniDawn Treos, a dynamic light scattering DynaPro NANOSTAR, and a refractive index Optilab rEX detectors. The analysis was made with the software ASTRA, v5.4.3.20 (Wyatt, Santa-Barbara, USA). Samples of 10 to 60 µL were injected at 0.5 mL min^{-1} on a Superdex 200 10/300 GL (GE Healthcare), equilibrated with the elution buffer. Bovine serum albumin at 2 mg mL^{-1} in PBS buffer was injected as a control in each experiment. The extinction coefficient and refractive index increments for the proteins were calculated from the amino-acid sequences using the program SEDFIT described above. For LMNG, we used $\partial n/\partial c$ = 0.146 mL g^{-1} determined by AUC.

2.15. SAXS and SANS samples

A first series of SAXS measurements was carried out with 14 samples of LMNG in H_2O, at concentrations between 0.31 and 20 mM, and a second series, measured by SAXS and SANS, with four samples of LMNG in H_2O and in D_2O, at 20 and 10 mM. SANS contrast variation determination was achieved for LMNG at 20 mM in 25 mM Tris pH 8, 150 mM NaCl, 10% glycerol, with different D_2O %s. LMNG concentrations were precisely determined using weighing-controlled solubilization and dilutions.

2.16. SAXS experiment

SAXS experiments were conducted on the BM29 beamline at the European Synchrotron Radiation Facility (Grenoble, France). The data were recorded for $0.004 < Q < 0.5$ Å^{-1} ($Q = (4\pi/\lambda)\sin\Theta$ is the modulus of the scattering vector, with 2Θ being the scattering angle, and λ the wavelength), using a two-dimensional 1 M Pilatus detector, at 20 °C, with a monochromatic X-ray beam with λ = 0.9919 Å and a sample to detector distance of 2.864 m. Measurements were performed with 50 µL loaded sample, in a quartz capillary, with a continuous flow. In the first series, 10 acquisitions with 1 s irradiation per acquisition (flow of 2.7 µL/s), in the second series, 10 and 30 acquisitions with 0.5 s irradiation (flows of 5 and 1 µL/s), were recorded for the samples and the solvents. The scattering curves were indistinguishable with the two flows. Data reduction was performed using the automated standard beamline software (BSxCuBE) [72], and data processing, including the elimination of data suffering from radiation damage, averaging, buffer subtraction, Guinier plots, using PRIMUS of the software suite ATSAS [73]. Absolute scales were obtained using the scattering of water.

2.17. SANS experiment

SANS experiments were carried out on the small-angle diffractometer D22 at the Institut Laue Langevin (Grenoble, France), at 20 °C, using neutron wavelengths λ of 6 and 12 Å, with samples measured in Hellma quartz cells 100QS with 1-mm optical path length. Scattering data for LMNG at 10 and 20 mM in H_2O and D_2O were recorded at 20 °C for $0.003 < Q < 0.45$ Å^{-1}, using a neutron wavelength λ of 6 Å, and sample-detector/collimation distances (SD/coll) of 17.6 m/17.6 m, 5.6 m/5.6 m, and 1.4 m/2.8 m for 15, 5 and 5 min, respectively. For LMNG at 20 mM in D_2O, additional data were recorded at (SD/coll) of 17.6 m/17.6 m at 12 Å, leading to a total Q-range of 0.0012–0.45 Å^{-1}.Transmissions were measured at 17 m for 1 min. For the determination of the contrast match point, samples were measured at 10 °C, with SD/coll of 5.6 m/5.6 m, 1.4 m/2.8 m, for 5 and 1 min respectively, and transmissions were measured at 5.6 m for 1 min. LMNG at its match point, in 21.4% D_2O, was measured at 15 °C, with SD/coll of 8 m/8 m and 1.4 m/2 m for 60 and 15 min, respectively. Data reduction to obtain scattering curves in absolute scale, and manipulation -merging, buffer subtraction- were done in the usual way (see *e.g.* [74]) using Grasp (a Matlab™ script application produced by ILL) and SANS reduction macros provided by NIST Center running on IGOR (Wavemetrics) [75]. Absolute intensities are obtained using the direct beam measurement.

2.18. SAXS and SANS Guinier analysis

The radii of gyration (Rg) and the intensities scattered in the forward direction ($I(0)$) were extracted by the Guinier approximation, with $RgQ \leq 1.3$. Aggregation number were derived from the molar mass of LMNG micelle, M (g mol^{-1}) obtained from the absolute forward intensity, $I(0)$ (cm^{-1}), using $M = (I(0)/c)N_A/(\partial\rho_{el}/\partial c)^2$, in SAXS, and $M = (I(0)/c)N_A/(\partial\rho_N/\partial c)^2$, in SANS. N_A is Avogadro's number, c the concentration (g mL^{-1}), and $\partial\rho_{el}/\partial c$ and $\partial\rho_N/\partial$c (cm g^{-1}) the increment of electron and neutron, respectively, scattering length density per g of LMNG. $\partial\rho_{el}/\partial c = (\rho_{el} - \rho^{\circ}_{el})\ r_{el}\ \bar{v}$, with $\rho_{el} = 4.105 \cdot 10^{23}$ (from composition and $\bar{v}$) and $\rho^{\circ}_{el} = 3.297 \cdot 10^{23}$ the numbers of electron per mL of LMNG and solvent, respectively, and $\rho_{el} = 2.818 \cdot 10^{-13}$ cm the scattering length of an electron. $\partial\rho_N/\partial$c was calculated to be 1.108 10^{10} cm g^{-1} in H_2O, and $-3.509 \cdot 10^{10}$ cm g^{-1} in D_2O.

2.19. SAXS and SANS combined analysis for LMNG shape

SAXS and SANS data were analyzed using shape-dependent models in SASview [76]. The scattered intensity from a homogeneous dispersion of particles is written as:

$I(Q) = N\ V^2\ (\Delta\rho)^2\ P(Q)\ S(Q)$

where N is the number density of particles, V their volume, $\Delta\rho$ (cm^{-2}) is the scattering contrast, $P(Q)$ is the inter particle form factor and $S(Q)$ is the interparticle structure factor.

In the present case, SAXS and SANS data have been fitted simultaneously with a core shell cylinder form factor and hard sphere potential with beta approximation using SASview software. The cylinder form factor included size polydispersity on radius (fixed at 5%) using a Gaussian distribution. The scale factor was fixed by the surfactant concentration. The head group X-ray/neutron scattering length densities (Å^{-2}) (SLD) were fitted using the same hydration level of the anhydrous polar hear. Radius, length and shell thickness of the cylinder were constrained and kept equal for X-ray and neutrons. Fitting was performed using the optimizer DREAM which allows to set simultaneous fits as well as proper error determination.

3. Results

3.1. Hydrodynamic characterization of LMNG

Our first aim was to characterize the assembly properties of LMNG molecules by itself. AUC-SV experiments were done for LMNG solubilized in water at different concentrations. The SV profiles and analysis in terms of continuous distributions $c(s_{20w})$ of sedimentation coefficients, s_{20w}, showed a unique or main boundary. The mean s_{20w}-value

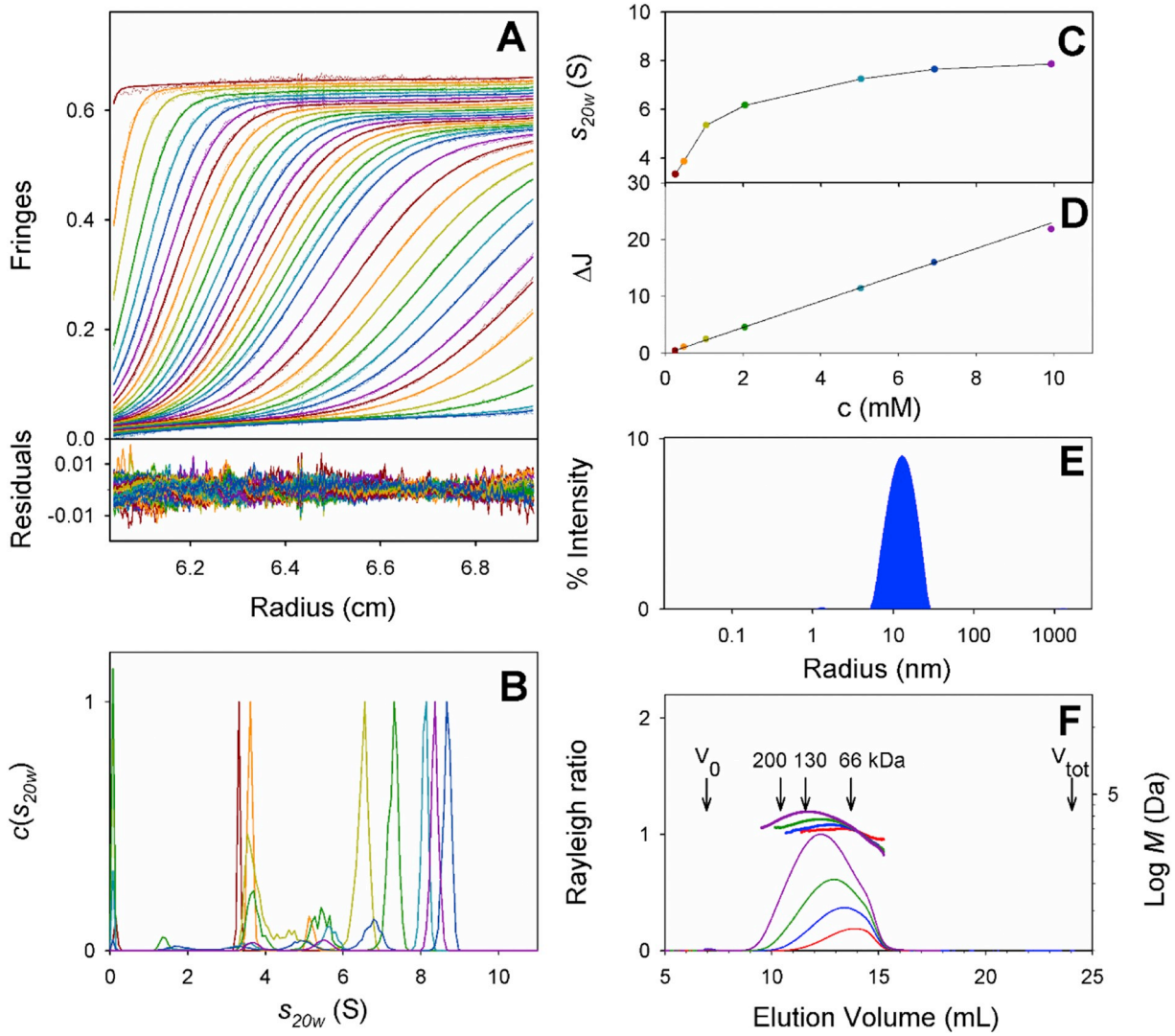

Fig. 1. LMNG in AUC-SV, DLS, and SEC-LS.
AUC-SV: A: Superposition of experimental and fitted sedimentation velocity profiles (top) and residuals (bottom), obtained at 130,000*g* and 20 °C during ≈ 5 h using interference optics and 12 mm optical path centerpiece, for LMNG at 0.25 mM in water. B: Superposition of the normalized $c(s)$ distributions for LMNG at 0.25 (brown), 0.5 (orange), 1 (yellow-green), 2 (green), 5 (cyan), 7 (blue), and 10 (purple) mM. C: plot of the mean sedimentation coefficient s_{20w} *versus* LMNG concentration. Note that the mean s_{20w} is obtained from the integration of the $c(s_{20w})$ over the whole s_{20w}-range; At 10 mM compared to 7 mM, as seen in Panel B, s_{20w} the for the main species is decreased, while, as seen in Panel C, the mean s_{20w} is slightly increased. D: Fringe number ΔJ, normalized to 1 cm optical path-length, for the micelle contributions *vs.* total LMNG concentration, and linear fit. DLS: E: Hydrodynamic radius distribution of LMNG at 20 mM in water. SEC-LS: F: Rayleigh ratio measured along the elution profiles, for 30 µL LMNG injected at 2, 5, 10, and 20 mM (red, blue, green, and purple thin lines, respectively) on a Superdex 200 10/300 GL (GE Healthcare) column eluted with 50 mM Tris-HCl pH 7.0, 300 mM NaCl, 0.05 mM LMNG, and molar masses (thick lines, right axis) derived from the light scattering and refractive index detections. V_0 is the dead volume, V_{tot} the total volume of the column, and the arrows indicate the elution volumes of BSA as a monomer, dimer, and trimer (66, 130, and 200 kDa) from a different injection. (For interpretation of the references to color in this figure legend, the reader is referred to the web version of this article.)

increased with concentration, from 3.3 S at 0.25 mM to 7.9 S at 9.8 mM (Fig. 1A–C). This indicates that LMNG micelle aggregation number increases with concentration, an atypical behavior compared to usual detergents. Complementary AUC-SV in a dilute buffer (20 mM Tris-HCl pH 8.0, 150 mM NaCl), at larger LMNG concentrations of 23 and 35 mM, gave estimates for s_{20w} of 7.7 and 8.7S, respectively. By integrating the signal for the micelles at the different LMNG concentrations (Fig. 1D), we determine, in water, a refractive index increment for LMNG $\partial n/\partial c = 0.146\ \mathrm{mL\,g^{-1}}$ (close to that of DDM, $0.143\ \mathrm{mL\,g^{-1}}$ [65]), and a CMC of 40 µM. The knowledge of the partial specific volume, $\bar{\nu}$, of LMNG is required to correlate s_{20w} and molar mass, or aggregation numbers $N_{agg.}$ We measured, with density measurement, $\bar{\nu} = 0.797\ \mathrm{mL\,g^{-1}}$, a value close to that of DDM: $0.82\ \mathrm{mL\,g^{-1}}$ from [65] and $0.81–0.837\ \mathrm{mL\,g^{-1}}$ from [1].

Minimum aggregation numbers N_{agg} of 63 and 230 are calculated at 0.25 and 10 mM considering globular compact micelles (frictional ratio of 1.25), but N_{agg} are larger, at least for the larger micelles, since their shape is anisotropic (see below). Dynamic light scattering (DLS) of 20 mM LMNG in water showed essentially one population with a polydispersity index of 35% and a hydrodynamic radius, R_H, of 14 nm (Fig. 1E), in line with the reported value of 7.2 nm at 5 mM [49]. Combining s_{20w} and R_H values at 5 and 20 mM provides N_{agg} estimates of 300 and 620, corresponding to frictional ratios of 1.65 and 2.4, indicating moderately and strongly elongated shapes, respectively.

In SEC-LS experiments with 0.05 mM LMNG in the equilibration and elution buffer (buffer A), LMNG injected at 2, 5, 10 and 20 mM eluted as a very large peak covering the elution volumes of BSA monomer (65 kDa) to BSA trimer (Fig. 1F). When LMNG

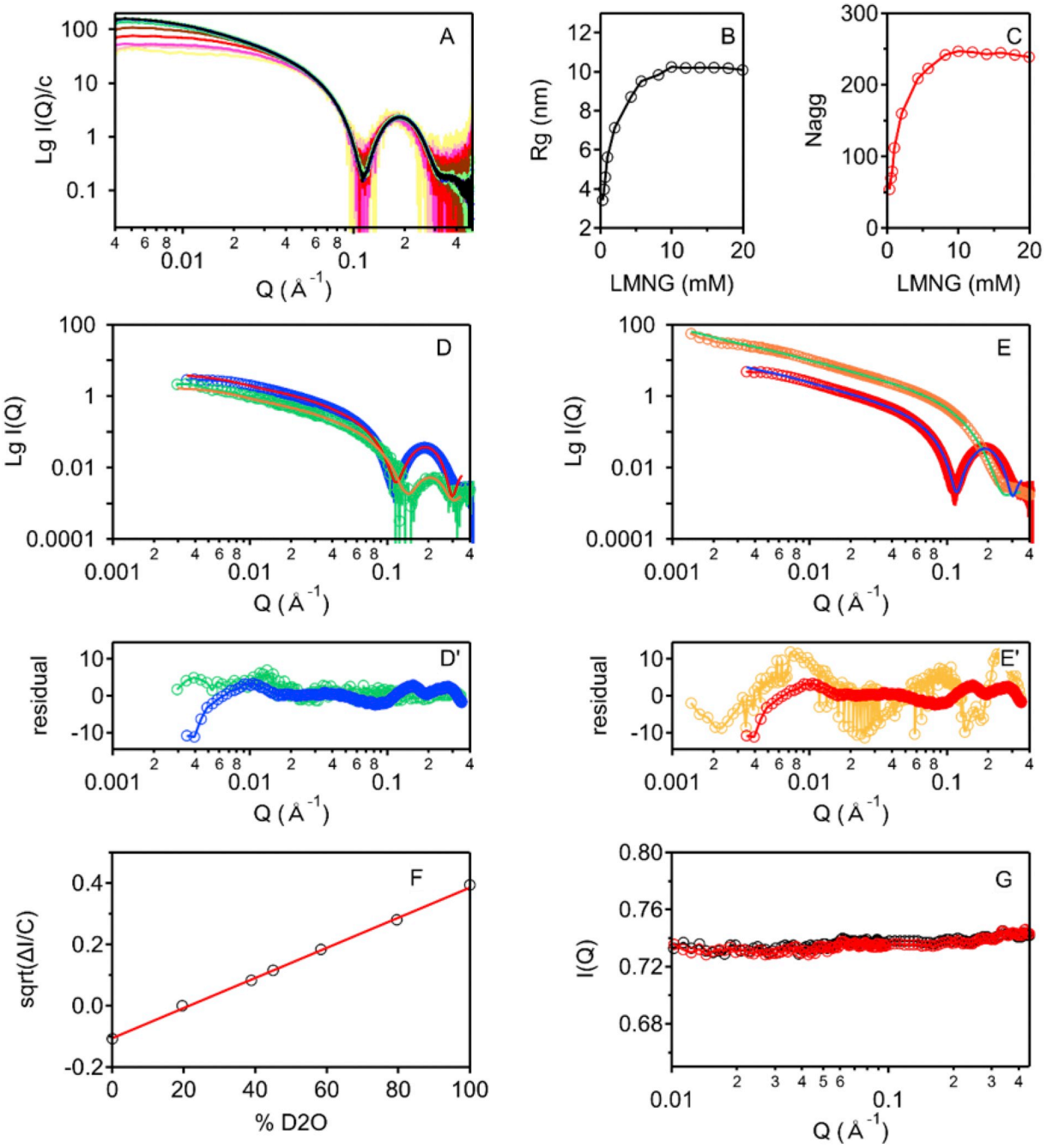

Fig. 2. SAXS and SANS analysis of LMNG.

A: Superposition of 13 SAXS profiles obtained at 0.3 (yellow), 0.5 (pale pink), 0.7 (pink), 1 (red), 2 (brown), 6 (green), 8 (light green), 10 (light blue), 12 (blue), 14 (navy), 16 (purple), 18 (grey), and 20 (black) mM LMNG, in H_2O, at 10 °C. B: corresponding *Rg*, and, C: aggregation numbers, *versus* LMNG concentrations. D, E: Superposition, for LMNG at 20 mM in H_2O (D), and D_2O (E) of the experimental scattering curves obtained by SAXS (blue and red dots, respectively) and SANS (green and orange dots, respectively), and of the fitted curves, in the model of a core-shell cylinder, in SAXS (red and blue lines in H_2O and D_2O, respectively), and in SANS (orange and green lines in H_2O and D_2O, respectively); D′, E′: respective normalized by data error residuals. SAXS and SANS data in each solvent were globally fitted (Table 1). F: Match point determination from SANS scattering curves obtained for 20 mM LMNG in 0, 20, 40, 45, 60, 80, and 100% D_2O. G: Superposition of raw scattering curves obtained in a solvent with 21.4% D_2O for LMNG at 2 mM (black) and of the solvent alone (red). (For interpretation of the references to color in this figure legend, the reader is referred to the web version of this article.)

concentration increased, the elution volume decreased. However, the molar masses determined from coupled refractive index and light scattering detections did not change significantly, neither along the elution, nor with the injected LMNG concentration: from 67 kDa (N_{agg} = 67) at 2 mM to 76 kDa (N_{agg} = 76) at 20 mM (Fig. 1F). This suggests the dissociation of the largest LMNG complexes upon sample dilution on the column.

3.2. Structural characterization of LMNG by small angle scattering

SAXS and SANS experiments were performed to get additional information on the size and shape of LMNG micelles. A first set of SAXS experiments were done with LMNG between 0.3 and 20 mM (0.03 and 2%) (Fig. 2A). From the Guinier analysis, the size of the micelle increases with *Rg* and aggregation numbers increasing from 3.4 nm to

10 nm, and from 55 to 240, respectively, when LMNG concentration is raised from 0.3 to 10 mM. (Fig. 2B and C). These values remain constant for LMNG concentrations increasing from 10 to 20 mM, and indeed the scattering curves are superimposed (Fig. 2A). All curves are superimposed at the largest angles, representing the smallest distances in the real space, compatible with an identical circular cross section. To ascertain the shape of the LMNG micelles, 10 and 20 mM LMNG samples were measured by SAXS and SANS, in H_2O and D_2O. In the same buffer, the scattering curves normalized by concentration were superimposable for the 10 and 20 mM LMNG samples. From Guinier plots, the radii of gyration from SAXS were 11.5 and 11.6 nm at 10 and 20 mM in H_2O, and 17.7 and 17.2 nm at 10 and 20 mM in D_2O. The aggregation numbers were 285 in H_2O, and 528 in D_2O. The *Rg* and aggregation numbers from SAXS, in H_2O were slightly larger but similar to those of the first set of experiments. The size of the micelles appears significantly larger here for LMNG in D_2O than in H_2O. However, as will be discussed below, the significance of this difference is not ascertained.

The SAXS and SANS scattering curves of 20 mM LMNG in H_2O and D_2O were analyzed globally. We used a model of a core shell cylinder with hard sphere interaction, defined by a core representing the hydrophobic tails (*i.e.* the hydrocarbon chains) covered by a shell representing the hydrated polar heads. The SLD of the core and of the solvent were fixed to the theoretical values. The SLD of the polar head (different in SAXS and SANS), and the dimensions of the micelles (radius of the cylinder core, thickness of the shell, and length, common in SAXS and SANS) were globally fitted keeping the same hydration level in X-ray and neutron. The results are presented in Table 1. The fitted values for the SLD of the anhydrous shell values are in the same order of magnitude as those calculated for the anhydrous polar head. We extracted reasonable hydration of 30% in H_2O and 44% in D_2O. The radius of the hydrophobic core, 14 Å, and that of the shell thickness, 7–9 Å, are in line with those expected from the LMNG size.

Finally, we investigated whether LMNG could be totally matched out in SANS. This is required to be able to focus on protein contribution in an protein-LMNG complex. The differential distribution of detergent hydrophobic tails and hydrophilic heads in the detergent micelles and bound detergent indeed corresponds to ordered scattering density fluctuations, which makes the scattering curve of the micelles and bound detergent possibly not flat even at the detergent match point [77]. We thus measured for LMNG a set of contrast variation curves, using a solvent with different %s of D_2O. We determined a contrast match point of 21.4% D_2O (Fig. 2F). The scattering curve of the 2 mM LMNG sample in 21.4% D_2O perfectly superimposes that of the solvent (Fig. 2G). Thus LMNG can be homogeneously masked. The analysis of the neutron scattering curves of membrane proteins solubilized in LMNG, in 21.4% D_2O will not require the fastidious step of detergent modelling to access membrane protein envelope structure. Because the contrast match point of hydrogenated proteins is ≈44% D_2O, membrane proteins should be deuterated to improve their scattering signal, but this is not problematic, since deuterating proteins, in general, is not an issue.

To summarize, SAXS and SANS showed that LMNG forms large elongated rod-like micelles above the mM concentration. Given this observation, the question of the homogeneity of different membrane proteins at various LMNG concentrations was addressed below.

3.3. FhuA-LMNG assemblies

FhuA is an *E. coli* outer membrane ferrichome-iron transporter involved in bacteriophage infection [78,79]. The structure of this robust β-barrel protein was solved in 1998 [80]. We investigated FhuA stability, homogeneity and association state at different LMNG concentrations, and whether the protein can crystallize in LMNG.

We first compared the thermal stability of FhuA in LDAO and in LMNG by DSF, allowing to measure the melting temperature (T_m) of the protein by probing the fluorescence emission (F_{350nm}/F_{330nm} ratio) of the aromatic residues upon increasing temperature. Simultaneous light back-reflection measurements permit to detect qualitatively aggregation events. Detergent was exchanged by a 48 times dilution, leading to a final residual concentration of LDAO that was much below its CMC (20 times). The melting curves are similar whatever the final detergent concentration, corresponding to CMC + 0.2, 0.5 mM and 1–2 mM, *i.e.* LDAO at 1.2, 1.5, and 2.2 mM and LMNG at 0.21, 0.51 and 2.01 mM. They show (Fig. 3A) two unfolding events, attributed to, first, the unfolding of the cork, and then of the barrel [81] (both domains contain tryptophans). From light back-reflection, the onset of protein aggregation coincides with the first T_m, and significant aggregation to the second T_m. In LDAO, the T_m at 63 and 69 °C are in line with the published values of 60–65 and 74–75 °C, from scanning calorimetry [81], or synchrotron radiation circular dichroism [78] in slightly different buffers with 1.3 or 4.4 mM LDAO. In LMNG, unfolding is shifted to higher temperatures. The first T_m is at 67 °C, showing a moderate stabilization (+4 °C) of the cork, the second one at 80 °C indicating a significant stabilization (+11 °C) of the barrel. T_m values are reported in Table 2. For comparison, binding of ferrichrome, the natural ligand, was described to have a strong stabilizing effect on FhuA cork, shifting the first transition by 6 °C [81]; binding of phage T5 Receptor Binding Protein pb5 leads to one unique unfolding event at 89 °C (+15 °C *vs.* T_m of barrel for FhuA alone) [78]. Thus, LMNG significantly stabilizes both the flexible parts and the rigid domain of this β-barrel protein.

Table 1
Rod analysis of SAXS and SANS data for 20 mM LMNG.

	LMNG 20 mM in H_2O		LMNG 20 mM in D_2O	
	SAXS	*SANS*	*SAXS*	*SANS*
Q range ($Å^{-1}$)	0.0035–0.35	0.0030–0.35	0.0035–0.35	0.0015–0.35
χ^2_R	3.2	3.2	2.3	26.7
Background, fixed (cm^{-1})	0.0008	0.001	0.0012	0.0015
SLD solvent, fixed (10^{-6} $Å^{-2}$)	9.4	−0.56	9.4	6.4
SLD core, fixed (10^{-6} $Å^{-2}$)	8.3	−0.3	8.3	−0.3
SLD anhydrous head, fixed (10^{-6} $Å^{-2}$)	14.75	1.88	14.75	3.99
SLD shell, fitted (10^{-6} $Å^{-2}$)	13.12 ± 0.02	1.134[a]	12.42 ± 0.02	5.048[a]
Fitted shell hydration (%)	30		44	
Radius (Å)[b]	14.51 ± 0.02		13.29 ± 0.01	
Thickness (Å)	7.33 ± 0.04		9.25 ± 0.03	
Length (Å)	603 ± 7		5376 ± 16	
Vol fraction	0.02 ± 0.00001		0.01951 ± 0.00006	

χ^2_R: reduced χ^2.
[a] Linked parameter.
[b] A polydispersity on radius width was fixed to 5%.

Table 2
Melting temperatures of FhuA, SpNOX, BmrA, and bR.

Protein	Detergent type	Detergent conc. (mM)	Micelle conc. (mM)	T_m (°C)	T_{agg} (°C)
FhuA	LDAO	1.2, 1.5, 2.2	0.2, 0.5, 1.2	63.0 + 69.0	65
FhuA	LMNG	0.21, 0.51, 2.0	0.2, 0.5, 1.0	67.0 + 80.0	74
SpNOX	DDM	1,27	1.1	40.5	56
SpNOX	LMNG	0.21	0.2	53.9	60
BmrA Apo	DDM	2	1.8	41.2	54
BmrA Apo	LMNG	0.1	0.1	45.7	70
BmrA Vi-inh	DDM	2	1.8	46.4	45
BmrA Vi-inh	LMNG	0.1	0.1	59.3	50
bR	OTG	11	2.0	53.6	43
bR	DDM	2.01	1.8	59.9	52
bR	LMNG	2.17	2.2	65.9	63

T_m: melting temperature measured by differential scanning fluorimetry; T_{agg}: onset temperature for aggregation from light back reflexion. BmrA Vi-inh, Vi-inhibited forms were incubated with 10 mM ATP, 10 mM $MgCl_2$, and 1 mM vanadate. Standard deviations of typically 0.2 were determined from triplicates experiments in BmrA, otherwise the precision on T_m is estimated at 1 °C. Micelle concentrations (*i.e.* above the CMC concentrations) were calculated considering CMC-values of 1, 0.01, 0.17 and 9 mM for LDAO, LMNG, DDM, and OTG, respectively.

For FhuA, detergent exchange can easily be done, by dilution of the purified protein solution well below the CMC of the first detergent, and re-solubilization of the pellet in the desired detergent. The resulting sample in LMNG, also used for crystallization assays, contained ≈7.5 mg mL^{-1} FhuA and 12 mM (total concentration) LMNG. SV-AUC analysis shows a main contribution (≈75% of the absorbance) at s_{20w} = 7.8 S, *i.e.* the same value as that published for FhuA in DDM [82]. Additional contributions are detected at s_{20w} = 10.7 S (≈5%) and 6.2 S (15–20%), which correspond reasonably to FhuA dimer and LMNG free micelles, respectively (Fig. 4A, B). Analysis of the absorbance of interference fringe signals provides an estimate of 1 g g^{-1} (80 mol/mol) of bound LMNG, and a free micelle concentration of 4.5 mM. In order to investigate the effect of LMNG concentration on FhuA homogeneity, complementary SV-AUC experiments were done on a similarly prepared sample with nominal concentrations of 5.4 mg mL^{-1} FhuA and 13 mM LMNG, and two derived samples, with FhuA diluted twice, and increased LMNG nominal concentrations to 18 and 24 mM. For these three samples too, only one main boundary is observed (> 80%) at about 7 S (Table 3). Probably, due to the large total concentrations of LMNG and FhuA, the fit is poor and the s_{20w} values imprecise (data not shown). The data can be interpreted by the non-ideal co-sedimentation of FhuA complexes and of LMNG free micelles, sedimenting at nearly the same s_{20w} value (Table 3). Nevertheless the membrane protein appears to remain monomeric in the presence of even very large concentrations of LMNG, where the latter forms large micelles. SEC-LS performed on a similar sample injected after 10 times dilution, showed traces of aggregates, FhuA dimer as a shoulder, FhuA monomer as the main contribution at 12.3 mL, and LMNG micelles at 14.5 mL (Fig. 4C). The molar mass analysis gives for the main peak 79.3 kDa for FhuA molar mass contribution, in agreement with the protein sequence (79.9 kDa), and 98.5 kDa for LMNG contribution, corresponding to 1.2 g g^{-1} (95 mol/mol) bound detergent.

3.4. FhuA crystallization

480 conditions were screened for the crystallization of FhuA solubilized in 1.2% (12 mM) LMNG or, for comparison, 1.6% (79.4 mM) decyldimethylamide-*N*-oxide (DDAO). DDAO is the detergent in which the protein was historically crystallized [56], and in our hands, FhuA-

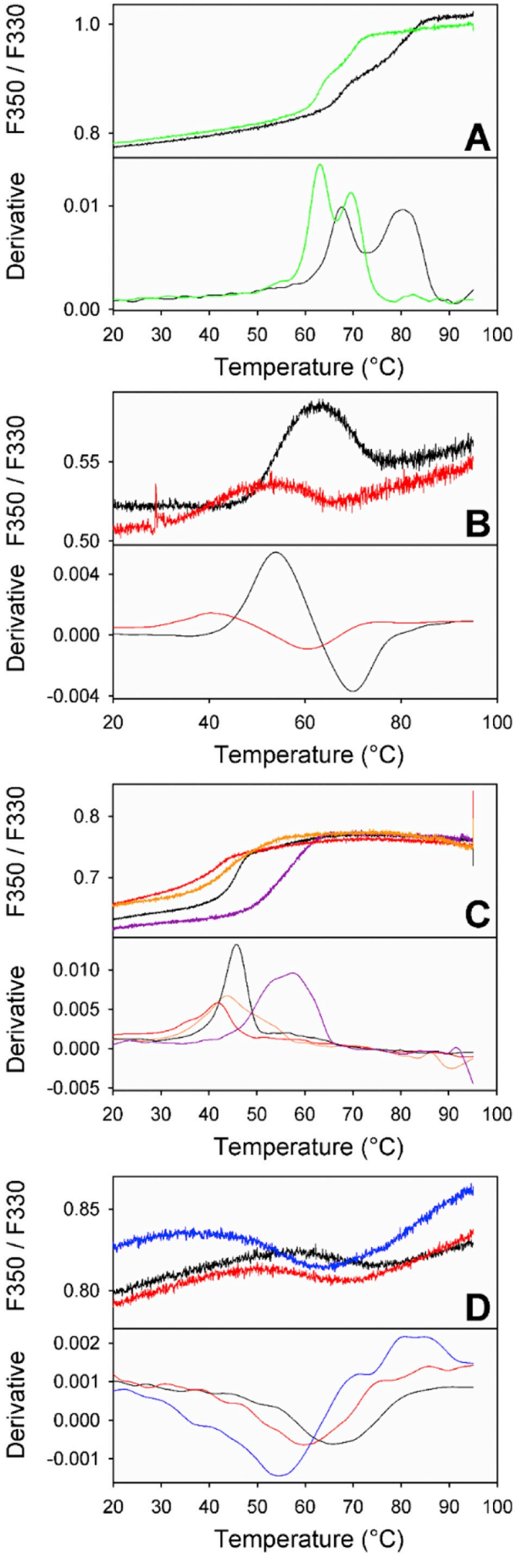

(caption on next page)

Fig. 3. Thermal denaturation of FhuA, SpNOX, BmrA, and bR, by differential scanning fluorimetry.
Ratio of the fluorescence emitted at 350 and 330 nm (top panels), and derivative (bottom panels) for A: FhuA at 0.04 mg mL^{-1} in the presence of LDAO 1.2 mM (green) or LMNG 0.21 mM (black); B: SpNOX at 8.3 mg mL^{-1} in the presence of DDM 1.27 mM (red) or LMNG 0.21 mM (black); C: BmrA at 1 mg mL^{-1}, in DDM 2 mM, in the Apo (red), or Vi-inhibited (orange) forms, and in LMNG 0.1 mM, in the Apo (black), or Vi-inhibited (purple) forms. The Vi-inhibited forms were incubated with 1 mM Vi, 10 mM ATP and 10 mM $MgCl_2$ for 15 min. D: bR at 0.14 mg mL^{-1} in OTG 11 mM (blue), DDM 2.17 mM (red), or LMNG 0.21 mM (black). (For interpretation of the references to color in this figure legend, the reader is referred to the web version of this article.)

DDAO crystals diffracting to 2.2 Å could be obtained (Arnaud and Breyton, unpublished data).

The FhuA-LMNG complex is clearly more susceptible to precipitating conditions: only 53.7% of the drops remained clear (*vs.* 86% for FhuA-DDAO). In addition, 13.3% of the conditions with LMNG yielded unambiguous crystal formation *vs.* only 3% in DDAO, and 10 *vs.* 8 conditions, respectively showed single crystals. Whereas conditions allowing single crystal growth in DDAO were closely related (high molar mass PEG, pH 6–7 and $MgCl_2$), those in LMNG displayed more differences: different precipitants, including wide ranges of PEG molar mass (400–8000) and pH (4–9) and a variety of co-crystallization salts. The shapes of the crystals were also very different, with feather-like shapes for FhuA-DDAO and more rod for FhuA-LMNG crystals (Fig. 4D). X-ray diffraction data were collected on FhuA-LMNG crystals (Table 4). Crystals grown in the screening assay, with little optimization, diffracted up to 4 Å, which allowed to get a model at low resolution and to determine the crystal packing. Interestingly, these crystals have a different space groups ($C222_1$) than crystals obtained with DDAO ($P6_1$).

Thus, LMNG largely expanded the number of potential conditions in which FhuA crystals are grown, possibly by allowing different crystal packing. These data seemingly support the idea that LMNG enhances successful crystallization of membrane proteins [26].

3.5. SpNOX-LMNG assemblies

We then investigated the prokaryotic enzyme SpNOX [62]. This protein is a recently identified analog to the eukaryotic NOX membrane proteins. They are the central catalytic component, involved in transmembrane electrons transfer, within NADPH oxidase complexes, which play essential roles in *e.g.* immunity, cardiovascular physiology, *etc.* Despite the progress done in the characterization of the soluble subunits of the NADPH oxidase complexes [83,84], there were very few structural information on the NOX α-helical membranous component up to the recent composite structure of a NOX5 isoform from a cyanobacteria [85]. Apart from its fundamental biological interest, this protein displays several features that make it a convenient model to test and develop new methods or processes in membrane protein biochemistry. Indeed, the red color brought by the presence of two hemes *b* within the transmembrane protein constitutes a good reporter in all steps of protein manipulation as well as a precious indicator of the correct folding of the protein. Moreover, SpNOX has an enzymatic activity that can be measured spectrophotometrically in a fast and convenient way.

For SpNOX solubilization and purification, maltoside detergents were identified as essential in order to preserve protein activity [62]. However, several lines of improvement have been observed by using LMNG instead of DDM. First, from the elution profile from size exclusion chromatography of the second purification step (Fig. 5A), the peak of SpNOX aggregates, at 45 mL, decreases drastically from DDM to LMNG while, in addition to minor amounts of dimers detected in the two conditions, that of monomeric SpNOX, at 70 mL, increases. SpNOX is obtained with an improved homogeneity in LMNG compared to DDM. Moreover, SpNOX shows a significantly increased specific activity in

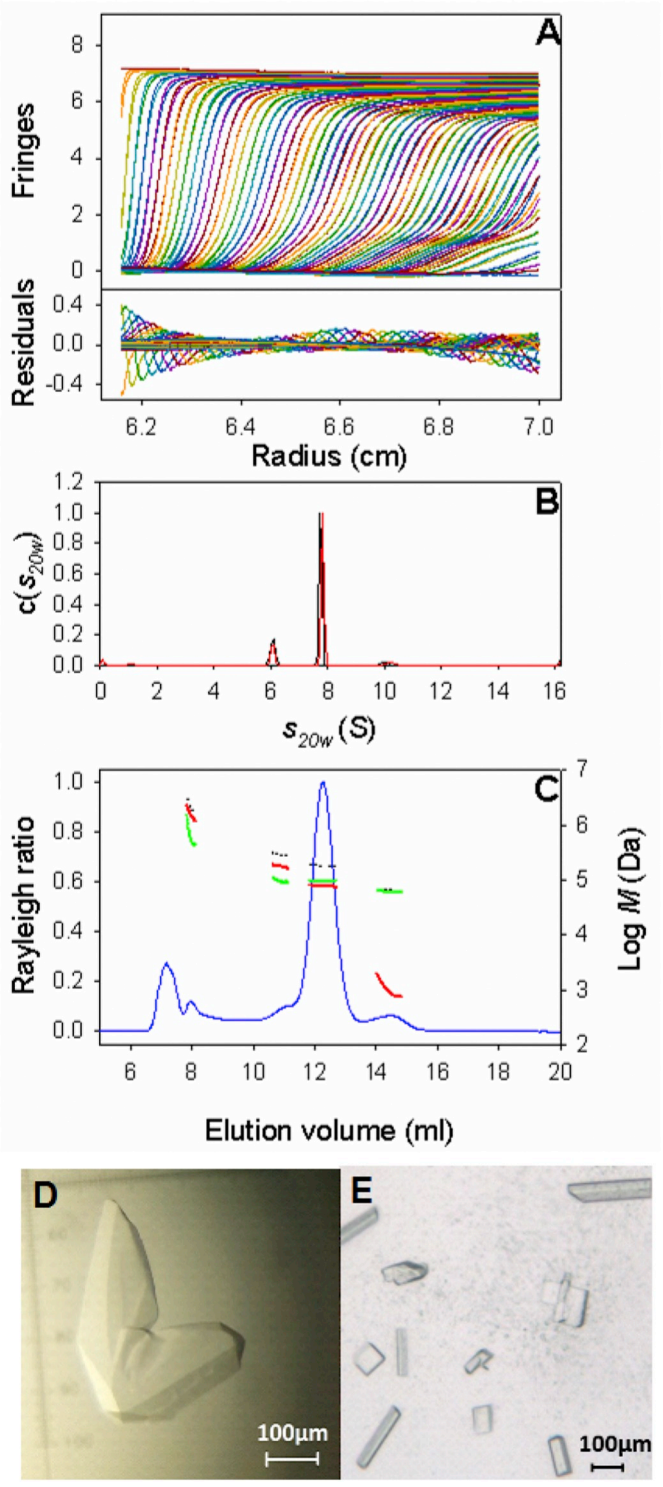

(caption on next page)

LMNG compared to DDM (Table 5). We evaluate the relative thermal stability of SpNOX in LMNG compared to DDM. T_m in LMNG is drastically increased (+13 °C) (Table 2).

We then investigated, using SV-AUC, homogeneity and association state of SpNOX solubilized in LMNG, at different concentrations of SpNOX and LMNG. After a final SEC purification step with 0.03 mM LMNG in the elution buffer (buffer A, see legend to Fig. 5), SpNOX was obtained at 0.1 mg mL^{-1} (sample *c0.1*). Then the protein was concentrated 30 times by ultrafiltration with a 30-kDa cut off membrane

Fig. 4. Characterization and crystallization of LMNG solubilized FhuA.
AUC-SV: A: Superposition of experimental and fitted sedimentation velocity profiles (top) and residuals (bottom), obtained at 130,000*g* and 4 °C during ≈4.5 h using interference optics and 1.5 mm optical path centerpiece, for 7.5 mg mL^{-1} FhuA solubilized with 12 mM LMNG in 20 mM Tris-HCl pH 8.0, 150 mM NaCl. Reference channel was filled with solvent without LMNG. B: Superposition of the normalized $c(s_{20w})$ distributions obtained at 280 nm (red line) and with interference optics (black line). SEC-LS: C: Rayleigh ratio measured along the elution profiles, for 35 µL of FhuA at 1 mg mL^{-1} and LMNG at 1.2 mM injected on a Superdex 200 10/300 GL (GE Healthcare) column equilibrated at 6 °C with 100 mM Tris-HCl pH 8.0, 150 mM NaCl, 1 mM EDTA, 0.5 mM LMNG, and molar masses (thick lines, right axis) for the whole complex (black), and LMNG (green) and FhuA (red) contributions, derived from combining light scattering, refractive index, and absorbance at 280 nm detections. D. Typical DDAO-solubilized FhuA crystals grown in 0.1 M MES pH 6.0, 10% PEG 6000, 2% DDAO. E. Typical LMNG-solubilized FhuA crystals grown in 0.1 M ADA pH 6.5, 12% PEG 6000, 1.2% LMNG. (For interpretation of the references to color in this figure legend, the reader is referred to the web version of this article.)

Table 3
LMNG solubilized FhuA in AUC-SV.

exp	FhuA (mg mL^{-1})	total LMNG (mM)	free LMNG[a] (mM)	Main s_{20w} (S) from A_{280}[b]	Main s_{20w} (S) from ΔJ[b]	s_{20w} (S) for LMNG[c]
1	7.5	12	4.5	7.8	7.8	6.8
2	5.4	13	7.6	6.8	6.8	7.6
3	2.7	18	15.3	6.4	7.1	7.6
4	2.7	24	21.3	7.0	7.5	7.7

LMNG free micelles and FhuA complexes sediment separately (Fig. 4) in exp. 1, but are not resolved in exp. 2–4. [a]Calculated with the hypothesis of 1 g g^{-1} LMNG bound to FhuA, except for exp. 1, where free LMNG micelle concentration was measured in AUC-SV. [b]For FhuA complex in exp. 1, and unresolved LMNG free micelles and FhuA complex in exp. 2–4. [c]From AUC-SV experiments of pure LMNG (Fig. 1) for the LMNG concentrations reported on the fourth column.

Table 4
Characteristics of LMNG solubilized FhuA crystals.

Crystal data collection statistics for FhuA – LMNG	
Space group	C 2 2 21
Unit cell dimension (Å)	149.53 210.96 188.7 90 90 90
Number of reflections	371,461 (37,282)
Number of unique reflections	25,522 (2481)
Resolution limits (Å)	40.61–4.0
Higher resolution shell (Å)	4.143–4.0
Completeness	98.13% (98.06%)
Redundancy	14.6 (14.8)
Rmerged	0.1771 (7.384)
Rmeasured	0.1838 (7.648)
I/σ(I)	9.51 (0.50)
Molecular replacement with Phaser	
LLG = 3,698.6 TFZ = 16.4	
Crystallographic refinement statistics	
Resolution range (Å)	40.61–4.0
Number of reflections	25,098
R/FreeR	0.3141/0.3546
Number of atoms (total)	11,024
Mean B value (Å^2)	209.52
rms deviation from ideal values:	
bond length (Å)	0.007
bond angle (degree)	1.52

(sample *c3*). To further investigate the effects of protein and LMNG concentrations on the size and composition of the LMNG/SpNOX complexes, part of *c3* was rediluted 12 or 30 times in buffer A (containing 0.03 mM LMNG) and 12 times with the same buffer but containing LMNG at 1.5 mM (samples *c0.25d*, *c0.1d*, *c0.25dLMNG*, respectively). AUC-SV of these samples was followed at 412 nm, in addition to the usual 280 nm and interference detection, which allows following the heme b cofactors. The normalized *c*(*s*) curves (Fig. 5B) at 280 and 412 nm superimpose showing that the different SpNOX complexes in all samples have the same heme content. The measured ratio A_{412}/A_{280} = 1.75 ± 0.05 is that expected for pure SpNOX [62]. The main SpNOX species (typically 85%) sediments at s_{20w} = 6.0 ± 0.1 S. A minor contribution (typically 8%) is detected at ≈8.2 S, in addition to poorly-defined aggregates (typically 7%). *c0.25dLMNG* appears to be more homogeneous, and *c0.25d* more heterogeneous, but we cannot ascertain the relevance of these subtle variations. We conclude that SpNOX main assemblies have clearly the same composition in all samples, and increasing LMNG or protein concentration does not lead to larger complexes. Interference optics allows the additional detection of LMNG micelles below 4 S, in the expected *s*-range, since we measured *s* at 2.5 and 5 S for pure LMNG at 0.05 and 1.5 mM in buffer A. From the integration of the signal, we derived a concentration of 1.2 mM free micelles in *c3*, which indicated an almost stoechiometrical co-concentration of LMNG and SpNOX. For the main SpNOX complex, the ratio of the interference fringes and A_{280} signals is the same for *c0.1*, *c3*, *c0.25d*, suggesting that no or few LMNG micelles co-sediment (the ratio is however larger for *c0.25dLMNG* and *c0.1d*, but it may be related to the uncertainty of the analysis). It provides a rough estimate of 1 ± 0.1 g g^{-1} LMNG bound to SpNOX (this value is imprecise, as discussed below).

Complementary SEC-LS-DLS in buffer A with 0.05 mM LMNG was performed on four samples of SpNOX from a different purification. One at 0.16 mg mL^{-1} is from SEC as the last step of purification, the three others are from subsequent concentration to 1.0, 2.9 and 8.7 mg mL^{-1} (concentration by a factor of 8, 18 and 54, respectively) by ultrafiltration. The elution profiles of the four SpNOX samples are very similar, and one example is shown on Fig. 5C. The main SpNOX complex elutes at 12.8 mL with a R_H = 4.0 nm measured from DLS. The analysis provides molar masses for the main complex of 68 ± 3 kDa and 59 ± 3 kDa for SpNOX and LMNG- components, remarkably constant for the four samples. These values correspond to a detergent/protein ratio similar to that estimated from AUC. The protein molar mass, however is intermediate between the theoretical ones for a monomer (48 kDa) and a dimer. This suggests a systematical error in the input value, used in AUC and SEC-LS, of the SpNOX extinction coefficient. We thus rather consider the total molar mass of the complex of 126 kDa, derived from LS and RI detection to derive, in the hypothesis of a monomeric protein, an amount of bound detergent of 1.6 g g^{-1}. Combining *s* from AUC and R_H from DLS, a buoyant molar mass of 26.2 kDa is derived, which corresponds to a globular compact monomer of SpNOX binding 1.6 g g^{-1} of LMNG, with a frictional ratio of 1.2, thus a globular compact shape.

3.6. BmrA-LMNG assemblies

BmrA (for 'Bacillus multidrug resistance ATP') is a member of the ABC ("ATP-Binding Cassette") transporters family. It is capable to export multiple drugs with no chemical relationship [86]. In human, its closest homologue MDR1 confers resistance to chemotherapeutic treatments [63]. Crystal structures of homologs stabilized in different states [87,88] suggest that, to permit drug translocation, large conformational changes must occur in an alternating access model. BmrA could be purified in a functional homodimeric form in 0.05% DDM [89,90], and, indeed it was shown to be flexible and adopt different conformations [91–94].

Since then, the protein was purified in LMNG [95]. It was noticed that LMNG, in contrast to DDM, significantly reduced BmrA aggregation with time. Moreover, the ATPase activity of BmrA was significantly increased, by a factor of about 1.5 to 2, in LMNG compared to DDM

Table 5
Compared activities, in LMNG and DDM, of SpNOX and BmrA.

Protein	Environment	Activity	
SpNOX	DDM 1.27 mM	5.9 ± 0.5	mol Cyt *c* reduced s^{-1} mol^{-1} SpNOX
SpNOX	LMNG 0.21 mM	9.3 ± 0.2	mol Cyt *c* reduced s^{-1} mol^{-1} SpNOX
BmrA	DDM 2 mM	0.8 ± 0.1	µmol ATP hydrolyzed min^{-1} mg^{-1} BmrA
BmrA	LMNG 0.1 mM	1.4 ± 0.2	µmol ATP hydrolyzed min^{-1} mg^{-1} BmrA
BmrA	Liposome	5.0 ± 0.6	µmol ATP hydrolyzed min^{-1} mg^{-1} BmrA

(Table 5). The activity in LMNG is thus getting closer to that of the protein reconstituted into liposomes: 1.4 *vs.* 5, respectively, µmol ATP hydrolyzed/min/mg protein (Table 5).

We evaluated by DSF the protein's thermal stability for two freshly purified - in either DDM or LMNG - batches of BmrA. Measurements were done on the Apo and the vanadate (Vi) inhibited forms. The Apo-form is expected to be in an open conformation, the Vi-inhibited form would exist in a closed conformation ([64,93] and unpublished results). Fig. 3 shows the measurements for BmrA Apo and Vi-inhibited forms, and Table 2 reports the melting temperatures T_m. In DDM and in LMNG, the T_m increases steadily from the less stable Apo to the more stable Vi-inhibited form. For the two forms, BmrA unfolds at higher temperature when purified in LMNG compared to DDM: by 4.5 °C for BmrA Apo, and ≈13 °C for the Vi-inhibited BmrA (Table 2).

Limited proteolysis experiments were performed on the Apo- and Vi-inhibited BmrA forms, to evaluate differences in protein flexibility between the two forms, in DDM and in LMNG. After incubation for different times with a protease, BrmA samples were run on SDS-PAGE. Fig. 6A–D show clearly, for BmrA purified in DDM and LMNG, respectively, and incubated with trypsin, the increased robustness of Vi-inhibited BmrA compared to the Apo form. In DDM, the 55 kDa band representing the intact protein essentially disappeared after 30 min of incubation for the Apo form, and > 300 min for the Vi-inhibited form, in agreement with previously published results [93]. In LMNG, 60 min are required for an almost full disappearance of the intact Apo BmrA, and the Vi-inhibited form is essentially preserved for the entire time period tested. The reduced kinetics of proteolysis in LMNG compared to DDM is also observed with protease V8 (Fig. 6E–F). We checked that the detergent type had no effect on protease activity by itself.

In order to evaluate protein homogeneity in LMNG, samples of BmrA were purified with a last step of SEC in a buffer containing LMNG at 0.1 mM, concentrated by ultrafiltration by a factor of 4.4 for a final BmrA concentration of 1.3 mg mL^{-1}. SV-AUC revealed a very homogeneous preparation, with one protein complex at s_{20w} = 8.2 S (experimental value of 4.2S, at 10 °C, in the buffer containing glycerol) (Fig. 7A). SEC-LS experiments, done with a BmrA sample at 2.7 mg mL^{-1}, prepared in a similar way, stored frozen at −80 °C and injected on a column equilibrated with buffer A, showed minor (total ≈5%) contributions of large and small aggregates eluting at 7.8 mL and as a shoulder at 9.7 mL. In addition, the main complex eluted at 10.7 mL, with a R_H = 5.5 nm measured from DLS, and a total molar mass of 240 kDa, corresponding to a dimer with 0.8 g g^{-1} bound detergent (Fig. 7B). Combining R_H and the *s*-values, we derived a buoyant molar mass of 45.9 kDa, corresponding to a dimer with 0.6 g g^{-1} bound LMNG, and a frictional ratio of 1.35. Excess LMNG micelles were undetected in the AUC experiments; in SEC-LS their amount corresponds to an injected LMNG concentration of 0.2 mM. In conclusion, very homogeneous BmrA samples can be prepared in LMNG with protein concentration in the mg mL^{-1} range, which remains essentially homogeneous after storage at −80 °C.

3.7. bR homogeneity, and time and thermal stability

Lastly, we investigated the homogeneity and stability over time of bR. bR is a light-driven proton pump purified from the archaea *Halobacterium*. It is composed of seven transmembrane α-helices and binds a covalent cofactor, a retinal molecule that confers purple color to the protein.

Sucrose gradients are a convenient means to perform both detergent exchange and evaluate the colloidal homogeneity of the protein-detergent complex. In the case of colored proteins, this latter information is directly visible after centrifugation, by the broadness of the protein-detergent band. We routinely use this method to evaluate the potentialities of fluorinated surfactants in the biochemistry of membrane proteins, using the bR. Fig. 8A shows the results of sucrose density gradient experiments in the presence of 1 mM DDM, or 0.2, 2 and 20 mM LMNG. After 15 h centrifugation, the protein migrated past the middle of the gradient, insuring total detergent exchange, as checked by TLC. In all LMNG conditions, the protein band migrates at the same depth and appears to have the same width/broadness as that in DDM, suggesting that the bR-LMNG complexes are homogeneous monomers as the bR-DDM complexes. The retinal molecule, whose visible absorption spectrum is very sensitive to its local environment, is a convenient reporter of the state of the protein: the trimeric protein in its native membrane reveals a visible absorption spectrum with a maximum at λ_{max} = 570 nm; when solubilized in detergent, the protein monomerizes and displays λ_{max} = 554 nm; in both cases, the protein appears purple. When the protein denatures, the retinal is released, and λ_{max} shifts to 400–380 nm: the protein solution turns yellow. Fig. 8B and C report the absorption spectra of the protein recovered just after centrifugation and three months after, stored on ice in the dark. The DDM sample, which appears pinkish in the gradient, displays a broad absorption peak, with a λ_{max} ~ 530 nm (Fig. 8B), suggesting a poorly folded protein. After three months however, the spectrum shows a usual peak, with λ_{max} = 555 nm. The protein probably started to denature in OTG, the detergent used for its solubilization, but returned to its native fold when transferred to DDM. In all LMNG samples, the absorption peak displays a λ_{max} = 564 nm (Fig. 8C), suggesting that the dynamics of the bR monomer in LMNG is different than in classical detergents. After three months incubation, the absorption spectra are unchanged, indicating that the protein is very stable.

Lastly, bR thermal denaturation assays were performed. Solubilized bR samples were incubated with biobeads to decrease the OTG concentration, and diluted 18 times (leading to a residual OTG concentration of 0.4 times the CMC) in OTG, DDM, or LMNG, at a concentration of 2 mM above the CMC of each detergent, for thermal denaturation assays. Result are presented on Fig. 3 and Table 2. bR has an increased thermostability in DDM compared to OTG, and LMNG is even more stabilizing, with T_m increased by 6 and 12 °C, respectively.

4. Discussion and conclusion

4.1. On the self-assembly of LMNG

From AUC experiments, we determined the CMC of LMNG to be 40 µM. This is coherent with previously published value from hydrophobic dye solubilization measurements (10 µM) [26], while isothermal titration calorimetry measurements yielded a significantly lower concentration (11.3 nM) [44]. The CMC is not an absolute value, rather a range of concentrations, and different techniques used to determine the

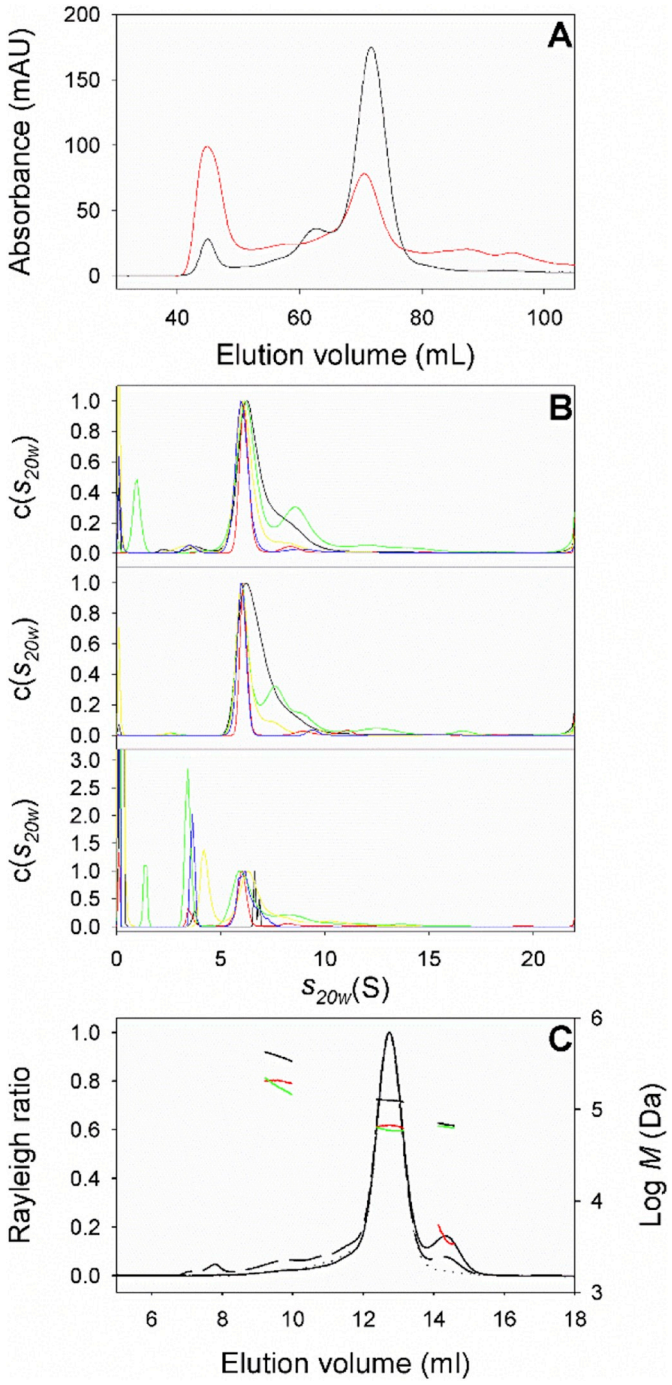

Fig. 5. LMNG solubilized SpNOX: preparative SEC, AUC-SV and SEC-LS. A: Superdex 200 16/60 elution profiles, in the second step of SpNOX purification, in 50 mM Tris-HCl pH7, 300 mM NaCl, with either 0.3 mM DDM (red line) or 0.03 mM LMNG (black line). Aggregates elute at 45 mL, monomeric SpNOX elutes at 70 mL. B: Normalized $c(s_{20w})$ distributions from AUC-SV at 280 nm (top), 412 nm (middle) and by interference optics (bottom), for SpNOX samples *c0.1*, *c3*, *c0.25d*, *c0.1d*, *c0.25dLMNG* (black, red, green, yellow, and blue lines, respectively). The vertical dashed line at 6S indicates the main SpNOX complex C: SEC-LS normalized elution profiles obtained at 280 nm (dotted line), by refractive index (continuous line), and light scattering (dashed line), for 30 µL of SpNOX at 2.9 mgmL^{-1} injected on a Superdex 200 10/300 GL at 4°C in 50 mM Tris-HCl pH7.0, 300 mM NaCl, 0.05 mM LMNG, and molar masses (thick lines, right axis) for the whole complex (black), and LMNG (green) and SpNOX (red) contributions, derived from combining static light scattering, refractive index, and absorbance at 280 nm. A hydrodynamic radius of 4.0 nm was measured by DLS at the maximum of the main peak. (For interpretation of the references to color in this figure legend, the reader is referred to the web version of this article.)

CMC probe different properties of micelle formation. Thus, it is not unusual to find different values depending on the technique used, and discrepancies become exacerbated when the CMC is very low.

Regarding the size of the micelles, the s_{20w}-value of LMNG at 0.25 mM (0.025%) is 3.3 S. This value is in the same range than that of DDM (3.12 S) that forms globular compact micelles of about 60 kDa in a large range of detergent concentration [65]. If LMNG forms quite small micelles at 0.25 mM, AUC, DLS, SAXS, and SANS, clearly indicate it forms larger micelles, rods of increasing length, when increasing the concentration above 0.25 mM. The lateral dimension of the hydrophobic core radius is 14 Å, and that of the shell thickness is 7 Å in H_2O (9 Å in D_2O). These values correspond to that of DDM micelles, described from SAXS to form oblate ellipsoids with, in the minor axis, a hydrophobic core of ≈15 Å surrounded by a hydrophilic layer of ≈6 Å thickness [96,97] (Scheme 2). The differences of 1 Å between our LMNG and the published DDM dimensions are not significant since different techniques and buffers, thus contrasts (in terms of electron density or neutron scattering length densities), were used. To this date, this is only one membrane protein pdb file (4b4a) containing LMNG as a ligand (pdf identifier "LMN"). The maximum C—O, C—C and O—O distances in the whole molecule, in the two tails, and in the two heads, respectively, are 21.9, 13 and 11, 9.8 and 9.7 Å, respectively (we note that in this unique structure, the hydrophilic head is quite open: we measure a maximal distance between the O of the two sugars of LMNG of 19 Å). For DDM as a ligand (pdf identifier "LMT"), in an arbitrary selection of membrane protein pdb files (6haw, 6hqb, 4kfm, 6cnn), we measure maximal distances for the whole molecule, the tail, and the head, of 20.5 ± 1, 12 ± 1, and 9.2 ± 0.8 Å, respectively. These values are logically similar to that of LMNG. The maximum length of the tail is logically lower than 16.7 Å corresponding to the dimension of an extended alkyl chain with 12 carbons [97].

If DDM is described to form slightly elongated micelles, for LMNG at 20 mM however, we measured lengths of 600 Å in H_2O and > 5000 Å in D_2O. It corresponds to LMNG rods with ratios of the total length over the total diameter, of 14 and 120. For LMNG in H_2O, the rod length value coincides with the maximum distances estimated between 10 and 20 mM LMNG, from the pair distribution analysis of the – measured independently – SAXS data of Fig. 2A. In a preliminary independent SANS experiment, however, rods of only 1200 Å long were modelled for LMNG micelles at 20 mM in D_2O. It corresponds to a length over diameter ratio of 28, 4–5 times smaller than that presented above. It is likely that the precise length of LMNG rods depends on uncontrolled parameters during sample preparation. It is possible that LMNG forms longer rods in D_2O, compared to H_2O, but we cannot ascertain it. For both SAXS and SANS, the shape and size of the micelles does not change between 10 and 20 mM.

Israelachvili et al. [98,99] have provided a rational to explain how the molecular geometry of individual surfactant molecules affects and controls the shape and size of the assemblies they form. The geometry of the molecule can be described by three parameters: the area of the hydrated polar head, a_0, the volume, v, and the extension, l_c, of the hydrophobic tail. The value of the related critical packing parameter, $v/(a_0\ l_c)$, representing the ratio of the mean area of the hydrophobic tail on that of the hydrophilic head, determines the geometry of the assemblies: for $v/(a_0\ l_c) < 1/3$ (large hydrophilic surface), spherical micelles are formed; for $1/3 < v/(a_0\ l_c) < 1/2$, rods are favored; then, for $v/(a_0\ l_c) < 1$, ~1, and > 1 (with increasingly large hydrophobic lateral extensions), flexible or planar bilayers, and inverted micelles, respectively, are stabilized. The LMNG molecule corresponds to two linked DDM molecules. The linkage is done through a quaternary carbon, localized on the lauryl chain, at the second carbon following the ether group belonging to the maltose moiety. It is thus at the junction between the hydrophilic head and the hydrophobic tail of the detergent. The constraints of this link on each moiety dimensions are hardly intuitively predictable. The fact that DDM forms globular micelle while LMNG forms rod means that the packing parameter $v/(a_0\ l_c)$

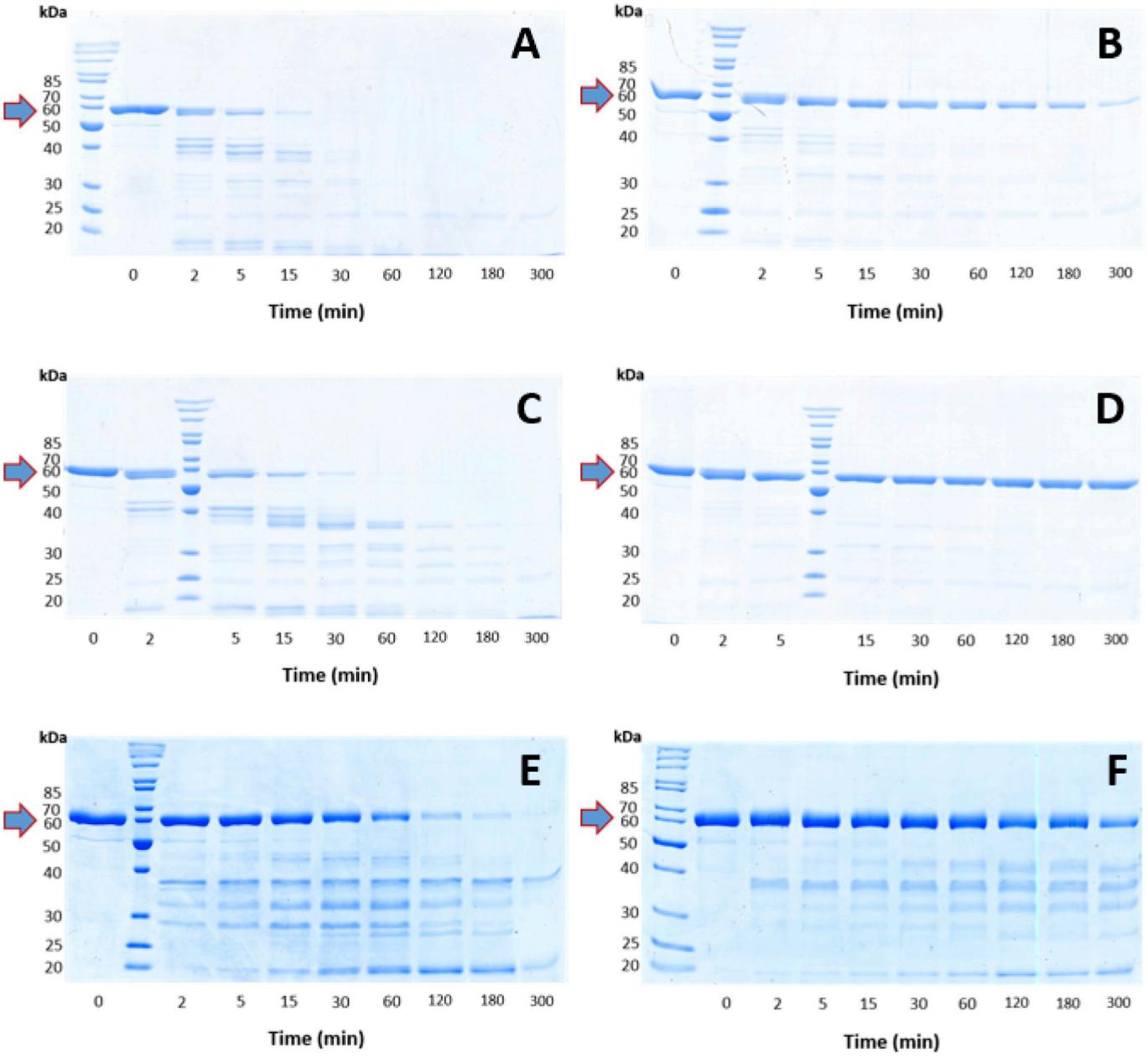

Fig. 6. BmrA limited proteolysis experiments.
A–D: incubation with trypsin at 1 µg/250 µg of protein, for A: Apo BmrA in DDM, B: Vi-inhibited BmrA in DDM, C: Apo BmrA in LMNG, D: Vi-inhibited BmrA in LMNG. E–F: incubation with protease V8 at 1 µg/20 µg of protein, for Apo BmrA, in E: DDM, and F: LMNG. DDM and LMNG concentrations are 2 and 0.1 mM, respectively. Time zero is taken after 15 min of pre-incubation before adding the proteases. The arrows indicate intact BmrA.

increases from DDM to LMNG, which can be related to an decrease, in LMNG compared to DDM of the hydrophilic surface per maltose group, and/or of the mean length of the hydrophobic chain, corresponding to changes in their landscape of the molecular conformational stability and/or dynamics.

Rod formation has noticeable consequences for biochemists. When using ultrafiltration centrifugal devices to concentrate proteins, LMNG co-concentrates with the membrane protein by the same factor. Depending on the initial detergent concentration, typically from 0.02 to 0.1 mM, LMNG in the concentrated sample will form small to very large assemblies. Concentrated LMNG dissociates upon SEC, but elutes as a very broad peak, preventing membrane protein in concentrated LMNG to be recovered with a well-defined LMNG concentration.

4.2. On the relative stabilization of proteins in LMNG compared to DDM

Our work corroborates the stabilizing propensity of LMNG towards membrane proteins, already described in the literature (see the introduction). All four proteins investigated here are thermally stabilized in LMNG compared to DDM. The temperature shift is very large, both for FhuA (+11 °C), a very stable β-barrel protein, and for SpNOX (+13 °C), a fragile α-helical protein. For the flexible BmrA, temperature shifts between 4 and 13 °C are observed depending on the presence or absence of ligands. For bR, the gain is 6 °C. SpNOX solubilized and partially purified in LMNG shows a significantly decreased content of aggregates, corresponding to an increased stability. The reduced kinetics of limited proteolysis in LMNG compared to DDM for the Apo and the Vi-inhibited forms of BmrA, expected to represent the open and

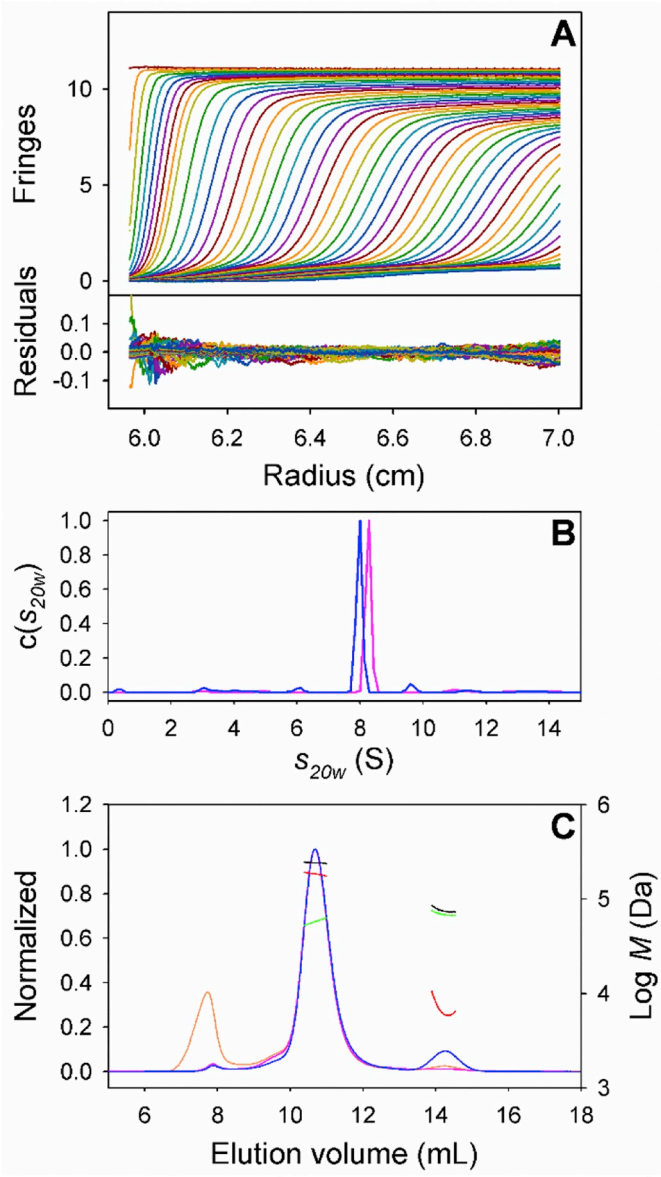

Fig. 7. LMNG solubilized BmrA in AUC-SV and SEC-MALS.
AUC-SV: A: Superposition of experimental and fitted sedimentation velocity profiles (top) and residuals (bottom), obtained at 130,000*g* and 10 °C during ≈8 h using interference optics and 12 mm optical path centerpiece, for BmrA at 2.3 mg mL^{-1} and free LMNG at 0.44 mM (putative concentration) in 25 mM Tris-HCl pH 8.0, 150 mM NaCl, 10% glycerol. Reference channel was filled with solvent without LMNG. B: Superposition of the normalized $c(s_{20w})$ distributions obtained at 280 nm (pink line) and with interference optics (blue line). SEC-LS: C: Rayleigh ratio, refractive index, and absorbance at 280 nm (orange, blue, and pink lines, respectively) measured along the elution profiles, for 50 µL of BmrA at 2.7 mg mL^{-1} and free LMNG at 0.06 mM, this concentration being experimentally determined in SEC-LS, injected on a Superdex 200 10/300 GL (GE Healthcare) column equilibrated at 4 °C with 50 mM Tris-HCl pH 7.0, 300 mM NaCl, 0.05 mM LMNG (buffer A), and molar masses (thick lines, right axis) for the whole complex (black), and LMNG (green) and BmrA (red) contributions, derived from combining the three detections. The protein elutes as a main species at 10.7 mL, together with large and small aggregates, in minor amounts, in the void volume (7.8 mL) and as a shoulder at 9.7 mL, respectively; free LMNG elutes at 14.2 mL. (For interpretation of the references to color in this figure legend, the reader is referred to the web version of this article.)

closed conformations, could have suggested some restricted flexibility of the protein. However, the protein is more active in LMNG as compared to DDM thereby indicating that the flexibility required for ATPase activity is not impaired in LMNG. Indeed, in LMNG, BmrA seems to be more prone to reach or stabilize the closed conformation which is required to get a high ATPase activity. Hence, BmrA is in a more stable and perhaps, more physiologically relevant conformations in LMNG as compared to DDM. Restricted protein flexibility is also suggested for bR, which UV–visible spectrum displays a maximum absorption peak close to that of the constrained trimer in the purple membrane, far from that of the more flexible monomer in DDM. These results are in the line with the restraint of protein inter-conversion dynamics measured for GPCRs. The reduced dynamics of proteins may be related to the strong binding of the LMNG correlated to its low CMC, deriving from the connection of the two hydrophobic tails in its structure. As for BmrA, SpNOX displays an increased specific activity in LMNG compared to DDM, which may reflect a significantly higher proportion of inactive protein in DDM compared to LMNG, or be related to a difference in SpNOX flexibility, or to the stabilization of some conformations.

4.3. On the assembly of LMNG-membrane proteins

The solubilized membrane proteins investigated in this work have the same quaternary structure in LMNG as in their usual detergent: FhuA, SpNOX, and bR, are monomeric and BmrA is dimeric. In the case of SpNOX, dimers of the main species – probably inactivated forms – are detected in LMNG, for typically 10%, the proportion varying slightly depending on the purification. These species are also detected in DDM. In the AUC experiments where LMNG concentration was voluntarily raised to 24 mM, FhuA and SpNOX association states were not affected. The amount of bound detergent did not vary either, despite rod micelles of LMNG are expected at these large concentrations. This behavior was not anticipated. We previously investigated fluorinated surfactants (for reviews, see [8,16,17]), and, in a series of surfactants whose polar head size was modulated by the presence of one, two, or three glucose moieties, homogeneous complexes with bR and cytochrome b_6f were obtained only with the compounds that form homogeneous micelles, *i.e.* the surfactants with the more voluminous head. In the surfactant forming long rods, with only one glucose, the membrane proteins were soluble and active, but formed heterogeneous detergent protein complexes. We anticipated it could be related to the heterogeneity in the amount of bound detergent [100]. Other fluorinated surfactants with relatively small head groups (lactoside, maltoside, octaethylene glycol ether) formed large and polydisperse, probably rod-like assemblies, and indeed formed also large and heterogeneous complexes with membrane proteins (refs in [100]). By contrast, the fluorinated surfactant F-TAC (now commercialized by Calixar), which has a voluminous polymeric hydrophilic head, was shown to assemble into small micelles and form well defined complexes with membrane proteins. The present work on LMNG shows that large size of surfactant micelle does not necessarily translate into protein detergent complex heterogeneity.

4.4. On the assembly of LMNG-membrane proteins: bound detergent

In the case of FhuA, previous measurements determined 1.2 g of bound DDM per g of protein, using SEC in the presence of radiolabeled DDM [82]. This value is close to 1 and 1.2 g g^{-1} determined in the present work for the protein solubilized in LMNG by AUC and SEC-LS. For BmrA, the amount of bound LMNG (0.6 g g^{-1}) we determined by combining *s*- and R_H-values, is lower but in the same order of magnitude than that determined for bound DDM by the same technique (0.9 g g^{-1}) [101]. A similar trend, in the comparison of DDM and LMNG bound to BmrA, was reported using MALDI/TOF for the evaluation of bound detergent [7]. These estimates of bound DDM to BmrA are much lower than that determined by SEC in the presence of radiolabeled DDM (1.5 g g^{-1}) [89], which emphasizes the difficulty to determine precisely bound detergent. Nevertheless, these comparisons presented in Table 6, show that the amounts of bound detergent are

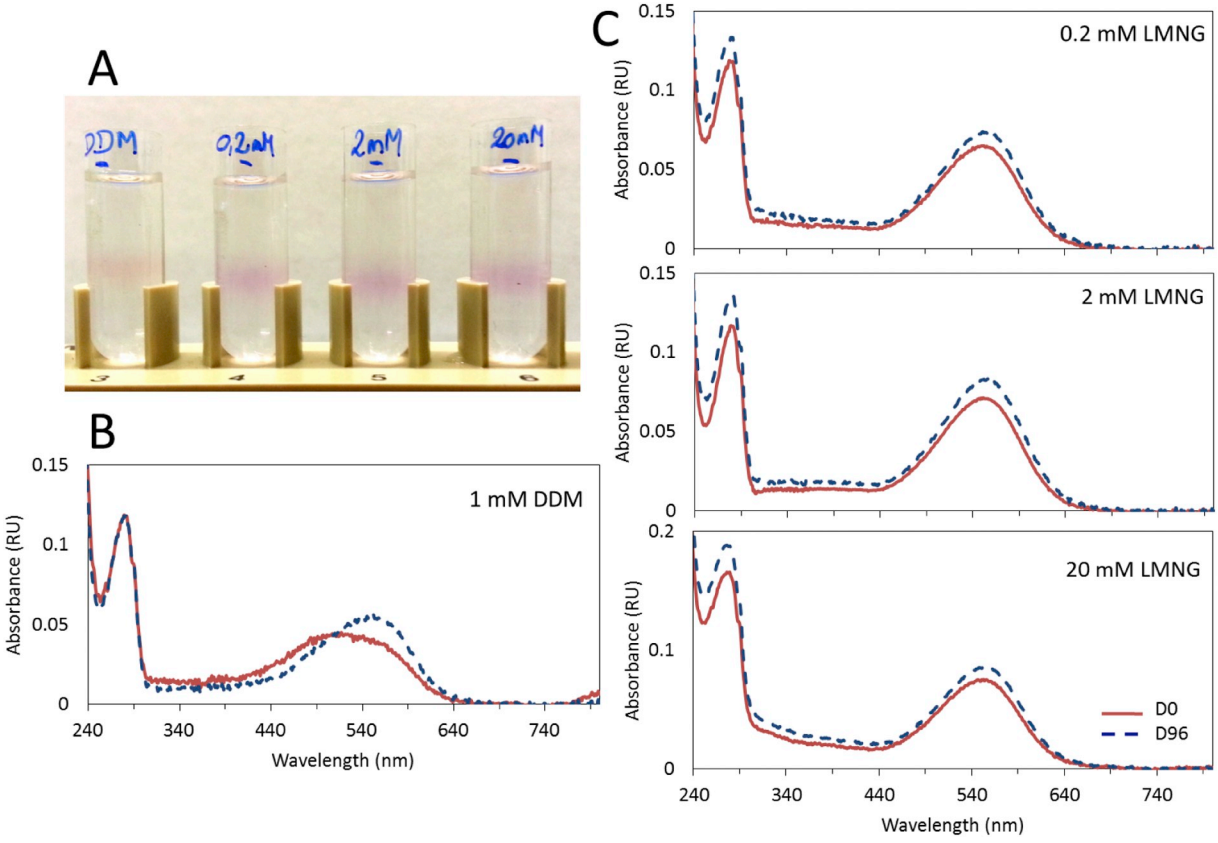

Fig. 8. bR sucrose gradient.
A: Migration of bR in 10–30% sucrose gradients in the presence of either 1 mM DDM, 0.2, 2 or 20 mM LMNG. Gradients were centrifuged 15 h at 200,000 ×*g*. bR was recovered from the gradients and its UV–visible spectrum measured immediately (D0, solid line) or three months after incubation at 4 °C in the dark (D96, dashed line). B: bR in 1 mM DDM, C: bR in 0.2, 2 and 20 mM LMNG.

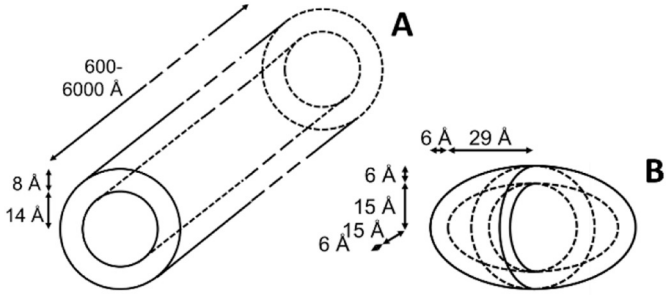

Scheme 2. Schematic representation of LMNG and DDM micelles.
A: LMNG micelles at 20 mM in H_2O or D_2O, from modelling of combined SANS and SAXS data (this work) B: DDM micelles from modelling of SAXS data [96,97].

Table 6
Bound LMNG and DDM to FhuA, BmrA, and SpNOX.

Protein	Detergent	Bound detergent		Technique	Reference
		g g^{-1}	mol/mol[a]		
FhuA	DDM	1.2	188	SEC/[^{14}C]DDM	[82]
FhuA	LMNG	1.0	80	AUC	Present work
FhuA	LMNG	1.2	95	SEC-LS	Present work
BmrA	DDM	0.9	234	AUC+ SEC-LS	[101]
BmrA	DDM	1.3–1.6	388–416	MALDI/TOF	[7]
BmrA	DDM	1.5	390	SEC/[^{14}C]DDM	[89]
BmrA	LMNG	0.6	79	AUC+ SEC-LS	Present work
BmrA	LMNG	1.1–1.3	145–171	MALDI/TOF	[7]
SpNOX	LMNG	1.6	77	AUC+ SEC-LS	Present work

[a] Considering FhuA and SpNOX as monomers, and BmrA as a dimer.

similar whether the protein is solubilized in DDM or LMNG. It means that the amount in mol/mol is nearly twice for DDM than for LMNG, and it is possible that the amount (in g g^{-1}) of bound LMNG is slightly less compared to that of DDM.

4.5. On the crystallization of LMNG-membrane protein

The high resolution structures of several GPCRs were obtained thanks to purification in LMNG (*cf* Introduction) followed by crystallization in mesophase, a process in which the membrane protein in the crystal is stripped off from its bound detergent [102]. Crystallization in LMNG using vapor diffusion was described for *e.g.* the cytochrome b_6f complex [26], the TatC core of the twin-arginine protein transporter [50], an ABC transporter lipid-linked oligosaccharide flippase [41], a borate efflux transporter [51], and a plant voltage-gated two-pore channel [52]. FhuA is yet another one. One of our motivations, in crystallizing this well described protein, was to check whether the ability to obtain crystals was prevented by the presence of large LMNG assemblies in the membrane protein sample. It is clearly not the case, and on the contrary, comparing the behavior of the protein in crystallization screens, we observed that the number of initial hits was larger when the protein was solubilized in LMNG when compared to the classically used DDAO. The space group of crystals of FhuA grown in LMNG is not the same as that of the protein grown in DDAO. However, this is not remarkable, as the same space group is found when the protein is crystallized in LDAO.

4.6. To summarize

The interest of structural biologists for LMNG is very strong, since it stabilizes noticeably most membrane proteins compared to other detergents. Due to its low desorption kinetics, it would stabilize membrane proteins even in sub-CMC concentrations. It forms large rod assemblies at concentrations above the sub mM range, but, for the examples we investigated, the solubilized proteins remain as homogeneous as in usual detergents, with similar amounts of bound detergent, and the presence of the large LMNG micelles does not prohibit membrane protein crystallization using vapor diffusion or mesophase.

Transparency document

The Transparency document associated with this article can be found, in online version.

Acknowledgment

This work used the platforms of the Grenoble Instruct centre (ISBG; UMS 3518 CNRS-CEA-UJF-EMBL) with support from FRISBI (ANR-10-INSB-05-02) and GRAL (ANR-10-LABX-49-01) within the Grenoble Partnership for Structural Biology (PSB). Gina Reyes-Mejia, Marie-Ange Marrel, Séraphine Crassac, and Emma Lundell (UGA) performed BmrA and FhuA preparations, FhuA and bR thermal denaturation assays, respectively, during their master internships at IBS. We thank Marie-Pierre Candusso for advices with BmrA limited proteolysis; Adam Round and Martha Brennich (ESRF), and Frank Gabel (IBS), for help in SAXS data acquisistion. This work benefited from the use of the SasView application, originally developed under NSF Award DMR-0520547. SasView also contains code developed with funding from the EU Horizon 2020 programme under the SINE2020 project Grant No 654000. This work was supported by the French Agence Nationale de la Recherche (ANR-16-CE92-0001) to CE and CB, (ANR-14-CE09-0024B) to JMJ and (ANR-17-CE11-0013) to JD, CH, FF, AV, IPH, MT. A. Vermot thanks her support through the Emergence program from the Univ. Grenoble Alpes.

References

[1] M. le Maire, P. Champeil, J.V. Moller, Interaction of membrane proteins and lipids with solubilizing detergents, Biochim. Biophys. Acta 1508 (2000) 86–111.
[2] J.-L. Popot, Extracting membrane proteins from their native environment, Membr. Proteins Aqueous Solut. Deterg. Amphipols, Springer International Publishing, 2018, pp. 59–95.
[3] C. Breyton, C. Tribet, J. Olive, J.-P. Dubacq, J.-L. Popot, Dimer to monomer conversion of the cytochrome b6f complex. Causes and consequences, J. Biol. Chem. 272 (1997) 21892–21900.
[4] S. Lee, A. Mao, S. Bhattacharya, N. Robertson, R. Grisshammer, C.G. Tate, N. Vaidehi, How do short chain nonionic detergents destabilize G-protein-coupled receptors? J. Am. Chem. Soc. 138 (2016) 15425–15433, https://doi.org/10.1021/jacs.6b08742.
[5] C. Chipot, F. Dehez, J.R. Schnell, N. Zitzmann, E. Pebay-Peyroula, L.J. Catoire, B. Miroux, E.R.S. Kunji, G. Veglia, T.A. Cross, P. Schanda, Perturbations of native membrane protein structure in alkyl phosphocholine detergents: a critical assessment of NMR and biophysical studies, Chem. Rev. 118 (2018) 3559–3607, https://doi.org/10.1021/acs.chemrev.7b00570.
[6] Q. Zhang, H. Tao, W.-X. Hong, New amphiphiles for membrane protein structural biology, Methods 55 (2011) 318–323, https://doi.org/10.1016/j.ymeth.2011.09.015.
[7] V. Chaptal, F. Delolme, A. Kilburg, S. Magnard, C. Montigny, M. Picard, C. Prier, L. Monticelli, O. Bornert, M. Agez, S. Ravaud, C. Orelle, R. Wagner, A. Jawhari, I. Broutin, E. Pebay-Peyroula, J.-M. Jault, H.R. Kaback, M. le Maire, P. Falson, Quantification of detergents complexed with membrane proteins, Sci. Rep. 7 (2017) 41751, , https://doi.org/10.1038/srep41751.
[8] G. Durand, M. Abla, C. Ebel, C. Breyton, New amphiphiles to handle membrane proteins: “ménage à trois” between chemistry, physical-chemistry and biochemistry, in: I. Muss-Veteau (Ed.), Membr. Proteins Prod. Struct. Anal. Springer, 2014.
[9] J.-L. Popot, Alternatives to detergents for handling membrane proteins in aqueous solutions, Membr. Proteins Aqueous Solut. Deterg. Amphipols, Springer International Publishing, 2018, pp. 97–149.
[10] C.E. Schafmeister, L.J.W. Miercke, R.A. Stroud, Structure at 2.5 Å of a designed peptide that maintains solubility of membrane proteins, Science 262 (1993) 734–738.
[11] X. Zhao, Y. Nagai, P.J. Reeves, P. Kiley, H.G. Khorana, S. Zhang, Designer short peptide surfactants stabilize G protein-coupled receptor bovine rhodopsin, Proc. Natl. Acad. Sci. U. S. A. 103 (2006) 17707–17712, https://doi.org/10.1073/pnas.0607167103.
[12] K. Corin, P. Baaske, D.B. Ravel, J. Song, E. Brown, X. Wang, C.J. Wienken, M. Jerabek-Willemsen, S. Duhr, Y. Luo, D. Braun, S. Zhang, Designer lipid-like peptides: a class of detergents for studying functional olfactory receptors using commercial cell-free systems, PLoS One 6 (2011) e25067, , https://doi.org/10.1371/journal.pone.0025067.
[13] H. Tao, S.C. Lee, A. Moeller, R.S. Roy, F.Y. Siu, J. Zimmermann, R.C. Stevens, C.S. Potter, B. Carragher, Q. Zhang, Engineered nanostructured β-sheet peptides protect membrane proteins, Nat. Methods 10 (2013) 759–761, https://doi.org/10.1038/nmeth.2533.
[14] C. Tribet, R. Audebert, J.-L. Popot, Amphipols: polymers that keep membrane proteins soluble in detergent-free aqueous solutions, Proc. Natl. Acad. Sci. U. S. A. 93 (1996) 15047–15050.
[15] J.-L. Popot, Membrane Proteins in Aqueous Solutions: From Detergents to Amphipols, Springer International Publishing, 2018, https://www.springer.com/de/book/9783319731469 , Accessed date: 13 June 2018.
[16] C. Breyton, B. Pucci, J.-L. Popot, Amphipols and fluorinated surfactants: two alternatives to detergents for studying membrane proteins in vitro, Methods Mol. Biol. 601 (2010) 219–245, https://doi.org/10.1007/978-1-60761-344-2_14.
[17] J.-L. Popot, Amphipols, nanodiscs, and fluorinated surfactants: three nonconventional approaches to studying membrane proteins in aqueous solutions, Annu. Rev. Biochem. 79 (2010) 737–775, https://doi.org/10.1146/annurev.biochem.052208.114057.
[18] R. Matar-Merheb, M. Rhimi, A. Leydier, F. Huché, C. Galián, E. Desuzinges-Mandon, D. Ficheux, D. Flot, N. Aghajari, R. Kahn, A. Di Pietro, J.-M. Jault, A.W. Coleman, P. Falson, Structuring detergents for extracting and stabilizing functional membrane proteins, PLoS One 6 (2011) e18036, , https://doi.org/10.1371/journal.pone.0018036.
[19] P.S. Chae, P.D. Laible, S.H. Gellman, Tripod amphiphiles for membrane protein manipulation, Mol. BioSyst. 6 (2010) 89–94.
[20] P.S. Chae, K.H. Cho, M.J. Wander, H.E. Bae, S.H. Gellman, P.D. Laible, Hydrophobic variants of ganglio-tripod amphiphiles for membrane protein manipulation, Biochim. Biophys. Acta 1838 (2014) 278–286, https://doi.org/10.1016/j.bbamem.2013.09.011.
[21] Q. Zhang, X. Ma, A. Ward, W.-X. Hong, V.-P. Jaakola, R.C. Stevens, M.G. Finn, G. Chang, Designing facial amphiphiles for the stabilization of integral membrane proteins, Angew. Chem. Int. Ed. Eng. 46 (2007) 7023–7025, https://doi.org/10.1002/anie.200701556.
[22] P.S. Chae, K. Gotfryd, J. Pacyna, L.J.W. Miercke, S.G.F. Rasmussen, R.A. Robbins, R.R. Rana, C.J. Loland, B. Kobilka, R. Stroud, B. Byrne, U. Gether, S.H. Gellman, Tandem facial amphiphiles for membrane protein stabilization, J. Am. Chem. Soc. 132 (2010) 16750–16752, https://doi.org/10.1021/ja1072959.
[23] S.C. Lee, B.C. Bennett, W.-X. Hong, Y. Fu, K.A. Baker, J. Marcoux, C.V. Robinson, A.B. Ward, J.R. Halpert, R.C. Stevens, C.D. Stout, M.J. Yeager, Q. Zhang, Steroid-based facial amphiphiles for stabilization and crystallization of membrane proteins, Proc. Natl. Acad. Sci. U. S. A. 110 (2013) E1203–E1211, https://doi.org/10.1073/pnas.1221442110.
[24] P.S. Chae, S.G.F. Rasmussen, R.R. Rana, K. Gotfryd, A.C. Kruse, A. Manglik, K.H. Cho, S. Nurva, U. Gether, L. Guan, C.J. Loland, B. Byrne, B.K. Kobilka, S.H. Gellman, A new class of amphiphiles bearing rigid hydrophobic groups for solubilization and stabilization of membrane proteins, Angew. Chem. Weinheim Bergstr. Ger. 18 (2012) 9485–9490, https://doi.org/10.1002/chem.201200069.
[25] P.S. Chae, R.R. Rana, K. Gotfryd, S.G.F. Rasmussen, A.C. Kruse, K.H. Cho, S. Capaldi, E. Carlsson, B. Kobilka, C.J. Loland, U. Gether, S. Banerjee, B. Byrne, J.K. Lee, S.H. Gellman, Glucose-neopentyl glycol (GNG) amphiphiles for membrane protein study, Chem. Commun. (Camb.) 49 (2013) 2287–2289, https://doi.org/10.1039/c2cc36844g.
[26] P.S. Chae, S.G.F. Rasmussen, R.R. Rana, K. Gotfryd, R. Chandra, M.A. Goren, A.C. Kruse, S. Nurva, C.J. Loland, Y. Pierre, D. Drew, J.-L. Popot, D. Picot, B.G. Fox, L. Guan, U. Gether, B. Byrne, B. Kobilka, S.H. Gellman, Maltose-neopentyl glycol (MNG) amphiphiles for solubilization, stabilization and crystallization of membrane proteins, Nat. Methods 7 (2010) 1003–1008, https://doi.org/10.1038/nmeth.1526.
[27] A. Sadaf, J.S. Mortensen, S. Capaldi, E. Tikhonova, P. Hariharan, O. de Castro Ribeiro, C.J. Loland, L. Guan, B. Byrne, P.S. Chae, A class of rigid linker-bearing glucosides for membrane protein structural study, Chem. Sci. 7 (2016) 1933–1939, https://doi.org/10.1039/C5SC02900G.
[28] M. Ehsan, Y. Du, N.J. Scull, E. Tikhonova, J. Tarrasch, J.S. Mortensen, C.J. Loland, G. Skiniotis, L. Guan, B. Byrne, B.K. Kobilka, P.S. Chae, Highly branched pentasaccharide-bearing amphiphiles for membrane protein studies, J. Am. Chem. Soc. 138 (2016) 3789–3796, https://doi.org/10.1021/jacs.5b13233.
[29] H. Hussain, J.S. Mortensen, Y. Du, C. Santillan, O. Ribeiro, J. Go, P. Hariharan, C.J. Loland, L. Guan, B.K. Kobilka, B. Byrne, P.S. Chae, Tandem malonate-based glucosides (TMGs) for membrane protein structural studies, Sci. Rep. 7 (2017) 3963, , https://doi.org/10.1038/s41598-017-03809-3.
[30] K.H. Cho, O. Ribeiro, Y. Du, E. Tikhonova, J.S. Mortensen, K. Markham, P. Hariharan, C.J. Loland, L. Guan, B.K. Kobilka, B. Byrne, P.S. Chae, Mesitylene-cored glucoside amphiphiles (MGAs) for membrane protein studies: importance of alkyl chain density in detergent efficacy, Angew. Chem. Weinheim Bergstr. Ger. 22 (2016) 18833–18839, https://doi.org/10.1002/chem.201603338.
[31] M. Das, Y. Du, J.S. Mortensen, O. Ribeiro, P. Hariharan, L. Guan, C.J. Loland, B.K. Kobilka, B. Byrne, P.S. Chae, Butane-1,2,3,4-tetraol-based amphiphilic

stereoisomers for membrane protein study: importance of chirality in the linker region, Chem. Sci. 8 (2017) 1169–1177, https://doi.org/10.1039/c6sc02981g.
[32] P.S. Chae, M.J. Wander, K.H. Cho, P.D. Laible, S.H. Gellman, Carbohydrate-containing Triton X-100 analogues for membrane protein solubilization and stabilization, Mol. BioSyst. 9 (2013) 626–629, https://doi.org/10.1039/c3mb25584k.
[33] P.S. Chae, H.E. Bae, M. Das, Adamantane-based amphiphiles (ADAs) for membrane protein study: importance of a detergent hydrophobic group in membrane protein solubilisation, Chem. Commun. (Camb.) 50 (2014) 12300–12303, https://doi.org/10.1039/c4cc05746e.
[34] S.G.F. Rasmussen, H.-J. Choi, J.J. Fung, E. Pardon, P. Casarosa, P.S. Chae, B.T. Devree, D.M. Rosenbaum, F.S. Thian, T.S. Kobilka, A. Schnapp, I. Konetzki, R.K. Sunahara, S.H. Gellman, A. Pautsch, J. Steyaert, W.I. Weis, B.K. Kobilka, Structure of a nanobody-stabilized active state of the β(2) adrenoceptor, Nature 469 (2011) 175–180, https://doi.org/10.1038/nature09648.
[35] D.M. Rosenbaum, C. Zhang, J.A. Lyons, R. Holl, D. Aragao, D.H. Arlow, S.G.F. Rasmussen, H.-J. Choi, B.T. Devree, R.K. Sunahara, P.S. Chae, S.H. Gellman, R.O. Dror, D.E. Shaw, W.I. Weis, M. Caffrey, P. Gmeiner, B.K. Kobilka, Structure and function of an irreversible agonist-β(2) adrenoceptor complex, Nature 469 (2011) 236–240, https://doi.org/10.1038/nature09665.
[36] T.T. Selao, R. Branca, P.S. Chae, J. Lehtiö, S.H. Gellman, S.G.F. Rasmussen, S. Nordlund, A. Norén, Identification of chromatophore membrane protein complexes formed under different nitrogen availability conditions in Rhodospirillum rubrum, J. Proteome Res. 10 (2011) 2703–2714, https://doi.org/10.1021/pr100838x.
[37] X. Jiang, L. Guan, Y. Zhou, W.-X. Hong, Q. Zhang, H.R. Kaback, Evidence for an intermediate conformational state of LacY, Proc. Natl. Acad. Sci. U. S. A. 109 (2012) E698–E704, https://doi.org/10.1073/pnas.1201107109.
[38] A. Amin, P. Hariharan, P.S. Chae, L. Guan, Effect of detergents on galactoside binding by Melibiose permeases, Biochemistry 54 (2015) 5849–5855, https://doi.org/10.1021/acs.biochem.5b00660.
[39] C. Nasrallah, K. Rottier, R. Marcellin, V. Compan, J. Font, A. Llebaria, J.-P. Pin, J.-L. Banères, G. Lebon, Direct coupling of detergent purified human mGlu5 receptor to the heterotrimeric G proteins Gq and Gs, Sci. Rep. 8 (2018) 4407, , https://doi.org/10.1038/s41598-018-22729-4.
[40] T.S. Owen, D. Salom, W. Sun, K. Palczewski, Increasing the stability of recombinant human green cone pigment, Biochemistry 57 (2018) 1022–1030, https://doi.org/10.1021/acs.biochem.7b01118.
[41] C. Perez, S. Gerber, J. Boilevin, M. Bucher, T. Darbre, M. Aebi, J.-L. Reymond, K.P. Locher, Structure and mechanism of an active lipid-linked oligosaccharide flippase, Nature 524 (2015) 433–438, https://doi.org/10.1038/nature14953.
[42] E.M. Quistgaard, M. Martinez Molledo, C. Löw, Structure determination of a major facilitator peptide transporter: inward facing PepTSt from Streptococcus thermophilus crystallized in space group P3121, PLoS One 12 (2017) e0173126, , https://doi.org/10.1371/journal.pone.0173126.
[43] Y. Gao, G. Westfield, J.W. Erickson, R.A. Cerione, G. Skiniotis, S. Ramachandran, Isolation and structure-function characterization of a signaling-active rhodopsin-G protein complex, J. Biol. Chem. 292 (2017) 14280–14289, https://doi.org/10.1074/jbc.M117.797100.
[44] K.Y. Chung, T.H. Kim, A. Manglik, R. Alvares, B.K. Kobilka, R.S. Prosser, Role of detergents in conformational exchange of a G protein-coupled receptor, J. Biol. Chem. 287 (2012) 36305–36311, https://doi.org/10.1074/jbc.M112.406371.
[45] K.Y. Chung, S.G.F. Rasmussen, T. Liu, S. Li, B.T. DeVree, P.S. Chae, D. Calinski, B.K. Kobilka, V.L. Woods Jr., R.K. Sunahara, Conformational changes in the G protein Gs induced by the β2 adrenergic receptor, Nature 477 (2011) 611–615, https://doi.org/10.1038/nature10488.
[46] G.H. Westfield, S.G.F. Rasmussen, M. Su, S. Dutta, B.T. DeVree, K.Y. Chung, D. Calinski, G. Velez-Ruiz, A.N. Oleskie, E. Pardon, P.S. Chae, T. Liu, S. Li, V.L. Woods Jr., J. Steyaert, B.K. Kobilka, R.K. Sunahara, G. Skiniotis, Structural flexibility of the G alpha s alpha-helical domain in the beta2-adrenoceptor Gs complex, Proc. Natl. Acad. Sci. U. S. A. 108 (2011) 16086–16091, https://doi.org/10.1073/pnas.1113645108.
[47] F. Hauer, C. Gerle, N. Fischer, A. Oshima, K. Shinzawa-Itoh, S. Shimada, K. Yokoyama, Y. Fujiyoshi, H. Stark, GraDeR: membrane protein complex preparation for single-particle cryo-EM, Structure (23) (2015) 1769–1775, https://doi.org/10.1016/j.str.2015.06.029.
[48] T.E. Kraft, R.C. Hresko, P.W. Hruz, Expression, purification, and functional characterization of the insulin-responsive facilitative glucose transporter GLUT4, Protein Sci. 24 (2015) 2008–2019, https://doi.org/10.1002/pro.2812.
[49] K.H. Cho, M. Husri, A. Amin, K. Gotfryd, H.J. Lee, J. Go, J.W. Kim, C.J. Loland, L. Guan, B. Byrne, P.S. Chae, Maltose neopentyl glycol-3 (MNG-3) analogues for membrane protein study, Analyst 140 (2015) 3157–3163, https://doi.org/10.1039/c5an00240k.
[50] S.E. Rollauer, M.J. Tarry, J.E. Graham, M. Jääskeläinen, F. Jäger, S. Johnson, M. Krehenbrink, S.-M. Liu, M.J. Lukey, J. Marcoux, M.A. McDowell, F. Rodriguez, P. Roversi, P.J. Stansfeld, C.V. Robinson, M.S.P. Sansom, T. Palmer, M. Högbom, B.C. Berks, S.M. Lea, Structure of the TatC core of the twin-arginine protein transport system, Nature 492 (2012) 210–214, https://doi.org/10.1038/nature11683.
[51] B.H. Thurtle-Schmidt, R.M. Stroud, Structure of Bor1 supports an elevator transport mechanism for SLC4 anion exchangers, Proc. Natl. Acad. Sci. U. S. A. 113 (2016) 10542–10546, https://doi.org/10.1073/pnas.1612603113.
[52] J. Guo, W. Zeng, Q. Chen, C. Lee, L. Chen, Y. Yang, C. Cang, D. Ren, Y. Jiang, Structure of the voltage-gated two-pore channel TPC1 from Arabidopsis thaliana, Nature 531 (2016) 196–201, https://doi.org/10.1038/nature16446.
[53] K.W. Huynh, M.R. Cohen, J. Jiang, A. Samanta, D.T. Lodowski, Z.H. Zhou, V.Y. Moiseenkova-Bell, Structure of the full-length TRPV2 channel by cryo-EM, Nat. Commun. 7 (2016) 11130, , https://doi.org/10.1038/ncomms11130.
[54] A. Oshima, K. Tani, Y. Fujiyoshi, Atomic structure of the innexin-6 gap junction channel determined by cryo-EM, Nat. Commun. 7 (2016) 13681, , https://doi.org/10.1038/ncomms13681.
[55] S. Dang, S. Feng, J. Tien, C.J. Peters, D. Bulkley, M. Lolicato, J. Zhao, K. Zuberbühler, W. Ye, L. Qi, T. Chen, C.S. Craik, Y.N. Jan, D.L. Minor, Y. Cheng, L.Y. Jan, Cryo-EM structures of the TMEM16A calcium-activated chloride channel, Nature 552 (2017) 426–429, https://doi.org/10.1038/nature25024.
[56] A.D. Ferguson, J. Breed, K. Diederichs, W. Welte, J.W. Coulton, An internal affinity-tag for purification and crystallization of the siderophore receptor FhuA, integral outer membrane protein from Escherichia coli K-12, Protein Sci. 7 (1998) 1636–1638.
[57] M. Roth, P. Carpentier, O. Kaïkati, J. Joly, P. Charrault, M. Pirocchi, R. Kahn, E. Fanchon, L. Jacquamet, F. Borel, A. Bertoni, P. Israel-Gouy, J.L. Ferrer, FIP: a highly automated beamline for multiwavelength anomalous diffraction experiments, Acta Crystallogr. D Biol. Crystallogr. 58 (2002) 805–814.
[58] W. Kabsch, XDS, Acta Crystallogr. D Biol. Crystallogr. 66 (2010) 125–132, https://doi.org/10.1107/S0907444909047337.
[59] A.J. McCoy, R.W. Grosse-Kunstleve, P.D. Adams, M.D. Winn, L.C. Storoni, R.J. Read, Phaser crystallographic software, J. Appl. Crystallogr. 40 (2007) 658–674, https://doi.org/10.1107/S0021889807021206.
[60] P.V. Afonine, R.W. Grosse-Kunstleve, N. Echols, J.J. Headd, N.W. Moriarty, M. Mustyakimov, T.C. Terwilliger, A. Urzhumtsev, P.H. Zwart, P.D. Adams, Towards automated crystallographic structure refinement with phenix.refine, Acta Crystallogr. D Biol. Crystallogr. 68 (2012) 352–367, https://doi.org/10.1107/S0907444912001308.
[61] J.J. Headd, N. Echols, P.V. Afonine, R.W. Grosse-Kunstleve, V.B. Chen, N.W. Moriarty, D.C. Richardson, J.S. Richardson, P.D. Adams, Use of knowledge-based restraints in phenix.refine to improve macromolecular refinement at low resolution, Acta Crystallogr. D Biol. Crystallogr. 68 (2012) 381–390, https://doi.org/10.1107/S0907444911047834.
[62] C. Hajjar, M.V. Cherrier, G. Dias Mirandela, I. Petit-Hartlein, M.J. Stasia, J.C. Fontecilla-Camps, F. Fieschi, J. Dupuy, The NOX family of proteins is also present in bacteria, MBio 8 (2017), https://doi.org/10.1128/mBio.01487-17.
[63] E. Steinfels, C. Orelle, O. Dalmas, F. Penin, B. Miroux, A. Di Pietro, J.-M. Jault, Highly efficient over-production in E. coli of YvcC, a multidrug-like ATP-binding cassette transporter from Bacillus subtilis, Biochim. Biophys. Acta 1565 (2002) 1–5.
[64] C. Orelle, O. Dalmas, P. Gros, A. Di Pietro, J.-M. Jault, The conserved glutamate residue adjacent to the Walker-B motif is the catalytic base for ATP hydrolysis in the ATP-binding cassette transporter BmrA, J. Biol. Chem. 278 (2003) 47002–47008, https://doi.org/10.1074/jbc.M308268200.
[65] A. Salvay, C. Ebel, Analytical ultracentrifuge for the characterization of detergent in solution, Prog. Colloid Polym. Sci. 2006, pp. 74–82, , https://doi.org/10.1007/2882_006.
[66] P. Schuck, Size-distribution analysis of macromolecules by sedimentation velocity ultracentrifugation and lamm equation modeling, Biophys. J. 78 (2000) 1606–1619, https://doi.org/10.1016/S0006-3495(00)76713-0.
[67] H. Zhao, R. Ghirlando, C. Alfonso, F. Arisaka, I. Attali, D.L. Bain, M.M. Bakhtina, D.F. Becker, G.J. Bedwell, A. Bekdemir, T.M.D. Besong, C. Birck, C.A. Brautigam, W. Brennerman, O. Byron, A. Bzowska, J.B. Chaires, C.T. Chaton, H. Cölfen, K.D. Connaghan, K.A. Crowley, U. Curth, T. Daviter, W.L. Dean, A.I. Díez, C. Ebel, D.M. Eckert, L.E. Eisele, E. Eisenstein, P. England, C. Escalante, J.A. Fagan, R. Fairman, R.M. Finn, W. Fischle, J.G. de la Torre, J. Gor, H. Gustafsson, D. Hall, S.E. Harding, J.G.H. Cifre, A.B. Herr, E.E. Howell, R.S. Isaac, S.-C. Jao, D. Jose, S.-J. Kim, B. Kokona, J.A. Kornblatt, D. Kosek, E. Krayukhina, D. Krzizike, E.A. Kusznir, H. Kwon, A. Larson, T.M. Laue, A. Le Roy, A.P. Leech, H. Lilie, K. Luger, J.R. Luque-Ortega, J. Ma, C.A. May, E.L. Maynard, A. Modrak-Wojcik, Y.-F. Mok, N. Mücke, L. Nagel-Steger, G.J. Narlikar, M. Noda, A. Nourse, T. Obsil, C.K. Park, J.-K. Park, P.D. Pawelek, E.E. Perdue, S.J. Perkins, M.A. Perugini, C.L. Peterson, M.G. Peverelli, G. Piszczek, G. Prag, P.E. Prevelige, B.D.E. Raynal, L. Rezabkova, K. Richter, A.E. Ringel, R. Rosenberg, A.J. Rowe, A.C. Rufer, D.J. Scott, J.G. Seravalli, A.S. Solovyova, R. Song, D. Staunton, C. Stoddard, K. Stott, H.M. Strauss, W.W. Streicher, J.P. Sumida, S.G. Swygert, R.H. Szczepanowski, I. Tessmer, R.T. Toth, A. Tripathy, S. Uchiyama, S.F.W. Uebel, S. Unzai, A.V. Gruber, P.H. von Hippel, C. Wandrey, S.-H. Wang, S.E. Weitzel, B. Wielgus-Kutrowska, C. Wolberger, M. Wolff, E. Wright, Y.-S. Wu, J.M. Wubben, P. Schuck, A multilaboratory comparison of calibration accuracy and the performance of external references in analytical ultracentrifugation, PLoS One 10 (2015) e0126420, , https://doi.org/10.1371/journal.pone.0126420.
[68] C.A. Brautigam, Calculations and publication-quality illustrations for analytical ultracentrifugation data, Methods Enzymol. 562 (2015) 109–133, https://doi.org/10.1016/bs.mie.2015.05.001.
[69] A. Le Roy, H. Nury, B. Wiseman, J. Sarwan, J.-M. Jault, C. Ebel, Sedimentation velocity analytical ultracentrifugation in hydrogenated and deuterated solvents for the characterization of membrane proteins, Methods Mol. Biol. 1033 (2013) 219–251, https://doi.org/10.1007/978-1-62703-487-6_15.
[70] A. Le Roy, K. Wang, B. Schaack, P. Schuck, C. Breyton, C. Ebel, AUC and small-angle scattering for membrane proteins, Methods Enzymol. 562 (2015) 257–286, https://doi.org/10.1016/bs.mie.2015.06.010.
[71] A.G. Salvay, M. Santamaria, M. le Maire, C. Ebel, Analytical ultracentrifugation sedimentation velocity for the characterization of detergent-solubilized membrane proteins Ca++-ATPase and ExbB, J. Biol. Phys. 33 (2007) 399–419, https://doi.org/10.1007/s10867-008-9058-3.
[72] P. Pernot, A. Round, R. Barrett, A. De Maria Antolinos, A. Gobbo, E. Gordon, J. Huet, J. Kieffer, M. Lentini, M. Mattenet, C. Morawe, C. Mueller-Dieckmann,

S. Ohlsson, W. Schmid, J. Surr, P. Theveneau, L. Zerrad, S. McSweeney, Upgraded ESRF BM29 beamline for SAXS on macromolecules in solution, J. Synchrotron Radiat. 20 (2013) 660–664, https://doi.org/10.1107/S0909049513010431.
[73] M.V. Petoukhov, D. Franke, A.V. Shkumatov, G. Tria, A.G. Kikhney, M. Gajda, C. Gorba, H.D.T. Mertens, P.V. Konarev, D.I. Svergun, New developments in the ATSAS program package for small-angle scattering data analysis, J. Appl. Crystallogr. 45 (2012) 342–350, https://doi.org/10.1107/S0021889812007662.
[74] C. Ebel, C. Breyton, A. Martel, Examining membrane proteins by neutron scattering, in: Vincent Postis, Adrian Goldmann (Eds.), Biophys. Membr. Proteins Methods Protoc. Springer, 2018.
[75] S.R. Kline, Reduction and analysis of SANS and USANS data using IGOR Pro, J. Appl. Crystallogr. 39 (2006) 895–900, https://doi.org/10.1107/S0021889806035059.
[76] M. Doucet, J.H. Cho, G. Alina, J. Bakker, W. Bouwman, P. Butler, K. Campbell, M. Gonzales, R. Heenan, A. Jackson, P. Juhas, S. King, P. Kienzle, J. Krzywon, A. Markvardsen, T. Nielsen, L. O'Driscoll, W. Potrzebowski, R. Ferraz Leal, T. Richter, P. Rozycko, T. Snow, A. Washington, SasView Version 4.2, Zenodo, (2018), https://doi.org/10.5281/zenodo.1412041.
[77] C. Breyton, F. Gabel, M. Lethier, A. Flayhan, G. Durand, J.-M. Jault, C. Juillan-Binard, L. Imbert, M. Moulin, S. Ravaud, M. Härtlein, C. Ebel, Small angle neutron scattering for the study of solubilised membrane proteins, Eur. Phys. J. E Soft Matter 36 (2013) 9889, https://doi.org/10.1140/epje/i2013-13071-6.
[78] A. Flayhan, F. Wien, M. Paternostre, P. Boulanger, C. Breyton, New insights into pb5, the receptor binding protein of bacteriophage T5, and its interaction with its Escherichia coli receptor FhuA, Biochimie 94 (2012) 1982–1989, https://doi.org/10.1016/j.biochi.2012.05.021.
[79] C. Breyton, A. Flayhan, F. Gabel, M. Lethier, G. Durand, P. Boulanger, M. Chami, C. Ebel, Assessing the conformational changes of pb5, the receptor-binding protein of phage T5, upon binding to its Escherichia coli receptor FhuA, J. Biol. Chem. 288 (2013) 30763–30772, https://doi.org/10.1074/jbc.M113.501536.
[80] A.D. Ferguson, E. Hofmann, J.W. Coulton, K. Diederichs, W. Welte, Siderophore-mediated iron transport: crystal structure of FhuA with bound lipopolysaccharide, Science 282 (1998) 2215–2220.
[81] M. Bonhivers, M. Desmadril, G.S. Moeck, P. Boulanger, A. Colomer-Pallas, L. Letellier, Stability studies of FhuA, a two-domain outer membrane protein from Escherichia coli, Biochemistry 40 (2001) 2606–2613.
[82] P. Boulanger, M. le Maire, M. Bonhivers, S. Dubois, M. Desmadril, L. Letellier, Purification and structural and functional characterization of FhuA, a transporter of the Escherichia coli outer membrane, Biochemistry 35 (1996) 14216–14224, https://doi.org/10.1021/bi9608673.
[83] D. Durand, C. Vivès, D. Cannella, J. Pérez, E. Pebay-Peyroula, P. Vachette, F. Fieschi, NADPH oxidase activator p67(phox) behaves in solution as a multi-domain protein with semi-flexible linkers, J. Struct. Biol. 169 (2010) 45–53, https://doi.org/10.1016/j.jsb.2009.08.009.
[84] J. Marcoux, P. Man, I. Petit-Haertlein, C. Vivès, E. Forest, F. Fieschi, p47phox molecular activation for assembly of the neutrophil NADPH oxidase complex, J. Biol. Chem. 285 (2010) 28980–28990, https://doi.org/10.1074/jbc.M110.139824.
[85] F. Magnani, S. Nenci, E. Millana Fananas, M. Ceccon, E. Romero, M.W. Fraaije, A. Mattevi, Crystal structures and atomic model of NADPH oxidase, Proc. Natl. Acad. Sci. U. S. A. 114 (2017) 6764–6769, https://doi.org/10.1073/pnas.1702293114.
[86] E. Steinfels, C. Orelle, J.-R. Fantino, O. Dalmas, J.-L. Rigaud, F. Denizot, A. Di Pietro, J.-M. Jault, Characterization of YvcC (BmrA), a multidrug ABC transporter constitutively expressed in Bacillus subtilis, Biochemistry 43 (2004) 7491–7502, https://doi.org/10.1021/bi0362018.
[87] A. Ward, C.L. Reyes, J. Yu, C.B. Roth, G. Chang, Flexibility in the ABC transporter MsbA: alternating access with a twist, Proc. Natl. Acad. Sci. U. S. A. 104 (2007) 19005–19010, https://doi.org/10.1073/pnas.0709388104.
[88] M.S. Jin, M.L. Oldham, Q. Zhang, J. Chen, Crystal structure of the multidrug transporter P-glycoprotein from Caenorhabditis elegans, Nature 490 (2012) 566–569, https://doi.org/10.1038/nature11448.
[89] S. Ravaud, M.-A. Do Cao, M. Jidenko, C. Ebel, M. Le Maire, J.-M. Jault, A. Di Pietro, R. Haser, N. Aghajari, The ABC transporter BmrA from Bacillus subtilis is a functional dimer when in a detergent-solubilized state, Biochem. J. 395 (2006) 345–353.
[90] O. Dalmas, M.-A. Do Cao, M.R. Lugo, F.J. Sharom, A. Di Pietro, J.-M. Jault, Time-resolved fluorescence resonance energy transfer shows that the bacterial multidrug ABC half-transporter BmrA functions as a homodimer, Biochemistry 44 (2005) 4312–4321, https://doi.org/10.1021/bi0482809.
[91] C. Orelle, F. Gubellini, A. Durand, S. Marco, D. Lévy, P. Gros, A. Di Pietro, J.-M. Jault, Conformational change induced by ATP binding in the multidrug ATP-binding cassette transporter BmrA, Biochemistry 47 (2008) 2404–2412, https://doi.org/10.1021/bi702303s.
[92] M.-A. Do Cao, S. Crouzy, M. Kim, M. Becchi, D.S. Cafiso, A. Di Pietro, J.-M. Jault, Probing the conformation of the resting state of a bacterial multidrug ABC transporter, BmrA, by a site-directed spin labeling approach, Protein Sci. 18 (2009) 1507–1520, https://doi.org/10.1002/pro.141.
[93] S. Mehmood, C. Domene, E. Forest, J.-M. Jault, Dynamics of a bacterial multidrug ABC transporter in the inward- and outward-facing conformations, Proc. Natl. Acad. Sci. U. S. A. 109 (2012) 10832–10836, https://doi.org/10.1073/pnas.1204067109.
[94] P.F. Fribourg, M. Chami, C.O.S. Sorzano, F. Gubellini, R. Marabini, S. Marco, J.-M. Jault, D. Lévy, 3D cryo-electron reconstruction of BmrA, a bacterial multidrug ABC transporter in an inward-facing conformation and in a lipidic environment, J. Mol. Biol. 426 (2014) 2059–2069, https://doi.org/10.1016/j.jmb.2014.03.002.
[95] B. Wiseman, A. Kilburg, V. Chaptal, G.C. Reyes-Mejia, J. Sarwan, P. Falson, J.-M. Jault, Stubborn contaminants: influence of detergents on the purity of the multidrug ABC transporter BmrA, PLoS One 9 (2014) e114864, , https://doi.org/10.1371/journal.pone.0114864.
[96] J. Lipfert, L. Columbus, V.B. Chu, S.A. Lesley, S. Doniach, Size and shape of detergent micelles determined by small-angle X-ray scattering, J. Phys. Chem. B 111 (2007) 12427–12438, https://doi.org/10.1021/jp073016l.
[97] R.C. Oliver, S.V. Pingali, V.S. Urban, Designing mixed detergent micelles for uniform neutron contrast, J. Phys. Chem. Lett. 8 (2017) 5041–5046, https://doi.org/10.1021/acs.jpclett.7b02149.
[98] J.N. Israelachvili, D.J. Mitchell, B.W. Barry, W. Ninham, Theory of self-assembly of lipid bilayers and vesicles, Biochim. Biophys. Acta Biomembr. 470 (1977) 185–201.
[99] J.N. Israelachvili, Intermolecular and Surface Forces, 3rd edition, Academic Press, London, 1992https://www.elsevier.com/books/intermolecular-and-surface-forces/israelachvili/978-0-12-391927-4 , Accessed date: 24 July 2018.
[100] C. Breyton, F. Gabel, M. Abla, Y. Pierre, F. Lebaupain, G. Durand, J.-L. Popot, C. Ebel, B. Pucci, Micellar and biochemical properties of (hemi)fluorinated surfactants are controlled by the size of the polar head, Biophys. J. 97 (2009) 1077–1086, https://doi.org/10.1016/j.bpj.2009.05.053.
[101] E. Boncoeur, C. Durmort, B. Bernay, C. Ebel, A.M. Di Guilmi, J. Croizé, T. Vernet, J.-M. Jault, PatA and PatB form a functional heterodimeric ABC multidrug efflux transporter responsible for the resistance of Streptococcus pneumoniae to fluoroquinolones, Biochemistry 51 (2012) 7755–7765, https://doi.org/10.1021/bi300762p.
[102] E. Pebay-Peyroula, G. Rummel, J.P. Rosenbusch, E. Landau, X-ray structure of bacteriorhodopsin at 2.5 Å from microcrystals grown in lipidic cubic phases, Science 277 (1997) 1676–1881.

Annex

Antimicrobial class	Modes of action: drug targets	Mechanisms of resistance		
		Drug inactivating enzymes	Drug target alteration/protection	Cell envelope membrane permeability/drug efflux pump
β-Lactams	Inhibition of cell wall synthesis by targeting to penicillin-binding proteins	Ambler class A, B, C and D β-lactamases	Mutations in PBP with reduced affinity to β-lactams	OM permeability with reduced porin production; RND pumps
Aminoglycosides	Inhibition of protein synthesis (30S ribosome inhibitors affecting initiation and translocation)	*N*-acetyltransferases, *O*-nucleotidyltransferases, *O*-phosphotransferases	Mutations in ribosome	Lipopolysaccharide alterations; RND pumps
Amphenicols	Inhibition of protein synthesis (50S ribosome inhibitors blocking the peptidyl transferase)	Chloramphenicol acetyltransferase	Mutations in 23S rRNA	RND and MFS pumps
Cationic peptides	Disruption of cell membranes and/or intracellular targets (cell wall, nucleic acid, or protein synthesis)	Proteolytic degradation	Membrane alteration	Cell membrane and lipopolysaccharide alterations; efflux
Coumarins (novobiocin)	Inhibition of RNA synthesis (DNA gyrase B)		Mutations in DNA gyrase B	OM permeability; RND pumps
Ethambutol	Disruption of cell wall synthesis (by inhibiting the polymerization of cell wall arabinan)		Mutations in or overexpression of mycobacterial arabinosyl transferases	Efflux
Fluoroquinolones	Inhibition of DNA synthesis by targeting topoisomerases to block DNA replication and repair	*N*-acetyltransferase AAC(6′)-Ib-cr	Alterations of DNA gyrase and topoisomerase IV; Qnr pentapeptide family proteins	OM permeability with reduced porin production; RND, MFS, and ABC pumps
Glycopeptides (vancomycin)	Disruption of cell wall synthesis (binding to *N*-acyl-D-Ala-D-Ala termini of peptidoglycan precursors)		Acquisition of genes generating alternative peptidoglycan termini (D-Ala-D-lactate and D-Ala-D-Ser)	Cell wall thickening; outer membrane permeability

Annex 1. Major antibiotic classes with their mode of action and resistance mechanism (Li, 2016)

Antimicrobial class	Modes of action: drug targets	Mechanisms of resistance		
		Drug inactivating enzymes	Drug target alteration/protection	Cell envelope membrane permeability/drug efflux pump
Glycylcyclines (tigecycline)	Inhibition of protein synthesis (30S ribosome inhibitors to block tRNA delivery)		Mutations in the ribosomal S10 protein	RND pumps
Isoniazid	Inhibition of fatty acid synthesis	Loss of drug activation (mutations in catalase-peroxidase)	Target modification (InhA)	Efflux
Ketolides	Inhibition of protein synthesis (50S ribosome inhibitors by binding to 23S rRNA to block nascent chain elongation)		Mutations in 23S rRNA and ribosomal L4 protein	OM permeability; efflux
Lincosamides	Inhibition of protein synthesis (50S ribosome inhibitors by binding to 23S rRNA and causing premature dissociation of the peptidyl-tRNA)		Target modification by Erm methylases (mutations in 23S rRNA)	OM permeability; efflux
Lipopeptides (daptomycin)	Disruption of cell membrane	Inactivation by daptomycin hydrolase	Mutations in lysylphosphatidylglycerol synthetase	Cell wall thickening; cell membrane lipid and protein modification; outer membrane permeability
Macrolides	Inhibition of protein synthesis (50S ribosome inhibitors by binding to 23S rRNA to block nascent chain elongation)	Macrolide esterase or phosphotransferase	Target modification by Erm methylases (mutations in 23S rRNA)	OM permeability; efflux
Nitrofurans	Disruption of DNA synthesis (by cross-linking to DNA)	Loss of drug activation (mutations in nitroreductase)		

Annex 1. Major antibiotic classes with their mode of action and resistance mechanism (Li, 2016), continued

Nitroimidazole	Disruption of DNA synthesis	Loss of drug activation		Efflux
Oxazolidinones	Inhibition of protein synthesis (50S ribosome inhibitors by binding to the peptidyl transferase center)		Mutations in 23S rRNA; inactivation of methyltransferase (RlmN)	OM permeability; efflux by RND pumps
Pleuromutilins	Inhibition of protein synthesis (50S ribosome inhibitors by binding to the peptidyl transferase center)		Mutations in the 50S ribosome (23S rRNA)	OM permeability; efflux
Polyketides (mupirocin)	Inhibition of protein synthesis (inhibiting the Ile-tRNA synthetases)		Mutations or acquisition of Ile-tRNA synthetases	
Polymyxins	Disruption of outer membrane		Lipopolysaccharide alteration	Lipopolysaccharide alteration; efflux
Pyrazinamide	Inhibition of fatty acid synthase; interference with ATP production	Loss of drug activation (mutations in or lack of pyrazinamidase)	Target protein overexpression (ribosomal protein S1)	Efflux (in non-*M. tuberculosis*)
Rifamycins	Inhibition of RNA synthesis (targeting the DNA-dependent RNA polymerase)	ADP-ribosyltransferases, phospherases, glycosyltransferase	Mutations in the *rpoB* gene	OM permeability; efflux
Streptogramins	Inhibition of protein synthesis (50S ribosome inhibitors)		Target modification by Erm methylases (mutations in 23S rRNA)	OM permeability; efflux
Sulfonamides	Interference of folic acid synthesis		Mutations or overproduction of dihydropteroate synthases (encoded by *sul1* and *sul2*)	Efflux by RND pumps
Trimethoprim	Interference of folic acid synthesis		Mutations or overproduction of dihydrofolate reductases (encoded by *dhfr* or *dfrA* genes)	OM permeability; efflux by RND pumps
Tetracyclines	Inhibition of protein synthesis (30S ribosome inhibitors by preventing aminoacyl-tRNA association with the ribosome)	Tetracycline-inactivating enzymes: Tet(X) protein; tetracycline destructases	Target ribosomal protection	OM permeability; efflux by MFS and RND pumps

Annex 1. Major antibiotic classes with their mode of action and resistance mechanism (Li, 2016)

Antibiotic Approved or Released	Year Released	Resistant Germ Identified	Year Identified
Penicillin	1941	Penicillin-resistant *Staphylococcus aureus* Penicillin-resistant *Streptococcus pneumoniae* Penicillinase-producing *Neisseria gonorrhoeae*	1942 1967 1976
Vancomycin	1958	Plasmid-mediated vancomycin-resistant *Enterococcus faecium* Vancomycin-resistant *Staphylococcus aureus*	1988 2002
Amphotericin B	1959	Amphotericin B-resistant *Candida auris*	2016
Methicillin	1960	Methicillin-resistant *Staphylococcus aureus*	1960
Extended-spectrum cephalosporin	1980 (Cefotaxime)	Extended-spectrum beta-lactamase-producing *Escherichia coli*	1983
Azithromycin	1980	Azithromycin-resistant *Neisseria gonorrhoeae*	2011
Imipenem	1985	*Klebsiella pneumoniae* carbapenemase (KPC)-producing *Klebsiella pneumoniae*	1996
Ciprofloxacin	1987	Ciprofloxacin-resistant *Neisseria gonorrhoeae*	2007
Fluconazole	1990 (FDA approved)	Fluconazole-resistant *Candida*	1988
Caspofungin	2001	Caspofungin-resistant *Candida*	2004
Daptomycin	2003	Daptomycin-resistant methicillin-resistant *Staphylococcus aureus*	2004
Ceftazidime-avibactam	2015	Ceftazidime-avibactam-resistant KPC-producing *Klebsiella pneumoniae*	2015

Annex 2. Timeline showing the year in which antibiotic resistant microorganism (bacteria or fungi) was identified against some of the major classes of antibiotics (CDC, 2019)

	Type/fold I	Type/fold II	Type/fold III	Type/fold IV	Type/fold V	Type/fold VI	Type/fold VII
Function	**Importers**			**Exporters/importers**[a]		**Extractors**	**Mechanotransmitters**
Structural features	(5–6) + (5–6/8) TM helices	10+10 TM helices	4–8 (EcfT)+6 (EcfS) TM helices	6+6 TM helices (helix swap), elbow helices, TMD0[b], L_0[c]	6+6 TM helices, elbow helices, large ECDs in ABCA	6+6 TM helices, periplasmic β-jellyroll domains	4+4 TM helices, elbow helices, large periplasmic domains
Representatives in prokaryotes	Maltose importer ($MalFGK_2$)	Cobalamin importer ($BtuC_2D_2$)	Folate importer	Sav1866, MsbA, TmrAB	Wzm-Wzt	$LptB_2FG$	MacB
Representatives in humans	Nonexistent	Nonexistent	Nonexistent	P-gp, TAP, MRP1, CFTR[d], SUR[d] (B/C/D subfamily)	ABCA1, ABCG5/8, ABCG2 (A/G subfamily)	Nonexistent	Nonexistent
Substrates	E.g., sugars, amino acids, peptides	Micronutrients	Micronutrients	Very diverse (e.g., xenobiotics, lipids, peptides, ions, hormones)	O-antigen, sterols, xenobiotics, uric acid, phospholipids, cholesterol	Lipopolysaccharide	Macrolide antibiotics, polypeptide virulence factors
Translocation pathway	Cavity with defined binding site (cf. type II importers)	Hydrophobic, Teflon-like pathway	EcfS acts as translocation module	Large cavity	Channel or slit-like cavity	Large V-shaped cavity	No transmembrane transport pathway
Coupling helices	Each CH interacts with NBD of same transporter half	Each CH interacts with NBD of same transporter half	Provided by EcfT (crossover): contact NBD and EcfS	CH1 and CH2: contact different NBDs	CpH (and CnH) contact NBD of same transporter half/half-transporter	CHs of LptF and LptG interact with LptB of same transporter half	CH1 and CH2: both contact NBD of same monomer

Abbreviations: CH, coupling helix; NBD, nucleotide-binding domain; P-gp, P-glycoprotein; TM, transmembrane.

[a]Not all type IV systems function as transporters.

[b]In some members of the ABCB and ABCC subfamilies.

[c]ABCC-specific structural element.

[d]CFTR and SUR function as an ion channel and a regulatory module, respectively.

Annex 3. Classification of ABC transporters according to TMD types/folds summarizing their key structural and functional features (Thomas & Tampe, 2020)

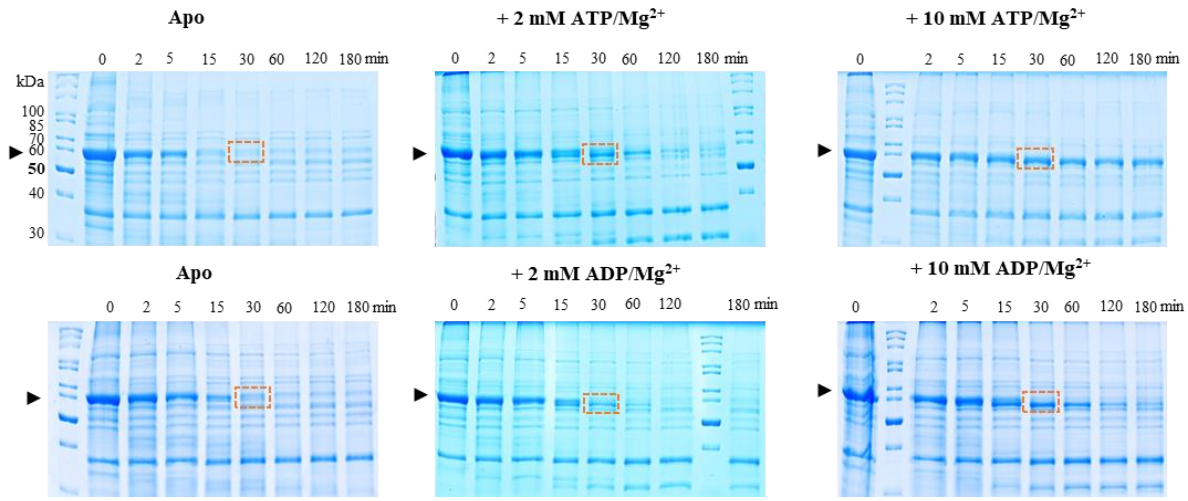

Annex 4. The effect of ATP and ADP on WT BmrA in IMVs monitored by limited proteolysis using trypsin. IMVs containing overexpressed BmrA were proteolysed in the presence or absence of mentioned ligands, for the indicated periods of time and the progress was visualized on SDS-PAGE gels stained with coommassie blue. The black arrows indicate the intact BmrA band and the red dotted rectangles highlight the progress at 30 min of digestion.

HDX sequence coverage maps

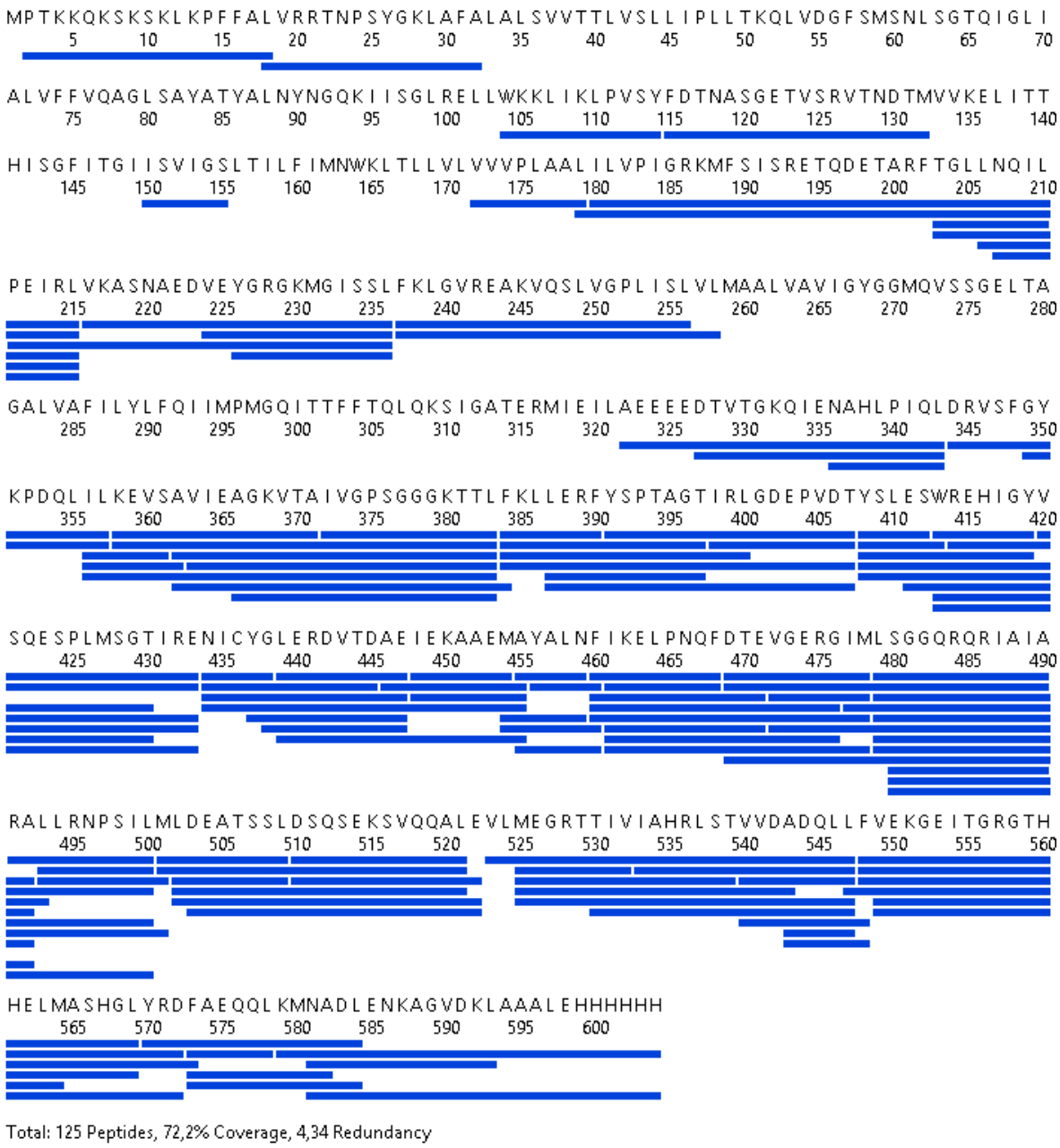

Annex 5. Sequence coverage map of WT BmrA in LMNG. The blue bars represent the recovered peptides, mapped on the primary sequence of the protein. A 72 % final sequence coverage was achieved. Note that residues 29-309 constitute TMD and 341-576 form the NBD.

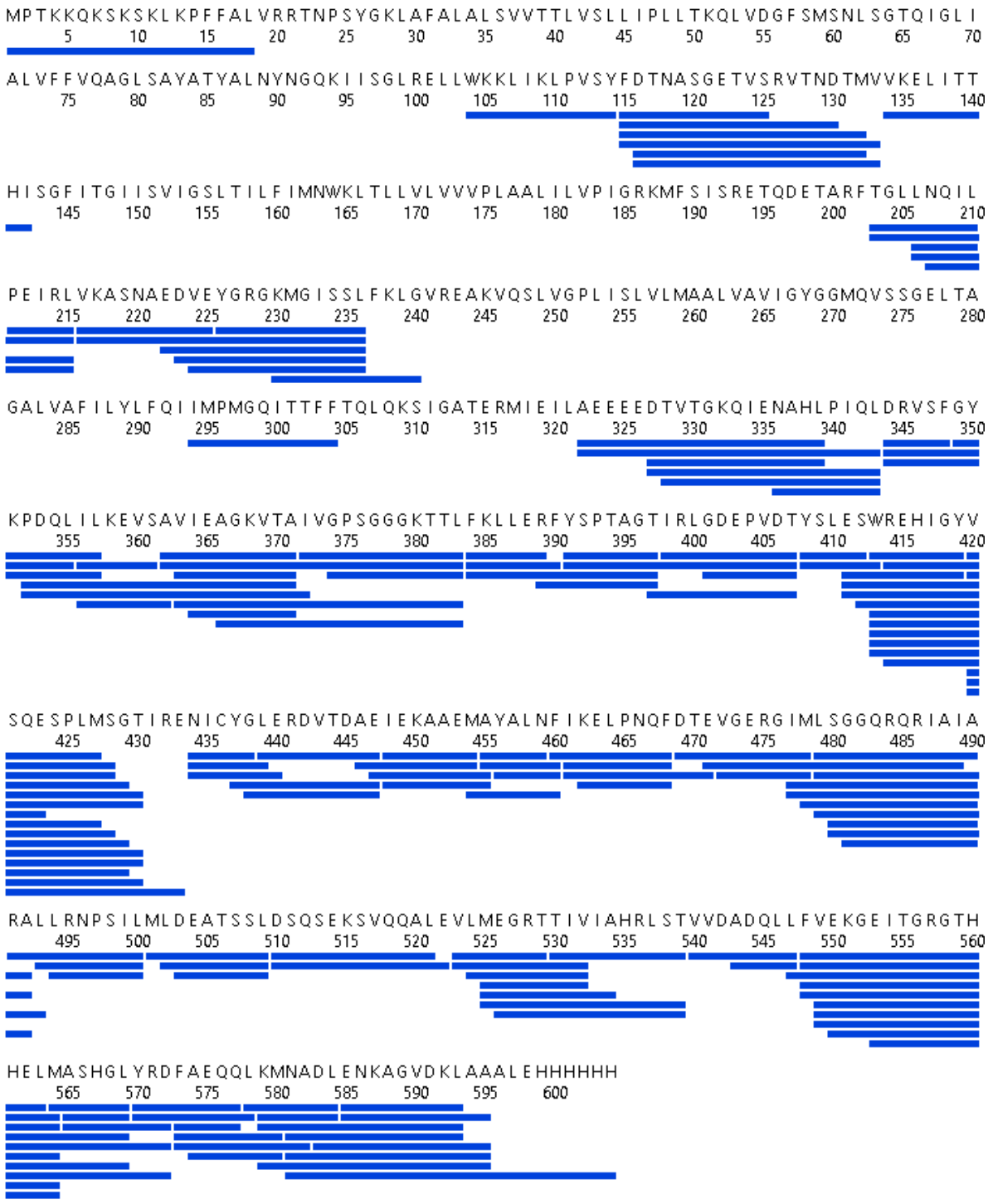

Annex 6. Sequence coverage map of WT BmrA in nanodiscs (LMNG). The blue bars represent the recovered peptides, mapped on the primary sequence of the protein. A 64 % final sequence coverage was achieved. Note that residues 29-309 constitute TMD and 341-576 form the NBD.

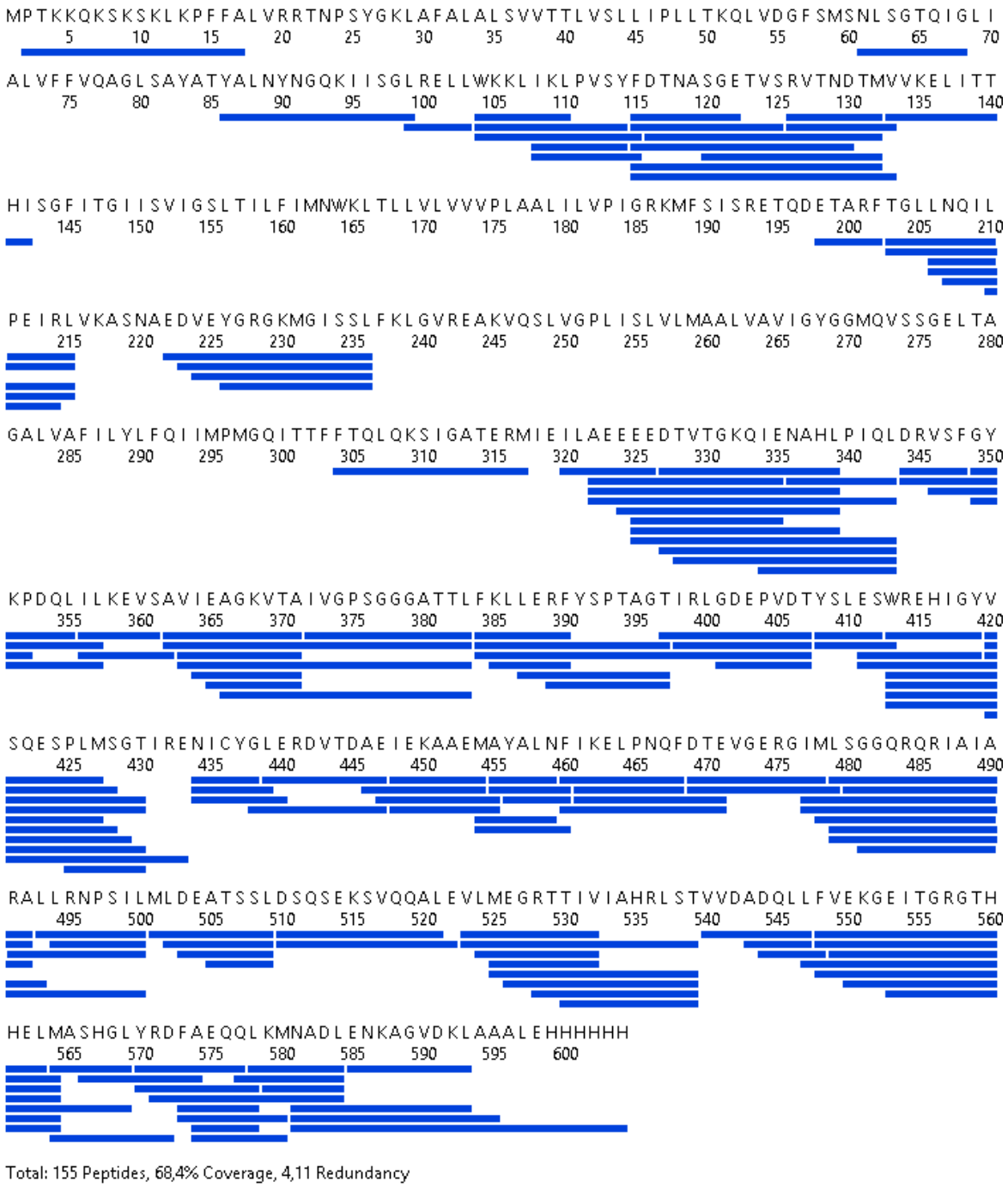

Total: 155 Peptides, 68,4% Coverage, 4,11 Redundancy

Annex 7. Sequence coverage map of K380A BmrA in LMNG. The blue bars represent the recovered peptides, mapped on the primary sequence of the protein. A 68 % final sequence coverage was achieved. Note that residues 29-309 constitute TMD and 341-576 form the NBD.

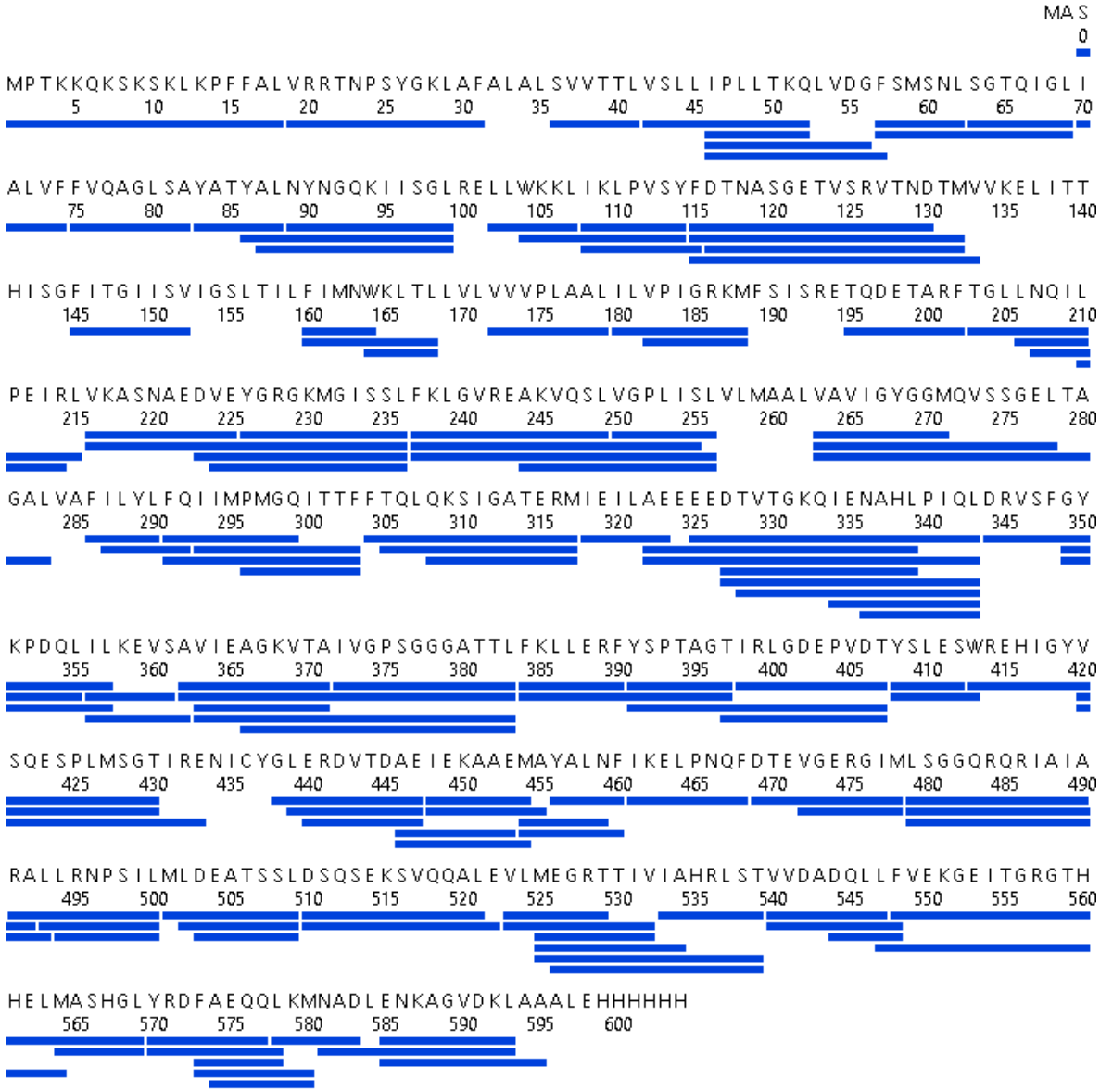

Total: 135 Peptides, 90,8% Coverage, 2,62 Redundancy

Annex 8. Sequence coverage map of K380A BmrA in nanodiscs (DDM/cholate). The blue bars represent the recovered peptides, mapped on the primary sequence of the protein. A 91 % final sequence coverage was achieved. Note that residues 29-309 constitute TMD and 341-576 form the NBD.

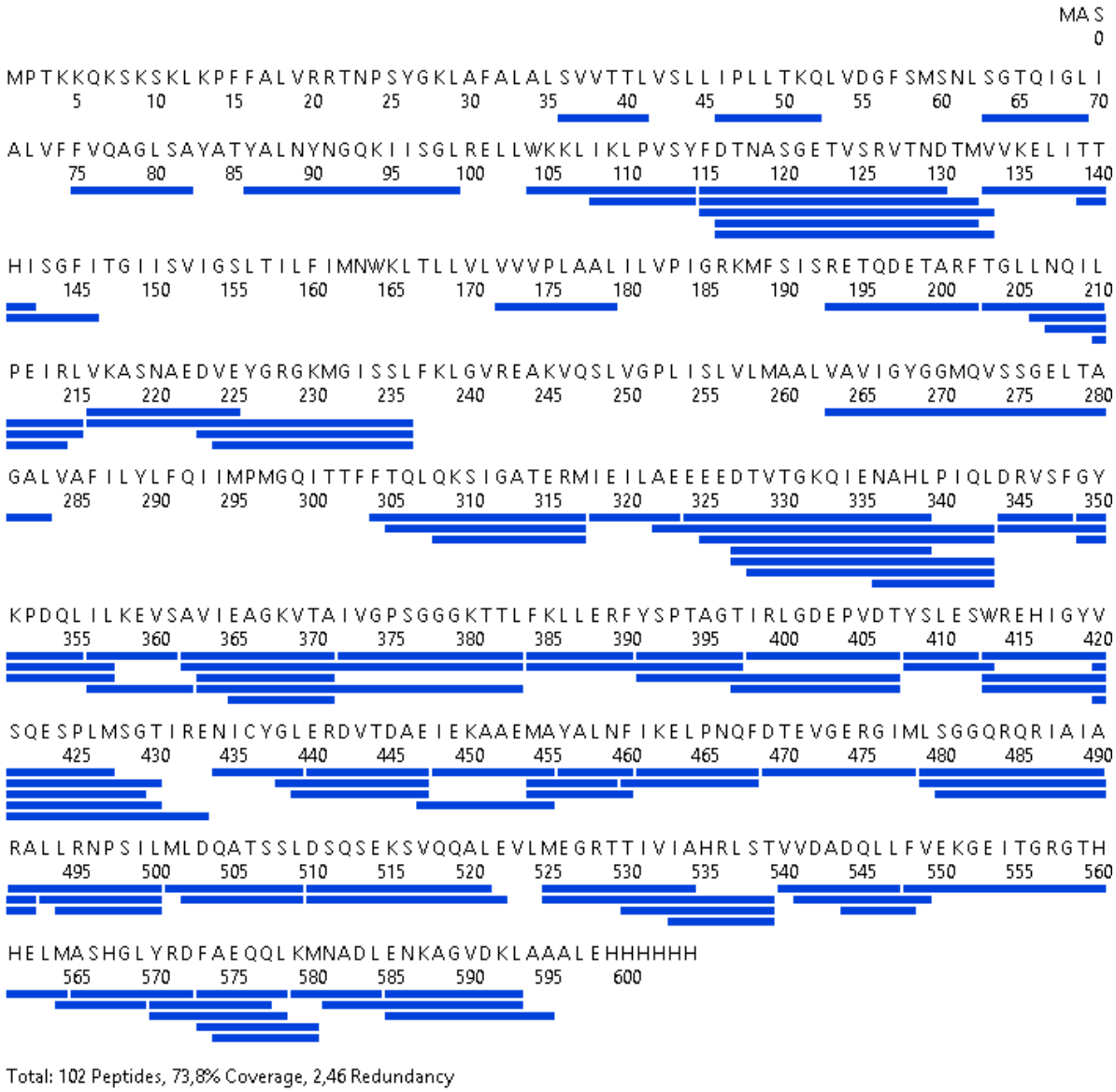

Annex 9. Sequence coverage map of E504Q BmrA in nanodiscs (DDM/cholate). The blue bars represent the recovered peptides, mapped on the primary sequence of the protein. A 74 % final sequence coverage was achieved. Note that residues 29-309 constitute TMD and 341-576 form the NBD.

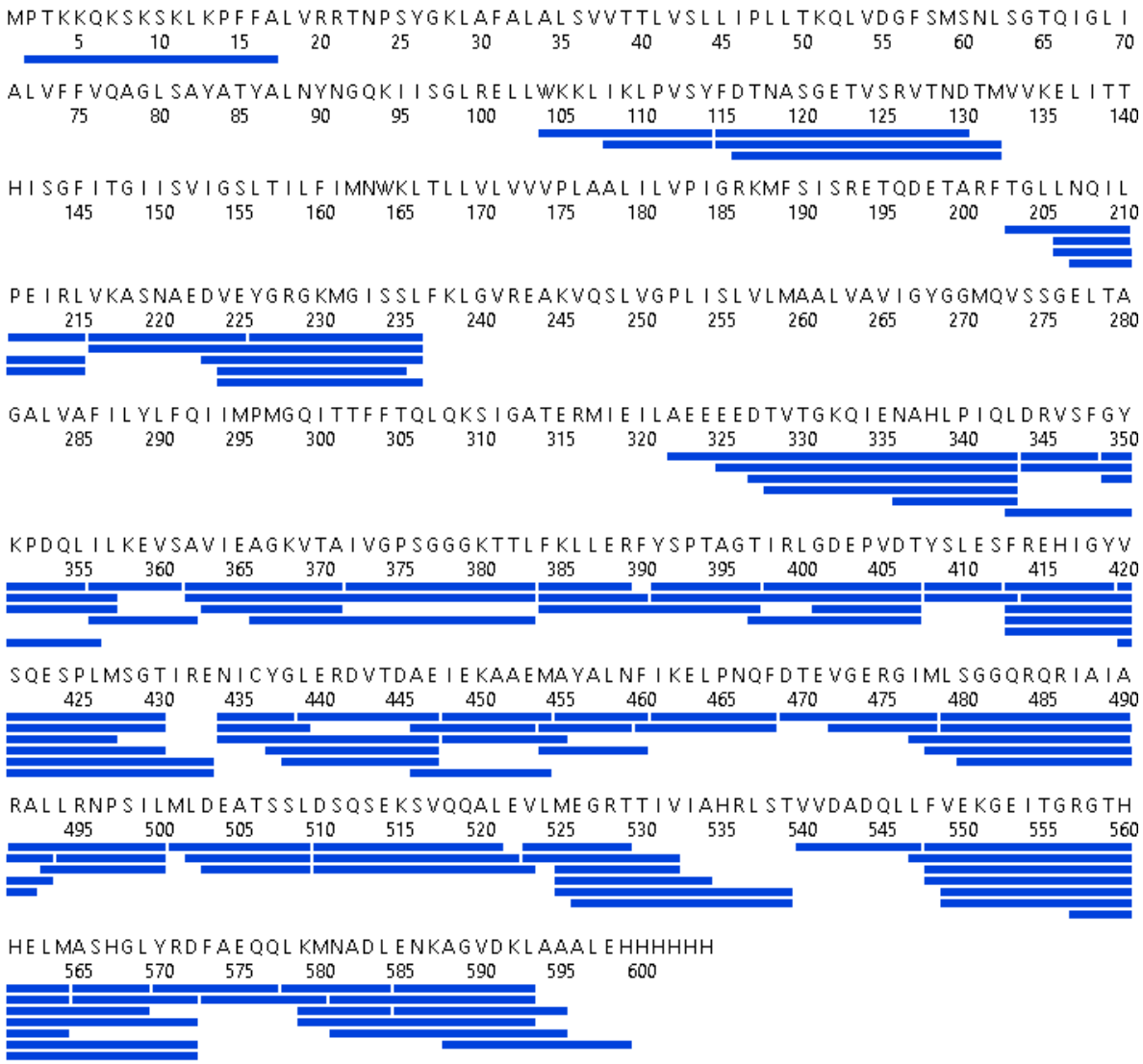

Total: 108 Peptides, 59,1% Coverage, 3,46 Redundancy

Annex 10. Sequence coverage map of W413F BmrA in nanodiscs (LMNG). The blue bars represent the recovered peptides, mapped on the primary sequence of the protein. A 59 % final sequence coverage was achieved. Note that residues 29-309 constitute TMD and 341-576 form the NBD.

Annex 11. Sequence coverage map of WT BmrA in IMVs. The blue bars represent the recovered peptides, mapped on the primary sequence of the protein. A 78 % final sequence coverage was achieved. Note that residues 29-309 constitute TMD and 341-576 form the NBD

Uptake Plots

Annex 12. Deuterium uptake plots of WT BmrA in LMNG in the Apo and Vi-trapped condition

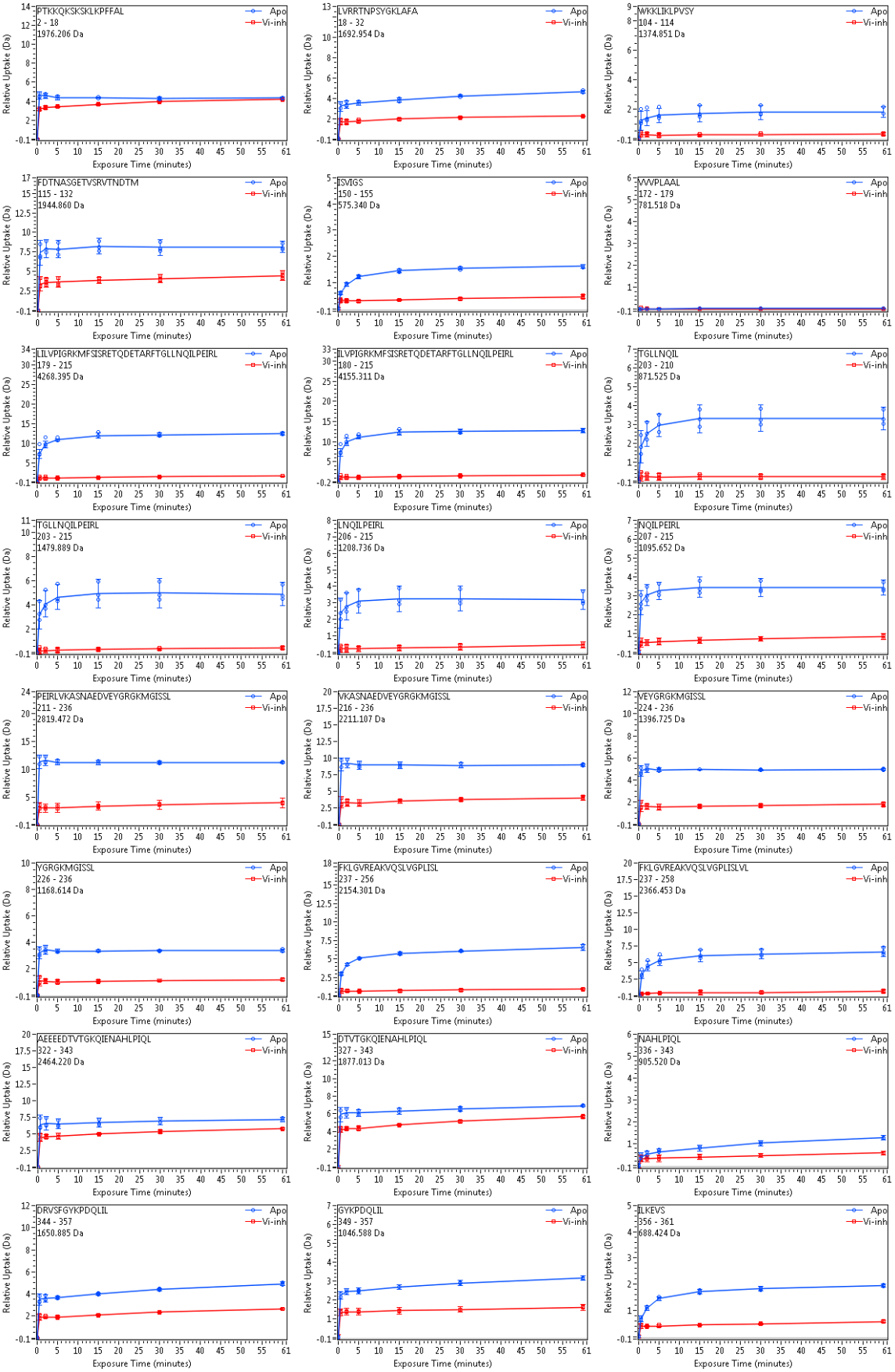

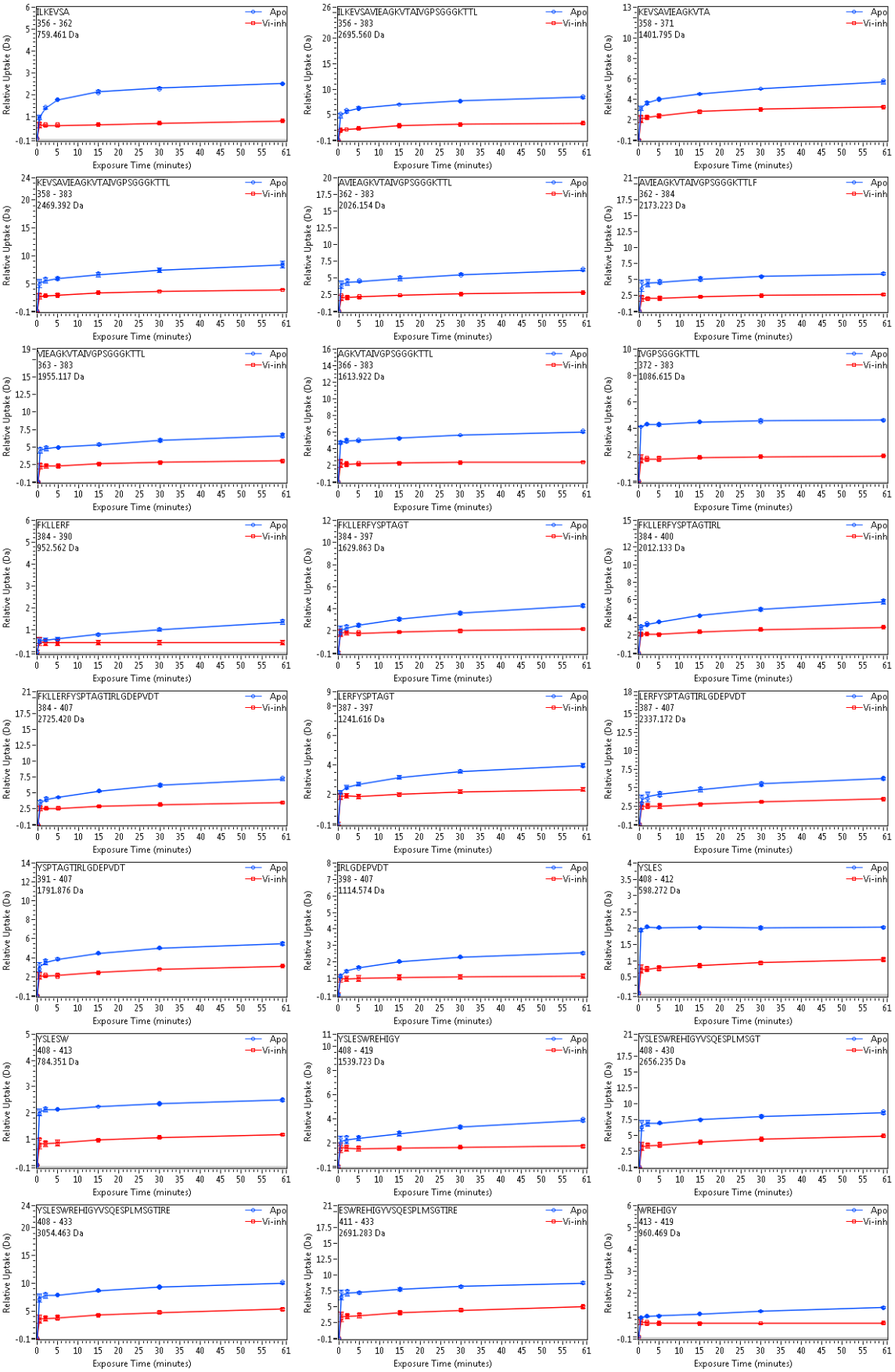
ILKEVSA
356 - 362
759.461 Da
ILKEVSAVIEAGKVTAIVGPSGGGKTTL
356 - 383
2695.560 Da
KEVSAVIEAGKVTA
358 - 371
1401.795 Da
KEVSAVIEAGKVTAIVGPSGGGKTTL
358 - 383
2469.392 Da
AVIEAGKVTAIVGPSGGGKTTL
362 - 383
2026.154 Da
AVIEAGKVTAIVGPSGGGKTTLF
362 - 384
2173.223 Da
VIEAGKVTAIVGPSGGGKTTL
363 - 383
1955.117 Da
AGKVTAIVGPSGGGKTTL
366 - 383
1613.922 Da
IVGPSGGGKTTL
372 - 383
1086.615 Da
FKLLERF
384 - 390
952.562 Da
FKLLERFYSPTAGT
384 - 397
1629.863 Da
FKLLERFYSPTAGTIRL
384 - 400
2012.133 Da
FKLLERFYSPTAGTIRLGDEPVDT
384 - 407
2725.420 Da
LERFYSPTAGT
387 - 397
1241.616 Da
LERFYSPTAGTIRLGDEPVDT
387 - 407
2337.172 Da
YSPTAGTIRLGDEPVDT
391 - 407
1791.876 Da
IRLGDEPVDT
398 - 407
1114.574 Da
YSLES
408 - 412
598.272 Da
YSLESW
408 - 413
784.351 Da
YSLESWREHIGY
408 - 419
1539.723 Da
YSLESWREHIGYVSQESPLMSGT
408 - 430
2656.235 Da
YSLESWREHIGYVSQESPLMSGTIRE
408 - 433
3054.463 Da
ESWREHIGYVSQESPLMSGTIRE
411 - 433
2691.283 Da
WREHIGY
413 - 419
960.469 Da
Apo
Vi-inh
Relative Uptake (Da)
Exposure Time (minutes)

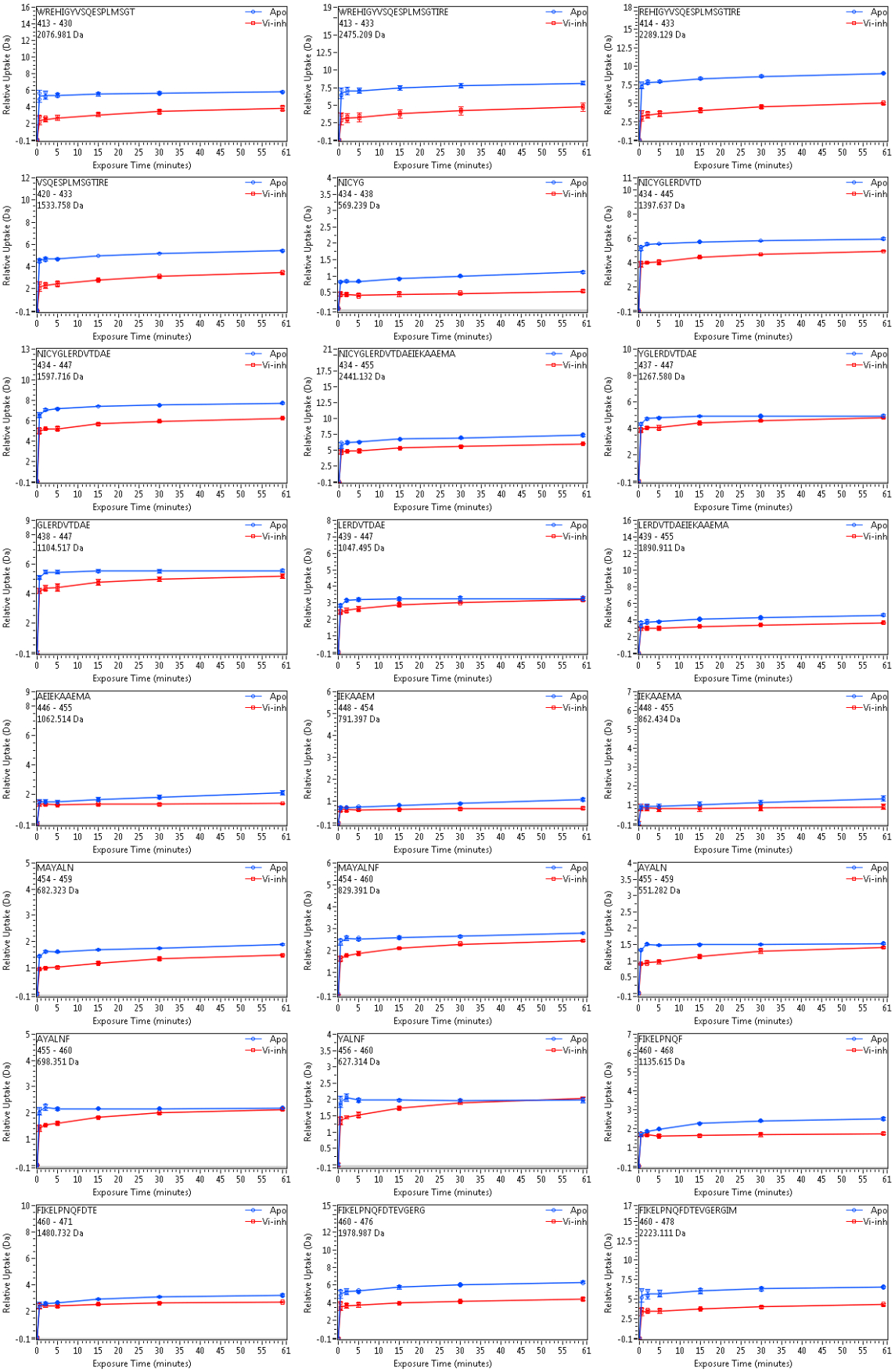
WREHIGYVSQESPLMSGT
413 - 430
2076.981 Da
WREHIGYVSQESPLMSGTIRE
413 - 433
2475.209 Da
REHIGYVSQESPLMSGTIRE
414 - 433
2289.129 Da
VSQESPLMSGTIRE
420 - 433
1533.758 Da
NICYG
434 - 438
569.239 Da
NICYGLERDVTD
434 - 445
1397.637 Da
NICYGLERDVTDAE
434 - 447
1597.716 Da
NICYGLERDVTDAEIEKAAEMA
434 - 455
2441.132 Da
YGLERDVTDAE
437 - 447
1267.580 Da
GLERDVTDAE
438 - 447
1104.517 Da
LERDVTDAE
439 - 447
1047.495 Da
LERDVTDAEIEKAAEMA
439 - 455
1890.911 Da
AEIEKAAEMA
446 - 455
1062.514 Da
IEKAAEM
448 - 454
791.397 Da
IEKAAEMA
448 - 455
862.434 Da
MAYALN
454 - 459
682.323 Da
MAYALNF
454 - 460
829.391 Da
AYALN
455 - 459
551.282 Da
AYALNF
455 - 460
698.351 Da
YALNF
456 - 460
627.314 Da
FIKELPNQF
460 - 468
1135.615 Da
FIKELPNQFDTE
460 - 471
1480.732 Da
FIKELPNQFDTEVGERG
460 - 476
1978.987 Da
FIKELPNQFDTEVGERGIM
460 - 478
2223.111 Da
Apo
Vi-inh
Relative Uptake (Da)
Exposure Time (minutes)

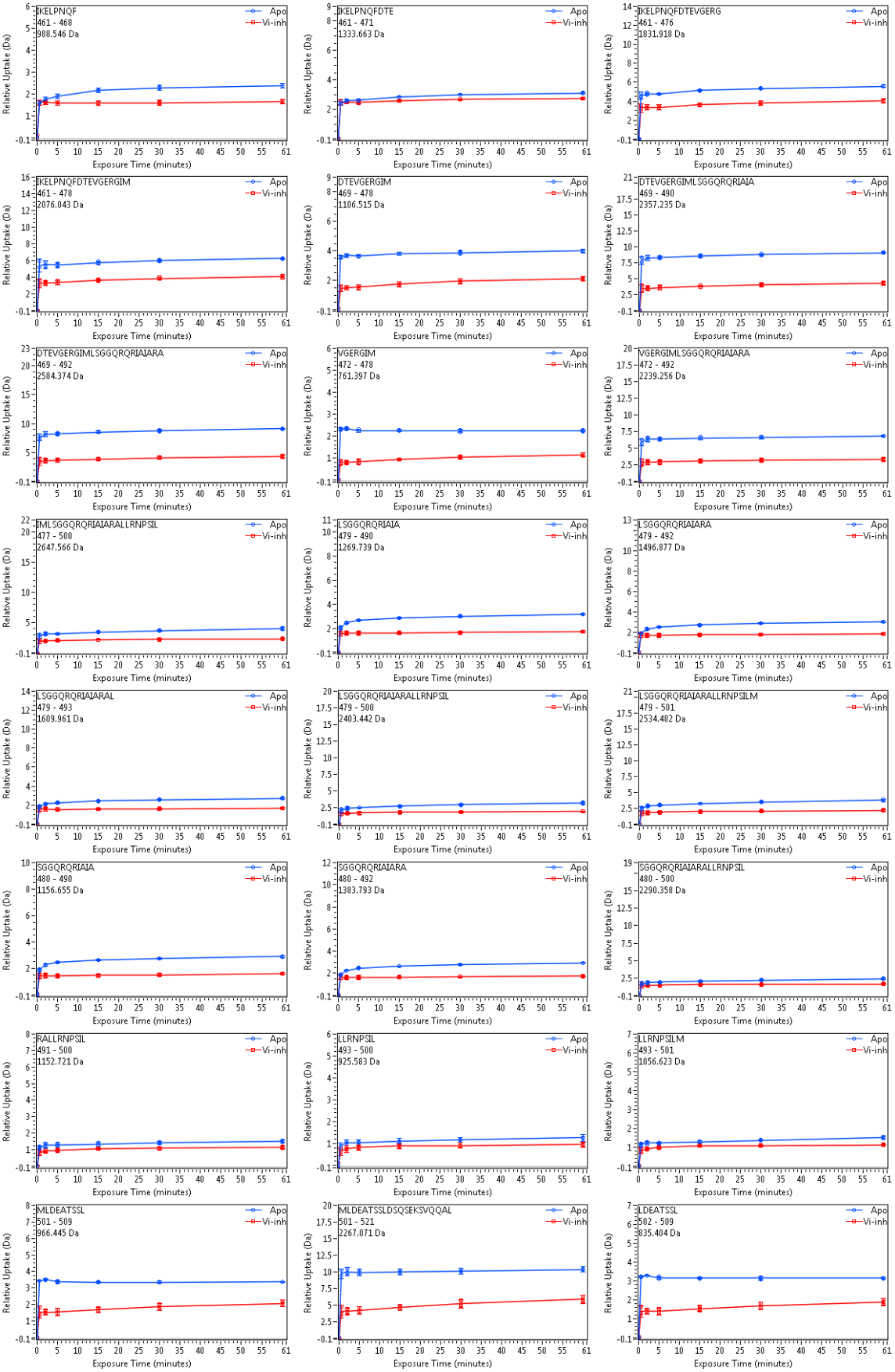
IKELPNQF
461 - 468
988.546 Da
IKELPNQFDTE
461 - 471
1333.663 Da
IKELPNQFDTEVGERG
461 - 476
1831.918 Da
IKELPNQFDTEVGERGIM
461 - 478
2076.043 Da
DTEVGERGIM
469 - 478
1106.515 Da
DTEVGERGIMLSGGQRQRIAIA
469 - 490
2357.235 Da
DTEVGERGIMLSGGQRQRIAIARA
469 - 492
2584.374 Da
VGERGIM
472 - 478
761.397 Da
VGERGIMLSGGQRQRIAIARA
472 - 492
2239.256 Da
IMLSGGQRQRIAIARALLRNPSIL
477 - 500
2647.566 Da
LSGGQRQRIAIA
479 - 490
1269.739 Da
LSGGQRQRIAIARA
479 - 492
1496.877 Da
LSGGQRQRIAIARAL
479 - 493
1609.961 Da
LSGGQRQRIAIARALLRNPSIL
479 - 500
2403.442 Da
LSGGQRQRIAIARALLRNPSILM
479 - 501
2534.482 Da
SGGQRQRIAIA
480 - 490
1156.655 Da
SGGQRQRIAIARA
480 - 492
1383.793 Da
SGGQRQRIAIARALLRNPSIL
480 - 500
2290.358 Da
RALLRNPSIL
491 - 500
1152.721 Da
LLRNPSIL
493 - 500
925.583 Da
LLRNPSILM
493 - 501
1056.623 Da
MLDEATSSL
501 - 509
966.445 Da
MLDEATSSLDSQSEKSVQQAL
501 - 521
2267.071 Da
LDEATSSL
502 - 509
835.404 Da
Apo
Vi-inh
Relative Uptake (Da)
Exposure Time (minutes)

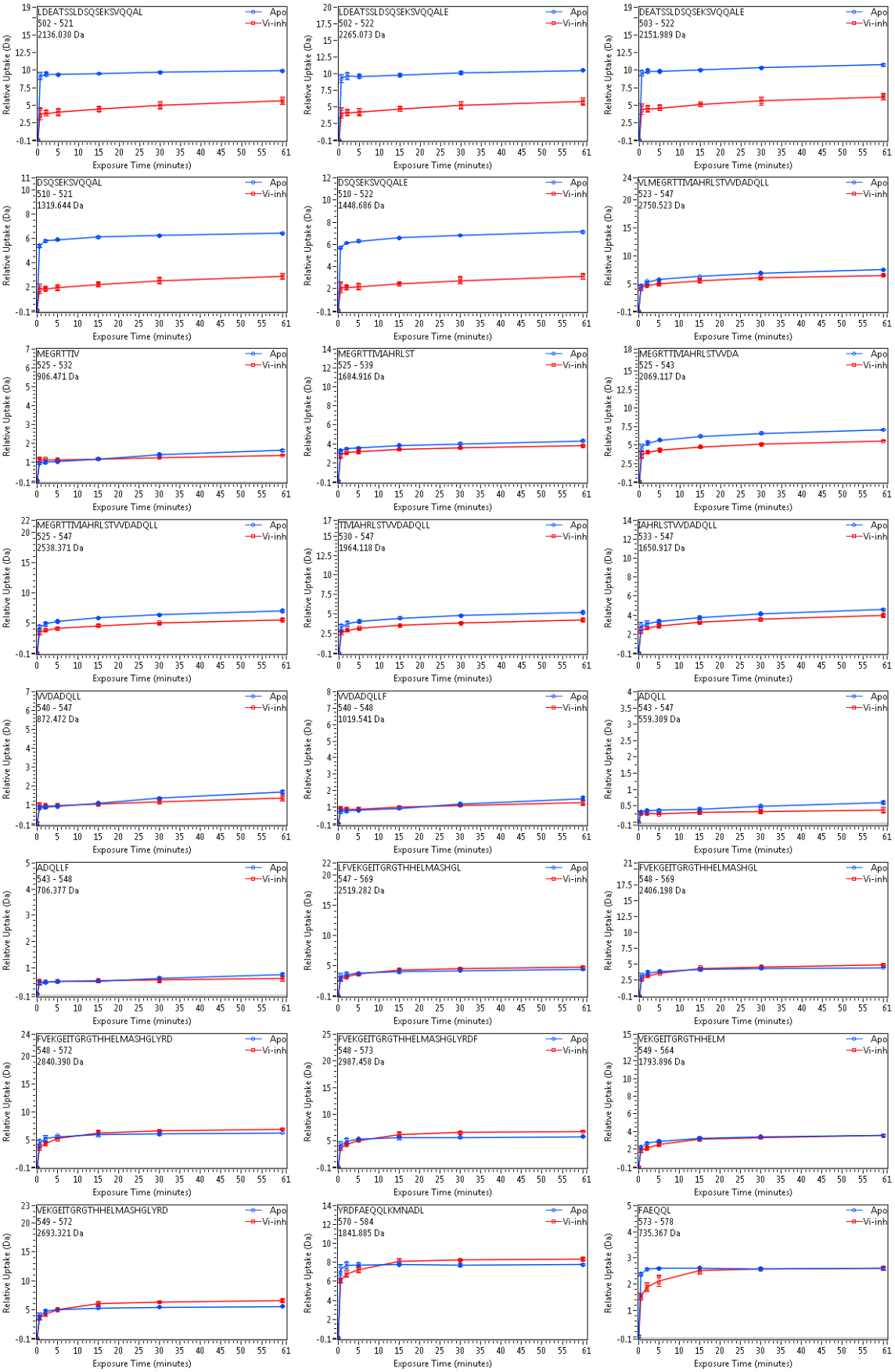
LDEATSSLDSQSEKSVQQAL
502 - 521
2136.030 Da
LDEATSSLDSQSEKSVQQALE
502 - 522
2265.073 Da
DEATSSLDSQSEKSVQQALE
503 - 522
2151.989 Da
DSQSEKSVQQAL
510 - 521
1319.644 Da
DSQSEKSVQQALE
510 - 522
1448.686 Da
VLMEGRTTTVIAHRLSTVVDADQLL
523 - 547
2750.523 Da
MEGRTTTV
525 - 532
906.471 Da
MEGRTTTVIAHRLST
525 - 539
1684.916 Da
MEGRTTTVIAHRLSTVVDA
525 - 543
2069.117 Da
MEGRTTTVIAHRLSTVVDADQLL
525 - 547
2538.371 Da
TTVIAHRLSTVVDADQLL
530 - 547
1964.118 Da
IAHRLSTVVDADQLL
533 - 547
1650.917 Da
VVDADQLL
540 - 547
872.472 Da
VVDADQLLF
540 - 548
1019.541 Da
ADQLL
543 - 547
559.309 Da
ADQLLF
543 - 548
706.377 Da
LFVEKGEITGRGTHHELMASHGL
547 - 569
2519.282 Da
FVEKGEITGRGTHHELMASHGL
548 - 569
2406.198 Da
FVEKGEITGRGTHHELMASHGLYRD
548 - 572
2840.390 Da
FVEKGEITGRGTHHELMASHGLYRDF
548 - 573
2987.458 Da
VEKGEITGRGTHHELM
549 - 564
1793.896 Da
VEKGEITGRGTHHELMASHGLYRD
549 - 572
2693.321 Da
YRDFAEQQLKMNADL
570 - 584
1841.885 Da
FAEQQL
573 - 578
735.367 Da
Apo
Vi-inh
Relative Uptake (Da)
Exposure Time (minutes)

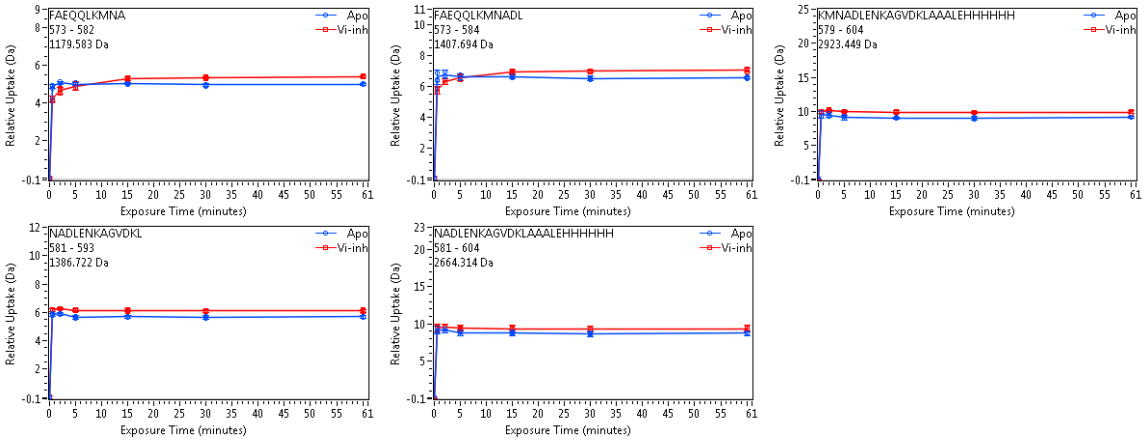
FAEQQLKMNA
573 - 582
1179.583 Da
Apo
Vi-inh
Relative Uptake (Da)
Exposure Time (minutes)
FAEQQLKMNADL
573 - 584
1407.694 Da
KMNADLENKAGVDKLAAALEHHHHHH
579 - 604
2923.449 Da
NADLENKAGVDKL
581 - 593
1386.722 Da
NADLENKAGVDKLAAALEHHHHHH
581 - 604
2664.314 Da

Annex 13 : Deuterium uptake plots of WT BmrA in nanodiscs (LMNG) in the Apo and Vi-trapped condition

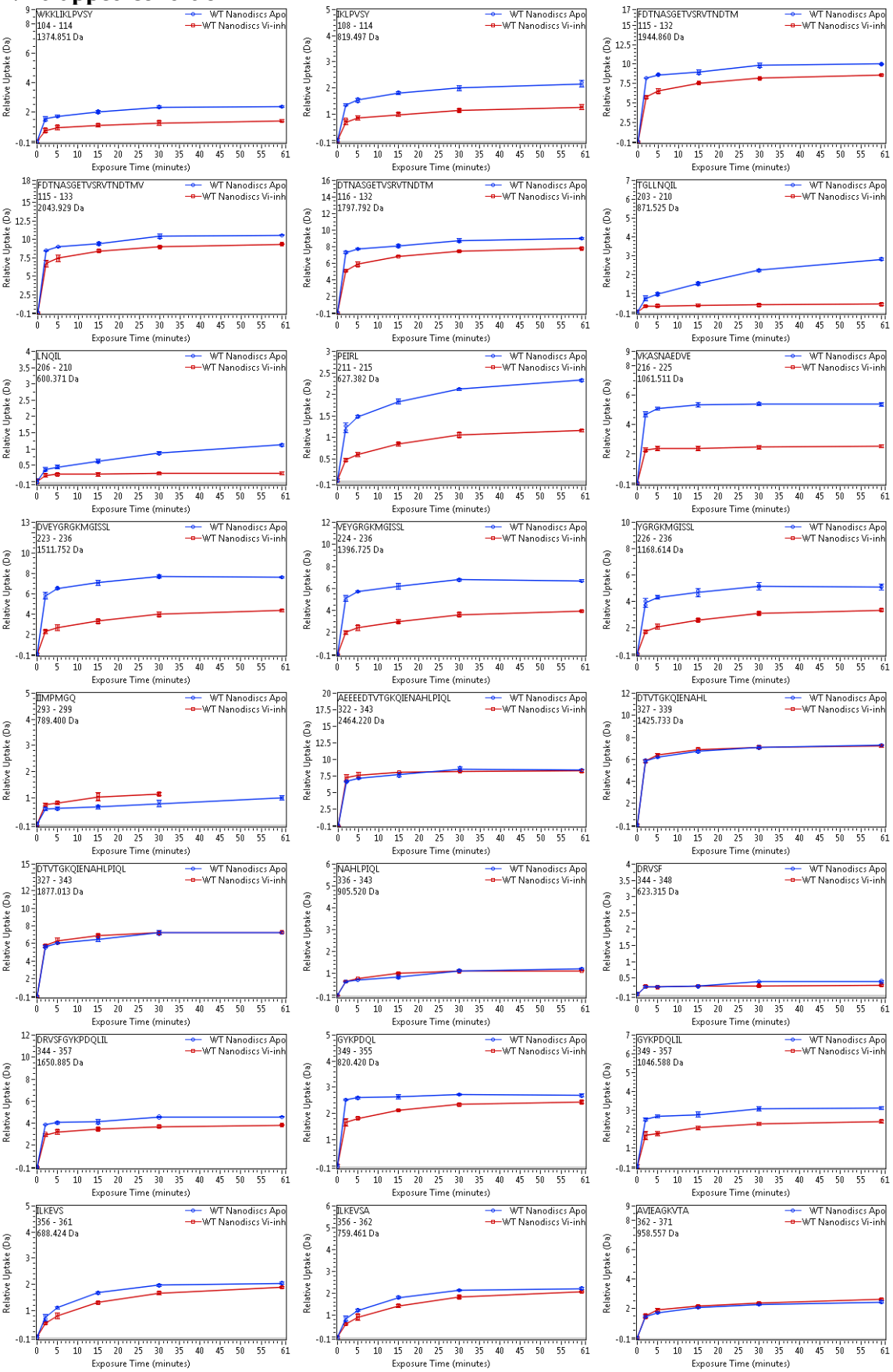

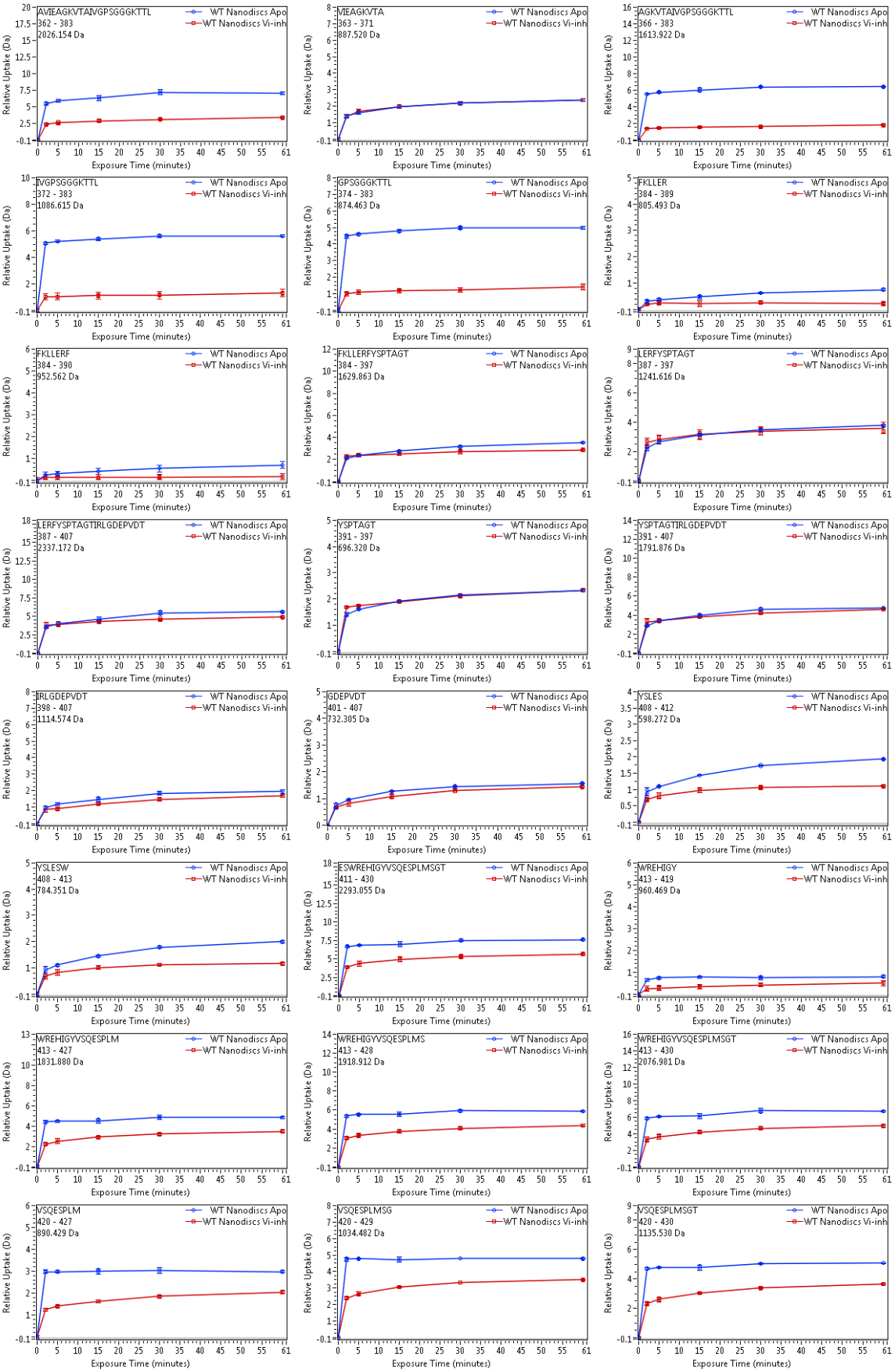
AVIEAGKVTAIVGPSGGGKTTL
362 - 383
2026.154 Da
VIEAGKVTA
363 - 371
887.520 Da
AGKVTAIVGPSGGGKTTL
366 - 383
1613.922 Da
IVGPSGGGKTTL
372 - 383
1086.615 Da
GPSGGGKTTL
374 - 383
874.463 Da
FKLLER
384 - 389
805.493 Da
FKLLERF
384 - 390
952.562 Da
FKLLERFYSPTAGT
384 - 397
1629.863 Da
LERFYSPTAGT
387 - 397
1241.616 Da
LERFYSPTAGTIRLGDEPVDT
387 - 407
2337.172 Da
YSPTAGT
391 - 397
696.320 Da
YSPTAGTIRLGDEPVDT
391 - 407
1791.876 Da
IRLGDEPVDT
398 - 407
1114.574 Da
GDEPVDT
401 - 407
732.305 Da
YSLES
408 - 412
598.272 Da
YSLESW
408 - 413
784.351 Da
ESWREHIGYVSQESPLMSGT
411 - 430
2293.055 Da
WREHIGY
413 - 419
960.469 Da
WREHIGYVSQESPLM
413 - 427
1831.880 Da
WREHIGYVSQESPLMS
413 - 428
1918.912 Da
WREHIGYVSQESPLMSGT
413 - 430
2076.981 Da
VSQESPLM
420 - 427
890.429 Da
VSQESPLMSG
420 - 429
1034.482 Da
VSQESPLMSGT
420 - 430
1135.530 Da
WT Nanodiscs Apo
WT Nanodiscs Vi-inh
Relative Uptake (Da)
Exposure Time (minutes)

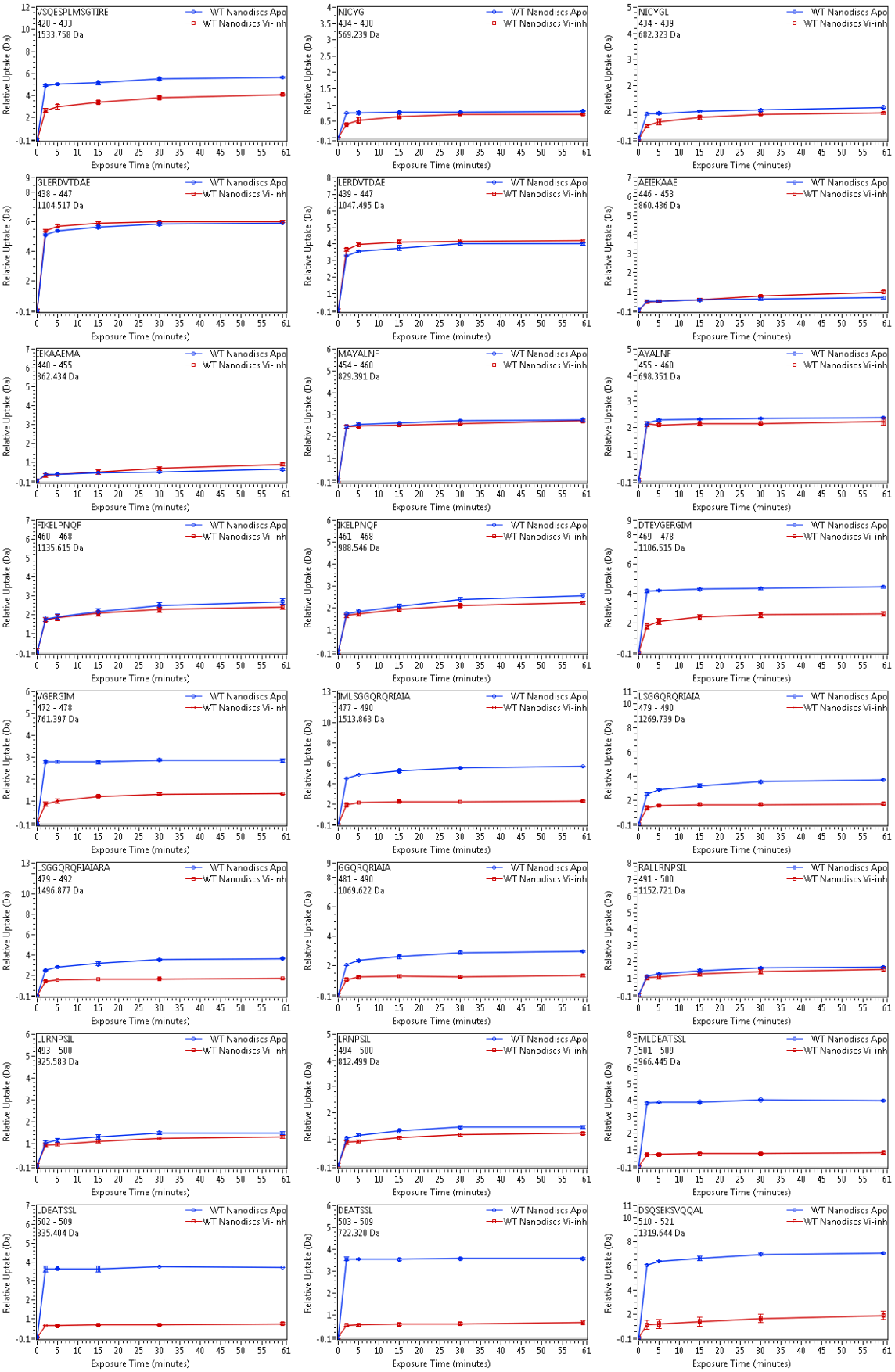
VSQESPLMSGTIRE
420 - 433
1533.758 Da
NICYG
434 - 438
569.239 Da
NICYGL
434 - 439
682.323 Da
GLERDVTDAE
438 - 447
1104.517 Da
LERDVTDAE
439 - 447
1047.495 Da
AEIEKAAE
446 - 453
860.436 Da
IEKAAEMA
448 - 455
862.434 Da
MAYALNF
454 - 460
829.391 Da
AYALNF
455 - 460
698.351 Da
FIKELPNQF
460 - 468
1135.615 Da
IKELPNQF
461 - 468
988.546 Da
DTEVGERGIM
469 - 478
1106.515 Da
VGERGIM
472 - 478
761.397 Da
MLSGGQRQRIAIA
477 - 490
1513.863 Da
LSGGQRQRIAIA
479 - 490
1269.739 Da
LSGGQRQRIAIARA
479 - 492
1496.877 Da
GGQRQRIAIA
481 - 490
1069.622 Da
RALLRNPSIL
491 - 500
1152.721 Da
LLRNPSIL
493 - 500
925.583 Da
LRNPSIL
494 - 500
812.499 Da
MLDEATSSL
501 - 509
966.445 Da
LDEATSSL
502 - 509
835.404 Da
DEATSSL
503 - 509
722.320 Da
DSQSEKSVQQAL
510 - 521
1319.644 Da
WT Nanodiscs Apo
WT Nanodiscs Vi-inh
Relative Uptake (Da)
Exposure Time (minutes)

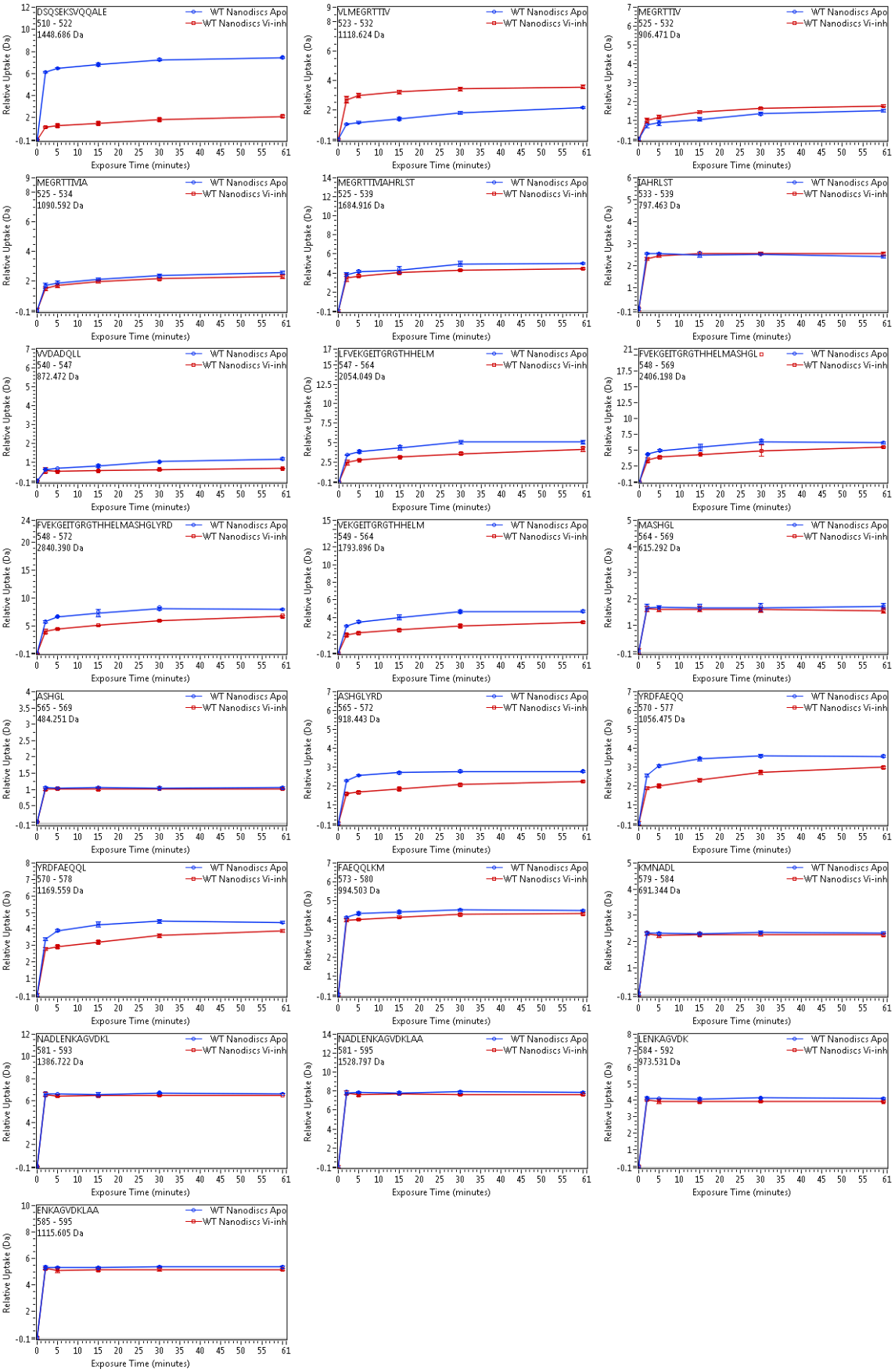
DSQSEKSVQQALE
510 - 522
1448.686 Da
VLMEGRTTIV
523 - 532
1118.624 Da
MEGRTTIV
525 - 532
906.471 Da
MEGRTTIVIA
525 - 534
1090.592 Da
MEGRTTIVIAHRLST
525 - 539
1684.916 Da
IAHRLST
533 - 539
797.463 Da
VVDADQLL
540 - 547
872.472 Da
LFVEKGEITGRGTHHELM
547 - 564
2054.049 Da
FVEKGEITGRGTHHELMASHGL
548 - 569
2406.198 Da
FVEKGEITGRGTHHELMASHGLYRD
548 - 572
2840.390 Da
VEKGEITGRGTHHELM
549 - 564
1793.896 Da
MASHGL
564 - 569
615.292 Da
ASHGL
565 - 569
484.251 Da
ASHGLYRD
565 - 572
918.443 Da
YRDFAEQQ
570 - 577
1056.475 Da
YRDFAEQQL
570 - 578
1169.559 Da
FAEQQLKM
573 - 580
994.503 Da
KMNADL
579 - 584
691.344 Da
NADLENKAGVDKL
581 - 593
1386.722 Da
NADLENKAGVDKLAA
581 - 595
1528.797 Da
LENKAGVDK
584 - 592
973.531 Da
ENKAGVDKLAA
585 - 595
1115.605 Da
WT Nanodiscs Apo
WT Nanodiscs Vi-inh
Relative Uptake (Da)
Exposure Time (minutes)

Annex 14 : Deuterium uptake plots of WT BmrA in nanodiscs (LMNG) in the Apo and doxorubicin-bound condition

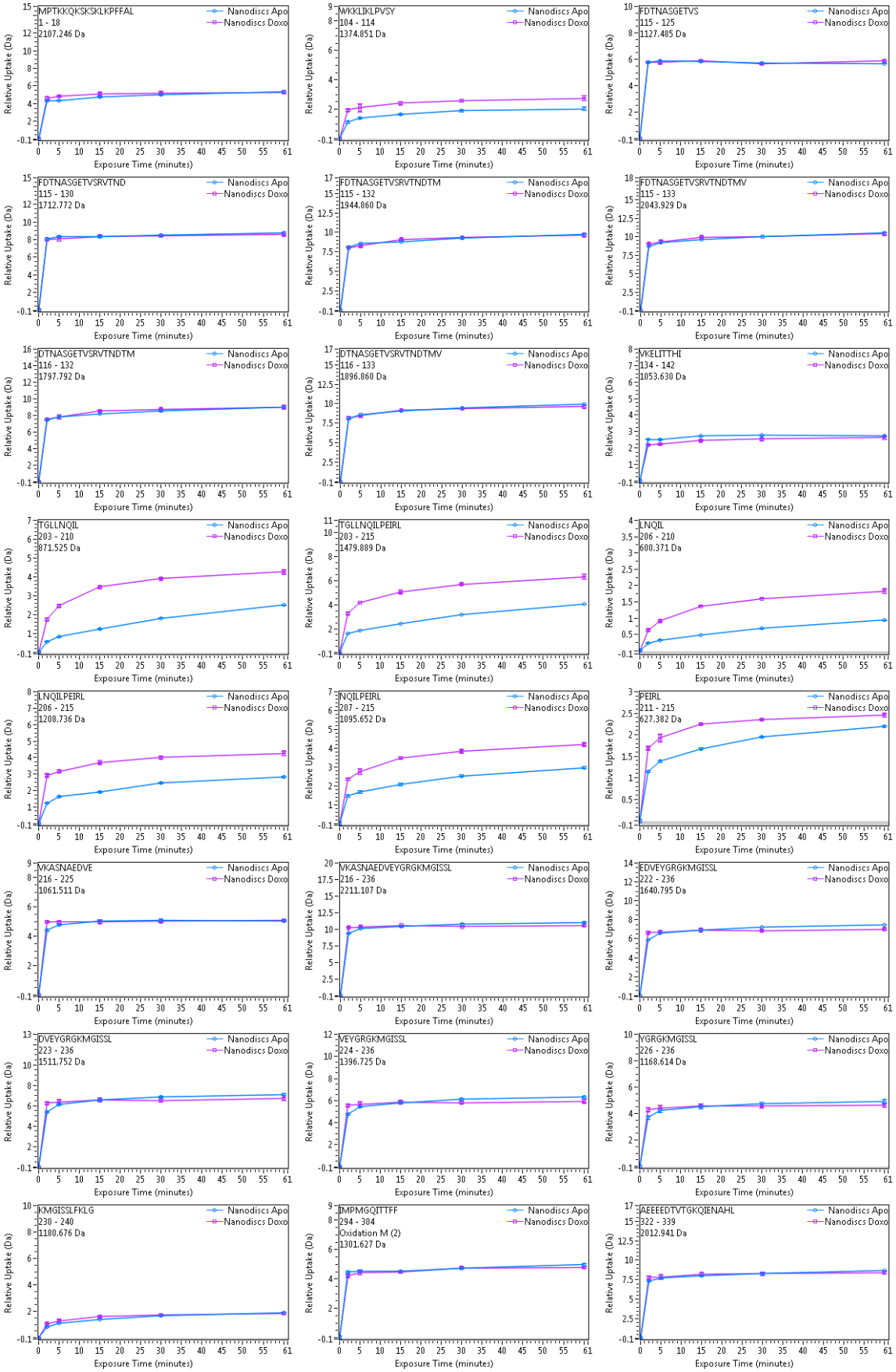

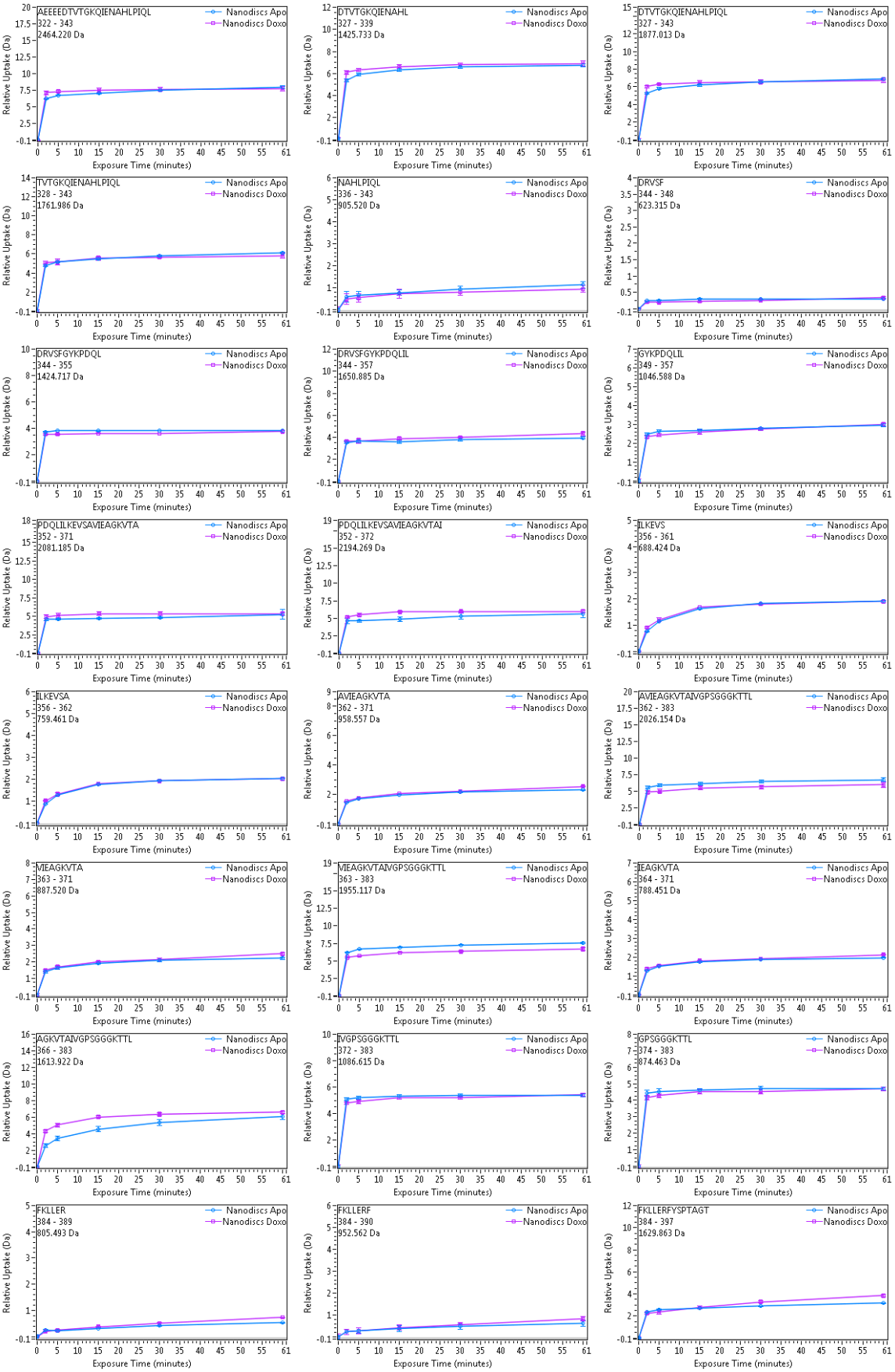
AEEEEDTVTGKQIENAHLPIQL
322 - 343
2464.220 Da
DTVTGKQIENAHL
327 - 339
1425.733 Da
DTVTGKQIENAHLPIQL
327 - 343
1877.013 Da
TVTGKQIENAHLPIQL
328 - 343
1761.986 Da
NAHLPIQL
336 - 343
905.520 Da
DRVSF
344 - 348
623.315 Da
DRVSFGYKPDQL
344 - 355
1424.717 Da
DRVSFGYKPDQLIL
344 - 357
1650.885 Da
GYKPDQLIL
349 - 357
1046.588 Da
PDQLILKEVSAVIEAGKVTA
352 - 371
2081.185 Da
PDQLILKEVSAVIEAGKVTAI
352 - 372
2194.269 Da
ILKEVS
356 - 361
688.424 Da
ILKEVSA
356 - 362
759.461 Da
AVIEAGKVTA
362 - 371
958.557 Da
AVIEAGKVTAIVGPSGGGKTTL
362 - 383
2026.154 Da
VIEAGKVTA
363 - 371
887.520 Da
VIEAGKVTAIVGPSGGGKTTL
363 - 383
1955.117 Da
IEAGKVTA
364 - 371
788.451 Da
AGKVTAIVGPSGGGKTTL
366 - 383
1613.922 Da
IVGPSGGGKTTL
372 - 383
1086.615 Da
GPSGGGKTTL
374 - 383
874.463 Da
FKLLER
384 - 389
805.493 Da
FKLLERF
384 - 390
952.562 Da
FKLLERFYSPTAGT
384 - 397
1629.863 Da
Nanodiscs Apo
Nanodiscs Doxo
Relative Uptake (Da)
Exposure Time (minutes)

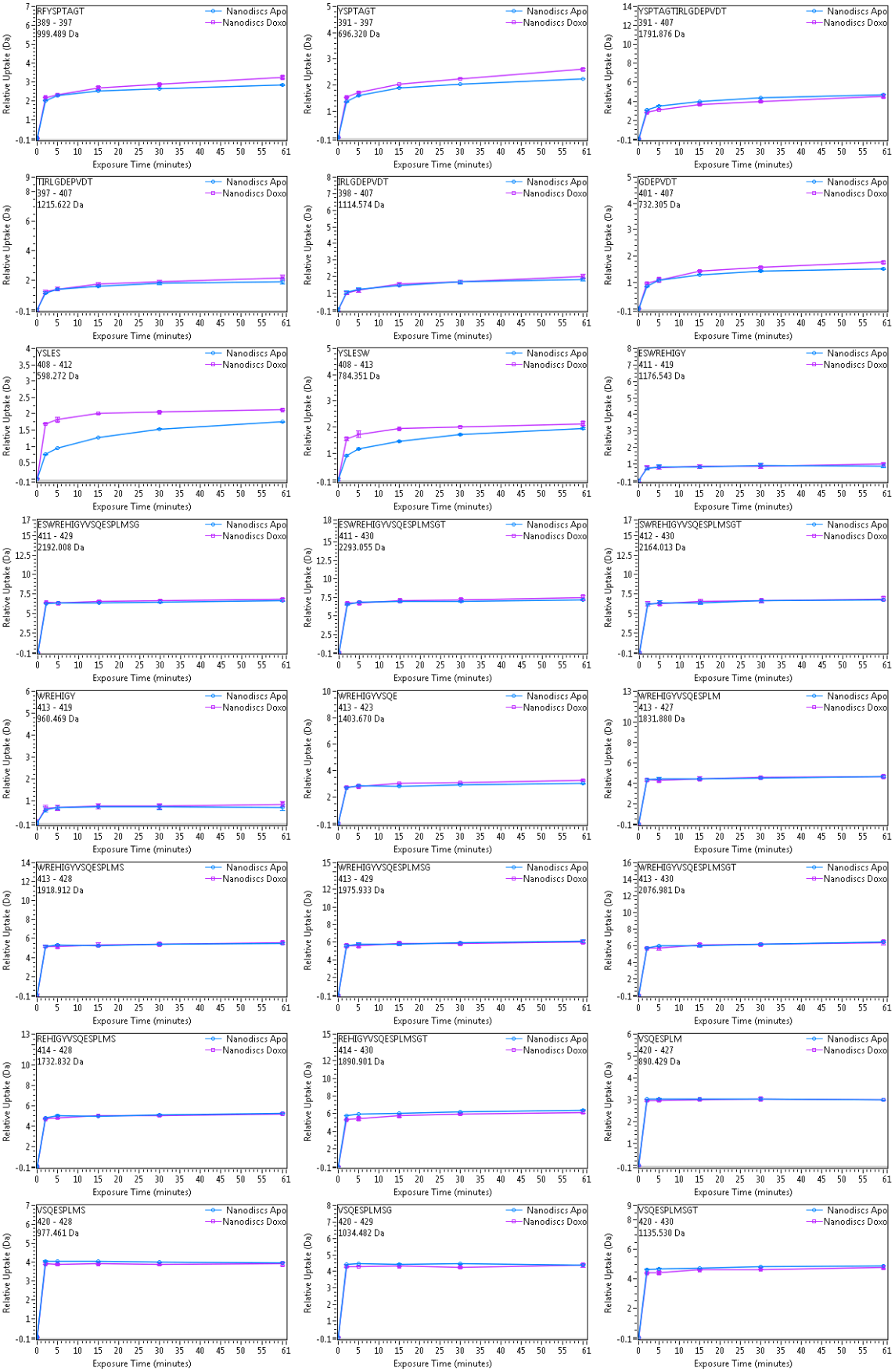
RFYSPTAGT
389 - 397
999.489 Da
YSPTAGT
391 - 397
696.320 Da
YSPTAGTIRLGDEPVDT
391 - 407
1791.876 Da
TIRLGDEPVDT
397 - 407
1215.622 Da
RLGDEPVDT
398 - 407
1114.574 Da
GDEPVDT
401 - 407
732.305 Da
YSLES
408 - 412
598.272 Da
YSLESW
408 - 413
784.351 Da
ESWREHIGY
411 - 419
1176.543 Da
ESWREHIGYVSQESPLMSG
411 - 429
2192.008 Da
ESWREHIGYVSQESPLMSGT
411 - 430
2293.055 Da
SWREHIGYVSQESPLMSGT
412 - 430
2164.013 Da
WREHIGY
413 - 419
960.469 Da
WREHIGYVSQE
413 - 423
1403.670 Da
WREHIGYVSQESPLM
413 - 427
1831.880 Da
WREHIGYVSQESPLMS
413 - 428
1918.912 Da
WREHIGYVSQESPLMSG
413 - 429
1975.933 Da
WREHIGYVSQESPLMSGT
413 - 430
2076.981 Da
REHIGYVSQESPLMS
414 - 428
1732.832 Da
REHIGYVSQESPLMSGT
414 - 430
1890.901 Da
VSQESPLM
420 - 427
890.429 Da
VSQESPLMS
420 - 428
977.461 Da
VSQESPLMSG
420 - 429
1034.482 Da
VSQESPLMSGT
420 - 430
1135.530 Da
Nanodiscs Apo
Nanodiscs Doxo
Relative Uptake (Da)
Exposure Time (minutes)

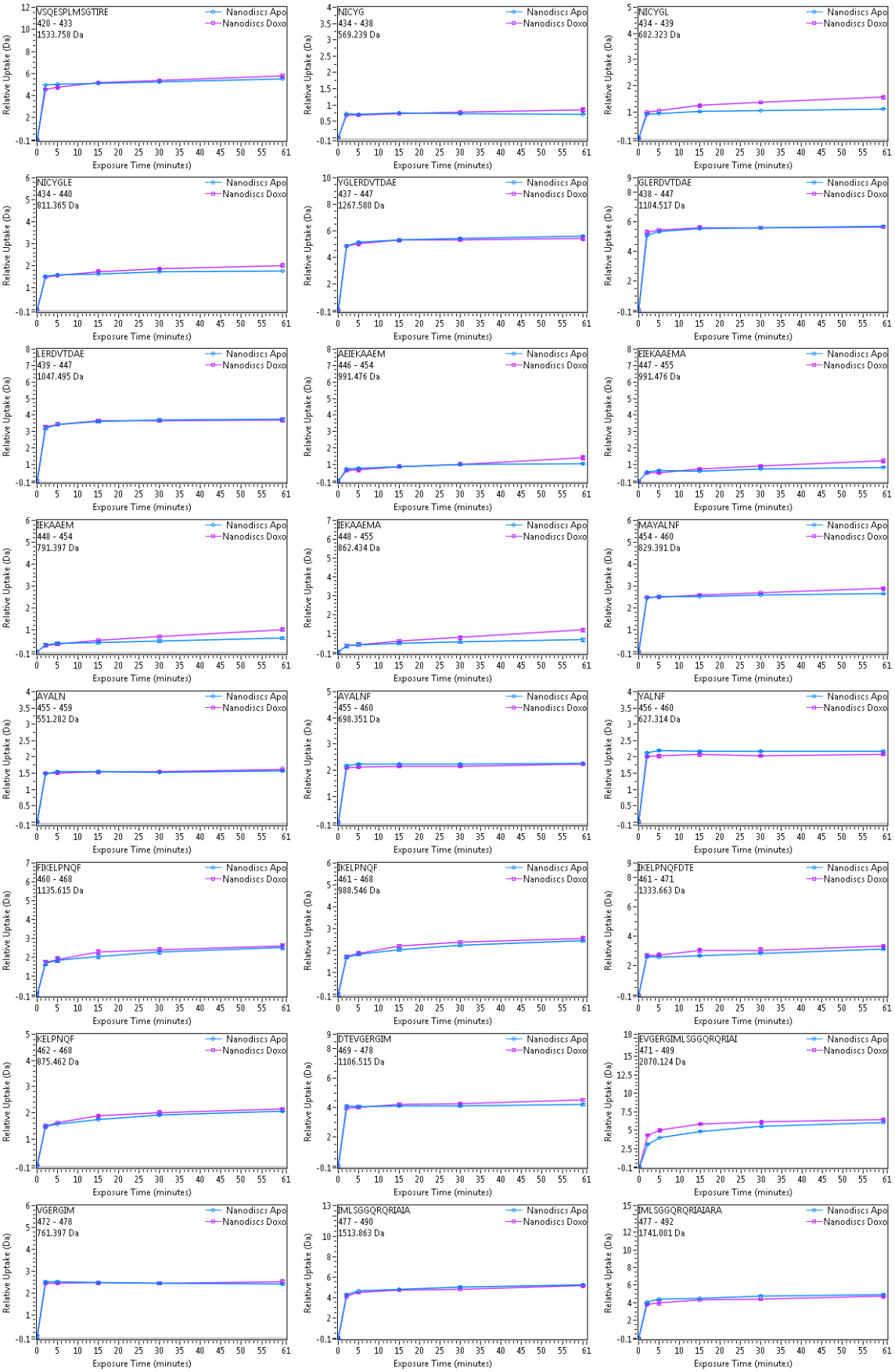
VSQESPLMSGTIRE
420 - 433
1533.758 Da
NICYG
434 - 438
569.239 Da
NICYGL
434 - 439
682.323 Da
NICYGLE
434 - 440
811.365 Da
YGLERDVTDAE
437 - 447
1267.580 Da
GLERDVTDAE
438 - 447
1104.517 Da
LERDVTDAE
439 - 447
1047.495 Da
AEIEKAAEM
446 - 454
991.476 Da
EIEKAAEMA
447 - 455
991.476 Da
IEKAAEM
448 - 454
791.397 Da
IEKAAEMA
448 - 455
862.434 Da
MAYALNF
454 - 460
829.391 Da
AYALN
455 - 459
551.282 Da
AYALNF
455 - 460
698.351 Da
YALNF
456 - 460
627.314 Da
FIKELPNQF
460 - 468
1135.615 Da
IKELPNQF
461 - 468
988.546 Da
IKELPNQFDTE
461 - 471
1333.663 Da
KELPNQF
462 - 468
875.462 Da
DTEVGERGIM
469 - 478
1106.515 Da
EVGERGIMLSGGQRQRIAI
471 - 489
2070.124 Da
VGERGIM
472 - 478
761.397 Da
IMLSGGQRQRIAIA
477 - 490
1513.863 Da
IMLSGGQRQRIAIARA
477 - 492
1741.001 Da
Nanodiscs Apo
Nanodiscs Doxo
Relative Uptake (Da)
Exposure Time (minutes)

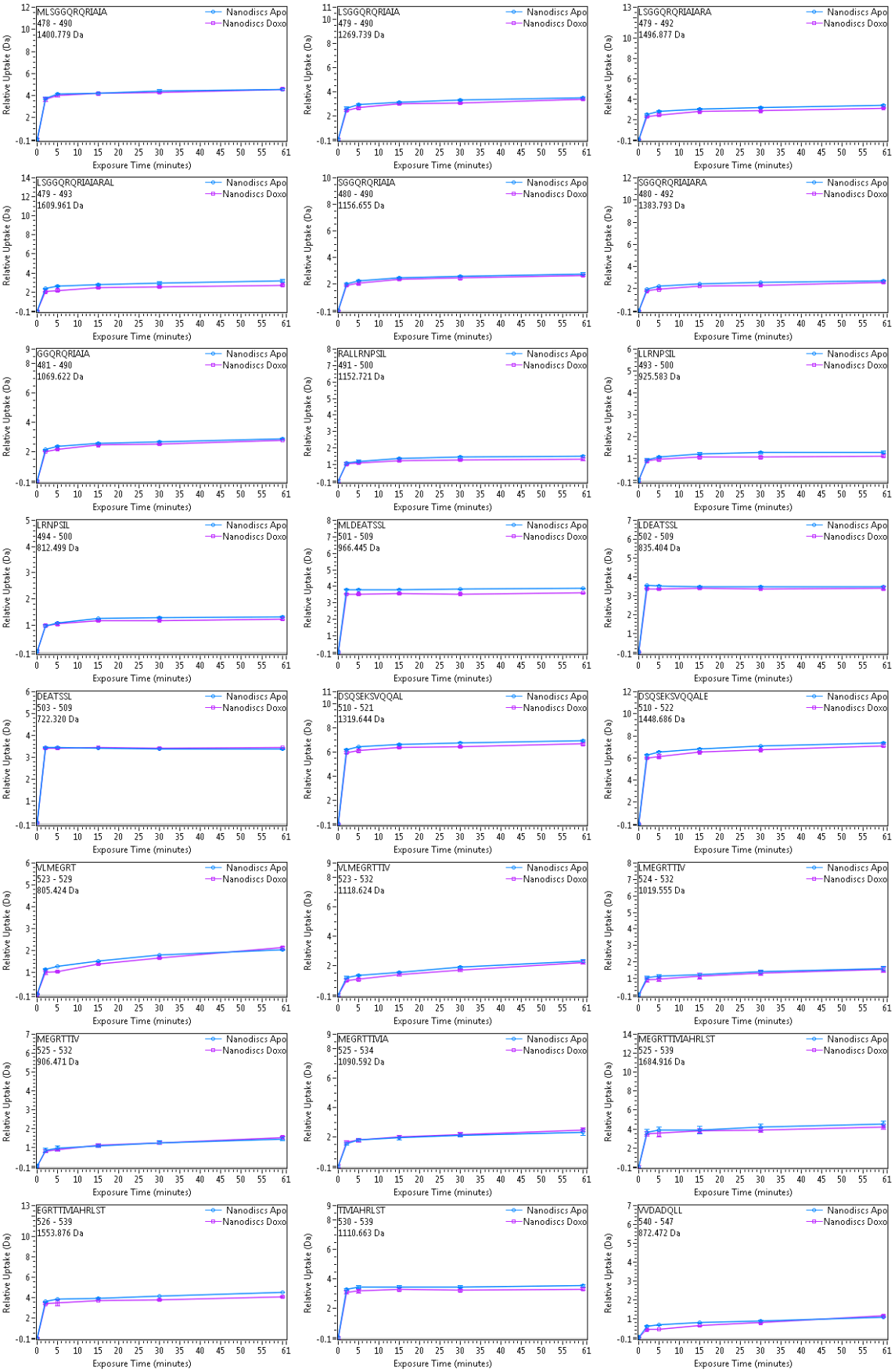
MLSGGQRQRIAIA
478 - 490
1400.779 Da
LSGGQRQRIAIA
479 - 490
1269.739 Da
LSGGQRQRIAIARA
479 - 492
1496.877 Da
LSGGQRQRIAIARAL
479 - 493
1609.961 Da
SGGQRQRIAIA
480 - 490
1156.655 Da
SGGQRQRIAIARA
480 - 492
1383.793 Da
GGQRQRIAIA
481 - 490
1069.622 Da
RALLRNPSIL
491 - 500
1152.721 Da
LLRNPSIL
493 - 500
925.583 Da
LRNPSIL
494 - 500
812.499 Da
MLDEATSSL
501 - 509
966.445 Da
LDEATSSL
502 - 509
835.404 Da
DEATSSL
503 - 509
722.320 Da
DSQSEKSVQQAL
510 - 521
1319.644 Da
DSQSEKSVQQALE
510 - 522
1448.686 Da
VLMEGRT
523 - 529
805.424 Da
VLMEGRTTIV
523 - 532
1118.624 Da
LMEGRTTIV
524 - 532
1019.555 Da
MEGRTTIV
525 - 532
906.471 Da
MEGRTTIVIA
525 - 534
1090.592 Da
MEGRTTIVIAHRLST
525 - 539
1684.916 Da
EGRTTIVIAHRLST
526 - 539
1553.876 Da
TIVIAHRLST
530 - 539
1110.663 Da
VVDADQLL
540 - 547
872.472 Da
Nanodiscs Apo
Nanodiscs Doxo
Relative Uptake (Da)
Exposure Time (minutes)

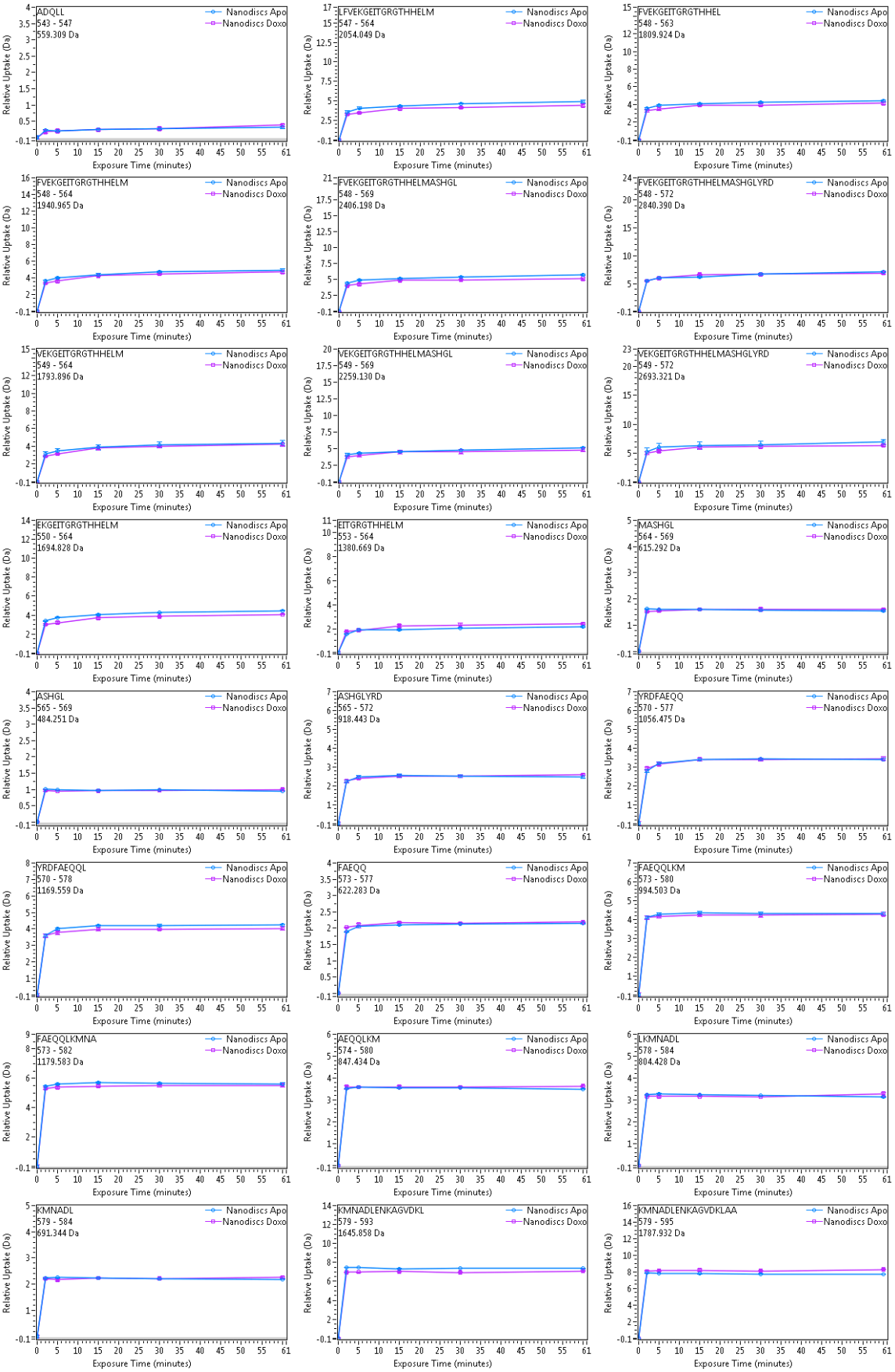
ADQLL
543 - 547
559.309 Da
LFVEKGEITGRGTHHELM
547 - 564
2054.049 Da
FVEKGEITGRGTHHEL
548 - 563
1809.924 Da
FVEKGEITGRGTHHELM
548 - 564
1940.965 Da
FVEKGEITGRGTHHELMASHGL
548 - 569
2406.198 Da
FVEKGEITGRGTHHELMASHGLYRD
548 - 572
2840.390 Da
VEKGEITGRGTHHELM
549 - 564
1793.896 Da
VEKGEITGRGTHHELMASHGL
549 - 569
2259.130 Da
VEKGEITGRGTHHELMASHGLYRD
549 - 572
2693.321 Da
EKGEITGRGTHHELM
550 - 564
1694.828 Da
EITGRGTHHELM
553 - 564
1380.669 Da
MASHGL
564 - 569
615.292 Da
ASHGL
565 - 569
484.251 Da
ASHGLYRD
565 - 572
918.443 Da
YRDFAEQQ
570 - 577
1056.475 Da
YRDFAEQQL
570 - 578
1169.559 Da
FAEQQ
573 - 577
622.283 Da
FAEQQLKM
573 - 580
994.503 Da
FAEQQLKMNA
573 - 582
1179.583 Da
AEQQLKM
574 - 580
847.434 Da
LKMNADL
578 - 584
804.428 Da
KMNADL
579 - 584
691.344 Da
KMNADLENKAGVDKL
579 - 593
1645.858 Da
KMNADLENKAGVDKLAA
579 - 595
1787.932 Da
Nanodiscs Apo
Nanodiscs Doxo
Relative Uptake (Da)
Exposure Time (minutes)

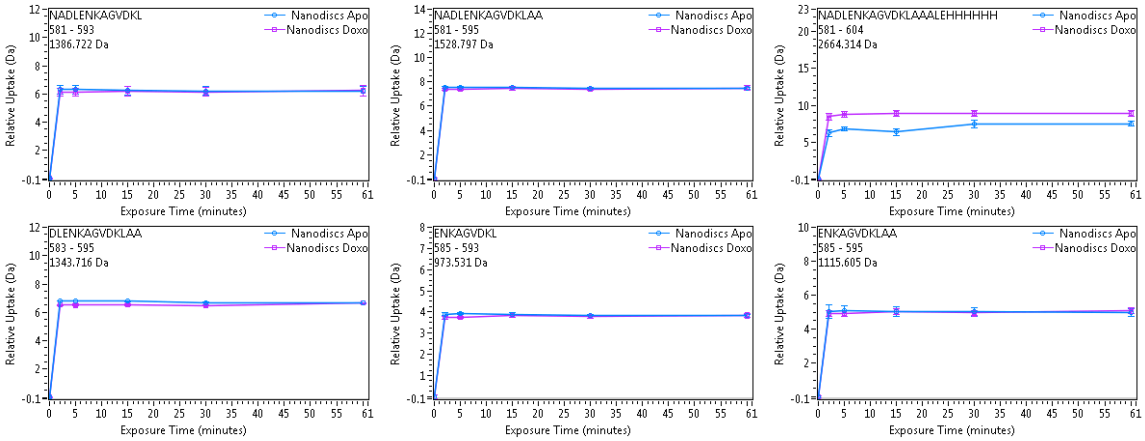
NADLENKAGVDKL
581 - 593
1386.722 Da
Nanodiscs Apo
Nanodiscs Doxo
Relative Uptake (Da)
Exposure Time (minutes)
NADLENKAGVDKLAA
581 - 595
1528.797 Da
NADLENKAGVDKLAAALEHHHHHH
581 - 604
2664.314 Da
DLENKAGVDKLAA
583 - 595
1343.716 Da
ENKAGVDKL
585 - 593
973.531 Da
ENKAGVDKLAA
585 - 595
1115.605 Da

Annex 15 : Deuterium uptake plots of WT BmrA in nanodiscs (DDM/cholate) in the Apo and Vi-trapped condition

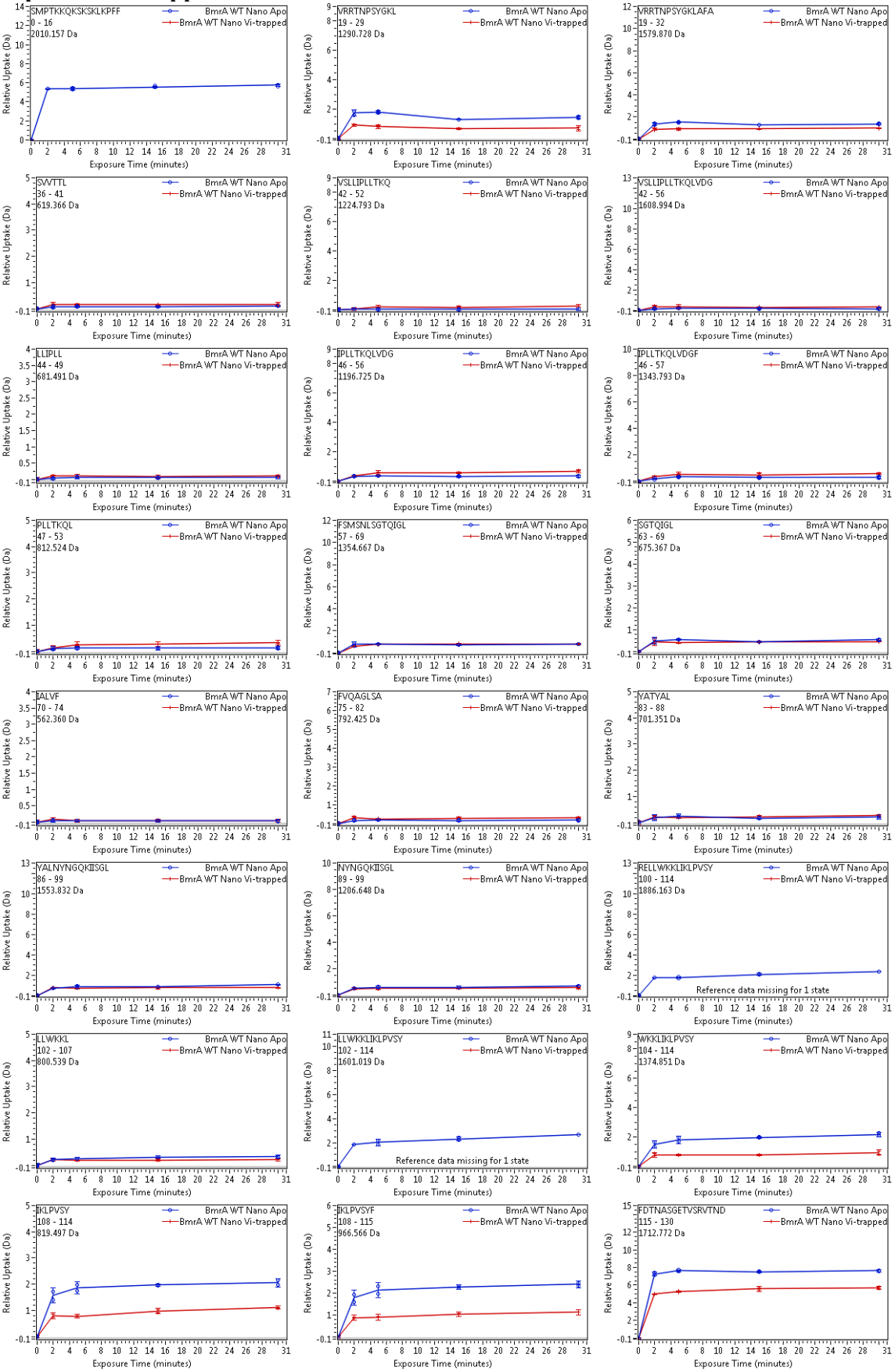

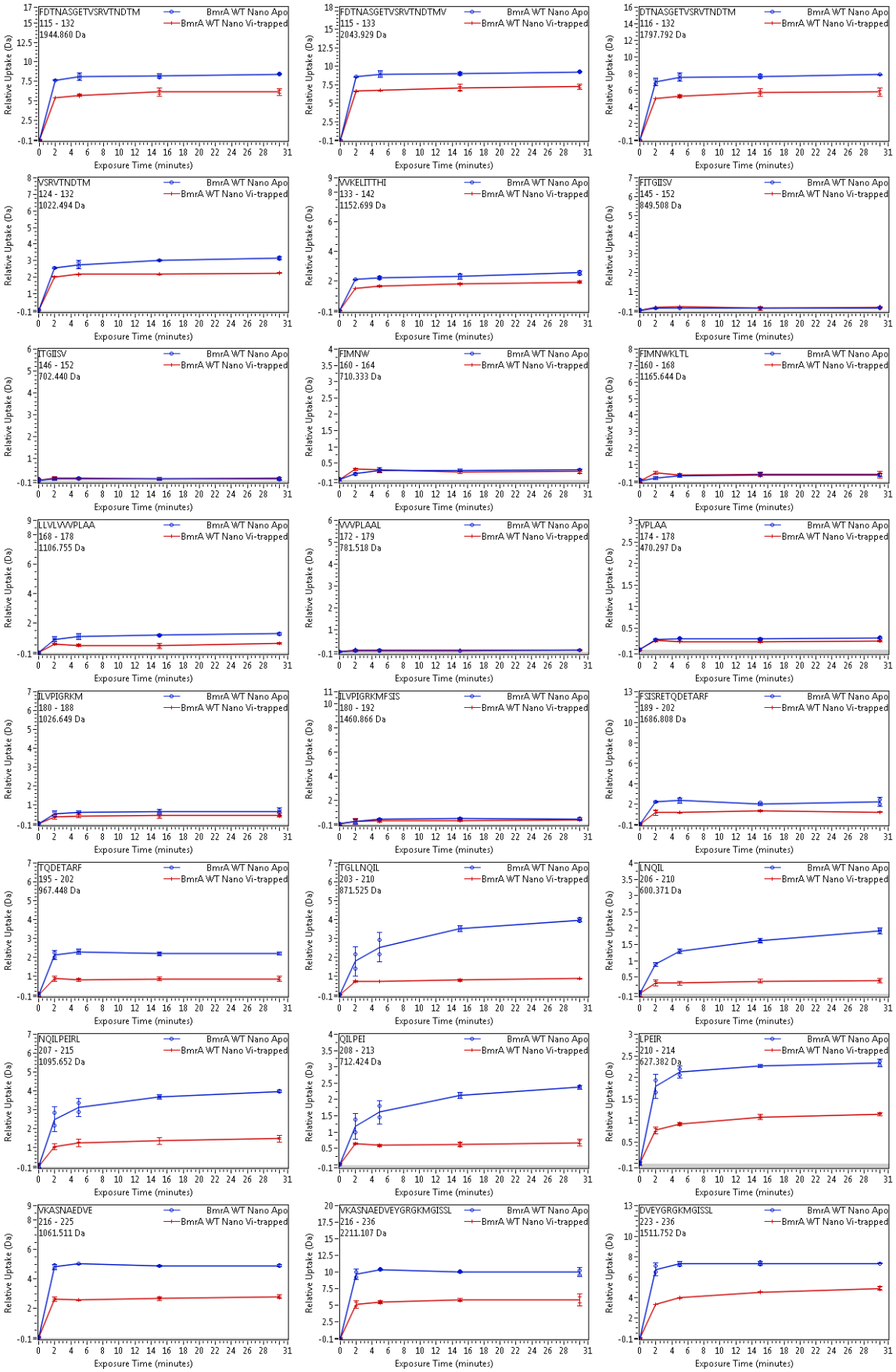
FDTNASGETVSRVTNDTM
115 - 132
1944.860 Da
FDTNASGETVSRVTNDTMV
115 - 133
2043.929 Da
DTNASGETVSRVTNDTM
116 - 132
1797.792 Da
VSRVTNDTM
124 - 132
1022.494 Da
VVKELITTHI
133 - 142
1152.699 Da
FITGIISV
145 - 152
849.508 Da
ITGIISV
146 - 152
702.440 Da
FIMNW
160 - 164
710.333 Da
FIMNWKLTL
160 - 168
1165.644 Da
LLVLVVVPLAA
168 - 178
1106.755 Da
VVVPLAAL
172 - 179
781.518 Da
VPLAA
174 - 178
470.297 Da
ILVPIGRKM
180 - 188
1026.649 Da
ILVPIGRKMFSIS
180 - 192
1460.866 Da
FSISRETQDETARF
189 - 202
1686.808 Da
TQDETARF
195 - 202
967.448 Da
TGLLNQIL
203 - 210
871.525 Da
LNQIL
206 - 210
600.371 Da
NQILPEIRL
207 - 215
1095.652 Da
QILPEI
208 - 213
712.424 Da
LPEIR
210 - 214
627.382 Da
VKASNAEDVE
216 - 225
1061.511 Da
VKASNAEDVEYGRGKMGISSL
216 - 236
2211.107 Da
DVEYGRGKMGISSL
223 - 236
1511.752 Da
BmrA WT Nano Apo
BmrA WT Nano Vi-trapped
Relative Uptake (Da)
Exposure Time (minutes)

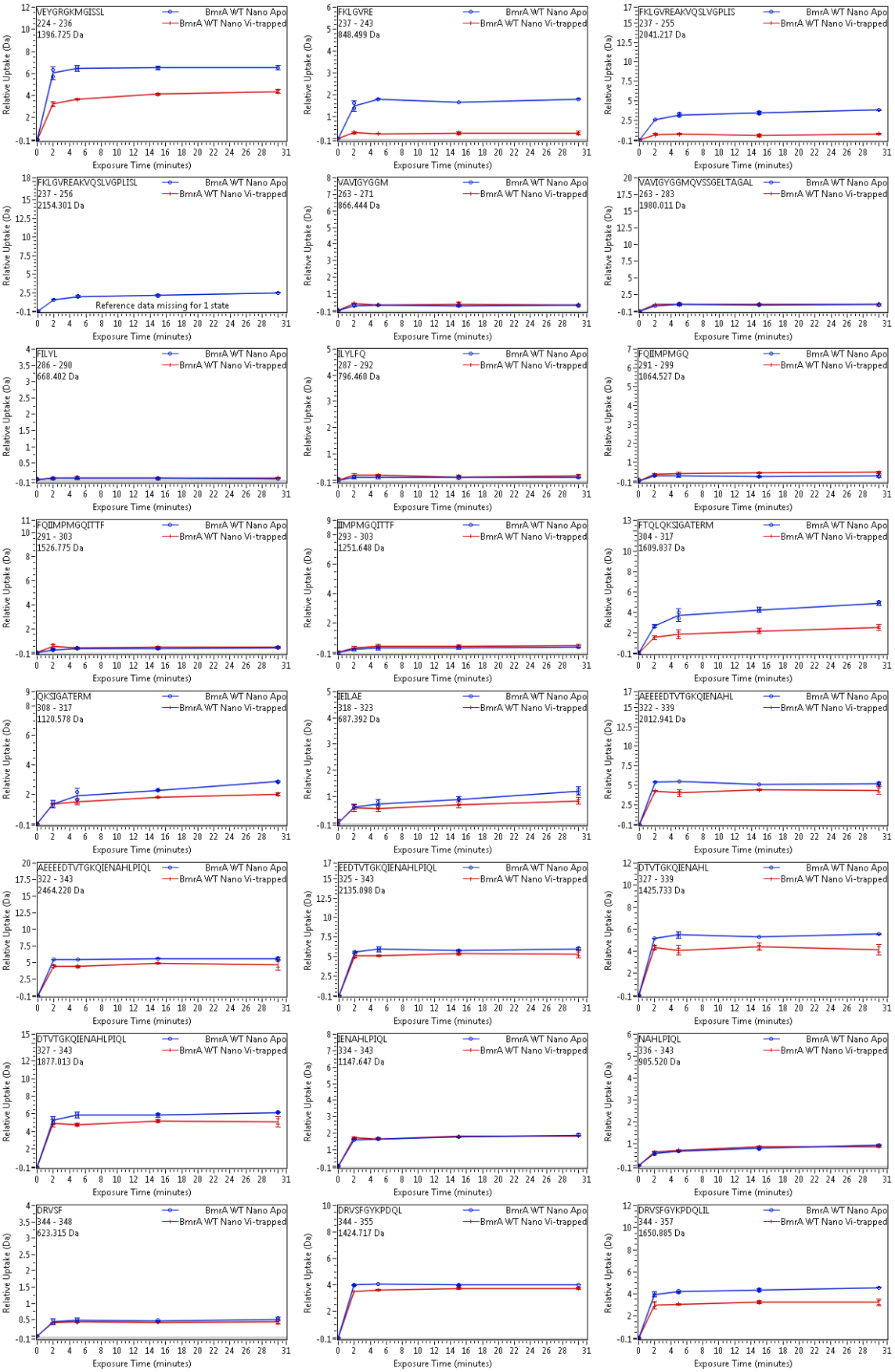
VEYGRGKMGISSL
224 - 236
1396.725 Da
FKLGVRE
237 - 243
848.499 Da
FKLGVREAKVQSLVGPLIS
237 - 255
2041.217 Da
FKLGVREAKVQSLVGPLISL
237 - 256
2154.301 Da
Reference data missing for 1 state
VAVIGYGGM
263 - 271
866.444 Da
VAVIGYGGMQVSSGELTAGAL
263 - 283
1980.011 Da
FILYL
286 - 290
668.402 Da
ILYLFQ
287 - 292
796.460 Da
FQIIMPMGQ
291 - 299
1064.527 Da
FQIIMPMGQITTF
291 - 303
1526.775 Da
IIMPMGQITTF
293 - 303
1251.648 Da
FTQLQKSIGATERM
304 - 317
1609.837 Da
QKSIGATERM
308 - 317
1120.578 Da
EILAE
318 - 323
687.392 Da
AEEEEDTVTGKQIENAHL
322 - 339
2012.941 Da
AEEEEDTVTGKQIENAHLPIQL
322 - 343
2464.220 Da
EEDTVTGKQIENAHLPIQL
325 - 343
2135.098 Da
DTVTGKQIENAHL
327 - 339
1425.733 Da
DTVTGKQIENAHLPIQL
327 - 343
1877.013 Da
IENAHLPIQL
334 - 343
1147.647 Da
NAHLPIQL
336 - 343
905.520 Da
DRVSF
344 - 348
623.315 Da
DRVSFGYKPDQL
344 - 355
1424.717 Da
DRVSFGYKPDQLIL
344 - 357
1650.885 Da
BmrA WT Nano Apo
BmrA WT Nano Vi-trapped
Relative Uptake (Da)
Exposure Time (minutes)

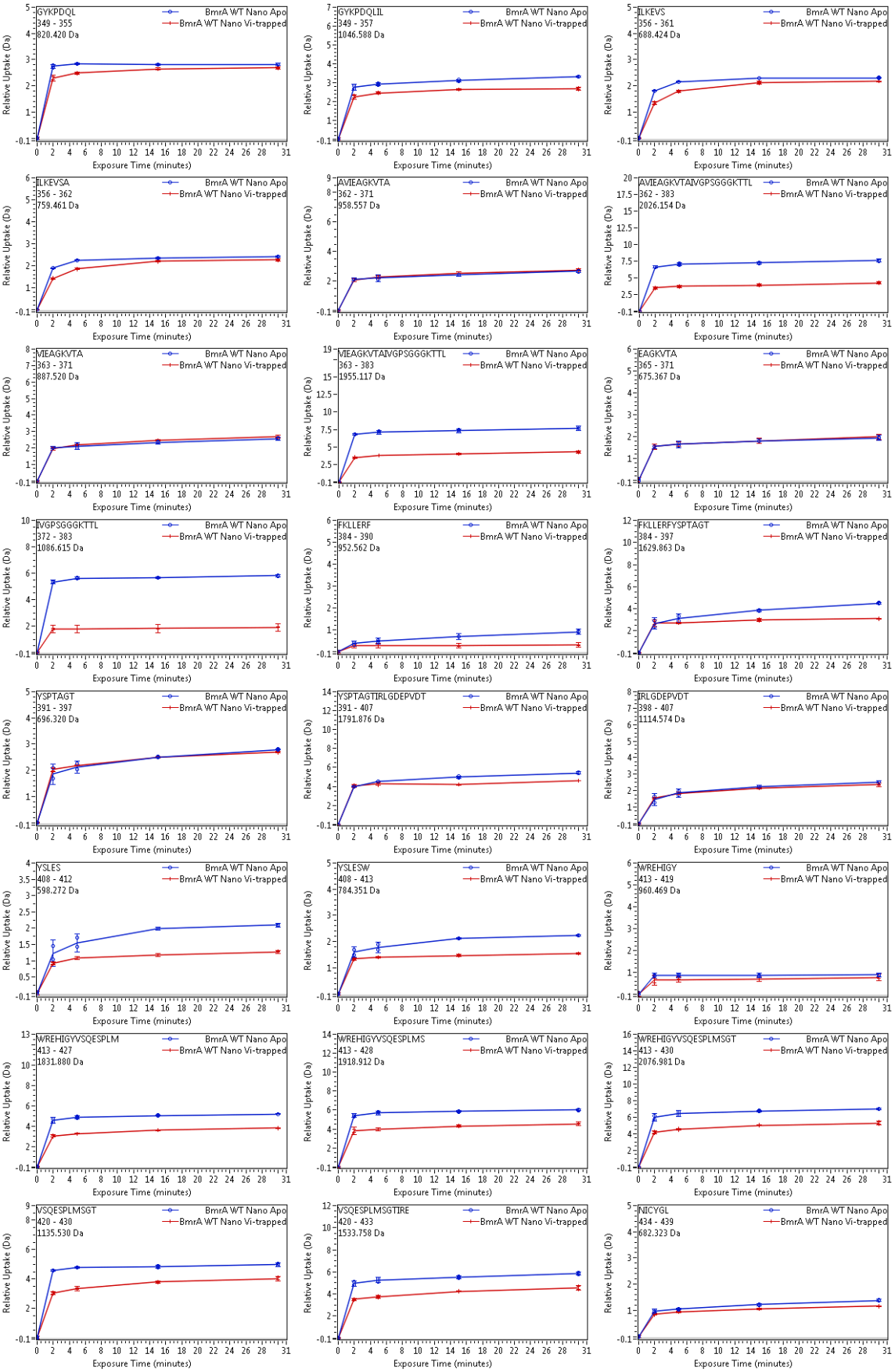
GYKPDQL
349 - 355
820.420 Da
GYKPDQLIL
349 - 357
1046.588 Da
ILKEVS
356 - 361
688.424 Da
ILKEVSA
356 - 362
759.461 Da
AVIEAGKVTA
362 - 371
958.557 Da
AVIEAGKVTAIVGPSGGGKTTL
362 - 383
2026.154 Da
VIEAGKVTA
363 - 371
887.520 Da
VIEAGKVTAIVGPSGGGKTTL
363 - 383
1955.117 Da
EAGKVTA
365 - 371
675.367 Da
IVGPSGGGKTTL
372 - 383
1086.615 Da
FKLLERF
384 - 390
952.562 Da
FKLLERFYSPTAGT
384 - 397
1629.863 Da
YSPTAGT
391 - 397
696.320 Da
YSPTAGTIRLGDEPVDT
391 - 407
1791.876 Da
IRLGDEPVDT
398 - 407
1114.574 Da
YSLES
408 - 412
598.272 Da
YSLESW
408 - 413
784.351 Da
WREHIGY
413 - 419
960.469 Da
WREHIGYVSQESPLM
413 - 427
1831.880 Da
WREHIGYVSQESPLMS
413 - 428
1918.912 Da
WREHIGYVSQESPLMSGT
413 - 430
2076.981 Da
VSQESPLMSGT
420 - 430
1135.530 Da
VSQESPLMSGTIRE
420 - 433
1533.758 Da
NICYGL
434 - 439
682.323 Da
BmrA WT Nano Apo
BmrA WT Nano Vi-trapped
Relative Uptake (Da)
Exposure Time (minutes)

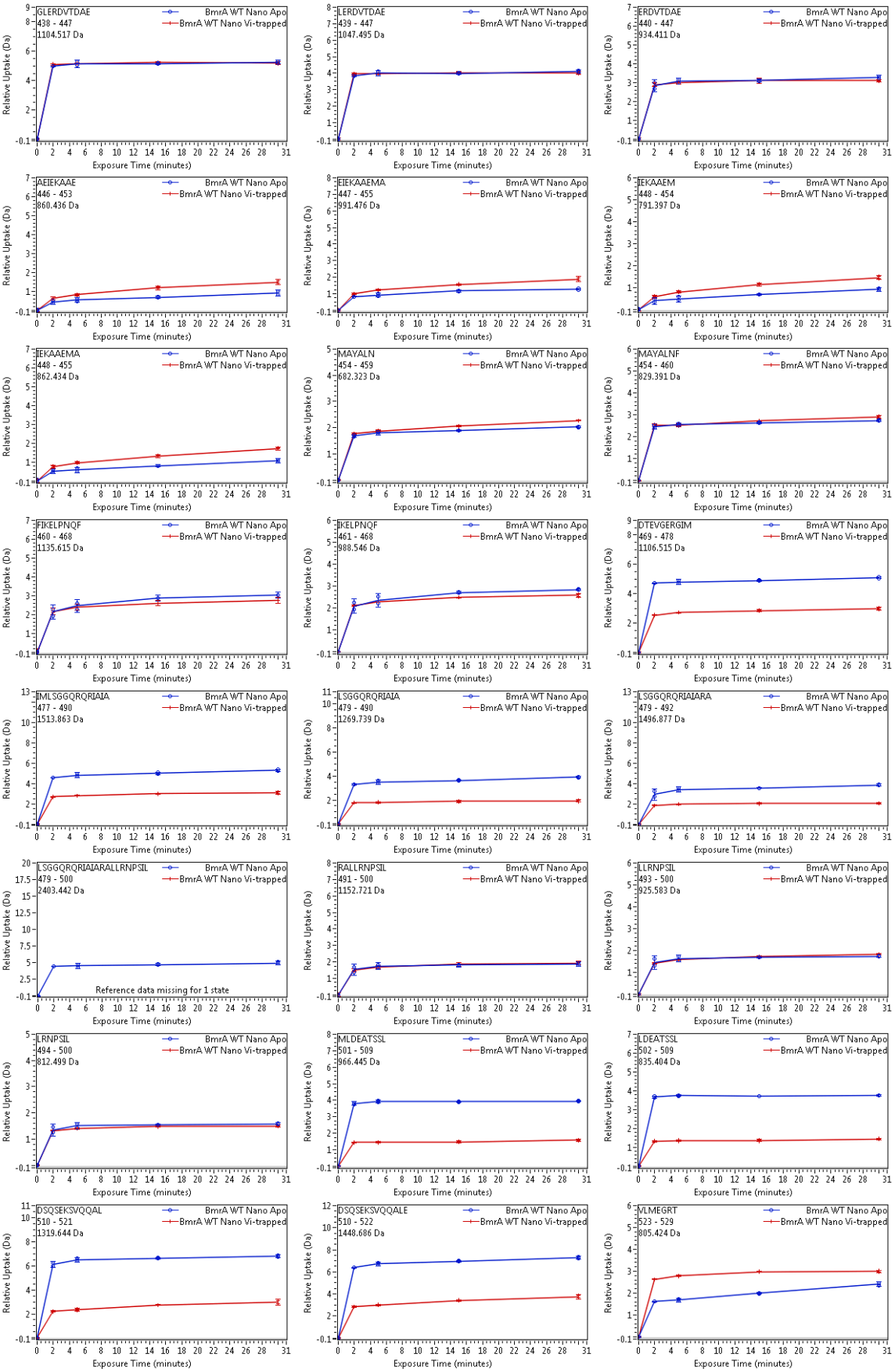
GLERDVTDAE
438 - 447
1104.517 Da
LERDVTDAE
439 - 447
1047.495 Da
ERDVTDAE
440 - 447
934.411 Da
AEIEKAAE
446 - 453
860.436 Da
EIEKAAEMA
447 - 455
991.476 Da
IEKAAEM
448 - 454
791.397 Da
IEKAAEMA
448 - 455
862.434 Da
MAYALN
454 - 459
682.323 Da
MAYALNF
454 - 460
829.391 Da
FIKELPNQF
460 - 468
1135.615 Da
IKELPNQF
461 - 468
988.546 Da
DTEVGERGIM
469 - 478
1106.515 Da
IMLSGGQRQRIAIA
477 - 490
1513.863 Da
LSGGQRQRIAIA
479 - 490
1269.739 Da
LSGGQRQRIAIARA
479 - 492
1496.877 Da
LSGGQRQRIAIARALLRNPSIL
479 - 500
2403.442 Da
Reference data missing for 1 state
RALLRNPSIL
491 - 500
1152.721 Da
LLRNPSIL
493 - 500
925.583 Da
LRNPSIL
494 - 500
812.499 Da
MLDEATSSL
501 - 509
966.445 Da
LDEATSSL
502 - 509
835.404 Da
DSQSEKSVQQAL
510 - 521
1319.644 Da
DSQSEKSVQQALE
510 - 522
1448.686 Da
VLMEGRT
523 - 529
805.424 Da
BmrA WT Nano Apo
BmrA WT Nano Vi-trapped
Relative Uptake (Da)
Exposure Time (minutes)

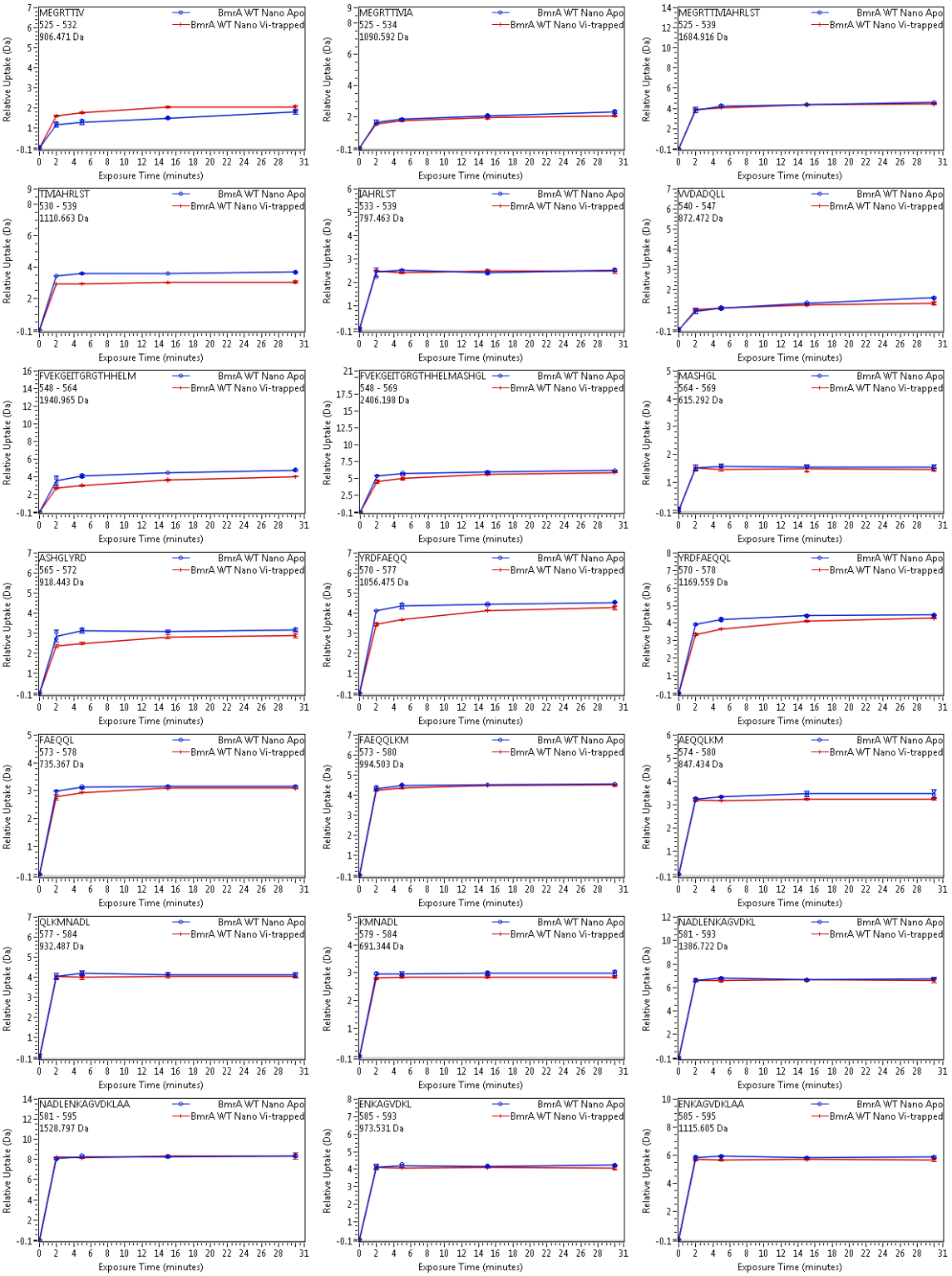
MEGRTTIV
525 - 532
906.471 Da
MEGRTTIVIA
525 - 534
1090.592 Da
MEGRTTIVIAHRLST
525 - 539
1684.916 Da
TTVIAHRLST
530 - 539
1110.663 Da
AHRLST
533 - 539
797.463 Da
VVDADQLL
540 - 547
872.472 Da
FVEKGEITGRGTHHELM
548 - 564
1940.965 Da
FVEKGEITGRGTHHELMASHGL
548 - 569
2406.198 Da
MASHGL
564 - 569
615.292 Da
ASHGLYRD
565 - 572
918.443 Da
YRDFAEQQ
570 - 577
1056.475 Da
YRDFAEQQL
570 - 578
1169.559 Da
FAEQQL
573 - 578
735.367 Da
FAEQQLKM
573 - 580
994.503 Da
AEQQLKM
574 - 580
847.434 Da
QLKMNADL
577 - 584
932.487 Da
KMNADL
579 - 584
691.344 Da
NADLENKAGVDKL
581 - 593
1386.722 Da
NADLENKAGVDKLAA
581 - 595
1528.797 Da
ENKAGVDKL
585 - 593
973.531 Da
ENKAGVDKLAA
585 - 595
1115.605 Da
BmrA WT Nano Apo
BmrA WT Nano Vi-trapped
Relative Uptake (Da)
Exposure Time (minutes)

Annex 16 : Deuterium uptake plots of WT BmrA in nanodiscs (DDM/cholate) in the Apo and doxorubicin-bound condition

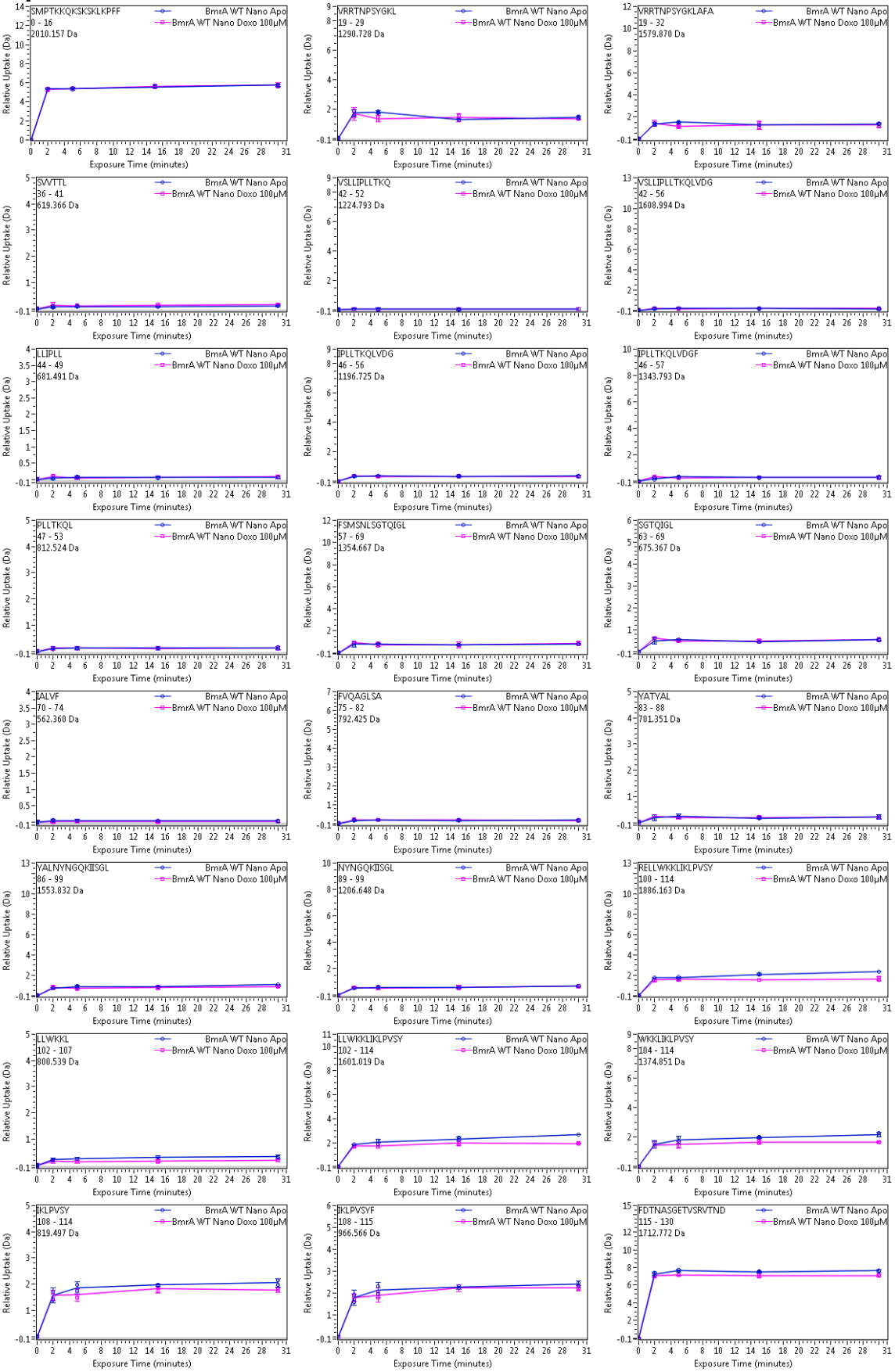

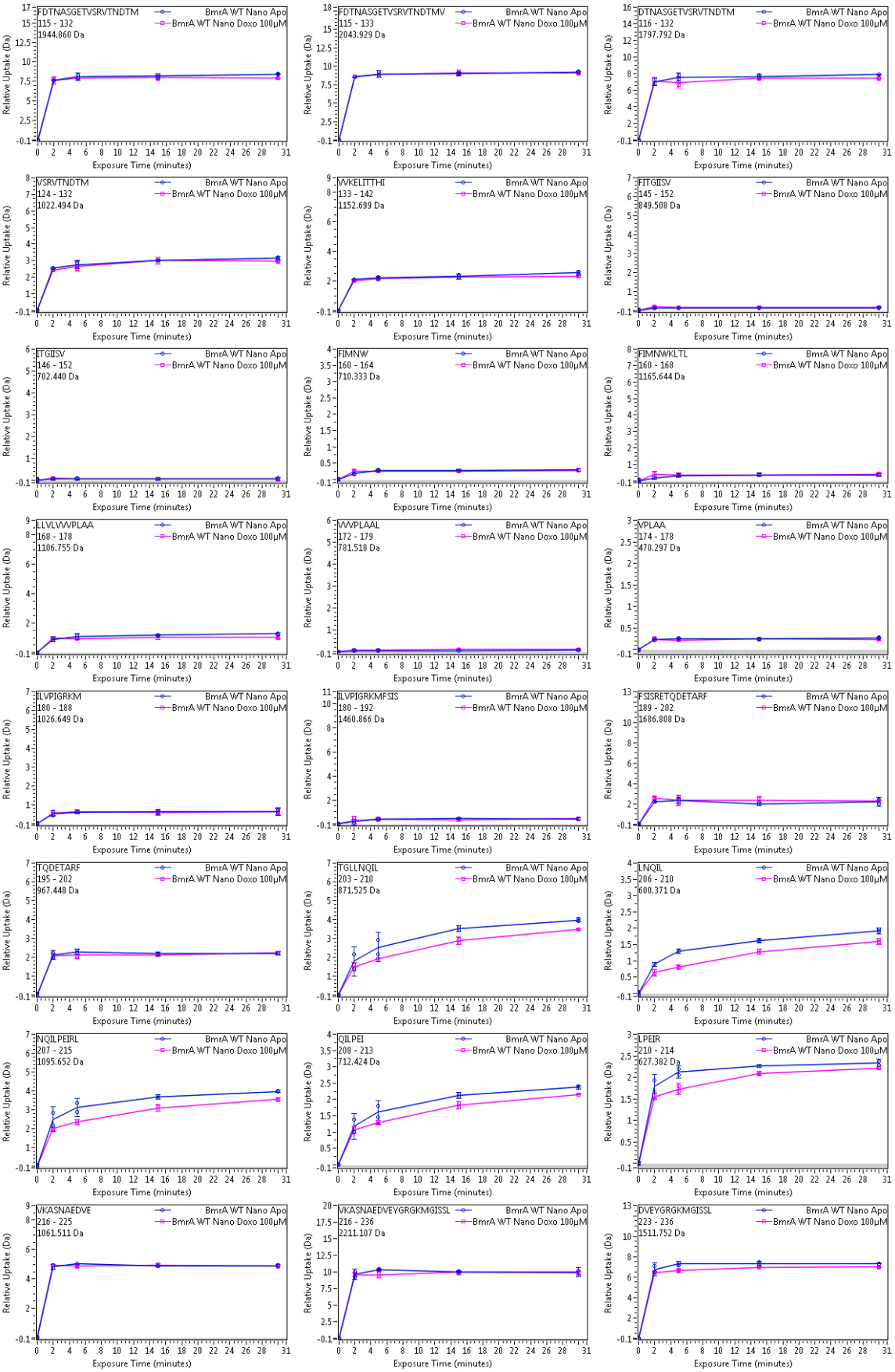
FDTNASGETVSRVTNDTM
115 - 132
1944.860 Da
FDTNASGETVSRVTNDTMV
115 - 133
2043.929 Da
DTNASGETVSRVTNDTM
116 - 132
1797.792 Da
VSRVTNDTM
124 - 132
1022.494 Da
VVKELITTHI
133 - 142
1152.699 Da
FITGIISV
145 - 152
849.508 Da
ITGIISV
146 - 152
702.440 Da
FIMNW
160 - 164
710.333 Da
FIMNWKLTL
160 - 168
1165.644 Da
LLVLVVVPLAA
168 - 178
1106.755 Da
VVVPLAAL
172 - 179
781.518 Da
VPLAA
174 - 178
470.297 Da
ILVPIGRKM
180 - 188
1026.649 Da
ILVPIGRKMFSIS
180 - 192
1460.866 Da
FSISRETQDETARF
189 - 202
1686.808 Da
TQDETARF
195 - 202
967.448 Da
TGLLNQIL
203 - 210
871.525 Da
LNQIL
206 - 210
600.371 Da
NQILPEIRL
207 - 215
1095.652 Da
QILPEI
208 - 213
712.424 Da
LPEIR
210 - 214
627.382 Da
VKASNAEDVE
216 - 225
1061.511 Da
VKASNAEDVEYGRGKMGISSL
216 - 236
2211.107 Da
DVEYGRGKMGISSL
223 - 236
1511.752 Da
BmrA WT Nano Apo
BmrA WT Nano Doxo 100µM
Relative Uptake (Da)
Exposure Time (minutes)

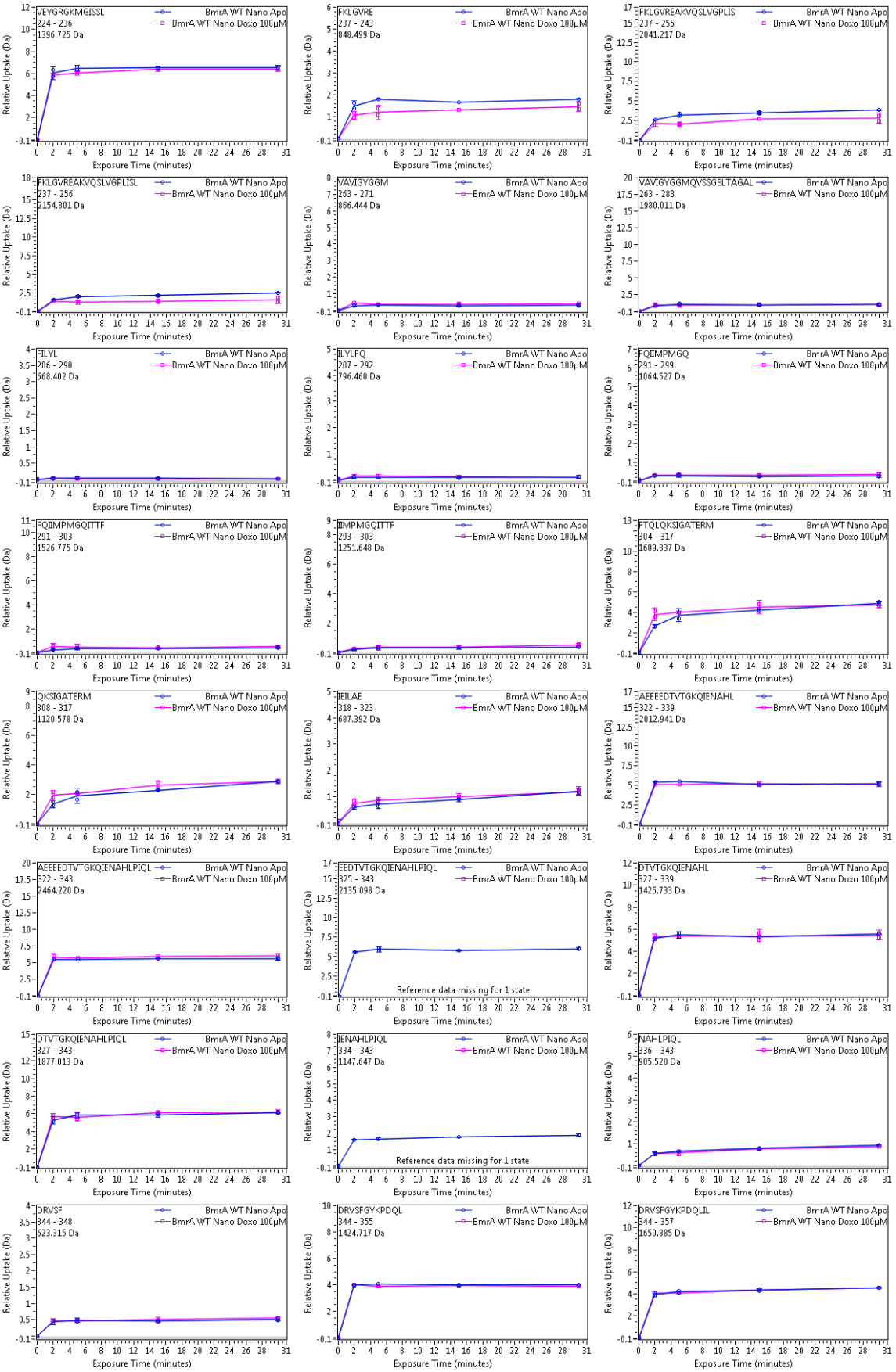
VEYGRGKMGISSL
224 - 236
1396.725 Da
FKLGVRE
237 - 243
848.499 Da
FKLGVREAKVQSLVGPLIS
237 - 255
2041.217 Da
FKLGVREAKVQSLVGPLISL
237 - 256
2154.301 Da
VAVIGYGGM
263 - 271
866.444 Da
VAVIGYGGMQVSSGELTAGAL
263 - 283
1980.011 Da
FILYL
286 - 290
668.402 Da
ILYLFQ
287 - 292
796.460 Da
FQIIMPMGQ
291 - 299
1064.527 Da
FQIIMPMGQITTF
291 - 303
1526.775 Da
IIMPMGQITTF
293 - 303
1251.648 Da
FTQLQKSIGATERM
304 - 317
1609.837 Da
QKSIGATERM
308 - 317
1120.578 Da
EILAE
318 - 323
687.392 Da
AEEEEDTVTGKQIENAHL
322 - 339
2012.941 Da
AEEEEDTVTGKQIENAHLPIQL
322 - 343
2464.220 Da
EEDTVTGKQIENAHLPIQL
325 - 343
2135.098 Da
Reference data missing for 1 state
DTVTGKQIENAHL
327 - 339
1425.733 Da
DTVTGKQIENAHLPIQL
327 - 343
1877.013 Da
IENAHLPIQL
334 - 343
1147.647 Da
Reference data missing for 1 state
NAHLPIQL
336 - 343
905.520 Da
DRVSF
344 - 348
623.315 Da
DRVSFGYKPDQL
344 - 355
1424.717 Da
DRVSFGYKPDQLIL
344 - 357
1650.885 Da
BmrA WT Nano Apo
BmrA WT Nano Doxo 100µM
Relative Uptake (Da)
Exposure Time (minutes)

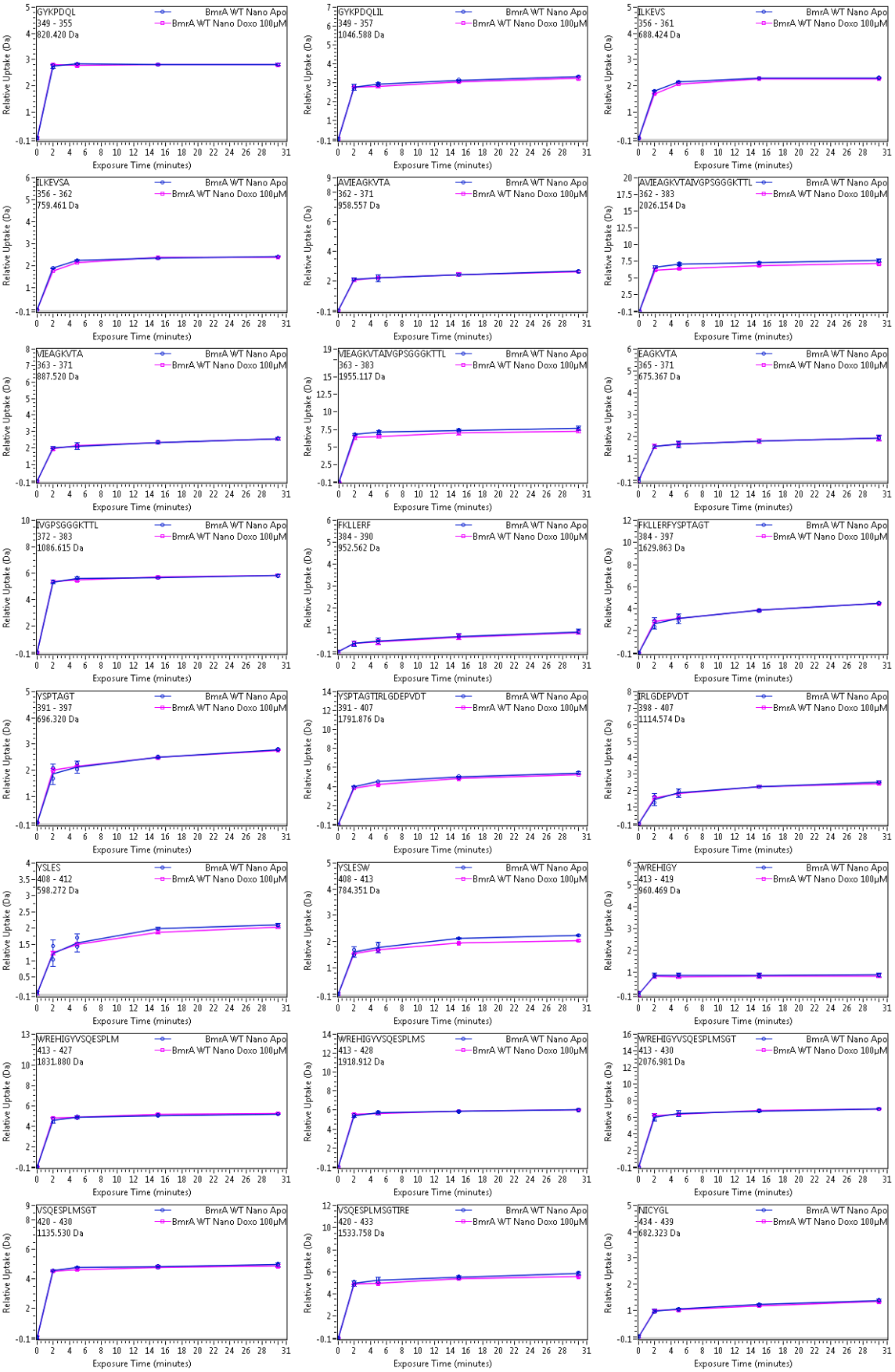
GYKPDQL
349 - 355
820.420 Da
GYKPDQLIL
349 - 357
1046.588 Da
ILKEVS
356 - 361
688.424 Da
ILKEVSA
356 - 362
759.461 Da
AVIEAGKVTA
362 - 371
958.557 Da
AVIEAGKVTAIVGPSGGGKTTL
362 - 383
2026.154 Da
VIEAGKVTA
363 - 371
887.520 Da
VIEAGKVTAIVGPSGGGKTTL
363 - 383
1955.117 Da
EAGKVTA
365 - 371
675.367 Da
IVGPSGGGKTTL
372 - 383
1086.615 Da
FKLLERF
384 - 390
952.562 Da
FKLLERFYSPTAGT
384 - 397
1629.863 Da
YSPTAGT
391 - 397
696.320 Da
YSPTAGTIRLGDEPVDT
391 - 407
1791.876 Da
IRLGDEPVDT
398 - 407
1114.574 Da
YSLES
408 - 412
598.272 Da
YSLESW
408 - 413
784.351 Da
WREHIGY
413 - 419
960.469 Da
WREHIGYVSQESPLM
413 - 427
1831.880 Da
WREHIGYVSQESPLMS
413 - 428
1918.912 Da
WREHIGYVSQESPLMSGT
413 - 430
2076.981 Da
VSQESPLMSGT
420 - 430
1135.530 Da
VSQESPLMSGTIRE
420 - 433
1533.758 Da
NICYGL
434 - 439
682.323 Da
BmrA WT Nano Apo
BmrA WT Nano Doxo 100µM
Relative Uptake (Da)
Exposure Time (minutes)

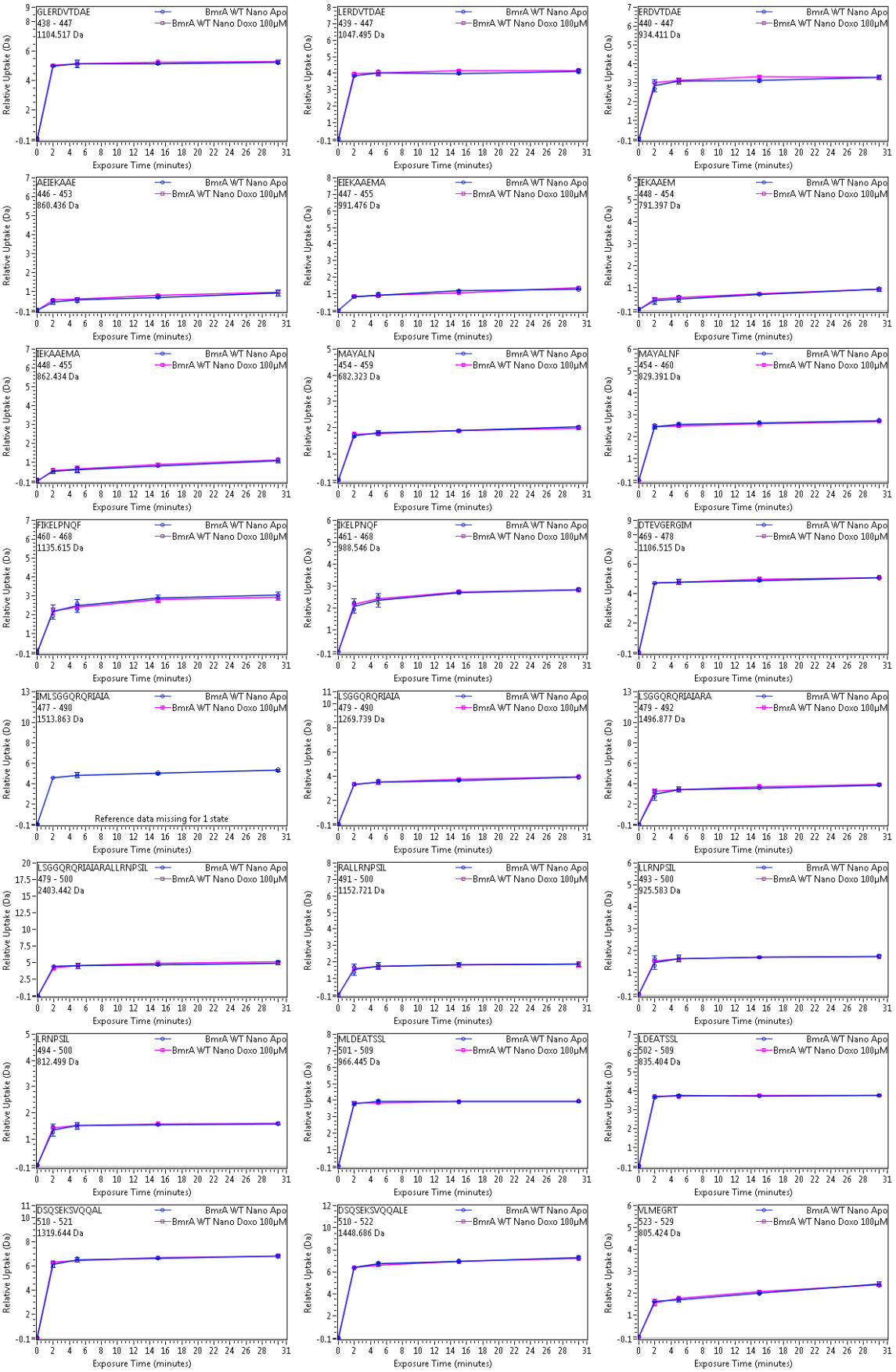
GLERDVTDAE
438 - 447
1104.517 Da
LERDVTDAE
439 - 447
1047.495 Da
ERDVTDAE
440 - 447
934.411 Da
AEIEKAAE
446 - 453
860.436 Da
EIEKAAEMA
447 - 455
991.476 Da
IEKAAEM
448 - 454
791.397 Da
IEKAAEMA
448 - 455
862.434 Da
MAYALN
454 - 459
682.323 Da
MAYALNF
454 - 460
829.391 Da
FIKELPNQF
460 - 468
1135.615 Da
IKELPNQF
461 - 468
988.546 Da
DTEVGERGIM
469 - 478
1106.515 Da
IMLSGGQRQRIAIA
477 - 490
1513.863 Da
Reference data missing for 1 state
LSGGQRQRIAIA
479 - 490
1269.739 Da
LSGGQRQRIAIARA
479 - 492
1496.877 Da
LSGGQRQRIAIARALLRNPSIL
479 - 500
2403.442 Da
RALLRNPSIL
491 - 500
1152.721 Da
LLRNPSIL
493 - 500
925.583 Da
LRNPSIL
494 - 500
812.499 Da
MLDEATSSL
501 - 509
966.445 Da
LDEATSSL
502 - 509
835.404 Da
DSQSEKSVQQAL
510 - 521
1319.644 Da
DSQSEKSVQQALE
510 - 522
1448.686 Da
VLMEGRT
523 - 529
805.424 Da
BmrA WT Nano Apo
BmrA WT Nano Doxo 100µM
Relative Uptake (Da)
Exposure Time (minutes)

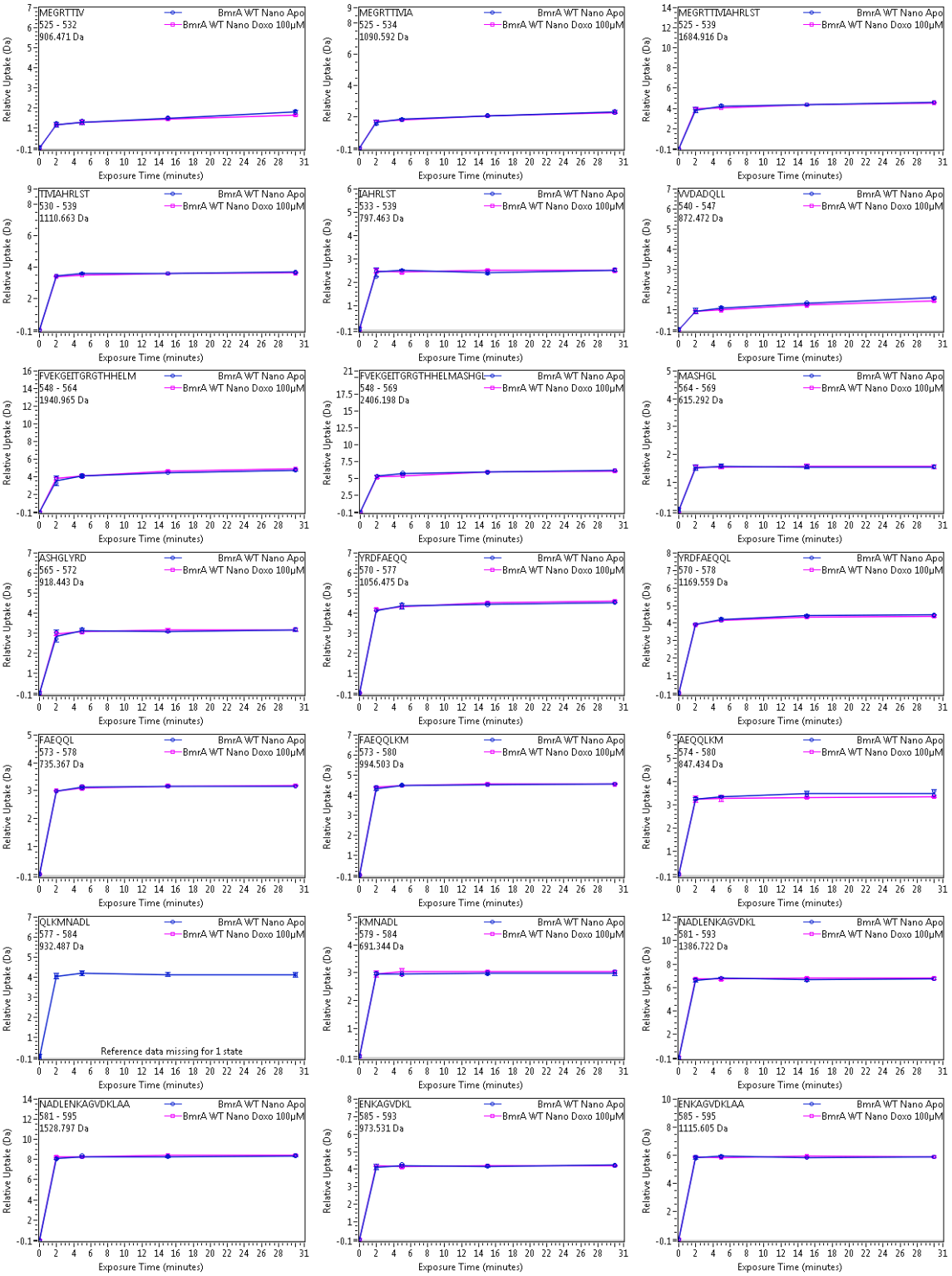
MEGRTTIV
525 - 532
906.471 Da
MEGRTTIVIA
525 - 534
1090.592 Da
MEGRTTIVIAHRLST
525 - 539
1684.916 Da
TTVIAHRLST
530 - 539
1110.663 Da
AHRLST
533 - 539
797.463 Da
VVDADQLL
540 - 547
872.472 Da
FVEKGEITGRGTHHELM
548 - 564
1940.965 Da
FVEKGEITGRGTHHELMASHGL
548 - 569
2406.198 Da
MASHGL
564 - 569
615.292 Da
ASHGLYRD
565 - 572
918.443 Da
YRDFAEQQ
570 - 577
1056.475 Da
YRDFAEQQL
570 - 578
1169.559 Da
FAEQQL
573 - 578
735.367 Da
FAEQQLKM
573 - 580
994.503 Da
AEQQLKM
574 - 580
847.434 Da
QLKMNADL
577 - 584
932.487 Da
Reference data missing for 1 state
KMNADL
579 - 584
691.344 Da
NADLENKAGVDKL
581 - 593
1386.722 Da
NADLENKAGVDKLAA
581 - 595
1528.797 Da
ENKAGVDKL
585 - 593
973.531 Da
ENKAGVDKLAA
585 - 595
1115.605 Da
BmrA WT Nano Apo
BmrA WT Nano Doxo 100µM
Relative Uptake (Da)
Exposure Time (minutes)

Annex 17 : Deuterium uptake plots of K380 BmrA mutant in LMNG in the Apo and ATP/Mg^{2+} incubated condition

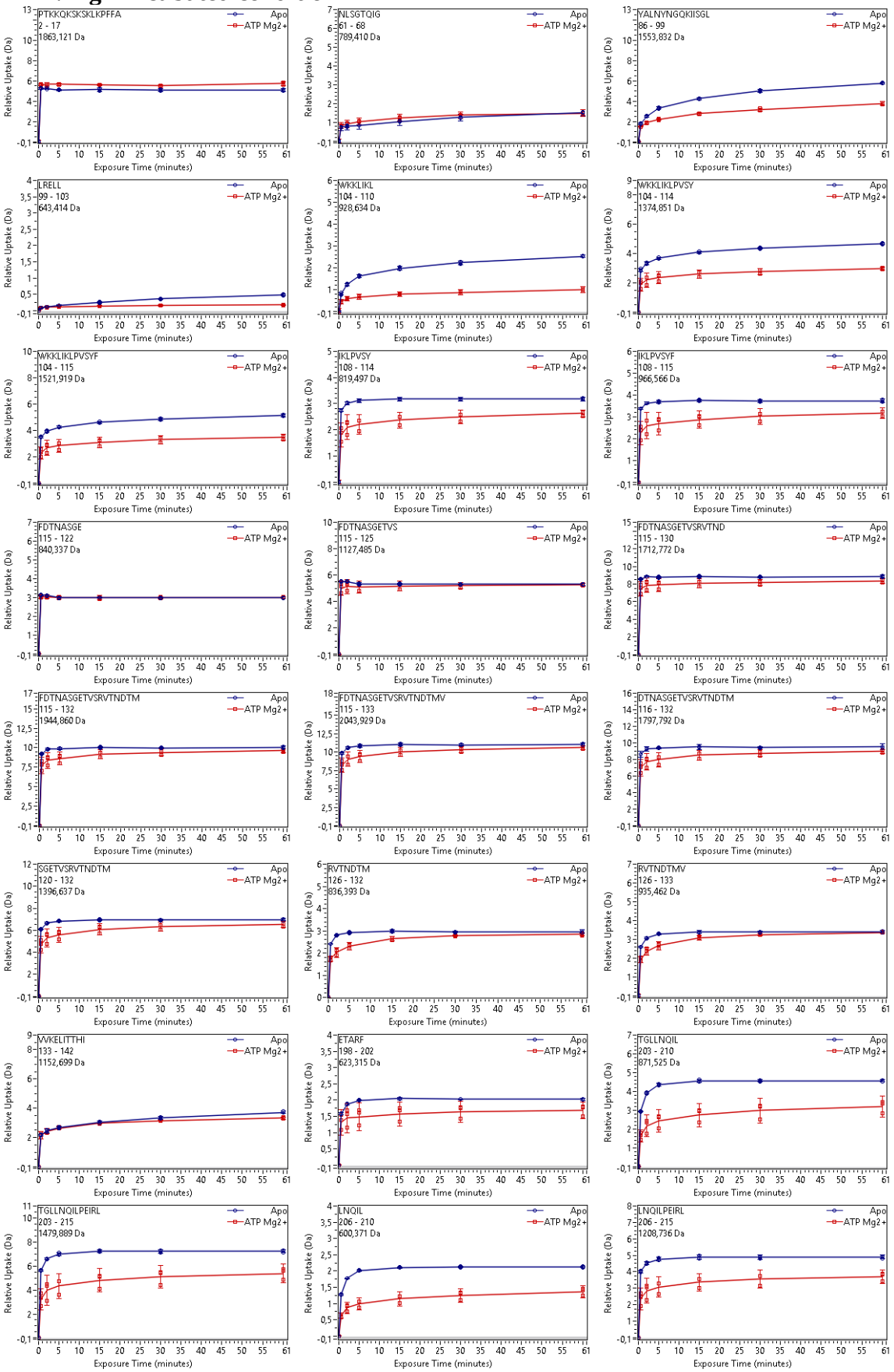

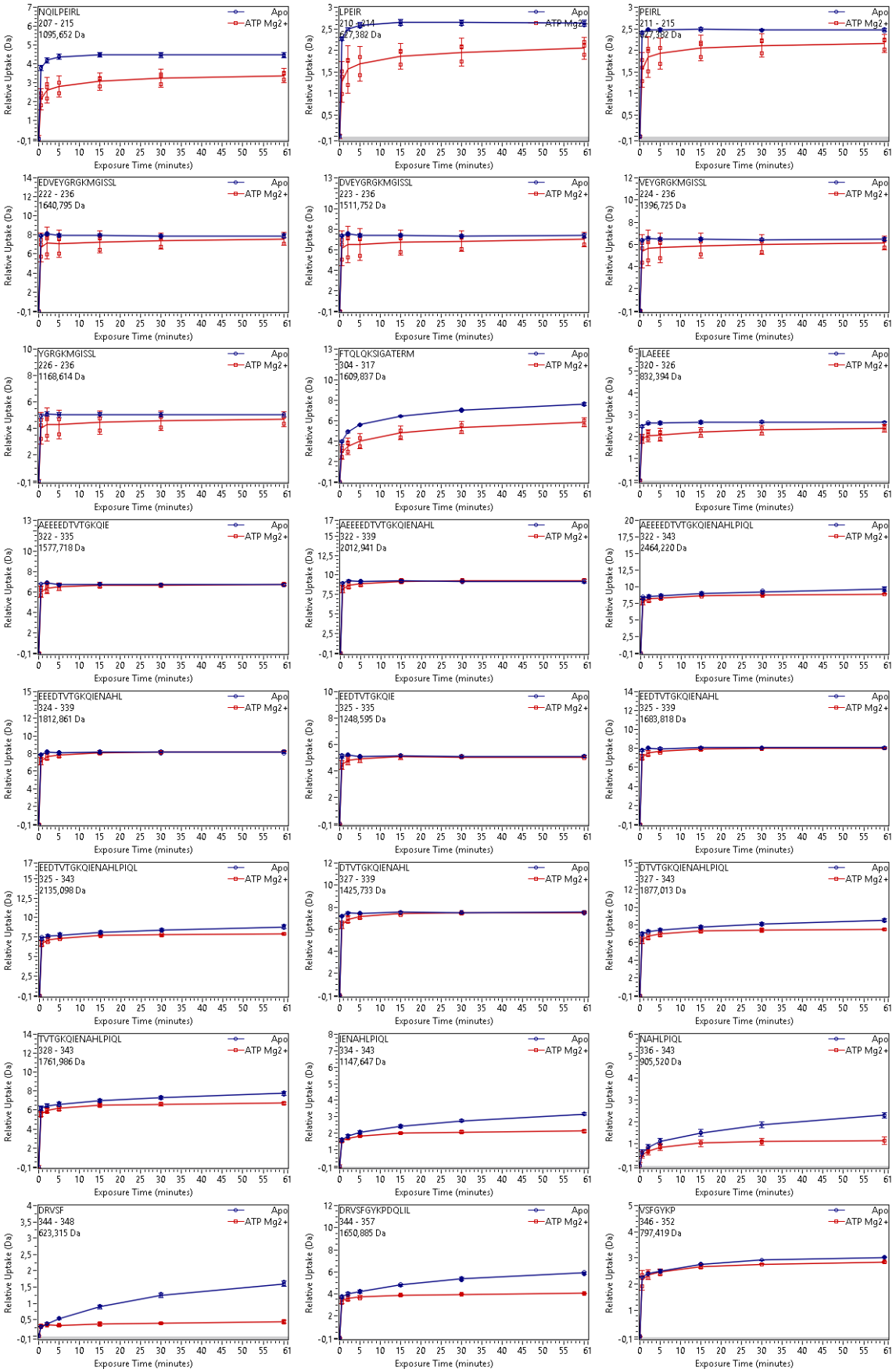
NQILPEIRL
207 - 215
1095,652 Da
LPEIR
210 - 214
627,382 Da
PEIRL
211 - 215
727,382 Da
EDVEYGRGKMGISSL
222 - 236
1640,795 Da
DVEYGRGKMGISSL
223 - 236
1511,752 Da
VEYGRGKMGISSL
224 - 236
1396,725 Da
YGRGKMGISSL
226 - 236
1168,614 Da
FTQLQKSIGATERM
304 - 317
1609,837 Da
ILAEEEE
320 - 326
832,394 Da
AEEEEDTVTGKQIE
322 - 335
1577,718 Da
AEEEEDTVTGKQIENAHL
322 - 339
2012,941 Da
AEEEEDTVTGKQIENAHLPIQL
322 - 343
2464,220 Da
EEEDTVTGKQIENAHL
324 - 339
1812,861 Da
EEDTVTGKQIE
325 - 335
1248,595 Da
EEDTVTGKQIENAHL
325 - 339
1683,818 Da
EEDTVTGKQIENAHLPIQL
325 - 343
2135,098 Da
DTVTGKQIENAHL
327 - 339
1425,733 Da
DTVTGKQIENAHLPIQL
327 - 343
1877,013 Da
TVTGKQIENAHLPIQL
328 - 343
1761,986 Da
IENAHLPIQL
334 - 343
1147,647 Da
NAHLPIQL
336 - 343
905,520 Da
DRVSF
344 - 348
623,315 Da
DRVSFGYKPDQLIL
344 - 357
1650,885 Da
VSFGYKP
346 - 352
797,419 Da
Apo
ATP Mg2+
Relative Uptake (Da)
Exposure Time (minutes)

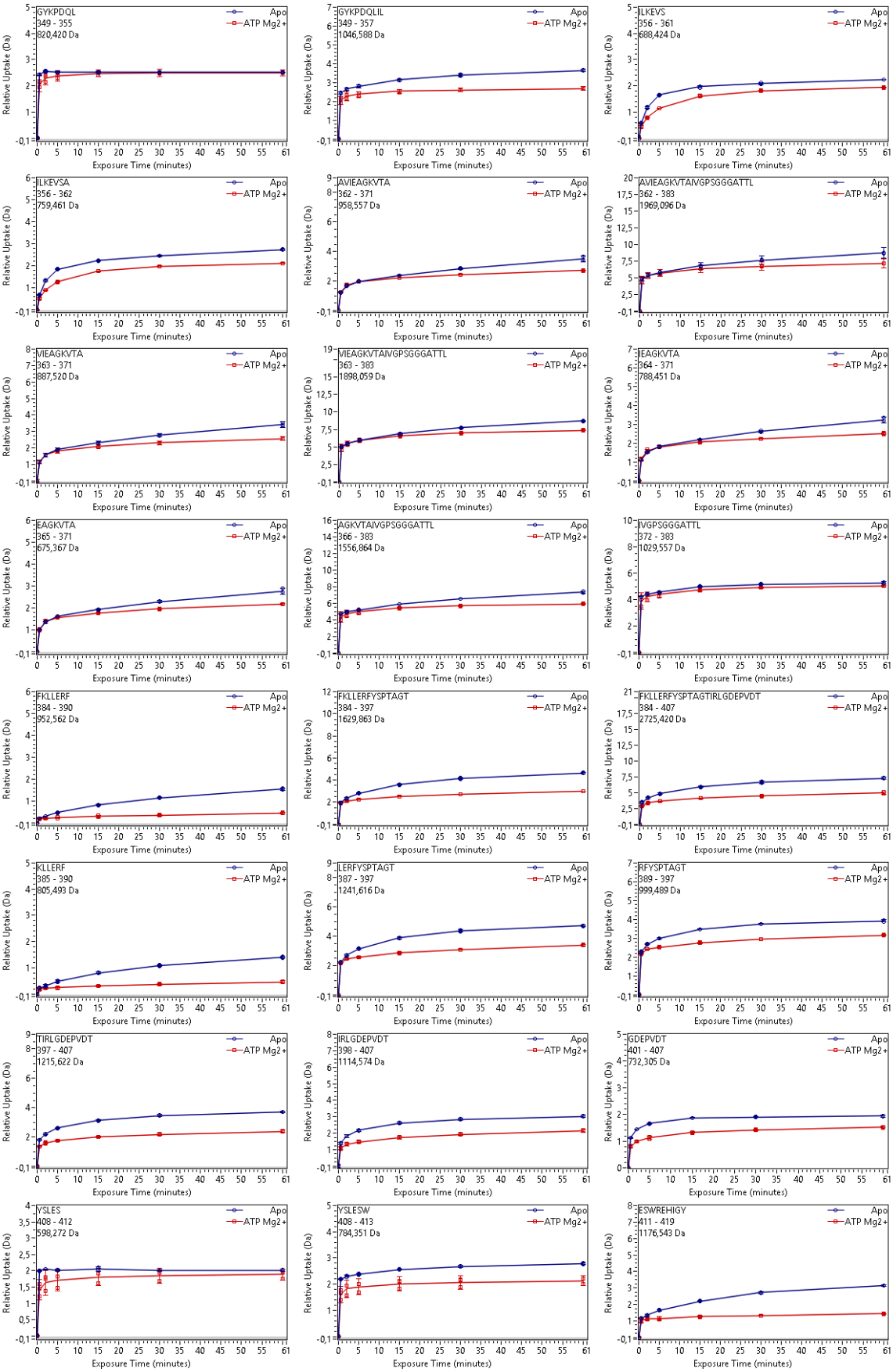
GYKPDQL
349 - 355
820,420 Da
GYKPDQLIL
349 - 357
1046,588 Da
ILKEVS
356 - 361
688,424 Da
ILKEVSA
356 - 362
759,461 Da
AVIEAGKVTA
362 - 371
958,557 Da
AVIEAGKVTAIVGPSGGGATTL
362 - 383
1969,096 Da
VIEAGKVTA
363 - 371
887,520 Da
VIEAGKVTAIVGPSGGGATTL
363 - 383
1898,059 Da
IEAGKVTA
364 - 371
788,451 Da
EAGKVTA
365 - 371
675,367 Da
AGKVTAIVGPSGGGATTL
366 - 383
1556,864 Da
IVGPSGGGATTL
372 - 383
1029,557 Da
FKLLERF
384 - 390
952,562 Da
FKLLERFYSPTAGT
384 - 397
1629,863 Da
FKLLERFYSPTAGTIRLGDEPVDT
384 - 407
2725,420 Da
KLLERF
385 - 390
805,493 Da
LERFYSPTAGT
387 - 397
1241,616 Da
RFYSPTAGT
389 - 397
999,489 Da
TIRLGDEPVDT
397 - 407
1215,622 Da
IRLGDEPVDT
398 - 407
1114,574 Da
GDEPVDT
401 - 407
732,305 Da
YSLES
408 - 412
598,272 Da
YSLESW
408 - 413
784,351 Da
ESWREHIGY
411 - 419
1176,543 Da
Apo
ATP Mg2+
Relative Uptake (Da)
Exposure Time (minutes)

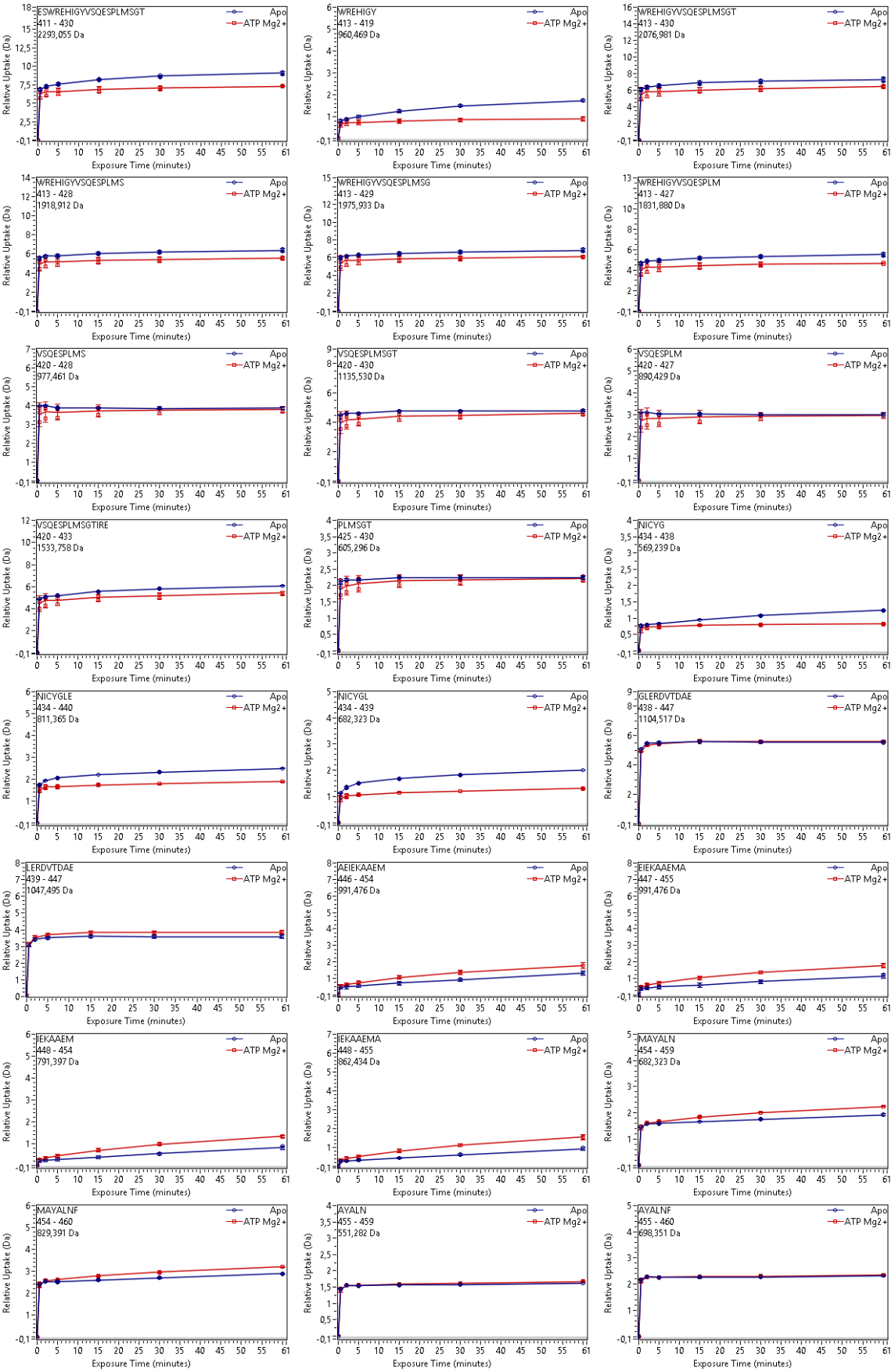
ESWREHIGYVSQESPLMSGT
411 - 430
2293,055 Da
WREHIGY
413 - 419
960,469 Da
WREHIGYVSQESPLMSGT
413 - 430
2076,981 Da
WREHIGYVSQESPLMS
413 - 428
1918,912 Da
WREHIGYVSQESPLMSG
413 - 429
1975,933 Da
WREHIGYVSQESPLM
413 - 427
1831,880 Da
VSQESPLMS
420 - 428
977,461 Da
VSQESPLMSGT
420 - 430
1135,530 Da
VSQESPLM
420 - 427
890,429 Da
VSQESPLMSGTIRE
420 - 433
1533,758 Da
PLMSGT
425 - 430
605,296 Da
NICYG
434 - 438
569,239 Da
NICYGLE
434 - 440
811,365 Da
NICYGL
434 - 439
682,323 Da
GLERDVTDAE
438 - 447
1104,517 Da
LERDVTDAE
439 - 447
1047,495 Da
AEIEKAAEM
446 - 454
991,476 Da
EIEKAAEMA
447 - 455
991,476 Da
IEKAAEM
448 - 454
791,397 Da
IEKAAEMA
448 - 455
862,434 Da
MAYALN
454 - 459
682,323 Da
MAYALNF
454 - 460
829,391 Da
AYALN
455 - 459
551,282 Da
AYALNF
455 - 460
698,351 Da
Apo
ATP Mg2+
Relative Uptake (Da)
Exposure Time (minutes)

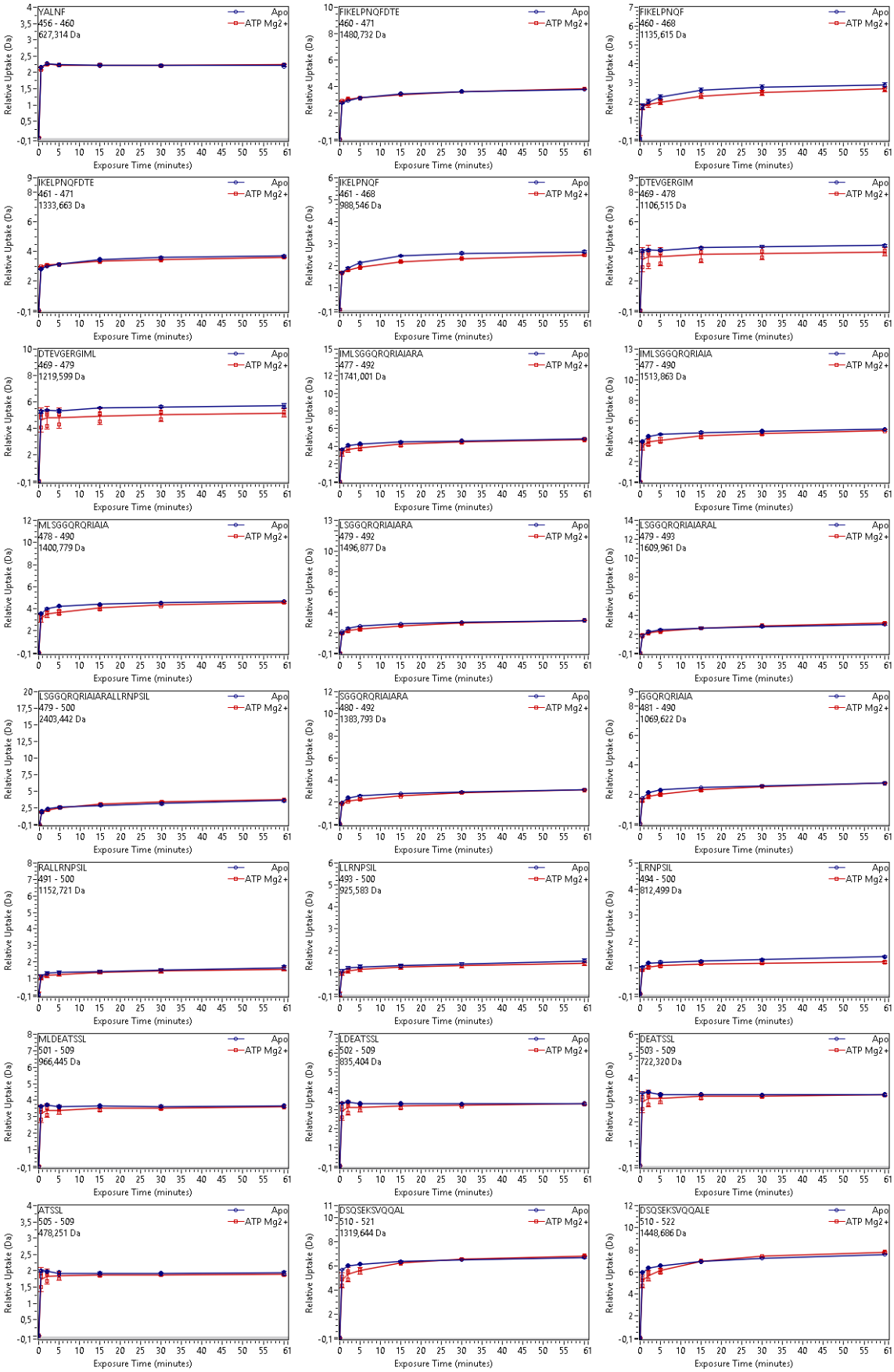
YALNF
456 - 460
627,314 Da
FIKELPNQFDTE
460 - 471
1480,732 Da
FIKELPNQF
460 - 468
1135,615 Da
IKELPNQFDTE
461 - 471
1333,663 Da
IKELPNQF
461 - 468
988,546 Da
DTEVGERGIM
469 - 478
1106,515 Da
DTEVGERGIML
469 - 479
1219,599 Da
IMLSGGQRQRIAIARA
477 - 492
1741,001 Da
IMLSGGQRQRIAIA
477 - 490
1513,863 Da
MLSGGQRQRIAIA
478 - 490
1400,779 Da
LSGGQRQRIAIARA
479 - 492
1496,877 Da
LSGGQRQRIAIARAL
479 - 493
1609,961 Da
LSGGQRQRIAIARALLRNPSIL
479 - 500
2403,442 Da
SGGQRQRIAIARA
480 - 492
1383,793 Da
GGQRQRIAIA
481 - 490
1069,622 Da
RALLRNPSIL
491 - 500
1152,721 Da
LLRNPSIL
493 - 500
925,583 Da
LRNPSIL
494 - 500
812,499 Da
MLDEATSSL
501 - 509
966,445 Da
LDEATSSL
502 - 509
835,404 Da
DEATSSL
503 - 509
722,320 Da
ATSSL
505 - 509
478,251 Da
DSQSEKSVQQAL
510 - 521
1319,644 Da
DSQSEKSVQQALE
510 - 522
1448,686 Da
Apo
ATP Mg2+
Relative Uptake (Da)
Exposure Time (minutes)

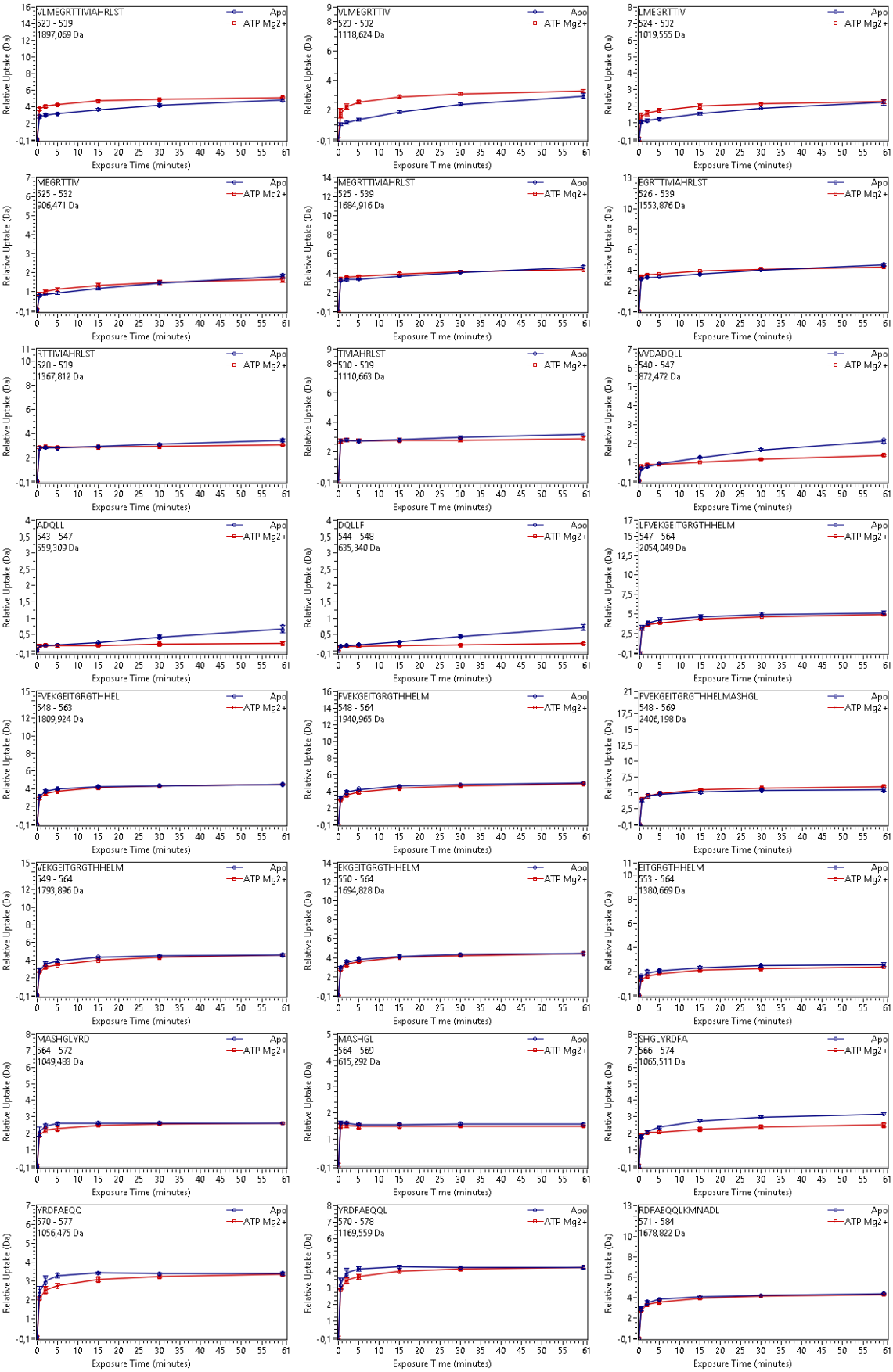
VLMEGRTTIVIAHRLST
523 - 539
1897,069 Da
VLMEGRTTIV
523 - 532
1118,624 Da
LMEGRTTIV
524 - 532
1019,555 Da
MEGRTTIV
525 - 532
906,471 Da
MEGRTTIVIAHRLST
525 - 539
1684,916 Da
EGRTTIVIAHRLST
526 - 539
1553,876 Da
RTTIVIAHRLST
528 - 539
1367,812 Da
TIVIAHRLST
530 - 539
1110,663 Da
VVDADQLL
540 - 547
872,472 Da
ADQLL
543 - 547
559,309 Da
DQLLF
544 - 548
635,340 Da
LFVEKGEITGRGTHHELM
547 - 564
2054,049 Da
FVEKGEITGRGTHHEL
548 - 563
1809,924 Da
FVEKGEITGRGTHHELM
548 - 564
1940,965 Da
FVEKGEITGRGTHHELMASHGL
548 - 569
2406,198 Da
VEKGEITGRGTHHELM
549 - 564
1793,896 Da
EKGEITGRGTHHELM
550 - 564
1694,828 Da
EITGRGTHHELM
553 - 564
1380,669 Da
MASHGLYRD
564 - 572
1049,483 Da
MASHGL
564 - 569
615,292 Da
SHGLYRDFA
566 - 574
1065,511 Da
YRDFAEQQ
570 - 577
1056,475 Da
YRDFAEQQL
570 - 578
1169,559 Da
RDFAEQQLKMNADL
571 - 584
1678,822 Da
Apo
ATP Mg2+
Relative Uptake (Da)
Exposure Time (minutes)

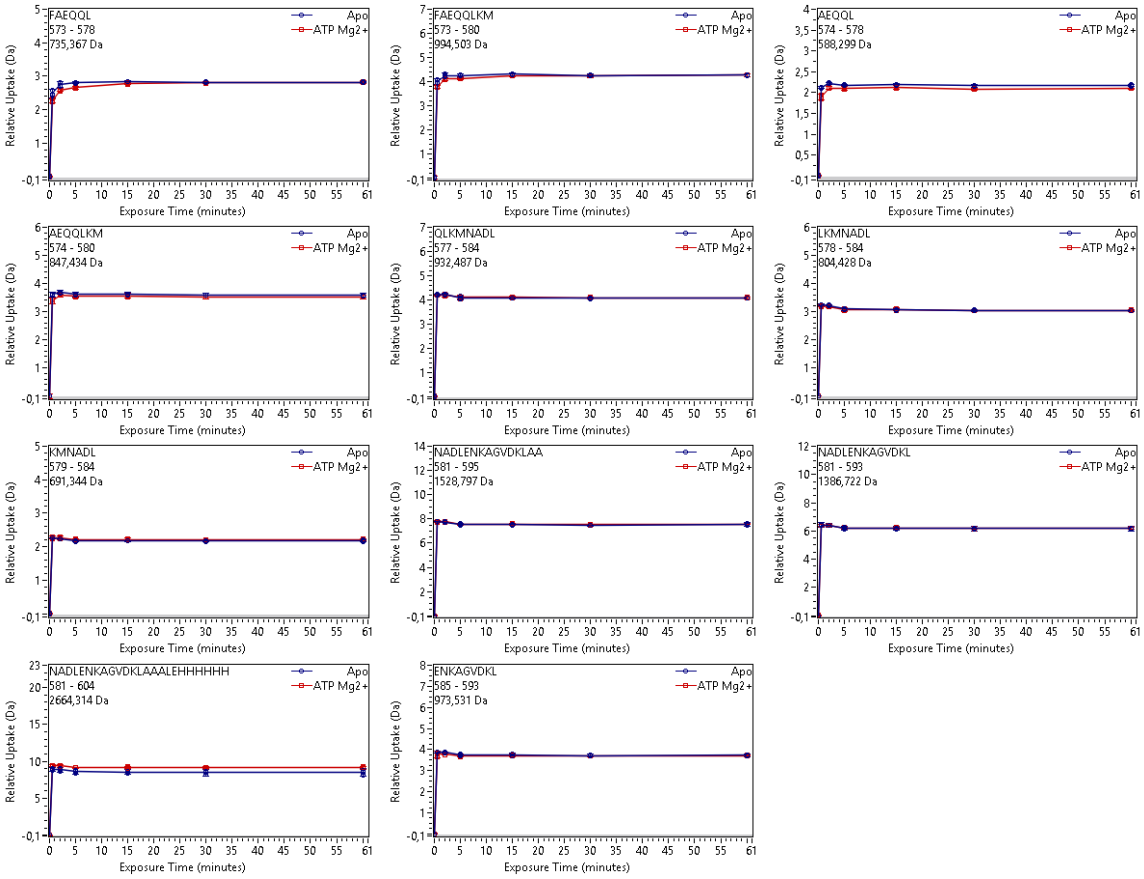
FAEQQL
573 - 578
735,367 Da
FAEQQLKM
573 - 580
994,503 Da
AEQQL
574 - 578
588,299 Da
AEQQLKM
574 - 580
847,434 Da
QLKMNADL
577 - 584
932,487 Da
LKMNADL
578 - 584
804,428 Da
KMNADL
579 - 584
691,344 Da
NADLENKAGVDKLAA
581 - 595
1528,797 Da
NADLENKAGVDKL
581 - 593
1386,722 Da
NADLENKAGVDKLAAALEHHHHHH
581 - 604
2664,314 Da
ENKAGVDKL
585 - 593
973,531 Da
Apo
ATP Mg2+
Relative Uptake (Da)
Exposure Time (minutes)

Annex 18 : Deuterium uptake plots of K380A BmrA mutant in nanodiscs (DDM/cholate) in the Apo and ATP/Mg^{2+}/Vi incubated condition

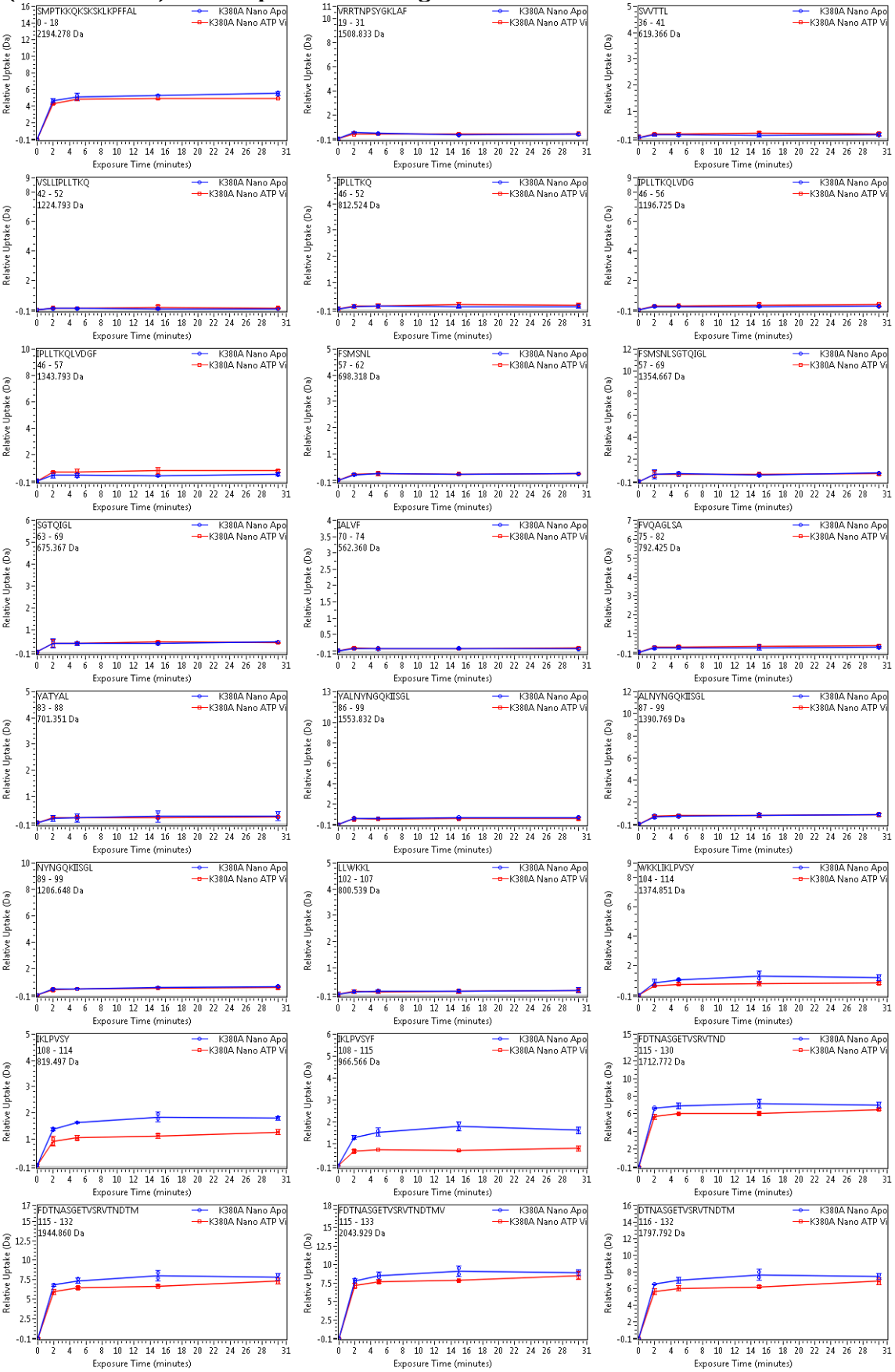

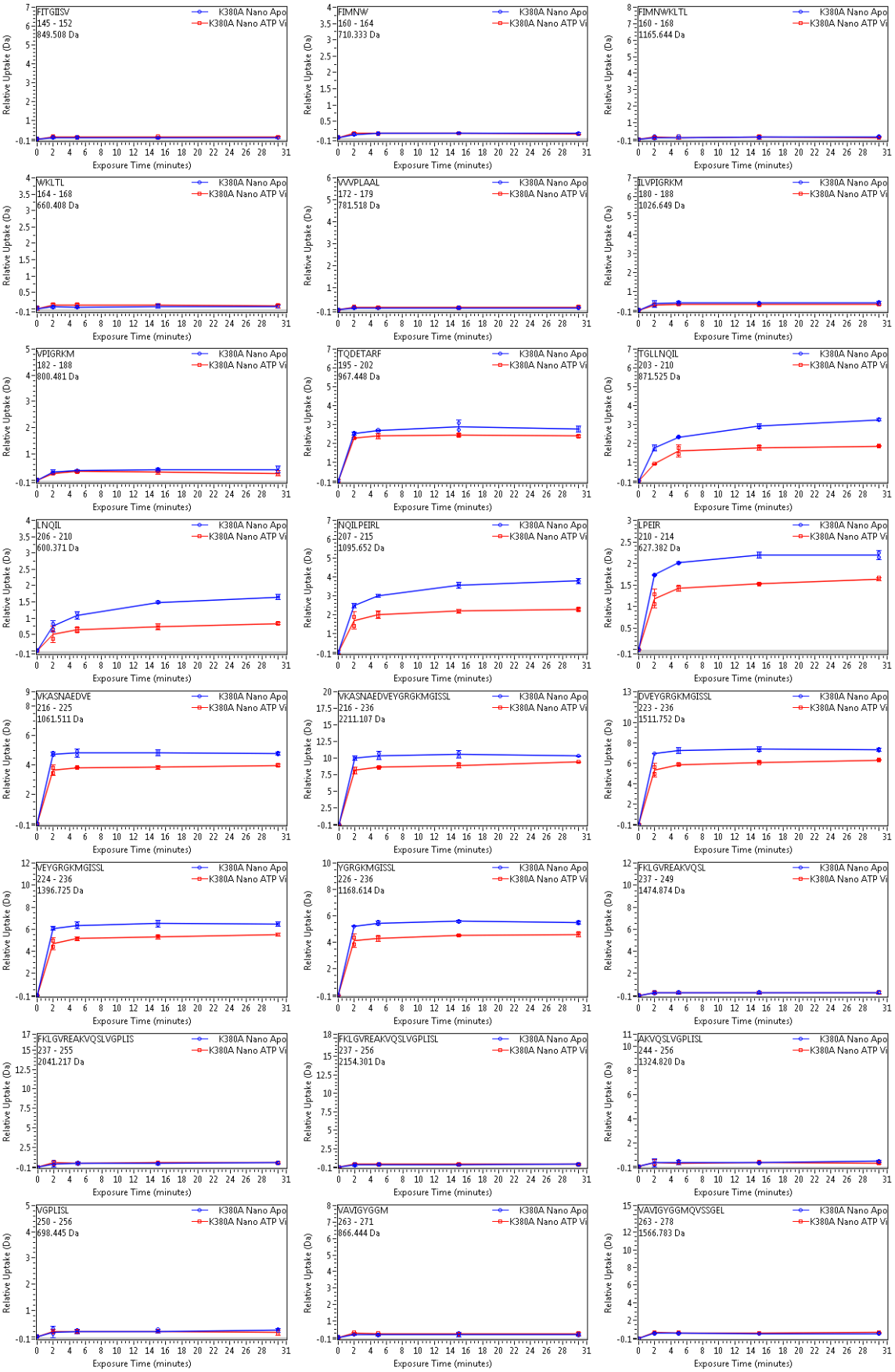
FITGIISV
145 - 152
849.508 Da
FIMNW
160 - 164
710.333 Da
FIMNWKLTL
160 - 168
1165.644 Da
WKLTL
164 - 168
660.408 Da
VVVPLAAL
172 - 179
781.518 Da
ILVPIGRKM
180 - 188
1026.649 Da
VPIGRKM
182 - 188
800.481 Da
TQDETARF
195 - 202
967.448 Da
TGLLNQIL
203 - 210
871.525 Da
LNQIL
206 - 210
600.371 Da
NQILPEIRL
207 - 215
1095.652 Da
LPEIR
210 - 214
627.382 Da
VKASNAEDVE
216 - 225
1061.511 Da
VKASNAEDVEYGRGKMGISSL
216 - 236
2211.107 Da
DVEYGRGKMGISSL
223 - 236
1511.752 Da
VEYGRGKMGISSL
224 - 236
1396.725 Da
YGRGKMGISSL
226 - 236
1168.614 Da
FKLGVREAKVQSL
237 - 249
1474.874 Da
FKLGVREAKVQSLVGPLIS
237 - 255
2041.217 Da
FKLGVREAKVQSLVGPLISL
237 - 256
2154.301 Da
AKVQSLVGPLISL
244 - 256
1324.820 Da
VGPLISL
250 - 256
698.445 Da
NAVIGYGGM
263 - 271
866.444 Da
NAVIGYGGMQVSSGEL
263 - 278
1566.783 Da
K380A Nano Apo
K380A Nano ATP Vi
Relative Uptake (Da)
Exposure Time (minutes)

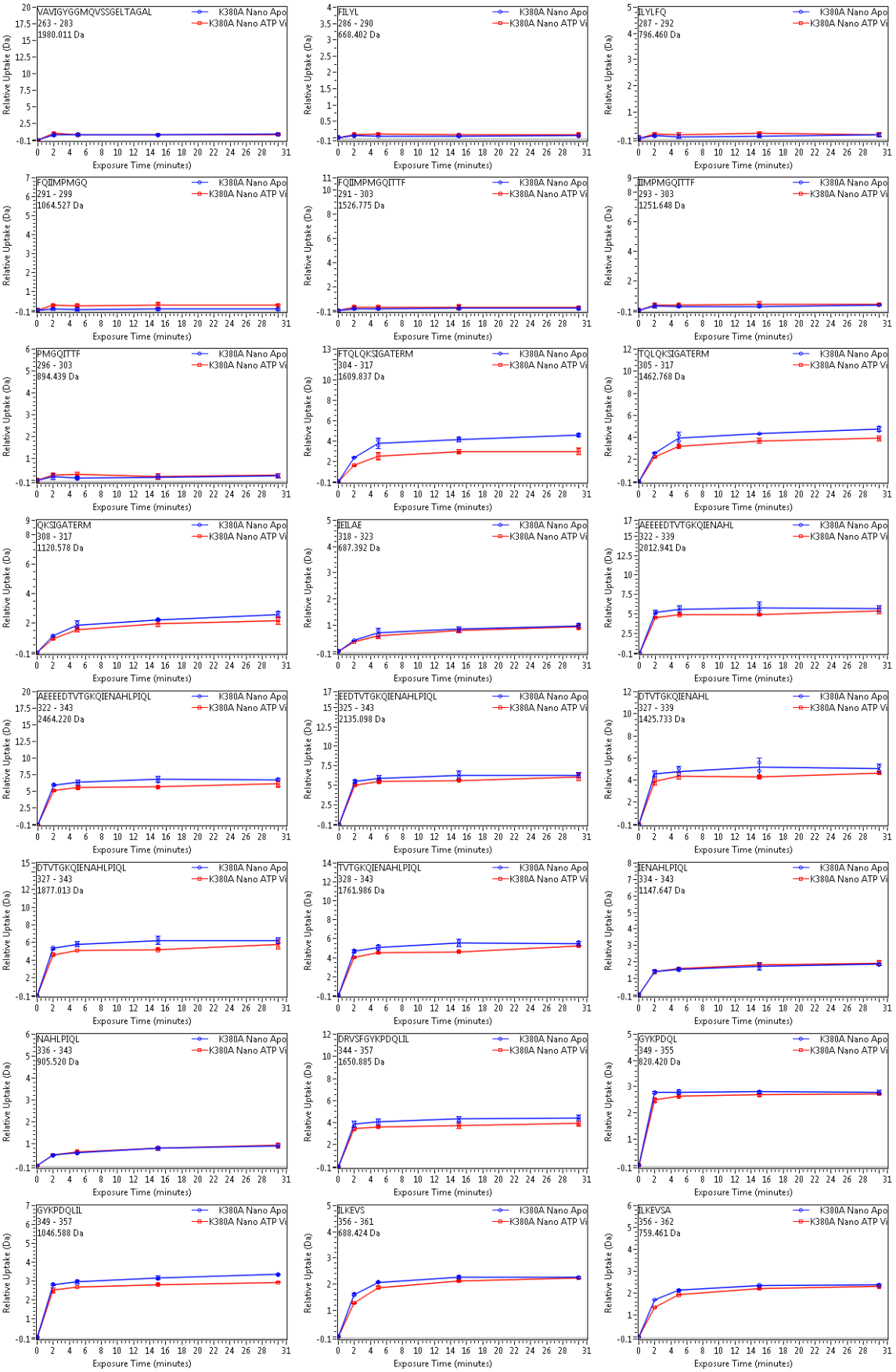
VAVIGYGGMQVSSGELTAGAL
263 - 283
1980.011 Da
FILYL
286 - 290
668.402 Da
ILYLFQ
287 - 292
796.460 Da
FQIIMPMGQ
291 - 299
1064.527 Da
FQIIMPMGQITTF
291 - 303
1526.775 Da
IIMPMGQITTF
293 - 303
1251.648 Da
PMGQITTF
296 - 303
894.439 Da
FTQLQKSIGATERM
304 - 317
1609.837 Da
TQLQKSIGATERM
305 - 317
1462.768 Da
QKSIGATERM
308 - 317
1120.578 Da
IEILAE
318 - 323
687.392 Da
AEEEEDTVTGKQIENAHL
322 - 339
2012.941 Da
AEEEEDTVTGKQIENAHLPIQL
322 - 343
2464.220 Da
EEDTVTGKQIENAHLPIQL
325 - 343
2135.098 Da
DTVTGKQIENAHL
327 - 339
1425.733 Da
DTVTGKQIENAHLPIQL
327 - 343
1877.013 Da
TVTGKQIENAHLPIQL
328 - 343
1761.986 Da
IENAHLPIQL
334 - 343
1147.647 Da
NAHLPIQL
336 - 343
905.520 Da
DRVSFGYKPDQLIL
344 - 357
1650.885 Da
GYKPDQL
349 - 355
820.420 Da
GYKPDQLIL
349 - 357
1046.588 Da
ILKEVS
356 - 361
688.424 Da
ILKEVSA
356 - 362
759.461 Da
K380A Nano Apo
K380A Nano ATP Vi
Relative Uptake (Da)
Exposure Time (minutes)

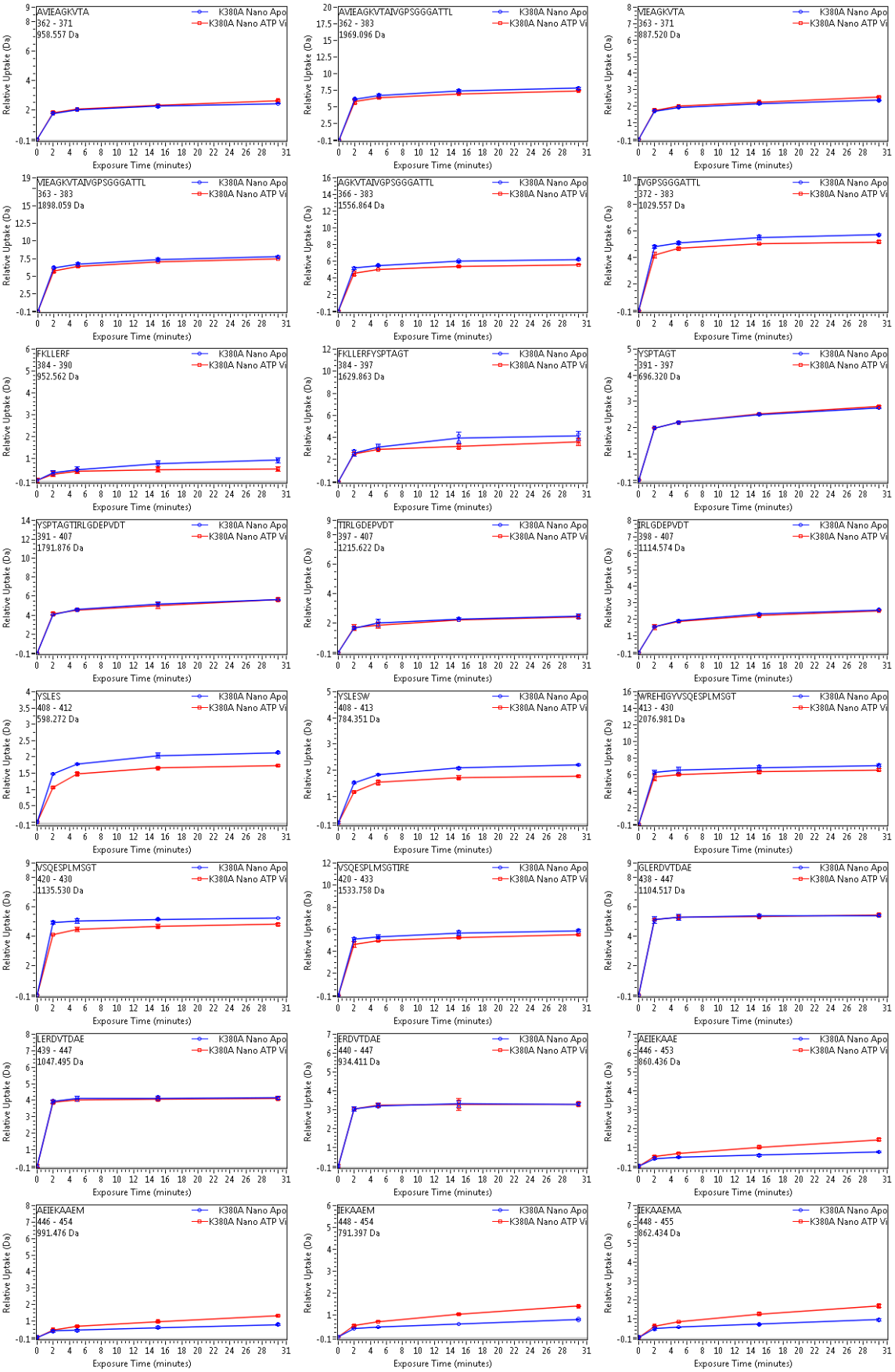
AVIEAGKVTA
362 - 371
958.557 Da
AVIEAGKVTAIVGPSGGGATTL
362 - 383
1969.096 Da
VIEAGKVTA
363 - 371
887.520 Da
VIEAGKVTAIVGPSGGGATTL
363 - 383
1898.059 Da
AGKVTAIVGPSGGGATTL
366 - 383
1556.864 Da
IVGPSGGGATTL
372 - 383
1029.557 Da
FKLLERF
384 - 390
952.562 Da
FKLLERFVSPTAGT
384 - 397
1629.863 Da
VSPTAGT
391 - 397
696.320 Da
VSPTAGTIRLGDEPVDT
391 - 407
1791.876 Da
TIRLGDEPVDT
397 - 407
1215.622 Da
IRLGDEPVDT
398 - 407
1114.574 Da
YSLES
408 - 412
598.272 Da
YSLESW
408 - 413
784.351 Da
WREHIGYVSQESPLMSGT
413 - 430
2076.981 Da
VSQESPLMSGT
420 - 430
1135.530 Da
VSQESPLMSGTIRE
420 - 433
1533.758 Da
GLERDVTDAE
438 - 447
1104.517 Da
LERDVTDAE
439 - 447
1047.495 Da
ERDVTDAE
440 - 447
934.411 Da
AEIEKAAE
446 - 453
860.436 Da
AEIEKAAEM
446 - 454
991.476 Da
IEKAAEM
448 - 454
791.397 Da
IEKAAEMA
448 - 455
862.434 Da
K380A Nano Apo
K380A Nano ATP Vi
Relative Uptake (Da)
Exposure Time (minutes)

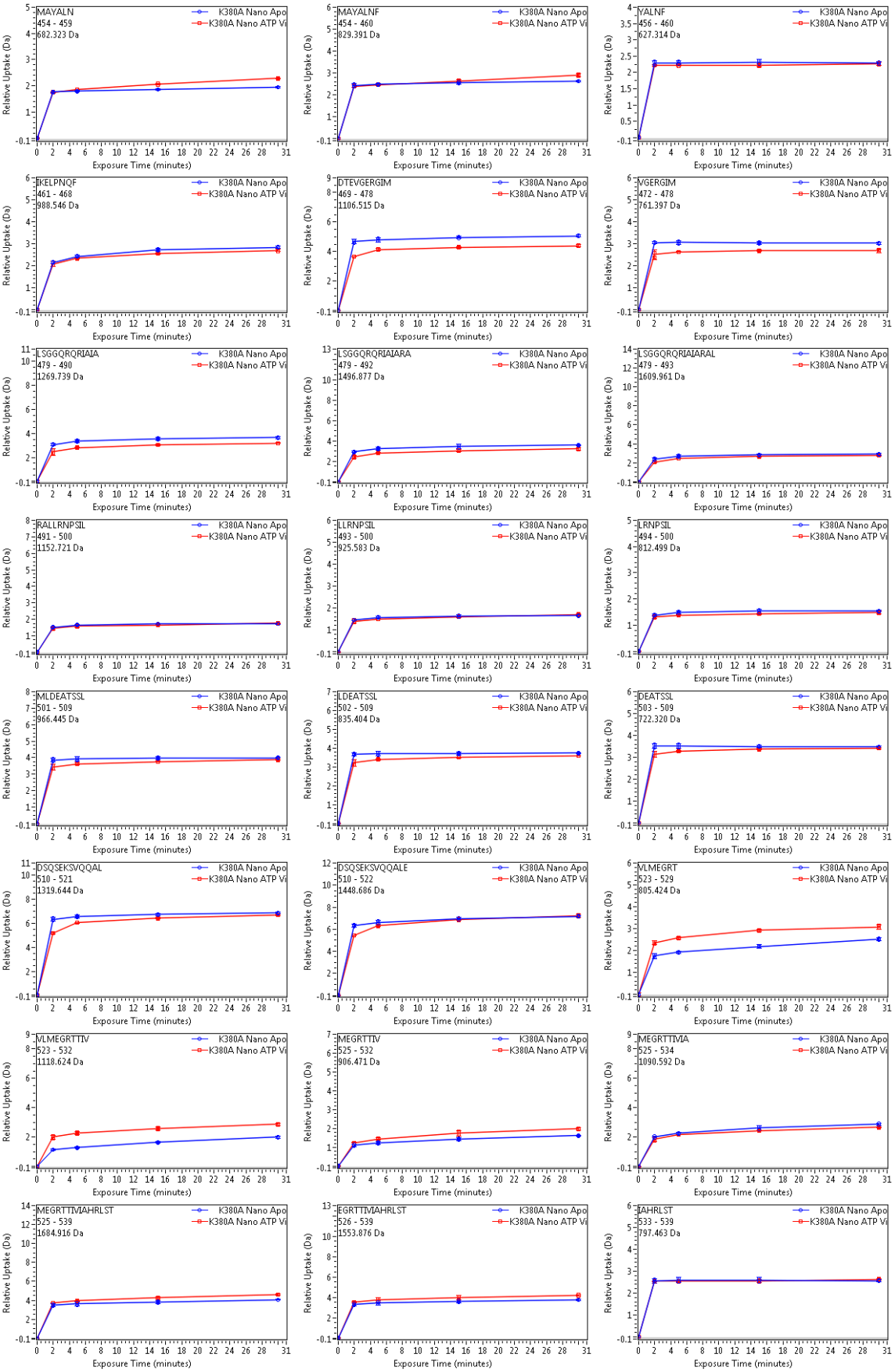
MAYALN
454 - 459
682.323 Da
MAYALNF
454 - 460
829.391 Da
YALNF
456 - 460
627.314 Da
IKELPNQF
461 - 468
988.546 Da
DTEVGERGIM
469 - 478
1106.515 Da
VGERGIM
472 - 478
761.397 Da
LSGGQRQRIAIA
479 - 490
1269.739 Da
LSGGQRQRIAIARA
479 - 492
1496.877 Da
LSGGQRQRIAIARAL
479 - 493
1609.961 Da
RALLRNPSIL
491 - 500
1152.721 Da
LLRNPSIL
493 - 500
925.583 Da
LRNPSIL
494 - 500
812.499 Da
MLDEATSSL
501 - 509
966.445 Da
LDEATSSL
502 - 509
835.404 Da
DEATSSL
503 - 509
722.320 Da
DSQSEKSVQQAL
510 - 521
1319.644 Da
DSQSEKSVQQALE
510 - 522
1448.686 Da
VLMEGRT
523 - 529
805.424 Da
VLMEGRTTIV
523 - 532
1118.624 Da
MEGRTTIV
525 - 532
906.471 Da
MEGRTTIVIA
525 - 534
1090.592 Da
MEGRTTIVIAHRLST
525 - 539
1684.916 Da
EGRTTIVIAHRLST
526 - 539
1553.876 Da
IAHRLST
533 - 539
797.463 Da
K380A Nano Apo
K380A Nano ATP Vi
Relative Uptake (Da)
Exposure Time (minutes)

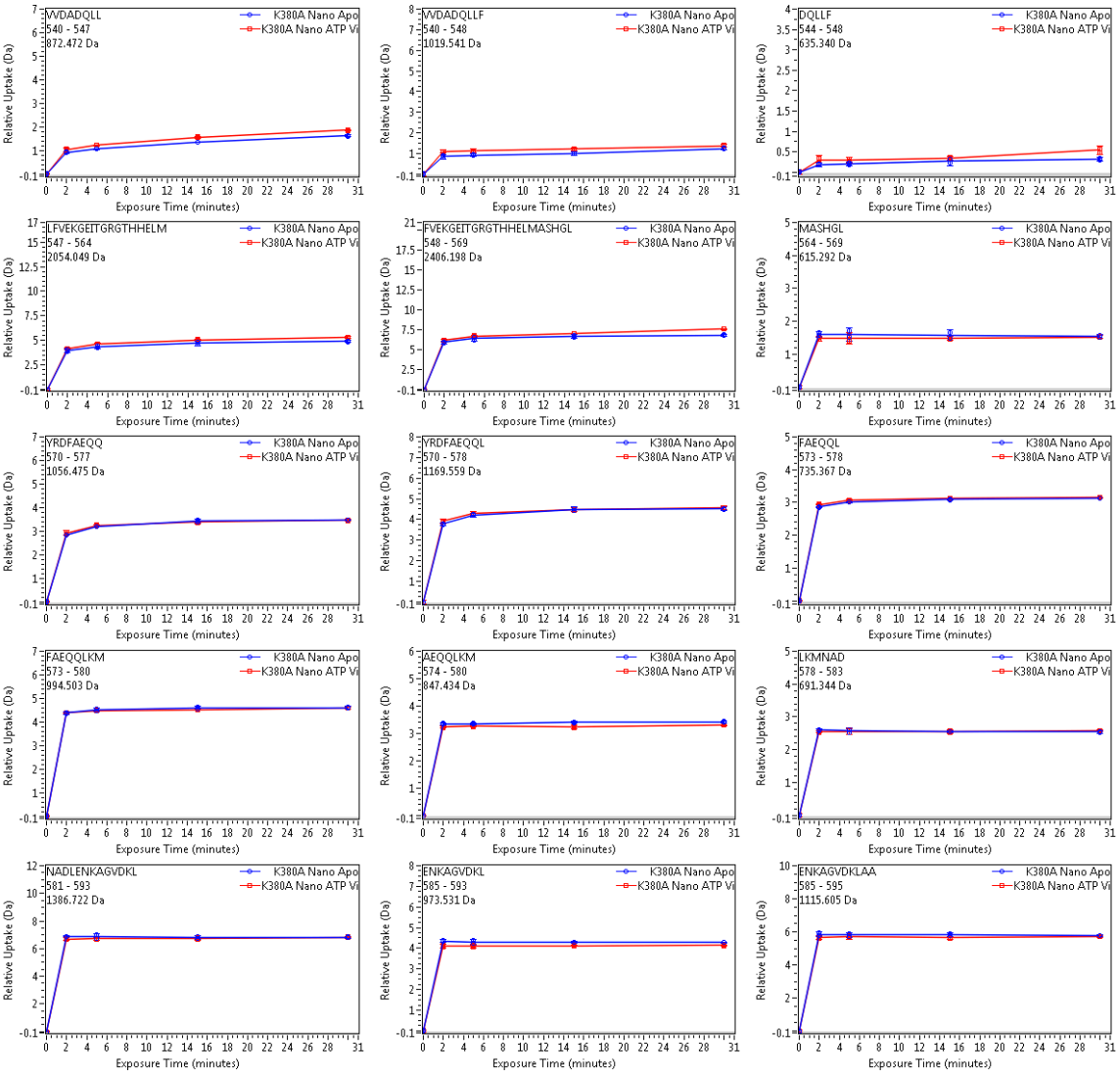
VVDADQLL
540 - 547
872.472 Da
VVDADQLLF
540 - 548
1019.541 Da
DQLLF
544 - 548
635.340 Da
LFVEKGEITGRGTHHELM
547 - 564
2054.049 Da
FVEKGEITGRGTHHELMASHGL
548 - 569
2406.198 Da
MASHGL
564 - 569
615.292 Da
YRDFAEQQ
570 - 577
1056.475 Da
YRDFAEQQL
570 - 578
1169.559 Da
FAEQQL
573 - 578
735.367 Da
FAEQQLKM
573 - 580
994.503 Da
AEQQLKM
574 - 580
847.434 Da
LKMNAD
578 - 583
691.344 Da
NADLENKAGVDKL
581 - 593
1386.722 Da
ENKAGVDKL
585 - 593
973.531 Da
ENKAGVDKLAA
585 - 595
1115.605 Da
K380A Nano Apo
K380A Nano ATP Vi
Relative Uptake (Da)
Exposure Time (minutes)

Annex 19 : Deuterium uptake plots of E504Q BmrA mutant in nanodiscs (DDM/cholate) in the Apo and ATP-trapped condition

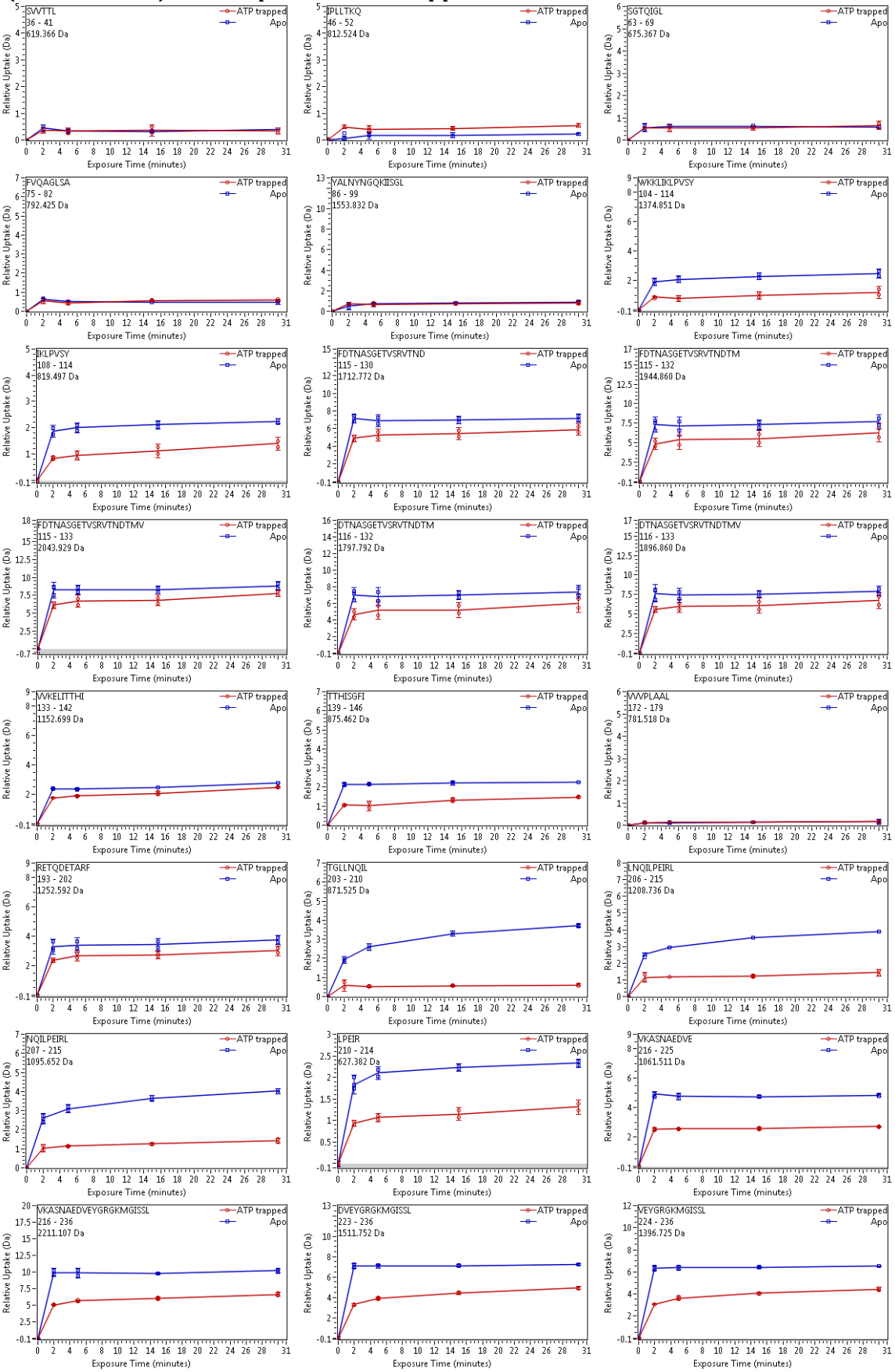

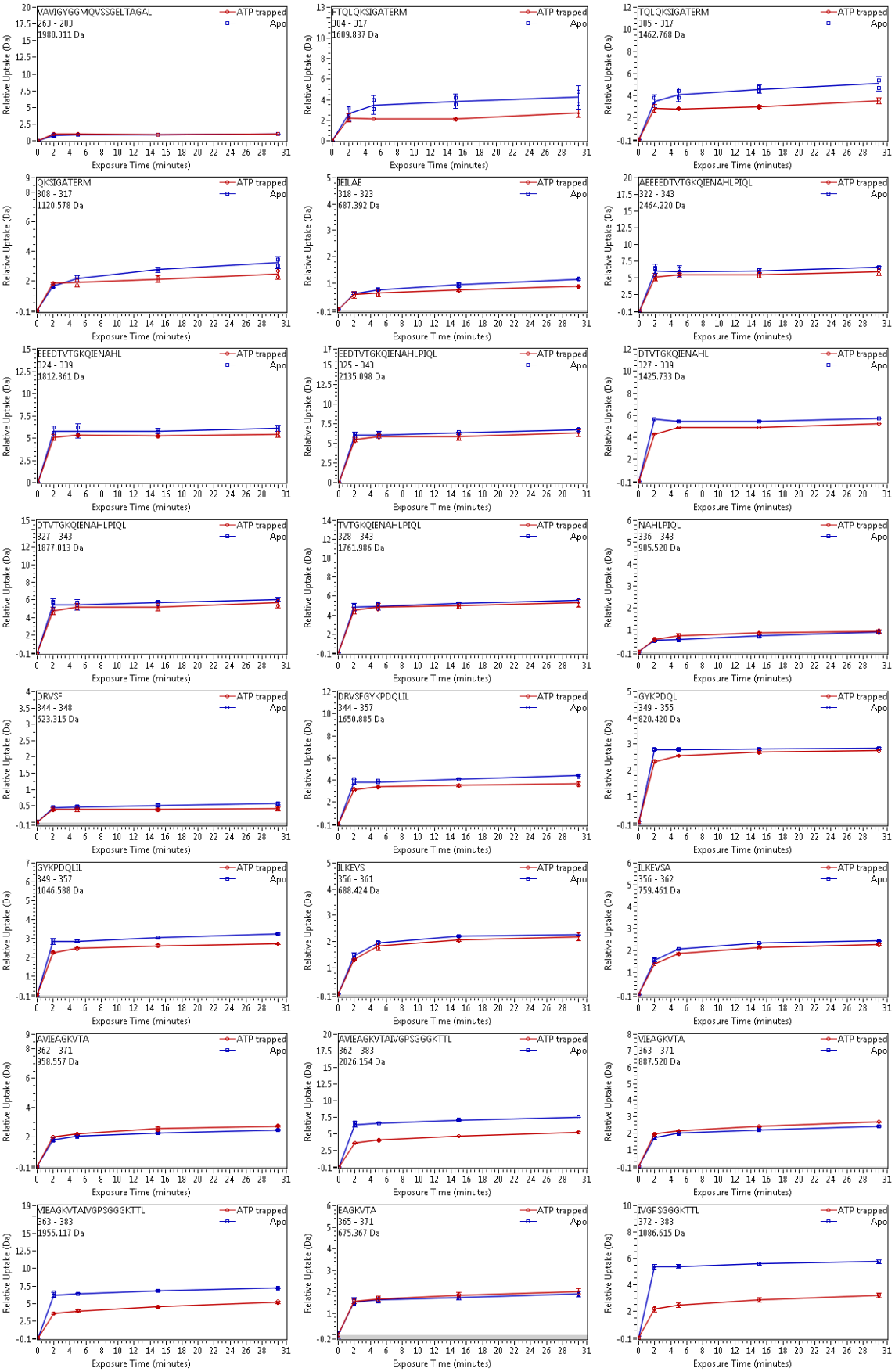
VAVIGYGGMQVSSGELTAGAL
263 - 283
1980.011 Da
FTQLQKSIGATERM
304 - 317
1609.837 Da
TQLQKSIGATERM
305 - 317
1462.768 Da
QKSIGATERM
308 - 317
1120.578 Da
EILAE
318 - 323
687.392 Da
AEEEEDTVTGKQIENAHLPIQL
322 - 343
2464.220 Da
EEEDTVTGKQIENAHL
324 - 339
1812.861 Da
EEDTVTGKQIENAHLPIQL
325 - 343
2135.098 Da
DTVTGKQIENAHL
327 - 339
1425.733 Da
DTVTGKQIENAHLPIQL
327 - 343
1877.013 Da
TVTGKQIENAHLPIQL
328 - 343
1761.986 Da
NAHLPIQL
336 - 343
905.520 Da
DRVSF
344 - 348
623.315 Da
DRVSFGYKPDQLIL
344 - 357
1650.885 Da
GVKPDQL
349 - 355
820.420 Da
GVKPDQLIL
349 - 357
1046.588 Da
ILKEVS
356 - 361
688.424 Da
ILKEVSA
356 - 362
759.461 Da
AVIEAGKVTA
362 - 371
958.557 Da
AVIEAGKVTAIVGPSGGGKTTL
362 - 383
2026.154 Da
VIEAGKVTA
363 - 371
887.520 Da
VIEAGKVTAIVGPSGGGKTTL
363 - 383
1955.117 Da
EAGKVTA
365 - 371
675.367 Da
IVGPSGGGKTTL
372 - 383
1086.615 Da
ATP trapped
Apo
Relative Uptake (Da)
Exposure Time (minutes)

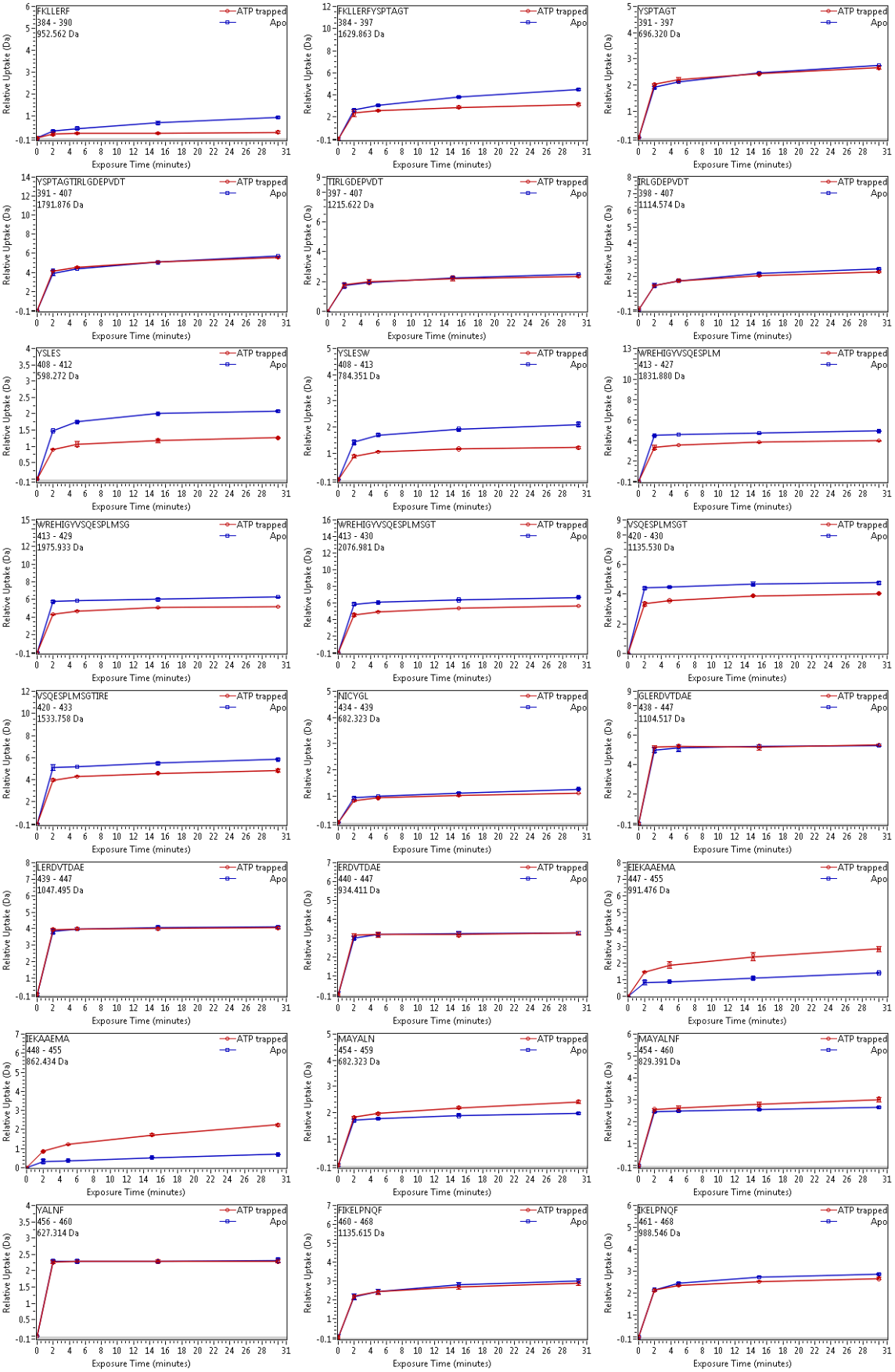
FKLLERF
384 - 390
952.562 Da
FKLLERFYSPTAGT
384 - 397
1629.863 Da
YSPTAGT
391 - 397
696.320 Da
YSPTAGTIRLGDEPVDT
391 - 407
1791.876 Da
IRLGDEPVDT
397 - 407
1215.622 Da
IRLGDEPVDT
398 - 407
1114.574 Da
YSLES
408 - 412
598.272 Da
YSLESW
408 - 413
784.351 Da
WREHIGYVSQESPLM
413 - 427
1831.880 Da
WREHIGYVSQESPLMSG
413 - 429
1975.933 Da
WREHIGYVSQESPLMSGT
413 - 430
2076.981 Da
VSQESPLMSGT
420 - 430
1135.530 Da
VSQESPLMSGTIRE
420 - 433
1533.758 Da
NICYGL
434 - 439
682.323 Da
GLERDVTDAE
438 - 447
1104.517 Da
LERDVTDAE
439 - 447
1047.495 Da
ERDVTDAE
440 - 447
934.411 Da
EIEKAAEMA
447 - 455
991.476 Da
IEKAAEMA
448 - 455
862.434 Da
MAYALN
454 - 459
682.323 Da
MAYALNF
454 - 460
829.391 Da
YALNF
456 - 460
627.314 Da
FIKELPNQF
460 - 468
1135.615 Da
IKELPNQF
461 - 468
988.546 Da
ATP trapped
Apo
Relative Uptake (Da)
Exposure Time (minutes)

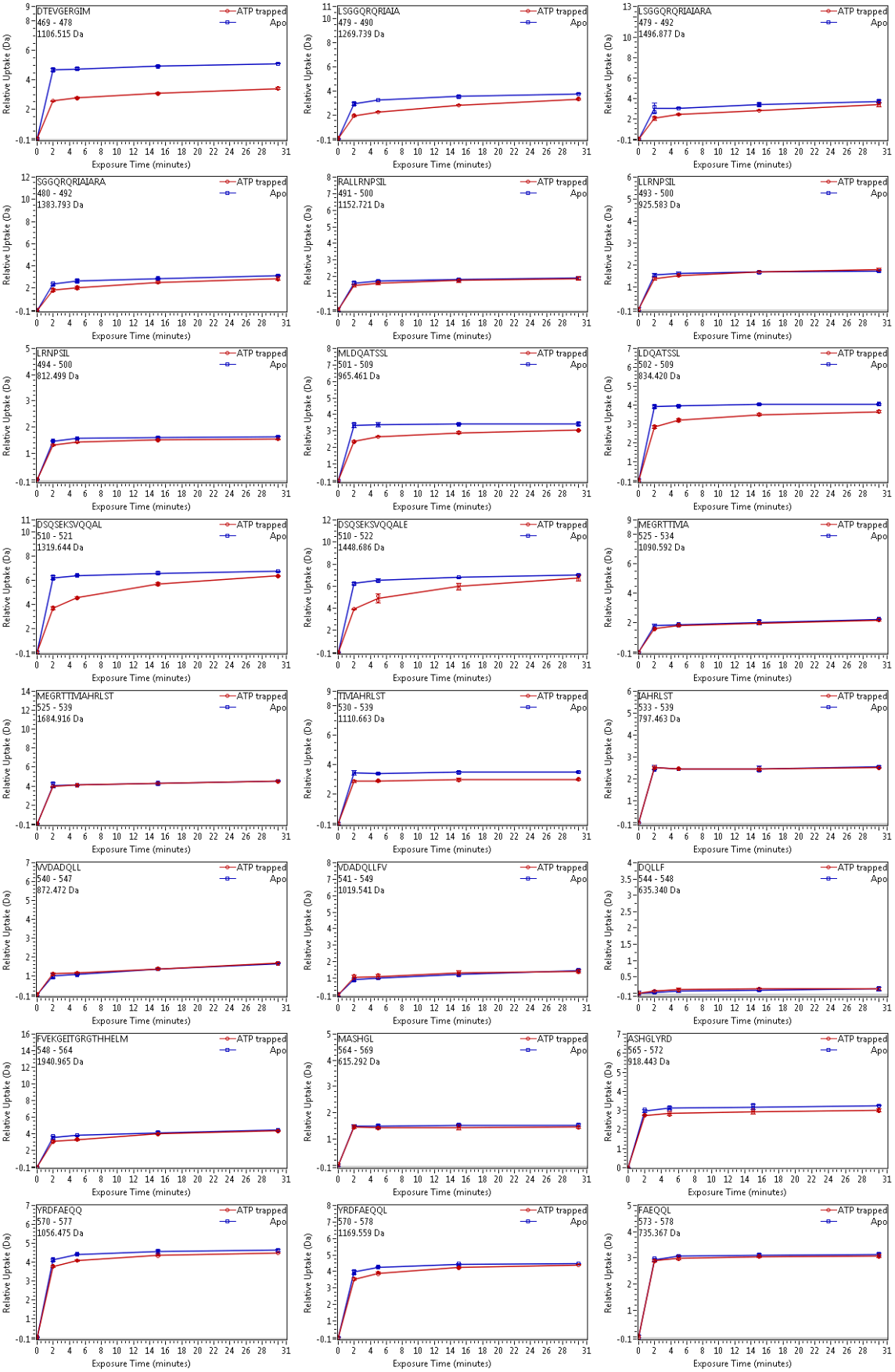
DTEVGERGIM
469 - 478
1106.515 Da
LSGGQRQRIAIA
479 - 490
1269.739 Da
LSGGQRQRIAIARA
479 - 492
1496.877 Da
SGGQRQRIAIARA
480 - 492
1383.793 Da
RALLRNPSIL
491 - 500
1152.721 Da
LLRNPSIL
493 - 500
925.583 Da
LRNPSIL
494 - 500
812.499 Da
MLDQATSSL
501 - 509
965.461 Da
LDQATSSL
502 - 509
834.420 Da
DSQSEKSVQQAL
510 - 521
1319.644 Da
DSQSEKSVQQALE
510 - 522
1448.686 Da
MEGRTTIVIA
525 - 534
1090.592 Da
MEGRTTIVIAHRLST
525 - 539
1684.916 Da
TIVIAHRLST
530 - 539
1110.663 Da
IAHRLST
533 - 539
797.463 Da
VVDADQLL
540 - 547
872.472 Da
VDADQLLFV
541 - 549
1019.541 Da
DQLLF
544 - 548
635.340 Da
FVEKGEITGRGTHHELM
548 - 564
1940.965 Da
MASHGL
564 - 569
615.292 Da
ASHGLYRD
565 - 572
918.443 Da
YRDFAEQQ
570 - 577
1056.475 Da
YRDFAEQQL
570 - 578
1169.559 Da
FAEQQL
573 - 578
735.367 Da
ATP trapped
Apo
Relative Uptake (Da)
Exposure Time (minutes)

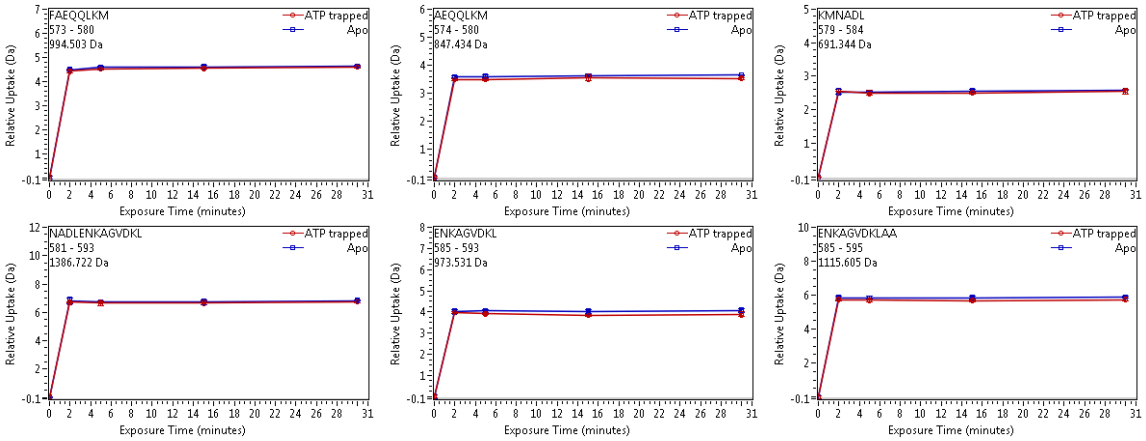
FAEQQLKM
573 - 580
994.503 Da
AEQQLKM
574 - 580
847.434 Da
KMNADL
579 - 584
691.344 Da
NADLENKAGVDKL
581 - 593
1386.722 Da
ENKAGVDKL
585 - 593
973.531 Da
ENKAGVDKLAA
585 - 595
1115.605 Da
ATP trapped
Apo
Relative Uptake (Da)
Exposure Time (minutes)

Annex 20 : Deuterium uptake plots of W413F BmrA mutant in nanodiscs (LMNG) in the Apo and Vi-trapped condition

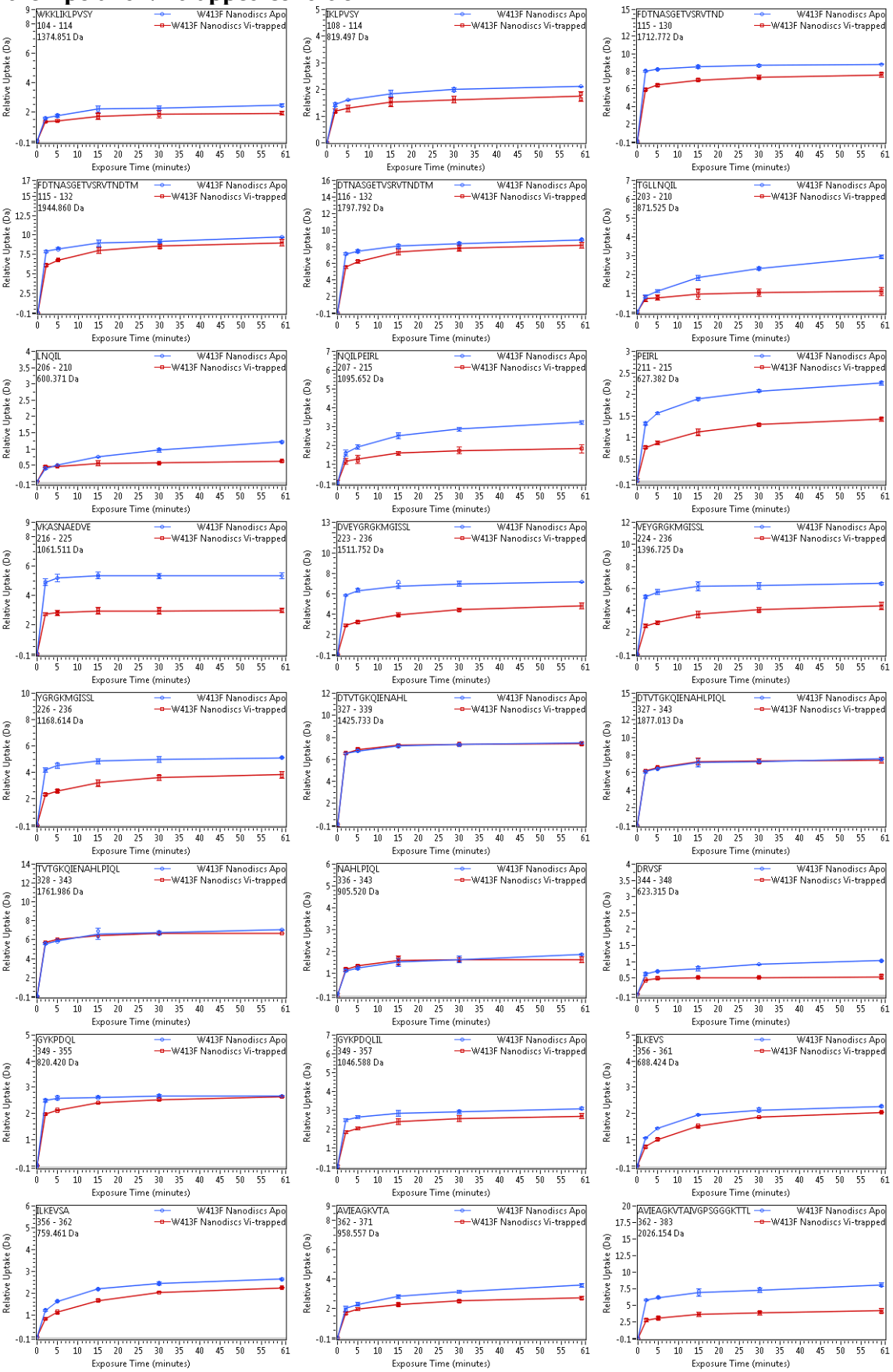

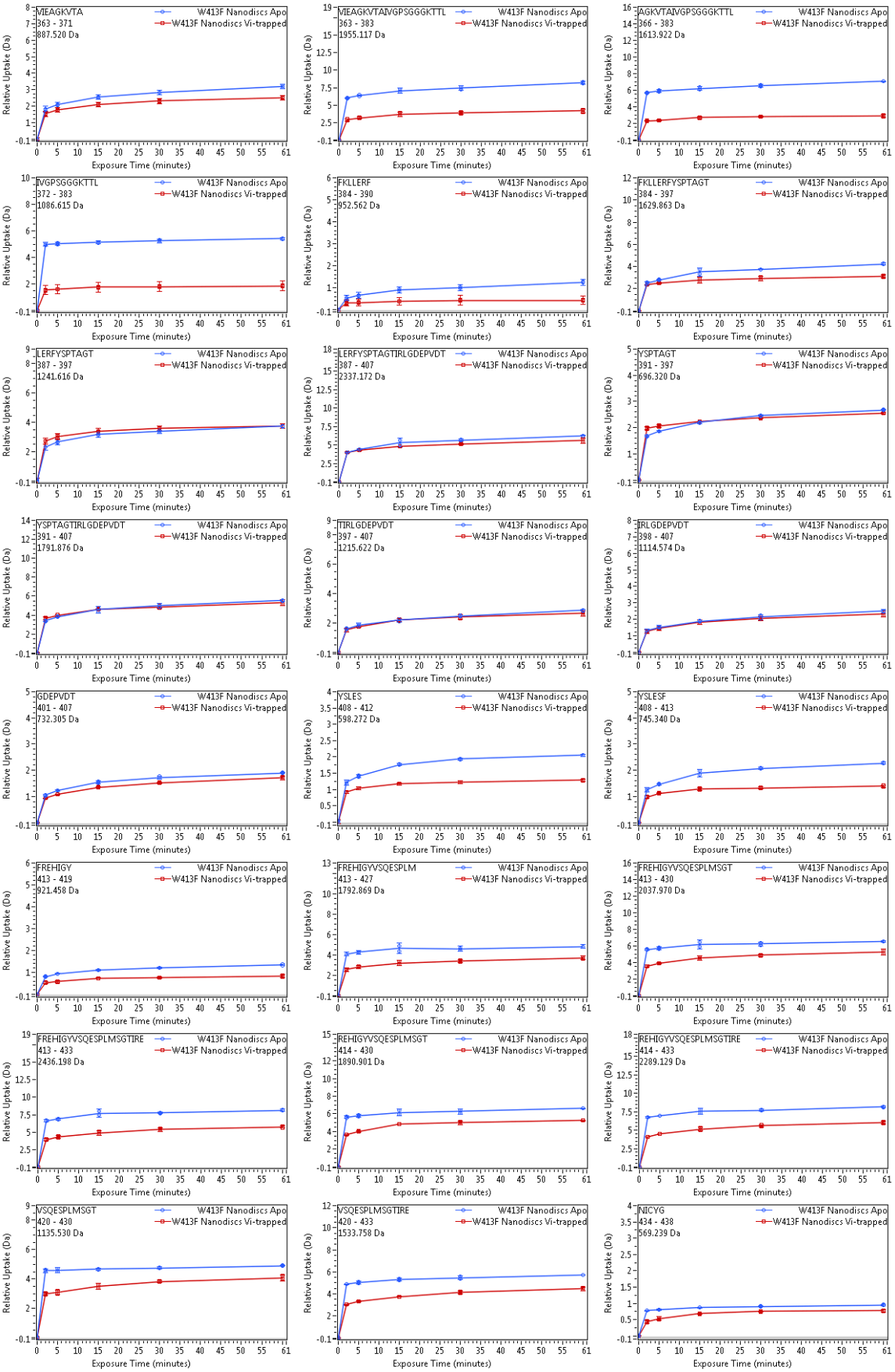
VIEAGKVTA
363 - 371
887.520 Da
VIEAGKVTAIVGPSGGGKTTL
363 - 383
1955.117 Da
AGKVTAIVGPSGGGKTTL
366 - 383
1613.922 Da
IVGPSGGGKTTL
372 - 383
1086.615 Da
FKLLERF
384 - 390
952.562 Da
FKLLERFYSPTAGT
384 - 397
1629.863 Da
LERFYSPTAGT
387 - 397
1241.616 Da
LERFYSPTAGTIRLGDEPVDT
387 - 407
2337.172 Da
YSPTAGT
391 - 397
696.320 Da
YSPTAGTIRLGDEPVDT
391 - 407
1791.876 Da
TIRLGDEPVDT
397 - 407
1215.622 Da
IRLGDEPVDT
398 - 407
1114.574 Da
GDEPVDT
401 - 407
732.305 Da
YSLES
408 - 412
598.272 Da
YSLESF
408 - 413
745.340 Da
FREHIGY
413 - 419
921.458 Da
FREHIGYVSQESPLM
413 - 427
1792.869 Da
FREHIGYVSQESPLMSGT
413 - 430
2037.970 Da
FREHIGYVSQESPLMSGTIRE
413 - 433
2436.198 Da
REHIGYVSQESPLMSGT
414 - 430
1890.901 Da
REHIGYVSQESPLMSGTIRE
414 - 433
2289.129 Da
VSQESPLMSGT
420 - 430
1135.530 Da
VSQESPLMSGTIRE
420 - 433
1533.758 Da
NICYG
434 - 438
569.239 Da
W413F Nanodiscs Apo
W413F Nanodiscs Vi-trapped
Relative Uptake (Da)
Exposure Time (minutes)

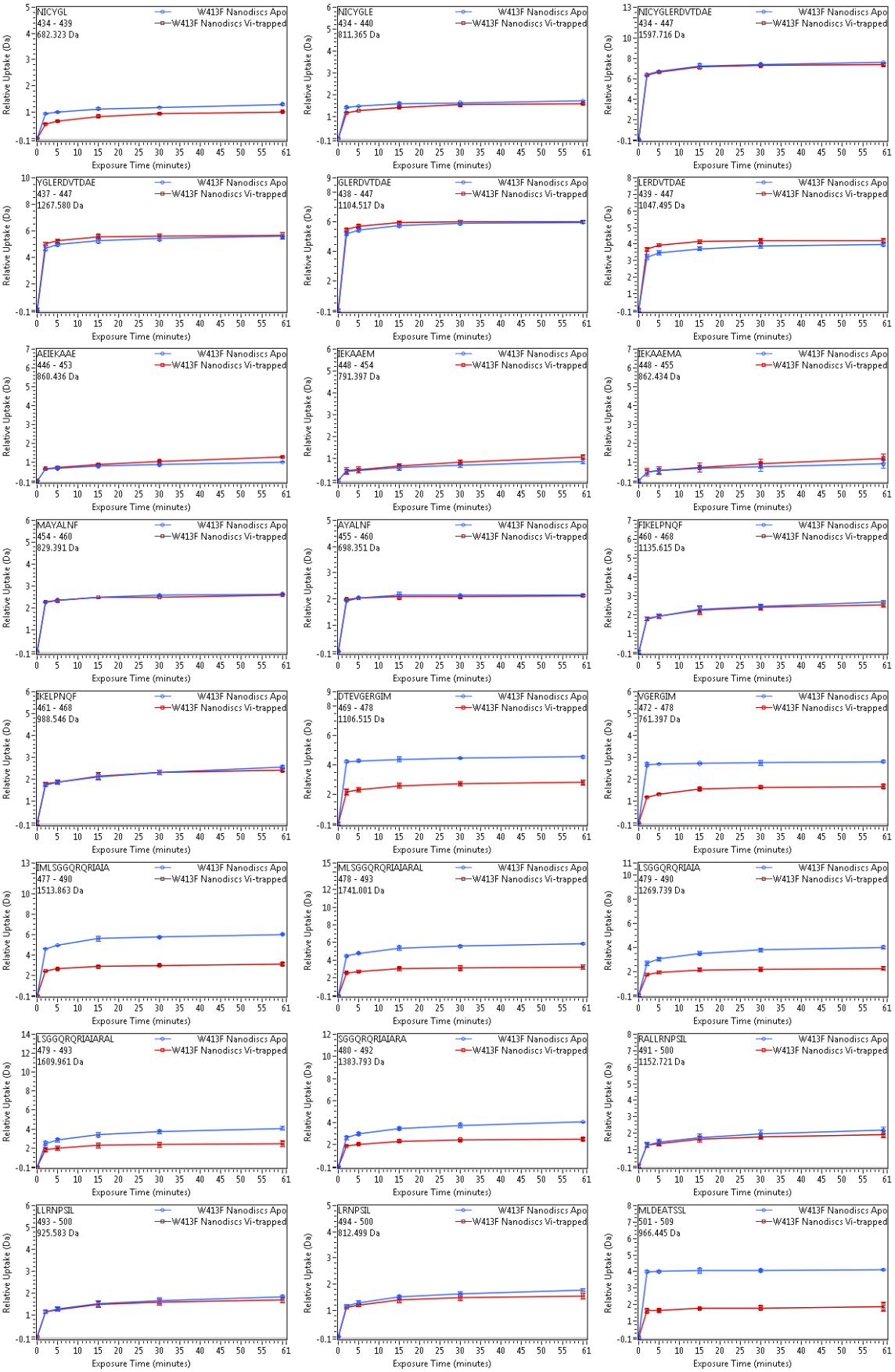
NICYGL
434 - 439
682.323 Da
NICYGLE
434 - 440
811.365 Da
NICYGLERDVTDAE
434 - 447
1597.716 Da
YGLERDVTDAE
437 - 447
1267.580 Da
GLERDVTDAE
438 - 447
1104.517 Da
LERDVTDAE
439 - 447
1047.495 Da
AEIEKAAE
446 - 453
860.436 Da
IEKAAEM
448 - 454
791.397 Da
IEKAAEMA
448 - 455
862.434 Da
MAYALNF
454 - 460
829.391 Da
AYALNF
455 - 460
698.351 Da
FIKELPNQF
460 - 468
1135.615 Da
IKELPNQF
461 - 468
988.546 Da
DTEVGERGIM
469 - 478
1106.515 Da
VGERGIM
472 - 478
761.397 Da
IMLSGGQRQRIAIA
477 - 490
1513.863 Da
MLSGGQRQRIAIARAL
478 - 493
1741.001 Da
LSGGQRQRIAIA
479 - 490
1269.739 Da
LSGGQRQRIAIARAL
479 - 493
1609.961 Da
SGGQRQRIAIARA
480 - 492
1383.793 Da
RALLRNPSIL
491 - 500
1152.721 Da
LLRNPSIL
493 - 500
925.583 Da
LRNPSIL
494 - 500
812.499 Da
MLDEATSSL
501 - 509
966.445 Da
W413F Nanodiscs Apo
W413F Nanodiscs Vi-trapped
Relative Uptake (Da)
Exposure Time (minutes)

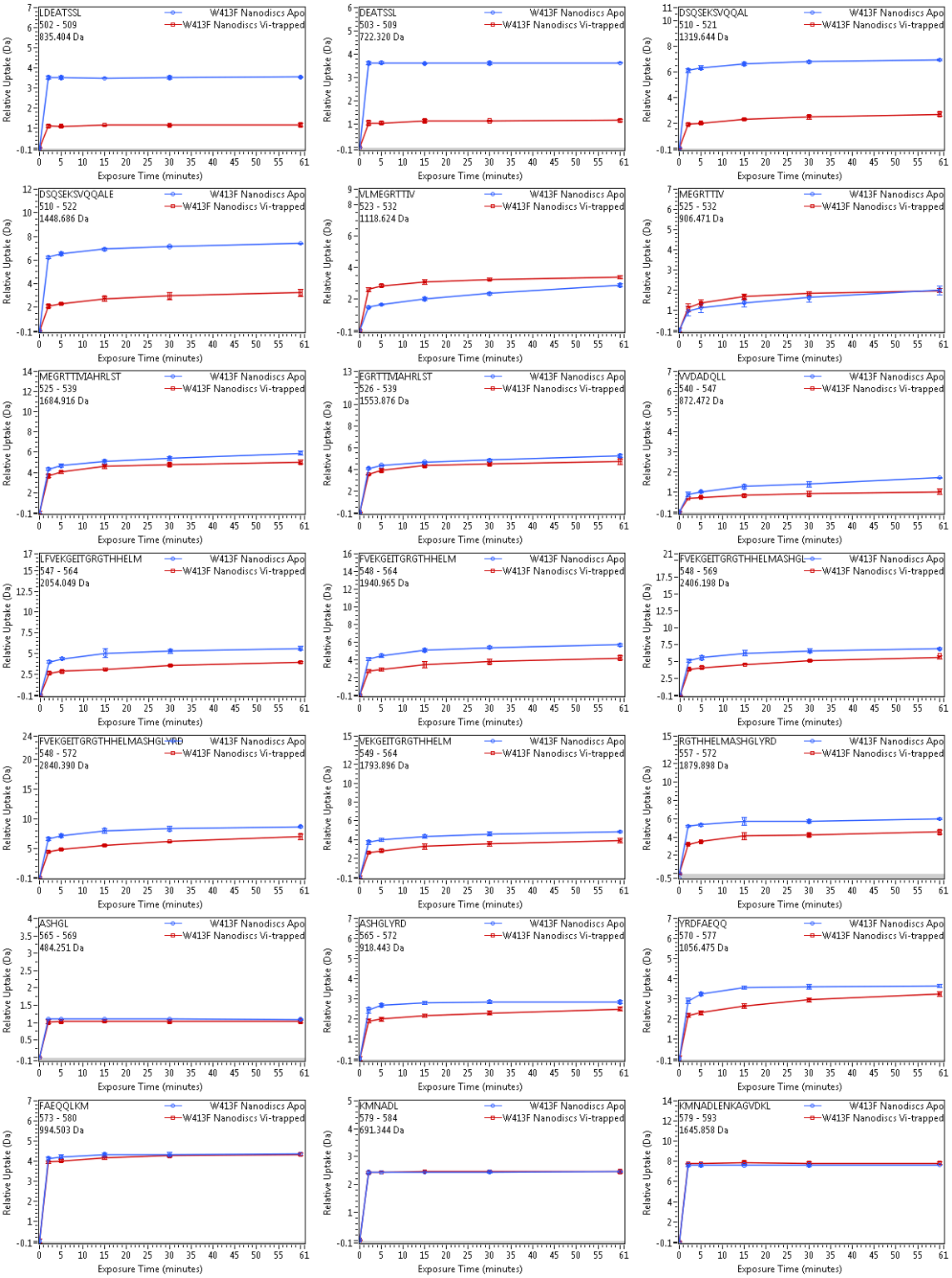
LDEATSSL
502 - 509
835.404 Da
DEATSSL
503 - 509
722.320 Da
DSQSEKSVQQAL
510 - 521
1319.644 Da
DSQSEKSVQQALE
510 - 522
1448.686 Da
VLMEGRTTIV
523 - 532
1118.624 Da
MEGRTTIV
525 - 532
906.471 Da
MEGRTTIVIAHRLST
525 - 539
1684.916 Da
EGRTTIVIAHRLST
526 - 539
1553.876 Da
VVDADQLL
540 - 547
872.472 Da
LFVEKGEITGRGTHHELM
547 - 564
2054.049 Da
FVEKGEITGRGTHHELM
548 - 564
1940.965 Da
FVEKGEITGRGTHHELMASHGL
548 - 569
2406.198 Da
FVEKGEITGRGTHHELMASHGLYRD
548 - 572
2840.390 Da
VEKGEITGRGTHHELM
549 - 564
1793.896 Da
RGTHHELMASHGLYRD
557 - 572
1879.898 Da
ASHGL
565 - 569
484.251 Da
ASHGLYRD
565 - 572
918.443 Da
YRDFAEQQ
570 - 577
1056.475 Da
FAEQQLKM
573 - 580
994.503 Da
KMNADL
579 - 584
691.344 Da
KMNADLENKAGVDKL
579 - 593
1645.858 Da
W413F Nanodiscs Apo
W413F Nanodiscs Vi-trapped
Relative Uptake (Da)
Exposure Time (minutes)

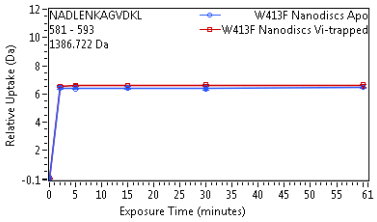
NADLENKAGVDKL
581 - 593
1386.722 Da
W413F Nanodiscs Apo
W413F Nanodiscs Vi-trapped
Relative Uptake (Da)
Exposure Time (minutes)

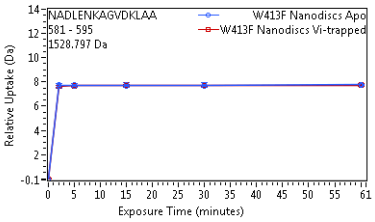
NADLENKAGVDKLAA
581 - 595
1528.797 Da
W413F Nanodiscs Apo
W413F Nanodiscs Vi-trapped
Relative Uptake (Da)
Exposure Time (minutes)

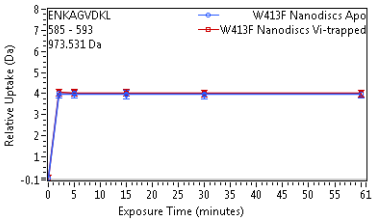
ENKAGVDKL
585 - 593
973.531 Da
W413F Nanodiscs Apo
W413F Nanodiscs Vi-trapped
Relative Uptake (Da)
Exposure Time (minutes)

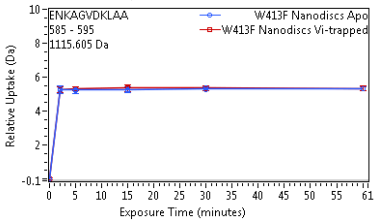
ENKAGVDKLAA
585 - 595
1115.605 Da
W413F Nanodiscs Apo
W413F Nanodiscs Vi-trapped
Relative Uptake (Da)
Exposure Time (minutes)

Annex 21 : Deuterium uptake plots of W413F BmrA mutant in nanodiscs (LMNG) in the Apo and doxorubicin-bound condition

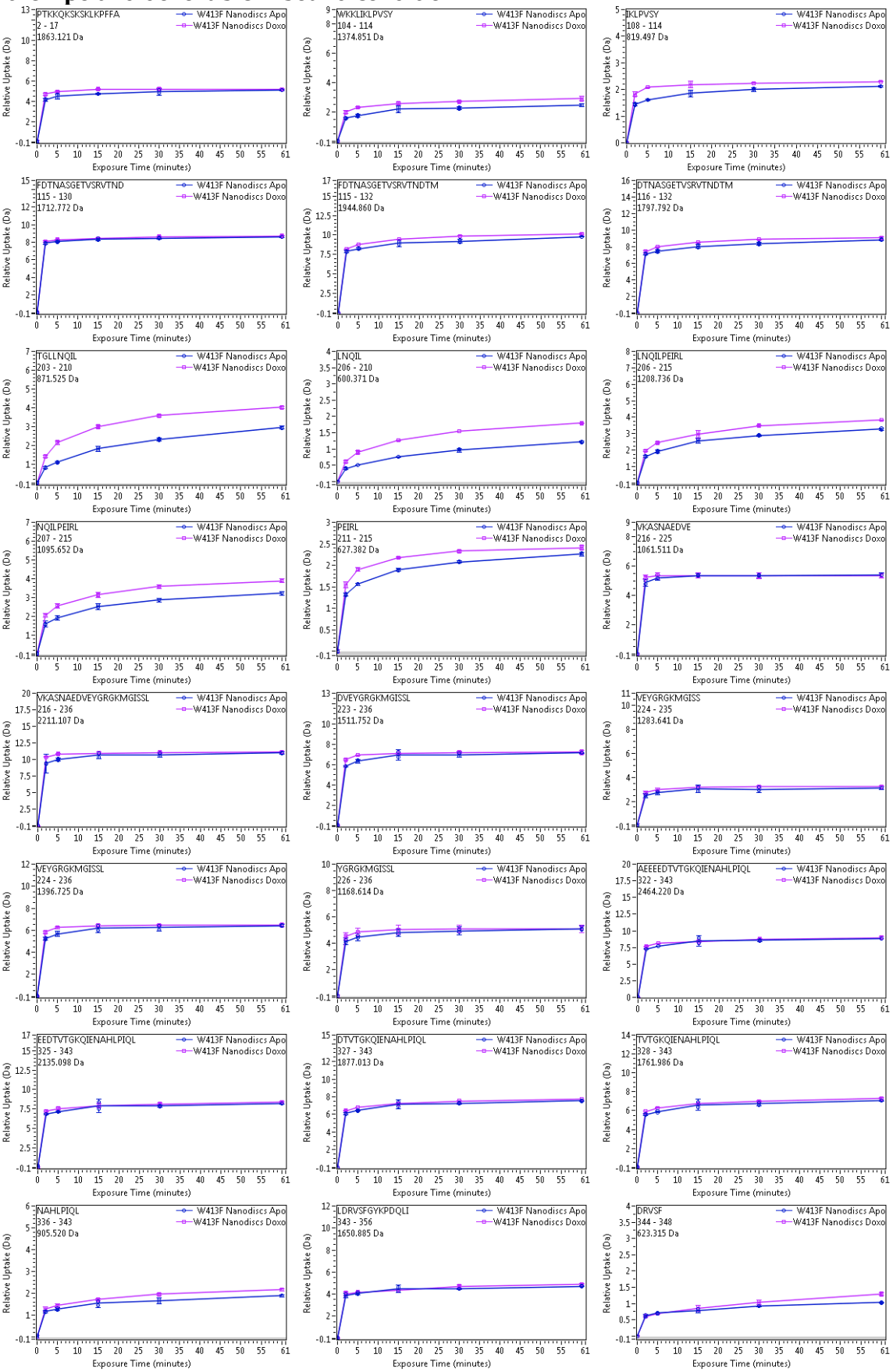

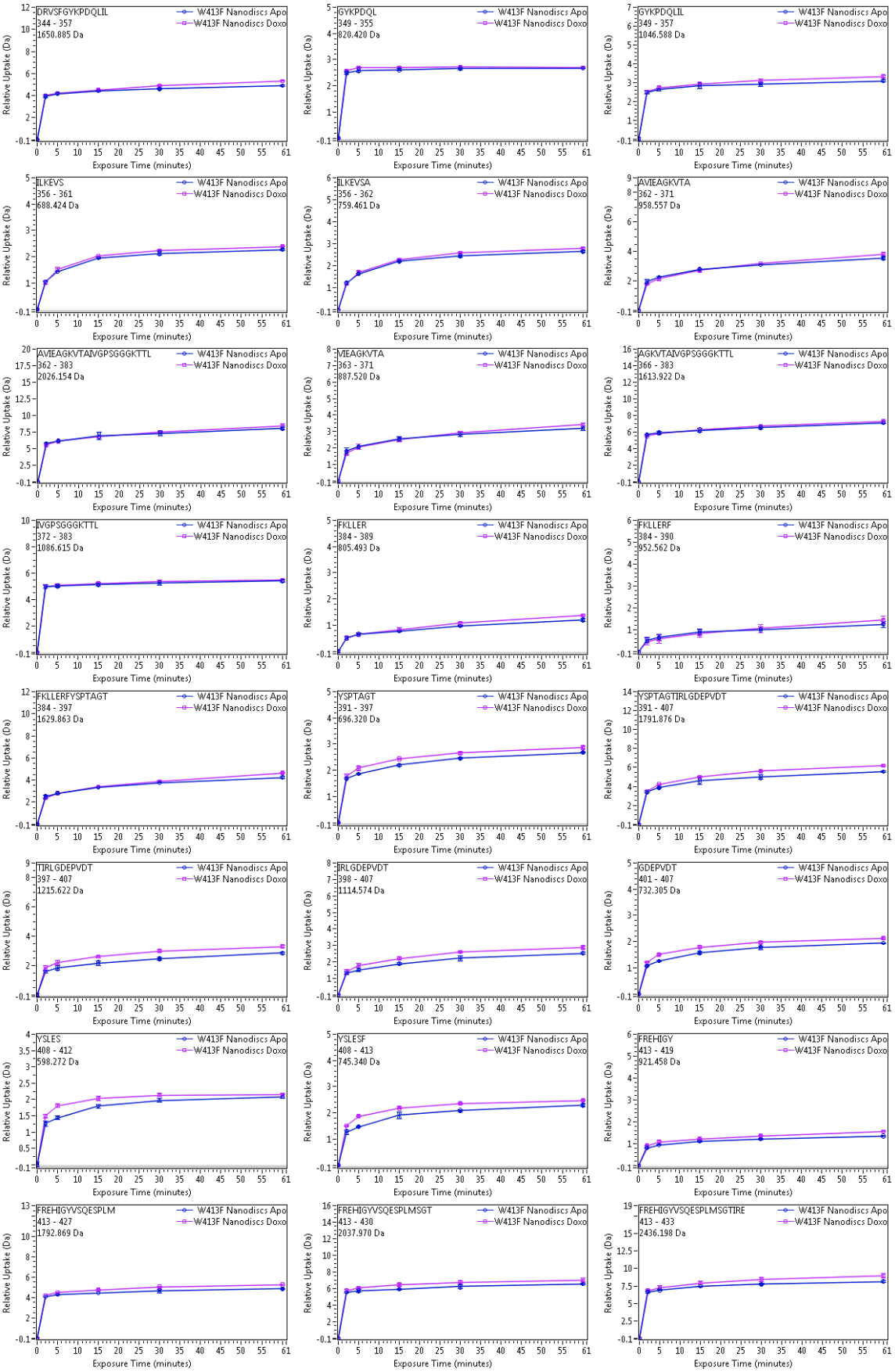
DRVSFGYKPDQLIL
344 - 357
1650.885 Da
GYKPDQL
349 - 355
820.420 Da
GYKPDQLIL
349 - 357
1046.588 Da
ILKEVS
356 - 361
688.424 Da
ILKEVSA
356 - 362
759.461 Da
AVIEAGKVTA
362 - 371
958.557 Da
AVIEAGKVTAIVGPSGGGKTTL
362 - 383
2026.154 Da
VIEAGKVTA
363 - 371
887.520 Da
AGKVTAIVGPSGGGKTTL
366 - 383
1613.922 Da
IVGPSGGGKTTL
372 - 383
1086.615 Da
FKLLER
384 - 389
805.493 Da
FKLLERF
384 - 390
952.562 Da
FKLLERFYSPTAGT
384 - 397
1629.863 Da
YSPTAGT
391 - 397
696.320 Da
YSPTAGTIRLGDEPVDT
391 - 407
1791.876 Da
TIRLGDEPVDT
397 - 407
1215.622 Da
IRLGDEPVDT
398 - 407
1114.574 Da
GDEPVDT
401 - 407
732.305 Da
YSLES
408 - 412
598.272 Da
YSLESF
408 - 413
745.340 Da
FREHIGY
413 - 419
921.458 Da
FREHIGYVSQESPLM
413 - 427
1792.869 Da
FREHIGYVSQESPLMSGT
413 - 430
2037.970 Da
FREHIGYVSQESPLMSGTIRE
413 - 433
2436.198 Da
W413F Nanodiscs Apo
W413F Nanodiscs Doxo
Relative Uptake (Da)
Exposure Time (minutes)

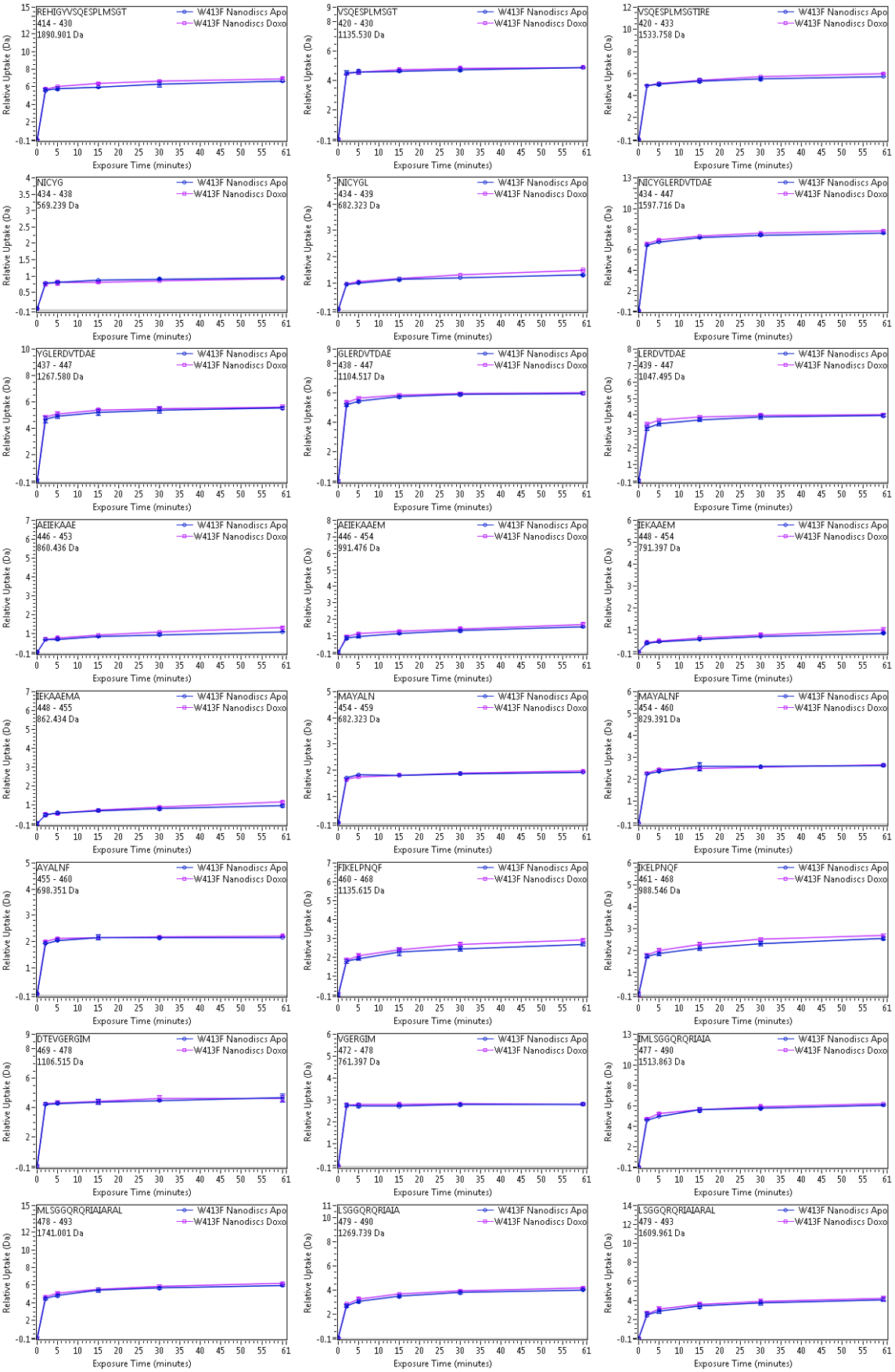
REHIGYVSQESPLMSGT
414 - 430
1890.901 Da
VSQESPLMSGT
420 - 430
1135.530 Da
VSQESPLMSGTIRE
420 - 433
1533.758 Da
NICYG
434 - 438
569.239 Da
NICYGL
434 - 439
682.323 Da
NICYGLERDVTDAE
434 - 447
1597.716 Da
YGLERDVTDAE
437 - 447
1267.580 Da
GLERDVTDAE
438 - 447
1104.517 Da
LERDVTDAE
439 - 447
1047.495 Da
AEIEKAAE
446 - 453
860.436 Da
AEIEKAAEM
446 - 454
991.476 Da
IEKAAEM
448 - 454
791.397 Da
IEKAAEMA
448 - 455
862.434 Da
MAYALN
454 - 459
682.323 Da
MAYALNF
454 - 460
829.391 Da
AYALNF
455 - 460
698.351 Da
FIKELPNQF
460 - 468
1135.615 Da
IKELPNQF
461 - 468
988.546 Da
DTEVGERGIM
469 - 478
1106.515 Da
VGERGIM
472 - 478
761.397 Da
IMLSGGQRQRIAIA
477 - 490
1513.863 Da
MLSGGQRQRIAIARAL
478 - 493
1741.001 Da
LSGGQRQRIAIA
479 - 490
1269.739 Da
LSGGQRQRIAIARAL
479 - 493
1609.961 Da
W413F Nanodiscs Apo
W413F Nanodiscs Doxo
Relative Uptake (Da)
Exposure Time (minutes)

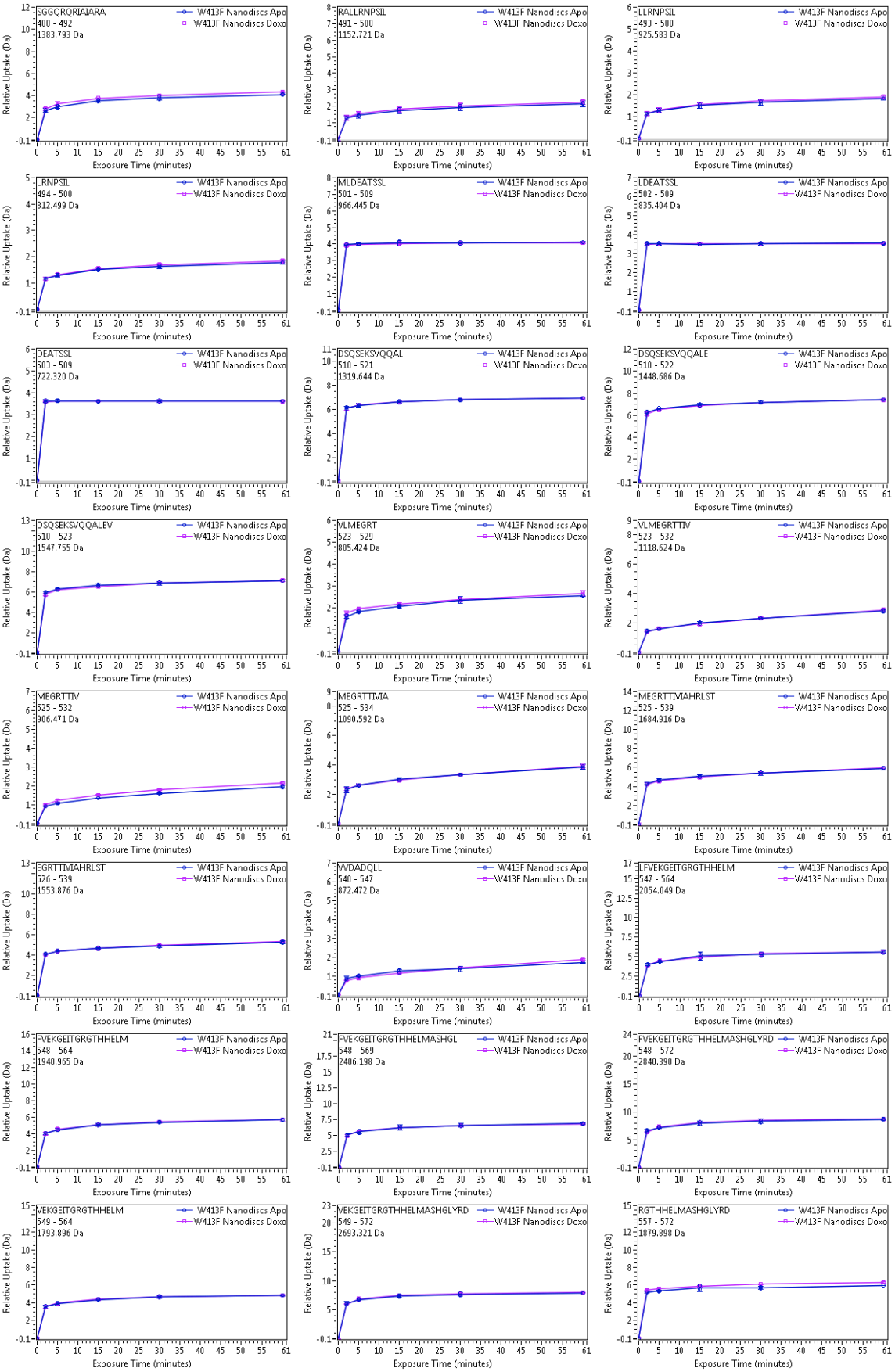
SGGQRQRIAIARA
480 - 492
1383.793 Da
RALLRNPSIL
491 - 500
1152.721 Da
LLRNPSIL
493 - 500
925.583 Da
LRNPSIL
494 - 500
812.499 Da
MLDEATSSL
501 - 509
966.445 Da
LDEATSSL
502 - 509
835.404 Da
DEATSSL
503 - 509
722.320 Da
DSQSEKSVQQAL
510 - 521
1319.644 Da
DSQSEKSVQQALE
510 - 522
1448.686 Da
DSQSEKSVQQALEV
510 - 523
1547.755 Da
VLMEGRT
523 - 529
805.424 Da
VLMEGRTTIV
523 - 532
1118.624 Da
MEGRTTIV
525 - 532
906.471 Da
MEGRTTIVIA
525 - 534
1090.592 Da
MEGRTTIVIAHRLST
525 - 539
1684.916 Da
EGRTTIVIAHRLST
526 - 539
1553.876 Da
VVDADQLL
540 - 547
872.472 Da
LFVEKGEITGRGTHHELM
547 - 564
2054.049 Da
FVEKGEITGRGTHHELM
548 - 564
1940.965 Da
FVEKGEITGRGTHHELMASHGL
548 - 569
2406.198 Da
FVEKGEITGRGTHHELMASHGLYRD
548 - 572
2840.390 Da
VEKGEITGRGTHHELM
549 - 564
1793.896 Da
VEKGEITGRGTHHELMASHGLYRD
549 - 572
2693.321 Da
RGTHHELMASHGLYRD
557 - 572
1879.898 Da
W413F Nanodiscs Apo
W413F Nanodiscs Doxo
Relative Uptake (Da)
Exposure Time (minutes)

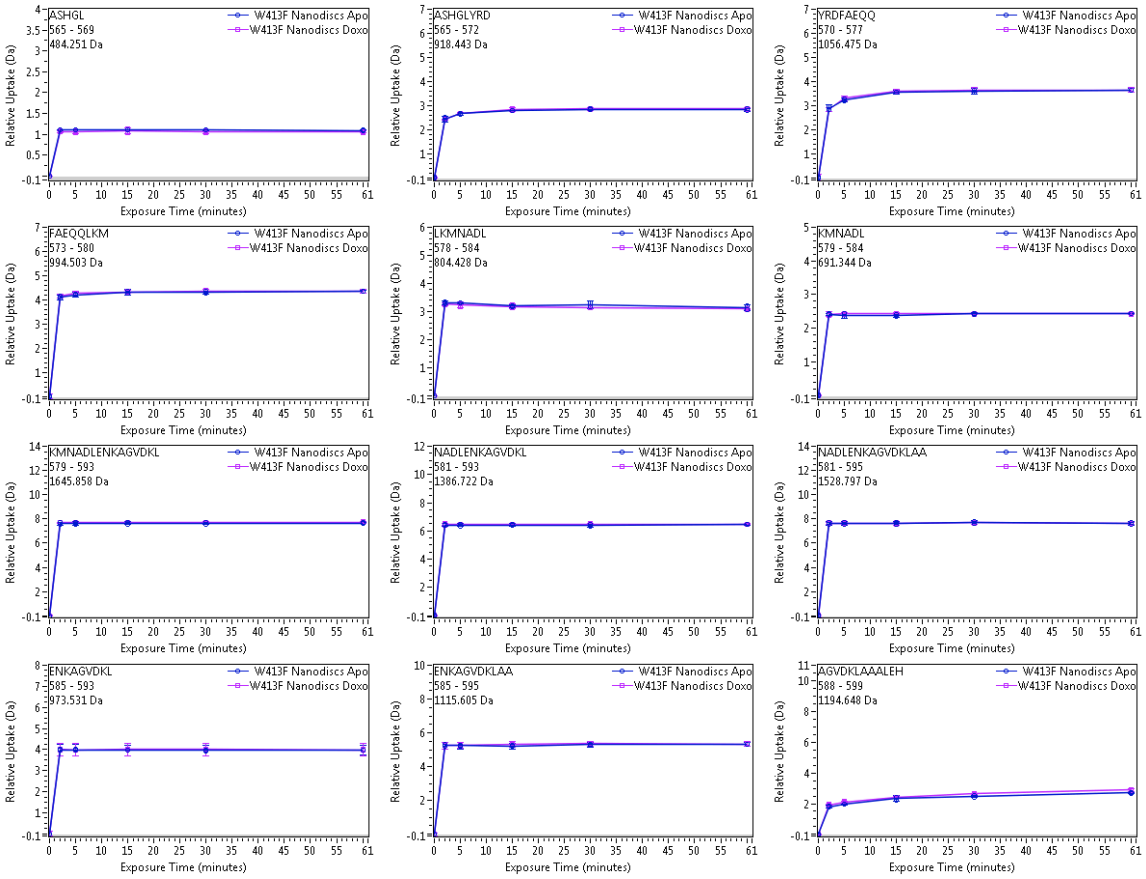
ASHGL
565 - 569
484.251 Da
ASHGLYRD
565 - 572
918.443 Da
YRDFAEQQ
570 - 577
1056.475 Da
FAEQQLKM
573 - 580
994.503 Da
LKMNADL
578 - 584
804.428 Da
KMNADL
579 - 584
691.344 Da
KMNADLENKAGVDKL
579 - 593
1645.858 Da
NADLENKAGVDKL
581 - 593
1386.722 Da
NADLENKAGVDKLAA
581 - 595
1528.797 Da
ENKAGVDKL
585 - 593
973.531 Da
ENKAGVDKLAA
585 - 595
1115.605 Da
AGVDKLAAALEH
588 - 599
1194.648 Da
W413F Nanodiscs Apo
W413F Nanodiscs Doxo
Relative Uptake (Da)
Exposure Time (minutes)

References

Alam, A., Kowal, J., Broude, E., Roninson, I., & Locher, K. P. (2019). Structural insight into substrate and inhibitor discrimination by human P-glycoprotein. *Science (New York, N.Y.)*, *363*(6428), 753–756. https://doi.org/10.1126/science.aav7102

Alam, A., Küng, R., Kowal, J., McLeod, R. A., Tremp, N., Broude, E. V., Roninson, I. B., Stahlberg, H., & Locher, K. P. (2018). Structure of a zosuquidar and UIC2-bound human-mouse chimeric ABCB1. *Proceedings of the National Academy of Sciences of the United States of America*, *115*(9), E1973–E1982. https://doi.org/10.1073/pnas.1717044115

Alvarez, F. J., Orelle, C., & Davidson, A. L. (2010). Functional reconstitution of an ABC transporter in nanodiscs for use in electron paramagnetic resonance spectroscopy. *Journal of the American Chemical Society*, *132*(28), 9513–9515. https://doi.org/10.1021/ja104047c

Alvarez, F. J. D., Orelle, C., Huang, Y., Bajaj, R., Everly, R. M., Klug, C. S., & Davidson, A. L. (2015). Full engagement of liganded maltose-binding protein stabilizes a semi-open ATP-binding cassette dimer in the maltose transporter. *Molecular Microbiology*, *98*(5), 878–894. https://doi.org/10.1111/mmi.13165

Ambudkar, S. V., Kim, I. W., Xia, D., & Sauna, Z. E. (2006). The A-loop, a novel conserved aromatic acid subdomain upstream of the Walker A motif in ABC transporters, is critical for ATP binding. *FEBS Letters*, *580*(4), 1049–1055. https://doi.org/10.1016/j.febslet.2005.12.051

Ambudkar, S. V., Kimchi-Sarfaty, C., Sauna, Z. E., & Gottesman, M. M. (2003). P-glycoprotein: From genomics to mechanism. *Oncogene*, *22*(47 REV. ISS. 6), 7468–7485. https://doi.org/10.1038/sj.onc.1206948

Anderson, K. W., Gallagher, E. S., & Hudgens, J. W. (2018). Automated Removal of Phospholipids from Membrane Proteins for H/D Exchange Mass Spectrometry Workflows. *Analytical Chemistry*, *90*(11), 6409–6412. https://doi.org/10.1021/acs.analchem.8b00429

Assaraf, Y. G., Brozovic, A., Gonçalves, A. C., Jurkovicova, D., Linē, A., Machuqueiro, M., Saponara, S., Sarmento-Ribeiro, A. B., Xavier, C. P. R., & Vasconcelos, M. H. (2019). The multi-factorial nature of clinical multidrug resistance in cancer. *Drug Resistance Updates*, *46*(September), 100645. https://doi.org/10.1016/j.drup.2019.100645

Bai, Y., Milne, J. S., Mayne, L., & Englander, S. W. (1993). Primary structure effects on peptide group hydrogen exchange. *Proteins: Structure, Function, and Bioinformatics*, *17*(1), 75–86. https://doi.org/10.1002/prot.340170110

Baker, M. (2010). Making membrane proteins for structures: A trillion tiny tweaks. *Nature Methods*, *7*(6), 429–434. https://doi.org/10.1038/nmeth0610-429

Bardiaux, B., Cordier, F., Brier, S., López-Castilla, A., Izadi-Pruneyre, N., & Nilges, M. (2019). Dynamics of a type 2 secretion system pseudopilus unraveled by complementary approaches. *Journal of Biomolecular NMR*, *73*(6–7), 293–303. https://doi.org/10.1007/s10858-019-00246-4

Barksdale AD, Rosenberg A. Acquisition and interpretation of hydrogen exchange data from peptides, polymers, and proteins. (1982). *Methods of Biochemical Analysis*, 28:1-113. https://doi.org/10.1002/9780470110485.ch1

Bay, D. C., Rommens, K. L., & Turner, R. J. (2008). Small multidrug resistance proteins: A

multidrug transporter family that continues to grow. *Biochimica et Biophysica Acta - Biomembranes*, *1778*(9), 1814–1838. https://doi.org/10.1016/j.bbamem.2007.08.015

Bayburt, T. H., Grinkova, Y. V., & Sligar, S. G. (2002). Self-Assembly of Discoidal Phospholipid Bilayer Nanoparticles with Membrane Scaffold Proteins. *Nano Letters*, *2*(8), 853–856. https://doi.org/10.1021/nl025623k

Bentley, G. A., Delepierre, M., Dobson, C. M., Wedin, R. E., Mason, S. A., & Poulsen, F. M. (1983). Exchange of individual hydrogens for a protein in a crystal and in solution. *Journal of Molecular Biology*, *170*(1), 243–247. https://doi.org/10.1016/S0022-2836(83)80235-6

Bereszczak, J. Z., Watts, N. R., Wingfield, P. T., Steven, A. C., & Heck, A. J. R. (2014). Assessment of differences in the conformational flexibility of hepatitis B virus core-antigen and e-antigen by hydrogen deuterium exchange-mass spectrometry. *Protein Science*, *23*(7), 884–896. https://doi.org/10.1002/pro.2470

Bhat, J. Y., Miličić, G., Thieulin-Pardo, G., Bracher, A., Maxwell, A., Ciniawsky, S., Mueller-Cajar, O., Engen, J. R., Hartl, F. U., Wendler, P., & Hayer-Hartl, M. (2017). Mechanism of Enzyme Repair by the AAA+ Chaperone Rubisco Activase. *Molecular Cell*, *67*(5), 744-756.e6. https://doi.org/10.1016/j.molcel.2017.07.004

Blanchet, C. E., & Svergun, D. I. (2013). Small-angle X-ray scattering on biological macromolecules and nanocomposites in solution. *Annual Review of Physical Chemistry*, *64*(November 2012), 37–54. https://doi.org/10.1146/annurev-physchem-040412-110132

Borst, P., & Oude Elferink, R. (2002). Mammalian ABC transporters in health and disease. *Annual Review of Biochemistry*, *71*, 537–592. https://doi.org/10.1146/annurev.biochem.71.102301.093055

Bouyssié, D., Lesne, J., Locard-Paulet, M., Albigot, R., Burlet-Schiltz, O., & Marcoux, J. (2019). HDX-Viewer: interactive 3D visualization of hydrogen-deuterium exchange data. *Bioinformatics (Oxford, England)*, *35*(24), 5331–5333. https://doi.org/10.1093/bioinformatics/btz550

Breyton, C., Javed, W., Vermot, A., Arnaud, C.-A., Hajjar, C., Dupuy, J., Petit-Hartlein, I., Le Roy, A., Martel, A., Thépaut, M., Orelle, C., Jault, J.-M., Fieschi, F., Porcar, L., & Ebel, C. (2019). Assemblies of lauryl maltose neopentyl glycol (LMNG) and LMNG-solubilized membrane proteins. *Biochimica et Biophysica Acta - Biomembranes*, *1861*(5). https://doi.org/10.1016/j.bbamem.2019.02.003

Breyton, C., Gabel, F., Lethier, M., Flayhan, A., Durand, G., Jault, J. M., Juillan-Binard, C., Imbert, L., Moulin, M., Ravaud, S., Härtlein, M., & Ebel, C. (2013). Small angle neutron scattering for the study of solubilised membrane proteins. *The European Physical Journal. E, Soft Matter*, *36*(7), 71. https://doi.org/10.1140/epje/i2013-13071-6

Brown, M. H., & Skurray, R. A. (2001). Staphylococcal multidrug efflux protein QacA. *Journal of Molecular Microbiology and Biotechnology*, *3*(2), 163–170.

Brown MH, Paulsen IT, Skurray RA. (1999). The multidrug efflux protein NorM is a prototype of a new family of transporters. *Mol Microbiol*, 31(1):394-5. doi: 10.1046/j.1365-2958.1999.01162.x

Buchaklian, A. H., & Klug, C. S. (2006). Characterization of the LSGGQ and H motifs from the Escherichia coli lipid A transporter MsbA. *Biochemistry*, *45*(41), 12539–12546. https://doi.org/10.1021/bi060830a

Bush, K., & Jacoby, G. A. (2010). Updated functional classification of beta-lactamases. Antimicrobial agents and chemotherapy, 54(3), 969–976. https://doi.org/10.1128/AAC.01009-09

CDC. Antibiotic Resistance Threats in the United States, 2019. Atlanta, GA: U.S. Department of Health and Human Services, CDC; 2019. http://dx.doi.org/10.15620/cdc:82532

C Reygaert, W. (2018). An overview of the antimicrobial resistance mechanisms of bacteria. *AIMS Microbiology*, *4*(3), 482–501. https://doi.org/10.3934/microbiol.2018.3.482

Chami M, Steinfels E, Orelle C, Jault JM, Di Pietro A, Rigaud JL, Marco S. (2002). Three-dimensional structure by cryo-electron microscopy of YvcC, an homodimeric ATP-binding cassette transporter from Bacillus subtilis. *Journal of Molecular Biology*, 315(5):1075-85. https://doi.org/10.1006/jmbi.2001.5309

Chen YJ, Pornillos O, Lieu S, Ma C, Chen AP, Chang G. (2007). X-ray structure of EmrE supports dual topology model. *Proc Natl Acad Sci U S A*, 104(48):18999-9004. https://doi.org/10.1073/pnas.0709387104.

Chitsaz, M., & Brown, M. H. (2017). The role played by drug efflux pumps in bacterial multidrug resistance. *Essays in Biochemistry*, *61*(1), 127–139. https://doi.org/10.1042/EBC20160064

Choi, K. H., & Morais, M. (2014). Use of small-angle X-ray scattering to investigate the structure and function of dengue virus NS3 and NS5. *Methods in molecular biology (Clifton, N.J.)*, *1138*, 241–252. https://doi.org/10.1007/978-1-4939-0348-1_15

Chowdhury, S. K., Katta, V., & Chait, B. T. (1990). Probing Conformational Changes in Proteins by Mass Spectrometry. *Journal of the American Chemical Society*, *112*(24), 9012–9013. https://doi.org/10.1021/ja00180a074

Chufan, E. E., Sim, H. M., & Ambudkar, S. V. (2015). Molecular Basis of the Polyspecificity of P-Glycoprotein (ABCB1). Recent Biochemical and Structural Studies. In *Advances in Cancer Research* (1st ed., Vol. 125). Elsevier Inc. https://doi.org/10.1016/bs.acr.2014.10.003

Coelho, D., Kim, J. C., Miousse, I. R., Fung, S., Du Moulin, M., Buers, I., Suormala, T., Burda, P., Frapolli, M., Stucki, M., Nürnberg, P., Thiele, H., Robenek, H., Höhne, W., Longo, N., Pasquali, M., Mengel, E., Watkins, D., Shoubridge, E. A., … Baumgartner, M. R. (2012). Mutations in ABCD4 cause a new inborn error of vitamin B12 metabolism. *Nature Genetics*, *44*(10), 1152–1155. https://doi.org/10.1038/ng.2386

Cooper, R. S., & Altenberg, G. A. (2013). Association/dissociation of the nucleotide-binding domains of the atp-binding cassette protein MSBA measured during continuous hydrolysis. *Journal of Biological Chemistry*, *288*(29), 20785–20796. https://doi.org/10.1074/jbc.M113.477976

Crow, A., Greene, N. P., Kaplan, E., & Koronakis, V. (2017). Structure and mechanotransmission mechanism of the MacB ABC transporter superfamily. *Proceedings of the National Academy of Sciences of the United States of America*, *114*(47), 12572–12577. https://doi.org/10.1073/pnas.1712153114

Csanády, L., Vergani, P., & Gadsby, D. C. (2019). Structure, gating, and regulation of the CFTR anion channel. *Physiological Reviews*, *99*(1), 707–738. https://doi.org/10.1152/physrev.00007.2018

Cui, L., Tominaga, E., Neoh, H. M., & Hiramatsu, K. (2006). Correlation between reduced daptomycin susceptibility and vancomycin resistance in vancomycin-intermediate Staphylococcus aureus. *Antimicrobial Agents and Chemotherapy*, *50*(3), 1079–1082. https://doi.org/10.1128/AAC.50.3.1079-1082.2006

Dalmas O, Do Cao MA, Lugo MR, Sharom FJ, Di Pietro A, Jault JM. (2005). Time-resolved fluorescence resonance energy transfer shows that the bacterial multidrug ABC half-transporter BmrA functions as a homodimer. *Biochemistry*, 44(11):4312-21. https://doi.org/10.1021/bi0482809

Dalmas O, Orelle C, Foucher AE, Geourjon C, Crouzy S, Di Pietro A, Jault JM. (2005). The Q-loop disengages from the first intracellular loop during the catalytic cycle of the multidrug ABC transporter BmrA. *Journal of Biological Chemistry*, 280(44):36857-64. https://doi.org/10.1074/jbc.M503266200

Dassa, E., & Bouige, P. (2001). The ABC of ABCs: A phylogenetic and functional classification of ABC systems in living organisms. *Research in Microbiology*, *152*(3–4), 211–229. https://doi.org/10.1016/S0923-2508(01)01194-9

Davidson, A. L., Dassa, E., Orelle, C., & Chen, J. (2008). Structure, Function, and Evolution of Bacterial ATP-Binding Cassette Systems. *Microbiology and Molecular Biology Reviews*, *72*(2), 317–364. https://doi.org/10.1128/mmbr.00031-07

Dawson, R. J. P., & Locher, K. P. (2006). Structure of a bacterial multidrug ABC transporter. *Nature*, *443*(7108), 180–185. https://doi.org/10.1038/nature05155

Dean, M., & Annilo, T. (2005). Evolution of the ATP-binding cassette (ABC) transporter superfamily in vertebrates. *Annual Review of Genomics and Human Genetics*, *6*, 123–142. https://doi.org/10.1146/annurev.genom.6.080604.162122

Delmar, J. A., & Yu, E. W. (2016). The AbgT family: A novel class of antimetabolite transporters. *Protein Science*, *25*(2), 322–337. https://doi.org/10.1002/pro.2820

Deng Y, Zhang Z, Smith DL. (1999). Comparison of continuous and pulsed labeling amide hydrogen exchange/mass spectrometry for studies of protein dynamics. Journal of the American Society for Mass Spectrometry, 10(8):675-84. https://doi.org/10.1016/S1044-0305(99)00038-0

Denisov, I. G., & Sligar, S. G. (2016). Nanodiscs for structural and functional studies of membrane proteins. *Nature Structural and Molecular Biology*, *23*(6), 481–486. https://doi.org/10.1038/nsmb.3195

Denisov, I. G., & Sligar, S. G. (2017). Nanodiscs in Membrane Biochemistry and Biophysics. *Chemical reviews*, *117*(6), 4669–4713. https://doi.org/10.1021/acs.chemrev.6b00690

Do Cao, M. A., Crouzy, S., Kim, M., Becchi, M., Cafiso, D. S., Di Pietro, A., & Jault, J. M. (2009). Probing the conformation of the resting state of a bacterial multidrug ABC transporter, BmrA, by a site-directed spin labeling approach. *Protein science : a publication of the Protein Society*, *18*(7), 1507–1520. https://doi.org/10.1002/pro.141

Dong, H., Zhang, Z., Tang, X., Paterson, N. G., & Dong, C. (2017). Structural and functional insights into the lipopolysaccharide ABC transporter LptB2FG. *Nature Communications*, *8*(1), 1–11. https://doi.org/10.1038/s41467-017-00273-5

Drawz, S. M., & Bonomo, R. A. (2010). Three decades of β-lactamase inhibitors. *Clinical*

Microbiology Reviews, *23*(1), 160–201. https://doi.org/10.1128/CMR.00037-09

Encyclopædia-Britannica (2012) Antibiotic resistance: Mechanisms of antibiotic resistance. Encyclopædia Britannica Online. https://www.britannica.com/science/antibiotic-resistance

Engen, J. R., & Komives, E. A. (2020). Complementarity of Hydrogen/Deuterium Exchange Mass Spectrometry and Cryo-Electron Microscopy. *Trends in Biochemical Sciences*, *45*(10), 906–918. https://doi.org/10.1016/j.tibs.2020.05.005

Englander, J. J., Calhoun, D. B., & Englander, S. W. (1979). Measurement and calibration of peptide group hydrogen-deuterium exchange by ultraviolet spectrophotometry. *Analytical Biochemistry*, *92*(2), 517–524. https://doi.org/10.1016/0003-2697(79)90693-6

Englander, S. W. (1963). A Hydrogen Exchange Method Using Tritium and Sephadex: Its Application to Ribonuclease. *Biochemistry*, *2*(4), 798–807. https://doi.org/10.1021/bi00904a030

Englander, S. W., & Kallenbach, N. R. (1983). Hydrogen exchange and structural dynamics of proteins and nucleic acids. *Quarterly Reviews of Biophysics*, *16*(4), 521–655. https://doi.org/10.1017/S0033583500005217

Esser, L., Zhou, F., Pluchino, K. M., Shiloach, J., Ma, J., Tang, W. K., Gutierrez, C., Zhang, A., Shukla, S., Madigan, J. P., Zhou, T., Kwong, P. D., Ambudkar, S. V., Gottesman, M. M., & Xia, D. (2017). Structures of the Multidrug Transporter P-glycoprotein Reveal Asymmetric ATP Binding and the Mechanism of Polyspecificity. *Journal of Biological Chemistry*, *292*(2), 446–461. https://doi.org/10.1074/jbc.M116.755884

Fang, J., Rand, K. D., Beuning, P. J., & Engen, J. R. (2011). False EX1 signatures caused by sample carryover during HX MS analyses. *International journal of mass spectrometry*, *302*(1-3), 19–25. https://doi.org/10.1016/j.ijms.2010.06.039

Fetsch, E. E., & Davidson, A. L. (2002). Vanadate-catalyzed photocleavage of the signature motif of an ATP-binding cassette (ABC) transporter. *Proceedings of the National Academy of Sciences of the United States of America*, *99*(15), 9685–9690. https://doi.org/10.1073/pnas.152204499

Fitzpatrick, A. W. P., Llabrés, S., Neuberger, A., Blaza, J. N., Bai, X. C., Okada, U., Murakami, S., Van Veen, H. W., Zachariae, U., Scheres, S. H. W., Luisi, B. F., & Du, D. (2017). Structure of the MacAB-TolC ABC-type tripartite multidrug efflux pump. *Nature Microbiology*, *2*, 0–3. https://doi.org/10.1038/nmicrobiol.2017.70

Frank, G. A., Shukla, S., Rao, P., Borgnia, M. J., Bartesaghi, A., Merk, A., Mobin, A., Esser, L., Earl, L. A., Gottesman, M. M., Xia, D., Ambudkar, S. V., & Subramaniam, S. (2016). Cryo-EM analysis of the conformational landscape of human P-glycoprotein (ABCB1) during its catalytic cycle. *Molecular Pharmacology*, *90*(1), 35–41. https://doi.org/10.1124/mol.116.104190

Franke D, Jeffries CM, Svergun DI. (2015). Correlation Map, a goodness-of-fit test for one-dimensional X-ray scattering spectra. *Nature Methods*, *12*(5):419-22. https://doi.org/10.1038/nmeth.3358

Franke, D., Petoukhov, M. V., Konarev, P. V., Panjkovich, A., Tuukkanen, A., Mertens, H. D. T., Kikhney, A. G., Hajizadeh, N. R., Franklin, J. M., Jeffries, C. M., & Svergun, D. I. (2017). ATSAS 2.8: A comprehensive data analysis suite for small-angle scattering from

macromolecular solutions. *Journal of Applied Crystallography*, *50*, 1212–1225. https://doi.org/10.1107/S1600576717007786

Fribourg PF, Chami M, Sorzano CO, Gubellini F, Marabini R, Marco S, Jault JM, Lévy D. (2014). 3D cryo-electron reconstruction of BmrA, a bacterial multidrug ABC transporter in an inward-facing conformation and in a lipidic environment. *Journal of Molecular Biology*, 426(10):2059-69. https://doi.org/10.1016/j.jmb.2014.03.002

Garvey, M. I., Baylay, A. J., Wong, R. L., & Piddock, L. J. V. (2011). Overexpression of patA and patB, which encode ABC transporters, is associated with fluoroquinolone resistance in clinical isolates of Streptococcus pneumoniae. *Antimicrobial Agents and Chemotherapy*, *55*(1), 190–196. https://doi.org/10.1128/AAC.00672-10

Geourjon, C., Orelle, C., Steinfels, E., Blanchet, C., Deléage, G., Di Pietro, A., & Jault, J. M. (2001). A common mechanism for ATP hydrolysis in ABC transporter and helicase superfamilies. *Trends in Biochemical Sciences*, *26*(9), 539–544. https://doi.org/10.1016/S0968-0004(01)01907-7

Goldstein, F. W., Gutmann, L., Williamson, R., Collatz, E., & Acar, J. F. (1983). In vivo and in vitro emergence of simultaneous resistance to both β-lactam and aminoglycoside antibiotics in a strain of Serratia marcescens. *Annales de l'Institut Pasteur Microbiology*, *134*(3), 329–337. https://doi.org/10.1016/S0769-2609(83)80058-1

Goosen, N., & Moolenaar, G. F. (2001). Role of ATP hydrolysis by UvrA and UvrB during nucleotide excision repair. *Research in Microbiology*, *152*(3–4), 401–409. https://doi.org/10.1016/S0923-2508(01)01211-6

Gottesman, M. M., & Ling, V. (2006). The molecular basis of multidrug resistance in cancer: The early years of P-glycoprotein research. *FEBS Letters*, *580*(4), 998–1009. https://doi.org/10.1016/j.febslet.2005.12.060

Greene, N. P., Kaplan, E., Crow, A., & Koronakis, V. (2018). Antibiotic resistance mediated by the MacB ABC transporter family: A structural and functional perspective. *Frontiers in Microbiology*, *9*(MAY). https://doi.org/10.3389/fmicb.2018.00950

Grossmann, N., Vakkasoglu, A. S., Hulpke, S., Abele, R., Gaudet, R., & Tampé, R. (2014). Mechanistic determinants of the directionality and energetics of active export by a heterodimeric ABC transporter. *Nature Communications*, *5*. https://doi.org/10.1038/ncomms6419

Guiral M, Viratelle O, Westerhoff HV, Lankelma J. (1994). Cooperative P-glycoprotein mediated daunorubicin transport into DNA-loaded plasma membrane vesicles. *FEBS Letters*, 346(2-3):141-5. https://doi.org/10.1016/0014-5793(94)00447-1

Gutmann, L., Williamson, R., Moreau, N., Kitzis, M. D., Collatz, E., Acar, J. F., & Goldstein, F. W. (1985). Cross-resistance to nalidixic acid, trimethoprim, and chloramphenicol associated with alterations in outer membrane proteins of klebsiella, enterobacter, and serratia. *Journal of Infectious Diseases*, *151*(3), 501–507. https://doi.org/10.1093/infdis/151.3.501

Haertlein M, Moulin M, Devos JM, Laux V, Dunne O, Forsyth VT. (2016). Biomolecular Deuteration for Neutron Structural Biology and Dynamics. *Methods in Enzymology*, *566*:113-57. https://doi.org/10.1016/bs.mie.2015.11.001

Hassan, K. A., Jackson, S. M., Penesyan, A., Patching, S. G., Tetu, S. G., Eijkelkamp, B. A.,

Brown, M. H., Henderson, P. J. F., & Paulsen, I. T. (2013). Transcriptomic and biochemical analyses identify a family of chlorhexidine efflux proteins. *Proceedings of the National Academy of Sciences of the United States of America*, *110*(50), 20254–20259. https://doi.org/10.1073/pnas.1317052110

Hassan, K. A., Liu, Q., Elbourne, L. D. H., Ahmad, I., Sharples, D., Naidu, V., Chan, C. L., Li, L., Harborne, S. P. D., Pokhrel, A., Postis, V. L. G., Goldman, A., Henderson, P. J. F., & Paulsen, I. T. (2018). Pacing across the membrane: the novel PACE family of efflux pumps is widespread in Gram-negative pathogens. *Research in Microbiology*, *169*(7–8), 450–454. https://doi.org/10.1016/j.resmic.2018.01.001

Hassan, K. A., Liu, Q., Henderson, P. J. F., & Paulsen, I. T. (2015). Homologs of the Acinetobacter baumannii acei transporter represent a new family of bacterial multidrug efflux systems. *MBio*, *6*(1), 1–5. https://doi.org/10.1128/mBio.01982-14

Hassan, K. A., Naidu, V., Edgerton, J. R., Mettrick, K. A., Liu, Q., Fahmy, L., Li, L., Jackson, S. M., Ahmad, I., Sharples, D., Henderson, P. J. F., & Paulsen, I. T. (2019). Short-chain diamines are the physiological substrates of PACE family efflux pumps. *Proceedings of the National Academy of Sciences of the United States of America*, *116*(36), 18015–18020. https://doi.org/10.1073/pnas.1901591116

Hebling, C. M., Morgan, C. R., Stafford, D. W., Jorgenson, J. W., Rand, K. D., & Engen, J. R. (2010). Conformational analysis of membrane proteins in phospholipid bilayer nanodiscs by hydrogen exchange mass spectrometry. *Analytical Chemistry*, *82*(13), 5415–5419. https://doi.org/10.1021/ac100962c

Henderson, G. B., Zevely, E. M., Kadner, R. J., & Huennekens, F. M. (1978). The folate and thiamine transport proteins of lactobacillus casei. *Progress in Clinical and Biological Research*, *VOL.22*, 165–173.

Heng, J., Zhao, Y., Liu, M., Liu, Y., Fan, J., Wang, X., Zhao, Y., Zhang, XC. (2015). Substrate-bound structure of the E. coli multidrug resistance transporter MdfA. *Cell Research*, 25(9):1060-73. https://doi.org/10.1038/cr.2015.94.

Higgins, C. F., & Linton, K. J. (2004). The ATP switch model for ABC transporters. *Nature Structural and Molecular Biology*, *11*(10), 918–926. https://doi.org/10.1038/nsmb836

Hofmann, S., Januliene, D., Mehdipour, A. R., Thomas, C., Stefan, E., Brüchert, S., Kuhn, B. T., Geertsma, E. R., Hummer, G., Tampé, R., & Moeller, A. (2019). Conformation space of a heterodimeric ABC exporter under turnover conditions. *Nature*, *571*(7766), 580–583. https://doi.org/10.1038/s41586-019-1391-0

Hoofnagle, A. N., Resing, K. A., & Ahn, N. G. (2003). Protein analysis by hydrogen exchange mass spectrometry. *Annual Review of Biophysics and Biomolecular Structure*, *32*, 1–25. https://doi.org/10.1146/annurev.biophys.32.110601.142417

Hooper, D. C., & Jacoby, G. A. (2015). Mechanisms of drug resistance: Quinolone resistance. *Annals of the New York Academy of Sciences*, *1354*(1), 12–31. https://doi.org/10.1111/nyas.12830

Hvorup, R. N., Winnen, B., Chang, A. B., Jiang, Y., Zhou, X. F., & Saier, M. H. (2003). The multidrug/oligosaccharidyl-lipid/polysaccharide (MOP) exporter superfamily. *European Journal of Biochemistry*, *270*(5), 799–813. https://doi.org/10.1046/j.1432-1033.2003.03418.x

Jack, D. L., Yang, N. M., & Saier, M. H. (2001). The drug/metabolite transporter superfamily. *European Journal of Biochemistry*, *268*(13), 3620–3639. https://doi.org/10.1046/j.1432-1327.2001.02265.x

Jacoby, G. A., Strahilevitz, J., & Hooper, D. C. (2015). *Plasmid-Mediated Quinolone Resistance*. *October 2014*, 1–24. https://doi.org/10.1128/microbiolspec.PLAS-0006

Jacrot, B. (1976). Scattering From Solution. *Reports on Progress in Physics*, *39*(156), 911–953.

Jardetzky O. (1966). Simple allosteric model for membrane pumps. *Nature*, 211(5052):969-70. https://doi.org/10.1038/211969a0

Jensen, P. F., Rand, K. D. (2016). Hydrogen Exchange Mass Spectrometry of Proteins: Fundamentals, Methods, and Applications (first ed.). Weis (Ed.), John Wiley and Sons, Chichester, pp. 1-17. https://doi.org/10.1002/9781118703748.ch1

Jiarong Li, M., Guttman, M., & Atkins, W. M. (2018). Conformational dynamics of P-glycoprotein in lipid nanodiscs and detergent micelles reveal complex motions on a wide time scale. *Journal of Biological Chemistry*, *293*(17), 6297–6307. https://doi.org/10.1074/jbc.RA118.002190

Jin, M. S., Oldham, M. L., Zhang, Q., & Chen, J. (2012). Crystal structure of the multidrug transporter P-glycoprotein from Caenorhabditis elegans. *Nature*, *490*(7421), 566–569. https://doi.org/10.1038/nature11448

Jones, P. M., & George, A. M. (1999). Subunit interactions in ABC transporters: Towards a functional architecture. *FEMS Microbiology Letters*, *179*(2), 187–202. https://doi.org/10.1016/S0378-1097(99)00411-5

Jones, P. M., & George, A. M. (2002). Mechanism of ABC transporters: A molecular dynamics simulation of a well characterized nucleotide-binding subunit. *Proceedings of the National Academy of Sciences of the United States of America*, *99*(20), 12639–12644. https://doi.org/10.1073/pnas.152439599

Jones, P. M., & George, A. M. (2009). Opening of the ADP-bound active site in the ABC transporter ATPase dimer: Evidence for a constant contact, alternating sites model for the catalytic cycle. *Proteins: Structure, Function and Bioinformatics*, *75*(2), 387–396. https://doi.org/10.1002/prot.22250

Jones, P. M., & George, A. M. (2012). Role of the D-loops in allosteric control of ATP hydrolysis in an ABC transporter. *Journal of Physical Chemistry A*, *116*(11), 3004–3013. https://doi.org/10.1021/jp211139s

Jones, P. M., & George, A. M. (2013). Mechanism of the ABC transporter ATPase domains: Catalytic models and the biochemical and biophysical record. *Critical Reviews in Biochemistry and Molecular Biology*, *48*(1), 39–50. https://doi.org/10.3109/10409238.2012.735644

Josts, I., Nitsche, J., Maric, S., Mertens, H. D., Moulin, M., Haertlein, M., Prevost, S., Svergun, D. I., Busch, S., Forsyth, V. T., & Tidow, H. (2018). Conformational States of ABC Transporter MsbA in a Lipid Environment Investigated by Small-Angle Scattering Using Stealth Carrier Nanodiscs. *Structure*, *26*(8), 1072-1079.e4. https://doi.org/10.1016/j.str.2018.05.007

Juliano, R. L., & Ling, V. (1976). A surface glycoprotein modulating drug permeability in Chinese hamster ovary cell mutants. *BBA - Biomembranes*, *455*(1), 152–162.

https://doi.org/10.1016/0005-2736(76)90160-7

Katta V, Chait BT. Conformational changes in proteins probed by hydrogen-exchange electrospray-ionization mass spectrometry. (1991). *Rapid Communications in Mass Spectrometry*, 5(4):214-7. https://doi.org/10.1002/rcm.1290050415

Kim, Y., & Chen, J. (2018). *Molecular structure of human P-glycoprotein in the ATP-bound, outward-facing conformation*. 2–7.

Kimura, Y., Kioka, N., Kato, H., Matsuo, M., & Ueda, K. (2007). Modulation of drug-stimulated ATPase activity of human MDR1/P-glycoprotein by cholesterol. *Biochemical Journal*, *401*(2), 597–605. https://doi.org/10.1042/BJ20060632

Kline, S. R. (2006). Reduction and analysis of SANS and USANS data using IGOR Pro. *Journal of Applied Crystallography*, *39*:895–900. https://doi.org/10.1107/S0021889806035059

Kluth, M., Stindt, J., Dröge, C., Linnemann, D., Kubitz, R., & Schmitt, L. (2015). A mutation within the extended X loop abolished substrateinduced ATPase activity of the human liver ATP-binding cassette (ABC) transporter MDR3. *Journal of Biological Chemistry*, *290*(8), 4896–4907. https://doi.org/10.1074/jbc.M114.588566

Knowles, T. J., Finka, R., Smith, C., Lin, Y. P., Dafforn, T., & Overduin, M. (2009). Membrane proteins solubilized intact in lipid containing nanoparticles bounded by styrene maleic acid copolymer. *Journal of the American Chemical Society*, *131*(22), 7484–7485. https://doi.org/10.1021/ja810046q

Kobayashi, N., Nishino, K., & Yamaguchi, A. (2001). Novel macrolide-specific ABC-type efflux transporter in Escherichia coli. *Journal of bacteriology*, *183*(19), 5639–5644. https://doi.org/10.1128/JB.183.19.5639-5644.2001

Koch, M. H. J., Vachette, P., & Svergun, D. I. (2003). Small-angle scattering: A view on the properties, structures and structural changes of biological macromolecules in solution. In *Quarterly Reviews of Biophysics* (Vol. 36, Issue 2). https://doi.org/10.1017/S0033583503003871

Konarev, P.V., Volkov, V.V., Sokolova, A.V., Koch, M.H.J., & Svergun D. I. (2003). PRIMUS - a Windows-PC based system for small-angle scattering data analysis. *Journal of Applied Crystallography, 36,* 1277-1282. https://doi.org/10.1107/S0021889803012779

Konermann, L., Pan, J., & Liu, Y. H. (2011). Hydrogen exchange mass spectrometry for studying protein structure and dynamics. *Chemical Society Reviews*, *40*(3), 1224–1234. https://doi.org/10.1039/c0cs00113a

Kopcho, N., Chang, G., & Komives, E. A. (2019). Dynamics of ABC Transporter P-glycoprotein in Three Conformational States. *Scientific Reports*, *9*(1), 1–11. https://doi.org/10.1038/s41598-019-50578-2

Korkhov, V. M., Mireku, S. A., & Locher, K. P. (2012). Structure of AMP-PNP-bound vitamin B 12 transporter BtuCD-F. *Nature*, *490*(7420), 367–372. https://doi.org/10.1038/nature11442

Krügel H, Licht A, Biedermann G, Petzold A, Lassak J, Hupfer Y, Schlott B, Hertweck C, Platzer M, Brantl S, Saluz HP. (2010). Cervimycin C resistance in Bacillus subtilis is due to a promoter up-mutation and increased mRNA stability of the constitutive ABC-transporter gene bmrA. *FEMS Microbiology Letters*, 313(2):155-63.

https://doi.org/10.1111/j.1574-6968.2010.02143.x

Kumar, A., & Schweizer, H. P. (2005). Bacterial resistance to antibiotics: Active efflux and reduced uptake. *Advanced Drug Delivery Reviews*, *57*(10), 1486–1513. https://doi.org/10.1016/j.addr.2005.04.004

Kuroda, T., & Tsuchiya, T. (2009). Multidrug efflux transporters in the MATE family. *Biochimica et Biophysica Acta - Proteins and Proteomics*, *1794*(5), 763–768. https://doi.org/10.1016/j.bbapap.2008.11.012

Lacabanne, D., Orelle, C., Lecoq, L., Kunert, B., Chuilon, C., Wiegand, T., Ravaud, S., Jault, J. M., Meier, B. H., & Böckmann, A. (2019). Flexible-to-rigid transition is central for substrate transport in the ABC transporter BmrA from Bacillus subtilis. *Communications Biology*, *2*(1), 1–9. https://doi.org/10.1038/s42003-019-0390-x

Lapinski, P. E., Neubig, R. R., & Raghavan, M. (2001). Walker A Lysine Mutations of TAP1 and TAP2 Interfere with Peptide Translocation but Not Peptide Binding. *Journal of Biological Chemistry*, *276*(10), 7526–7533. https://doi.org/10.1074/jbc.M009448200

Lau, A.M., Claesen, J., Hansen, K., Politis, A. (2020). Deuteros 2.0: Peptide-level significance testing of data from hydrogen deuterium exchange mass spectrometry. *Bioinformatics*, 28:btaa677. https://doi.org/10.1093/bioinformatics/btaa677.

Lee Jyh_Yeuan, Kinch Lisa N., Borek Dominika M., Wang Jin, Wang Junmei, Urbatsch Ina L., Xie Xiao-Song, Grishin NikolaiV., Cohen Johnathan C., Otwinowski Zbyszek, Hobbs Helen H., R. daniel M. (2016). Crystal structure of the human sterol transporter ABCG5/ABCG8. *Nature*, *553*(7604), 561–564. https://doi.org/10.1038/nature17666.

Lee, M., Choi, Y., Burla, B., Kim, Y. Y., Jeon, B., Maeshima, M., Yoo, J. Y., Martinoia, E., & Lee, Y. (2008). The ABC transporter AtABCB14 is a malate importer and modulates stomatal response to CO2. *Nature Cell Biology*, *10*(10), 1217–1223. https://doi.org/10.1038/ncb1782

Lenormant, H., & Blout, ER. (1953). Origin of the absorption band at 1,550 cm.-1 in proteins. *Nature*, *172*(4382):770-1. https://doi.org/10.1038/172770a0

Lewinson, O., & Livnat-Levanon, N. (2017). Mechanism of Action of ABC Importers: Conservation, Divergence, and Physiological Adaptations. *Journal of Molecular Biology*, *429*(5), 606–619. https://doi.org/10.1016/j.jmb.2017.01.010

Li, J., Jaimes, K. F., & Aller, S. G. (2014). Refined structures of mouse P-glycoprotein. *Protein Science*, *23*(1), 34–46. https://doi.org/10.1002/pro.2387

Li XZ. (2016) Antimicrobial Resistance in Bacteria: An Overview of Mechanisms and Role of Drug Efflux Pumps. In: Li XZ., Elkins C., Zgurskaya H. (eds) Efflux-Mediated Antimicrobial Resistance in Bacteria. Adis, Cham. https://doi.org/10.1007/978-3-319-39658-3_6

Li XZ. (2017) Active Efflux as a Mechanism of Resistance to Antimicrobial Drugs. In: Mayers D., Sobel J., Ouellette M., Kaye K., Marchaim D. (eds) *Antimicrobial Drug Resistance*. Springer, Cham. https://doi.org/10.1007/978-3-319-46718-4_10

Li XZ, Nikaido H. (2004). Efflux-mediated drug resistance in bacteria. *Drugs*, 64(2):159-204. https://doi.org/10.2165/00003495-200464020-00004

Li, X. Z., Plésiat, P., & Nikaido, H. (2015). The challenge of efflux-mediated antibiotic

resistance in Gram-negative bacteria. *Clinical Microbiology Reviews*, *28*(2), 337–418. https://doi.org/10.1128/CMR.00117-14

Li Yanyan, Orlando, B. J., & Liao, M. (2019). Structural basis of lipopolysaccharide extraction by the LptB2FGC complex. *Nature*, *567*(7749), 486–490. https://doi.org/10.1038/s41586-019-1025-6.

Lim, X. X., Chandramohan, A., Lim, X. Y. E., Bag, N., Sharma, K. K., Wirawan, M., Wohland, T., Lok, S. M., & Anand, G. S. (2017). Conformational changes in intact dengue virus reveal serotype-specific expansion. *Nature Communications*, *8*. https://doi.org/10.1038/ncomms14339

Lin, J., Zhou, D., Steitz, T. A., Polikanov, Y. S., & Gagnon, M. G. (2018). Ribosome-Targeting Antibiotics: Modes of Action, Mechanisms of Resistance, and Implications for Drug Design. *Annual Review of Biochemistry*, *87*, 451–478. https://doi.org/10.1146/annurev-biochem-062917-011942

Locher, K. P. (2016). Mechanistic diversity in ATP-binding cassette (ABC) transporters. *Nature Structural and Molecular Biology*, *23*(6), 487–493. https://doi.org/10.1038/nsmb.3216

Locher, K. P., Lee, A. T., & Rees, D. C. (2002). The E. coli BtuCD structure: A framework for ABC transporter architecture and mechanism. *Science*, *296*(5570), 1091–1098. https://doi.org/10.1126/science.1071142

Loo TW, Bartlett MC, Clarke DM. (2003). Drug binding in human P-glycoprotein causes conformational changes in both nucleotide-binding domains. *Journal of Biological Chemistry*, 17;278(3):1575-8. https://doi.org/10.1074/jbc.M211307200

Loo, T. W., Bartlett, M. C., Detty, M. R., & Clarke, D. M. (2012). The ATPase activity of the P-glycoprotein drug pump is highly activated when the N-terminal and central regions of the nucleotide-binding domains are linked closely together. *Journal of Biological Chemistry*, *287*(32), 26806–26816. https://doi.org/10.1074/jbc.M112.376202

Loo, T. W., & Clarke, D. M. (2014). Identification of the distance between the homologous halves of P-glycoprotein that triggers the high/low ATPase activity switch. *Journal of Biological Chemistry*, *289*(12), 8484–8492. https://doi.org/10.1074/jbc.M114.552075

Mahieu E, Gabel F. (2018). Biological small-angle neutron scattering: recent results and development. Acta Crystallographica Section D: Structural Biology, 74(Pt 8):715-726. doi: 10.1107/S2059798318005016

Maity, K., Heumann, J. M., McGrath, A. P., Kopcho, N. J., Hsu, P. K., Lee, C. W., Mapes, J. H., Garza, D., Krishnan, S., Morgan, G. P., Hendargo, K. J., Klose, T., Rees, S. D., Medrano-Soto, A., Saier, M. H., Piñeros, M., Komives, E. A., Schroeder, J. I., Chang, G., & Stowell, M. H. B. (2019). Cryo-EM structure of OSCA1.2 from Oryza sativa elucidates the mechanical basis of potential membrane hyperosmolality gating. *Proceedings of the National Academy of Sciences of the United States of America*, *116*(28), 14309–14318. https://doi.org/10.1073/pnas.1900774116

Maric, S., Skar-Gislinge, N., Midtgaard, S., Thygesen, M. B., Schiller, J., Frielinghaus, H., Moulin, M., Haertlein, M., Forsyth, V. T., Pomorski, T. G., & Arleth, L. (2014). Stealth carriers for low-resolution structure determination of membrane proteins in solution. *Acta Crystallographica Section D: Biological Crystallography*, *70*(2), 317–328. https://doi.org/10.1107/S1399004713027466

Martens, C., Shekhar, M., Lau, A. M., Tajkhorshid, E., & Politis, A. (2019). Integrating hydrogen–deuterium exchange mass spectrometry with molecular dynamics simulations to probe lipid-modulated conformational changes in membrane proteins. *Nature Protocols*, *14*(11), 3183–3204. https://doi.org/10.1038/s41596-019-0219-6

Martinez, L., Arnaud, O., Henin, E., Tao, H., Chaptal, V., Doshi, R., Andrieu, T., Dussurgey, S., Tod, M., Di Pietro, A., Zhang, Q., Chang, G., & Falson, P. (2014). Understanding polyspecificity within the substrate-binding cavity of the human multidrug resistance P-glycoprotein. *The FEBS journal*, *281*(3), 673–682. https://doi.org/10.1111/febs.12613

Mathieu, K., Javed, W., Vallet, S., Lesterlin, C., Candusso, M.-P., Ding, F., Xu, X. N., Ebel, C., Jault, J.-M., & Orelle, C. (2019). Functionality of membrane proteins overexpressed and purified from E. coli is highly dependent upon the strain. *Scientific Reports*, *9*(1). https://doi.org/10.1038/s41598-019-39382-0

McAleese, F., Petersen, P., Ruzin, A., Dunman, P. M., Murphy, E., Projan, S. J., & Bradford, P. A. (2005). A novel MATE family efflux pump contributes to the reduced susceptibility of laboratory-derived Staphylococcus aureus mutants to tigecycline. *Antimicrobial agents and chemotherapy*, 49(5), 1865–1871. https://doi.org/10.1128/AAC.49.5.1865-1871.2005

McMurry, L., Petrucci, R. E., & Levy, S. B. (1980). Active efflux of tetracycline encoded by four genetically different tetracyline resistance determinants in Escherichia coli. *Proceedings of the National Academy of Sciences of the United States of America*, *77*(7 II), 3974–3977. https://doi.org/10.1073/pnas.77.7.3974

Mehmood, S., Domene, C., Forest, E., & Jault, J. M. (2012). Dynamics of a bacterial multidrug ABC transporter in the inward- and outward-facing conformations. *Proceedings of the National Academy of Sciences of the United States of America*, *109*(27), 10832–10836. https://doi.org/10.1073/pnas.1204067109

Midtgaard, S. R., Darwish, T. A., Pedersen, M. C., Huda, P., Larsen, A. H., Jensen, G. V., Kynde, S. A. R., Skar-Gislinge, N., Nielsen, A. J. Z., Olesen, C., Blaise, M., Dorosz, J. J., Thorsen, T. S., Venskutonytė, R., Krintel, C., Møller, J. V., Frielinghaus, H., Gilbert, E. P., Martel, A., … Arleth, L. (2018). Invisible detergents for structure determination of membrane proteins by small-angle neutron scattering. *FEBS Journal*, *285*(2), 357–371. https://doi.org/10.1111/febs.14345

Moeller Arne, Lee Sung Chang , Tao Houchao , Speir Jeffrey A. , Chang Geoffrey, Urbatsch Ina L., Potter Clinton S., Carragher Bridget, and Z. Q. (2015). Distinct Conformational Spectrum of Homologous Multidrug ABC Transporters. *Structure*, *23*(3), 450–460. https://doi.org/10.1016/j.str.2014.12.013.Distinct

Moody, Jonathan E., Millen Linda, Binns Derk, Hunt John F., T. P. J. et al. (2002). Cooperative, ATP-dependent Association of the Nucleotide Binding Cassettes during the Catalytic Cycle of ATP-binding Cassette Transporters. *Biol*. https://doi.org/10.1074/jbc.C200228200

Morar, M., Pengelly, K., Koteva, K., & Wright, G. D. (2012). Mechanism and diversity of the erythromycin esterase family of enzymes. *Biochemistry*, *51*(8), 1740–1751. https://doi.org/10.1021/bi201790u

Morita, Y., Kataoka, A., Shiota, S., Mizushima, T., & Tsuchiya, T. (2000). NorM of Vibrio parahaemolyticus is an Na+-driven multidrug efflux pump. *Journal of Bacteriology*, *182*(23), 6694–6697. https://doi.org/10.1128/JB.182.23.6694-6697.2000

Morita, Yuji, Kodama, K., Shiota, S., Mine, T., Kataoka, A., Mizushima, T., & Tsuchiya, T. (1998). NorM, putative multidrug efflux protein, of Vibrio parahaemolyticus and its homolog in Escherichia coli. *Antimicrobial Agents and Chemotherapy*, *42*(7), 1778–1782. https://doi.org/10.1128/aac.42.7.1778

Narita, S. ichiro, & Tokuda, H. (2009). Biochemical characterization of an ABC transporter LptBFGC complex required for the outer membrane sorting of lipopolysaccharides. *FEBS Letters*, *583*(13), 2160–2164. https://doi.org/10.1016/j.febslet.2009.05.051

Nasie, I., Steiner-Mordoch, S., & Schuldiner, S. (2012). New substrates on the block: Clinically relevant resistances for EmrE and homologues. *Journal of Bacteriology*, *194*(24), 6766–6770. https://doi.org/10.1128/JB.01318-12

Neuberger A, Du D, Luisi BF. (2018). Structure and mechanism of bacterial tripartite efflux pumps. *Res Microbiol*, 169(7-8):401-413. https://doi.org/10.1016/j.resmic.2018.05.003

Neyfakh, A. A. (1992). The multidrug efflux transporter of Bacillus subtilis is a structural and functional homolog of the Staphylococcus norA protein. *Antimicrobial Agents and Chemotherapy*, *36*(2), 484–485. https://doi.org/10.1128/AAC.36.2.484

Nikaido, H. (2018). RND transporters in the living world. *Research in Microbiology*, *169*(7–8), 363–371. https://doi.org/10.1016/j.resmic.2018.03.001

Nishino, K., & Yamaguchi, A. (2001). Analysis of a complete library of putative drug transporter genes in Escherichia coli. Journal of bacteriology, 183(20), 5803–5812. https://doi.org/10.1128/JB.183.20.5803-5812.2001

Okada, U., Yamashita, E., Neuberger, A., Morimoto, M., Van Veen, H. W., & Murakami, S. (2017). Crystal structure of tripartite-type ABC transporter MacB from Acinetobacter baumannii. *Nature Communications*, *8*(1). https://doi.org/10.1038/s41467-017-01399-2

Oldham, M. L., & Chen, J. (2011). Snapshots of the maltose transporter during ATP hydrolysis. *Proceedings of the National Academy of Sciences of the United States of America*, *108*(37), 15152–15156. https://doi.org/10.1073/pnas.1108858108

Omote, H., Hiasa, M., Matsumoto, T., Otsuka, M., & Moriyama, Y. (2006). The MATE proteins as fundamental transporters of metabolic and xenobiotic organic cations. *Trends in Pharmacological Sciences*, *27*(11), 587–593. https://doi.org/10.1016/j.tips.2006.09.001

O'Neill J. Antimicrobial resistance: Tackling drug-resistant infections globally: Final report and recommendations. *Rev Antimicrob Resist*. 2016. http://amr-review.org/Publications

Orelle, C. (2004). Mécanisme d'hydrolyse de l'ATP st de transport de drogues par BmrA, homologue bactérien de la glycoprotéine-P. (Doctoral dissertation). Universite Claude Bernard Lyon 1, Lyon, France.

Orelle, C., Ayvaz, T., Everly, R. M., Klug, C. S., & Davidson, A. L. (2008b). Both maltose-binding protein and ATP are required for nucleotide-binding domain closure in the intact maltose ABC transporter. *Proceedings of the National Academy of Sciences of the United States of America*, *105*(35), 12837–12842. https://doi.org/10.1073/pnas.0803799105

Orelle C, Dalmas O, Gros P, Di Pietro A, Jault JM. (2003). The conserved glutamate residue adjacent to the Walker-B motif is the catalytic base for ATP hydrolysis in the ATP-binding cassette transporter BmrA. *J Biol Chem*, 278(47):47002-8. https://doi.org/10.1074/jbc.M308268200

Orelle C, Gubellini F, Durand A, Marco S, Lévy D, Gros P, Di Pietro A, Jault JM. (2008). Conformational change induced by ATP binding in the multidrug ATP-binding cassette transporter BmrA. *Biochemistry*, 47(8):2404-12. https://doi.org/10.1021/bi702303s

Orelle, C., Mathieu, K., & Jault, J. M. (2019). Multidrug ABC transporters in bacteria. *Research in Microbiology*, *170*(8), 381–391. https://doi.org/10.1016/j.resmic.2019.06.001

Oswald, C., Holland, I. B., & Schmitt, L. (2006). The motor domains of ABC-transporters: What can structures tell us? *Naunyn-Schmiedeberg's Archives of Pharmacology*, *372*(6), 385–399. https://doi.org/10.1007/s00210-005-0031-4

Overington, J. P., Al-Lazikani, B., & Hopkins, A. L. (2006). How many drug targets are there? *Nature Reviews Drug Discovery*, *5*(12), 993–996. https://doi.org/10.1038/nrd2199

Owens Tristan W., Rebecca Taylor J., Pahil Karanbir, Bertani Blake, Ruiz Natividad, Kruse Andrew C., K. D. (2019). Structural basis for unidirectional export of lipopolysaccharide to the cell surface. *Nature*, *567*(7749), 550–553. https://doi.org/10.1016/j.physbeh.2017.03.040

Pao, S. S., Paulsen, I. T., & Saier, M. H., Jr (1998). Major facilitator superfamily. *Microbiology and molecular biology reviews*, 62(1), 1–34.

Parcej D, Tampé R. (2010). ABC proteins in antigen translocation and viral inhibition. *Nat Chem Biol*, 6(8):572-80. https://doi.org/10.1038/nchembio.410

Parker, C. H., Morgan, C. R., Rand, K. D., Engen, J. R., Jorgenson, J. W., & Stafford, D. W. (2014). A conformational investigation of propeptide binding to the integral membrane protein γ-glutamyl carboxylase using nanodisc hydrogen exchange mass spectrometry. *Biochemistry*, *53*(9), 1511–1520. https://doi.org/10.1021/bi401536m

Paulsen, I. T., Skurray, R. A., Tam, R., Saier, M. H., Turner, R. J., Weiner, J. H., Goldberg, E. B., & Grinius, L. L. (1996). The SMR family: A novel family of multidrug efflux proteins involved with the efflux of lipophilic drugs. *Molecular Microbiology*, *19*(6), 1167–1175. https://doi.org/10.1111/j.1365-2958.1996.tb02462.x

Petoukhov, M.V., & Svergun, D.I. (2015). Ambiguity assessment of small-angle scattering curves from monodisperse systems. *Acta Crystallographica Section D: Structural Biology, D71*, 1051-1058. https://doi.org/10.1107/S1399004715002576

Pichler, K., Warner, K., Magrane, M., & UniProt Consortium (2018). SPIN: Submitting Sequences Determined at Protein Level to UniProt. *Current protocols in bioinformatics*, *62*(1), e52. https://doi.org/10.1002/cpbi.52

Pirrone, G. F., Iacob, R. E., & Engen, J. R. (2015). Applications of hydrogen/deuterium exchange MS from 2012 to 2014. *Analytical Chemistry*, *87*(1), 99–118. https://doi.org/10.1021/ac5040242

Prieß, M., Göddeke, H., Groenhof, G., & Schäfer, L. V. (2018). Molecular Mechanism of ATP Hydrolysis in an ABC Transporter. *ACS central science*, *4*(10), 1334–1343. https://doi.org/10.1021/acscentsci.8b00369

Puljung, M. C. (2018). Cryo-electron microscopy structures and progress toward a dynamic understanding of KATP channels. *Journal of General Physiology*, *150*(5), 653–669. https://doi.org/10.1085/jgp.201711978

Putman, M., Van Veen, H. W., Degener, J. E., & Konings, W. N. (2001). The lactococcal

secondary multidrug transporter LmrP confers resistance to lincosamides, macrolides, streptogramins and tetracyclines. *Microbiology*, *147*(10), 2873–2880. https://doi.org/10.1099/00221287-147-10-2873

Quazi, F., Lenevich, S., & Molday, R. S. (2012). ABCA4 is an N-retinylidene-phosphatidylethanolamine and phosphatidylethanolamine importer. *Nature Communications*, *3*(May), 925–929. https://doi.org/10.1038/ncomms1927

Quentin, Y., Fichant, G., & Denizot, F. (1999). Inventory, assembly and analysis of Bacillus subtilis ABC transport systems. *Journal of Molecular Biology*, *287*(3), 467–484. https://doi.org/10.1006/jmbi.1999.2624

Quistgaard, E. M., Löw, C., Guettou, F., & Nordlund, P. (2016). Understanding transport by the major facilitator superfamily (MFS): Structures pave the way. *Nature Reviews Molecular Cell Biology*, *17*(2), 123–132. https://doi.org/10.1038/nrm.2015.25

Ramirez, M. S., & Tolmasky, M. E. (2010). Aminoglycoside modifying enzymes. *Drug resistance updates* : reviews and commentaries in antimicrobial and anticancer chemotherapy, 13(6), 151–171. https://doi.org/10.1016/j.drup.2010.08.003

Ravaud, S., Do Cao, M. A., Jidenko, M., Ebel, C., Le Maire, M., Jault, J. M., Di Pietro, A., Haser, R., & Aghajari, N. (2006). The ABC transporter BmrA from Bacillus subtilis is a functional dimer when in a detergent-solubilized state. *The Biochemical journal*, *395*(2), 345–353. https://doi.org/10.1042/BJ20051719

Reading, E., Ahdash, Z., Fais, C., Ricci, V., Wang-Kan, X., Grimsey, E., Stone, J. W., Malloci, G., Lau, A. M., Findlay, H., Konijnenberg, A., Booth, P. J., Ruggerone, P., Vargiu, A. V., Piddock, L. J. V., & Politis, A. (2020). Perturbed structural dynamics underlie inhibition and altered specificity of the multidrug efflux pump AcrB. *BioRxiv*, 2020.04.27.063511. https://www.biorxiv.org/content/10.1101/2020.04.27.063511v1%0Ahttps://www.biorxiv.org/content/10.1101/2020.04.27.063511v1.abstract

Reading, E., Hall, Z., Martens, C., Haghighi, T., Findlay, H., Ahdash, Z., Politis, A., & Booth, P. J. (2017). Interrogating Membrane Protein Conformational Dynamics within Native Lipid Compositions. *Angewandte Chemie - International Edition*, *56*(49), 15654–15657. https://doi.org/10.1002/anie.201709657

Rédei, G. P. (2008). Major Facilitator Superfamily (MFS). *Encyclopedia of Genetics, Genomics, Proteomics and Informatics*, *62*(1), 1142–1142. https://doi.org/10.1007/978-1-4020-6754-9_9778

Rees, D. C., Johnson, E., & Lewinson, O. (2009). ABC transporters: The power to change. *Nature Reviews Molecular Cell Biology*, *10*(3), 218–227. https://doi.org/10.1038/nrm2646

Rempel, S., Stanek, W. K., & Slotboom, D. J. (2019). ECF-Type ATP-binding cassette transporters. *Annual Review of Biochemistry*, *88*, 551–576. https://doi.org/10.1146/annurev-biochem-013118-111705

Rey, M., Mrázek, H., Pompach, P., Novák, P., Pelosi, L., Brandolin, G., Forest, E., Havlíček, V., & Man, P. (2010). Effective removal of nonionic detergents in protein mass spectrometry, hydrogen/deuterium exchange, and proteomics. *Analytical Chemistry*, *82*(12), 5107–5116. https://doi.org/10.1021/ac100171m

Rigaud, J. L., Pitard, B., & Levy, D. (1995). Reconstitution of membrane proteins into liposomes: application to energy-transducing membrane proteins. *BBA - Bioenergetics*,

1231(3), 223–246. https://doi.org/10.1016/0005-2728(95)00091-V

Ritchie, T. K., Grinkova, Y. V., Bayburt, T. H., Denisov, I. G., Zolnerciks, J. K., Atkins, W. M., & Sligar, S. G. (2009). Chapter 11 - Reconstitution of membrane proteins in phospholipid bilayer nanodiscs. *Methods in enzymology*, *464*, 211–231. https://doi.org/10.1016/S0076-6879(09)64011-8

Rodionov, D. A., Hebbeln, P., Eudes, A., Ter Beek, J., Rodionova, I. A., Erkens, G. B., Slotboom, D. J., Gelfand, M. S., Osterman, A. L., Hanson, A. D., & Eitinger, T. (2009). A novel class of modular transporters for vitamins in prokaryotes. *Journal of Bacteriology*, *91*(1), 42–51. https://doi.org/10.1128/JB.01208-08

Rodríguez-Martínez, J. M., Poirel, L., & Nordmann, P. (2009). Molecular epidemiology and mechanisms of carbapenem resistance in Pseudomonas aeruginosa. *Antimicrobial Agents and Chemotherapy*, *53*(11), 4783–4788. https://doi.org/10.1128/AAC.00574-09

Rominski, A., Roditscheff, A., Selchow, P., Böttger, E. C., & Sander, P. (2017). Intrinsic rifamycin resistance of Mycobacterium abscessus is mediated by ADP-ribosyltransferase MAB_0591. *Journal of Antimicrobial Chemotherapy*, *72*(2), 376–384. https://doi.org/10.1093/jac/dkw466

Sanders, C. R., & Prosser, R. S. (1998). Bicelles: A model membrane system for all seasons? *Structure*, *6*(10), 1227–1234. https://doi.org/10.1016/S0969-2126(98)00123-3

Schindler, B. D., & Kaatz, G. W. (2016). Multidrug efflux pumps of Gram-positive bacteria. *Drug Resistance Updates*, *27*, 1–13. https://doi.org/10.1016/j.drup.2016.04.003

Schmees, G., Stein, A., Hunke, S., Landmesser, H., & Schneider, E. (1999). Functional consequences of mutations in the conserved "signature sequence" of the ATP-binding-cassette protein MalK. *European Journal of Biochemistry*, *266*(2), 420–430. https://doi.org/10.1046/j.1432-1327.1999.00871.x

Schuldiner, S., Granot, D., Mordoch, S. S., Ninio, S., Rotem, D., Soskin, M., & Yerushalmi, H. (2001). Precious things come in little packages. *Journal of Molecular Microbiology and Biotechnology*, *3*(2), 155–162.

Schuldiner, Shimon. (2009). EmrE, a model for studying evolution and mechanism of ion-coupled transporters. *Biochimica et Biophysica Acta - Proteins and Proteomics*, *1794*(5), 748–762. https://doi.org/10.1016/j.bbapap.2008.12.018

Schwarz, S., Kehrenberg, C., Doublet, B., & Cloeckaert, A. (2004). Molecular basis of bacterial resistance to chloramphenicol and florfenicol. *FEMS Microbiology Reviews*, *28*(5), 519–542. https://doi.org/10.1016/j.femsre.2004.04.001

Senior, A. E., Al-Shawi, M. K., & Urbatsch, I. L. (1995). The catalytic cycle of P-glycoprotein. *FEBS Letters*, *377*(3), 285–289. https://doi.org/10.1016/0014-5793(95)01345-8

Sheff, J. G., Farshidfar, F., Bathe, O. F., Kopciuk, K., Gentile, F., Tuszynski, J., Barakat, K., & Schriemer, D. C. (2017). Novel allosteric pathway of Eg5 regulation identified through multivariate statistical analysis of hydrogen-exchange mass spectrometry (HX-MS) ligand screening data. *Molecular and Cellular Proteomics*, *16*(3), 428–437. https://doi.org/10.1074/mcp.M116.064246

Silva, L. P., Vanzile, M., Bavari, S., Aman, J. M. J., & Schriemer, D. C. (2012). Assembly of ebola virus matrix protein VP40 is regulated by latch-like properties of N and C terminal tails. *PLoS ONE*, *7*(7). https://doi.org/10.1371/journal.pone.0039978

Silverton, L., Dean, M., & Moitra, K. (2011). Variation and evolution of the ABC transporter genes ABCB1, ABCC1, ABCG2, ABCG5 and ABCG8: implication for pharmacogenetics and disease. Drug metabolism and drug interactions, 26(4), 169–179. https://doi.org/10.1515/DMDI.2011.027

Smith, P. C., Karpowich, N., Millen, L., Moody, J. E., Rosen, J., Thomas, P. J., & Hunt, J. F. (2002). ATP binding to the motor domain from an ABC transporter drives formation of a nucleotide sandwich dimer. *Molecular Cell*, *10*(1), 139–149. https://doi.org/10.1016/S1097-2765(02)00576-2

Spanogiannopoulos, P., Thaker, M., Koteva, K., Waglechner, N., & Wright, G. D. (2012). Characterization of a rifampin-inactivating glycosyltransferase from a screen of environmental actinomycetes. *Antimicrobial Agents and Chemotherapy*, *56*(10), 5061–5069. https://doi.org/10.1128/AAC.01166-12

Spanogiannopoulos, P., Waglechner, N., Koteva, K., & Wright, G. D. (2014). A rifamycin inactivating phosphotransferase family shared by environmental and pathogenic bacteria. *Proceedings of the National Academy of Sciences of the United States of America*, *111*(19), 7102–7107. https://doi.org/10.1073/pnas.1402358111

Srinivasan, V. B., & Rajamohan, G. (2013). KpnEF, a new member of the Klebsiella pneumoniae cell envelope stress response regulon, is an SMR-type efflux pump involved in broad-spectrum antimicrobial resistance. *Antimicrobial Agents and Chemotherapy*, *57*(9), 4449–4462. https://doi.org/10.1128/AAC.02284-12

Srinivasan, V. B., Rajamohan, G., & Gebreyes, W. A. (2009). Role of AbeS, a novel efflux pump of the SMR family of transporters, in resistance to antimicrobial agents in Acinetobacter baumannii. *Antimicrobial Agents and Chemotherapy*, *53*(12), 5312–5316. https://doi.org/10.1128/AAC.00748-09

Steinfels, E., Orelle, C., Dalmas, O., Penin, F., Miroux, B., Di Pietro, A., & Jault, J. M. (2002). Highly efficient over-production in E. coli of YvcC, a multidrug-like ATP-binding cassette transporter from Bacillus subtilis. *Biochimica et Biophysica Acta - Biomembranes*, *1565*(1), 1–5. https://doi.org/10.1016/S0005-2736(02)00515-1

Steinfels, E., Orelle, C., Fantino, J. R., Dalmas, O., Rigaud, J. L., Denizot, F., Di Pietro, A., & Jault, J. M. (2004). Characterization of YvcC (BmrA), a multidrug ABC transporter constitutively expressed in Bacillus subtilis. *Biochemistry*, *43*(23), 7491–7502. https://doi.org/10.1021/bi0362018

Su CC, Bolla JR, Kumar N, Radhakrishnan A, Long F, Delmar JA, Chou TH, Rajashankar KR, Shafer WM, Yu EW. (2015). Structure and function of Neisseria gonorrhoeae MtrF illuminates a class of antimetabolite efflux pumps. *Cell Rep*, 11(1):61-70. https://doi.org/10.1016/j.celrep.2015.03.003.

Svergun, D.I. (1992). Determination of the regularization parameter in indirect-transform methods using perceptual criteria. *Journal of Applied Crystallography. 25*, 495-503. https://doi.org/10.1107/S0021889892001663

Svergun, D.I. (1999). Restoring low resolution structure of biological macromolecules from solution scattering using simulated annealing. *Biophysical Journal*, 2879-2886. https://doi.org/10.1016/S0006-3495(99)77443-6

Svergun, D. I. (2010). Small-angle X-ray and neutron scattering as a tool for structural systems biology. *Biological Chemistry*, *391*(7), 737–743. https://doi.org/10.1515/BC.2010.093

Swier, L. J. Y. M., Guskov, A., & Slotboom, D. J. (2016). Structural insight in the toppling mechanism of an energy-coupling factor transporter. *Nature Communications*, *7*, 1–11. https://doi.org/10.1038/ncomms11072

Szakács, G., Ozvegy, C., Bakos , E., Sarkadi, B., & Váradi, A. (2001). Role of glycine-534 and glycine-1179 of human multidrug resistance protein (MDR1) in drug-mediated control of ATP hydrolysis. *The Biochemical journal*, *356*(Pt 1), 71–75. https://doi.org/10.1042/0264-6021:3560071

Taylor NMI, Manolaridis I, Jackson SM, Kowal J, Stahlberg H, Locher KP. (2017). Structure of the human multidrug transporter ABCG2. *Nature*, 546(7659):504-509. https://doi.org/10.1038/nature22345

Ter Beek, J., Guskov, A., & Slotboom, D. J. (2014). Structural diversity of ABC transporters. *Journal of General Physiology*, *143*(4), 419–435. https://doi.org/10.1085/jgp.201411164

Thomas, C., & Tampé, R. (2018). Multifaceted structures and mechanisms of ABC transport systems in health and disease. *Current Opinion in Structural Biology*, *51*, 116–128. https://doi.org/10.1016/j.sbi.2018.03.016

Thomas, C., & Tampé, R. (2020). Structural and Mechanistic Principles of ABC Transporters. *Annual Review of Biochemistry*, *89*, 605–636. https://doi.org/10.1146/annurev-biochem-011520-105201

Tooke, C. L., Hinchliffe, P., Bragginton, E. C., Colenso, C. K., Hirvonen, V., Takebayashi, Y., & Spencer, J. (2019). β-Lactamases and β-Lactamase Inhibitors in the 21st Century. *Journal of molecular biology*, 431(18), 3472–3500. https://doi.org/10.1016/j.jmb.2019.04.002

Trabjerg, E., Nazari, Z. E., & Rand, K. D. (2018). Conformational analysis of complex protein states by hydrogen/deuterium exchange mass spectrometry (HDX-MS): Challenges and emerging solutions. *TrAC - Trends in Analytical Chemistry*, *106*, 125–138. https://doi.org/10.1016/j.trac.2018.06.008

Tribet, C., Audebert, R., & Popot, J. L. (1996). Amphipols: Polymers that keep membrane proteins soluble in aqueous solutions. *Proceedings of the National Academy of Sciences of the United States of America*, *93*(26), 15047–15050. https://doi.org/10.1073/pnas.93.26.15047

Tseng, T. T., Gratwick, K. S., Kollman, J., Park, D., Nies, D. H., Goffeau, A., & Saier, M. H. (1999). The RND permease superfamily: An ancient, ubiquitous and diverse family that includes human disease and development proteins. *Journal of Molecular Microbiology and Biotechnology*, *1*(1), 107–125.

Underbakke, E. S., Iavarone, A. T., Chalmers, M. J., Pascal, B. D., Novick, S., Griffin, P. R., & Marletta, M. A. (2014). Nitric oxide-induced conformational changes in soluble guanylate cyclase. *Structure*, *22*(4), 602–611. https://doi.org/10.1016/j.str.2014.01.008

Urbatsch IL, Tyndall GA, Tombline G, Senior AE. (2003). P-glycoprotein catalytic mechanism: studies of the ADP-vanadate inhibited state. *Journal of Biological Chemistry, 278*(25):23171-9. https://doi.org/10.1074/jbc.M301957200

van der Does, C., & Tampé, R. (2004). How do ABC transporters drive transport? *Biological Chemistry*, *385*(10), 927–933. https://doi.org/10.1515/BC.2004.121

van Veen HW, Callaghan R, Soceneantu L, Sardini A, Konings WN, Higgins CF. (1998). A

bacterial antibiotic-resistance gene that complements the human multidrug-resistance P-glycoprotein gene. *Nature*, 391(6664):291-5. https://doi.org/10.1038/34669

Van Veen, H. W., & Konings, W. N. (1998). The ABC family of multidrug transporters in microorganisms. *Biochimica et Biophysica Acta - Bioenergetics*, *1365*(1–2), 31–36. https://doi.org/10.1016/S0005-2728(98)00039-5

Van Veen, H. W., Venema, K., Bolhuis, H., Oussenko, I., Kok, J., Poolman, B., Driessen, A. J. M., & Konings, W. N. (1996). Multidrug resistance mediated by a bacterial homolog of the human multidrug transporter MDR1. *Proceedings of the National Academy of Sciences of the United States of America*, *93*(20), 10668–10672. https://doi.org/10.1073/pnas.93.20.10668

Van Wonderen, J. M., McMahon, R. M., OMara, M. L., McDevitt, C. A., Thomson, A. J., Kerr, I. D., MacMillan, F., & Callaghan, R. (2014). The central cavity of ABCB1 undergoes alternating access during ATP hydrolysis. *FEBS Journal*, *281*(9), 2190–2201. https://doi.org/10.1111/febs.12773

Verhalen, B., & Wilkens, S. (2011). P-glycoprotein retains drug-stimulated ATpase activity upon covalent linkage of the two nucleotide binding domains at their C-terminal ends. *Journal of Biological Chemistry*, *286*(12), 10476–10482. https://doi.org/10.1074/jbc.M110.193151

Vetter, I. R., & Wittinghofer, A. (1999). Nucleoside triphosphate-binding proteins: Different scaffolds to achieve phosphoryl transfer. *Quarterly Reviews of Biophysics*, *32*(1), 1–56. https://doi.org/10.1017/S0033583599003480

Volkov, V.V., & Svergun, D. I. (2003). Uniqueness of ab-initio shape determination in small-angle scattering. *Journal of Applied Crystallography, 36*, 860-864. https://doi.org/10.1107/S0021889803000268

Wales, T. E., & Engen, J. R. (2005). Hydrogen exchange mass spectrometry for the analysis of protein dynamics. *Mass Spectrometry Reviews*, *25*(1), 158–170. https://doi.org/10.1002/mas.20064

Walker, J. E., Saraste, M., Runswick, M. J., & Gay, N. J. (1982). Distantly related sequences in the alpha- and beta-subunits of ATP synthase, myosin, kinases and other ATP-requiring enzymes and a common nucleotide binding fold. *The EMBO journal*, 1(8), 945–951

Ward, A., Reyes, C. L., Yu, J., Roth, C. B., & Chang, G. (2007). Flexibility in the ABC transporter MsbA: Alternating access with a twist. *Proceedings of the National Academy of Sciences of the United States of America*, *104*(48), 19005–19010. https://doi.org/10.1073/pnas.0709388104

Weis, D. D., Wales, T. E., Engen, J. R., Hotchko, M., & Ten Eyck, L. F. (2006). Identification and Characterization of EX1 Kinetics in H/D Exchange Mass Spectrometry by Peak Width Analysis. *Journal of the American Society for Mass Spectrometry*, *17*(11), 1498–1509. https://doi.org/10.1016/j.jasms.2006.05.014

Yang, H., & Smith, D. L. (1997). Kinetics of cytochrome c folding examined by hydrogen exchange and mass spectrometry. *Biochemistry*, *36*(48), 14992–14999. https://doi.org/10.1021/bi9717183

Yeung, Y. G., Nieves, E., Angeletti, R. H., & Stanley, E. R. (2008). Removal of detergents from protein digests for mass spectrometry analysis. *Analytical biochemistry*, *382*(2), 135–

137. https://doi.org/10.1016/j.ab.2008.07.034

Zaitseva, J., Jenewein, S., Jumpertz, T., Holland, I. B., & Schmitt, L. (2005). H662 is the linchpin of ATP hydrolysis in the nucleotide-binding domain of the ABC transporter HlyB. *EMBO Journal*, *24*(11), 1901–1910. https://doi.org/10.1038/sj.emboj.7600657

Zapun, A., Contreras-Martel, C., & Vernet, T. (2008). Penicillin-binding proteins and β-lactam resistance. *FEMS Microbiology Reviews*, *32*(2), 361–385. https://doi.org/10.1111/j.1574-6976.2007.00095.x

Zhang, J., Chalmers, M. J., Stayrook, K. R., Burris, L. L., Garcia-, R. D., Pascal, B. D., Burris, T. P., Dodge, J. A., & Griffin, P. R. (2010). Hydrogen/Deuterium Exchange Reveals Distinct Agonist/Partial Agonist Receptor Dynamics within the intact Vitamin D Receptor/Retinoid X Receptor Heterodimer. *Structure*, *18*(10), 1332–1341. https://doi.org/10.1016/j.str.2010.07.007

Zhang, Z., & Smith, D. L. (1993). Determination of amide hydrogen exchange by mass spectrometry: A new tool for protein structure elucidation. *Protein Science*, *2*(4), 522–531. https://doi.org/10.1002/pro.5560020404

Zhao, Q., Wang, C., Wang, C., Guo, H., Bao, Z., Zhang, M., & Zhang, P. (2015). Structures of FolT in substrate-bound and substrate-released conformations reveal a gating mechanism for ECF transporters. *Nature Communications*, *6*(May), 1–7. https://doi.org/10.1038/ncomms8661

Zheng, J., Strutzenberg, T., Pascal, B. D., & Griffin, P. R. (2019). Protein dynamics and conformational changes explored by hydrogen/deuterium exchange mass spectrometry. *Current Opinion in Structural Biology*, *58*, 305–313. https://doi.org/10.1016/j.sbi.2019.06.007

Zoghbi, M. E., Mok, L., Swartz, D. J., Singh, A., Fendley, G. A., Urbatsch, I. L., & Altenberg, G. A. (2017). Substrate-induced conformational changes in the nucleotide-binding domains of lipid bilayer-associated P-glycoprotein during ATP hydrolysis. *Journal of Biological Chemistry*, *292*(50), 20412–20424. https://doi.org/10.1074/jbc.M117.814186